STUDIES OF SOME EXOTIC MATERIALS

THESIS

SUBMITTED FOR THE AWARD OF THE DEGREE OF

Doctor of Science

IN

PHYSICS

BY

DR. MD. SHAFIKUDDIN MOLLAH

SENIOR LECTURER

DEPARTMENT OF PHYSICS
ALIGARH MUSLIM UNIVERSITY
ALIGARH (INDIA)

2005

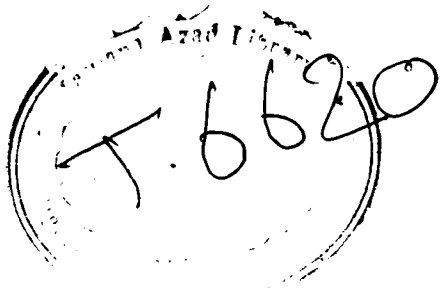
T.6620

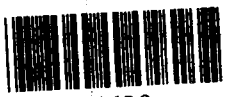
T6620

Dedicated to the memory

of my deceased father

Dr. Muhammad Irfan
Professor & Chairman

DEPARTMENT OF PHYSICS
ALIGARH MUSLIM UNIVERSITY
ALIGARH – 202 002, INDIA
Tel: (Off.) +91 571 2701001

Date: 28th February, 2005

Certificate

This is to certify that a major portion of the work submitted by Dr. Md. Shafikuddin Mollah, Senior Lecturer, Department of Physics, Aligarh Muslim University, Aligarh-202002, India, in the D.Sc Thesis entitled "Studies on some Exotic Materials" is an original contribution made by him. Dr. Mollah has the original contribution in his field of specialization under the following heads.

(i) Papers published independently: 6

(ii) Papers in which he is a senior author: 24

(iii) Papers in which he is a junior author: 20

(Professor Muhammad Irfan)
Chairman

Chairman
Deptt. of Physics
A. M. U. Aligarh

Acknowledgement

It is a great pleasure to express my sincere thanks and gratitude to the Committee for Advanced Studies and Research (CASR), Aligarh Muslim University (AMU), Aligarh 202002, India, for considering and approving my application to supplicate my D.Sc. thesis entitled "Studies on some Exotic Materials". It would be impossible without the help and cooperation of Professor Muhammad Irfan (Chairman, Department of Physics), Professor S. H. Israili (Dean, Faculty of Science), Mr. Naseem Ahmad, IAS (Honorable Vice-Chancellor), and all other Chairmen of different Departments, Faculty of Science, AMU, Aligarh, India.

I express my heartiest appreciation to different funding agencies in India and abroad like Council for Scientific and Industrial Research (CSIR), Government of India; University Grants Commission (UGC), Government of India; Israeli Ministry of Science, Israel; MONBUSHO, Government of Japan; National Science Council (NSC), Government of Taiwan, ROC; Third World Academy of Science (TWAS), Italy; and The Abdus Salam International Centre for Theoretical Physics (ICTP), Italy; for financially supporting me to carry out my research work. All my achievements have come into reality because of the brilliant discussions and co-operations of my co-workers from India and abroad.

I gratefully acknowledge to all my colleagues, Department of Physics, AMU, Aligarh, India, for helping and encouraging me in different occasions. The office staffs of the Department of Physics, Faculty of Science and Administrative office are conceded for their various assistances.

It is impossible to express my debt to my wife who is constantly encouraging me in research to achieve my goal and assisting me in solving several problems. I have no words to articulate for my son and daughter whose love and affection is the light of my daily life. I am very much obliged to my mother and other relatives who always wish me to be very successful in life.

Last of all, I want to express my thankfulness to the common people of India who are silently supporting our research work.

(Dr. Md. Shafikuddin Mollah)

Senior Lecturer, Department of Physics,

Aligah Muslim University,

Aligarh-2002, India

28th February, 2005

Contents

Curriculum Vitae

Curriculum Vitae

Name: Dr. Md. Shafikuddin Mollah

Present position: Senior Lecturer of Physics

Institution: Aligarh Muslim University

Nationality: Indian

Corresponding address: Department of Physics, Aligarh Muslim University, Aligarh- 202002, India.

Tel & Fax: +91-571-2701001

Email: smollah@rediffmail.com, s.mollahm@lycos.com

Permanent address: Flat No. S. F. 6, Shahil Apartments, Anupshahar Road, Kabir Colony, Aligarh-202002, India. **Tel:** +91-571-2705707

Educational qualifications:

Ph.D (Science), 1993, Indian Association for the Cultivation of Science, Kolkata, India.

M.Sc. (Physics), 1989, University of Calcutta, Kolkata, India.

B.Sc. (Physics Honours), 1987, University of Calcutta, Kolkata, India.

Research experience: 15 years

Teaching experience: 8 years

Specialization: Solid State Physics, Amorphous Semiconductor, Superconductor and Colossal Magnetoresistance (CMR).

Positions held in India:

(i) Senior Lecturer (Assistant Professor), Department of Physics, Aligarh Muslim University, Aligarh-202002, India. August, 1998- till date.

(ii) Assistant Professor, Department of Applied Physics, Birla Institute of Technology, Mesra, Ranchi, India. September, 1997 – July, 1998.

(iii) Postdoctoral Research Associate, Pressure standards, National Physical Laboratory, New Delhi, India. April, 1997 – August, 1997.

(iv) Postdoctoral Research Associate, Department of Solid State Physics, Indian Association for the Cultivation of Science, Kolkata, India. October, 1993 – February, 1994 and March, 1995 – October, 1995.

(v) Junior & Senior Research Fellow, Department of Solid State Physics, Indian Association for the Cultivation of Science, Kolkata, India. December, 1990 – October, 1993.

Positions held in abroad:

(i) Postdoctoral Fellow, Department of Physics, National Sun Yat Sen University, Kaohsiung 804, Taiwan, ROC. September, 2001 – July, 2004.

(ii) Visiting Fellow, The Abdus Salam International Centre for Theoretical Physics, Trieste, Italy. July, 2000 – August, 2000.

(iii) Postdoctoral Research Associate, Department of Electrical and Electronic Engineering, Toyohashi University of Technology, Toyohashi, Japan. October, 1995 –March, 1997.

(iv) Postdoctoral Research Associate, Materials Engineering Department, Ben Gurion University of the Negev, Beer Sheva, Israel. February, 1994 – March, 1995.

Scholarships/Fellowships awarded from India and abroad:

(i) Postdoctoral fellowship from National Science Council, Taiwan, ROC, 2001

(ii) Senior Research Associateship (Scientist's Pool Scheme), CSIR, India, 1997

(iii) Japanese Government Scholarship (MONBUSHO), Japan, 1995

(iv) Fellowship from Israeli Ministry of Science, Israel, 1994

(v) Fellowship from CSIR, India, 1990

(vi) National Scholarship of India, 1982

Membership of scientific bodies:

(i) Membership of the New York Academy of Sciences, USA, 1996

(ii) Life Member of Indian Association for the Cultivation of Science, Kolkata, India, 1994-95

Seminars/Symposiums/Workshops attended in India and abroad:

Year	Name and place

(i) **2005:** XIth Workshop on "Neutrons as probes of Condensed Matter", Bhabha Atomic Research Centre, Mumbai, India.

(ii) **2004:** 49th DAE-Solid State Physics Symposium, Guru Nanak Dev University, Amritsar, India.

(iii) **2004:** Accelerator Users' Workshop, Nuclear Science Centre, New Delhi, India.

(iv) **2004:** 2004 Taiwan International Conference on Superconductivity & 7th Workshop on Low Temperature Physics, Penghu, Taiwan.

(v) **2004:** National Symposium of the Physical Society of ROC, Hsinchu, Taiwan.

(vi) **2002:** International Conference on the Physics and Chemistry of Molecular and Oxide Superconductors, Hsinchu, Taiwan.

(vii) **2000:** International Conference on Magnetic Materials, Saha Institute of Nuclear Physics, Kolkata, India.

(viii) **2000:** XII International Workshop on Strongly Correlated Electron System, The Abdus Salam International Centre for Theoretical Physics, Trieste, Italy.

(ix) **1999:** DAE-Solid State Physics Symposium, Indira Gandhi Centre for Atomic Research, Kalpakkam, India.

(x) **1999:** Tenth International Workshop on Physics of Semiconductor Devices, Solid State Physics Laboratory, Delhi, India.

(xi) **1999:** Workshop on Experiments at Low Temperature, Inter University Consortium, Indore, India.

(xii) **1994:** National Symposium on Superconductor, Technion, Haifa, Israel.

(xiii) **1994:** Solid State Physics Symposium, Indian Association for the Cultivation of Science, Kolkata, India.

(xiv) **1993:** Solid State Physics Symposium, Bhaba Atomic Research Centre, Mumbai, India.

(xv) **1992:** INDO-US Workshop on Perspectives in New Materials, National Physical Laboratory, New Delhi, India.

(xvi) **1991:** Workshop on "Materials Research", Inter University Consortium, Indore, India.

Invited talk:

I have been invited to give an Invited talk on the "Properties of $Pr_{0.65}Ca_{0.35-x}Sr_xMnO_3$ Manganites" in 49th DAE-Solid State Physics Symposium, Guru Nanak Dev University, Amritsar, India, in December, 2004. This is the biggest conference in India and about 600 participants usually take part from all over the World.

Research projects granted/completed/submitted:

(i) Research Project entitled "AC conductivity and dielectric constant of $CaCu_3Ti_4O_{12}$-type materials" by **S. Mollah** has been submitted to **Third World Academy of Sciences (TWAS)**, ICTP, Trieste, Italy, in 2004.

(ii) Research Project entitled "Effect of Mn-site substitution on the ferromagnetic insulating state of $RE_{0.85}A_{0.15}MnO_3$ manganites (RE = La, Pr, Nd, Sm and A = Ca, Sr, Pb)" by **S. Mollah** has been submitted to **Council of Scientific & Industrial Research (CSIR)**, India, in 2004.

(iii) Research Project (Code No. UFUP dated 01.02.2005) entitled "SHI irradiation induced modification in multiferroic thin film of RMn_2O_5 system" by **S. Mollah** has been sanctioned by **Nuclear Science Center (NSC)**, New Delhi, India.

(iv) Research Project (No. 00-332 RG/PHYS/AS dated 10.8.2001) entitled "AC conductivity of semiconducting oxynitride glasses" by **S. Mollah**, was granted by **Third World Academy of Sciences (TWAS)**, ICTP, Trieste, Italy, in 2001.

(v) A Major Research Project (No.F 10-31/98 dated 23.10.1998) from University Grants Commission (**UGC**), **Government of India,** entitled "Study on electronic conduction of semiconducting oxynitride glasses and their application" by **S. Mollah**, has been completed under my direct supervision on 23.10.2001.

Research scholar guiding experience:

I have guided two M.Phil. leading to Ph.D. research scholars. They have worked on amorphous semiconductor and superconductivity. Presently one Ph.D research scholar and one M. Phil. student are working with me. The Ph.D research scholar is engaged to SHI irradiation induced modification in multiferroic thin film of RMn_2O_5 system and the M. Phil. student is working on the properties of colossal magnetoresistive (CMR) materials. I have also guided the M.Sc. project of 7 students.

Research collaborators:

(i) Prof. H. Sakata, Department of Applied Chemistry, Tokai University, Japan.

(ii) Prof. B. K. Chaudhuri, Department of Solid State Physics, Indian Association for the Cultivation of Science, Kolkata, India.

(iii) Dr. Ravi Kumar, Materials Science Division, Nuclear Science Centre, New Delhi, India.

Laboratory set up:

When I joined as a lecturer the Department of Physics, Aligarh Muslim University, in 1998, there was no research laboratory of my field of interest. For financial assistance to set up a laboratory, I applied for a Major Research Project in the University Grants Commission (UGC), Government of India and got it. Then I set up a Glass-Ceramic Laboratory where we have the synthesis and characterization facility of CMR/superconductor and amorphous materials. I also set up four new experiments in the M.Sc. Solid State Physics (special) laboratory. Several experiments were introduced by me in Birla Institute of Technology, Mesra, Ranchi, India.

Working experience in different laboratories:

1. Glass-Ceramic Laboratory, Department of Solid State Physics, Indian Association for the Cultivation of Science, Jadavpur, Kolkata-32, India.
2. Materials Processing Laboratory, Materials Engineering Department, Ben Gurion University of the Negev, Beer Sheva, Israel.
3. Superconductivity Laboratory, Department of Electrical and Electronic Engineering, Toyohashi University of Technology, Toyohashi, Japan.
4. Low Temperature Physics Laboratory, Department of Physics, National Sun Yat Sen University, Kaohsiung, Taiwan, ROC.
5. Pressure Standard, National Physical Laboratory, New Delhi, India.
6. Materials Science Laboratory, Birla Institute of Technology, Mesra, Ranchi, India.

7. Glass-Ceramic Laboratory, Department of Physics, Aligarh Muslim University, Aligarh, India.

Sample preparation experience:

1. Preparation of glassy amorphous materials by melt quenching technique.
2. Synthesis of superconducting, relaxor, CMR and multiferroic RMn_2O_5 materials by solid-state reaction route.
3. Preparation of thin films by chemical vapor deposition technique.
4. Synthesis of superconducting, CMR and multiferroic RMn_2O_5 materials by sol-gel route.
5. Fabrication of single filament and multi-filament Ag-sheathed Bi-based 2212/2223 superconducting wires/tapes.

Instruments operating experience:

I can operate the following instruments needed to characterize our samples.

1. X-ray diffractometer
2. Scanning electron microscope
3. Differential thermal analyzer
4. Thermal gravimetric analyzer
5. Differential scanning calorimeter
6. Two probe dc conductivity measuring system for glassy materials
7. Four probe resistivity measuring system with cryo-cooler and also with liquid helium temperature for transport property measurement of superconductor, relaxor and CMR materials
8. AC conductivity and dielectric property measuring Impedance analyzer
9. Low temperature magnetic field dependence of specific heat measuring instrument.

10. High temperature specific heat measuring instrument by the AC calorimeteric technique
11. Superconducting Quantum Interference Device (SQUID) for magnetization measurement
12. High pressure system for magnetic susceptibility measurement under pressure
13. Thermoelectric power measuring instrument
14. Superconductors' critical current density (J_c) measuring instrument both by ac pulsed method and using constant current sources.
15. I can work with a high temperature (~ 1500 °C) furnace for the synthesis of CMR materials.

I can analyze the data obtained from:

1. Electron paramagnetic resonance (EPR) machine and
2. X-ray photo emission spectrometer (XPS)

Significant achievements:

1. It has been confirmed that the strong electron-phonon interaction in the glassy phase of some transition metal oxide glasses like $Bi_4Sr_3Ca_3Cu_yO_x$ (y = 0-5), $Bi_4Sr_3Ca_{3-z}Li_zCu_4O_x$ (z=0.1-1) and $Bi_{4-n}Pb_nSr_3Ca_3Cu_4O_x$ (n = 0-1) causes the formation of small polarons and becomes superconductor in their respective glass ceramic phases.
2. The conduction in these glasses is by the hopping of polarons in the non-adiabatic regime.
3. The carriers of the glasses are having distribution of relaxation times.
4. The hydrostatic pressure increases the superconducting transition temperature of $MgCNi_3$.

5. Spinel $LiTi_2O_4$ can be well described by a typical type-II, BCS-like, moderate coupling, and fully gapped superconductor in the dirty limit.
6. The connectivity effect of metal/alloy between superconducting grains can explain the critical currents in Ag/Ag-Cu/Ag-In doped Bi-based superconductors.
7. A huge enhancement of magnetoresistance, MR (10% at H = 100 Oe and 99% at H = 0.5 T) observed in $Pr_{0.65}Ca_{0.25}Sr_{0.1}MnO_3$ sample around the metal-insulator (MI) transition temperature ($T_{MI} \sim 80$ K) is induced by the phase separation (PS).
8. Non-adiabatic small polaron hopping conduction mechanism is followed by $Pr_{0.65}Ca_{0.35-x}Sr_xMnO_3$ (x = 0-0.35) manganites above the respective T_{MI}.
9. Invited articles are contributed in Encyclopedia of Nanoscience and Nanotechnology, Studies of High Temperature Superconductors, and Topical Review of J. Phys.: Condens. Matter.
10. Published several articles in Internationally reputed journals.

Computing knowledge:

I can write preliminary programs in BASIC and FORTRAIN languages. I can successfully operate MS Word and Origin programs. The internet system is widely known to me.

Orientation programmes/Refresher courses completed:

I have completed the following Refresher courses/Orientation programme as required by the University Grants Commission (UGC), Government of India, for university teachers.

(i) Refresher course in Physics (Concepts of Physics) from Academic Staff College, Aligarh Muslim University, Aligarh, during 19.11.2004-10.12.2004.

(ii) Refresher course in Physics from Academic Staff College, Aligarh Muslim University, Aligarh, during 10.4.2001-9.5.2001.

(iii) Orientation Programme from Academic Staff College, Aligarh Muslim University, Aligarh, during 15.5.2000-13.6.2000.

Description of working experience in different Universities/Institutions:

From August 1998 to date, I am working in the Department of Physics, Aligarh Muslim University (**AMU**), Aligarh, India, as a senior lecturer (Assistant Professor). I have been teaching undergraduate and postgraduate students. I am teaching **Solid State Physics** ***Special paper*** of M.Sc. 4th Semester and taking the laboratory classes. A Glass-Ceramic Laboratory has been set up by me. I am guiding the M.Sc students to prepare their seminar lectures, which are essential for their M.Sc. degree. I have also guided two M. Phil. leading to Ph. D students in AMU and presently guiding one Ph. D and one M. Phil. student. I have completed successfully a major research project from University Grants Commission, Government of India. The work of that project was on the preparation and characterization of oxynitride glasses and to find their pressure and gas sensing property. I got a research project from Third World Academy of Science (TWAS), Italy. Recently, I have got another Research Project (Code No. UFUP dated 01.02.2005) entitled "SHI irradiation induced modification in multiferroic thin film of RMn_2O_5 system" sanctioned by Nuclear Science Center (NSC), New Delhi, India. I have also worked on the electron paramagnetic resonance (EPR) of Fe^{3+} ions in Fe_2O_3-PbO-Bi_2O_3 glasses in AMU and on the x-ray photoelectron spectroscopy of VN-PbO-TeO_2 glasses with the collaboration of Prof. H. Sakata, Tokai University, Japan.

From October, 2001 to July, 2004, I was on study leave from the Department of Physics, **AMU**, Aligarh, India, and was working as a postdoctoral fellow with Prof. H. D.

Yang, Department of Physics, National Sun Yat Sen University (**NSYSU**), Kaohsiung, Taiwan, R.O.C. During this period, I have been working on the resistivity, magnetization, low and high temperature specific heat, thermoelectric power and change of property due to pressure effect of different colossal magnetoresistive (CMR), superconducting (SC) and antiferromagnetic-ferroelectric (AFM-FE) materials in the frontier areas of Solid State Physics viz. $Pr_{0.65}Ca_{0.35-x}Sr_xMnO_3$, $(Nd/Sm)_{0.5}(Sr,Ca)_{0.5}MnO_3$, $La_{0.7}Ca_{0.3-y}NayMnO_3$, $Ca_{1-x}(Na,K)_xMn_{1-y}Cr_yO_3$ etc. CMR materials, $Pr1_{.85}Ce_{.15}Cu_{1-x}ZnxO_4$, MgB_2, $MgCNi_3$, $LiTi_2O_4$ etc. superconductors and RMn_2O_5 (R = La, Pr, Sm, Nd, Tb, Y) AFM-FE materials. The polycrystalline CMR, SC and AFM-FE materials were prepared in our laboratory following appropriate routes and characterized. The magnetic field dependent (0-8 T) specific heat (C) down to 1.5 K gives the information about the type of superconductivity as well as different important parameters of SC materials and anomalies corresponding to various transitions of CMR materials. The field cooled (FC) and zero field cooled (ZFC) magnetization (M) up to 8 T and down to 10 K were measured in our laboratory by commercial SQUID magnetometer. The pressure dependent (up to 2 GPa) ac susceptibility (χ_{ac}) were evaluated down to 1.5 K to get the information of its effect on the T_c of SC and different phase transition temperatures of CMR materials.

I have served the Department of Applied Physics, Birla Institute of Technology (**BIT**), Mesra, Ranchi, India, as an Assistant Professor from September 1997 to July 1998. During this period of my service, I have taught undergraduate and postgraduate students and continued my research work on amorphous semiconductors and superconductors. Several experimental courses were guided by me. New experiments were also set up by me.

From April to August, 1997, I worked in Pressure Standard Division, National Physical Laboratory (**NPL**), New Delhi, India, on ferroelectric relaxor materials. We studied the pressure and temperature effect on the dielectric constant and dielectric loss of Pb-Fe-Nb-O, Pb-Zn-Nb-O, Pb-Fe-W-O etc. relaxor materials. We achieved some ferroelectric materials to be used as pressure sensing materials and dielectric of multilayer capacitors.

I have been employed for one and half years (October, 1995 – March, 1997) as a postdoctoral fellow in Toyohashi University of Technology (**TUT**), Japan. During this period, I have fabricated and characterized Ag-sheathed Bi-2212/2223 superconducting wires/tapes. Two types of tapes were fabricated according to the handling method of the precursor material. One series was prepared by the hand packing (HP) of the precursor powder and another was prepared with cold isostatic pressed (CIP) precursor. Both series of tapes were pressed several times with subsequent heat treatment. It was found that the CIP tapes gave better critical current density (J_c) than the HP tapes. It was concluded that the higher packing density of CIP tapes enhanced the formation of 2223 phases and made their connectivity better.

I have worked in Materials Engineering Department, Ben Gurion University (**BGU**) of the Negev, Beer Sheva, Israel, for one year (February, 1994 – March, 1995). Doping effect of Ag and Ag-Cu on the superconducting properties of bulk $Bi_{1.6}Pb_{0.4}Sr_2Ca_2Cu_3O_x$ ceramics has been investigated. Lower wt% of Ag and Ag-Cu addition was found to enhance the critical currents of the ceramic composites. From elemental mapping and back scattering measurements, we found that Ag was widely dispersed in the material for lower concentration whereas the granular size of Ag increased with the increase of Ag and Ag-Cu addition acting as weak links for

superconducting currents. Some superconducting materials were also prepared as thin films by chemical vapor deposition technique.

I started my research work on the preparation and characterization of some transition metal oxide glasses becoming high temperature superconductors in their glass ceramic phases in Solid State Physics Department, Indian Association for the Cultivation of Science (**IACS**), Jadavpur, Kolkata-32, India. Dc&ac conductivity, dielectric properties, XRD, SEM, DTA, TGA, DSC and IR of these glasses were investigated. Dc conductivity of these glasses was found to fit with Mott's variable range hopping (VRH) model in the intermediate temperature region. Ac conductivity of these glasses was fitted with the existing theoretical models i.e. Quantum Mechanical Tunneling (QMT), Small Polaron Tunneling (SPT), Overlapping Large Polaron Tunneling (OLPT) and Correlated Barrier Hopping (CBH) models. The CBH model was found to be the most suitable one to explain the ac conductivity as well as the frequency exponent data. Thermoelectric power of some of the glasses and glass ceramics were measured and fitted with the theoretical models to get the nature of the carriers in the glasses and glass ceramics. Ba-K-Bi-O system was also studied in the glassy phase. Some unusual behavior of temperature dependence of dielectric constant, dielectric loss and dc conductivity was observed for these glasses. This may be due to the rotational/ orientational motion of BiO_3 and BiO_6 structural units. In addition, $BaTiO_3$ doped V_2O_5-Bi_2O_3 glasses and Y-Ba-Cu-O superconductors were prepared and their properties were explored.

References:

My biographical sketch will be available in the 20th and 21st editions of Marquis "Who's Who in the World". It is also available at the 8th edition of Marquis "Who's Who

in Science and Technology in the World". Recently, it has been included in the list of Leading Scientists of the World, 2005 in the International Biographical Centre, England.

List of Publications

(Accepted and Published papers)

1. Transformation of high T_c superconducting phase in $Bi_{2-x}Pb_xSr_2Ca_2Cu_{3-y}A_yO_\delta$ (A = K, Na; x = 0.1-0.3; y = 0.1-0.3) to the ferroelectric phase by K and Na doping: S. Mukherjee, **S. Mollah**, H. D. Yang and B. K. Chaudhuri, accepted for publication in ***Chin. J. Phys.*** (2005).
2. Properties of $Pr_{0.65}Ca_{0.35-x}Sr_xMnO_3$ manganites: **S. Mollah, *Solid State Physics***, Uiversity Press, (2005) (Invited article in Proceedings of 49th DAE-Solid State Physics Symposium, held at GNDU, Amritsar, during December 26-30, 2004).
3. Non-adiabatic small polaron hopping conduction in $Pr_{0.65}Ca_{0.35-x}Sr_xMnO_3$ perovskites above the metal-insulator transition temperature: **S. Mollah**, H. L. Huang, H. D. Yang, S. Pal, S. Taran and B. K. Chaudhuri, ***J. Magn. Magn. Mater.*, 284** (2004) 383-394.
4. The Physics of non-oxide perovskite superconductor $MgCNi_3$: **S. Mollah**, ***J. Phys.: Condens. Matter* 16** (2004) R1237-R1276 **(Topical Review)**.
5. Magnetic field dependence of low temperature specific heat of spinel oxide superconductor $LiTi_2O_4$: C. P. Sun, J. -Y. Lin, **S. Mollah**, P. L. Ho, H. D. Yang, C. F. Hsu, Y. C. Liao and M. K. Wu, ***Phys. Rev. B*, 70** (2004) 054519.
6. Phase separation and huge enhancement of magnetoresistance in $Pr_{0.65}Ca_{0.35-x}Sr_xMnO_3$: **S. Mollah**, C. P. Sun, H. L. Huang, P. L. Ho and H. D. Yang, ***J. Appl. Phys.*, 95** (2004) 6813-6815.
7. Non-adiabatic small polaron hopping conduction in VN-PbO-TeO_2 glasses: **S. Mollah**, K. Hirota, K. Sega, B. K. Chaudhuri and H. Sakata, ***Phil. Mag. B.*, 84** (2004) 1697-1715.

8. Development of pulsed magnetic field and study of magnetotransport properties of K-doped $La_{1-x}Ca_{x-y}K_yMnO_3$ CMR materials: S. Bhattacharya, S. Pal, R. K. Mukherjee, B. K. Chaudhuri, S. Neeleshwar, Y. Y. Chen, **S. Mollah** and H. D. Yang, ***J. Magn. Magn. Mater.***, **269** (2004) 359-371.

9. Ferroelectric nanocrystals dispersed oxide glasses: B. K. Chaudhuri, H. Sakata, **S. Mollah** and H. D. Yang, in "***Encyclopedia of Nanoscience and Nanotechnology***", Ed. H. S. Nalwa and forwarded by R. Smalley, Nobel Prize Laureate, (American scientific publishers) Vol. **3** (2004) pp 335-357.

10. Pressure effects on the transition temperature of superconducting MgC_xNi_3: H. D. Yang, **S. Mollah**, W. L. Huang, P. L. Ho, H. L. Huang, C. -J. Liu, J. -Y. Lin, Y. -L. Zhang, R. -C. Yu and C. -Q. Jin, ***Phys. Rev. B*, 68** (2003) 092507.

11. Comment on "Evidence for the immobile bipolaron formation in the paramagnetic state of the magnetoresistive manganites" A. Banerjee, S. Bhattacharya, **S. Mollah**, H. Sakata, H. D. Yang and B. K. Chaudhuri, ***Phys. Rev. B*, 68** (2003) 186401.

12. Low temperature specific heat of bi-layered manganites $La_{2-2x}Sr_{1+2x}Mn_2O_7$ (x = 0.3 and 0.5): H. D. Yang, I. P. Hong, F. H. Hsu, H. H. Li, S. Y. Tu, H. L. Huang, S. Chatterjee, **S. Mollah**, Y. -K. Kuo, T. I. Hsu, H. C. Ku and W. -H. Li, ***Solid State Commun.***, **27** (2003) 229-232.

13. Transport and dielectric properties of K doped glassy precursor for high T_c superconductor showing ferroelectric behavior due to embedded nanocrystalline ferroelectric phase: S. Mukherjee, H. Sakata, B. K. Chaudhuri, **S. Mollah** and H. D. Yang, ***J. Appl. Phys.***, **94** (2003) 1211-1217.

14. Electronic and magnetic instability in $Pr_{0.65}Ca_{0.25}Sr_{0.1}MnO_3$: **S. Mollah**, H. L. Huang, P. L. Ho, W. L. Huang, C. W. Huang, C. P. Sun, J. -Y. Lin, S. J. Liu, Y. S. Gou, W. -H. Li and H. D. Yang, ***J. Mag. Mag. Mater.*, 265** (2003) 215-221.

15. Specific heat studies on the charge and magnetic ordering in manganites: H. D. Yang, H. L. Huang, P. L. Ho, W.L. Huang, C. W. Huang, **S. Mollah**, S. J. Liu and J. -Y. Lin, ***Physica B*, 329-333** (2003) 801-802.

16. MgB2 Superconductor: A review: **S. Mollah**, H. D. Yang and B. K. Chaudhuri, ***Ind. J. Phys.***, **77A** (2003) 9-22.

17. X-ray photoelectron spectroscopy of VN-PbO-TeO_2 glasses: **S. Mollah**, K. Hirota and H. Sakata, ***Physica Scripta***, **T97** (2002) 160-162.

18. Critical temperature and critical current of PbBiSCCO-Ag/AgCu/AgIn composites: **S. Mollah**, ***Materlas Letters***, **52** (2002) 159-165.

19. Preparation and Characterization of Bi_2O_3-PbO-R (R = Fe_2O_3, MnO_2, CuO and V_2O_5) semiconducting oxide glasses: C. Prakash, A. Firdous and **S. Mollah** in "***Physics of Semiconductor Devices***". Eds. V. Kumar and P. K. Basu, Allied Publishers, **Vol. II** (2001) P 1166-1169 (Proceedings of Eleventh International Workshop on the Physics of Semiconductor Devices held at SSPL, Delhi, during December, 2001).

20. Electron Paramagnetic resonance of Fe^{3+} ions in Bi_2O_3-PbO-Fe_2O_3 glasses: C. Prakash, S. Husain, R. J. Singh and **S. Mollah**, ***J. Alloys and Compounds***, **326** (2001) 47-49.

21. DC conductivity of VN-PbO-TeO_2 glasses: **S. Mollah** in "***Physics of Semiconductor Devices***" Eds. V. Kumar and S.K. Aggarawal, Allied Publishers, **Vol. II** (1999) P-1388 (Proceedings of Tenth International Workshop on Physics of Semiconductor Devices held in SSPL, Delhi, India, during December, 1999).

22. Role of normal metal inclusions in the critical current of PbBiSCCO-Ag/AgCu/AgIn composites: **S. Mollah, *Solid State Physics***, Eds. R. Mukhopadhyay, B. K. Godwal and S. M. Yusuf, Uiversity Press, **Vol. 42** (1999) P-459 (proceedings of 42^{nd} DAE-Solid State Physics Symposium, held at IGCAR, Kalpakkam, during December 20-24, 1999).

23. Transport properties of Pb-doped $Bi_4Sr_3Ca_3Cu_4O_x$ semiconducting glasses and glass-ceramic superconductors: S. Chatterjee, S. Banerjee, **S. Mollah** and B. K. Chaudhuri, ***Phys. Rev. B.***, **53** (1996) 5942-5952.

24. Phases evolution during the fabrication of bulk Bi-based superconducting glass ceramics: **S. Mollah**, N. Froumin and J. Baram, In "***Studies of High Temperature Superconductors***", Ed. A. V. Narlikar, NY, Nova Science Publishers Inc. Commark, **Vol. 16** (1996) pp.155-174.

25. Critical currents of PbBiSCCO Ag/AgCu composites: **S. Mollah**, N. Froumin, M. Polak and J. Baram, ***Materials Letts.***, **27** (1996) 187-193.

26. ac conductivity of glassy $Bi_{4-n}Pb_nSr_3Ca_3Cu_4O_x$ semiconductors (with n = 0.0, 0.1, 0.5 and 1.0): Precursors for high T_c superconductors: **S. Mollah**, K. K. Som, S. Chakraborty, A. K. Bera, S. Chatterjee, S. Banerjee and B. K. Chaudhuri, ***Phys. Rev. B.***, **51** (1995) 17512-17520.

27. Dielectric properties of semiconducting $Bi_{4-n}Pb_nSr_3Ca_3Cu_4O_x$ ($0 \leq n \leq 1$) glasses: Precursors for high T_c superconductors: **S. Mollah**, S. Chatterjee, S. Banerjee, S. Chakraborty and B. K. Chaudhuri, ***Phil. Mag. B***, **71** (1995) 151-162.

28. Anomalous dielectric relaxation behavior of K doped amorphous $Ba_{1-x}K_xO_{3-\delta}$ (x = 0 to 0.75) oxides: **S. Mollah**, A. K. Bera, S. Chakraborty and B. K. Chaudhuri, ***Phys. Rev. B***, **49** (1994) 15017-15022.

29. High dielectric constants in $BaTiO_3$ doped $90V_2O_5$-$10Bi_2O_3$ oxide glasses obeying Debye-type dielectric relaxation behavior: S. Chakraborty, A. K. Bera, **S. Mollah** and B. K. Chaudhuri, ***J. Mater. Research***, **9** (1994) 1932-1935.

30. Study of dielectric relaxation behavior in Li-doped semiconducting Bi-Sr-Ca-Cu-O glasses: **S. Mollah**, A. K. Chakraborty, S. Chakraborty, K. K. Som and B. K. Chaudhuri, ***J. Non-Cryst. Solids***, **167** (1994) 192-198.

31. Debye type dielectric behavior of Bi-Sr-Ca-Cu-O based transition metal oxide glasses: Precursor for oxide superconductors: K. K. Som, **S. Mollah**, K. Bose and B. K. Chaudhuri, ***Phys. Rev. B*, 47** (1993) 534-537.

32. ac conductivity in $Bi_4Sr_3Ca_3Cu_yO_x$ (y = 0-5) and $Bi_4Sr_3Ca_{3-z}Li_zCu_4O_x$ (z = 0.1-1.0) semiconducting oxide glasses: **S. Mollah**, K. K. Som, K. Bose and B. K. Chaudhuri, ***J. Appl. Phys.*, 74** (1993) 931-937.

33. Metallic behaviour of the electrochemically deposited Tl-Bi-Pb-Sr-Ca-Cu-O films down to 10 K: S. Chatterjee, S. Banerjee, **S. Mollah**, K. K. Som and B. K. Chaudhuri, ***Ind. J. Phys. A*, 67** (1993) 421-424.

34. Nonadiabatic small polaron hopping conduction in Li-doped and undoped $Bi_4Sr_3Ca_3Cu_yO_x$ ($0 \leq y \leq 5$): **S. Mollah**, K. K. Som, K. Bose, A. K. Chakraborty and B. K. Chaudhuri, ***Phys. Rev. B*, 46** (1992) 11075-11083.

35. Nonlinear physical properties of amorphous $Bi_4Sr_3Ca_3Cu_yO_x$ semiconducting oxides with y between 0 and 5: K. K. Som, **S. Mollah**, K. Bose and B. K. Chaudhuri, ***Phys. Rev. B*, 45** (1992) 1655-1659.

36. Preparation and characterization of superconducting ($YBa_2Cu_3O_x$-Ag) composites obtained by sol-gel method: P. K. Pal, **S. Mollah**, K. Bose, K. K. Som and B. K. Chaudhuri, ***J. Mat. Sci. (Materials in Electronics)*, 3** (1992) 120-123.

37. Concentration-dependent physical properties of $Bi_2Ca_3Sr_3Cu_4O_x$ oxide glasses with z = 1-5: **S. Mollah**, K. Bose, K. K. Som and B. K. Chaudhuri, ***J. Mat. Sci. Lett.*, 11** (1992) 1294-1297.

38. Preparation and characterization of $YBa_2Cu_3O_x$ high temperature superconductor obtained by sol-gel method: P. K. Pal, K. Bose, **S. Mollah** and B. K. Chaudhuri, ***Ind. J. Phys. A*, 65** (1991) 269-275.

Symposium Papers (abstracts only):

1. Synthesis and Physical properties of $PrMn_2O_5$: **S. Mollah**, C. J. Chou and H. D. Yang, ***49th Conference on Magnetism and Magnetic Materials***, November 7-11, Florida, USA, 2004.
2. Interplay of charge and spin ordering in $Pr_{0.65}Ca_{0.35-x}Sr_xMnO_3$: **S. Mollah**, C. P. Sun, H. L. Huang, P. L. Ho and H. D. Yang, ***2004 Taiwan International Conference on Superconductivity and the 7th Workshop on Low Temperature Physics*** (***TICS'04 & WLTP7***), Penghu, Taiwan, July 5-9, 2004.
3. Magnetotransport properties of alkali metal doped La-Ca-Mn-O system under pulsed magnetic field: B. K. Chaudhuri, **S. Mollah** and H. D. Yang, ***2004 Taiwan International Conference on Superconductivity and the 7th Workshop on Low Temperature Physics*** (***TICS'04 & WLTP7***), Penghu, Taiwan, July 5-9, 2004.
4. DC conductivity and Electron Paramagnetic Resonance of xLi_2CO_3-(20-x)Na_2CO_3-$20MnO_2$-$60P_2O_5$ (x = 0, 5, 10, 20) glasses" A. Firdous and **S. Mollah**, ***"First International Meeting on Applied Physics, aphys2003"***, Badajoz, Spain, October 13-18, 2003.
5. Magnetic field dependent magnetic and transport properties of $Pr_{0.65}(Ca_{0.35-x}Sr_x)MnO_3$ CMR materials: **S. Mollah**, S. Bhattacharya, A. Banerjee, S. Pal, H. D. Yang and B. K. Chaudhuri, ***"Proc. of thirteenth National Conference on Cryogenics"***, IACS, Kolkata, India, March 23-26, 2003.
6. BCS-like superconductor $LiTi_2O_4$: C. P. Sun, H. D. Yang, C. W. Huang, W. L. Huang, **S. Mollah**, J. -Y. Lin, C. F. Hsu, Y. C. Liao and M. K. Wu, ***"Proc. of thirteenth National Conference on Cryogenics"***, IACS, Kolkata, India, March 23-26, 2003.

7. Critical currents of metal/alloy doped PbBiSCCO superconductors: **S. Mollah,** ***"National seminar in Gowalior University"***, M. P., India, 1998.

8. Superconducting properties of electrochemically deposited film on silver wires and tapes: S. Chatterjee, S. Banerjee, **S. Mollah** and B. K. Chaudhuri, in "***Thirteenth National Symposium on Cryogenics, Shivaji University, Kolhapur***" December 3-5, 1993.

9. Application of pair approximation type and random walk type models in the ac conductivity of Pb doped $Bi_{4-n}Pb_nSr_3Ca_3Cu_4O_x$ ($0 \leq n \leq 1$) semiconducting oxides: **S. Mollah**, S. Chakraborty and B. K. Chaudhuri in ***"Solid State Physics Symposium 1993, BARC, Bombay; Dec.27-31, 1993"*** P-151.

10. Large dielectric permitivity in $BaTiO_3$ doped V_2O_5-Bi_2O_3 oxide glasses obeying Debye-type dielectric relaxation behavior: S. Chakraborty and **S. Mollah**, in "***Solid State Physics Symposium 1993, BARC, Bombay, Dec.27-31, 1993***" P-150.

11. Properties of Bi-based oxide glasses and the corresponding superconducting glass-ceramics: B. K. Chaudhuri, **S. Mollah** and K. K. Som, in "***INDO-US workshop on perspectives in new materials, 22-23 March, 1992, NPL, New Delhi, India***" P-53.

12. Non-adiabatic small polaron hopping in Bi-Sr-(Ca,Li)-Cu-O glass: **S. Mollah**, K. K. Som, G. Dey and B. K. Chaudhuri in "***Proc. of the Solid State Physics Symposium; India***" Vol.35-C, P.181.

Synopsis

Synopsis

The D.Sc Thesis entitled "Studies on some Exotic Materials" is a compilation of research work done by Dr. S. Mollah on the glassy amorphous semiconducting, superconducting and colossal magnetoresistive (CMR) materials. These are structurally characterized by different techniques such as x-ray diffraction (XRD), scanning electron microscopy (SEM), differential thermal analysis (DTA), thermo-gravimetric analysis (TGA), differential scanning calorimetry (DSC), infra-red (IR), electron paramagnetic resonance (EPR), x-ray photoemission spectroscopy (XPS) etc. Their physical properties are determined by the measurement of dc&ac conductivities, dielectric properties, thermoelectric power (TEP), specific heat (C) and magnetization (M) with or without the application of magnetic field (0-8 T) or high pressure (0-17 kbar) at temperatures down to 0.5 K. The work on glassy amorphous semiconducting, superconducting and CMR materials are summarized step by step in the following.

Ceramics and glasses with large dielectric constants are very important for their technological applications. They are used for developing barrier layer capacitors. Multi-component transition metal oxide (TMO) and other metal oxide glasses have been studied because of their probable technological applications in optical and electrical memory switches, oxygen gas sensors etc. It is considered that highly conducting telluride glasses are potential candidates for O_2 gas sensors. Vanadium-lead-telluride glasses are perspective candidates for pressure and gas sensors. Some TMO glasses are used as precursor materials for preparing superconductors by proper annealing. The

superconductors obtained from the glassy phase are found to be very dense as well as homogeneous.

Non-linear behaviors of density (ρ) and mean molar oxygen volume (V_o^*) of $Bi_4Sr_3Ca_3Cu_yO_x$ (y = 0-5) glasses are observed with the variation of CuO concentration. IR-spectroscopic data and V_o^* in these glasses indicate a change of (BiO_6) octahedral to a pyramidal (BiO_3) structural unit with a change of CuO content in the glasses. However, there is no direct evidence of structural change from XRD data. It is concluded that the nonlinear variation of the ratio of Cu^+/Cu(total) in the glasses depending on the CuO concentration can explain the properties of these glasses. The temperature (80-450 K) and CuO concentration dependence of dc conductivity (σ_{dc}) of $Bi_4Sr_3Ca_3Cu_yO_x$ (y = 0-5), $Bi_4Sr_3Ca_{3-z}Li_zCu_4O_x$ (z = 0.l-l) and $Bi_{4-n}Pb_nSr_3Ca_3Cu_4O_x$ (n = 0-1) glasses are elaborately studied. The variation of activation energy (W) with glass composition dominates the conductivity. A strong pre-exponential factor containing the small polaron tunneling term exp(-2αR) is observed in dc conductivity unlike many other glasses with transition metal ions (TMI). The electron-phonon interaction in these glasses is strong enough to form the small polaron and the electrical conduction occurs due to their hopping. Non-adiabatic small polaron hopping conduction mechanism is found to be appropriate for explaining the conductivity data of these glasses. The addition of Li decreases the conductivity and causes appreciable changes in the model parameters though the overall thermal behavior of electrical transport remains the same. This indicates that a small amount (less than 10 wt.%) of Li act as flux in these glasses to keep the oxygen content fixed in the corresponding glass-ceramic phases. This lowers the sintering as well as melting temperature of the glasses. Though the Li doping reduces the σ_{dc}, Pb doping increases it.

Pb^{+2} substituted for Bi^{+3} as well as Sr defects act as hole donors in the $Bi_{4-n}Pb_nSr_3Ca_3Cu_4O_x$ glass system. Since the valency of Pb is +2 and that of Bi is +3, one Pb atom can dope a hole to the system. Thus the dc conductivity increases with the increase of Pb doping.

The temperature (80-450 K) and frequency (50-10^4 Hz) variation of ac conductivity $\sigma_{ac}(\omega)$ of $Bi_4Sr_3Ca_3Cu_yO_x$ (y = 0-5), $Bi_4Sr_3Ca_{3-z}Li_zCu_4O_x$ (z = 0.1-1) and $Bi_{4-n}Pb_nSr_3Ca_3Cu_4O_x$ (n = 0-1) have been ornately investigated. The universal power-law behavior [$\sigma_{ac}(\omega) = \sigma_{ac}(0) + A\omega^s$ with exponent $s < 1$] is found to be valid for most of these glasses where $\omega = 2\pi f$, f being the linear frequency and A is a constant. Little deviation from this limiting performance is also observed for some glass compositions in the low-temperature and higher frequency regions. The s value is found to be little higher than unity (1.1-1.2) in the low temperature regime where $\sigma_{ac}(\omega)$ also illustrates the non-linear variation with temperature. It is retrieved that the quantum mechanical tunneling (QMT) and over-lapping large polaron tunneling (OLPT) models are inadequate to explain the general behavior of both temperature and frequency dependent $\sigma_{ac}(\omega)$ and s. However, the correlated barrier hopping (CBH) model based on the pair approximation is noticed to be the most appropriate one for explaining the frequency and temperature-dependent ac conductivity data. The extended-pair approximation and percolation models are also found to fit the ac conductivity data for $s < 1$. Nevertheless, the fitting with CBH model is better. The random walk type of model is found to be valid for a limited range of temperature too.

Frequency (50-10^4 Hz) and temperature (80-450 K) dependence of dielectric constant (ε') and dielectric loss (ε'') are studied for $Bi_4Sr_3Ca_3Cu_yO_x$ (y = 0-5),

$Bi_4Sr_3Ca_{3-z}Li_zCu_4O_x$ (z = 0.1-1) and $Bi_{4-n}Pb_nSr_3Ca_3Cu_4O_x$ (n = 0-1) glasses. Both of ε' and ε" do not show any peak in the temperature range of our study. However, the imaginary part (M") of the dielectric modulus (M^*) demonstrates peaks. The dielectric properties of these glasses are found to follow the Debye type relaxation behavior with relaxation frequency f_c [$= \nu_c \exp(-W_c/k_BT)$] where W_c is the activation energy, k_B is the Boltzman constant and T is the absolute temperature. There is a distribution of carriers' relaxation times which has been confirmed from the Cole-Cole plots. The relaxation performance is thermally activated in nature like the dc electrical conduction process of these glasses.

The dielectric properties of glassy $Ba_{1-x}K_xBiO_3$ (x = 0 to 0.75) at different temperatures (80-450 K) and frequencies (1-10 kHz) are also examined. Large increase in ε' and ε" are observed in all these glasses between the temperatures 297 and 320 K. Metal-insulator transition is as well detected in these. The anomalies are considered to be associated with the orientational motion of the BiO_3 and BiO_6 structural units present in the glasses. These motions are giving rise to the structural instability and different kinds of phase transitions including a superconducting transition in the crystalline phases.

$BaTiO_3$ doped $90V_2O_5$-$10Bi_2O_3$ glasses show a larger ε' ($10^2 - 10^4$) compared to the undoped glass (~ 10^2). They all reveal Debye type relaxation behavior though the 15 wt.% $BaTiO_3$ doping demonstrates the highest ε'. The increase in ε' is due to the formation of microcrystalline clusters of $BaTiO_3$ (1.8-8 μm, depending on the doping concentration). The Bi_2O_3 also plays some important role on the dielectric properties of the glasses.

Electron paramagnetic resonance (EPR) study of Fe^{3+} ions in Bi_2O_3–PbO–Fe_2O_3 glasses has been carried out in room temperature for different molar percentages of

Fe_2O_3. In each spectrum, there is more than one line. 'g' values of all the lines in each spectrum have been determined. The origin of each spectral line is explained.

The σ_{dc} and x-ray photoemission spectroscopy (XPS) of oxynitride VN-PbO-TeO_2 glasses with different mol% of VN, PbO and TeO_2 are studied. The XPS analysis reveals the presence of VN, V^{4+}, V^{5+}, Pb^{2+}, Pb^{4+}, Te^{4+} and Te in the glasses. The manifestation of VN containing 8-10 at.%VN confirms vanadium-lead-tellurous oxynitride glasses. The VN contents correspond to an equivalent content of 1-2 at.% N in the glasses. Values of $C_v = V^{4+}/V(total)$ are calculated from the areas of separated XPS peaks corresponding to V^{4+} and V^{5+} ions for different glass compositions. Some redox reactions assumed in the glass melts explain qualitatively changes in the C_v value. The σ_{dc} increases with VN content for a fixed mol% of PbO. Neither Mott's variable-range hopping (VRH) model at low temperatures ($T < \theta_D/4$, θ_D = Debye temperature) nor Greaves' VRH model at intermediate temperatures ($\theta_D/4 < T < \theta_D/2$) describes the dc conductivity data for these glasses. Multi-phonon tunneling transport of strongly coupled electrons is also unable to account for the carrier transport. However, at high temperatures ($T > \theta_D/2$), conduction is found to be due to small-polaron hopping in the non-adiabatic regime. Alteration of the VN content causes a change in the model parameters achieved from the best-fitting curves for the glasses.

The dielectric constants of TMO glasses are, in general, very low and follow Debye type dielectric relaxation behavior as discussed above. Ag_2O doped Bi-Sr-Ca-Cu-O glasses, dispersed with nanocrystalline silver particles show high value of density of states (DOS) at the Fermi level, $N(E_F)$, estimated from the VRH model. But none of these nanocrystal-dispersed glasses are ferroelectric (FE) or they do not show

high dielectric permittivity. However, some of the TMO glasses containing $BaTiO_3$, $PbTiO_3$, TeO_2 etc. are found to illustrate FE behavior due to the presence of nanocrystalline phases.

Nanophase materials and nanocomposites characterized by an ultrafine grain size (< 50 nm); have created high interest in recent years by virtue of their unusual mechanical, electrical, optical and magnetic properties. Nanocrystalline particles/clusters embedded in the alkali metal doped glasses are considered to be responsible for the FE activities of bulk glass nanocrystal composite (GNC). Pure nanocrystalline ferroelectric $PbTiO_3$ generally illustrates a critical size of the nanocrystals (different for different systems) at which dielectric constant exhibits a maximum value. There is, however, large difference in the ferroelectric behavior (Curie temperature, dielectric constant, polarization etc.) of the bulk and its nanocrystalline counterpart. The synthesis, characterization and transport properties of such FE glass-nanocomposite materials are studied. The K-doped glasses viz. $Bi_{2-x}Pb_xSr_2Ca_2Cu_{3-y}K_yO_z$ (x = 0.1-03, y = 0.2-0.3) show FE transitions (between 500-330 K depending on y). The K free glasses are, however, not ferroelectric but are precursors for high T_c superconductors. Nanocrystalline particles/clusters (~10-50 nm size) embedded in the K doped glasses, observed from transmission electron microscopic studies, are considered to be responsible for the ferroelectric performance of the bulk GNC. Though their dielectric behavior is different, both the K free and K containing glassy systems are semiconductors and follow non-adiabatic small polaron hopping conduction mechanism.

Superconductors are extensively studied since its discovery in 1911. There was tremendous work on the high temperature oxide superconductors from the time of the

discovery of $YBa_2Cu_3O_7$ superconductor with superconducting transition temperature (T_c ~ 90 K). Scientists all over the world were deeply involved in searching for superconductors with higher T_c and were successful in obtaining several new oxide superconductors with T_c > 77 K. However, most of these superconductors are multi-phased and brittle in nature. Therefore, several ductile sheath materials like Ag, Ag-Cu etc. are used for fabricating superconducting wires/tapes for the technological applications. Critical temperatures (T_c) and critical currents (I_c) of Pb–Bi–Sr–Ca–Cu–O (PbBiSCCO) superconductors containing 10, 25 or 30 wt.% Ag or AgCu or AgIn are studied. Specimens of 24-h annealed, 10 wt.% added metal/alloy composites show the highest critical currents, which is much higher than pure PbBiSCCO. Samples annealed for 24 h bestow better transport property than the 48-h annealed samples for the same composition. The connectivity effect of metal/alloy between superconducting grains can explain this finding. The I_c of AgIn composites is superior to AgCu but inferior to Ag composites. This finding is explained in terms of supercurrent transport properties. Partial substitution of Cu by K in multi-component glassy precursors for high T_c superconductor viz. $Bi_{2-x}Pb_xSr_2Ca_2Cu_3O_\delta$ (x = 0.1-0.3) is found to destroy superconductivity of the corresponding annealed phases. Unlike K free glasses, the K-containing $Bi_{2-x}Pb_xSr_2Ca_2Cu_{3-y}K_yO_z$ (x = 0.1-03, y = 0.2-0.3) does not become superconductor by annealing it at higher temperatures. This indicates the suppression of superconductivity by the precipitation of ferroelectric nanoparticles in the K doped glass nanocrystal composite (GNC). As a small amount (less than 10 wt.%) of Li acts as flux in $Bi_4Sr_3Ca_{3-z}Li_zCu_4O_x$ (z = 0.l, 0.5, and l) glasses to keep the oxygen content fixed, it helps to increase the superconducting transition temperature of corresponding glass-ceramics.

The thermoelectric power (TEP) of $Bi_{4-n}Pb_nSr_3Ca_3Cu_4O_x$ (n = 0-1) glasses and glass ceramics has been investigated. Seebeck coefficient (S) of the partially annealed glass system is found to increase linearly with temperature. The S value of the corresponding glass ceramic superconductor shows broad peaks around T_c. A change over from positive (below 290 K) to negative (above 290 K) in thermal variation of S indicates the coexistence of both electrons and holes in these superconductors. The TEP data can be fitted with both the two-band and Nagaosa-Lee models. Therefore, the bosonic contribution in the transport properties of these superconductors, as expected by the Nagaosa-Lee model, is supported. $YBa_2Cu_3O_x$ (123) and ($YBa_2Cu_3O_x$–Ag) superconductors are prepared by sol-gel method and their electrical resistivity as well as magnetic susceptibility is studied. The T_c is found to be ~ 93 K. The critical current density (J_c) is determined to be around 200 A/cm^2 at self-field and 80 K temperature.

Synthesis, structure and properties of the most intensively studied newly discovered intermetallic binary superconductor MgB_2 have been discussed. Though this material has been known since 1950s, it is recently ascertained to be superconductive with a record high T_c ~ 40 K. The detection of this binary superconductor initiates the basic research to find out other binary and ternary intermetallic superconductors like $BeB_{2.75}$, $MgCNi_3$ etc. It has a hexagonal unit cell with parameters a ~ 3.1432 Å and c ~ 3.5193 Å. MgB_2 bulk samples synthesized under high pressure (~3.5 GPa) and high temperature (~1000 °C) has density ~2.63 g/cm^3. The normal state carriers of MgB_2 are holes as established from the positive thermoelectric power and Hall coefficient measurements. The external pressure decreases the T_c with dT_c/dP in the range of -1 to -2 K/GPa. The T_c also decreases rapidly by the doping of Mn, Li, Co, C, Al, Ni and Fe

but increases slightly by Zn doping. However, no significant change of T_c is observed by the doping of Si and Be. It is further noticed that the anisotropic ratio γ (= H_{c2}^{ab} /H_{c2}^{c}) ~ 1- 5 with lower critical field $H_{c1}(0)$ ~ 25-48 mT and upper critical field, $H_{c2}(0)$ ~ 40 T. The J_c of it is as high as 1.3×10^6 A/cm^2 in the self-field and 9.4×10^4 A/cm^2 in a magnetic field of 2 T at the temperature of 20 K. The most interesting feature of this superconductor is the appearance of two superconducting energy gaps: one is at Δ_1 ~ 1.92 meV and the other is at Δ_2 ~ 3.45 meV. From theoretical studies, it is found that MgB_2 superconductor has a minimum of the density of states (DOS) just above the Fermi level that can account for the decrease of T_c with the increase of pressure. Copper oxide based high temperature cuprate superconductors (HTSC) are limited in their use as their J_c is governed by many factors like size of the superconducting grains, intra- and inter grain connectivity, texture of the superconducting grains etc. Though the wires/tapes made of HTSC can be operated above liquid nitrogen temperature (77 K), these are expensive due to the use of 70% silver for their fabrication. MgB_2 offers the possibility of a new class of superconducting materials having low cost and high performance for magnetic and electronic applications. The advantages of MgB_2 are of its lower anisotropy compared to that of HTSC, larger coherence lengths and comparatively cleaner grain boundaries to current flow. Its high T_c value, simple crystal structure, large coherence lengths, high critical current densities and fields promise that MgB_2 would be the most probable candidate for large scale applications and devices. Considering its higher T_c and J_c values in addition to lower cost compared to the existing metallic superconductor NbTi etc., there is an immense possibility of MgB_2 to be emerging out as the next generation

superconductor for technological applications. It would also provide higher operating temperatures compared to the present Nb based electronics with higher device speed.

Another intermetallic superconductor $MgCNi_3$ has many interesting properties and is focused for the understanding of its complicated physics. Energy band calculations show that the DOS at the Fermi level, $N(E_F)$, is dominated by Ni d states and there is a von Hove singularity (vHs) of the DOS just below (< 50-120 meV) the E_F. It is surprising that the conduction electrons in it are derived from the partially filled Ni d states, which typically lead to the ferromagnetism in metallic Ni and many Ni-based binary alloys. The MgC_xNi_3 has a simple cubic perovskite structure with space group Pm-3m and the lattice parameter a is ~ 3.812 Å for x ~ 0.97 at ambient temperature and pressure. However, the $Ni_6(O_6)$ octahedral is locally distorted from those expected in perfect cubic Pm-3m. Six Ni atoms at the face-centered positions and eight Mg atoms at the cube corners surround the carbon atom of $MgCNi_3$ at the body center. The carriers in it are electron type in normal state though theoretically it is predicted to be hole type. Its T_c increases with the increase of x in MgC_xNi_3 but generally decreases due to the Ni site doping by Co, Fe, Mn, Cu etc. Theoretically, DOS peak is greatly reduced by the doping at Mg or Ni site, which accounts for the reduced T_c. The effect of hydrostatic pressure (P) up to 17 kbar on the T_c of MgC_xNi_3 (x = 1-1.5) has been examined. The T_c is found to increase with increasing P at a rate of dT_c/dP ~ 0.0134 to 0.0155 K/kbar depending on the value of carbon content x. The absolute value of dT_c/dP for MgC_xNi_3 is about the same as that of intermetallic RNi_2B_2C (R = rare earths) and metallic superconductors but about one order of magnitude smaller than that of MgB_2. However, the $d\ln T_c/dP$ ~ 0.00181 to 0.00224 $kbar^{-1}$ and the rate of change of T_c with unit cell volume (V), $d\ln T_c/d\ln V$ ~ –3.18 to –2.58

of MgC_xNi_3 are having the comparable magnitude to that of MgB_2 with opposite sign. The increase of T_c with P in MgC_xNi_3 can be explained in the frame works of DOS effect. Controversial magnetoresistance is reported on it. It has been observed that the electronic contribution is slightly higher than the lattice one in the normal state thermal conductivity. The specific heat and tunneling spectroscopic studies indicate that this is an s-wave BCS-type weak/moderate coupling type-II superconductor which needs further confirmation as the penetration depth exhibits distinctly a non s-wave BCS low temperature behavior and theoretically suggested as a d-wave superconductor.

Magnetic field dependence of low temperature specific heat of spinel oxide superconductor $LiTi_2O_4$ has been elaborately investigated. In the normal state, the obtained electronic coefficient of specific heat γ_n = 19.15 mJ/mol K^2 and the Debye temperature θ_D = 657 K. The $T_c \sim 11.4$ K is very sharp ($\Delta T_c \sim 0.3$ K) and the estimated $\delta C/\gamma_n T_c$ is ~ 1.78. In the superconducting state, the best fit of data leads to the electronic specific heat $C_{es}/\gamma_n T_c = 9.87 \exp(-1.58\ T_c/T)$ without field and $\gamma(H) \propto H^{0.95}$ with fields. In addition, $H_{c2}(0) \sim 11.7$ T, thermodynamic critical field $H_c(0) \sim 0.32$ T, Grinzburg-Landau parameter $\xi_{GL}(0) \sim 55$ Å, London penetration depth $\lambda_{GL}(0) \sim 1600$ Å, and $H_{c1}(0) \sim 26$ mT are estimated from Werthamer-Helfand-Hohenberg (WHH) theory or other relevant relations. All the obtained results indicate that $LiTi_2O_4$ can be well described by a typical type-II, BCS-like, moderate coupling, and fully gapped superconductor in the dirty limit. It is suggested that $LiTi_2O_4$ is a moderately electron-electron correlated system.

Colossal magnetoresistivity (CMR) in manganites like $RE_{1-x}A_xMnO_3$ (RE = rare earth and A = alkaline earth material) is an example in which spin, charge and lattice

degrees of freedom conspire to produce a dramatic effect. This system has many significant properties like metal-insulator transition (MIT), ferromagnetic (FM)-paramagnetic (PM) and FM-antiferromagnetic (AFM) phase change, charge and orbital ordering (CO-OO), spin ordering etc. The interplay between double exchange (DE) interaction and CO-OO can be tuned by changing the value of x, by varying the radius of RE or A, by applying the electric/magnetic field, by irradiating with x-ray/infra-red radiation, by applying external pressure and by Mn-site substitution. The ground state of CMR materials have electronic phase separation (PS) which is the simultaneous presence of submicrometer FM metallic phase percolated in an insulating CO-OO AFM matrix. A little change of the fraction or arrangement of the domains can induce the percolation. There are several chemical and physical applications of the CMR materials. The chemical applications include catalysts for auto exhausts and electrochemical engineering, where they are employed as electrodes in oxygen sensors and solid oxide fuel cells. The catalytic activity is associated with Mn^{3+}-Mn^{4+} mixed valence where the mixed ionic-electronic conductivity is associated with the formation of oxygen vacancies in the solid. The potential physical applications include magnetic sensors, magnetoresistive read/write heads and magnetoresistive random access memory.

The specific heat of bi-layered manganites $La_{2-2x}Sr_{1+2x}Mn_2O_7$ (x = 0.3 and 0.5) is examined for the ground state of low temperature excitations. A $T^{3/2}$ dependent term in the low-temperature specific heat (LTSH) is identified at zero magnetic field and suppressed by magnetic fields for x = 0.3 sample, which is consistent with a ferromagnetic metallic ground state. For x = 0.5 sample, a T^2 term is observed and is consistent with a two-dimensional (2D) antiferromagnetic insulator. However, it is almost

independent of magnetic field within the range of measured temperature (0.6-10 K) and magnetic field (6 T). Specific heat C of polycrystalline manganites $Pr_{1-x}Ca_xMnO_3$ (113-PCMO) with x = 0.3-0.4, $La_{1-y}Ca_yMnO_3$ (113-LCMO) with y = 0.3 and 0.5, and $La_{2-2z}Sr_{1+2z}Mn_2O_7$ (327-LSMO) with z = 0.3 and 0.5 have been investigated for a wide range of temperatures (T = 80-300 K). Clear anomalies in C are identified which are associated with CO, AFM and FM ordering transitions. The anomalies in 113-PCMO and 113-LSMO are bigger than those of 327-LSMO. The possible explanations for these are due to the dimensionality effects.

A systematic study of resistivity (ρ), magnetization (M) and specific heat (C) on polycrystalline $Pr_{0.65}Ca_{0.35-x}Sr_xMnO_3$ (x = 0-0.35) perovskite manganites has been carried out. The T-x phase diagram presenting their electrical and magnetic properties is prevailed. The $Pr_{0.65}Ca_{0.25}Sr_{0.1}MnO_3$ (for x = 0.1) sample is particularly unique showing a CO transition at T_{CO} ~ 200 K, an AFM ordering transition at T_N ~ 175 K, a metal-insulator (MI) transition at T_{MI} ~ 80 K and an unusual magnetic ordering transition at T_M^* ~ 45 K in the absence of magnetic fields. However, the specific heat data do not show any anomaly at T_{MI} for MI transition but illustrate a much smaller anomaly than expected one at T_M^* and is suppressed by magnetic fields. This may indicate that the FM ordering in $Pr_{0.65}Ca_{0.25}Sr_{0.1}MnO_3$, commonly related to MI transition, is of canted or fluctuated of phase separation of FM and AFM in nature. This is established from the T-H phase diagram, as well as the thermal and magnetic hysteresis in ρ, M and C. A huge enhancement of magnetoresistance, MR (10% at H = 100 Oe and 99% at H = 0.5 T) has been observed in $Pr_{0.65}Ca_{0.25}Sr_{0.1}MnO_3$ sample around T_{MI} ~ 80 K which is induced by the phase separation (PS).

In fact, a competition between a CO insulating and a FM metallic phase is accomplished in $Pr_{0.65}Ca_{0.35-x}Sr_xMnO_3$ perovskites as the sample for x = 0 exposes an insulating and that for x = 0.35 reveals a metallic behavior below room temperature. The doping of Sr introduces the nanosize FM clusters in CO/AFM matrix of $Pr_{0.65}Ca_{0.35}MnO_3$. At lower concentration of Sr, the number of nanosize FM clusters is very small and the system resembles a regular array of charge short of Wigner crystal and it remains an insulator as no percolation is possible through the AFM matrix. The increase of Sr concentration (x), enhances the number as well as volume of FM clusters, the percolation among some FM clusters starts and the ρ decreases. When x = 0.1, the number and volume of CO/AFM and FM clusters become nearly equal causing to disorder induced PS with prominent and intrinsic inhomogeneities in the form of coexisting competing phases and leading to MI transition and unusual magnetic ordering in these materials. Therefore, the application of a low magnetic field ($\leq$ 0.5 T) on the samples with x ~ 0.1 is sufficient to partially melt the CO insulating phases and facilitate to percolate the FM phases to enhance the metallicity leading to huge magnetoresistance. The volumes as well as the number of FM clusters increase with further increase of x in expense to those of CO/AFM clusters. Thus practically all the matrix become FM leaving embedded nanosize CO/AFM phases in x = 0.35 sample which is metallic at all temperatures as the nanosize CO/AFM phases cannot block the percolation.

Non-adiabatic small polaron hopping conduction mechanism is followed by $Pr_{0.65}Ca_{0.35-x}Sr_xMnO_3$ (x = 0-0.35) manganites above the respective T_{MI}. Variable range hopping (VRH) has been found less important with the increase of Sr concentration in the low temperature semiconducting region ($T > T_{MI}$). A non-linear change in the activation

energy (E_p) and θ_D with applied magnetic field has been observed for all the samples. The metallic conduction below T_{MI} shows the electron-magnon scattering behavior similar to other manganites. Activation energy E_s, estimated from the temperature dependent Seebeck coefficient data, is observed to be much smaller than E_p determined from the resistivity data, which also supports the small polaron hopping conduction. The transport in the high temperature phase of oxygen isotope diffused epitaxial thin films of $La_{0.75}Ca_{0.25}MnO_3$ (LCMO) and $Nd_{0.75}Sr_{0.25}MnO_3$ (NSMO) are also explained by small polaron hopping conduction mechanism.

Temperature dependent magnetization, magnetoresistance and magneto-thermoelectric power of the K doped $La_{1-x}Ca_{x-y}K_yMnO_3$ type samples with $x = 0.3$ and $0 \leq y \leq 0.15$ has been studied. All the samples exhibit sharp MIT around T_p accompanied by a FM metallic to paramagnetic (PM) semiconducting phase transition with a well-defined Curie temperature T_c (almost equal to T_p). Doping of mono-valent K in the divalent Ca site of $La_{1-x}Ca_{x-y}K_yMnO_3$ drives the system from a high resistivity regime with lower T_p to a lower resistivity regime with higher T_p. Systematic increase of Curie temperature with increase of K doing is observed from the magnetization measurement down to 5 K. Low temperature resistivity (ρ) and thermoelectric power (Seebeck coefficient, S) data well fit the relations $\rho = \rho_0 + \rho_2 T^2$ and $S = S_0 + S_{3/2}T^{3/2} + S_4T^4$ respectively signifying the importance of electron-magnon scattering process ($\rho_2 T^2$ and $S_{3/2}T^{3/2}$ term). Alternatively, the high temperature ($T > T_p$ up to 320 K) conductivity data satisfy VRH model. For $T > 320$ K, small polaron hopping model is more appropriate than the VRH model. High temperature TEP data also signifies the formation of thermally activated small polarons. Even with very small change of y, the DOS at the

Fermi level $N(E_F)$ changes considerably. The magnetotransport properties have been measured under pulsed magnetic field of microsecond duration. The decay time of the magnetic pulse within the sample (τ) varies with field strength, which indicates that with change of magnetic field, ordering of the spin in the ferromagnetic regime changes. The details of the work on the exotic materials will be obtained from the attached reprints in the following chapters.

The thesis consists of three chapters of reprints. Chapter-I contains the reprints on amorphous semiconducting glasses and high dielectric constant materials. Chapter-II incorporates the reprints on superconducting materials. The published work on CMR materials is comprised in Chapter-III.

Chapter-I

Chapter-I

This Chapter contains the reprints on amorphous semiconducting glasses and high dielectric constant materials. These glasses are structurally characterized by x-ray diffraction (XRD), scanning electron microscopy (SEM), differential thermal analysis (DTA), thermo-gravimetric analysis (TGA), differential scanning calorimetry (DSC), infra-red (IR), electron paramagnetic resonance (EPR) and x-ray photoemission spectroscopic (XPS) techniques.

The dc & ac conductivities and dielectric properties of $Bi_4Sr_3Ca_3Cu_yO_x$ (y = 0-5), $Bi_4Sr_3Ca_{3-z}Li_zCu_4O_x$ (z=0.1-1), $Bi_{4-n}Pb_nSr_3Ca_3Cu_4O_x$ (n = 0-1) and VN-PbO-TeO_2 glasses are measured and fitted with different theoretical models. It is found that the dc conductivity of all the glasses is due to the small polaron hopping conduction. The ac conductivity and the frequency exponent are explained by the correlated barrier hopping (CBH) model. There is a distribution of relaxation times of the carriers which has been confirmed from the Cole-Cole plot. The relaxation behavior is also thermally activated in nature.

Dielectric properties of $Ba_{1-x}K_xBiO_3$ (x = 0 to 0.75) and $BaTiO_3$ doped $90V_2O_5$-$10Bi_2O_3$ glasses are also given in this chapter. The room temperature electron paramagnetic resonance (EPR) of Fe^{3+} ions in Bi_2O_3–PbO–Fe_2O_3 glasses for different molar percentages of Fe_2O_3 are included here. The reprint on K-doped glasses viz. $Bi_{2-x}Pb_xSr_2Ca_2Cu_{3-y}K_yO_z$ (x = 0.1-03, y = 0.2-0.3) showing ferroelectric transitions (between 500-330 K depending on y) is as well attached here. This chapter also contains the invited article on ferroelectric nanocrystals dispersed oxide glasses published in Encyclopedia of Nanoscience and Nanotechnology.

PHILOSOPHICAL MAGAZINE, 11 June 2004
VOL. 84, NO. 17, 1697–1715

Taylor & Francis
Taylor & Francis Group

Non-adiabatic small-polaron hopping conduction in VN–PbO–TeO_2 glasses

S. MOLLAH†¶, K. HIROTA‡, K. SEGA§, B. K. CHAUDHURI‖ and H. SAKATA§††

† Department of Physics, Aligarh Muslim University, Aligarh-202002, India
‡ Department of Chemistry, School of Science, Tokai University, Hiratsuka, Kanagawa 259-1292, Japan
§ Department of Applied Chemistry, School of Engineering, Tokai University, Hiratsuka, Kanagawa 259-1292, Japan
‖ Department of Solid State Physics, Indian Association for the Cultivation of Science, Jadavpur, Kolkata-700032, India

[*Received 17 March 2003 and accepted in revised form 3 December 2003*]

ABSTRACT

The dc conductivity of VN–PbO–TeO_2 glasses with different mole percentages of VN, PbO and TeO_2 has been measured in the temperature range 125–450 K. The conductivity of the glasses increases with increasing VN content for a fixed mole percentage of PbO. Neither Mott's variable-range hopping (VRH) model at low temperatures ($T < \Theta_D/4$, where Θ_D is the Debye temperature) nor Greaves' VRH model at intermediate temperatures ($\Theta_D/4 < T < \Theta_D/2$) describe the dc conductivity data for these glasses. Multiphonon tunnelling transport of strongly coupled electrons is also unable to account for the carrier transport. However, at high temperatures ($T > \Theta_D/2$), conduction is shown to be due to small-polaron hopping in the non-adiabatic regime. Alteration of the VN content causes a change in the model parameters achieved from best-fitting curves for the glasses. Modulated differential scanning calorimetry analysis shows that the glass transition temperatures T_g in this system vary from 269 to 302°C.

§ 1. INTRODUCTION

Semiconducting transition-metal oxide (TMO) glasses are of special interest for many technological applications (Sakurai and Yamaki 1985, Hirashima *et al.* 1987, Nakamura and Ichinose 1987). The presence of transition-metal ions (TMIs) in more than one valence state is a general condition for the semiconducting behaviour of these glasses. The dc conduction occurs by transfer of electron from a low to a high valence state of the TMIs. It has been hypothesized that electrical conduction in these glasses is controlled by strong electron–phonon interaction, resulting in the formation of small polarons (Mott 1968, Austin and Mott 1969, Mott and Davis 1979). This indeed was found in oxide glasses containing Cu (Mollah *et al.* 1992, 1995, Som *et al.* 1992, Chatterjee *et al.* 1996), V (Doweidar *et al.* 1985, 1991,

¶Present address: Department of Physics, National Sun Yat Sen University, Kaohsiung 804, Taiwan.
††Author for correspondence: skt@keyaki.cc.u-tokai.ac.jp.

Philosophical Magazine ISSN 1478-6435 print/ISSN 1478-6443 online © 2004 Taylor & Francis Ltd
http://www.tandf.co.uk/journals
DOI: 10.1080/14786430310001659795

Sakata *et al.* 1999) and Fe (Qiu *et al.* 1995, Satou and Sakata 2000) ions. Small-polaron hopping (SPH) (Mott 1968, Austin and Mott 1969) has been invoked to explain the dc conduction and transport properties of vanadate glasses (Sayer and Mansingh 1972, 1983, Dhawan *et al.* 1982, Ghosh and Chaudhuri 1986, Mori *et al.* 1994, Qiu *et al.* 1995, 1997, Satou and Sakata 2000). Three-dimensional variable-range hopping (VRH) conduction (Mott 1969) takes place in these glasses at low temperature (below $\Theta_D/2$, Θ_D being the Debye temperature) where the polaron binding energy is less than k_BT (k_B is the Boltzmann constant and T is the absolute temperature).

Recently, there has been considerable interest in the study of semiconducting glasses with tellurium oxide as the (non-conventional) glass former. It is considered that highly conductive tellurite glasses are potential candidates for O_2 gas sensors. Some glasses containing TMOs, for example V_2O_5–PbO–TeO_2 (Sakata *et al.* 1996), V_2O_5–SnO–TeO_2 (Mori and Sakata 1997) and Fe_2O_3–Sb–TeO_2 (Chakraborty *et al.* 1997) have revealed O_2-gas-sensing properties.

The effect of N (3–18 wt%) incorporation on the electrical conductivity, the strength and the structure of Si-based oxynitride glasses have been studied for almost three decades (Mulfinger 1966, Elmer and Nordberg 1967, Jack 1976, Frischat and Schrimpf 1980, Loehman 1980, Makishima *et al.* 1980). N incorporation in the SiO_2 structure enhances the ionic conductivity and the strength of the glass owing to a compaction of the structure (Frischat and Schrimpf 1980, Makishima *et al.* 1980). To the present authors' knowledge, no work has been done on the transport properties of VN-containing vanadium–lead–tellurium oxynitride glasses. VN–PbO–TeO_2 glasses are perspective materials for pressure and gas sensors if their conductivity is sufficiently large. The aim of this work is to investigate the effect of N incorporation on the physical and electrical properties of vanadium–lead–tellurium oxynitride glasses.

This paper reports the preparation, chemical analysis and temperature dependence of the dc conductivity of VN–PbO–TeO_2 glasses. Different model parameters are evaluated from the dc conductivity data to explain the transport property of these glasses. The thermal characterization of the glasses and the results of X-ray photoelectron spectroscopy (XPS) are also discussed.

§2. Experimental details

Reagent-grade VN (purity, 97.5%), PbO (purity, 99.9%) and TeO_2 (purity, 98.0%) were used to prepare the glass samples. For each sample, 5 g of these raw materials with appropriate masses for the constituents, were thoroughly mixed in an agate mortar and sintered at 200°C for 2 h to evaporate any moisture. Thereafter, the mixture was melted in an electric furnace in flowing N_2 gas (50 ml min^{-1}) at 750°C. Each melt was kept at this temperature for 1 h. The glasses were prepared from the melt at 750°C by rapid quenching to room temperature (25°C) by compression between two highly polished Cu blocks. The resulting glasses were black with shiny surfaces of area 10 mm × 10 mm and had a thickness of 1.0 mm. Six samples with different compositions were prepared. They will be hereafter referred to as follows: sample A, VN : PbO : TeO_2 = 50 : 10 : 40); sample B, VN : PbO : TeO_2 = 40 : 10 : 50; sample C, VN : PbO : TeO_2 = 30 : 10 : 60; sample D, VN : PbO : TeO_2 = 20 : 10 : 70; sample E, VN : PbO : TeO_2 = 40 : 20 : 40; sample F, VN : PbO : TeO_2 = 30 : 20 : 50. Their densities ρ were ascertained by the Gay–Lussac method in toluene at 293 K. These data were used to compute the apparent molar volume V_O^* occupied

by 1 g atom of O in these glasses. V_O^* was calculated from the formula $V_O^* = M/\rho n$, where M is molecular weight calculated from the composition and n is the number of O atoms in one formula unit. The amorphous character of the glasses was established by X-ray diffraction (XRD) of the samples in powder form, using a Rotofax 300 RU diffractometer and Cu Kα radiation at room temperature. The glass transition temperature T_g of the samples was determined from modulated differential scanning calorimetry (MDSC) analysis using a DSC 2910, a modulated differential scanning calorimeter and a thermal analysis instrument. The samples (15–20 mg) in powder form were heated from 150 to 350°C at 10°C min^{-1} for MDSC analysis. XPS of the glasses was accomplished using an X-ray photoelectron spectrometer (model ULVAC-PHI). The XPS data were taken after sputter etching of the samples for 10 s with Ar. A C correction for all the spectra was carried out. Part of the bulk samples were shaped with emery paper, cleaned with acetone and Au coated on both sides, for dc conductivity measurements in the temperature range 125–450 K by a two-probe method with a programmable electrometer (Keithley 617).

§3. Results and discussion

3.1. *Physical properties*

The density ρ of the glasses increases from 4.73 to 5.49 g cm^{-3}, while the apparent molar volume V_O^* decreases from 27.86 to 18.45 cm^3 g-$atom^{-1}$ with decrease in VN content (table 1). The variation in V_O^* with VN concentration suggests that the geometry and topology of the random network of the glasses change with VN concentration. Figure 1 shows XRD spectra of the six glass samples. All show only a broad hump at $2\theta \approx 30°$, confirming the amorphous nature of the samples. MDSC measurements are shown in figure 2. T_g of the glasses varies from 269 to 302°C, increasing with the decrease in VN (table 1). These values are higher than those reported for other tellurite glasses (Sakata *et al.* 1996). Sample C has the highest T_g of 302°C, while sample A has the lowest T_g of 269°C. XPS analysis (Mollah *et al.* 2002) revealed the presence of VN, V^{4+}, V^{5+}, Pb^{2+}, Pb^{4+}, Te^{4+} and Te in the glasses (table 2). The occupancy of 8–10 at.% VN confirmed the oxynitride nature of the vanadium–lead–tellurium glasses. These VN contents correspond to an equivalent content of 1–2 at.% N in the glasses (Mollah *et al.* 2002). Values of $C_v = [V^{4+}]/([V^{4+}]+[V^{5+}])$ were estimated from the area of separated XPS peaks

Table 1. Some physical parameters of VN–PbO–TeO_2 glasses.

Sample	A	B	C	D	E	F
ρ (g cm^{-3})	4.73	4.85	5.15	5.31	5.20	5.49
V_O^* (cm^3 g-$atom^{-1}$)	27.86	24.01	20.57	18.45	25.85	21.84
N (10^{22} cm^{-3})	2.40	2.28	2.25	2.17	2.32	2.29
R (nm)	0.34	0.35	0.35	0.36	0.35	0.35
r_p (nm)	0.21	0.25	0.25	0.24	0.23	0.24
T_g (°C)	269	277	302	291	275	281
W^a (eV)	0.34	0.38	0.46	0.52	0.57	0.49
$W_h{}^a$ (eV)	0.19	0.18	0.18	0.21	0.25	0.22
ΔW^a (eV)	0.15	0.20	0.28	0.32	0.32	0.28
$W_d{}^b$ (eV)	0.04	0.04	0.04	0.04	0.04	0.04

[a] $\Delta W = W - W_h$. W is the value at 444 K.
[b] ε_s is taken as 30 for all the glasses to calculate W_d.

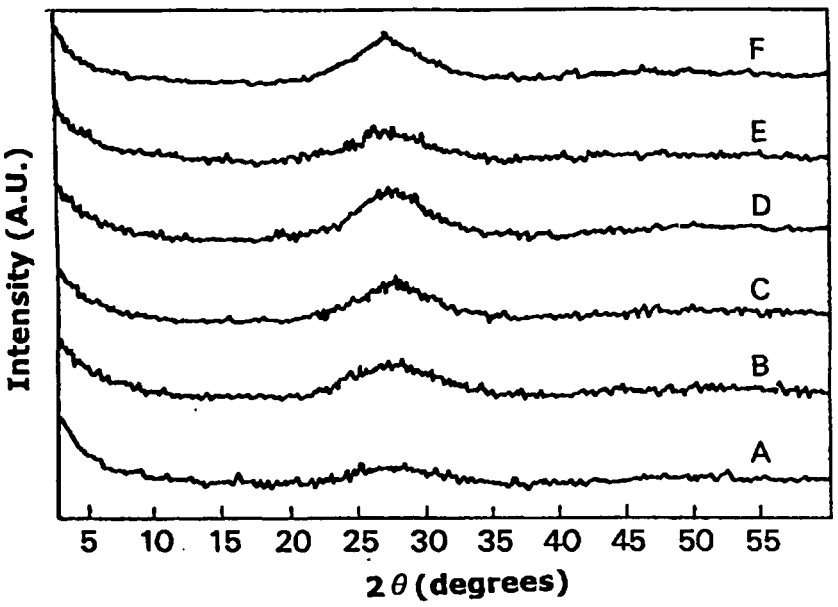

Figure 1. XRD patterns of VN–PbO–TeO_2 glasses (all arbitrary units).

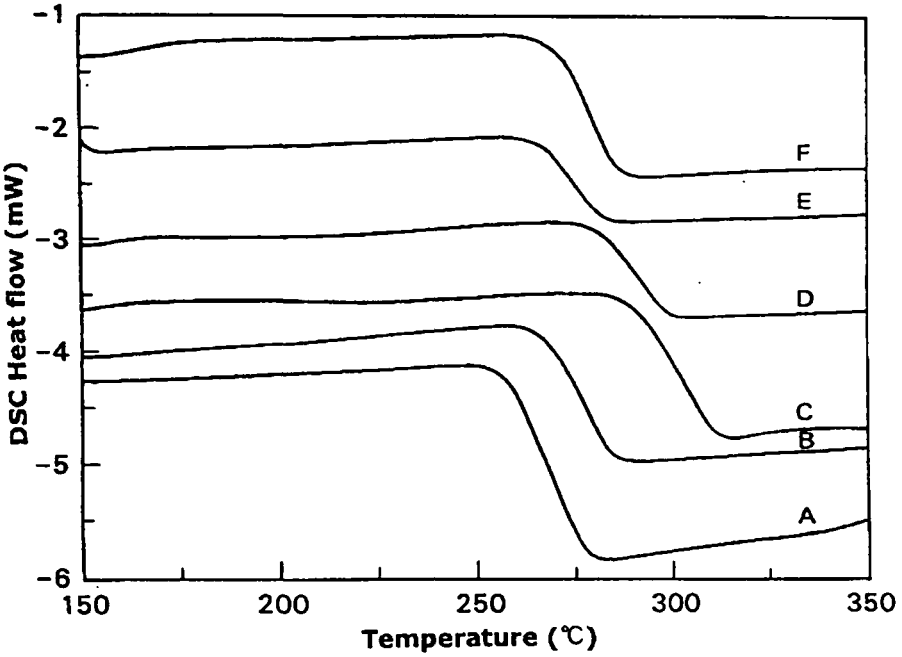

Figure 2. MDSC curves of VN–PbO–TeO_2 glasses.

corresponding to V^{4+} and V^{5+} for different glass compositions. The C_v values were consistent with the dc conductivity (tables 2 and 3) of the glasses.

Figure 3 shows the X-ray photoelectron spectra for V $2p_{3/2}$ of glass A. The main peak is separated from the peak corresponding to V^{5+} with a binding energy of

Table 2. Percentages of V, Pb and Te ions in the glasses, from XPS data.

Glass sample	Composition (at.%) from XPS data										
	V^a	V^{5+}	V^{4+}	VN	$C_v{}^b$	Pb^a	Pb^{2+}	Pb^{4+}	Te^a	Te^{4+}	Te
A	24.09	26.64	65.11	8.25	0.71	5.13	24.90	75.10	11.51	65.60	34.40
B	17.97	29.62	60.92	9.47	0.67	4.64	31.58	68.42	20.57	75.65	24.35
C	12.81	30.36	60.57	8.89	0.66	5.84	39.45	60.55	22.80	85.70	14.30
D	7.06	31.26	58.64	10.10	0.65	4.46	45.80	52.50	39.09	95.53	4.47

[a] Total atomic percentages in the glasses.
[b] $C_v = [V^{4+}]/([V^{4+}]+[V^{5+}])$.

Table 3. Physical parameters obtained from the dc conductivity data.

Sample	σ_0 (Ω^{-1} cm^{-1} K)		Θ_D (K)		α^a (nm^{-1})		$\nu_{ph}{}^b$ (10^{13} Hz)	
	(i)	(ii)	(i)	(ii)	(i)	(ii)	(i)	(ii)
A	3.41×10^{-12}	2.15×10^{-12}	285.7	277.7	55.0	61.9	1.02	1.01
B	1.00×10^{-11}	2.92×10^{-12}	307.6	320.0	53.0	54.7	1.29	0.94
C	1.84×10^{-11}	4.64×10^{-12}	333.3	333.3	51.5	53.4	0.97	0.94
D	2.92×10^{-11}	6.30×10^{-12}	347.8	363.6	50.6	52.8	0.14	0.95
E	3.0×10^{-10}	1.84×10^{-11}	363.6	388.3	—	—	—	—
F	1.16×10^{-9}	3.41×10^{-10}	400.0	416.6	—	—	—	—

(i) Obtained from the $\log_{10}\sigma_{dc}$ versus $10^3/T$ curves (not shown).
(ii) Obtained from the $\log_{10}(\sigma_{dc}T)$ versus $10^3/T$ curves (figure 5).
[a] Calculated from σ_0 at 400 K assuming that $\nu_{ph} = 10^{13}$ Hz.
[b] Calculated from σ_0 at 400 K using the corresponding α values from this table.

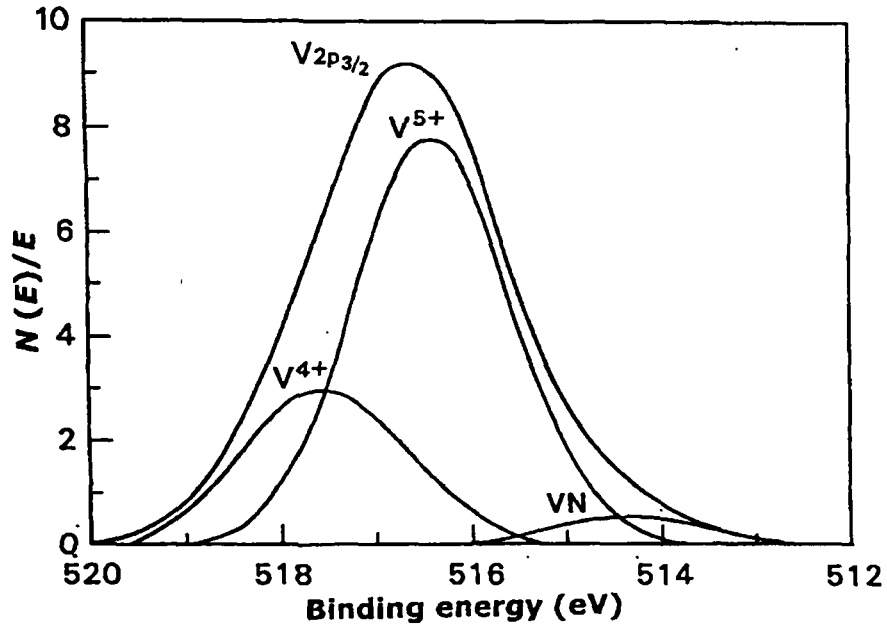

Figure 3. X-ray photoelectron spectra (V $2p_{3/2}$) of 50 mol% VN–10 mol% PbO–40 mol% TeO_2 glass (Mollah *et al.* 2002).

516.60 eV and that corresponding to V^{4-} with a binding energy of 517.56 eV. A peak due to VN with a binding energy of 514.60 eV is observed, suggesting the presence of VN structural units in the glass network. Possible structural units in the glass network may be =V=N–O or ≡V=N–O. The X-ray photoclectron spectra of Pb $4f_{7/2}$ and Te $3d_{5/2}$ of the glasses were also studied. Figures 4(a), (b) and (c) show the relative atomic percentages for V, Pb and Te ions respectively with different valences for the glasses A–D, calculated from an integrated area of each XPS

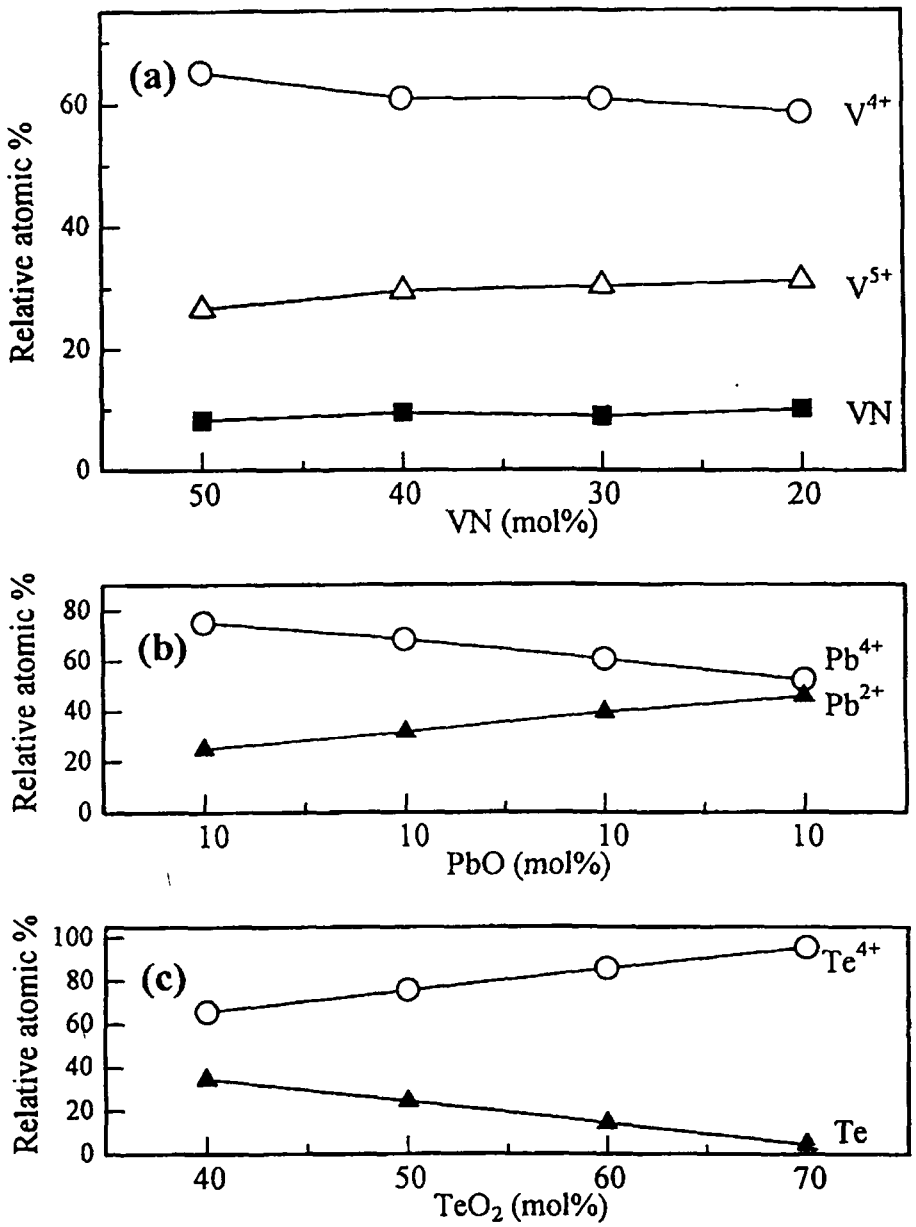

Figure 4. Relative atomic percentages of (a) VN and V, (b) Pb and (c) Te ions in the glasses determined from X-ray photoelectron spectra (Mollah *et al.* 2002).

peak. In figure 4(a), for 50–20 mol% VN (40–70 mol% TeO_2), the VN content present in the glasses varies from 8.25 to 10.10 (table 2). With increasing TeO_2 content, the relative concentration of V^{4+} decreases but that of V^{5+} increases (figure 4 and table 2). This indicates the formation of vanadium oxynitride glasses in the TeO_2 glass network, similar to the oxynitride glasses obtained for SiO_2-based glasses using AlN raw material (Loehman 1979). Figure 4(b) specifies the relative atomic percentages of Pb^{2+} and Pb^{4+} ions in the glasses. The former concentration increases and the latter decreases with increasing TeO_2 content. This may be due to the preferred oxidation of the V ion by O_2 decomposed from TeO_2, which decreases the amount of O_2 necessary for oxidizing PbO. The concentration of Te^{2+} in the glass increases with increase in the TeO_2 content (figure 4(c)), but the Te content decreases with increasing TeO_2. The increasing Te content for larger amounts of VN accompanied by the V^{4+} and V^{5+} contents (figure 4(a)), suggests a reducing reaction of TeO_2 which oxidizes V ions in the glasses on melting. From the presence of VN, V^{4+}, V^{5+}, Pb^{2+}, Pb^{4+}, Te^{4+} and Te ions in the glasses (table 2), the following redox reactions in the melts are inferred:

$$TeO_2 \rightarrow Te + O_2, \tag{1}$$

$$VN + O_2 \rightarrow VO_2 + \tfrac{1}{2}N_2, \tag{2}$$

$$2VO_2 + \tfrac{1}{2}O_2 \rightarrow V_2O_5, \tag{3}$$

$$PbO + \tfrac{1}{2}O_2 \rightarrow PbO_2. \tag{4}$$

Consequently, the above XPS data (figures 3 and 4, and table 2) indicate that N depolymerizes the glass network, as the VN content in the glasses is smaller for the higher stoichiometric VN contents (table 2). This could explain the decrease in T_g and Θ_D with increase in the VN content as found from MDSC and dc conductivity data (tables 1–3).

3.2. *Electrical properties*

The dc conductivity σ_{dc} behaviour of these glasses can be explained using a polaron hopping mechanism with an expression (in the non-adiabatic approximation) of the form (Mott 1968, Austin and Mott 1969, Mott and Davis 1979)

$$\sigma_{dc} = \frac{\sigma_0}{T} \exp\left(\frac{-W}{k_B T}\right), \tag{5}$$

where σ_0 is a pre-exponential factor given by $\nu_{ph} N e^2 R^2 C_v (1 - C_v) \exp(-2\alpha R)/k_B$ where N is the number of TMIs per unit volume, C_v is the ratio of the TMI concentration in the low-valence state to the total TMI concentration as defined earlier, ν_{ph} is an optical-phonon frequency (about 10^{13} Hz), e is the electronic charge, R is the average V–V spacing (proportional to $N^{-1/3}$), α is the wave function decay constant, W is the activation energy, k_B is the Boltzmann constant and T is the absolute temperature. Some of the important parameters such as N, R and C_v of the glasses are given in tables 1 and 2. In the adiabatic case, the integral $I = \exp(-2\alpha R)$ reduces to 1.0.

The activation energy W is given by (Mott 1968, Austin and Mott 1969, Mott and Davis 1979)

$$W = \begin{cases} W_h + \frac{W_d}{2} & \text{for } \begin{cases} T > \frac{\Theta_D}{2}, \\ T < \frac{\Theta_D}{4}, \end{cases} \\ W_d \end{cases} \tag{6}$$

where Θ_D is the Debye temperature defined by $h\nu_{ph} = k_B\Theta_D$, h being the Planck constant, W_h is the polaron-hopping energy equal to $W_p/2$, W_p is the polaron binding energy and W_d is the disorder energy arising from the energy difference of the neighbouring sites.

The value of W_h is estimated from the following relation (Mott 1968, Austin and Mott 1969, Mott and Davis 1979):

$$W_h = \frac{W_p}{2} = \frac{e^2}{4\varepsilon_p}(r_p^{-1} - R^{-1}), \tag{7}$$

where r_p is the polaron radius and ε_p is the effective dielectric constant. The r_p for these glasses are about 0.21–0.25 nm (table 1). The disorder energy W_d is obtained from the Millar–Abrahams (1960) theory as (Mott 1968, Murawski and Gzowski 1976, Murawski *et al.* 1979, Isard 1980)

$$W_d = \frac{0.3e^2}{\varepsilon_s R}, \tag{8}$$

where ε_s is the static dielectric constants of the glasses at high temperatures and low frequencies. This disorder energy W_d might exist between the initial and final sites owing to variations in the local arrangements of ions (Sayer and Mansingh 1972). Mott (1968) proposed that the carriers, having insufficient energy to hop to nearest neighbours, will hop further afield to find sites of comparable energy, in spite of a smaller electron overlap. This approach leads to the dependence of W_d on R (equation (8)). Isard (1980) suggested that it is more appropriate to use an extrapolation of the low-frequency dielectric constant ε_s from electrical measurements down to zero frequency, which are typically in the range 20–30, for the calculation of W_d for the vanadate glasses. However, it should be mentioned that, for the calculation of W_h from equation (7), the value of $1/\varepsilon_p$ $(= 1/\varepsilon_\infty - 1/\varepsilon_s)$ has been proposed by Isard (1980) taking ε_∞ and ε_s as the limiting values above and below respectively the phonon frequency (10^{13} Hz). For this case, ε_s is taken as the limiting high-frequency (10^{10} Hz) value (about 8) from electrical measurements (Isard 1980). We assume here that $\varepsilon_s = 30$, and this value is reasonable as $\varepsilon_s \approx 36$–54 at 500 Hz for V_2O_5–MnO–TeO_2 glasses (Pal *et al.* 2003) and $\varepsilon_s \approx 20$–30 for the vanadate glasses (Isard 1980). The calculated values of W_d are then found to be about 0.04 eV (table 1).

Figure 5 shows an Arrhenius plot of $\log_{10}(\sigma_{dc}T)$. At a particular temperature, the dc conductivity of the glass A is a maximum and that of the glass F is the minimum, consistent with the variation in C_v (table 2). At 360 K, the dc conductivity of the glasses is found to vary from 1.78×10^{-6} to $7.43 \times 10^{-9}\,\Omega^{-1}\,cm^{-1}$ depending on the concentration of VN. This large variation may be due to the change in VN content in the glasses. The slopes of the curves (figure 5) change slightly with T at high temperatures, indicating little modification of the activation energy W. At 444 K, W changes from 0.34 to 0.57 eV and W_h varies between 0.18 and 0.25 eV (table 1).

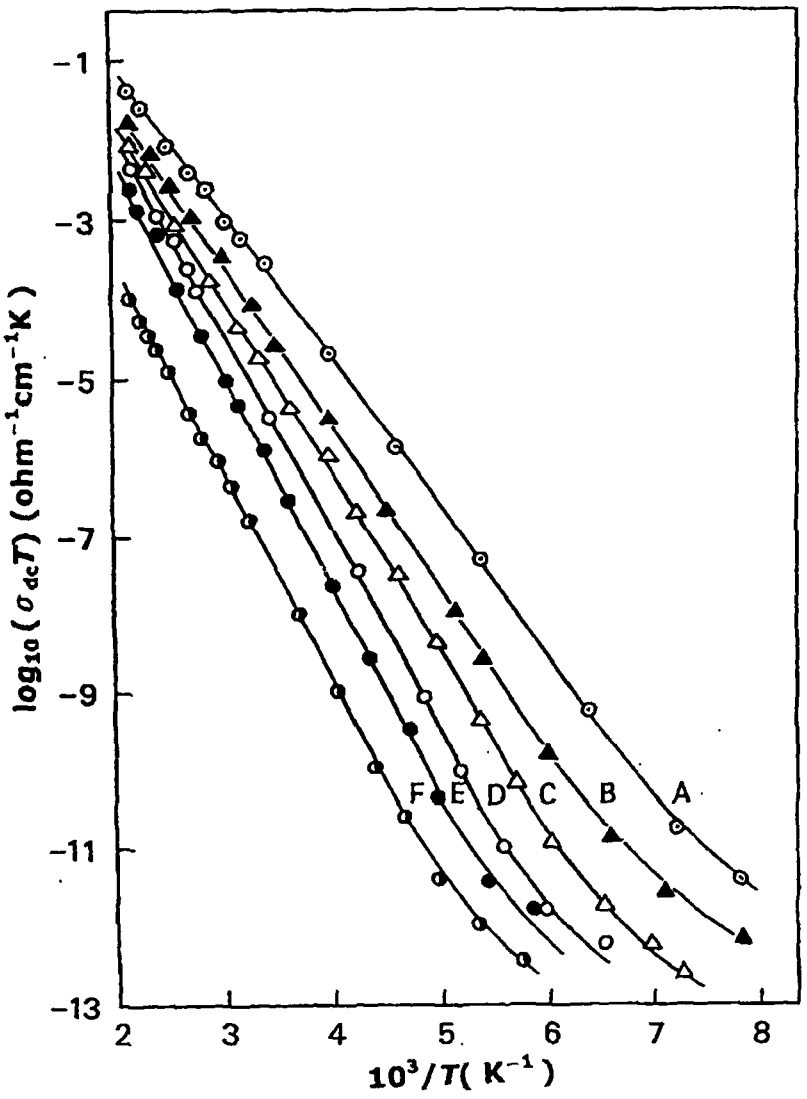

Figure 5. Inverse temperature dependence of the product of dc conductivity and absolute temperature.

The temperature where the linearity of the curves of $\log_{10}(\sigma_{dc}T)$ versus $10^3/T$ (figure 5) deviates is taken as $\Theta_D/2$. Θ_D is the Debye temperature which varies from 277.7 to 416.6 K (table 3), increasing with the decrease in VN content. The variation in $\log_{10}\sigma_{dc}$ and the activation energy W with mole percentage of VN for a fixed mole percentage of PbO is shown in figure 6 at two fixed temperatures (250 and 400 K). σ_{dc} increases and W decreases with increase in VN content.

The significance of the tunnelling term $\exp(-2\alpha R)$ in the σ_0 term of equation (5) can be seen by plotting $\log_{10}\sigma_{dc}$ against W at a fixed temperature. Since the temperature of measurement is T in equation (5), the plot has a slope of $1/k_BT$ for adiabatic hopping as σ_0 is unchanged, while for non-adiabatic hopping the term $\exp(-2\alpha R)$ will also contribute (equation (5)); so a different temperature T will be

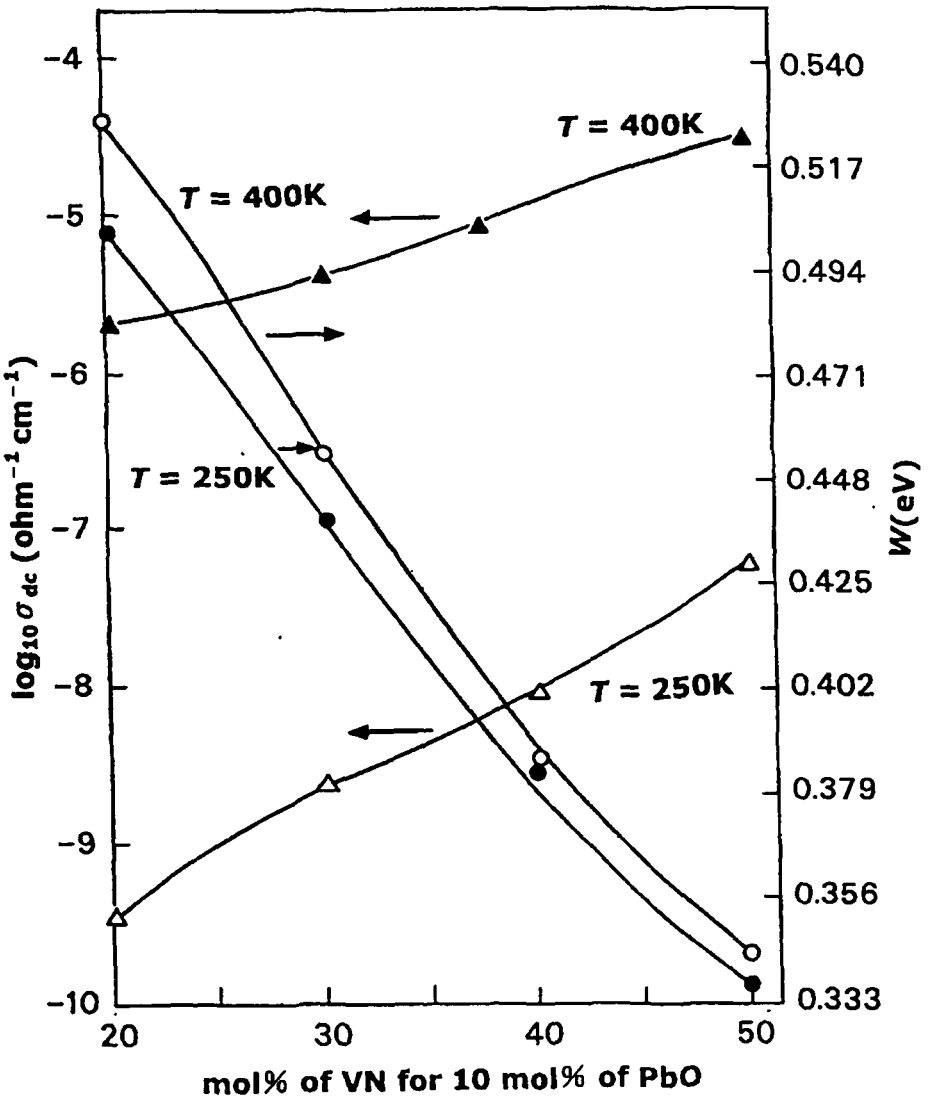

Figure 6. Dependences of dc conductivity and activation energy of vanadium–lead–tellurium oxynitride glasses on mole percentage of VN with a fixed mole percentage 10 mol% of PbO.

calculated from the slope. Thus the temperature T_e estimated from the slope of such a plot (figure 7) should be equal to the experimental temperature T when hopping is considered to be in the adiabatic regime but T_e should become greatly different from T if hopping is thought to be over in the non-adiabatic regime (Sayer and Mansingh 1972, 1983, Dhawan *et al.* 1982, Ghosh and Chaudhuri 1986). Again, if $2\alpha k_B RT \ll W$, equation (5) will reduce to the form in the adiabatic region and $T \approx T_e$. However, if $2\alpha k_B RT \approx W$ and α is independent of composition, then the variation in R with composition will cause a change in the slope of $\log_{10}\sigma_{dc}$ versus W plots, giving T_e different from T. Good agreement between T_e and T can be obtained even if $2\alpha k_B RT \approx W$ and αR is independent of composition

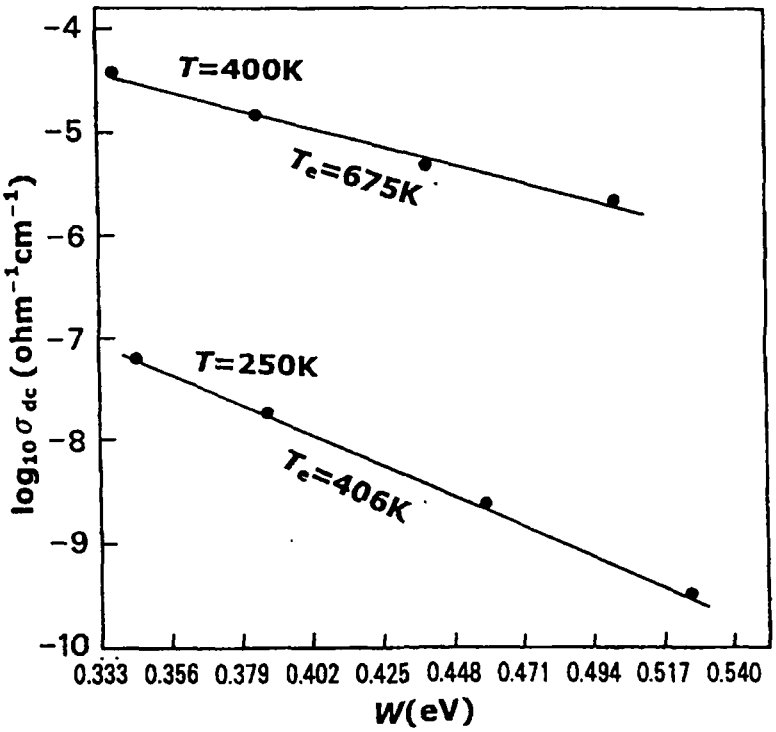

Figure 7. Variation in σ_{dc} with activation energy W for two fixed temperatures (250 and 400 K). The estimated temperatures T_e are obtained from the slopes of the curves (for details, see the text).

(Sayer and Mansingh 1972, 1983). Thus, the degree of agreement between T and T_e is not always sufficient to be able to classify the systems into adiabatic or non-adiabatic; it can, however, provide an indication. In our system, the temperatures predicted from such plots (figure 7) for the experimental temperatures $T=250$ and 400 K are found as $T_e=406$ and 675 K respectively. Thus the higher values of T_e from the corresponding experimental temperatures indicate non-adiabatic SPH conduction in these glasses. However, adiabatic SPH conduction in V_2O_5-containing tellurite glasses for V_2O_5 contents greater than 50 mol% and transport in the non-adiabatic regime for V_2O_5 contents less than 50 mol% have been reported (Mori *et al.* 1993a,b, 1995, 2000, Sakata *et al.* 1996, 1999).

In another approach from Holstein's (1959) relation, one can also infer whether the hopping conduction is in the adiabatic or non-adiabatic region. According to that relation, the polaron bandwidth J should obey the following conditions:

$$J\begin{cases} > H & \text{for adiabatic hopping,} \\ < H & \text{for non-adiabatic hopping conduction,} \end{cases} \tag{9}$$

where

$$H = \left(\frac{2k_B T W_h}{\pi}\right)^{1/4} \left(\frac{h\nu_{ph}}{\pi}\right)^{1/2}. \tag{10}$$

The condition for small-polaron formation is $J < W_h/3$. An evaluation of J can be made from the approximate relation (Holstein 1959) for high temperatures:

$$J(T) \approx 0.67 h\nu_{ph}\left(\frac{T}{\Theta_D}\right)^{1/4} = 0.027\left(\frac{T}{\Theta_D}\right)^{1/4}, \tag{11}$$

and for ground-state bandwidth $J(0) = 3h\nu_{ph} = 0.12$ eV. In the present system, from table 4, we find that $H \approx 0.05$ eV, $J(400\text{ K}) \approx 0.03$ eV, $J(80\text{ K}) \approx 0.02$ eV and $W_h/3 \approx$ 0.06–0.08 eV. Since J (for both 400 and 80 K) is less than H and J (for both 400 and 80 K) is less than $W_h/3$, we conclude that dc conduction in the vanadium–lead–tellurium oxynitride glasses occurs by SPH in the non-adiabatic regime. The value of the small-polaron coupling constant γ_p, which is a measure of electron–phonon interaction in these glasses, can be estimated from the relation $\gamma_p = 2W_h/h\nu_{ph}$ (Mott 1968, Austin and Mott 1969, Mott and Davis 1979). The values for γ_p, using $\nu_{ph} = 10^{13}$ Hz, vary from 8.75 to 14.16 (table 4). Austin and Mott (1969) suggested that a value of $\gamma_p > 4$ usually indicates strong electron–phonon interaction in the solids. From the values of γ_p, we have evaluated the ratio of the polaron mass m_p to the rigid-lattice effective mass m^* using the relation (Mott 1968)

$$m_p = \frac{h^2}{8\pi^2 JR^2}\exp(\gamma_p) = m^*\exp(\gamma_p). \tag{12}$$

The calculated values of m_p/m^* are found to vary from 6.32×10^3 to 1.42×10^6 (table 4), values that are very large and indicate strong electron–phonon interaction in these glasses.

Schnakenberg (1968) suggested that, with decreasing temperature, a single optical-phonon process replaces the multiphonon processes and the activation energy for conduction should follow the relation

$$\frac{W}{W'} = \frac{\tanh(h\nu_{ph}/4k_BT)}{h\nu_{ph}/4k_BT}, \tag{13}$$

where W' is the high-temperature activation energy. The variation in the theoretical as well as the experimental W/W' for glass A with temperature is shown in figure 8. It is seen that they both decrease with decrease in temperature. The same behaviour

Table 4. Parameters for non-adiabatic SPH conduction.

	J (eV)							
	$T = 400$ K		$T = 80$ K		H^a	$W_h/3$		
Sample	(i)	(ii)	(i)	(ii)	(eV)	(eV)	γ_p	m_p/m^*
A	0.03	0.03	0.02	0.02	0.05	0.06	14.16	1.42×10^6
B	0.03	0.03	0.02	0.02	0.05	0.06	8.75	6.32×10^3
C	0.03	0.03	0.02	0.02	0.05	0.06	8.84	6.69×10^3
D	0.03	0.03	0.02	0.02	0.05	0.07	9.96	2.11×10^4
E	0.03	0.03	0.02	0.02	0.05	0.08	11.99	1.61×10^5
F	0.03	0.03	0.02	0.02	0.05	0.07	10.39	3.27×10^4

(i) Values of Θ_D used for the calculation of J is obtained from the $10^3/T$ versus $\log_{10}\sigma_{dc}$ curves (not shown).
(ii) Values of Θ_D used for the calculation of J is obtained from the $10^3/T$ versus $\log_{10}(\sigma_{dc}T)$ curves (figure 5).
[a] H is calculated for $T = 300$ K which is within the range 80–400 K for which J values are given.

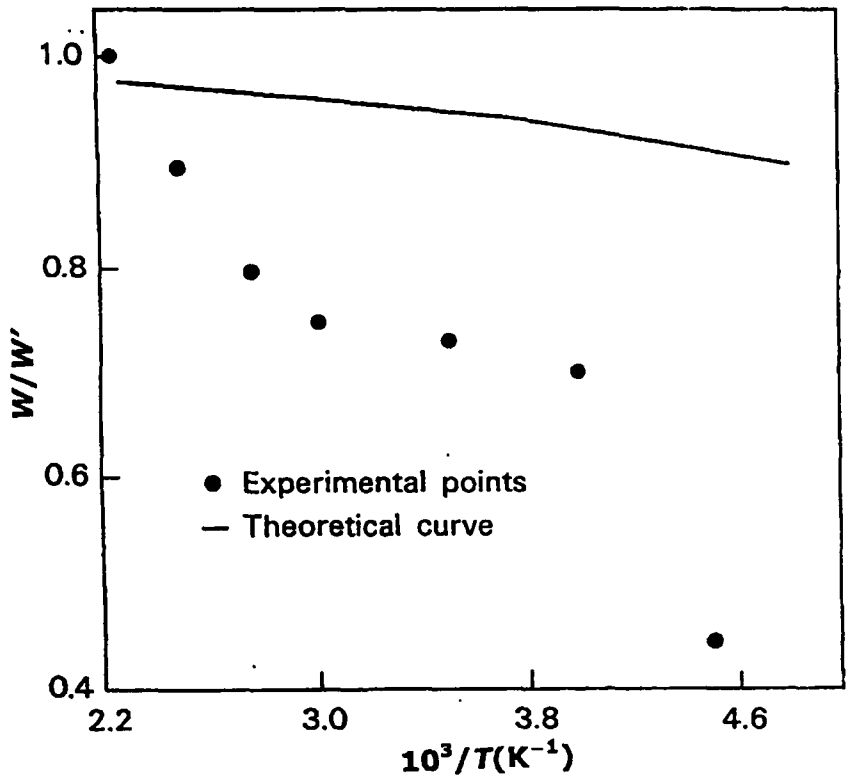

Figure 8. Plot of W/W' versus $10^3/T$ for the 50 mol% VN–10 mol% PbO–40 mol% TeO_2 glass (sample A). The theoretical curve is obtained from equation (13). The same behaviour is also observed for other glasses.

has also been observed for other glasses in this series as well as other TMO glasses (Mollah *et al.* 1992, 1995, Som *et al.* 1992, Chatterjee *et al.* 1996). The decrease in activation energy with decrease in temperature is consistent with the polaron-hopping model for dc conduction. Consequently the dc conduction in this glass system can be well explained by non-adiabatic SPH conduction.

At sufficiently low temperatures (below $\Theta_D/4$), where the polaron binding energy is small, the static disorder energy of the glass plays a dominant role in the conduction process. In this temperature range, Mott's (1968) VRH model might be considered applicable. According to this model, the conductivity is given by

$$\sigma_{dc} = Q \exp\left(-\frac{P}{T^{1/4}}\right), \tag{14}$$

where

$$P = 4\left(\frac{2\alpha^3}{9\pi k_B N(E_F)}\right)^{1/4} \tag{15}$$

and

$$Q = \frac{e^2}{2(8\pi)^{1/2}} \nu_{ph} \left(\frac{N(E_F)}{\alpha k_B T}\right)^{1/2}, \tag{16}$$

$N(E_F)$ being the density of states at the Fermi level. According to equation (14), plots of $\log_{10}\sigma_{dc}$ versus $T^{-1/4}$ should be straight lines. In contrast we see from figure 9 that this is not the case and so the VRH model is not appropriate to explain the data at low temperatures ($T < \Theta_D/2$).

Greaves (1973, 1982) suggested VRH conduction for the intermediate temperature range (temperatures between $\Theta_D/4$ and $\Theta_D/2$) and derived an expression for the conductivity as

$$\sigma_{dc}T^{1/2} = L\exp\left(-\frac{Q}{T^{1/4}}\right), \tag{17}$$

where Q and L are constants. The slope of $\log_{10}(\sigma_{dc}T^{1/2})$ versus $T^{1/4}$ plots is given by

$$Q = 2.1\left(\frac{\alpha^3}{k_B N(E_F)}\right)^{1/4} = 2.4\left(\frac{W_d(\alpha R)^3}{k_B}\right)^{1/4}. \tag{18}$$

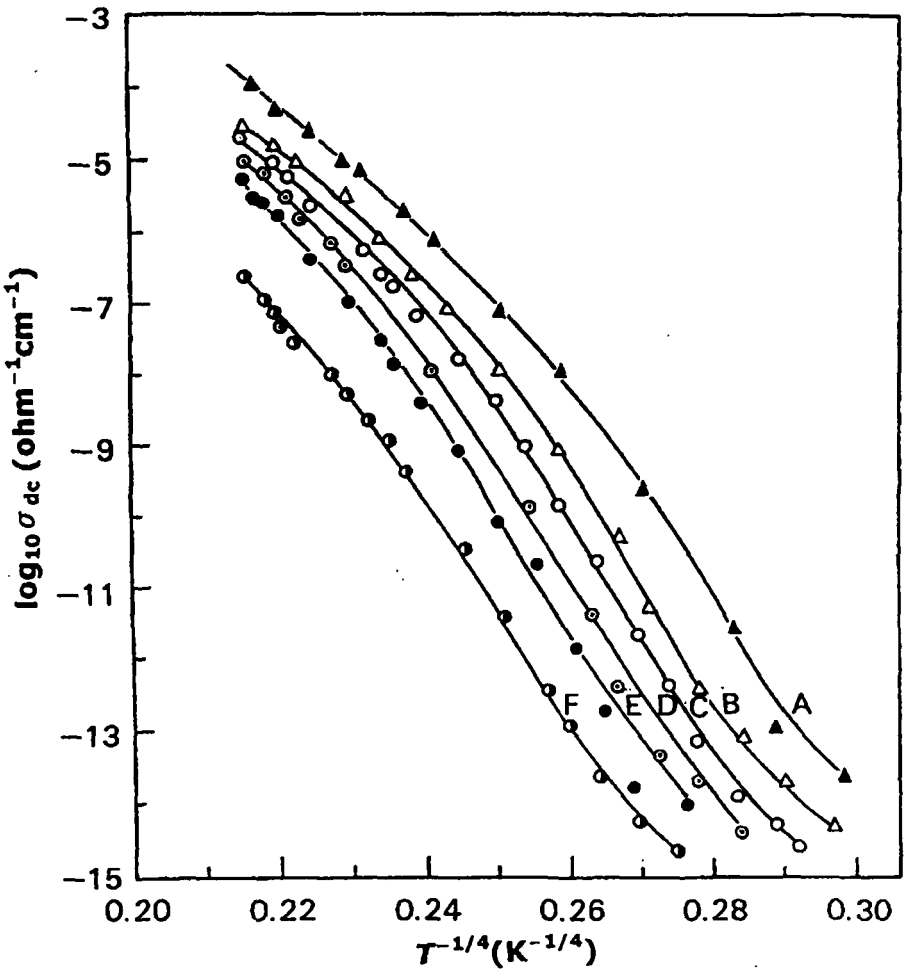

Figure 9. Plots of $\log_{10}\sigma_{dc}$ versus $T^{1/4}$ for the different VN–PbO–TeO_2 glasses.

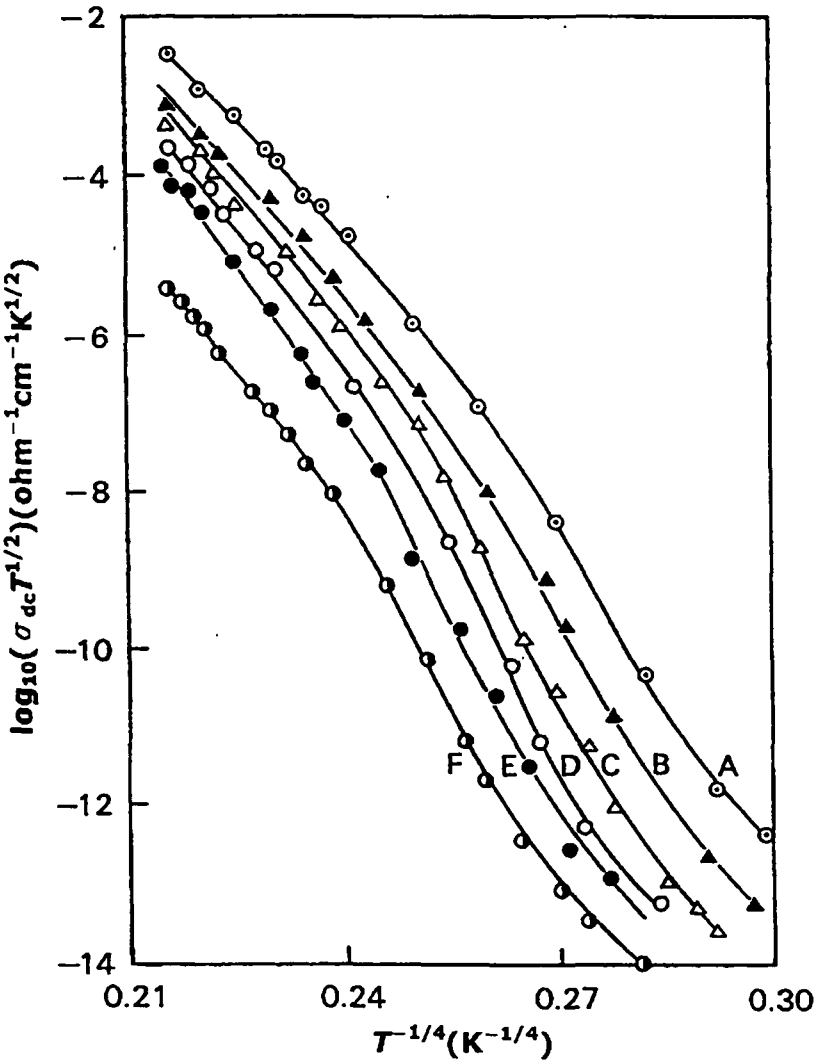

Figure 10. Plots of $\log_{10}(\sigma_{dc}T^{1/2})$ versus $T^{1/4}$ for the different VN–PbO–TeO_2 glasses.

Figure 10 shows that such plots are nonlinear. Thus neither of the VRH models (Mott 1968, Greaves 1973, 1982) is suitable for explaining the dc conductivity data of these glasses at temperatures lower than $\Theta_D/2$.

In an alternative approach, we tried to fit the dc conductivity data to a multi-phonon tunnelling model (Shimakawa and Miyake 1988, Shimakawa 1989) over the entire temperature range. According to Mott and Davis (1979), the dc hopping conductivity is given by

$$\sigma_{dc} = \frac{N(ed)^2\Gamma}{6k_BT}, \tag{19}$$

where N is the number of localized electrons, d is the hopping distance and Γ is the hopping rate. If the disorder energy Δ is less than the maximum phonon energy $h\nu_D$,

Table 5. Parameters for multiphonon tunnelling conduction.

Sample	A	B	C	D	E	F
ν_D[a] (10^{12} Hz)	5.83	6.49	6.89	7.35	7.78	8.44
ν_0[b] (10^{11} Hz)	5.04	5.71	6.09	6.57	6.80	7.42
$-\log_{10}\sigma'_{dc}$ (Ω^{-1} cm^{-1})	9.73	10.80	11.39	11.79	13.00	14.86
p	12.4	11.4	13.0	13.0	15.3	16.7
γ	3.12	3.17	3.08	3.07	2.99	3.11
Δ (eV)	0.03	0.03	0.03	0.04	0.04	0.05
E_M (10^{-4} eV)	4.22	4.17	5.58	5.95	6.67	8.36
G	3.17	2.44	2.87	2.63	2.74	2.90

[a] ν_D is calculated from $h\nu_D = k_B\Theta_D$.
[b] $\nu_0 = (R/\alpha^{-1})\nu_D$.

a single-phonon process (either nearest-neighbour or VRH) should explain the dc conduction (Mott 1968, Emin 1974, 1975, Shimakawa and Miyake 1988, Shimakawa 1989). When Δ is comparable with $h\nu_D$, and the Bohr radius α^{-1} is much larger than the lattice constant R, single-phonon tunnelling becomes less important (Mott 1968) and multiphonon processes make the dominant contribution to the electronic conduction. In the present system, the maximum $h\nu_D$ is equal to 0.034 eV (using the maximum ν_D from table 5), which is comparable with the disorder energy (about 0.04 eV) of these glasses (table 1). So it seemed that multiphonon tunnelling processes might be the more appropriate one to describe the dc conductivity data.

In multiphonon tunnelling of localized electrons, the hopping rate is given by (Shimakawa and Miyake 1988, Shimakawa 1989)

$$\Gamma = \nu_0 \exp(-\gamma p) \exp(-2\alpha d)\left(\frac{T}{T_0}\right)^p, \tag{20}$$

where $p = \Delta/h\nu_0$, $T_0 = h\nu_0/k_B$ and ν_0 is the acoustic phonon frequency. Since localized electrons with large radius couple only with long-wavelength phonons, ν_0 is smaller than ν_D, and is given by $\nu_0 = (R/\alpha^{-1})\nu_D$. For the weak-coupling case, γ lies between 2 and 3 (Shimakawa and Miyake 1988, Shimakawa 1989, Sakata *et al.* 1999). Once again as $N = k_B T N(E_F)$, σ_{dc} is proportional to T^p (from equations (19) and (20)). The exponent p may have a finite distribution but the average value is a non-integral number and ν_0 is distributed around a certain value (Shimakawa and Miyake 1988, Shimakawa 1989). According to this model the dc conductivity is given by $\sigma_{dc} = \sigma'_0 T^p$ where σ'_0 is a constant. However $\log_{10}\sigma_{dc}$ versus $\log_{10} T$ curves, as shown in figure 11, do not present a linear relationship of σ_{dc} with T. In spite of this, approximate values of p can be obtained from the data. The values are comparable with those obtained for V_2O_5–TeO_2, V_2O_5–P_2O_5 (Shimakawa and Miyake 1988, Shimakawa 1989) and V_2O_5–CoO–TeO_2 (Sakata *et al.* 1999) glasses. We have also calculated ν_D with the relation $h\nu_D = k_B\Theta_D$ using the values of Θ_D from table 3. Assuming that $\alpha^{-1} = 4$ nm and using R from table 1, together with the above ν_D, we have calculated ν_0. Typical values of ν_D, ν_0, T_0 and p for these glasses are given in table 5. The value of the disorder energy Δ is estimated from the relation $\Delta/h\nu_0 = p$ and found to be comparable with W_d (tables 1 and 5). γ of these glasses is found to vary from 2.99 to 3.17 (table 5). Again $\gamma = \ln(\Delta/E_M) - 1$, where E_M is a measure of the electron–lattice coupling strength (Mott 1968, Austin and Mott 1969, Mott and Davis 1979) and $G = E_M k_B T/(h\nu_0)^2$. The calculated values of E_M and G are shown

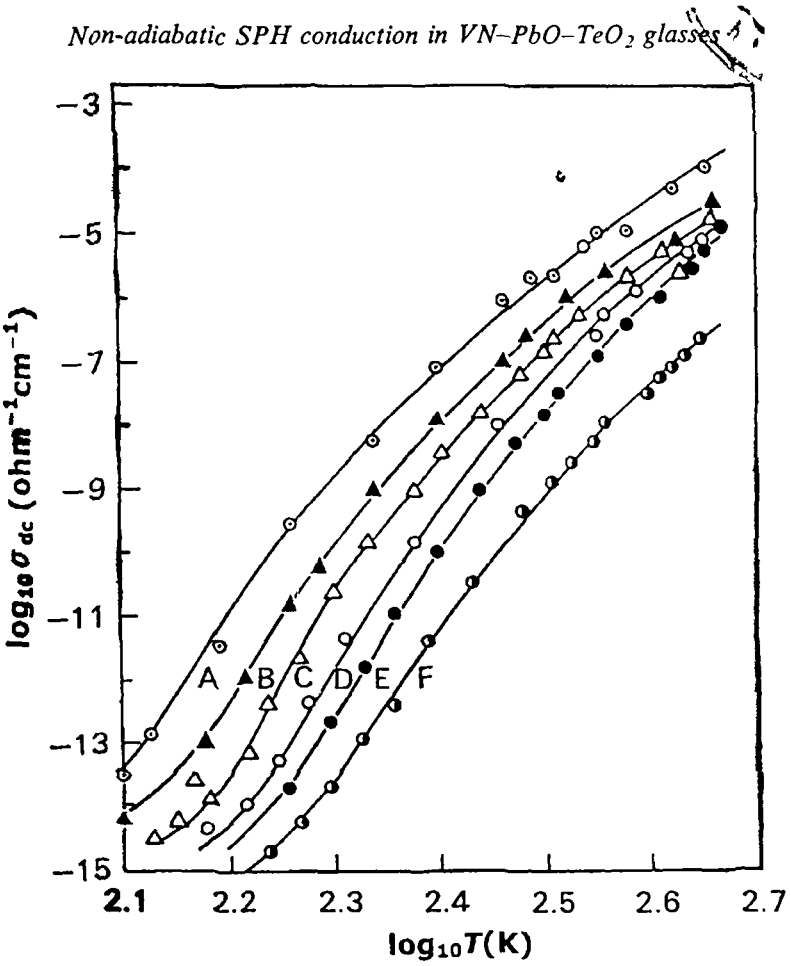

Figure 11. Graphs of $\log_{10}\sigma_{dc}$ and $\log_{10}T$ for the different vanadium–lead–tellurium oxynitride glasses

in table 5. If $\gamma = 2$–3 (Mott 1968) and $G < 1$ (Englman and Jortner 1970), multiphonon conduction of weakly coupled electrons is expected to be the most probable carrier transport process. In contrast, for the present vanadium–lead–tellurium oxynitride glasses, $\gamma > 3$ and $G > 1$ (table 5) This, together with the nonlinearity of the plots in figure 11, lead us to conclude that multiphonon tunnelling does not provide an adequate explanation of the dc conductivity data.

§4. Conclusions

Oxynitride glasses in the system VN–PbO–TeO_2 have been prepared by melt quenching, and the mechanism of dc conduction in these glasses investigated XPS analysis reveals the presence of VN (equivalent content of 1–2 at % N in the glasses) and suggests either =V=N–O or ≡V=N–O as a possible structural unit The T_g and Θ_D of the glasses are found to decrease with increase in the VN content The dc conductivity of the glasses decreases with reduction in the VN content (for a fixed mole percentage of PbO). VRH models (below $\Theta_D/2$) and multiphonon tunnelling (for the entire temperature region) cannot explain the dc conductivity data The estimated temperature from the slope of W versus $\log_{10}\sigma_{dc}$ at fixed temperatures

suggests that conduction occurs by SPH in the non-adiabatic region. By utilizing the SPH model of Mott (1968) and Austin and Mott (1969), the Holstein (1959) condition and Schnakenberg's (1968) suggestion, it is indeed most likely that transport of electrons in this glassy system occurs by SPH conduction in the non-adiabatic regime for temperatures above $\Theta_D/2$ (139–208 K, for the present glasses).

ACKNOWLEDGEMENTS

The authors are grateful to Inter University Consortium, Department of Atomic Energy Facilities (DAEF), Indore, India, for providing XRD and MDSC measurement facilities. We are also indebted to Tokyo Metropolitan Industrial Technology Research Institute, Japan, for their expertise in XPS assessment. This work was financially supported by University Grants Commission (UGC), Government of India, from UGC project (F. 10-31/98).

REFERENCES

AUSTIN, I. G., and MOTT, N. F., 1969, *Adv. Phys.*, **18**, 41.
CHAKRABORTY, S., SATOU, H., and SAKATA, H., 1997, *J. appl. Phys.*, **82**, 5520.
CHATTERJEE, S., BANERJEE, S., MOLLAH, S., and CHAUDHURI, B. K., 1996, *Phys. Rev.* B, **53**, 5942.
DHAWAN, V. K., MANSINGH, A., and SAYER, M., 1982, *J. non-crystalline Solids*, **51**, 87.
DOWEIDAR, H., GOHAR, I. A., MEHAHED, A. A., and EL DAMRAWI, G. M., 1991, *Solid St. Ionics*, **46**, 275.
DOWEIDAR, H., MEHAHED, A. A., and GOHAR, I. A., 1985, *J. Phys.* D, **19**, 1939.
ELMER, T. H., and NORDBERG, M. E., 1967, *J. Am. Ceram. Soc.*, **50**, 275.
EMIN, D., 1974, *Phys. Rev. Lett.*, **32**, 303; 1975, *Adv. Phys.*, **24**, 305.
ENGLMAN, R., and JORTNER, J., 1970, *Molec. Phys.*, **18**, 145.
FRISCHAT, G. H., and SCHRIMPF, C., 1980, *J. Am. Ceram. Soc.*, **63**, 714.
GHOSH, A., and CHAUDHURI, B. K.,1986, *J. non-crystalline Solids*, **83**, 151.
GREAVES, G. N., 1973, *J. non-crystalline Solids*, **11**, 427; 1982, *ibid.*, **51**, 87.
HIRASHIMA, H., WATANABE, Y., and YOSHIDA, T., 1987, *J. non-crystalline Solids*, **95–96**, 825.
HOLSTEIN, T., 1959, *Ann. Phys. (N.Y.)*, **8**, 325, 343.
ISARD, J. O., 1980, *J. non-crystalline Solids*, **42**, 371.
JACK, K. H., 1976, *J. Mater. Sci.*, **11**, 1135.
LOEHMAN, R. E., 1979, *J. Am. Ceram. Soc.*, **62**, 491; 1980, *J. non-crystalline Solids*, **42**, 433.
MAKISHIMA, A., MITOMO, M., TANAKA, H., LI, N., and TSUTUMI, M., 1980, *J. Ceram. Soc. Japan*, **88**, 701.
MILLER, A., and ABRAHAMS, E., 1960, *Phys. Rev.*, **120**, 745.
MOLLAH, S., HIROTA, K., and SAKATA, H., 2002, *Physica scripta*, **T97**, 160.
MOLLAH, S., SOM, K. K., BOSE, K., CHAKRABORTY, A. K., and CHAUDHURI, B. K., 1992, *Phys. Rev.* B, **46**, 11 075.
MOLLAH, S., SOM, K. K., CHAKRABORTY, S., BERA, A. K., CHATTERJEE, S., BANERJEE, S., and CHAUDHURI, B. K., 1995, *Phys. Rev.* B, **51**, 17 512.
MORI, H., IGARASHI, J., and SAKATA, H., 1993a, *J. Ceram. Soc. Japan*, **101**, 1351; 1995, *Glastech. Ber.*, **68**, 327.
MORI, H., KITAMI, T., and SAKATA, H., 1993b, *J. Ceram. Soc. Japan*, **101**, 347; 1994, *J. non-crystalline Solids*, **168**, 157.
MORI, H., MATSUNO, H., and SAKATA, H., 2000, *J. non-crystalline Solids*, **276**, 78.
MORI, H., and SAKATA, H., J. 1997, *J. Mater. Sci.*, **32**, 5243.
MOTT, N. F., 1968, *J. non-crystalline Solids*, **1**, 1; 1969, *Phil. Mag.*, **19**, 835.
MOTT, N. F., and DAVIS, E. A., 1979, *Electronic Processes in Non Crystalline Materials*, Second edition (Oxford: Clarendon).
MULFINGER, O. H., 1966, *J. Am. Ceram. Soc.*, **49**, 462.
MURAWSKI, L., CHUNG, C. H., and MACKENZIE, J. D., 1979, *J. non-crystalline Solids*, **32**, 91.
MURAWSKI, L., and GZOWSKI, O., 1976, *Acta Phys. Polonica* A, **50**, 463.
NAKAMURA, S., and ICHINOSE, N., 1987, *J. non-crystalline Solids*, **95–96**, 849.

PAL, M., SEGA, K., CHANDHURI, B. K., and SAKATA, H., 2003, *Phil. Mag.*, **83**, 1379.
QIU, H. H., KUDO, M., and SAKATA, H., 1997, *Mater. Chem. Phys.*, **51**, 233.
QIU, H. H., MORI, H., SAKATA, H., and HIRAYAMA, T., 1995, *J. Ceram. Soc. Japan*, **103**, 32.
SAKATA, H., AMANO, M., and YAGI, T., 1996, *J. non-crystalline Solids*, **194**, 198.
SAKATA, H., SEGA, K., and CHAUDHURI, B. K., 1999, *Phys. Rev.* B, **60**, 3230.
SAKURAI, Y., and YAMAKI, J., 1985, *J. Electrochem. Soc.*, **132**, 512.
SATOU, H., and SAKATA, H., 2000, *Mater. Chem. Phys.*, **65**, 186.
SAYER, M., and MANSINGH, A., 1972, *Phys. Rev.* B, **6**, 4629; 1983, *J. non-crystalline Solids*, **58**, 91.
SCHNAKENBERG, J., 1968, *Phys. Stat. Sol.*, **28**, 623.
SHIMAKAWA, K., 1989, *Phil. Mag.* B, **60**, 377.
SHIMAKAWA, K., and MIYAKE, K., 1988, *Phys. Rev. Lett.*, **61**, 994.
SOM, K. K., MOLLAH, S., BOSE, K., and CHAUDHURI, B. K., 1992, *Phys. Rev.* B, **45**, 1655.

ENN Encyclopedia of Nanoscience and Nanotechnology
www.aspbs.com/enn

Ferroelectric Nanocrystal Dispersed Oxide Glasses

B. K. Chaudhuri

Indian Association for the Cultivation of Science, Kolkata, India; and National Sun-Yat Sen University, Kaohsiung, Taiwan, Republic of China

H. Sakata

Tokai University, Kitakaname, Hiratsuka, Kanagawa, Japan

S. Mollah

National Sun-Yat Sen University, Kaohsiung, Taiwan, Republic of China; and Aligarh Muslim University, Aligarh, India

H. D. Yang

National Sun-Yat Sen University, Kaohsiung, Taiwan, Republic of China

CONTENTS

1. INTRODUCTION

During the last two decades, semiconducting properties of many multicomponent and transition metal oxide (TMO) and other metal oxide glasses have been studied because of their probable technological applications [1–4] in optical and electrical memory switches, oxygen sensors, etc. The high temperature ($T > \theta_D/2$, θ_D being the Debye temperature) conductivity data in many of these glasses, for example, V_2O_5–TeO_2 [5], V_2O_5–Bi_2O_3 [6], V_2O_5–P_2O_5 [7], V_2O_5–MnO–TeO_2 [8], V_2O_5–SnO–TeO_2 [9], V_2O_5–P_2O_5–TiO_2 [10], V_2O_5–CoO–TeO_2 [11], etc., were explained by using the "small polaron" hopping (SPH) model [12–15] based on strong electron–phonon interaction. On the other hand, in the low temperature phase ($T < \theta_D/2$), a variable-range hopping (VRH) conduction mechanism [15, 16] with $T^{-1/4}$ dependence was used to explain the conductivity data. The dielectric constants of these glasses are, in general, very low and follow Debye-type dielectric relaxation behavior. Another class of semiconducting glasses like CdS nanoparticles dispersed in sol–gel derived polymers [17], NiO–SiO_2 nanocomposites [18], ZnS nanocrystals stabilized in silica [19], etc. have been studied. Recently Itoigawa et al. [20] also observed the formation of nanosize silver and bismuth particles, respectively, in the Na_2O–B_2O_3–Ag_2O and Na_2O–B_2O_3–BiO_3 glasses. Lately Sakuri and Yamaki [2] reported the presence of such nanocrystalline phases in the V_2O_5–CoO–TeO_2 glass following multiphonon tunneling conduction mechanism. In the high temperature range (above $\theta_D/2$), these glasses also followed the SPH conduction mechanism but the VRH mechanism was found to be

ISBN: 1-58883-059-4/$35.00

not strictly followed [2] as these glasses showed extremely large values of the density of states (DOS) at the Fermi level $N(E_F)$, which is not possible. Similarly, Ag_2O doped Bi–Sr–Ca–Cu–O glasses, precursors for high T_c superconductors, also dispersed with nanocrystalline silver particles showed a high value [21] of $N(E_F)$ estimated from the VRH model. But none of these nanocrystal-dispersed glasses are ferroelectric (FE) or they do not show high dielectric permittivity. However, some of the TMO glasses containing $BaTiO_3$, $PbTiO_3$, TeO_2, etc. are found to show FE behavior due to the presence of nanocrystalline phases.

The aforementioned ferroelectric behavior in nanocrystals of pure FE material like $PbTiO_3$ is, however, not new [22]. Glass ceramics containing ferroelectric phases have been studied for long time to obtain useful dielectric and electro-optic properties [23–26]. Nanophase materials and nanocomposites, characterized by an ultrafine grain size (<50 nm), have created high interest in recent years by virtue of their unusual mechanical, electrical, optical, and magnetic properties. Pure nanocrystalline ferroelectric $PbTiO_3$ studied earlier showed a critical size of the nanocrystals [27] (different for different systems) at which the dielectric constant showed a maximum value. There is, however, a large difference in the ferroelectric behavior (Curie temperature, dielectric constant, polarization, etc.) of the bulk and its nanocrystalline counterpart [27]. But still today, ferroelectricity in pure glass has not been discovered. Ferroelectricity in liquid crystalline phase has, however, been observed [28].

Our major interest in this chapter is to report the synthesis, characterization, and study of transport and other properties of such FE glass–nanocomposite (hereafter referred to as FGNC) materials. It has also been shown how different theoretical models are used to explain the electrical transport and dielectric relaxation behavior of these FGNCs. This chapter will foeus on this new class of materials for further theoretical and experimental studies and also find new applications of the glass–nanocrystal composites showing giant dielectric permittivity.

2. FERROELECTRIC NANOCRYSTAL DISPERSED OXIDE GLASSES

Recently it has been observed that some multicomponent oxide glasses [29–39] dispersed with ferroelectric nanocrystalline phases are formed for suitable choice of the glass compositions with TiO_2, $BaTiO_3$, $PbTiO_3$, $SrTiO_3$, $PbZrO_3$, $KTiOPO_4$, $Bi_2VO_{5.5}$, $Li_2Ge_7O_{15}$, PbS, etc. Some of these nanocrystal-dispersed glasses (referred to as FGNC) are found to show ferroelectric or relaxor type ferroelectric behavior [29–30, 40–43]. Figure 1 schematically represents the nanocrystals dispersed in the glassy matrix. Some important parameters of studied FGNC materials (both opaque and transparent) are shown in Table 1 for comparison.

Many low melting TMO glasses like vanadium phosphate glasses (V_2O_5–P_2O_5, for example), containing different concentrations of TiO_2, $BaTiO_3$, $PbTiO_3$ etc., have been prepared in recent years, which contain nanocrystalline ferroelectric phases embedded in the glass matrix [29, 30]. All these FGNCs are, however, opaque. The alkali metal doped

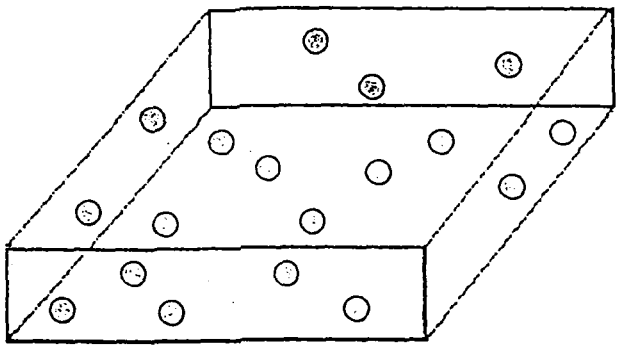

Figure 1. Schematic diagram of a ferroelectric nanocomposite glass. The dispersed nanocrystals are shown by dark black spots in the glass matrix.

Bi–Sr–Ca–Cu–A–O (A = Li, K, Na) glasses are also found to be ferroelectric for typical concentrations [42, 44]. As mentioned, the dielectric constants of these opaque TMO glasses are found to be extremely large (more than $BaTiO_3$) [30, 44]. Such a giant dielectric constant has also been obtained very recently in crystalline $CaCu_3Ti_4O_{12}$ oxide [45, 46] and La containing $PbTiO_3$ [47]. These materials of high dielectric constant are very important for their applications in devices. However, the origin of such a high dielectric constant is not yet clearly elucidated. In the nanoparticle dispersed glassy systems, the presence of nanocrystalline TiO_2, $BaTiO_3$, $PbTiO_3$, $SrTiO_3$, $PbZrO_3$, $KTiOPO_4$, $Bi_2VO_{5.5}$, $Li_2Ge_7O_{15}$, PbS, etc. phases are considered to be responsible for giant dielectric constant. As stated, this is a new class of material of immense technological as well as fundamental importance. By varying the glass compositions or the quenching rate, the size as well as the concentration of the FE nanoparticles/clusters can be varied.

The amorphous characters in the aforementioned oxide glasses and FGNCs are, in general, examined by an X-ray powder diffraction (XRD) technique. Nevertheless, depending on the smaller size and concentrations of the embedded nanocrystals, XRD is not sufficient to detect the presence of the nanocrystals in these glasses and FGNCs. XRD simply indicates amorphous character of these systems. Transmission electron microscopic (TEM) study can clearly reveal the presence of nanocrystalline phases in these FGNC materials. Some physical properties (like high dielectric constant) also indicate the presence of such nanocrystalline phase in some typical TMO glasses. It is also noticed from the TEM studies that many of the semiconducting TMO glasses, earlier reported to be pure homogeneous glasses, are found to contain nanocrystalline particles or clusters of different sizes (5–100 nm) and concentrations embedded in the corresponding glass matrices. Using the TEM technique, very little microstructural study of the semiconducting glassy system was, however, accomplished earlier [6, 11]. It is found that the size and concentration of the nanocrystals affect the transport, optical, and other properties of these ferroelectric nanocrystal-dispersed glasses. This behavior is similar to that observed in ferroelectric materials, for example, $PbTiO_3$ where dielectric permittivity and other properties strongly depend on the grain sizes [22].

Table 1. Some important physical parameters of different ferroelectric glass nanocrystal composites.

Glass matrix/FE nanoparticle	Cluster size (nm)	T_g (K)	T_c (K)	ε' at 1 kHz and 300 K	Ref.
$70(80V_2O_5–20PbO)/30BaTiO_3$	70–90	300	393	3.5×10^4	[30]
$50SrB_4O_7/50Bi_2VO_{5.5}$	15	730	763	3.2×10^3	[31, 32]
$50.5PbO–25.5ZrO_2 24TiO_2/PbS$	15.3	—	—	3.5×10^3	[34]
$80SiO_2/20KTiOPO_4$(KTP)	10–50	600	—	—	[35]
$(12Li_2O–88GeO_2)/Li_2Ge_7O_{15}$	10	—	283	—	[36–38]
$10(90V_2O_5–10P_2O_5)/90BaTiO_3$	~100	250	290	—	[50]

Note: T_g, T_c, and ε' represent, respectively, the glass transition temperature, Curie temperatures, and dielectric constants.

It was reported earlier [48] that the TMO glasses prepared with $BaTiO_3$, etc. contain nanocrystalline clusters and these FGNC samples, for example, $V_2O_5–Bi_2O_3 + xBaTiO_3$, showed giant dielectric constants because of the presence of nanocrystal/clusters of $BaTiO_3$ embedded in the glass matrix. The transport and dielectric properties of the pure host glasses, viz. $80V_2O_5–20P_2O_5$, $80V_2O_5–10Bi_2O_3$, $80V_2O_5–20PbO$, etc., where FE nanocrystals are precipitated (hereafter referred to as VP glass) by adding TiO_2, $BaTiO_3$ etc., have been well studied and reported in the literature [6, 7, 49]. Dielectric constants of these VP type base glasses are, on the other hand, very small and none of them exhibited ferroelectric behavior as mentioned earlier. The TiO_2, $PbTiO_3$, $BaTiO_3$, etc. with high melting oxide content in the VP glasses or similar other mostly binary TMO glasses, in spite of this, show extremely high dielectric constant [48] (compared to the pure base glass, VP, or similar other TMO glasses). Very little increase of conductivity observed in these systems is assigned to the appearance of nanocrystalline phases. Interestingly, the general behavior of all the ferroelectric FGNC composites, studied so far, is found to be similar.

Another class of nanocrystal-dispersed glasses [35, 39], for example, $KTiOPO_4$ dispersed oxide glasses, is found to be transparent. The transparent ferroelectric glass nanocomposites (TFGNCs) are suitable for second harmonic generation. More about these glass nanocomposites will be discussed separately in Section 8. Some of the important parameters of these TFGNCs are shown in Table 1 for comparison.

3. SYNTHESIS

3.1. Melt Quenching Technique

The melt quenching technique is widely used to prepare glasses and glass–ceramics. It needs higher temperature compared to that required for the sol–gel technique, but it takes less time. The TiO_2, $BaTiO_3$, $SrTiO_3$, $PbTiO_3$, etc. doped vanadate glasses (or the VP glasses) or other low melting TMO glasses (VP type base glasses), in general, can be prepared by a fast quenching method [48, 50]. For example, VP glass can be used to prepare a typical $(80V_2O_5–20P_2O_5) + xTiO_2$ type FGNC with different concentrations of TiO_2 ($x = 0.5, 5, 10, 20$, and 30 wt% TiO_2). Here $80V_2O_5–20P_2O_5$ (or VP glass) acts as the base glass. In brief, V_2O_5, $NH_4H_2PO_4$, and TiO_2 (or $BaTiO_3$, $SrTiO_3$, $PbTiO_3$, etc. can be used), each of purity 99.99% or better, were well mixed in appropriate proportions and preheated in air at about 500 °C for five hours with occasional grinding [48, 50]. The preheated mixed oxide samples were melted in air taking in a platinum crucible at about 1100 to 1250 °C (depending on the TiO_2, $BaTiO_3$, $SrTiO_3$, etc concentrations) for about 30 minutes. The homogeneous melt was then quickly quenched between two cooled copper or steel blocks resulting in thin (0.6–0.7 mm thickness) pellets of the glassy FGNC samples. Ferroelectric glass nanocomposites in the pseudobinary systems like $(100 – x)SrB_4O_7–xBi_2VO_{5.5}$ $(0 \leq x \leq 70)$ were prepared by the splat quenching technique [31, 32]. Strontium borate and bismuth vanadate were melted in a platinum crucible at 1100 °C. The melt was then quenched between two flat stainless steel blocks placed at a temperature around 100 °C to prevent cracking at the time of glass formation. The prepared glasses were then annealed well below the glass transition temperature (T_g). The Cr^{3+} doped lithium germanate glasses were also obtained [36–38] by similar fast quenching of the $12\%Li_2O–88\%GeO_2{:}0.5\%Cr_2O_3$ melt from 1350 °C. Subsequent annealing of the glass at different (480–520 °C) temperatures resulted in the precipitation of ferroelectric $Li_2Ge_7O_{15}$ nanocrystals in the glass matrix [36–38]. More details about the preparation of some other nanocrystal–glass composite samples by the melt quenching technique are available in the literature [51–53].

3.2. Sol–Gel Technique

The sol–gel technique is one of the most important methods to prepare glasses and ceramics of uniform grain sizes. The advantage of this technique is the mixing of the raw materials in the atomic scale during preparation. The disadvantage of this technique is that it is time consuming and the glass/ceramic may get through unnecessary water molecules. Glass–ceramics containing micrometer sized lead zirconate titanate (PZT) was synthesized by the sol–gel method and subsequently nanometer-size lead sulfide (PbS) phase was grown by treatment in hydrogen sulphide gas [33, 34]. A typical sol–gel method is as follows. One first needs to synthesize a gel of the target composition, viz. $50.5PbO–25.5ZrO_2–24TiO_2$. Here a solution of ethyl alcohol and acetic acid in the volume ratio of 75:25 was used. An appropriate amount of tetra-isopropyl orthotitanate ($C_{12}H_{28}O_4Ti$) was added to the solution and stirred for one hour. Subsequently, a suitable amount of lead acetate–acetic acid solution was added and stirred for more than one hour. An adequate amount of $Zr[O(CH_2)_3CH_3]_4$ was then added and

stirred for two hours. The sol was dried at 70 °C for 72 hours. Then it was subjected to several heat treatments [33, 34] to get the crystalline PZT phase in the glass matrix. This glass–ceramic was cold pressed and sintered at 900 °C for 2 hours in PbO atmosphere. The sintered pellet was polished with alumina powder and reduced in H_2S at different temperatures. Nanometer size particles of PbS were precipitated in the glass ceramic matrix. The detailed preparation procedure of transparent glass–nanocomposites, like xKTiOPO$_4$(KTP)–$(1-x)$SiO$_2$, by the sol–gel method has been described elsewhere [35, 39]. Multicomponent K_2O–TiO_2–P_2O_5–SiO_2 glass was prepared by the sol–gel method first [35, 39]. When this glass was heated above 650 °C, it was transformed into a dense nanocomposite of glass and KTP nanocrystals [35, 39]. Preparation of nanocomposites in some other techniques are also found in the literature [54–58].

4. DENSITY

The density of the FGNCs is generally measured by using the Archimedies method. Concentration dependent density of the FGNCs showed nonlinear variation [42]. This is an important property of nanocrystal-dispersed glasses. Since both size and concentrations of the nanocrystals depend on the compositions and there is also a critical size of the nanocrystals above which physical properties change [42] abruptly; the density of the FGNC system showed nonlinear variation with concentration. Both density and the glass transition temperature (T_g) showed little increase with increasing TiO_2 or $BaTiO_3$ concentration in these glass–nanocrystal composites [59]. But the corresponding increase of the average intersite separation (R) between two TMO (vanadium, for example) ions (V–O–V) with large increase of TiO_2 content (5–30 wt%) was relatively small (about 5%). R was calculated from the relation $(R = 1/N)^{1/3}$, where N is the vanadium ion concentrations. A similar small variation of R was also observed for the $BaTiO_3$ containing V_2O_5–Bi_2O_3–xSrTiO$_3$ glass–nanocrystal composites [29, 41] that followed the nonadiabatic hopping conduction mechanism.

The relationship between the density and the composition of nanocrystal-dispersed glasses is frequently expressed by the effective volume occupied by 1 g. wt of oxygen (V_o^*). The values of V_o^* can be determined from the theoretical formula given by Drake et al. [60]. Both density and V_o^* change in a similar manner with composition indicating that the topology of the glass–nanocrystal composites do not change appreciably for higher concentration of $SrTiO_3$ (or $BaTiO_3$). Variation of density (ρ) of the $(1-x)(90V_2O_5$–$10P_2O_5) + x$BaTiO$_3$ glass–nanocomposites [50] with concentrations (x) of $BaTiO_3$ is shown in Figure 2. Initially, the density decreases with x and then shows a maximum for the highest concentration of $BaTiO_3$ (Fig. 2). The particle diameters of a typical composite also show a nonlinear variation with the change of concentration of composite components [34]. Density of the 20KTP–80SiO_2 type FGNC system increased with the increase of heat treatment (annealing) time and temperature (being 2.34 g/cm^3 at 850 °C with 0.2% porosity) [35]. The density and V_o^* values of a typical TiO_2 containing FGNC for different TiO_2 concentrations (along with average size of the precipitated nanoparticles/clusters) are shown in Table 2.

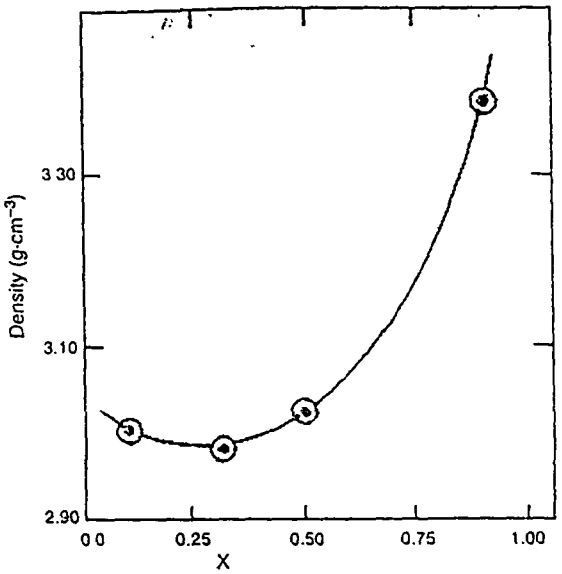

Figure 2. Variation of density of a typical glassy ferroelectric nanocomposite, viz. $(1-x)(90V_2O_5$–$10P_2O_5) + x$BaTiO$_3$ with concentrations (x) of $BaTiO_3$. Reprinted with permission from [50], M. Sadhukhan et al., *J. Chem. Phys.* 105, 11326 (1996). © 1996, American Institute of Physics.

5. DIFFERENTIAL THERMAL ANALYSIS STUDY

The glass transition temperature (T_g) is being measured from the differential thermal analysis (DTA) curve with heating rate 10 °C per minute (say). Figure 3 shows the DTA traces for typical as-quenched and heat-treated $50SrB_4O_7$–$50Bi_2VO_{5.5}$ ferroelectric glass nanocomposites [31]. In Figure 3a, the first exotherm was attributed to the crystallization of $Bi_2VO_{5.5}$. The second exothermic peak was associated with the crystallization of $Bi_{12}V_2O_{23}$ and $BiVO_4$ impurity phases. The third peak was attributed to the reformation of $Bi_2VO_{5.5}$ due to reaction of $Bi_{12}V_2O_{23}$ and $BiVO_4$ impurity phases. The fourth peak was due to the crystallization of the host glass matrix SrB_4O_7. All these findings were consistent with the XRD study of the sample [31]. The heat-treated samples did not show the first exotherm peak as shown in Figure 3b and c. Elaborate DTA study of $50SrB_4O_7$–$50Bi_2VO_{5.5}$ glass-nanocomposites has also been made [32]. The DTA curve of the $(80V_2O_5$–$20PbO) + x$ wt% $BaTiO_3$ type glass-nanocomposites showed [30] an increase of T_g with the corresponding increase of $BaTiO_3$ concentration (x). DTA traces of several glasses [60–63] indicated a clear correlation of T_g with the change of coordination number of the network former and the formation of nonbridging oxygen (NBO) atoms which means a destruction or depolymerization of the network structure. The increase of T_g, in general, indicates the increase of coordination number of the network former. In contradiction to this, formation of NBO causes a decrease of T_g as observed in lead vanadate glasses [15]. Thus the continuous increase of T_g with

Table 2. Certain significant physical structures of a typical ferroelectric glass nanocrystal composite system, viz. ($80V_2O_5$–$20P_2O_5$) glass embedded with x wt% TiO_2 nanocrystalline particles/clusters [64].

Values of x (wt%)	Grain/cluster size (nm)[a]	ρ[b] (gm/c.c.)	γ_ρ	V_o^* (c.c.)	Q (μV K^{-1})	η	T_g (°C)
5	10	3.063	25.25	11.38	−146	0.734	270 ± 5
10	20	3.065	24.47		−142	0.780	278 ± 5
20	40	3.082	17.38	11.99	−138	0.827	284 ± 5
30	80	3.216	12.25	12.03	−135	0.861	298 ± 5

Note: Seebeck coefficients (Q) were obtained from the best fitting of the experimental thermoelectric power data with Eq. (1).
[a] Indicates average size of the grains/cluters present in the FGNC.
[b] Error in the estimation of density was within ±0.005%.

x indicated strengthening of the bond [30]. The difference between T_g and crystallization temperature (T_{cr}) was less than 30 °C and it increased with the increase of x. Accordingly, the stability of the glasses increased with the increase of $BaTiO_3$. The values of T_g for TiO_2 containing FGNCs are given in Table 2.

6. SPECTROSCOPIC CHARACTERIZATION

6.1. X-Ray Diffraction

The amorphous character of all the ($80V_2O_5$–$20PbO$) + x wt% T (where T = $BaTiO_3$) type nanocrystal dispersed glassy system is demonstrated from the study of XRD patterns (with Cu K_α radiation) as shown in Figure 4a and b [30]. No crystalline peak was seen from the XRD patterns of this system. The corresponding annealed samples, however, showed the presence of $BaTiO_3$ as demonstrated in Figure 4c and d. The nanocrystals precipitated in these glasses (referred to as VPTI glasses) during glass formation are mostly $BaTiO_3$ or TiO_2 as indicated from the XRD patterns of the corresponding glass–ceramic samples obtained by annealing the as-quenched glass samples at 300 °C for a few hours in air (Fig. 4c and d). The very large dielectric permittivity of these multicomponent glasses compared to that of the base glasses V_2O_5–PbO or many other TMO glasses [12, 43, 48] also confirmed the presence of nanocrystalline $BaTiO_3$ or TiO_2 in the glass matrix. This result supported the earlier observation [48] that the dielectric constant of nanocrystalline TiO_2 or $BaTiO_3$ was much higher than that of bulk TiO_2 or $BaTiO_3$. The infrared (IR) spectra of all the glass samples exhibited almost identical

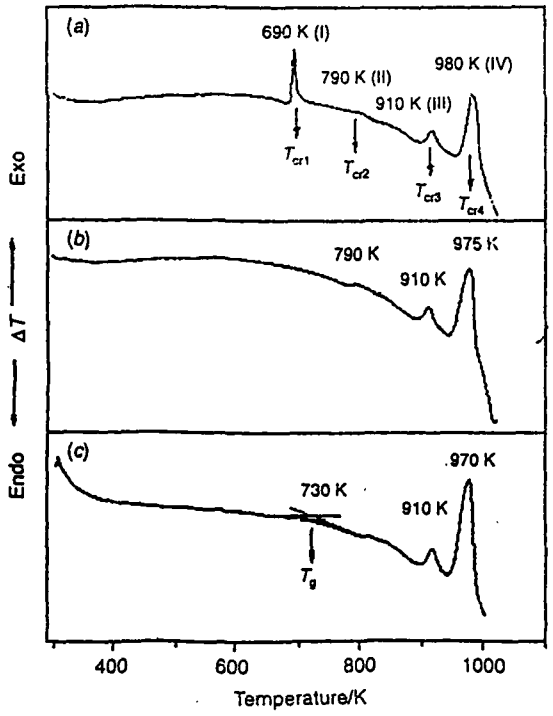

Figure 3. Differential thermal analysis traces for (a) as-quenched, (b) 447 °C, and (c) 547 °C heat-treated $50SrB_4O_7$–$50Bi_2VO_{5.5}$ glass nanocomposites. T_g and T_{cr} stand, respectively, for glass-transition and crystallization temperatures. Reprinted with permission from [31], N. S. Prasad and K. B. R. Varma, *J. Mater. Chem.* 11, 1912 (2001). © 2001, The Royal Society of Chemistry.

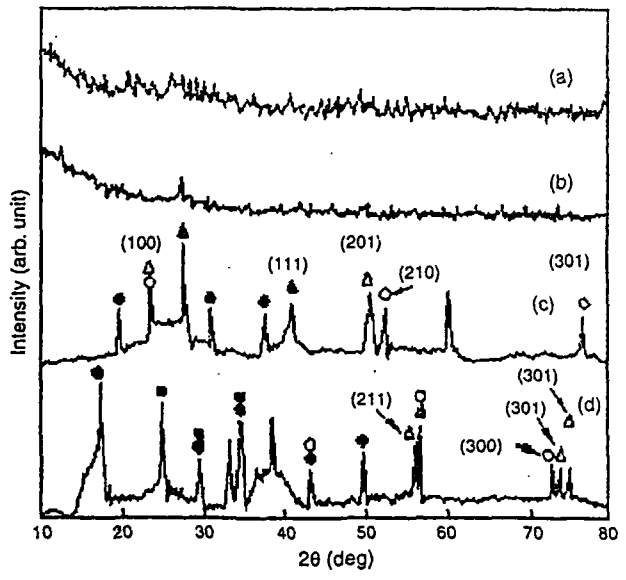

Figure 4. X-ray diffraction pattern of the as-quenched ($80V_2O_5$–$20PbO$) + x wt% $BaTiO_3$ glassy nanocomposite for (a) x = 15 and (b) x = 30 wt%. XRD of the corresponding annealed samples (annealed at 300 °C for 9 h) for (c) x = 15 and (d) x = 30 wt% with some of the identified crystalline peaks: PbV_2O_6(●), $PbTiO_3$ (○), PbV_2O_7 (♦), $BaTiO_3$ (△), and TiO_2(▲). Reprinted with permission from [30], M. Sadhukhan et al., *J. Appl. Phys.* 85, 3477 (1999). © 1999, American Institute of Physics.

features [30, 43] as will be discussed. The observed fine $Bi_2VO_{5.5}$ crystallites present in the SrB_4O_7 glass matrix were also confirmed by XRD studies [31, 32]. Systematic XRD studies corroborated the crystallization of $Bi_2VO_{5.5}$ phase along with minor impurity phases like $Bi_{12}V_2O_{23}$ and $BiVO_4$, depending on the temperature range of heating of the as-quenched samples [31, 32]. The XRD spectra well confirmed the presence of PZT crystals embedded in the glass matrix and the diffraction lines corresponding to PbS phase were broadened due to the small size of these crystallites [34].

6.2. Scanning Electron Microscopy

The scanning electron microscopic (SEM) study of the nanocrystal dispersed glassy composite gives clear evidence of the presence of crystallites in the glass matrix. The glassy character of the as-quenched FGNC samples was confirmed by SEM study as shown in Figure 5a and b for the two samples $(80V_2O_5–20PbO) + x$ wt% A (where A = $BaTiO_3$, etc.) with x = 15 and 30 wt% respectively [30]. The SEM micrographs of a typical sample (with x = 30 wt%) annealed at two different temperatures (290 and 300 °C) are shown, respectively, in Figure 5c and d. It is concluded from the SEM photographs (Fig. 5) that no crystallite was present before annealing the glasses. The presence of nanocrystals was, however, observed in the corresponding annealed samples consistent with the XRD pattern (Fig. 4). The SEM micrographs of ferroelectric PZT in glass–nanocrystal composite samples also showed identical results [34].

6.3. Transmission Electron Microscopy

Transmission electron microscopy is very important for the microstructural study of nanocomposites. The TEM studies of fine glass powder are made on carbon grids [21], which clearly reports the presence of nanocrystalline particles/clusters present in all the annealed glasses [48, 50]. The nanocrystals of TiO_2 or $BaTiO_3$ are formed in the glass matrices because of the large difference between the melting point of TiO_2 or $BaTiO_3$ than those of the base glasses (VP glasses). TEM indicated the presence of nanocrystalline $BaTiO_3$ or TiO_2 particles/clusters in these glasses (with maximum grain/cluster sizes varying from 5 to 80 nm with change of $BaTiO_3$, TiO_2, etc. content from 5 to 30 wt%). For lower concentration (x = 5–10 wt%), the size as well as concentration of the nanoparticles was very low. The TEM micrographs of $(80V_2O_5–20PbO) + 30$ wt% $BaTiO_3$ glass and the corresponding glass ceramic (annealed at 300 °C for 9 h) samples are shown, respectively, in Figure 6a and b. The selective area electron diffraction (SAED) pattern of the same glass and glass ceramics sample are shown correspondingly in Figure 6c and d. The TEM as well as the SAED patterns of the glass showed their amorphous nature (Fig. 6a and c) and those of the glass ceramic sample (Fig. 6b and d) indicated the distributed nanocrystalline particles/clusters in the glass matrix. These findings were in agreement with the XRD and SEM patterns of these samples [30]. Similar nanocrystalline particles were also observed in the $V_2O_5–CoO–TeO_2$ glasses [11] and also in the $(Bi_3Pb_2)Sr_3Ca_{4-m}(M_m)O_x$ glasses [44, 64] with M = Li, K, Cr, Mn, Zn, Ti, Ag. Prasad and Varma [31] found the presence of $Bi_2VO_{5.5}$ crystallites in SrB_4O_7 glass matrix by TEM and SAED study. Li et al. [35] also located the presence of KTP nanocrystals in SiO_2 transparent glass matrix.

6.4. Infrared Characterization

The IR spectra of the ferroelectric nanocrystals dispersed oxide glasses are generally studied in KBr matrix. Figure 7 shows the IR spectra of the $(80V_2O_5–20PbO) + x$ wt%

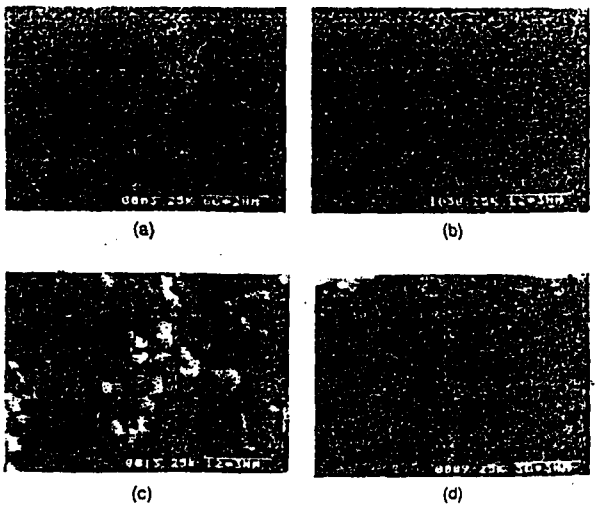

Figure 5. Scanning electron micrographs of the $(80V_2O_5–20PbO) + x$ wt% $BaTiO_3$ glasses for (a) x = 10 and (b) x = 30 wt% and those of the glass ceramics with x = 30 wt% annealed at different temperatures: (c) 290 °C and (d) 300 °C for 9 h each. Reprinted with permission from [30], M. Sadhukhan et al., *J. Appl. Phys.* 85, 3477 (1999). © 1999, American Institute of Physics.

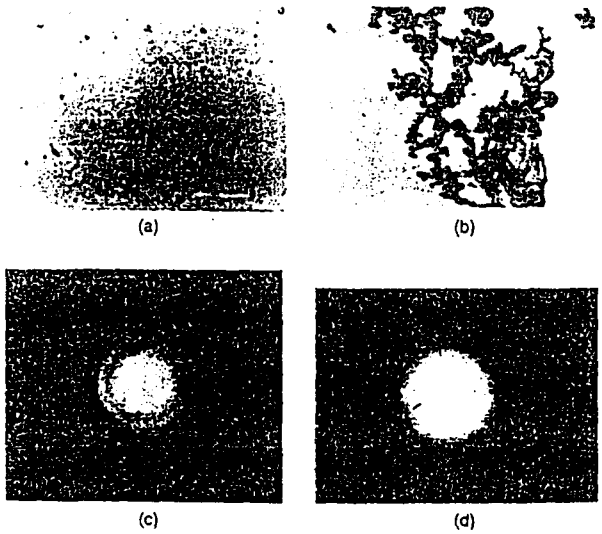

Figure 6. Tunneling electron micrographs of the $(80V_2O_5–20PbO) + x$ wt% $BaTiO_3$ glass-nanocomposite with x = 30 wt% (a) and the corresponding glass ceramic sample (obtained by annealed at 300 °C for 9 h) (b). The selective area electron diffraction pattern of the same glass (c) and the corresponding glass ceramic sample (d). Reprinted with permission from [30], M. Sadhukhan et al., *J. Appl. Phys.* 85, 3477 (1999). © 1999, American Institute of Physics.

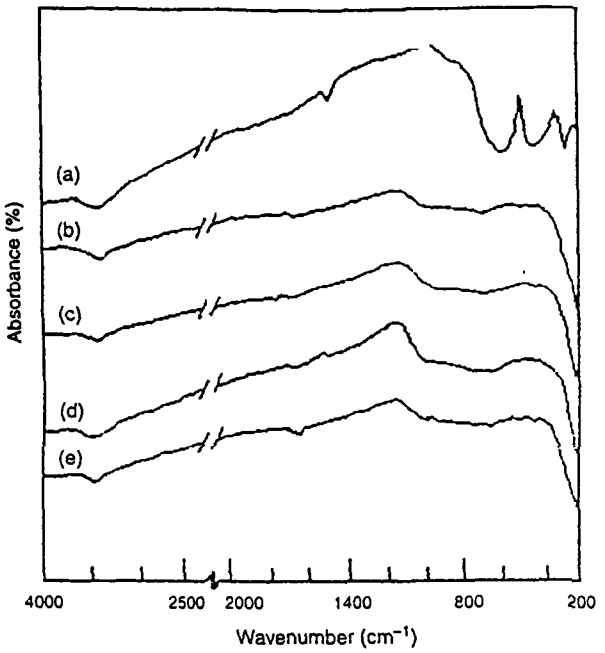

Figure 7. Infrared absorption spectra of (a) pure $BaTiO_3$, and $(80V_2O_5–20PbO) + x$ wt% $BaTiO_3$ glass-nanocomposites, respectively, for $x = 10$ (b), 15 (c), 20 (d), and 30 (e) wt% of $BaTiO_3$. Reprinted with permission from [30], M. Sadhukhan et al., *J. Appl. Phys.* 85, 3477 (1999). © 1999, American Institute of Physics.

$BaTiO_3$ ($x = 10$, 15, 20, and 30) glass–nanocomposites along with the pure $BaTiO_3$. The characteristic features of the IR spectra of all the glasses were found to be identical. The vibrational frequencies corresponding to the $Pb_2V_2O_7$ and $Pb_3V_2O_8$ structural units as reported for the lead vanadate glasses [65, 66] are not clearly observed from the IR spectra of these $(80V_2O_5–20PbO) + x$ wt% $BaTiO_3$ glasses [30]. Sadhukhan et al. [30] found a water band around 3400 cm^{-1} and an –OH stretching peak at 2920 cm^{-1} in all the glasses and crystalline $BaTiO_3$ due to the hygroscopic nature of the powder sample [67, 68]. In all the glass composites, signatures of the bonds and peaks of $BaTiO_3$ were not well visualized. However, instead of a band around 1500 cm^{-1} present in crystalline $BaTiO_3$, a new band around 1600 cm^{-1} was present in all the glasses. This might be due to the glassy environment of $BaTiO_3$ nanoparticles. The characteristic phonon frequency (ν_{ph}) estimated from the IR spectra was of the order of 10^{13} Hz corresponding to an IR band around 1000 and 1600 cm^{-1} for different glasses. This value of the phonon frequency agreed with that obtained from the conductivity data [30] of the sample.

7. PROPERTIES

7.1. Thermal Properties and Thermoelectric Power

The study of thermal property of glassy materials is difficult due to the higher thermal resistivity of the materials. However, that of glass–ceramics becomes much easier due to the crystalline nature of the glass–ceramics. The Seebeck coefficient (Q) of the FGNC sample is higher than that of the pure base glass as it contains crystalline nanoparticles of relatively higher conductivity [29, 41]. The Q values of FGNCs are determined by measuring the thermoelectric power (TEP) of the samples with a temperature difference around ~8 K between the two electrodes [29, 41]. For TEP measurements, samples of higher thickness (~1 mm or more) were generally used. All the FGNC systems showed negative values of thermoelectric power between 300 and 450 K. Table 2 shows the Q values of a typical TiO_2 containing FGNC system indicating it as an n-type semiconductor. Like many ternary vanadate glasses [49, 69–73], no appreciable temperature dependence of the TEP was observed between 300 and 400 K for the FGNCs. However, the magnitude of Q decreased with an increase in TiO_2 or $BaTiO_3$, etc. concentrations in the FGNCs (that is, with increase of grain size and their concentrations). The Q values were fitted with Heike's formula [73], viz.

$$Q = k_B/e[\ln\{C/(1-C)\} + \eta] \quad (1)$$

where e is the electronic charge and η is a constant of proportionality between the heat transfer and the kinetic energy of carrier. Values of $\eta < 1$ indicated a small polaron hopping transport mechanism [5, 29, 72–77] while for $\eta > 2$, the conduction was due to large polaron hopping [15, 60]. Equation (1) implies no temperature dependence of Q. Though it was reported earlier that the values of Seebeck coefficients of the glasses followed [5, 72–74] Heike's law, this model was also found to be applicable to FGNCs and the estimated values of η were almost constant and less than one (Table 2) indicating the validity of the small polaron hopping conduction mechanism in these FGNCs. Similar values of η (=0.44–0.98 depending on the concentrations) were also reported in other multicomponent vanadate glasses [49, 70] dispersed with nanocrystals. Interestingly, the values of η for these FGNCs were also positive and <1. For many TMO glasses η values are large and negative [42, 44].

7.2. Electrical Conductivity

7.2.1. dc Conductivity

For the temperature dependent dc conductivity (σ_{dc}) measurement, the thin pellets of the composites (diameters ~8 mm and thickness 0.3–0.4 mm) are generally used. The two polished faces of the pellets are gold plated by sputtering. Interestingly, like density, concentration dependent conductivity of the FGNC also showed an anomaly (change of slope) around the same concentration where density illustrated an anomaly between 5 and 10 wt% TiO_2 as shown in Figure 8 for typical $80V_2O_5–20P_2O_5 + xTiO_2$ glass-nanocomposites [64]. The dielectric constant of the same sample (discussed in a separate section) also decreased for TiO_2 content higher than 5 wt% as shown in Figure 8 for 0.1 kHz. This indicates that the dielectric constant is smaller (or larger) for the FGNC with grain/cluster size greater (or smaller) than a critical size (between 5 and 10 nm) [64]. This new result also supported the outcome of Zhang and co-workers [78]. It was shown by Wang et al. [22] that there was a critical grain size (~10 nm) around which the

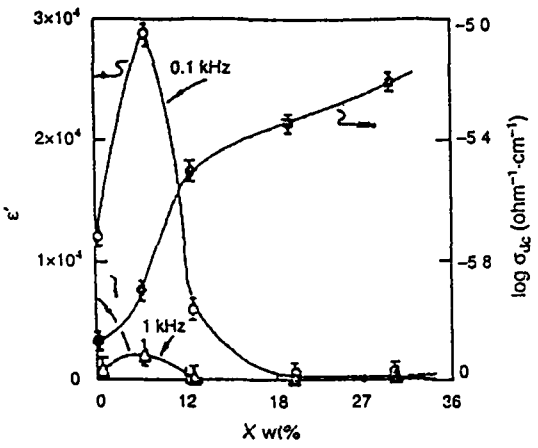

Figure 8. TiO_2 concentration (x) dependent logarithmic dc conductivity (log σ_{dc}) of the $(80V_2O_5\text{–}20P_2O_5) + xTiO_2$ glass–nanocrystal composites at a fixed temperature (300 K). The dielectric constant (ε') at two different frequencies (0.1 and 1 kHz) and at a fixed temperature (300 K) of the same glass-nanocomposite. Reprinted with permission from [64], D. K. Modak et al., *Sol. State Phys.* 43, 368 (2000).

dielectric constant of nanocrystalline ferroelectric $PbTiO_3$ was maximum. Most of the FGNC systems also behave in a similar way.

Thermal variations of the dc electrical conductivity (σ_{dc}) of the ferroelectric nanoparticle dispersed glassy system have been shown by different groups [29, 30, 50]. The logarithm of the dc conductivity (log σ_{dc}) vs $10^3/T$ curve (Fig. 9) for a typical FGNC ($80V_2O_5$–20PbO + x wt% $BaTiO_3$ with x = 10–30) indicated a change of slope around $\theta_D/2$ (Debye temperature θ_D being different for different samples) [30] All the other FGNCs also showed an analogous nature of variation of conductivity with change of temperature. As mentioned, density increased with increasing TiO_2 or $BaTiO_3$ concentration (x) exhibiting a break around x = 5 wt% (Fig. 2) which was also reflected in the dc conductivity vs TiO_2 concentration (x) curves shown earlier (Fig. 8). For lower concentrations (x < 10 wt%), σ_{dc} at a fixed temperature (300 K) increased slowly with increase of TiO_2 content in the FGNC (Fig. 8). This behavior was in sharp contrast to those of other pure vanadate glasses (base glasses), for example, V_2O_5–MnO_2–TeO_2 [8] and V_2O_5–CoO–TeO_2 [11], where a decrease in conductivity with increase of the second transition metal ion, viz. Mn or Co ions, was observed. The increase of σ_{dc} in these VPTI type FGNCs with increasing TiO_2 content (say) was comparatively very small [6] (the values of log σ_{dc} at room temperature are −5.90, −5.5, −5.35, and −5.20 $ohm^{-1}\,cm^{-1}$, respectively, for 5, 10, 20, and 30 wt% TiO_2). The corresponding increase of R (from 0.498 to 0.526 nm for x = 5–30 wt% TiO_2) was also little. As the V ion concentration in all the glasses was fixed (since the glass composition $80V_2O_5$–$20P_2O_5$ or $80V_2O_5$–20PbO was fixed for all the VPTI type FGNCs), this small increase of conductivity was not supposed to be due to an increase of V ion concentration. Again, little increase in the estimated values of average intersite separation R (separation between the transition metal ions) with increasing TiO_2 concentration in the VPTI type FGNC samples

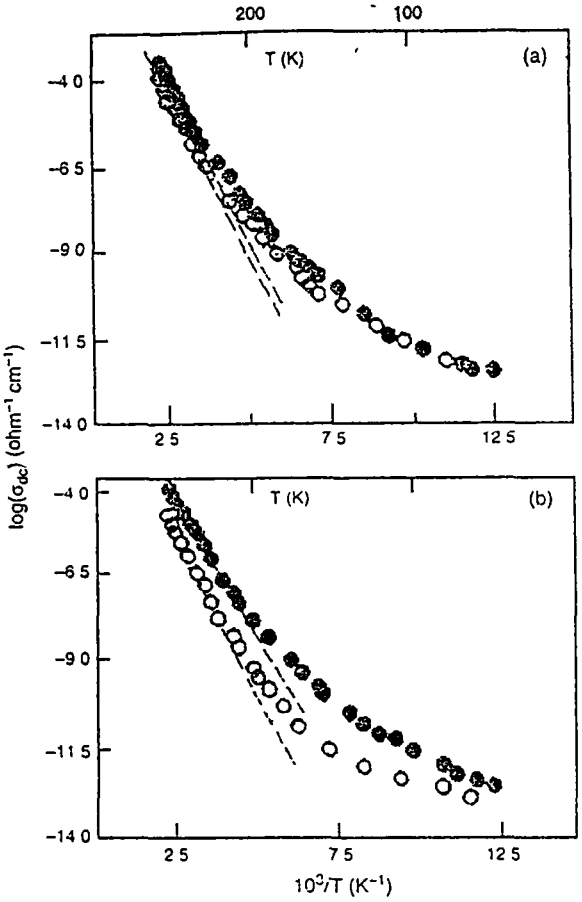

Figure 9. The logarithmic dc conductivity (log σ_{dc}) as a function of inverse temperature ($10^3/T$) of the $(80V_2O_5$–20PbO) + x wt% $BaTiO_3$ glass-nanocomposites with (a) x = 10 (●), 20 (○), (b) 15 (●), and 30 wt% (○) The labels on the top x axis give temperature (T) Reprinted with permission from [30], M Sadhukhan et al., *J Appl Phys* 85, 3477 (1999) © 1999, American Institute of Physics

should rather cause a decrease of conductivity The corresponding decrease of activation energy (W) and hence the observed small increase of conductivity with increase of TiO_2 (for example) content was, therefore, considered to be due to the presence of precipitated nanocrystalline particles/clusters uniformly dispersed in the glass–nanocrystal composites. This conclusion was also supported from the results of earlier observation [73] that the conductivity in nanocrystalline phase increased in glasses and in ceramic semiconductors while it decreased in the metallic systems. This is an interesting property of the nanocrystalline grains No theoretical model has yet been developed explaining this increase of conductivity in the glassy system with the appearance of nanocrystalline phase. Therefore, dc conductivity of the FGNCs is not solely due to the hopping between the TMO ions. In fact, the precipitated nanoclusters also contribute to the total conductivity. The magnitude of this contribution also depends on the size and concentration of the nanoclusters as in other FGNCs. With increase of TiO_2 content (from x = 5 to 30 wt%) in the FGNC system, like $80V_2O_5$–$20P_2O_5$ + $xTiO_2$ FGNCs, the rise of conductivity

was quite sharp between 5 and 10 wt% TiO_2 (where nanoparticle size varying between 5 and 20 nm) and for the values of x between 10 to 30 wt% (maximum grain/cluster size varying from 20 to 80 nm), the corresponding rise in conductivity with concentration was slow (Fig. 8). These two regions of conductivity are separated by an anomaly (change of slope) occurring between $x = 5$ and 10 wt% TiO_2 (Fig. 8). Similar types of concentration (x) dependent anomalies in the conductivity and other properties, above a particular (or critical) size and concentration of the nanoparticles, were also present in many other nontransition metal semiconducting oxide glasses. The importance of the contribution of such nanoclusters in the transport and other properties of glasses is, in general, overlooked as the overall behavior of the nanocrystal dispersed glasses and pure nanocrystal free glasses appears identical.

The relation between $\log \sigma_{dc}$ and inverse temperature (T^{-1}) is almost linear (Fig. 9) indicating the temperature dependent activation energy (W). This behavior of dc conductivity was described by the relation $\sigma_{dc} = (\sigma_o/T)\exp(-W/k_BT)$, where σ_o is the pre-exponential factor. The values of W were obtained from the plot of $\log \sigma_{dc}$ vs $1000/T$ (Fig. 9). At temperatures lower than $\theta_D/2$, the linearity in the $\log \sigma_{dc}$ vs T^{-1} curve deviated as seen from Figure 9. Similar thermal variation of dc conductivity (σ_{dc}) was also exhibited in V_2O_5–P_2O_5 [79] and many other TMO glasses [4, 69, 70] and followed a polaron hopping conduction mechanism. The high temperature ($T > \theta_D/2$) conductivity data of the VPTI type FGNCs thick pellets were interpreted in terms of the phonon-assisted hopping model given by [15]

$$\sigma_{dc} = (\sigma_o/T)\exp(-W/k_BT) \tag{2}$$

where $W = W_H + W_D/2$ (for $T > \theta_D/2$), $W = W_H + W_D/4$ (for $T < \theta_D/4$), and

$$\sigma_o = \nu_{ph} N e^2 R^2 C(1 - C)\exp(-2\alpha R)/k_B \tag{3}$$

ν_{ph} is the optical phonon frequency ($\sim 10^{13}$ Hz), α is the decay constant of the localized wave function, W_H is the polaron hopping energy, W_D is the disorder energy, and other parameters have usual meanings as mentioned earlier. The importance of the tunneling term $\exp(-2\alpha R)$ in Eq. (3) for the FGNCs could be understood [79] by plotting $\log \sigma_{dc}$ against W at a chosen temperature for all the VPTI type FGNCs. The temperature T_e (say), estimated from the slope of such a plot, would be close to the experimental temperature when the hopping is considered in the adiabatic regime [5, 79]. On the other hand, T_e would be very different from the experimental temperature when the hopping is considered in the nonadiabatic regime. The FGNC system was found to follow a nonadiabatic hopping conduction mechanism [64]. It is interesting to mention that Sayer and Mansingh [79] reported an adiabatic hopping conduction mechanism for the TiO_2 free base glass $80V_2O_5$–$20P_2O_5$. Therefore, a change of conduction mechanism occurred in the TiO_2 containing VPTI air quenched FGNCs. It is, however, rather difficult to uniquely identify the type of small polaron hopping conduction mechanism, adiabatic or nonadiabatic, only if the temperature dependence of conductivity is used, because a hopping process of nonadiabatic small polarons requires several restrictions on the electron transfer integral between neighboring hopping sites. So we have also attempted to confirm the nature of hopping conduction using other theoretical methods discussed later.

Dc conductivity data of FGNCs were well fitted with Eq. (2) above $\theta/2$. The estimated phonon frequencies agreed well with those estimated from the infrared spectra as mentioned (shown in Table 3). The polaron radius r_p was estimated from the formula [75], viz.

$$r_p = (1/2)(\pi/6N)^{1/3} \tag{4}$$

The estimated values of r_p (~0.2 Å) suggested strong localization in these FGNCs. The polaron hopping energy W_H was calculated from the relation [10]

$$W_H = e^2/4\varepsilon_p(1/r_p - 1/R) \tag{5}$$

where $1/\varepsilon_p$ ($=1/\varepsilon_\alpha - 1/\varepsilon_s$, ε_s and ε_α are the static and high frequency dielectric constants of the FGNCs, respectively). W_H can be calculated from Eqs. (4) and (5) under the approximation $\varepsilon_p = \varepsilon_\alpha = n^2$, where n is the refractive index of the FGNC. The values of W_H were obtained from fitting of the conductivity data with Schnakenberg's model [76] [Eq. (6)] and were found to be of the order of ~0.53, 0.42, 0.35, and 0.26 eV, respectively, for TiO_2 = 5, 10, 20, and 30 wt% in VPTI glass-nanocomposites [72]. These values of W_H were then used to estimate ε_p (=2.047, 2.486, 2.847, 3.932, respectively, for 5, 10, 20, and 30 wt% TiO_2 in VPTI glass-nanocomposites) [72]. The polaron binding energy (W_p) can be obtained from the formula [24] $W_p = e^2/\varepsilon_p r_p$. The calculated values of W_p are shown in Table 3. Using the values of ε_p, the calculated values of

Table 3. Selected valuable parameters of the TiO_2 nanocrystals dispersed $(80V_2O_5$–$20P_2O_5) + xTiO_2$ FGNCs [64] (FGNC in Table 2) obtained by the fitting of their high and low temperature dc conductivity data.

Values of x (wt%)	θ_D (K)	R (nm)	$\nu_{ph} \times 10^{13}$ (Hz)[a]	W^b (eV) at 450 K	W_H^b (eV)	W_p^b (eV)	W_D^b (eV)
5	664 ± 2	0.498	1.384 (3.00)	0.677	0 53	1 751	0 15 ± 0 01
10	625 ± 2	0.506	1.302 (3.03)	0.553	0 42	1 420	0 13 ± 0 01
20	583 ± 2	0.519	1.215 (3.03)	0.461	0.35	1 206	0 10 ± 0.01
30	555 ± 2	0.526	1.158 (3.03)	0.425	0.26	0 863	0 18 ± 0 1

[a] Values of ν_{ph} are obtained from the fitting of the high temperature conductivity data with Eq (2) and the corresponding values within the parenthesis are obtained from the infrared spectra of the samples with KBr.

[b] W, W_H, W_p, and W_D stand, respectively, for activation energy, polaron hopping energy, polaron binding energy, and disorder energy

refractive index (n) agree quite well with those determined from the Berwster angles [64]. The values of polaron binding energy W_p (Table 3) were found to decrease a little with increase of TiO_2 concentration (or with increase of nanocrystalline grain/cluster size) in the FGNCs. The disorder energy W_D can be estimated independently from the generalized polaron hopping model of Schnakenberg [72]. In this model, optical multiphonon and acoustical single-phonon processes determine the conductivity in the high temperature region. According to this model, the expression for the dc conductivity can be written as

$$\sigma_{dc}T \approx \sin h(h\nu_{ph}\beta)^{1/2} \exp[4W_H/h\nu_{ph} \tan h(h\nu_{ph}\beta/4)] \times \exp(-W_D\beta) \quad (6)$$

where $\beta = 1/k_BT$. Equation (6) is fitted to the experimental high temperature dc conductivity data by a least squares method. The values of the parameters W_H and W_D obtained from fitting the dc conductivity data with Eq. (6) are shown in Table 3. These values of W_H and W_D appeared to be a little higher than those of many other vanadate glasses referred in this chapter. This is considered to be due to the presence of dispersed nanocrystalline phases in the FGNCs. Precipitation of this phase caused some modifications of the glass network structure and hence some changes in the values of W_H and W_D (compared to those of the base glass without TiO_2) were observed. According to Eq. (2), the difference existing between W and W_H (Table 3) arose from the disordering energy term ($W_D/2$). This discrepancy had been explained as the effect of the partial charge of the cations of the glass forming oxides on activation energy for hopping conduction in transition metal oxides [4].

It has already been mentioned that Eq. (2) can only fit the high temperature (above $\theta_D/2$) dc conductivity data. For the low temperature regime ($T < \theta_D/2$) where the polaron binding energy is smaller [15, 16], σ_{dc} was explained, as usual, by the VRH models of Mott and Davis [15]. The expression for the conductivity in the three-dimensional VRH model is given by

$$\sigma_{dc} = A \exp[-(B/T)^{1/4}] \quad (7)$$

where A and B are constants, $B = 19.4\alpha^3/k_BN(E_F)$ with the $N(E_F)$ as the density of states at the Fermi level. Figure 10 shows the plot of $\log \sigma_{dc}$ against $T^{-1/4}$ for $(1-x)(90V_2O_5$–$10P_2O_5) + xBaTiO_3$ FGNCs. These curves indicate straight-line behavior with slightly different slopes. The values of

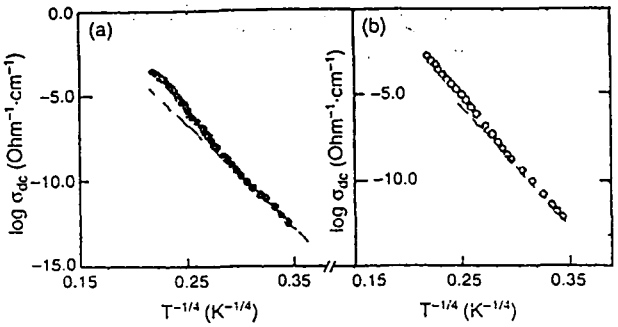

Figure 10. Plot of the logarithm of dc conductivity ($\log \sigma_{dc}$) as a function of $T^{-1/4}$ for different concentrations $x = 0.9$ (a) and $x = 0.3$ (b) of $BaTiO_3$ in $(1-x)(90V_2O_5$–$10P_2O_5) + xBaTiO_3$ glass nanocomposites. Reprinted with permission from [50], M. Sadhukhan et al., *J. Chem. Phys.* 105, 11326 (1996). © 1996, American Institute of Physics.

$N(E_F)$ were estimated from the best fitting of Eq. (7). The estimated values of $N(E_F)$ are shown in Table 4 for a typical FGNC $(80V_2O_5$–$20P_2O_5 + xTiO_2)$ [64]. Knowing $N(E_F)$ and other parameters, the nature of hopping conduction (adiabatic or nonadiabatic) can also be decided from the theory of Emin and Hilstein [74]. According to this theory, the hopping conduction mechanism is adiabatic for $J > \varphi$ and nonadiabatic for $J < \varphi$ where

$$\varphi = (2k_BTW_H/\pi)^{1/4}(h\nu_{ph}/\pi)^{1/2} \quad (8)$$

J is the polaron bandwidth related to the electron wave function overlap on the adjacent sites. For the present VPTI type glassy–nanocomposite system, the limiting values of φ estimated from the right hand side of Eq. (8) are 4.12×10^{-2}, 3.78×10^{-2}, 3.49×10^{-2}, and 3.54×10^{-2} eV, respectively, with 5, 10, 20, and 30 wt% TiO_2. The values of J were also estimated independently from the relation [15] $J = e^3[N(E_F)/\varepsilon_p^3]^{1/2}$. Using the values of $N(E_F)$ and ε_p one finds $J = 1.89 \times 10^{-3}$, 4.24×10^{-3}, 3.66×10^{-3}, and 2.99×10^{-3} eV for the VPTI type FGNCs with $x = 5$, 10, 20, and 30 wt% TiO_2, respectively. Comparing the estimated values of J and φ, it is observed that J is about one order of magnitude less than that of φ for all the glass compositions. This indicates nonadiabatic hopping conduction in all the VPTI type FGNCs, which is in agreement with the results obtained earlier from the plot of $\log \sigma_{dc}$ vs activation energy (W) curves [64]. So the TiO_2 containing VPTI

Table 4. Various model parameters obtained from the best fitting of the ac and dc conductivity data of the nanoparticle dispersed $(80V_2O_5$–$20P_2O_5) + xTiO_2$ (FGNC) [64] sample with different TiO_2 concentrations (x).

Values of x (wt%)	W_{HO}^a (eV)	r_p' (Å)	$N(E_F)$ (eV^{-1})^b	Exponent (s) at 300 K
5	0.8759	0.365	2.65×10^{17} (7.26×10^{18})	0.085
10	0.7102	0.408	1.01×10^{17} (2.46×10^{19})	0.095
20	0.6030	0.588	1.04×10^{17} (3.06×10^{19})	0.031
30	0.4315	0.806	1.82×10^{17} (5.04×10^{19})	0.028

[a] W_{HO} stands for polaron hopping energy between two sites at an infinite distance.
[b] Values of $N(E_F)$ were obtained from the fitting of the dc conductivity data with the VRH model [Eq. (7)]. The corresponding values within the brackets are obtained from the ac conductivity data of these FGNCs.

type FGNCs followed the nonadiabatic hopping conduction mechanism. A similar nonadiabatic hopping conduction mechanism was also reported for the $BaTiO_3$ doped V_2O_5–Bi_2O_3 FGNCs [29, 41, 50]

Attempts were made to fit the conductivity data of these nanoparticle dispersed glasses (FGNCs) with the percolation theoretical model of Triberis and Friedman [77] who applied percolation theory to the small polaron hopping regime. Considering correlation due to energy of a common site in a percolation cluster, they [77] obtained $\sigma_{dc} = \sigma_0' \exp[-(T_0'/T)^{1/4}]$, where σ_0' and $T_0'(= C'\alpha^3/k_B N_0)$ are constant. N_0 is the constant DOS in the mobility gap, and the constant C' has two values, 12.5 and 17.8, in the high and low temperature regimes, respectively. It may further be noted that this equation is similar to that of Mott's VRH model [Eq. (7)] with slightly different values of the constant T_0'. In Figure 10, two different slopes (high and low temperatures) are not clearly observed in the $\log \sigma_{dc}$ vs $T^{-1/4}$ plot for the FGNC system. The difference between the low and high temperature slopes might, however, be larger at higher temperatures beyond the range of measurements. So it was concluded that the percolation theory of Triberis and Friedman [77] was not suitable for application to these FGNCs in the measured temperature range.

An estimation of the small polaron coupling constant (γ_p), which is a measure of the electron–phonon interaction in the VPTI type nanocrystal dispersed glasses, was made from the relation [12] $\gamma_p = W_H/h\nu_{ph}$. Using the value of W_H from Table 3, the authors [64] calculated γ_p which varied from 25.25 to 12.44 for different VPTI type FGNCs. These values of γ_p were much larger compared to those of $BaTiO_3$-free V_2O_5–Bi_2O_3 glasses [60] or other TMO glasses where γ_p varied from 4 to 9. Such high values of γ_p were also obtained by Sega et al. [9] for the multicomponent V_2O_5–NiO–TeO_2 (γ_p = 19–23) and V_2O_5–MnO–TeO_2 (γ_p = 21–25) FGNCs of different concentrations. All these FGNCs, in addition, followed the nonadiabatic small polaron hopping conduction mechanism. According to Austin and Mott [12], higher values of γ_p (>4) indicate a strong electron–lattice (phonon) coupling. So it was found that the electron–lattice interaction decreased with the increase of TiO_2 content in the VPTI type FGNCs. The decrease of γ_p with decreasing TiO_2 concentrations indicated a decrease of electron–phonon interaction with an increase of concentration and size of the nanoclusters. Considering the diffusion of electrons in small polaron hopping, the hopping carrier mobility [75, 77] was estimated from the relation $\mu = 2\pi eR^2\beta/h(\pi\beta/4W_H)^{1/2}J^2\exp(-W\beta)$ (for nonadiabatic hopping). Using the aforementioned values of R and W_H, the values of μ estimated at 300 K are 4.24×10^{-8}, 5.17×10^{-7}, 5.33×10^{-6}, and 2.26×10^{-5} $cm^{-2}V^{-1}s^{-1}$, respectively, for x = 5, 10, 20, and 30 wt% TiO_2 FGNCs. These values of μ were comparable to those of other multicomponent vanadate glasses, viz. V_2O_5–Bi_2O_3–$SrTiO_3$ [29], V_2O_5–Sb_2O_3–TeO_3 [70], etc. The observed increase in mobility with concentration (x) was again attributed to the change of nanocrystalline grain sizes with increase of TiO_2 content in the VPTI type FGNCs. The localization condition for hopping electrons, viz. $\mu \ll 0.01$ $cm^{-2}V^{-1}s^{-1}$ [80], was satisfied for the VPTI type FGNCs. This result indicates that electrons in these FGNCs are localized mainly at the V ion site which is similar to that observed in the V_2O_5–Sb_2O_3–TeO_2 type of FGNCs [70]. Therefore, conduction in these glassy systems was primarily due to a polaron-hopping mechanism between the vanadium ions of different valence states though the authors [64] considered there to be little increase of conductivity due to the precipitation on nanocrystalline particles. The carrier concentrations N_c calculated from the relation [49, 70] $\sigma_{dc} = eN_c\mu$ were 5.56×10^{21}, 1.14×10^{22}, 1.57×10^{21}, and 5.24×10^{19} eV^{-1} for the VPBT type FGNCs, respectively, with TiO_2 concentration of 5, 10, 20, and 30 wt%. Concentration (x) dependent N_c showed little discontinuity (increase and then decrease with increasing x) around x = 10 wt% which might also be due to the phase separation in the FGNCs.

7.2.2. Ac Conductivity

For the frequency and temperature dependent dielectric constants (ε) and ac conductivity [$(\sigma_{ac}(\omega))$] measurements, the two polished faces of each of the samples (thickness 0.25–0.30 mm) were gold plated by sputtering and then annealed at about 150 °C for half an hour before conductivity measurement. This was done for better electrical contact with the sample surface. Conductivity measurements were made in the ohmic region as determined from the study of current–voltage (I–V) method.

It is well known that the frequency dependent ac conductivity data of amorphous or powdered semiconductors follow the relation [13, 14]

$$\sigma_{ac}(\omega) = A\omega^s \tag{9a}$$

where A is a constant weakly dependent on temperature and s is the frequency exponent, generally less than unity. The ac conductivity was calculated from the total conductivity $\sigma_t(\omega)$ measured at frequency ω and at a fixed temperature. Both dc conductivity (σ_{dc}) and total conductivity, $\sigma_t(\omega)$, are measured independently and then ac conductivity [$\sigma_{ac}(\omega)$] is estimated from the relation [13–14]

$$\sigma_t(\omega) = \sigma_{dc} + \sigma_{ac}(\omega) \tag{9b}$$

In the glassy FGNC system, the ac and dc conductivities arise due to completely different processes [81]. In other words, ac conductivity represents the dc conductivity in the limit [81] $\omega \to 0$. Analyses of the ac conductivity [$\sigma_{ac}(\omega) = \sigma_t(\omega) - \sigma_{dc}$] data of the semiconducting TMO glasses are generally made in the framework of quantum mechanical tunneling (QMT) [82], correlated barrier hopping (CBH) [12], and overlapping large polaron tunneling (OLPT) [83] models. In the following section, the temperature dependent ac conductivity data and the frequency exponent (s) of the nanoparticle dispersed glasses have been analyzed in terms of the OLPT model which is found to be the most appropriate for these nanocrystal–glass composite systems. Long [82] proposed the polaron tunneling model where the potential wells of two sites overlap thereby reducing the value of polaron hopping energy [84, 85] due to the long-range nature of the dominant Coulomb interaction. The polaron hopping energy has the form [81] $W_H = W_{HO}(1 - r_p/R)$ where W_{HO} is the polaron hopping between

two sites at infinite distance. The ac conductivity for the OLPT model [83] is given by

$$\sigma_{ac}(\omega) = (\pi^4/12)e^2(k_BT)^2[N(E_F)]^2 \times[\omega R_\omega^4/(2\alpha k_BT + W_{HO}r_p/R_\omega^2)] \quad (10)$$

where $R_\omega = (1/2\alpha)[\ln(1/\ln(\omega\tau))]$ is the optimum hopping length at a frequency ω calculated by the quadratic equation $R_\omega'^2 + [\beta W_{HO} + \ln(\omega\tau_0)]R_\omega' - \beta W_{HO}r_p' = 0$ (where $R_\omega' = 2\alpha R_\omega$, $r_p' = 2\alpha r_p$, and $\beta = 1/k_BT$). The frequency exponent (s) of $\sigma_{ac}(\omega)$ in this model is calculated from the relation

$$s = 1 - (4 + 6\beta W_{HO}r_p'/R_\omega')/(1 + \beta W_{HO}r_p'/R_\omega')^2/R_\omega' \quad (11)$$

Thus, the OLPT model [Eq. (11)] predicts that the exponent(s) [in Eq. (9a)] should be both temperature and frequency dependent.

At high temperatures (above $\theta_D/2$), the temperature dependence of both σ_{dc} and $\sigma_1(\omega)$ were strong and consequently the measured $\sigma_{ac}(\omega)$, at all frequencies, coincided with σ_{dc} in the high temperature region. Figure 11 represents the plots of $\log\sigma_{ac}$ of a typical glass nanocomposite [50] as a function of inverse temperature and frequency, viz. $\log\omega$. The solid lines are obtained by a least-square fitting procedure. It is evident that $\sigma_{ac}(\omega)$ obeys the universal relation $\sigma_{ac}(\omega) = A\omega^s$, suggesting that the loss mechanism should have a distribution of relaxation times. The plots of exponents s (calculated from the slopes of the curves) as a function of temperature are shown in Figure 12 (for two typical FGNC samples with $x = 10$ and 20 wt%) which indicated that the exponent (s) decreased with increasing temperature and then exhibited a minimum at a temperature around 300 K and subsequently increased. This typical behavior of s suggested that the OLPT model [Eq. (11)] was appropriate for these FGNC systems. In the intermediate temperature range (i.e., below 300 K), the values of s resided around the theoretical curves (solid lines in Fig. 12) for various values of the normalized polaron radius r_p' (shown in Table 4). In the high-temperature regime (above 300 K), an increase in s with increasing temperature was observed which was consistent with the behavior of the OLPT model. The best fit to the experimental points has been observed for the values of W_{HO} and r_p' as shown in Table 4. Both W_{HO} and s decrease with increasing TiO_2 content in the VPTI type FGNCs (i.e., with increase of nanocrystal size and concentration).

Ac conductivity of the FGNC system increased linearly with increasing temperature [i.e., $\sigma_{ac}(\omega)\alpha T^n$ with $n = 1$] over a limited range of temperature below 175 K as predicted by the QMT model [82]. Hence the experimental values of σ_{ac} could also be fitted with the QMT model that predicted a linear temperature dependence of $\sigma_{ac}(\omega)$ due to weak ac conductivity and the corresponding expression for the $\sigma_{ac}(\omega)$ can be written as

$$\sigma_{ac}(\omega) = \{\kappa K e^2 k_BT[N(E_F)]^2\omega R_\omega^4\}/\alpha \quad (12)$$

where κ is a constant factor and varies slightly between *different treatments, and* R_ω $[=(1/2\alpha)ln(1/\omega\tau_0)]$ *is the* characteristic tunneling distance and the corresponding frequency exponent has the form $s = 1 + 4/\ln(\omega\tau_0)$. Therefore, according to the QMT model, the exponent s was

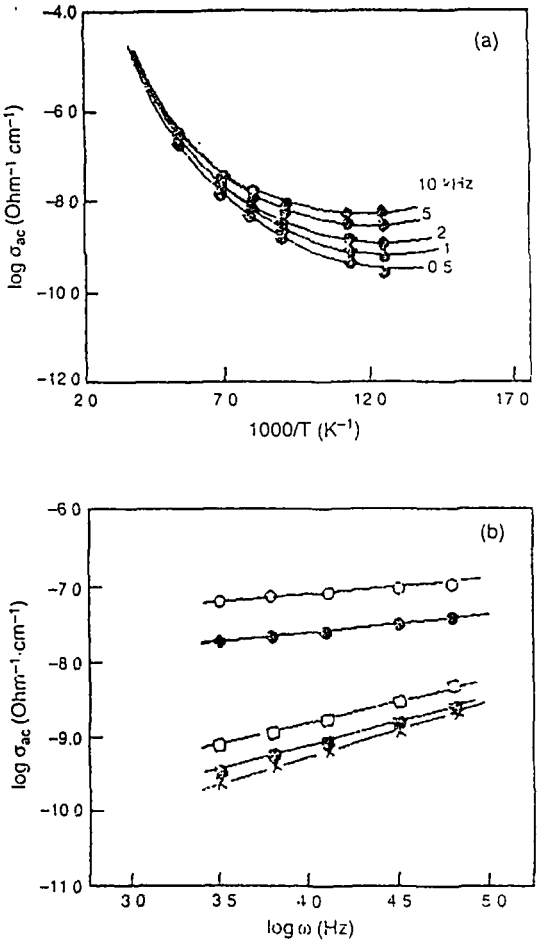

Figure 11. (a) Inverse temperature dependent logarithmic ac conductivity ($\log\sigma_{ac}$) of a typical $(1-x)(90V_2O_5{-}10P_2O_5) + xBaTiO_3$ glass-nanocomposite with $x = 0.3$ at different frequencies (0.5–10 kHz). (b) Frequency dependent ac conductivity of the same glass-nanocomposite sample with $x = 0.1$ at different temperatures [182 (○), 176 (●), 120 (□), 96 (♦), 88 K (x)]. From the slope of these curves, the values of s (frequency exponent) were estimated. Similar curves were obtained for other glass concentrations. (Solid lines are guides for the eyes.) Reprinted with permission from [50], M. Sadhukhan et al., *J. Chem. Phys.* 105, 11326 (1996). © 1996, American Institute of Physics.

independent of temperature that appeared to be valid for the FGNCs only in the low temperature region. The values of the DOS at the Fermi level, $N(E_F)$, were obtained by least-square fitting of the linear region in the low temperature phase for the same composition. The values of $N(E_F)$ presented in Table 4 seem to be reasonable and comparable to those obtained from the dc conductivity data (Table 4) of the same nanoparticle dispersed glasses. However, although the QMT mechanism appears to be consistent with the thermal variation in $\sigma_{ac}(\omega)$ of these VPTI nanocomposites in the low temperature regime, it completely *failed to interpret* the observed temperature dependence of the exponent s. The QMT model as discussed predicted a value of $s = 0.81$ (assuming $\tau_0 = 10^{-13}$ sec and $\omega/2\pi = 10^4$ sec^{-1}), independent of temperature. It has already been

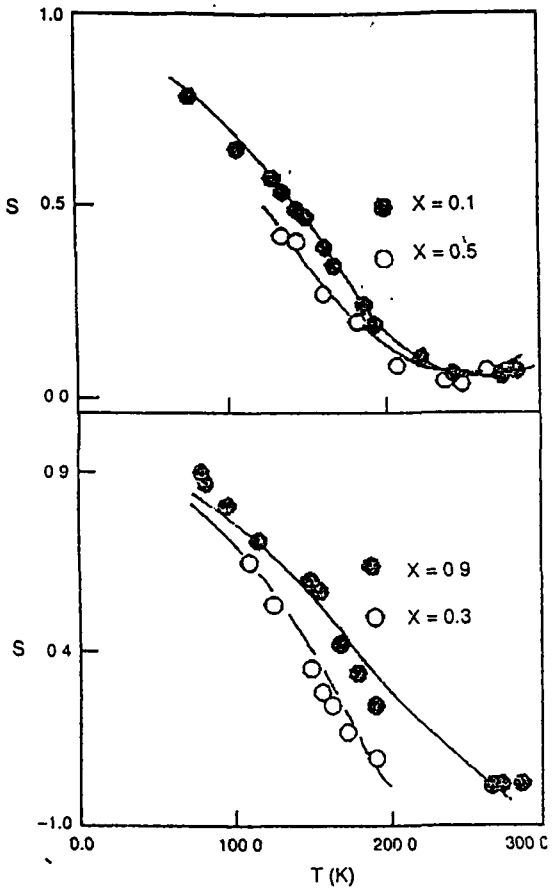

Figure 12. Thermal variation of frequency exponent (S) for $(1-x)\cdot(90V_2O_5{-}10P_2O_5) + xBaTiO_3$ (x = 0.1, 0.3, 0.5, and 0.9) glass-nanocomposites fitted with the OLPT model [Eq. (10)]. The continuous lines are the best-fit curves. Reprinted with permission from [50], M. Sadhukhan et al., *J. Chem. Phys.* 105, 11326 (1996). © 1996, American Institute of Physics.

shown in Figure 12 that s decreases with increasing temperature and then it increases after reaching a certain minimum value, which is also in complete contradiction to the prediction of the simple QMT model. However, at higher temperatures, the ac conductivity starts to deviate from linearity and the temperature (around $\theta_D/2$) at which deviation from linearity starts increases with increasing frequency. Thus the QMT model can explain only the experimental ac conductivity data at low temperature of these VPTI type FGNCs.

It is to be mentioned here that the OLPT model [Eq. (10)] is also applicable in the low temperature range if it is approximated to low temperature condition. One can show that at low temperature this equation reduces to the form

$$\sigma_{ac}(\omega) = (\pi^4/12)e^2(k_BT)^2[N(E_F)]^2[\omega R_\omega^4/2\alpha k_BT]$$
$$= (\pi^4/24)e^2(k_BT)[N(E_F)]^2\omega R_\omega^4/\alpha \qquad (13)$$

Equation (13) can explain the data of Figure 11 and the estimated $N(E_F)$ values fairly agree (within ±2%) with the corresponding values estimated from the QMT model. The OLPT model is, therefore, applicable for a wide range of temperature (both low and high) for these glass-nanocomposites. And the failure in temperature dependence of the exponent s as shown by the QMT model can also be avoided.

It was also observed that the CBH model [12] which correlates the barrier height W with the intersite separation R for single-electron hopping [84] was not applicable for the ac conductivity in these VPTI type nanoparticle dispersed glasses, even though this model was found to hold good for the base glass [69] V_2O_5–P_2O_5 (with 80–90 mol% V_2O_5) in the temperature range 80–400 K. A similar feature was observed as well for the $SrTiO_3$ doped V_2O_5–Bi_2O_3 FGNC system [41, 48]. The presence of TiO_2 in the V_2O_5–P_2O_5 glass, therefore, not only favors the formation of nanocrystals but also modifies the network structure, which in turn was responsible for the change of physical behavior of the nanocrystal dispersed glass. The nonlinear behavior of the TiO_2 doped VPTI type FGNCs, as discussed, was in addition a special property of these FGNCs which might be responsible for the observed differences in the conductivity mechanism in the TiO_2 doped FGNCs from that of the pure base glass, viz. vanadium phosphate (VP) glasses. The thermal variation of dielectric constant (both real and imaginary) of these glasses to be discussed is also interesting, indicating nonlinear behavior of these glasses with $x > 5$ wt% TiO_2 [64].

7.3. Dielectric Properties

Dielectric constants of the FGNC composites are, in general, measured by a GR-1615A Bridge and also by a HP 4291 impedance analyzer [48, 50]. Figures 13 and 14 show, respectively, the thermal variations of the real part (ε') of the dielectric constants of $80V_2O_5$–$20PbO$ + 30 wt% $BaTiO_3$ and $80V_2O_5$–$20P_2O_5$ + 10 wt% TiO_2 nanoparticle dispersed FGNCs for different frequencies (0.1–100 kHz) [30, 64]. Interestingly, the values of dielectric constants of these FGNCs were several orders (three to four) of magnitude higher than those of the undoped $80V_2O_5$–$20P_2O_5$ glasses [5]. It was also observed from the T vs ε' curve (Fig. 13) that this relaxation peak above 360 K was shifted to a higher temperature region with the increase of frequency. For higher concentrations ($x > 5$ wt% TiO_2, or $BaTiO_3$) at a fixed frequency [30, 64], where grain size became larger, or at higher frequencies (for a fixed concentration), the dielectric constant decreased (Figs. 13 and 14). A maximum dielectric constant for the VPTI type FGNC was observed with x around 5 wt% (having smallest grain/cluster size ~10 nm) at 100 kHz [64]. This behavior was also observed in the V_2O_5–P_2O_5–$KTiO_3$ glasses [86].

The Debye type relaxation behavior [87] can be characterized by a complex dielectric constant of the form $\varepsilon^* = \varepsilon_\alpha + (\varepsilon_s - \varepsilon_\alpha)/(1 + j\omega\tau)$ where ε_s and ε_α are the static and high frequency dielectric constants, respectively. ω is the angular frequency and τ is the dielectric relaxation time. Using the relation $\varepsilon^* = \varepsilon' + i\varepsilon''$, we get both real ($\varepsilon'$) and imaginary ($\varepsilon''$) parts of dielectric constants expressed as $\varepsilon' = \varepsilon_\infty + (\varepsilon_s - \varepsilon_\infty)/(1 + \omega^2\tau^2)$ and $\varepsilon'' = (\varepsilon_s - \varepsilon_\infty)\omega\tau/(1 + \omega^2\tau^2)$. Debye type dielectric relaxation

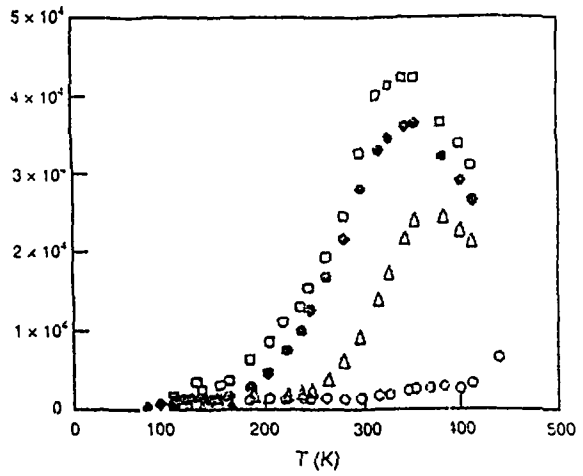

Figure 13. The thermal distinction real part of dielectric constant (ε) of the glass-nanocomposite sample ($80V_2O_5$–20PbO) + 30 wt% $BaTiO_3$ (annealed at 300 °C for 9 h in air) showing one broad peak around 390 K at four different frequencies, 100 Hz (□), 1 kHz (●), 10 kHz (△), and 100 kHz (○), corresponding to ferroelectric transition of $BaTiO_3$ at 393 K. Reprinted with permission from [30], M. Sadhukhan et al., *J. Appl. Phys.* 85, 3477 (1999). © 1999, American Institute of Physics.

behavior is also characterized by relaxation frequency $f_c = 1/2\pi\tau = \nu_{ph}\exp(-W/k_BT)$, where ν_{ph} is the characteristic phonon frequency. This relaxation process can be more clearly resolved [88] from the calculation of dielectric modulus M^* $(=M' + iM'') = \varepsilon^{*-1} = \omega\varepsilon_0 Z^*$, where ε_0 is the vacuum permittivity and Z^* is the complex impedance. The real (M') and imaginary (M'') parts of the complex dielectric modulus M^* are related to the dielectric constants as

$$M' = \varepsilon'/(\varepsilon'^2 + \varepsilon''^2) \quad \text{and} \quad M'' = \varepsilon''/(\varepsilon'^2 + \varepsilon''^2) \qquad (14)$$

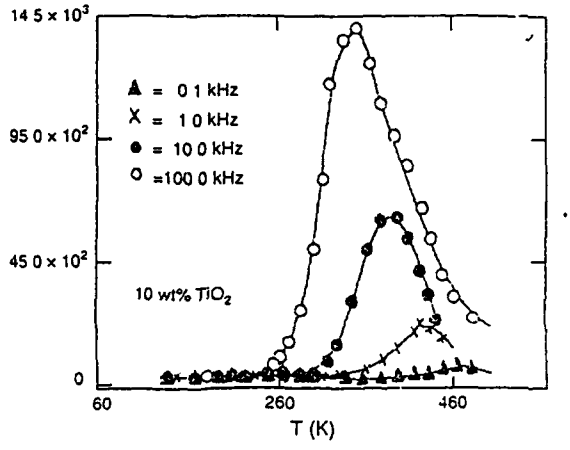

Figure 14. Real part of dielectric constant (ε) of ($80V_2O_5$–$20P_2O_5$) + xTiO_2 glass-nanocrystal composites for a fixed (x = 10 wt%) TiO_2 content at different frequencies (0.1 to 100 kHz) as a function of temperature. Reprinted with permission from [64], D. K. Modak et al., *Sol. State Phys.* 43, 368 (2000).

Again according to Cole and Cole [89], the complex dielectric constant can be expressed as

$$\varepsilon^* = \varepsilon_\infty + (\varepsilon_s - \varepsilon_\infty)/(1 + i\omega\tau_m)^{1-\phi} \qquad (15)$$

where τ_m is the mean relaxation time and ϕ is an empirical parameter lying between 0 and 1. The slope of the Cole–Cole plot [89] at $\varepsilon'' = 0$ gives the value of $(1 - \phi)\pi/2$. A value of $\phi = 0$ leads to a single relaxation time and $\phi = 1$ gives an infinite distribution of relaxation time which is very common in the glassy system.

The thermal variations of loss tangent $\tan\delta$ $(=\varepsilon''/\varepsilon')$ for TiO_2 doped nanoparticle dispersed FGNCs were large (since $\varepsilon'' > \varepsilon'$) indicating a very high loss factor in these FGNCs [64, 78]. The high loss of these glasses might be due to the more conducting nature of the precipitated nanocrystals embedded in the glass matrix, or the effects of space charge polarization [90] of nanocrystalline TiO_2. In the high temperature region, a sharp increase of the loss tangent was observed with increasing frequency. Interestingly, at lower concentrations ($x \leq 10$ wt% which was almost below the critical concentration x above which "phase transition" occurred), loss tangent of the VPTI type glass–nanocrystal composites showed peaks, which shifted to a higher temperature region for higher concentration for a constant frequency of 10 kHz. The $\tan\delta$ vs temperature curves of higher concentrations did not show any peak. It should be mentioned that Kundu et al. [34] did not observe any peak in temperature variation of $\tan\delta$ curves and the loss was also very low. Because of the absence of a well defined loss peak and the uncertainties involved in the subtraction of the dc conductivity from the total conductivity, it was difficult to use conventional methods of estimating the relaxation frequency f_c and the nature of the dispersion (i.e. whether it is characterized by a single relaxation time or by a distribution of relaxation times). However, the following two approaches may be used [79] for the analysis of the data. The first involves the dielectric modulus, defined by Macedo et al. [88], and the second approach is to extract information about the dielectric relaxation time from the temperature or frequency variation of the dielectric constant alone assuming a symmetric distribution of relaxation times. Although no peak was observed in the temperature dependent ε' curves of $80V_2O_5$–$20P_2O_5$ + 5 wt% TiO_2 nanoparticle dispersed FGNC (Fig. 15) for a fixed frequency up to the highest temperature limit measured (460 K), it exhibited Debye type dielectric relaxation behavior characterized by relaxation frequency f_c $(=1/2\pi\tau)$ [64]. It is interesting to note that Prasad et al. [31, 32], however, found peak in temperature variation of dielectric loss (ε'') data of $50SrB_4O_7$–$50Bi_2VO_{5.5}$ type FGNCs. The relaxation process in these FGNCs can be more clearly resolved by using Eq. (14). It was seen from the thermal variation of M' for a fixed (20 wt%) TiO_2 doped VPTI type FGNC (Fig. 16) that M' varies slowly with temperature for fixed measured frequency (10 kHz) above 260 K [64]. This type of temperature dependence of M' indicates that the dielectric constants of the samples are thermally activated. Similarly M'' vs T curves for a sample with 30 wt% TiO_2 (Fig. 17) at different fixed frequencies (1–100 kHz) showed peaks within the measured temperature limit around 110 K. The peak position of M

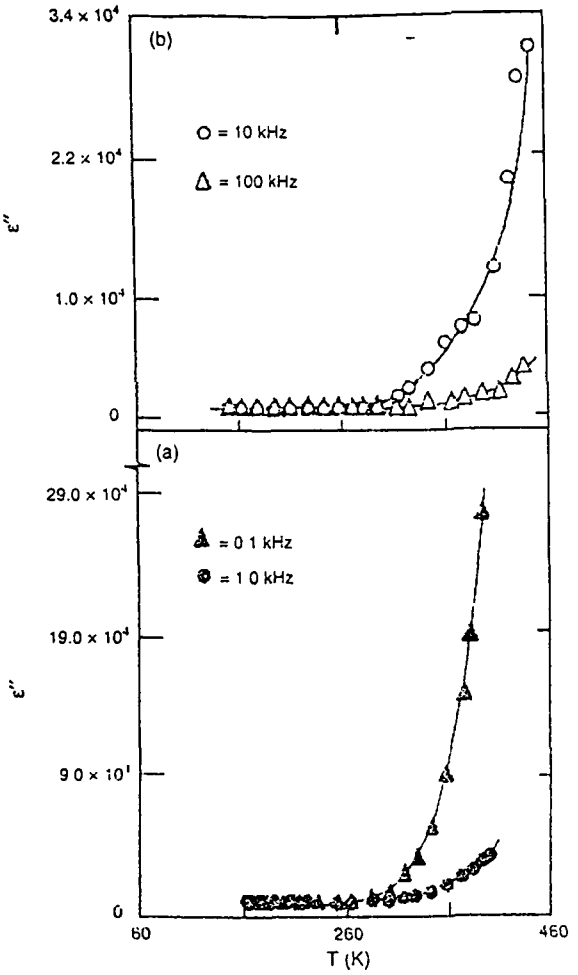

Figure 15. Imaginary part of dielectric constant (ε'') as a function of temperature for $(80V_2O_5\text{–}20P_2O_5) + x TiO_2$ glass-nanocrystal composites (with x = 5 wt% TiO_2) at frequencies 0.1 and 1.0 kHz (a) and 10 and 100 kHz (b). Reprinted with permission from [64], D. K. Modak et al., *Sol. State Phys.* 43, 368 (2000).

gave the temperature at which the measuring frequency was given by $f_c = \nu_{ph} \exp(-W/k_B T)$. Attempts were also made to find the nature of the dielectric relaxation behavior of these FGNCs from the Cole–Cole plot [89] of Eq. (15) at different fixed temperatures with different frequencies [64]. The semicircular nature of the curves as predicted from the Cole–Cole plot [89] for the TiO_2 or $BaTiO_3$ nanocrystal doped VPTI type FGNCs was not prominent [30, 50, 64]. From the Cole–Cole plot [89], it was also evident that ϕ resided between 0 and 1, which suggested that all these glass–nanocrystal composite samples had a distribution of relaxation times.

Grain size effects on ferro- and antiferroelectric oxides have been well investigated theoretically and experimentally [90, 91]. For ferroelectric $PbTiO_3$, the estimated critical size of the nanoparticle clusters [40] was between 8 and 12 nm. The high dielectric constant of these nanoparticle dispersed glasses might be related to the space charge polarization or ionic relaxation polarization occurring at the

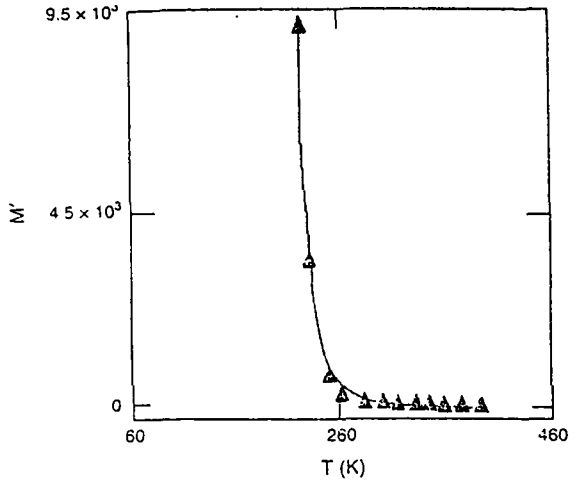

Figure 16. Thermal variation of the real part of dielectric modulus (M') for $(80V_2O_5\text{–}20P_2O_5) + x TiO_2$ glass-nanocrystal composites for a fixed TiO_2 concentration (x = 20 wt%) at 10 kHz. Reprinted with permission from [64], D. K. Modak et al., *Sol. State Phys.* 43, 368 (2000).

interface as suggested by Zhong et al. [90, 91]. The dielectric loss of the VPTI type nanoparticle dispersed FGNC was also very high which might be related to the more conducting character of the precipitated nanoclusters.

7.4. Ferroelectric Properties

For a typical FGNC system, viz. $Bi_{2-x}Pb_xSr_2Ca_2Cu_{3-y}K_y$ (x = 0.1–0.3, y = 0.2–0.3), the ferroelectric property is discussed. The T_g values of this system were found to be (340, 350, 360, and 400 K) depending on the values of x and y [44]. For a typical FGNC, viz. (x = 0.2, y = 0.2), its

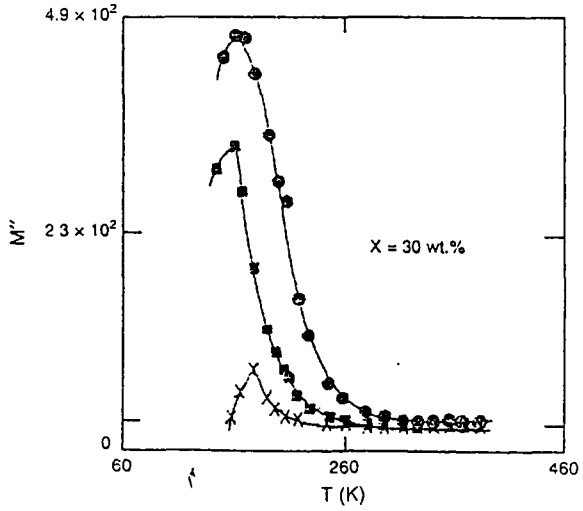

Figure 17. Thermal variation of imaginary part of dielectric modulus (M'') of $(80V_2O_5\text{–}20P_2O_5) + x TiO_2$ glass-nanocrystal composites for a fixed TiO_2 concentration (x = 30 wt%) at 1 (x), 10 (♦), and 100 (○) kHz. Reprinted with permission from [64], D. K. Modak et al., *Sol State Phys* 43, 368 (2000).

TEM micrograph clearly indicated the presence of microcrystals/clusters (10–50 nm size) The concentration of the nanoparticles slightly increased with the increase of Pb concentration As mentioned earlier, these nanoparticles are considered to be responsible for the ferroelectric behavior of K containing FGNCs since nanoparticle free glasses are not ferroelectric Interestingly, the K free glasses are reported to become also superconductors [59] by annealing around 840 °C Hereafter these K free glasses are referred to as SG glasses But due to the presence of alkali metal (partial substitution of Cu by K) in these glasses, they show FE behavior and do not become superconductors by annealing [44] around 840 °C The K doped ferroelectric glasses are termed FG glasses

The structure of Bi–Sr–Ca–Cu–O glasses depends to a great extent on the Cu content and its valence state [21] So the addition of alkali metal (K, say) in the Cu site distorted the average structure of the K free SG type glass to a great extent [44] Though both Bi_2O_3 and CuO are not glass-forming oxides, it is well established that both Bi_2O_3 and CuO are necessary to form a glassy state in the Bi–Si–Ca–Cu–O system as reported by several authors [78, 79] Bi_2O_3 enhances the glass-forming ability in the Bi-based FGNC systems, Bi_2O_3 acts as "glass former' in the presence of CuO It has been reported [92] that Bi ions are six coordinated (distorted BiO_6 octahedra) in the Bi-based glasses The oxygen coordination number of Cu^+ in Cu_2O is 2 and that of Cu^{2+} in CuO is 4 The density of CuO is more than Cu_2O, concluding that CuO structure is more compact than that of Cu_2O Recently Sato et al [93] proposed a glass network structure unit of $Bi_4Sr_3Ca_3Cu_4O_x$ glasses as shown in Figure 18 In this model, BiO_6 octahedra are connected to other octahedra through two coordinated Cu^+ ions and particularly in the K free SG type glasses Cu^+ ions take part mainly in the formation of networks The other cations of Cu^{2+} Ca^{2+} and Sr^{2+} may be distributed randomly in the surrounding network Partial replacement of Cu sites by K changed some ionic states of Cu and distorted the glass network structure in favor of dipolar ordering and hence appearance of ferroelectricity as observed from the dielectric properties discussed The difference between the glass structures of superconducting precursor glass (SG type glass) can be compared in terms of the oxygen molar volume [94, 95] V_o^* The value of V_o^* of the present FGNC was calculated using the equation

$$V_o^* = \frac{(M_{CuO} - 16C)X_{CuO} + M_K X_K + M_{Ca} X_{Ca} + M_{Sr} X_{Sr} + M_{Pb} X_{Pb} + M_{Bi} X_{Bi}}{d[(5-C)X_{CuO} + 3X_K + 3X_{Ca} + 3X_{Sr} + 1X_{Pb} + 3X_{Bi}]} \quad (16)$$

where M_{CuO}, M_K M_{Ca}, M_{Sr}, M_{Pb}, and M_{Bi} are the molecular weights of CuO, K_2CO_3, $CaCO_3$, $SrCO_3$ PbO, and Bi_2O_3 respectively X_{CuO}, X_K, X_{Ca}, X_{Sr}, Y_{Pb}, and X_{Bi} are the mole fractions of CuO, K_2CO $CaCO$, $SrCO_3$, PbO, and Bi_2O respectively The parameters d and C are the density of the glass and fraction of reduced Cu ions, respectively Both T_g (400 °C) and V_o^* (14 52) of the K containing FGNCs were a little higher than those of the K free SG glasses (T_g = 340 °C, V_o^* = 11 23) [44] This indicated that K doped glasses had a more stable glass network structure than that of the K free SG glasses However, the network structure also depended on the K and Pb concentrations

The dielectric constant of the Bi based glassy precursor ($Bi_4Sr_3Ca_3Cu_4O_x$) for high T_c superconductors (SG glasses) did not show any ferroelectric behavior [96–100] Figure 19a shows the variation of the dielectric constant (ε) of a typical K doped FGNC, viz (with $x = 0\,2$, $y = 0\,2$) as a function of temperature for different frequencies 0 1, 0 12, 1 0, 10, 100 kHz The appearance of small broad peak in the ($\varepsilon - T$) curve (Fig 19a) around 600 K along with the large peak for every frequency indicated the presence of the relaxation mode in the glass The ε' values of the FGNCs are of the same order as those of the Bi-based multicomponent SG glasses (Fig 19b) [96–100] It has already been shown [78] that the dielectric constant of nanocrystalline TiO_2 is much larger than that of the corresponding bulk sample As mentioned earlier [30–32, 34, 50 64], the Bi_2VO_5 PbS $BaTiO$ and TiO_2 ferroelectric nanocrystals containing FGNCs also showed high dielectric constants as shown in Table 1

The dielectric constant data of the K doped FGNC followed the Curie–Weiss relation $\varepsilon = C/(T - T_0)$, where C is the Curie constant T_0 is the extrapolated intersection of the high temperature part of the plot with the temperature axis as shown in Figure 20a [44] The order of transition was identified by finding the ratio of the slopes $\frac{\varepsilon(1)}{T}$ below and above T_{cf} [44] The value of this ratio (=−2 63) indicated that the transition was of first order type Prasad et al [31 32], also analyzed the dielectric constant data of the SrB_4O_7–$Bi_2VO_{5.5}$ type FGNCs in the same way In case of second order phase transition, T_0 is practically the same as the transition temperature or the Curie point T_{cf}, while in case of a first order transition T_0 is lower than the Curie temperature T_{cf} T_{cf} of this FGNC was found to vary from 500 to 530 K depending on K concentrations It is more interesting to mention here that for any of the K-free superconducting precursor glasses (SG glasses), becoming superconductors by annealing, the plot of $1/\varepsilon'$ vs T (Fig 20b) did not at all match with that of K doped FGNC showing ferroelectric behavior (Fig 20a) Detailed analysis of the dielectric properties of other SG glasses without showing ferroelectric behavior can be found in the text [96–100]

Here we like to mention that frequency dependent conductivity $\sigma_{ac}(\omega) \propto \omega^s$ (where $s < 1$ is frequency exponent [13, 14]) of these FGNCs also supported the small polaron hopping conduction mechanism [86] Murawski

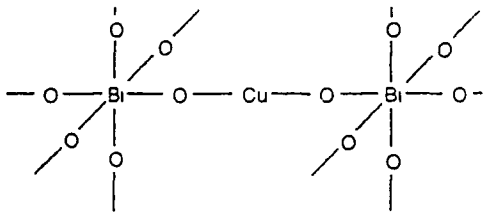

Figure 18 Network structure model of $Bi_4Sr_3Ca_3Cu_4O$ glasses In K doped glasses, Cu ions are partially replaced by K ions Reprinted with permission from [93], R Sato et al *J Non Cryst Solids* 160 180 (1993) © 1993, Elsevier Science

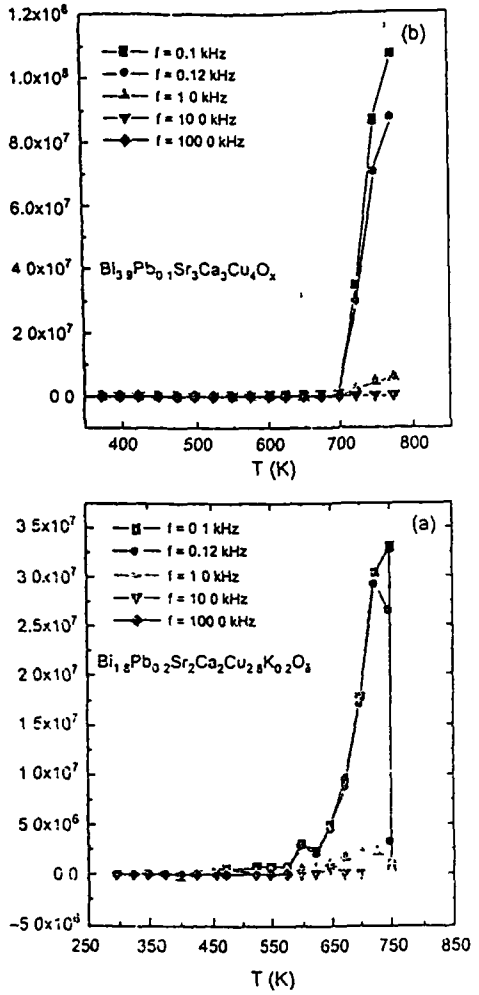

Figure 19. Thermal variation of real part of dielectric constant (ε') of (a) $Bi_{1.8}Pb_{0.2}Sr_2Ca_2Cu_{2.8}K_{0.2}O\delta$ and (b) $Bi_{3.9}Pb_{0.1}Sr_3Ca_3Cu_4O_x$ samples at different frequencies, 0.1–100 kHz. Reprinted with permission from [44], S. Mukherjee et al., *J. Appl. Phys.* 94, 1211 (2003), © 2003, American Institute of Physics.

and Barczynski [101] showed that a fractal structure was responsible for relaxation currents and the total conductivity $\sigma_t(\omega) = \sigma_{dc} + \sigma_{ac}(\omega)$ can be expressed as $\sigma_t = \sigma_{dc}[1 + K(d)(\omega/\omega_c)^r]$, where $r = 1 + d - d_f > 1$, d is the dimensionality of the space containing relevant clusters, and d_f is the fractal dimensionality of such clusters. For frequency $\omega < \omega_c = 2\pi f_c$, where f_c is the peak frequency at which dielectric constant data showed peaks and $K(d)$ is a dimensionally dependent constant related to the statistics of the contributing clusters ($K = 0.001$–0.0025) for many TMO glasses [90]. For a typical glass sample with $x = 30$ wt% of TiO_2, Mukherjee et al. [44] estimated d_f from the knowledge of ac conductivity and dielectric constant data of this sample. The estimated value of d_f was ~2.71 meaning that in the clusters the percolation paths also have three-dimensional character in the nanocrystal dispersed FGNCs.

Prasad et al. [31] observed that $50SrB_4O_7$–$50Bi_2VO_{5.5}$ glass nanocomposites heat-treated at 820 K/h did not show

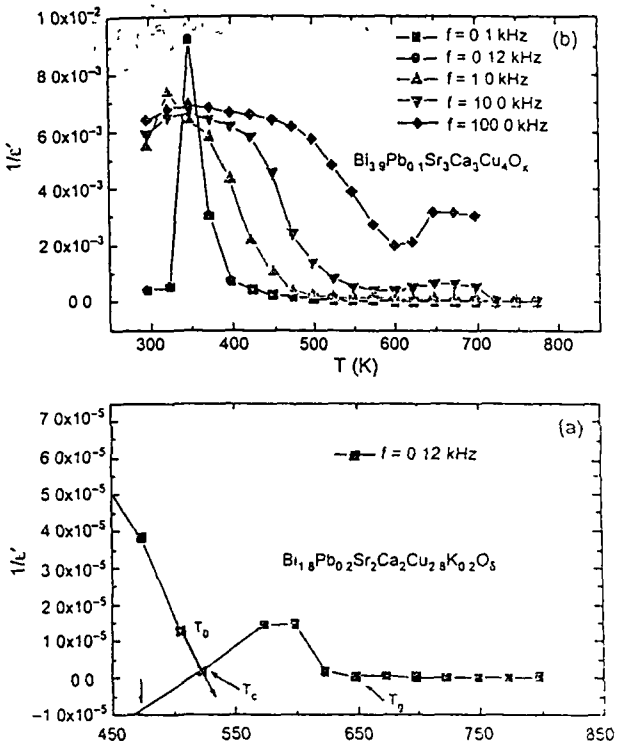

Figure 20. Variation of inverse dielectric constant ($1/\varepsilon$) with temperature of (a) $Bi_{1.8}Pb_{0.2}Sr_2Ca_2Cu_{2.8}O_\delta$ at a fixed frequency (0.12 kHz) and (b) $Bi_{3.9}Pb_{0.1}Sr_3Ca_3Cu_4O_x$ at different frequencies (0.1–100 kHz). Reprinted with permission from [44], S. Mukherjee et al. *J. Appl. Phys.* 94, 1211 (2003), © 2003, American Institute of Physics.

a polarization (P) versus electric field (E) hysteresis loop at room temperature (300 K) indicating that the coercive field required to switch on the polarization at this temperature was much higher. However, the sample exhibited a hysteresis loop in the vicinity of the ferroelectric to paraelectric transition temperature (720 K) associated with a remnant polarization (P_r) of 5.63×10^{-9} C cm^{-2} and coercive field (E_c) of 1250 V/cm (Fig. 21a). However, the values of P_r and E_c were, respectively [102], 2.25×10^{-8} C cm^{-2} and 650 V/cm for micrometer size crystallites containing $Bi_2VO_{5.5}$ ceramic. The loops disappeared and the plots became linear (Fig. 21b) at 780 K, which was beyond the phase transition temperature of this glass-nanocomposite. On cooling, the loops reappeared around 730 K, which was similar to that of the ferroelectric behavior of $Bi_2VO_{5.5}$ ceramics. Similar behavior was also exhibited by the K doped Bi–Sr–Ca–Cu–O FGNCs as discussed

7.5. Piezoelectric Properties

Though transport and other properties of the ferroelectric nanocrystal dispersed oxide glasses have been studied widely, the piezoelectric nanocrystal–glass composites have not been so extensively investigated. However, composites having perovskite dispersed polymer and glasses have been studied as electronic-ceramics [103–110]

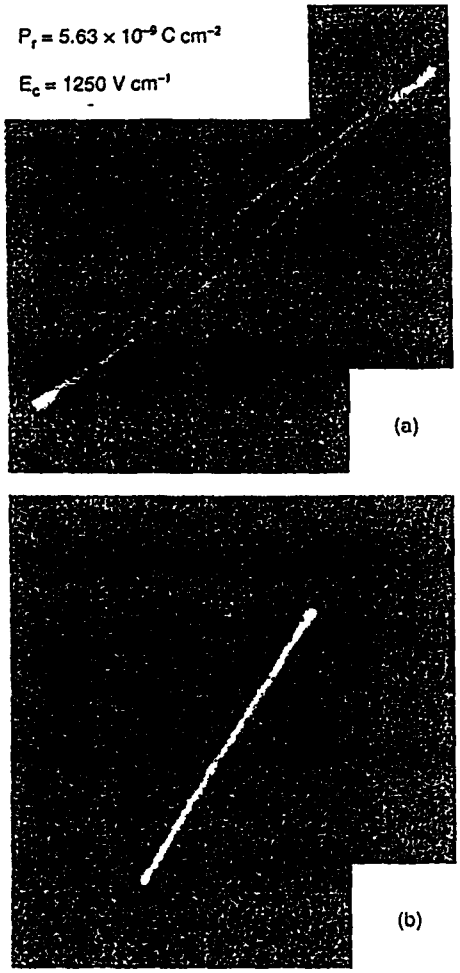

Figure 21. Hysteresis loops recorded on 820 K heat-treated $50SrB_4O_7$–$50Bi_2VO_{5.5}$ glass nanocomposites at two different temperatures, (a) 720 and (b) 780 K. P_r and E_c stand respectively for remnant polarization and coercive field. Reprinted with permission from [31], N. S. Prasad and K. B. R. Varma, *J. Mater. Chem.* 11, 1912 (2001). © 2001, The Royal Society of Chemistry.

The piezoelectric particulate reinforced nanocomposite ceramics have been broadly reported [111–119]. Various piezoelectric–nanocomposite systems like PZT/Ag, PZT/Al_2O_3, MgO/PZT, $BaTiO_3$/Ni, $BaTiO_3$/SiC, etc. have been explored by several groups [111–119]. The $PbZr_{0.5}Ti_{0.5}O_3$ type system can be used to prepare piezoelectric–glass nanocomposites [120]. The relative permittivity (ε') of these piezoelectric-nanocomposite systems is in the range of 1000–3000 at a temperature of 300 K and frequency of 1 kHz [119]. The dielectric constant and dielectric loss of the piezoelectric–nanocomposite system generally have an abrupt increase above the critical field as shown in Figure 22. This effect has been confirmed by different research groups [121]. Hagemann [122] proposed that this change is due to hysteretic domain wall motion and the resultant reorientation by spontaneous polarization. Similar to piezoelectric nanoparticle–glass composites,

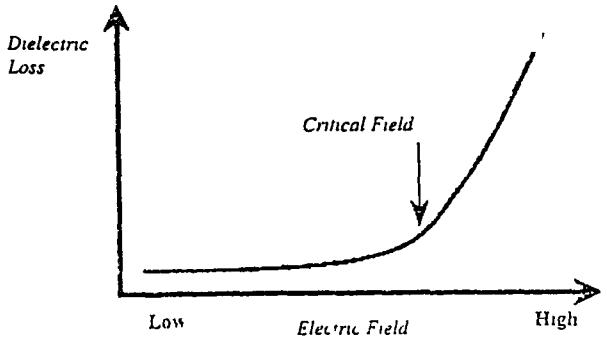

Figure 22. General trend of dielectric loss with applied electric field of piezoelectric glass-nanocomposites. Hysteretic domain wall motion above a critical field (indicated by arrow) leads to an increased dielectric loss. Reprinted with permission from [119a], S. R. Panteny et al., preprint (2002).

the pyroelectric nanoparticle–glass composites are not widely studied. Some composite films of lead titanate, PZT, lanthanum–lead titanate, and calsium–lanthanum–lead titanate into copolymer matrices for pyroelectric sensor application are already available in the literature [123–128].

7.6. Mechanical Properties

The mechanical behavior of a material is determined by its type of bonding and defect structure. Nanophase materials show increasing hardness with decreasing grain size. When the grain size of the material is reduced to the nanoscale, its mechanical property becomes strongly influenced due to the fact that a large fraction of the atoms in the material lie in the grain boundaries. So the material becomes superhard possessing hardness rivaling diamond [129, 130]. Glasses are generally very brittle. Dispersing nanocrystals inside the glass matrix can decrease its brittleness. Toughening is an extremely important property of glass for their practical use. A piezoelectric secondary phase (e.g., PZT particles) can increase the toughening when incorporated into the glass matrix. The works on PZT-containing ceramic matrix composites suggest that energy dissipation due to the piezoelectric effect as well as the motion of the domain wall should contribute to toughening. The sintering process of the mixtures containing different concentrations of PZT particles should be optimized in order to obtain a pore-free material. Transparent glass fiber reinforced silicate glass matrix composites with improved mechanical and optical properties are important for technical applications. The studies of mechanical properties of these products, viz. fracture strength, toughness, and thermal shock resistance, and the optical properties, viz. composite effective refractive index and light transmittance, are also very important for future investigation and analysis. Hot pressing is generally used to obtain dense glass-nanocomposite materials. The hardness of ferroelectric glass-nanocomposites are generally done by heat treatment of the material to produce a fine dispersion of particles within the microstructure which increases the resistance to domain wall motion [131].

8. TRANSPARENT FERROELECTRIC GLASS NANOCOMPOSITES

Some of the glass-nanocomposites are transparent since these have a big bandgap for light absorption for electrons, and so light absorption is very low and thus transmitted light fraction is very high. The nanoparticles in the glassy matrix are so small that light is unable to interact with them (i.e., the object is smaller than light wavelength) and thus the transparency of the glass-nanocomposite is not hampered by the inclusion of nanoparticles in the glass matrix. On the other hand, if the refractive index of the dispersed nanoparticles is the same as that of the base glass, it will also not affect the transparency of the glass. These materials have several advantages like easy formability, optical transparency, and low cost. Examples of some TFGNCs are $LiNbO_3$ nanocrystal embedded Li_2O–SiO_2–Al_2O_3 glass matrix and $KTiOPO_4$ (KTP) nanocrystals dispersed in SiO_2 glass matrix [35, 39].

In $KTiOPO_4$ (KTP)/SiO_2 TFGNC, the ferroelectric KTP nanocrystals were directly precipitated from K_2O–TiO_2–P_2O_5–SiO_2 parent glasses by heat treatment [35, 39]. The SAED, SEM, and TEM of these TFGNCs showed the distribution of the nanoparticles in the glass matrix beautifully before and after heat treatment. Particle sizes were measured from TEM photographs [35, 39]. The ultraviolet (UV) absorption band in these TFGNCs originated from the Ti–O band. There was also a strong absorption near 2800 nm, which corresponded to the well-known IR absorption band of the OH-band stretching mode. The transparency of these TFGNCs decreased with the increase of heat-treating temperature as shown in Figure 23. With the increase of heat-treatment temperature, the particle size increased and hence became able to interact with the light and as a result the transmittance decreased. However, these TFGNCs had a transmittance cutoff edge in the UV range at ~350 nm [35, 39].

The second order nonlinear susceptibility is generally induced only in a noncentrosymmetric crystal structure or anisotropic materials. In other words, second harmonic generation (SHG) in glasses should be forbidden as glasses have macroscopic inversion symmetry. Therefore, SHG and other electro-optical effects are usually unexpected in glassy systems. In fact, no SHG signal was observed in different SiO_2-based glasses [35] like $20P_2O_5$–$80SiO_2$, $10K_2O$–$10TiO_2$–$80SiO_2$, $10TiO_2$–$10P_2O_5$–$80SiO_2$, and $20TiO_2$–$80SiO_2$. But the SHG signal has been reported in some poled glasses [132] and photoinduced glasses [133–135] though the origin of the SHG signal was completely unclear. SHG was also observed in GeO_2-, CeO_2-, and Eu_2O_3-containing SiO_2 glass fibers which was due to the defects and additives and may be the origin of the SHG centers in the glasses [135–138]. The multicomponent K_2O–TiO_2–P_2O_5–SiO_2 parent glasses, when annealed at 550 °C, did not contain resolvable crystallites [39] as analyzed by XRD and hence did not exhibit any SHG signal (Fig 24a) Nevertheless, when annealed at 750 °C, it contained KTP nanocrystals dispersed in SiO_2 glass matrix and exhibited the SHG signal with a narrow bandwidth at 532 nm signifying a true SHG process (Fig. 24b). These results suggested that the SHG in KTP/SiO_2 TFGNC originated from KTP nanocrystals embedded in SiO_2 matrix [35]. It is to be noted here that a third order nonlinear optical susceptibility or third harmonic generation in silver nanocrystal dispersed BaO–B_2O_3–P_2O_5 glass was observed around the surface plasmon resonance band [51].

9. APPLICATIONS

Nanophase engineering with organic and inorganic materials is expanding enormously to manipulate optical and electronic functions. Semiconducting nanoparticles have been the subject of increasing interest since the demonstration in 1975 of the enhancement of their third order nonlinear optical properties [139]. Very small semiconductor (<10 nm) or metal particles in glass composites and semiconductor/polymer composites show interesting quantum effects and nonlinear electrical and optical properties. Nanocomposite materials consisting of small metal or oxide particles dispersed in glass matrices are attracting much

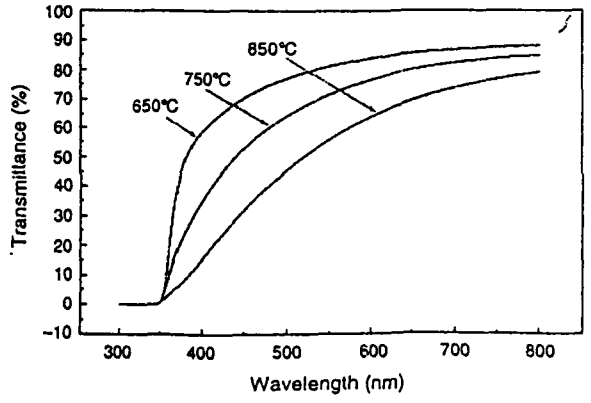

Figure 23. Wavelength variation of optical transmittance (%) of $20(K_2O$–TiO_2–$P_2O_5)$–$80SiO_2$ system heat-treated at various temperatures (650, 750, and 850 °C) for 4 hours. Reprinted with permission from [35], D. L. Li et al., *J. Non-Cryst. Solids* 271, 45 (2000). © 2000, Elsevier Science.

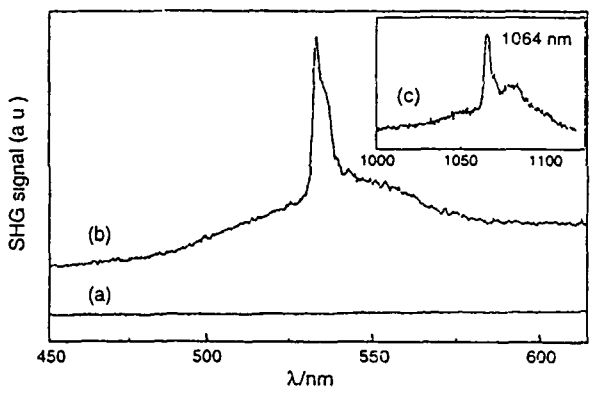

Figure 24. The SHG (532 nm) spectra for (a) $30(K_2O$–TiO_2–$P_2O_5)$–$70SiO_2$ multicomponent glass, (b) 30KTP–$70SiO_2$ nanocomposites prepared by heating at 750 °C, and (c) fundamental beam (1064 nm). Reprinted with permission from [39], D. L. Li et al., *J. Non-Cryst Solids* 261, 273 (2000). © 2000, Elsevier Science

attention because of their potential use in a variety of fields, such as optics, magnetism, and electronics [140–146]. Semiconducting nanoparticles are particularly interesting due to their possible applications in diverse areas like photocatalysis, solar cells, display panels, and new devices, viz. single electron transistors and so on [147–149] A high third order optical nonlinearity of semiconducting nanocrystal composites allow a wide range of useful function, such as high speed all-optical switching and other signal processing operations Ferroelectric nanoparticles can be treated as built in electrical dipoles, which can produce electro-optic effects, photorefraction, and harmonic generation The FGNC systems are both semiconducting and ferroelectric with a giant dielectric constant. The FGNCs with high permitivitty may be attractive for applications in microelectronics Because of the ferroelectric behavior of glass-nanocomposites, they have additional applications as sensor materials [150] When an ordinary glass is doped with quantized semiconductor colloids, it becomes a high-performance optical medium with potential applications in optical computing Very small particles have special atomic structures with discrete electronic states that give rise to an extraordinary property like superparamagnetism Magnetic nanocomposites have been used for mechanical force transfer (ferrofluids), high-density information storage, and magnetic refrigeration Piezoelectric nanocrystal–glass composites are more sensitive materials for high frequency hydrophones

Transparent FGNCs having nonlinear optical properties are used in transducers, sensors, and actuators in the fields of communication, energy, and health These new totally inorganic materials will be attractive for various optical applications (switching and memory devices) where currently standard monolithic glasses cannot be used due to poor mechanical properties More conventional applications of wide commercial interest such as architectural and building materials are also possible including applications where high fire and thermal shock resistance are required and where standard laminated glasses are not suitable due to their organic components The superhardness of the glass-nanocomposites can be used as a material requiring friction and wear resistance The superhard nanostructured films promise revolutionary improvements for wear protection for applications in high speed machining as well as in the emerging field of miniaturized moving parts in microelectromechanical systems [129, 130]

10. CONCLUSIONS

The ferroelectric glass-nanocomposites (FGNCs) are formed by uniformly dispersing nanocrystalline particles/clusters of TiO_2, $BaTiO_3$, $PbTiO_3$, $SrTiO_3$, $PbZrO_3$, $KTiOPO_4$, $Bi_2VO_{5.5}$, $Li_2Ge_7O_{15}$, PbS, etc in the glass matrices These FGNCs show giant dielectric constant, ferroelectric, and piezoelectric behavior depending on their composition The electrical and the dielectric properties of these FGNCs are found to depend on the size and concentration of the dispersed nanoclusters in the glass matrices For lower concentrations of FE nanocrystals ($\leq$5 wt% with average grain or cluster size <10 nm), the increase of conductivity was found to be small. A sharp rise of conductivity occurred for the FGNCs with 5 and 10 wt% TiO_2 embedded in $80V_2O_5$–$20P_2O_5$ glass For higher concentrations (>10 wt% with average grain or cluster size >20 nm), the conductivity increased slowly with increase of concentration The increase of electrical conductivity compared to the base glass was considered to be due to the precipitation of nanocrystalline phase in the base glass matrix A phase separation appeared in the FGNC between 5 and 10 wt% TiO_2 showing nonlinearity in the concentration dependent conductivity and dielectric permittivity The dielectric constant also showed the maximum value for the FGNC between 5 and 10 wt % The high dielectric constant of these FGNCs might be related to the space charge polarization or ionic relaxation polarization occurring at the interface as suggested by Zhang et al [78] Very strong polaronic couplings (γ varies from 12 to 25, generally for TMO glasses, $\gamma \sim 1$ indicates very strong electron–phonon interaction constant) observed for these FGNCs play an important role for their high dielectric constant It appears that there is an average critical grain/cluster size ($\sim$10 nm) above which dielectric constant of these FGNCs tends to decrease In the literature, grain size effects on ferro- and antiferroelectric oxide materials have been well established both theoretically and experimentally [29, 77] For ferroelectric $PbTiO_3$, the estimated critical size resides between 8.2 and 13.8 nm [29] Recently the high dielectric constant in $CaCu_3Ti_4O_{12}$ [45, 46] was also explained by considering semiconducting grains with insulating grain boundaries Further study of dielectric and conductivity relaxation behavior in these FGNCs would be interesting Problems related to the uniform size and distribution of the nanoparticles and preparation of the samples in the form of wire, tapes, thin films, etc from these nanoparticle-dispersed glasses are yet to be explored More elaborate theoretical analysis is necessary to understand the origin of the giant dielectric constant in these systems Moreover, our understanding of higher harmonic generations in nanocrystal dispersed glassy materials is no way complete Thorough experimental and theoretical investigations on such materials are highly encouraging SHG signal in TFGNCs was found to originate from the KTP nanocrystals embedded in SiO glassy matrix [35, 39]

The ferroelectric nanocrystal dispersed oxide glasses will most probably gain rapidly increasing importance in the near future In general properties, production, and characterization methods and their interrelations are, however, not yet satisfactorily understood Hence, efforts need to be made to enable the directed tailoring of nanophase, nanoscopic, and nanocomposite materials for future technological and industrial applications The main disadvantage of ferroelectric crystals grown within a glass medium is the difficulty in poling them because of the low dielectric permittivity of the glass matrix However, the precipitating of nanocrystalline FE metallic phase in glass matrix is easy and it enhances the dielectric constant of the glass enormously [33]

GLOSSARY

AC conductivity Frequency dependent conductivity The conductivity of the material changes both with temperature and frequency From the study of electric conductivity of solid materials (composites etc.), mechanism of electron or

ion transport, responsible for the electrical conductivity, can be explained.

Correlated barrier hopping (CBH) Mechanism of electrical conductivity. The charge carrier is assumed to hop between site pairs over the potential barrier (W) separating them. For the neighboring sites at a distance R the effective potential barrier will be reduced to a value Wo due to overlap of Coulomb potential of the two sites Thus the barrier height is correlated with the site separation R (for references see text).

Curie temperature The ferroelectric property of a crystal disappears above a critical temperature TC This temperature is called Curie temperature. Above the Curie temperature, the ferroelectric phase become paraelectric, like ferromagnetic to paramagnetic transition

Ferroelectricity It is a special property of some crystalline materials showing spontaneous polarization A necessary, but not sufficient, condition for a solid to be ferroelectric is the absence of a canter of symmetry. In total there are 21 classes of crystals, which lack a center of symmetry The classes are based on the rotational symmetry of crystals

Ferroelectric glass nanocrystal composite (FGNC) When some transition metal oxides are mixed with ferroelectric oxides PZT etc. nanocrystal of the ferroelectric oxides are precipitated in the glass matrix. These nanocrystals embedded glassy phase is called the glass-nanocrystal composite. Depending on the grain size and concentration of these nanoparticles, the properties of the FGNC change

Melt-quenching This technique is widely used for preparing disordered glassy and amorphous materials. The materials (metallic oxides, in particular) are melted to the liquid phase and quickly quenched to room temperature

Overlapping large polaron tunneling (OLPT) If there is appreciable overlap of the lattice distortion in the electron wave function, this model is used to explain ac conductivity of semiconductors in disordered materials The electronic wave function in this case extends over many atomic sites, hence the polaron is termed as large polaron. (See text for details).

Phonon The vibrations of the atoms or molecules are considered to be quantized and phonon is the quantized lattice vibration.

Piezoelectric Of the 21 classes of feroelectric crystals, 20 are piezoelectric, i.e. these crystals become polarized under the influence of external stress.

Polaron Localized charged carriers (formed due to strong interaction between the phonon and the carriers) which strongly interacts with the lattice. If the electron wave function extends over many atomic sites, the polarons are called large polarons, otherwise polarons are called small polarons

Pyroelectric Ten out of the 20 piezoelectric classes exhibit pyroelectric effects. These pyroelectric crystals are spontaneously polarized.

Quantum mechanical tunneling (QMT) In this process variable range phonon assisted quantum mechanical tunneling between sites close to Fermi level is considered for explaining electrical conductivity in disordered materials like composites, glass etc.

Scanning electron microscope (SEM) This is a technique for studying the surface structure of the materials.

Transition metal oxide (TMO) glasses The transition metal (Fe, Co, Ni, Cu, Mn etc) oxides when melted at higher temperature and quickly quenched to room temperature, forms oxide glasses. These glasses are semiconductors because of the the hopping of electrons/holes from higher valence to lower valence states of the transition metal ions Strong electron-phonon interaction is responsible for the polaron formation in these glasses

Transmission electron microscope (TEM) This is a technique for studying the surface structure of the materials

ACKNOWLEDGMENT

B K Chaudhuri is grateful to the National Science Council (NSC) ROC, for partial financial assistance during his visit to the Department of Physics, NSYSU, Kaohsiung, Taiwan ROC

REFERENCES

1 H Hirashima, Y Watanabe, and T Yoshida, *J Non Cryst Solids* 95 & 96, 825 (1987)
2 Y Sakuri and J Yamaki, *J Electrochem Soc* 132, 512 (1985)
3 S Chakraborty, H Satou, and H Sakata, *J Appl Phys* 82, 5520 (1997)
4 C H Chung and J D Mackenzie, *J Non Cryst Solids* 42, 357 (1980)
5 V K Dhawan, A Mansingh, and M Sayer, *J Non Cryst Solids* 51 87 (1982)
6 A Ghosh and B K Chaudhuri, *J Non Cryst Solids* 83, 151 (1986)
7 G N Greaves, *J Non Cryst Solids* 11, 427 (1973)
8 H Mori, T Kitami, and H Sakata, *J Non Cryst Solids* 168, 157 (1994)
9 K Sega, Y Kuroda, and H Sakata, *J Mater Sci* 33, 1303 (1998)
10 H Hirashima, K Nishii, and T Yoshida, *J Am Ceram Soc* 66 704 (1983)
11 H Sakata, K Sega, and B K Chaudhuri, *Phys Rev B* 60, 3230 (1999)
12 I G Austin and N F Mott, *Adv Phys* 18, 41 (1969)
13 N F Mott, *Adv Phys* 16, 49 (1967)
14 A M Ier and E Abrahams, *Phys Rev* 120, 745 (1960)
15 N F Mott and E A Davis, in "Electronic Processes in Non-Crystalline Materials," 2nd ed Clarendon, Oxford, 1979
16 N F Mott, *Philos Mag* 19, 835 (1969)
17 M Casu, A Lai, A Musinu, G Piccaluga, S S Solinas, S Bruni, F Cariati, and E Beretta, *J Mater Sci* 36, 3731 (2001)
18 B Capeon, T Gacoin, J M Nedelec, S Turrel, and M Bouazaoui, *J Mater Sci* 36, 2565 (2001)
19 N Hebalkar, A Cobo, S R Sainkar, S D Pradhan, W Vogel, J Urcan, and S K Kulkarni, *J Mater Sci* 36, 4377 (2001)
20 H Itoigawa, T Kamiyama and Y Nakamura, *J Non Cryst Solids* 210, 95 (1997), *ibid* 220, 210 (1997)
21 S Charterjee, S Banerjee, and B K Chaudhuri, *J Appl Phys* 81, 7320 (1997)
22 Y G Wang, W L Zhong, and P L Zhang, *Phys Rev B* 51, 11439 (1996)
23 A M Glass, K Nassau, and J W Shiever, *Appl Phys Lett* 31, 249 (1977)
24 M Takashinge, T Mitsui, T Nakamura, Y Akiawa, and M Jang, *Jpn J Appl Phys* 20, L159 (1981)

25 A M. Glass, K. Nassau, and J. W Shiever, *J Appl. Phys.* 48, 5213 (1977).
26 M Takashinge, T Nakamura, H Ozawa, R Uno, N Tsuyo, and K. Ari, *Jpn J Appl. Phys.* 19, L255 (1980).
27 G Burns and B A. Scott, *Phys Rev B* 7, 3088 (1993)
28 T Matsumoto, A Fukuda, M Johno, Y Motoyama, T Yui, S S Seomun, and M Yamashita, *J Chem Phys* 9, 2051 (1999)
29 M Sadhukhan, S Chakraborty, D K Modak, and B K Chaudhuri, *Philos Mag B* 72, 139 (1996)
30 M Sadhukhan, D K Modak, and B K Chaudhuri, *J Appl Phys* 85, 3477 (1999)
31 N S Prasad and K B R Varma, *J Mater Chem* 11, 1912 (2001)
32 N S Prasad, K V R Varma, and S B Lang, *J Phys Chem. Solids* 62, 1299 (2001)
33 T K Kundu and D Chakravorty, *Appl Phys Lett* 67, 2732 (1995)
34 T K Kundu, M Mukherjee, D Chakravorty, and L. E Cross, *J Appl Phys* 83, 4380 (1998)
35 D L. Li, L B Kong, L Y Zhang, and X Yao, *J Non-Cryst Solids* 271, 45 (2000)
36 R S Meltzer, W M Yen, H Zheng, S P Feofilov, M J Dejneka, B M Tissue, and H B Yuan, 64, 100201 (2001)
37 S A Basun, A A. Kaplyanskii, and S P. Feofilov, *Sov Phys Solid State* 34, 1807 (1992)
38 S A Basun, A A Kaplyanskii, and S P Feofilov, *Ferroelectrics* 143 163 (1993)
39 D Li, Y Lin, L Zhang, and X Yao *J Non Cryst Solids* 261, 273 (2000)
40 S Chottopadhyay, A Pushan, V R Palkar, and M Manu, *Phys Rev B* 52, 13177 (1995).
41 S Chakraborty, M Sadhukhan D K Modak, K K Som H S Maiti, and B K Chaudhuri, *Philos Mag B* 71, 1125 (1995)
42 A A Bhagat and T M Kamel *Phys Rev B* 63 012101 (2001)
43 S Bhattacharya, H Sakata, and B K Chaudhuri, *Phys Rev B*, 68 16201 (2003)
44 S Mukherjee H Sakata, B K Chaudhuri S Mollah, and H D Yang, *J Appl Phys.* 94, 1211 (2003)
45 D C Sinclair T B Adams, F D Morrison, and A R West *Appl Phys Lett* 80, 2153 (2002)
46 Y Lin Y B Chen T Garret, S W Liu, C L Chen, L Chen, R P Bontchev, A Jacobson, J C Jiang, E I Meletis J Horwitz, and H -D Wu, *Appl Phys Lett* 81, 631 (2002)
47 B G Kim, S M Cho, T Y Kim, and H M Jang, *Phys Rev Lett* 86, 3404 (2002)
48 S Chakraborty, M Sadhukhan, D K Mocak, and B K Chaudhuri, *J Mater Res* 30, 5139 (1995)
49 H Mori and H Sakata, *J Mater. Sci* 31, 1621 (1996)
50 M Sadhukhan, D K Modak, and B K. Chaudhuri, *J Chem Phys* 105, 11326 (1996)
51 Y Hamanaka, N Hayashi, A Nakamura, and S Omi, *J Lumin.* 87–89, 859 (2000)
52 K. Uchida, S. Kaneko, S Omi, C Hata, H. Tanji, Y Asahara, A J Ikushima, T. Tokizaki, and A Nakamura, *J Opt Soc Amer B* 11, 1236 (1994)
53 F Hache, D Ricard, and C Flytzanis, *J Opt Soc Amer B* 3, 1647 (1986)
54 M Fujii, A Mimura, S Hayashi, Y Yamamoto, and K. Murakami, *Phys Rev Lett* 89, 206805 (2002)
55 A Mimura, M Fujii, S Hayashi, D Kovalev, and F Koch, *Phys Rev B* 62, 12625 (2000)
56 M Fujii, A Mimura, S Hayashi, and K Yamamoto *Appl Phys Lett* 75, 184 (1999)
57 M Fujii, A Mimura, S Hayashi, K Yamamoto, C Urakawa, and H Ohta, *J Appl. Phys* 87, 1855 (2000)
58 H Hofmann, P Bowen, N Jongen, and J Lemaitre, *Scripta Mater* 44, 2197 (2001)
59 B K. Chaudhuri, *Chinese J Phys* 38, 211 (2000).
60 C F Drake, J A Stephens, and B Yates, *J Non-Cryst Solids* 28, 61 (1986)
61 J E Shelpy, *J Amer Ceram. Soc* 57, 436 (1975)
62 J E Shelpy, *J Appl Phys* 46, 193 (1975)
63 T Nishida, M Ogatta, and Y Takashina, *Bull. Chem Soc Jpn* 59, 2204 (1986).
64 D K Modak, U K Mondal, H Sakata, and B K Chaudhuri, *Sol State Phys* 43, 368 (2000)
65 S Mondal and A Ghosh, *Phys Rev B* 48, 9388 (1993)
66 V Dimitrov and Y Dimitrov, *J Non-Cryst Solids* 122 133 (1990)
67 N F Borrelle, B D Mc Swain, and G Su, *Phys Chem Glasses* 4, 119 (1963)
68 T Quan and C F Adams, *J Phys Chem* 70 331 (1966)
69 A Mansing and V K Dhawan *J Phys C* 11 3439 (1978)
70 H Mori and H Sakata, *J Ceram Soc Jpn* 102, 562 (1994)
71 J Appel, "Solid State Physics," Vol 21, p 193 Academic Press, New York, 1968
72 N N Ritten and T Abraham *Am Ceram Bull* 76, 51 (1997)
73 R R Heikes, A A Maradudin and R C Miller, *Ann Phys (NY)* 8, 733 (1963)
74 D Emin and T Hilstein, *Ann Phys (NY)* 53, 439 (1969)
75 D Emin, *Phys Rev Lett* 32, 303 (1975)
76 J Schnakenberg, *Phys Status Solidi* 28, 623 (1968)
77 G P Triberis and L. Friedman, *J Phys C* 18, 2281 (1985), G P Triberis, *J Non-Cryst Solids* 74, 1 (1979)
78 L D Zhang H F Zhang, G Z Wang, C M Mo, and Y Zhang, *Phys Status Solidi* 4 157, 483 (1996)
79 M Sayer and A Mansingh, *Phys Rev B* 6, 4629 (1972)
80 M H Cohen, *J Non Cryst Solids* 4, 391 (1970)
81 S R Elliott *Adv Phys* 36 135 (1987)
82 A R Long *Adv Phys* 31, 553 (1982)
83 M Polak *Phys Rev* 128 1822 (1965), *Philos Mag* 23, 317 (1971)
84 A L Efros, *Philos Mag B* 43, 829 (1981)
85 G E Pike *Phys Rev B* 6, 1572 (1972)
86 D K Modak Ph D Thesis Jadavpur University, Kolkata India 2000
87 H Frohlich Theory of Dielectrics ' Oxford University Press 1958
88 P B Macedo C T Moynihan and R Bose *Phys Chem Glasses* 13, 171 (1972)
89 K Cole and R H Cole, *J Chem Phys* 9 341 (1941)
90 W L Zhong, Y G Wang, P L Zhang, and B D Qu, *Phys Rev B* 50, 689 (1994)
91 W L Zhong, B Jiang, P L Ma H M Cheng, Z H Yang, and L X Li, *J Phys Condens Matter* 5, 2619 (1993)
92 W H Dumbaugh, *Phys Chem Glasses* 27, 119 (1986)
93 R Sato, T Komatsu, and K Matusita, *J Non Cryst Solids* 160, 180 (1993)
94 H Mori, H Matsumo, and H Sakata, *J Non Cryst Solids* 276 78 (2000)
95 T Szorenyi K Bali, and I Hevesi, *J Non Cryst Solids* 70, 297 (1985)
96 K K Som and B K. Chaudhuri, *Phys Rev B* 41, 1581 (1990)
97 S Chatterjee, S Banerjee, S Mollah, and B K Chaudhuri, *Phys Rev B* 53 5942 (1996)
98 T Komatsu, R Sato, C Hirose, K Matusita, and Y Matushita *Jpn J Appl Phys* 27, L2293 (1988)
99 Y Akamatsu, M Tatsumisago, N Tohge S Tsuboi and T Minami, *Jpn J Appl Phys* 27, L1696 (1988)
100 S Mollah, K K Som, K. Bose, and B K Chaudhuri *Phys Rev B* 46, 11075 (1992)
101 L Murawski and R J Barczynski, *J Non Cryst Solids* 185, 84 (1995)
102 K Shantha and K B R Varma, *J Amer Ceram Soc* 83 1122 (2000)

103 A Herczog, *J Amer. Ceram. Soc* 47, 107 (1964)
104 V F. Janas and A. Safari, *J. Amer. Ceram. Soc.* 78, 2345 (1995)
105 H I Hsiang and F S Yen, *Jpn J Appl Phys* 33, 3991 (1994)
106 T Yamamoto, K. Urabe, and H Banno, *Jpn J Appl. Phys* 32, 4272 (1993)
107 M H Lee, A Hallıyal, and R E Newnham, *J Amer Ceram Soc* 72, 986 (1989)
108 G S Gong, A. Safari, S J Jang, and R E Newnham, *Ferroelectr Lett* 5, 131 (1986)
109 F Duan, C P Fang, Z Y Ding, and H Q Zhu, *Mater Lett* 34 184 (1998)
110 B Houng, C Y Kim, and M J Haun *IEEE Trans Ultra Ferro Freq Contl* 47, 808 (2000)
111 K. Nihara, *J Ceram Soc Jpn* 99, 974 (1991)
112 T Nagai, H J Hwang, M Yasuoka, M Sando, and K Nihara, *J Kor Phys Soc* 32, S1271 (1998)
113 C E Borsa, S Jiao, R I Todd, and R J Brook, *J Microsc* 77, 305 (1995)
114 L C Stearns, J Zhao, and M P Harmer, *J Euro Ceram Soc* 10, 473 (1992)
115 H J Hwang, S Ueda, and K Nihara, *Ceram Trans* 44, 399 (1994)
116 T Nagai, H J Hwang, M Yasuoka, M Sando, and K Nihara, *Jpn J Appl Phys* 37, 3377 (1998)
117 H Hyuga, Y Hayashi, T Sekino, and K. Nihara, *Nanostruct Mater* 9, 547 (1997)
118 T Ohji, Y-K Jeong, Y-H Chao, and K Nihara, *J Amer Ceram Soc.* 81, 1453 (1998)
119 (a) S. R. Panteny, R. Stevens, and C R Bowen, preprint (2002) (b) S R. Panteny, C R Bowen, and R Stevens, *Key Eng Mater* 206, 1313 (2002)
120 A M Morales, M Gonzales, and J M Hruby, in "Proc 7th Fore sight Conference on Molecular Nanotechnology, 1999
121 K Wu and W Schulze, *J Amer Ceram Soc* 75, 3385 (1992)
122 H J Hagemann, *J Phys C Solid State Phys* 11, 3333 (1978)
123 Q Zhang, H L. Chan, Q Zhou and C L Choy, *Mater Res Innovat* 2, 283 (1999)
124 H L W Chan, Y Chen, C L Choy, *J Amer Ceram Soc* 81, 1231 (1998)
125 Q F. Zhou, H L W Chan, and C L Choy, *J Mater Proc Techn* 63, 281 (1997)
126 Q. F Zhou, L S Yin, J X Zhang, H L W Chan, and C L Choy, *J. Kor Phys Soc* 32, S1380 (1998)
127 N M Shorrocks, A. Patel, M J Walker, and A D Parasons, *Microelectron. Eng* 29, 59 (1995)
128 B Willing, M Kohli, K. Brooks, P Muralt, and N Setter, *Ferroelectrics* 201, 147 (1997)
129 S L. Grishick, W. W. Gerberich, J V R. Heberlein, and P H McMurry, NSF Foundation Nanostructure grant 9871863
130 F Di Fonzo, A Gidwani, M H Fan, D Neumann, D I Iordanoglou, J V R Heberlein, P H McMurry, S L Girshick, N Tymiak, W W Gerberich, and N P Rao, *Appl Phys Lett* 77, 910 (2000)
131 I Harris and T Bailey, in 'Nd-Fe Permanent Magnets Their Present and Future Applications' (I Mitchell, Ed) Elsevier England, 1985
132 R A Mayers, N Mukherjee, and S R J Bruek, *Opt Lett* 16 1732 (1991)
133 J Wasylak, J Kucharski, and I V Kityk *J Appl Phys* 85 425 (1999)
134 I V Kityk, E Golis, J Fihpecki, J Wasylak, and V M Zacharko, *J Mater Sci* 14, 1292 (1995)
135 T E Tasi, C G Askins, and E J Friebeble, *Appl Phys Lett* 61 390 (1992)
136 U Obsterberg and W Margulis, *Opt Lett* 11, 516 (1986)
137 Y Fuji, B S Kawasaki, K O Hill, and D C Johnson, *Opt Lett* 5, 48 (1980)
138 Y Sasaki and Y Ohmori, *Appl Phys Lett* 39, 466 (1981)
139 C Flystanis, in "Quantum Electronics A Treatise," Vol 1a Academic Press, New York, 1995
140 S Komaren, *J Mater Chem* 2, 1719 (1992)
141 W F Smith, in "Principles of Materials Science and Engineering ' McGraw-Hill, Singapore, 1986
142 R W Siegel, *Nanostruct Mater* 3, 1 (1993)
143 G Piccaluga, A Carnias, G Ennas and A Musinu, *J Mater Res* 13, 1 (2000) and references there in
144 R Uyeda, *Progr Mater Sci* 35, 1 (1991)
145 L E Brus, *J Chem Phys* 79, 5566 (1983)
146 A P Alivisatos, *Science* 271, 933 (1996)
147 D L Klein, R Roth, A K Lim, A P Alivisatos, and P Mceuen *Nature* 389, 699 (1997)
148 V L Colvin, M C Schlamp, and A P Alivisatos, *Nature* 370 354 (1994)
149 R N Bhargava, *J Lumin* 70, 85 (1996)
150 M E Lines and A M Glass, "Principles and Applications of Ferroelectricity and Related Materials" Clarendon, Oxford, 1979

JOURNAL OF APPLIED PHYSICS VOLUME 94, NUMBER 2 15 JULY 2003

Transport and dielectric properties of K doped glassy precursor for high T_C superconductor showing ferroelectric behavior due to embedded nanocrystalline ferroelectric phase

Soma Mukherjee
Department of Solid State Physics, Indian Association for the Cultivation of Science, Jadavpur, Kolkata-700032, India

H. Sakata
Department of Applied Chemistry, Tokai University, 1117, Kitakaname Hiratsuka Kanagawa 259-1292, Japan

B. K. Chaudhuri[a)]
Department of Solid State Physics, Indian Association for the Cultivation of Science, Jadavpur, Kolkata-700032, India and Department of Physics, National Sun Yat Sen University, Kaohsiung, Taiwan 804, Republic of China

S. Mollah
Department of Physics, National Sun Yat Sen University, Kaohsiung, Taiwan 804 Republic of China and Department of Physics, Aligarh Muslim University, Aligarh-202002, India

H. D. Yang
Department of Physics, National Sun Yat Sen University, Kaohsiung, Taiwan 804, Republic of China

(Received 26 September 2002; accepted 1 May 2003)

Partial substitution of Cu by K in multicomponent glassy precursor for high T_C superconductor *viz* $Bi_{2-x}Pb_xSr_2Ca_2Cu_3O_\delta$ ($x=0.1?$ .3) is found to destroy superconductivity of the corresponding annealed phase. These glasses *viz.* $Bi_{2-x}Pb_xSr_2Ca_2Cu_{3-y}K_yO_z$ ($x=0.1?$ .3, $y=0.2$), however, show ferroelectric transitions (between 500 and 530 K depending on x). The corresponding K free glasses are not ferroelectric but they are good precursors for high T_C superconductor. Nanocrystalline particles/clusters (~10? 0 nm size) embedded in the K doped glasses, observed from transmission electron microscopic studies, are considered to be responsible for the ferroelectric behavior of the bulk glass nanocrystal composite (GNC). Unlike K free glasses, the K-containing glasses do not become superconductor by annealing them at higher temperature. This indicates suppression of superconductivity by the precipitation of ferroelectric nanoparticles in the K doped GNC. Though their dielectric behavior is different, both the K free and K containing glassy systems are semiconductors and follow the similar nonadiabatic small polaron hopping conduction mechanism (obeying Holstein condition). A comparative study of the properties of the two glassy systems showing distinguishing behavior has been made. © *2003 American Institute of Physics* [DOI: 10.1063/1.1586971]

I. INTRODUCTION

Transition metal oxide glasses are interesting because of their probable technological applications.[1?] The semiconducting behavior in these glasses is due to the small polaron formation and hopping of these polarons from higher to the lower valence states of the transition metal ions (TMI). After the discovery of Bi based high T_C superconductors, it was noticed that some of the multicomponent glasses like $Bi_4Sr_3Ca_3Cu_4O_x$, $Bi_2Sr_2Ca_2Cu_3O_x$, $Bi_{4-y}Pb_ySr_3Ca_3Cu_4O_x$, etc. (referred to as SG glass) are very good precursors for high T_C superconductors.[4?] These glasses become superconductors (mostly 2223/2212 type)[4?] by annealing them around 840 ℃ for about 24 h. Recently Bahgat *et al*[9] prepared Bi based $Bi_{1.8}Pb_{0.3}Sr_2Ca_2Cu_{2.8}K_{0.2}O_\delta$ glass and considered it as a homogeneous multicomponent glass. They also reported ferroelectric (FE) behavior of this glass with ferroelectric Curie temperature T_{Cf} around 530 K. Here we should mention that it is a long-standing problem whether FE transition with spontaneous polarization is possible in pure homogeneous inorganic oxide glassy system. It is then difficult to justify ferroelectricity from crystal symmetry consideration. Lines[10] considered theoretically the possibility of FE phase in pure glass. But ferroelectricity has so far not been observed in pure glassy system even though FE ordering has been observed in liquid crystalline medium[11] where some kind of molecular order is present. Multicomponent vanadate and phosphate glasses doped $BaTiO_3$ and $SrTiO_3$ have also been studied earlier[12,13] showing high dielectric constant due to the presence of nanocrystalline ferroelectric phases embedded in the glass matrix (formed during glass formation from melt by fast quenching). Recently high dielectric constant observed in

a)Author to whom correspondence should be addressed, electronic mail sspbkc@mahendra.iacs.res.in

TABLE I. Some parameters for the $Bi_{2-x}Pb_xSr_2Ca_2Cu_{2.8}K_{0.2}O_\delta$ ($x=0.0, 0.1, 0.2$) and $Bi_{1.8}Pb_{0.3}Sr_2Ca_2Cu_{2.8}K_{0.2}O_\delta$ (Pb3K2) FG glasses T_g, T_x, density, and θ_D are obtained from the experimental data. Other parameters are obtained from the best fitting

Parameter	Pb0K2	Pb1K2	Pb2K2	Pb3K2
T_g (K)	340±5	350±5	360±5	400±5
T_x (K)	400±5	405±5	410±5	430±5
Density (g cm^{-3})	5.39±0.02	5.34±0.02	5.32±0.02	5.28±0.02
N (10^{21} cm^{-3})	9.017	8.932	8.899	8.821
R (Å)	4.805	4.820	4.826	4.839
C	0.777	0.8532	0.737	0.773
r_p (Å)	1.936	1.942	1.945	1.950
θ_D (K)	365	418	360	348
υ_{ph} (10^{12} Hz)[a]	7.6	8.72	7.51	7.26
α (Å^{-1})[a]	0.551	1.075	1.652	2.137
W (eV)[a]	0.2519	0.124	0.122	0.101
W_H (eV)[b]		0.08	0.122	0.201
W_D (eV)[b]		0.18	0.122	0.701
υ_{ph} (10^{12} Hz)[b]		9.8	8.2	7.86

[a]Indicates the parameters obtained from the Mott Eq. (1).
[b]Indicates the parameters obtained from the Schnakenberg Eq. (2).

$CaCu_3Ti_4O_{12}$ has also been attributed to the grain boundary (internal) instead of an intrinsic property associated with the crystal structure.[14] Even in the $Bi_{4-x}Pb_xSr_3Ca_3Cu_4O_\delta$ type glassy precursor for high T_C superconductor, we noticed nanocrystalline phases, precipitated during glass formation.[15,16] So the appearance of ferroelectricity in the homogeneous single-phase $Bi_{1.8}Pb_{0.3}Sr_2Ca_2Cu_{2.8}K_{0.2}O_\delta$ type glass (hereafter referred to as FG glass) is not beyond question. Microstructural, transport and dielectric properties of these K doped FE glasses are expected to be interesting for a deeper understanding of FE transition in this glass. A proper characterization of this glass is also interesting for technological application. Ferroelectric thin plates or films can also be prepared from the glassy phase.

In the present article, microstructural [using the transmission electron microscopic technique (TEM)], transport and dielectric properties of a typical K-containing (FG) glass have been studied and the results have been compared with those of the corresponding K free SG glasses which are not FE but good precursors for high T_C superconductor. We noticed that the K containing glasses showing FE behavior are not homogeneous single-phase glass but they are all glass-nanocrystal composites (GNC). Moreover, annealed K doped glasses are not superconductors. The nanocrystalline FE phase is considered responsible for the ferroelectricity in the K doped glasses and the suppression of superconductivity.

II. EXPERIMENT

The FG type $Bi_{2-x}Pb_xSr_2Ca_2Cu_{2.8}K_{0.2}O_\delta$ ($x=0.0$, 0.1, 0.2, and 0.3) glasses showing FE behavior are prepared by partially replacing Cu with K in a typical Bi-based glassy precursor for high T_C superconductor (SG) *viz.* $Bi_{2-x}Pb_xSr_2Ca_2Cu_3O_y$. The $Bi_{2-x}Pb_xSr_2Ca_2Cu_{2.8}K_{0.2}O_\delta$ type FG glasses, termed as Pb0K2, Pb1K2, Pb2K2, respectively, for $x=0.0$, 0.1, 0.2, and Pb3K2 (FG) for $Bi_{1.8}Pb_{0.3}Sr_2Ca_2Cu_{2.8}K_{0.2}O_\delta$ are prepared by a similar method as discussed in our earlier articles[4,7,8,15,16] by quick quenching from the respective high temperature melts at 1100–1500 °C depending on Pb concentration. X-ray diffraction (XRD) analysis using Cu K_α radiation confirmed the amorphous state of all the melt-quenched glasses. Differential thermal analysis (DTA) at a heating rate of 10 °C/min from room temperature to 900 °C was made to find the glass transition (T_g) and crystallization (T_x) temperatures. A small endothermic peak was also observed from the DTA curves varying between 500 and 530 K depending on Pb concentrations ($x=0.1$–.3). The room temperature susceptibility was measured with a vibrating sample magnetometer (model 150) for all the samples showing paramagnetic behavior. The transmission electron micrographs of the said FG type glasses were obtained by Hitachi model H600 with fine glass powder on carbon grids. The conductivity of the samples from 80 to 450 K was measured similarly to our earlier work[4,5,8,16] using programable electrometer (Keithley model 617). Gold electrodes were deposited on both the surfaces of the samples by the vacuum sputtering technique for better contact. The dielectric constant of the samples with the same type of electrodes was measured by the HPLCR meter similarly to our earlier work.[8,12,13] The temperature was measured with a nanovoltmeter (Keithley model 181) within an accuracy of 0.5 K.

III. RESULTS AND DISCUSSION

The T_g and T_x values of the FG glasses are shown in Table I. For a typical FG glass *viz.* (Pb3K2), the glass transition ($T_g \sim 673$ K), and crystallization ($T_x \sim 703$ K) temperatures observed from the DTA trace agree quite well, respectively, with those of 667 and 717 K reported in Ref. 9. The TEM micrograph of this Pb3K2 glass shown in Fig. 1(a) clearly indicated the presence of microcrystals/clusters (10–50 nm size). The large cluster of a selected region of (a) is shown in Fig. 1(b). The FG glasses are, therefore, not pure single-phase homogeneous glasses but they are glass nanocomposites (GNC). These nanocrystals are, however, not always clearly detected from the XRD patterns due to their relatively small size (~10–50 nm) and low concentrations embedded in the glass matrix.

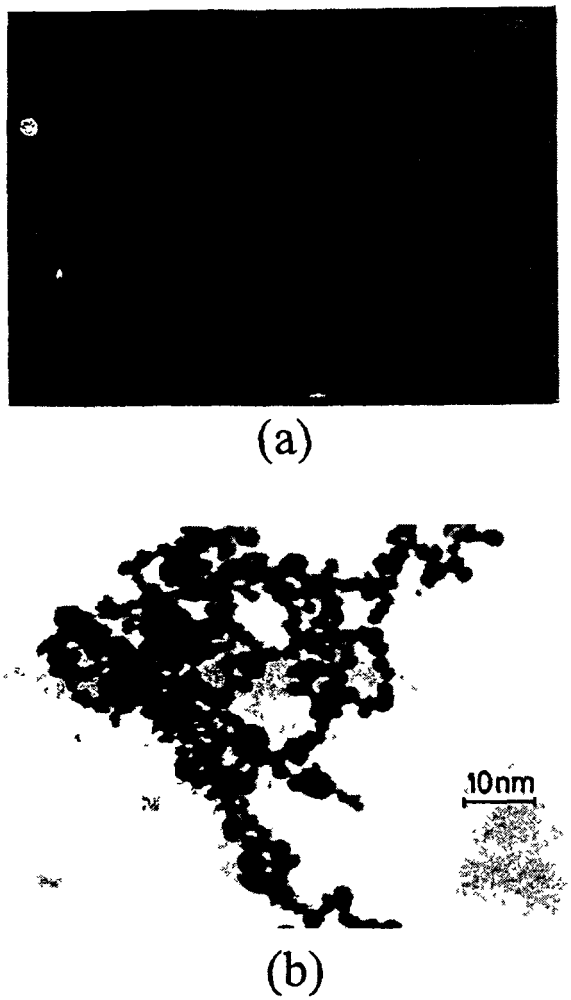

FIG 1 TEM for (a) the as quenched $Bi_{1.8}Pb_{0.3}Sr_2Ca_2Cu_{2.8}K_{0.2}O_\delta$ glass and (b) large cluster of the selected region of (a).

The concentration of the nanoparticles slightly increases with the increase of Pb concentration. These nanoparticles are considered to be responsible for the ferroelectric behavior of K containing glasses.

Interestingly, as mentioned earlier, the K free SG glass becomes a superconductor[15] by annealing around 840 K. But due to the presence of alkali metal (partial substitution of Cu by K) in the SG glasses, they show FE behavior and do not become superconductor by annealing around 840 K. Figure 2(a) shows the thermal variation of resistivity of the annealed FG glass and Fig. 2(b) demonstrates the same for the annealed SG glass showing its superconducting nature. Therefore, presence of K and, hence, the appearance of ferroelectricity suppresses superconducting behavior of the annealed FG glass sample. The electrical conductivity of Bi-based precursor glasses (SG) *viz.* $Bi_4Sr_3Ca_3Cu_4O_x+Ag_2O$, $(Bi,Pb)_4Sr_3Ca_3(Cu,A)_4O_x$ (A=Cr, Mn, Fe), elaborately studied earlier,[4,5,16,7,8] indicated that (i) these glasses become superconductors by annealing above the glass transition temperature, (ii) they are semiconductors between 450 and 10 K (studied so far) showing increase of resistance with decrease

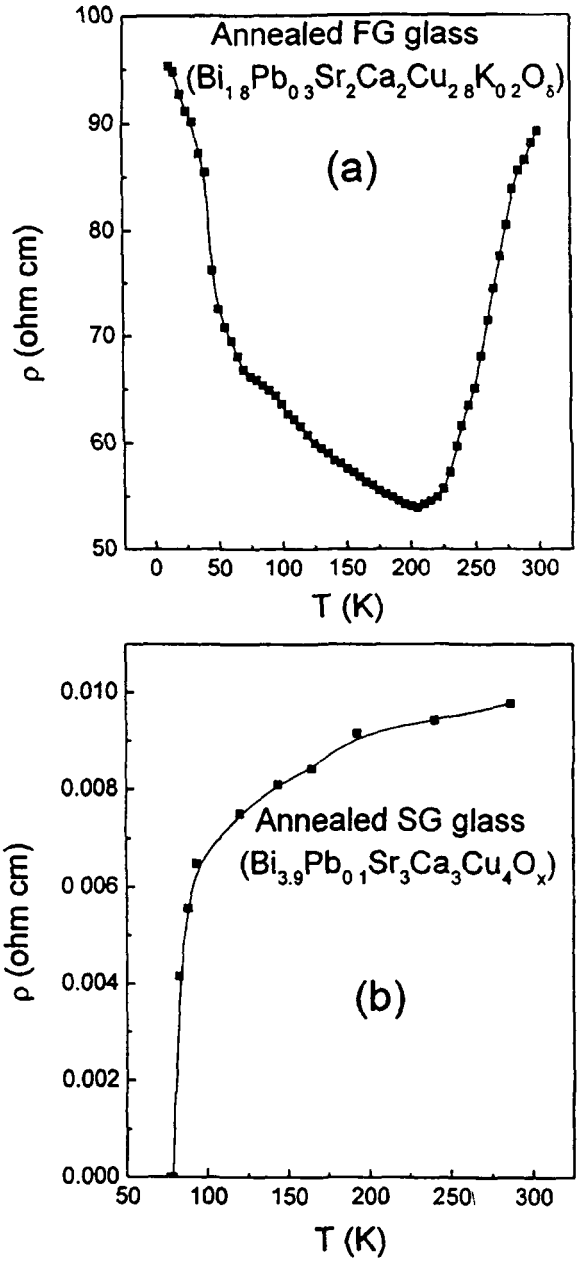

FIG 2 Thermal variation of the resistivity of (a) annealed $Bi_{1.8}Pb_{0.3}Sr_2Ca_2Cu_{2.8}K_{0.2}O_\delta$ (FG glass) which is a nonsuperconductor and (b) $Bi_{3.9}Pb_{0.1}Sr_3Ca_3Cu_4O_x$ (SG glass) showing superconducting behavior

of temperature, (iii) in the high temperature region ($T > 285\,K = \theta_D/2$, θ_D is the Debye temperature), the conduction process is dominated by thermally activated nearest neighbor hopping of small polarons, (iv) below $\theta_D/4$, the variable range hopping conduction is valid, and (v) the SG glasses are *n*-type semiconductors from the measurement of thermoelectric power. The Bi-based K doped FG glasses also show the same transport behavior except (i). The K containing FG glasses also showed little ionic conductivity and they are FE in contrast to the behavior of SG glass. Like SG glasses, the high temperature conductivity data of both the

FG and SG glasses can be well fitted with small polaron hopping model[19] *viz.*

$$\sigma = \nu_{ph}\left(\frac{Ne^2R^2}{kT}\right)C(1-C)\exp(-2\alpha R)\exp\left(-\frac{W}{kT}\right), \quad (1)$$

where ν_{ph} is the optical phonon frequency, R is the average Cu u spacing, N is the number of transition metal ions (Cu) per unit volume (Table I), and C is the ratio of the TMI concentration in the low valence states to the total TMI concentration. The values of C for all the glasses were estimated from the room temperature magnetic susceptibility and density data (Table I). In Eq. (1), α^{-1}, k, and T are, respectively, the localization length of the s-like wave function assumed to describe the localized states at each transition metal ion site, the Boltzmann constant, and the absolute temperature. The activation energy W arises from the electron-lattice interaction and/or the static disorder and can be expressed by, $W = W_H + W_D/2$, for $T > \theta_D/2$ and $W = W_D$ for $T < \theta_D/4$ (where W_H is the polaron hopping energy and W_D is due to static disorder). Figure 3(a) shows the plot of $\log \sigma_{dc}$ vs. T^{-1} for various compositions of Pb and similar curves were also obtained for the Bi-based precursor glasses (SG) studied earlier[4,15,16] as shown in Fig. 3(b). For the SG glasses, the conductivity increases with the Pb concentration and consequently activation energy W decreases. On the contrary, for the FG glasses like Pb3K2, the conductivity sharply decreases with Pb concentration. The values of W of FG type glasses are, however, comparable to those of other SG glasses like $Bi_4Sr_3Ca_3Cu_4O_x$, $(Bi_{4-x}Pb_x)Sr_3Ca_3(Cu_{4-y}A_y)O_x$ (A=Cr, Mn, Fe).[4,5,15,7,8] It is also noted that both concentrations and average particle/cluster sizes of the Pb0K2, Pb1K2, Pb2K2 glasses are smaller than those of the Pb3K2 (or FG) glass. A phase separation seems to occur around this particular concentration (Pb3K2) of the FG glasses showing lower value of conductivity with larger grain/cluster size (~50 nm average grain/cluster size). Insulating character of the larger ferroelectric particles/clusters of the FG glass is responsible for the lowering of conductivity of the glass. The values of θ_D, estimated from Fig. 3(a) (from the point where the change of slope occurred) are little less (Table I) than those of other binary or ternary transition metal oxide or SG glassy precursors.[4,15] All the parameters fitting the high temperature ($T > \theta_D/2$) conductivity data [Fig. 3(a)] with Eq. (1) are shown in Table I. The phonon frequency $\nu_{ph}(\sim 10^{12}$ Hz) of FG glass is little smaller than that of the SG glass ($\sim 10^{13}$ Hz) which become high T_C superconductors by annealing.[4,5,16,7,8]

For the FG glasses we also tried to check the conduction mechanism (adiabatic or nonadiabatic) using Holstein condition[20] *viz.* polaron band width $J > (2kTW_H/\pi)^{1/4}(h\nu_{ph}/\pi)^{1/2}$ for adiabatic and $J < (2kTW_H/\pi)^{1/4}(h\nu_{ph}/\pi)^{1/2}$ for nonadiabatic hopping mechanism. J can be independently calculated from $J = e^3[N(E_F)/\epsilon_p^3]^{1/2}$ where ϵ_p is the effective dielectric constant.[21] Using this relation and the earlier condition, FG glasses are found to follow the nonadiabatic small polaron hopping conduction mechanism similarly to that of the SG glasses. The estimated average site hopping distance, R, and

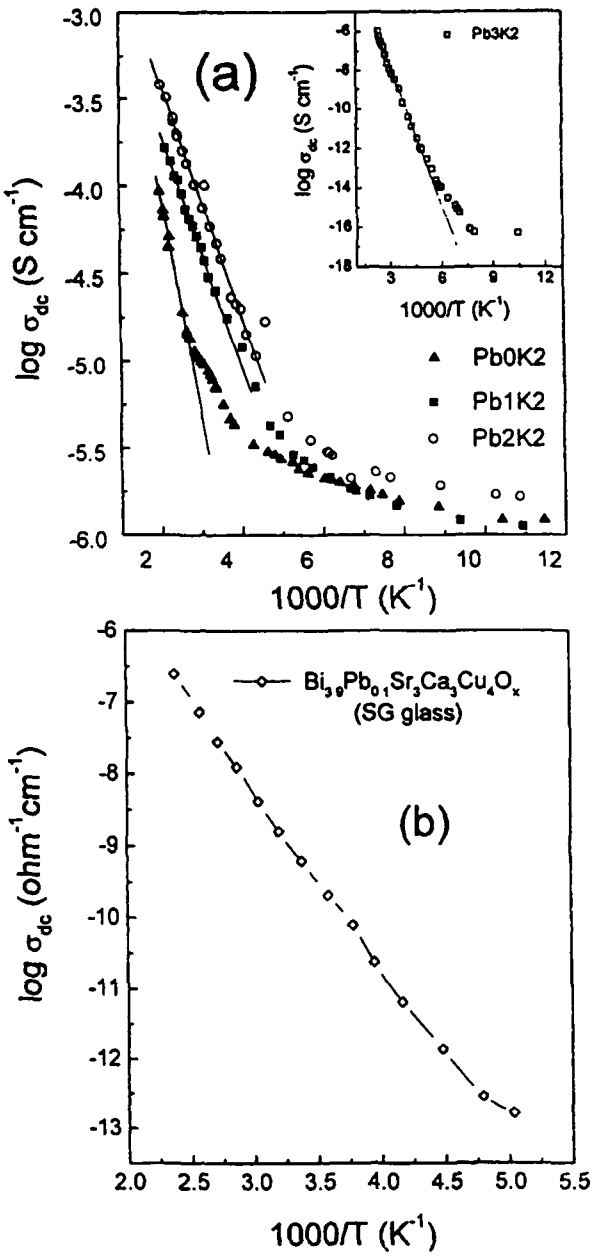

FIG 3 (a) Variation of $\log \sigma_{dc}$ vs $1000/T$ for $Bi_{2-x}Pb_xSr_2Ca_2Cu_{2.8}K_{0.2}O_y$ glasses The solid line is the best fit with Eq (1) (b) Thermal variation of $\log \sigma_{dc}$ as a function of $1000/T$ for $Bi_{3.9}Pb_{0.1}Sr_3Ca_3Cu_4O_x$ (SG glass)

polaron radius r_p (estimated from the equation[22,23] $r_p = 1/2(\pi/6N)^{1/3}$ shown Table I of the FG glasses are also comparable to those of other Bi-based SG glasses mentioned above[4,7,16,7,8] and satisfies the condition[24] ($r_p < R$) required for the small polaron hopping conduction mechanism. For all the FG glasses, ionic radii of Cu^+ and Cu^{2+} are, respectively, 0.96 and 0.69 Å and $< r_p < R$. Small polaron theory also requires[24] $\alpha^{-1} < r_p < R$ that is further satisfied for the FG type glasses similar to those of SG glasses. For an estimation of hopping energy W_H and disorder energy W_D, the conductivity data are also fitted with a generalized polaron-hopping model proposed by Schnakenberg.[25] The tempera-

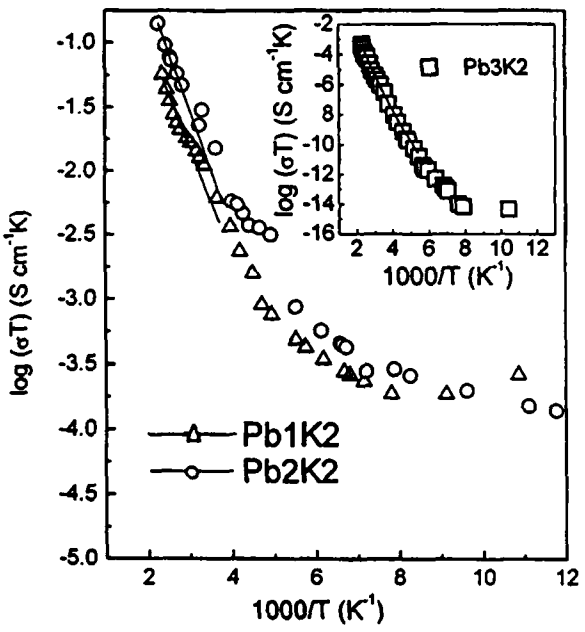

FIG 4 Variation of $\log(\sigma_{dc}T)$ vs $1000/T$ for $Bi_{2-x}Pb_xSr_2Ca_2Cu_{2.8}K_{0.2}O_\delta$ glasses The solid line is the best fit with Eq (2)

ture dependent conductivity in this model has the form (for $T > \theta_D/2$):

$$\sigma_{dc}T = \sigma_0[\sinh(h\nu_{ph})]^{1/2} \times \exp\left[-\left(\frac{4W_H}{h\nu_{ph}}\right)\tan\left(\frac{h\nu_{ph}\beta}{4}\right)\right]\exp\left(\frac{W_D}{\beta}\right), \quad (2)$$

where σ_0 is a temperature-independent parameter and $\beta = 1/kT$. The experimental conductivity data of the FG glasses fitted with Eq. (2) is shown in Fig. 4 (solid line). The corresponding parameters W_H, W_D, and ν_{ph} are given in Table I for comparison. The disorder energy W_D is also comparable to those of SG glasses.[47] It appears that only the dipolar ordering (causing ferroelectric behavior of the FG glass nanocomposite) in the nanoclusters of the FG type glasses suppresses superconducting behavior of these glasses in their annealed ceramic phases.

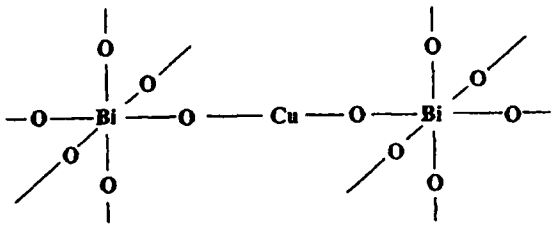

FIG 5 Network structure model of $Bi_4Sr_3Ca_3Cu_4O_x$ glasses Some fraction of Cu^+ ions connects distorted BiO_6 octahedra. In the K-doped FG glass, Cu ions are partially replaced by K ions

The structure of Bi r a u glasses depends to a great extent on the Cu content and its valence state.[26] So the addition of alkali metal (K, say) in the Cu site distorts the average structure of the K-free SG glass to a great extent. Though both Bi_2O_3 and CuO are not glass-forming oxides, it is well established that both Bi_2O_3 and CuO are necessary to form a glassy state in the Bi r a u system as reported by several authors.[27,28] Bi_2O_3 enhances the glass-forming ability in the Bi-based system and, hence, in the SG and FG systems, Bi_2O_3 acts as ?glass former? in the presence of CuO. It has been reported[29] that Bi^{3+} ions are six coordinated (distorted BiO_6 octahedra) in the Bi-based glasses. The oxygen coordination number of Cu^+ in Cu_2O is 2 and that of Cu^{2+} in CuO is 4. The density of CuO is more than Cu_2O, concluding that CuO structure is more compact than that of Cu_2O. Recently Sato *et al*[30] proposed a glass network structure unit shown in Fig. 5. In this model, BiO_6 octahedra are connected to other octahedra through two-coordinated Cu^+ ions and particularly in the K free SG type glasses Cu^+ ions take part mainly in the formation of networks. The other cations of Cu^{2+}, Ca^{2+}, and Sr^{2+} may be distributed randomly in the surrounding network. Partial replacement of Cu sites by K change some ionic states of Cu and distorts the glass network structure in favor of dipolar ordering and, hence, appearance of ferroelectricity as observed from the dielectric properties discussed later. The difference between the glass structures of SG and FG can be compared in terms of the oxygen molar volume[31,32] V_O^*. The value of V_O^* of the present glasses is calculated by using the equation

$$V_O^* = \frac{(M_{CuO} - 16C)X_{CuO} + M_K X_K + M_{Ca}X_{Ca} + M_{Sr}X_{Sr} + M_{Pb}X_{Pb} + M_{Bi}X_{Bi}}{d[(5-C)X_{CuO} + 3X_K + 3X_{Ca} + 3X_{Sr} + 1X_{Pb} + 3X_{Bi}]}.$$

where M_{CuO}, M_K, M_{Ca}, M_{Sr}, M_{Pb}, and M_{Bi} are the molecular weights of CuO, K_2CO_3, $CaCO_3$, $SrCO_3$, PbO, and Bi_2O_3, respectively. X_{CuO}, X_K, X_{Ca}, X_{Sr}, X_{Pb}, and X_{Bi} are the mole fraction of CuO, K_2CO_3, $CaCO_3$, $SrCO_3$, PbO, and Bi_2O_3, respectively. d and C are, respectively, the density of the glass and fraction of reduced Cu ion. Both T_g(400 ±1) and V_O^*(14.52) of the FG glass are little higher than those of the K free SG glass (T_g=340 ±1, V_O^* =11.23). This indicates K doped glass has a more stable glass network structure than that of the K free SG glass However, the network structure also depends on the K and Pb concentrations.

Dielectric constant of the Bi-based glassy precursor for high T_C superconductors (SG glasses) did not show any ferroelectricity.[47] The temperature measurement of the dielectric constant of the samples was repeated with different samples of same compositions and dielectric constant data were found to vary within 5% (as discussed later). Figure

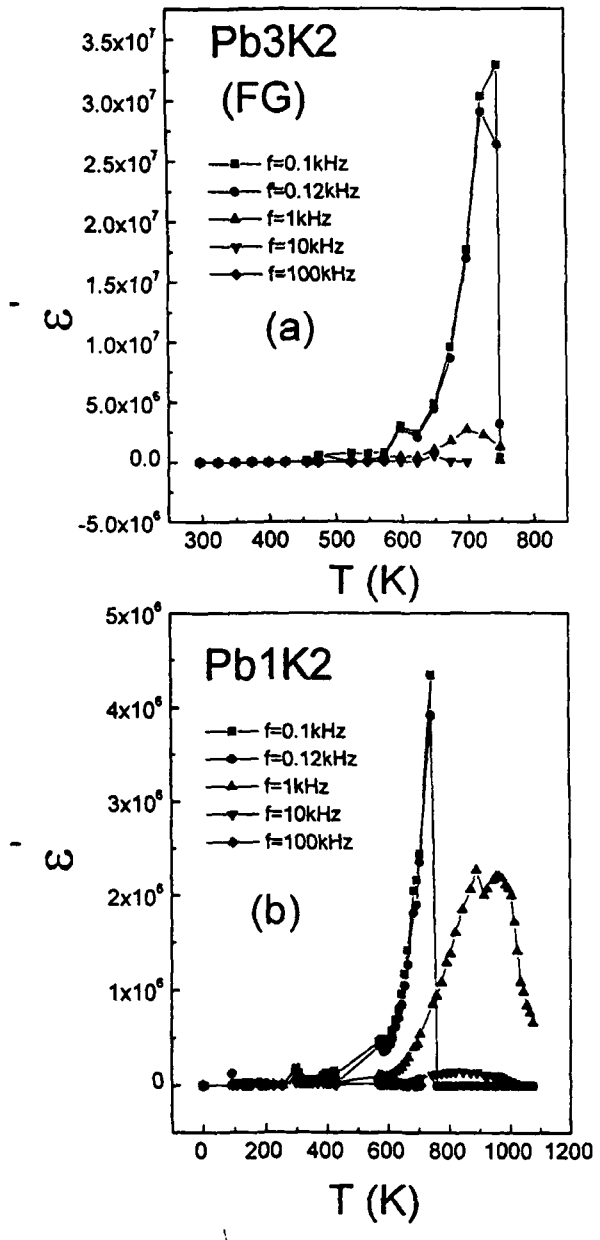

FIG. 6. Temperature variation of dielectric constant ϵ' for FG glasses (a) $Bi_{1.8}Pb_{0.3}Sr_2Ca_2Cu_{2.8}K_{0.2}O_\delta$ (Pb3K2) and (b) $Bi_{1.9}Pb_{0.1}Sr_2Ca_2Cu_{2.8}K_{0.2}O_\delta$ (Pb1K2) for different frequencies

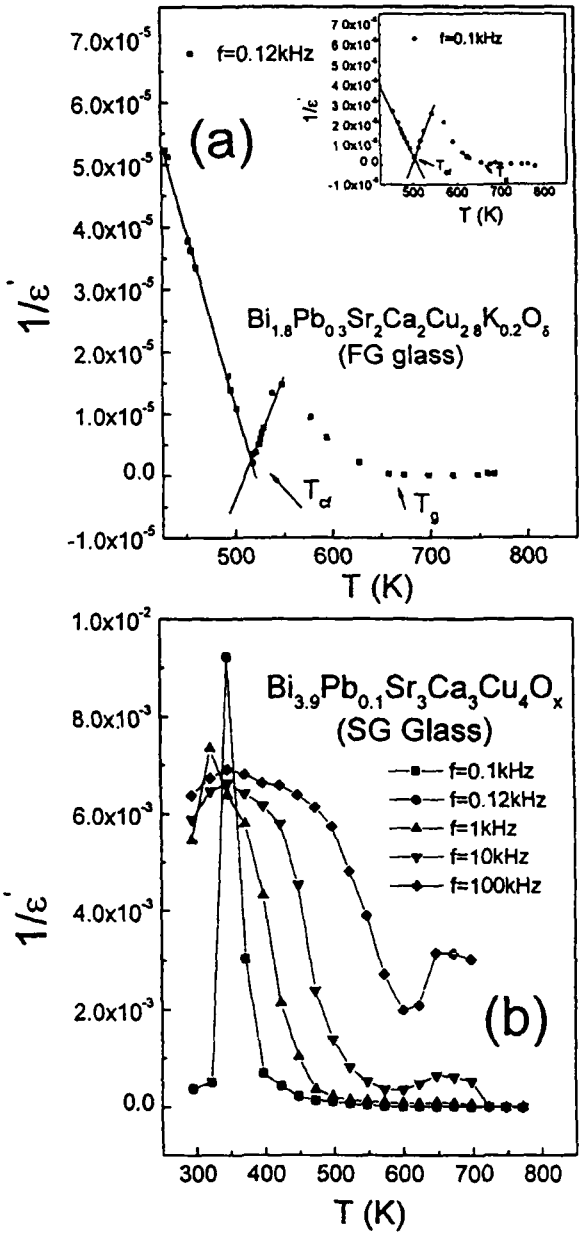

FIG. 7 Plot of $1/\epsilon'$ vs T for (a) $Bi_{1.8}Pb_{0.3}Sr_2Ca_2Cu_{2.8}K_{0.2}O_\delta$ (FG glass) showing FE transition and (b) $Bi_{3.9}Pb_{0.1}Sr_3Ca_3Cu_4O_x$ (SG glass) showing no FE transition

6(a) shows the variation of the dielectric constant of a typical FG glass Pb3K2 as a function of temperature for different frequencies 0.1, 0.12, 1.0, 10, and 100 kHz. The appearance of small broad peak in the $(\epsilon'-T)$ curve [Fig. 6(a)] around 600 K along with the large peak for every frequency indicates the presence of the relaxation mode in the glass. Figure 6(b) shows the same for the Pb1K2 glass. The ϵ' (real part of dielectric constant) values of the FG glasses are little larger than those of the Bi-based multicomponent SG glasses.[47] This is due to the presence of large number of nanocrystalline phases in the FG glasses with higher dielectric constants (lower conductivity). It has already been shown[34] that the dielectric constant of nanocrystalline TiO_2 is much larger than that of the corresponding bulk sample.

The dielectric constant data of the FG glass follow the Curie eiss relation $\epsilon' = C/(T-T_0)$, where C is the Curie constant. T_0 is the extrapolated intersection of the high temperature part of the plot with the temperature axis as shown in Fig. 7(a) with two different frequencies. Similar ferroelectric behavior was observed with the other two samples (Pb1K2 and Pb2k2) of different concentrations (not shown in the figure) with $T_0 = 454$ and 460 K for Pb1K2 and Pb2K2, respectively. The observed transition temperature $T_0 = 466$ K is close to the value 470 K observed by Bahgat *et al*[9] for similar sample. The order of the transition is iden-

tified by finding the ratio of the slopes $\partial(1/\epsilon)/\partial T$ [in Fig. 7(a)] below and above T_{Cf}. The value of this ratio($=-2.63$) indicates that the transition is of first order type. In case of second order phase transition, T_0 is practically the same as the transition temperature or the Curie point T_{Cf}, while in case of a first order transition T_0 is lower than the Curie temperature T_{Cf}. T_{Cf} is found to vary from 500 to 530 K depending on Pb concentrations. It is more interesting to mention here that for any of the K-free superconducting precursor glasses (SG glasses) becoming superconductor by annealing, the plot of $1/\epsilon'$ vs. T shown in Fig. 7(b) for a typical SG glass $Bi_{3.9}Pb_{0.1}Sr_3Ca_3Cu_4O_x$ does not at all match with that of FG glass showing ferroelectric behavior [Fig. 7(a)] Detailed analysis of the dielectric properties of other SG glasses without showing FE behavior has already been made earlier.[4,8]

IV. CONCLUSION

In conclusion, the glassy precursors for high T_C superconductors (SG glasses) show ferroelectric behavior when Cu is partially substituted by K. This K containing FG glass showing ferroelectric transition is not a single phase homogeneous glass but it is a GNC. Ferroelectricity in these glasses appears due to the presence of ferroelectric nanocrystalline particles/clusters embedded in the glass matrix. In the annealed FG glasses superconducting behavior is suppressed by alkali metal (like K) doping in the Cu site. Such substitution modifies the network structure of SG glass (Fig. 5). So ferroelectricty in pure single phase glass has not yet been observed. Present investigation also suggests that though ferromagnetism and superconductivity might coexist in the same material, coexistence of ferroelectricity and superconductivity in the same material is yet to be explored.

ACKNOWLEDGMENTS

The author S.M. is grateful to the Council of Scientific and Industrial Research (CSIR) for the financial support. The authors are also grateful to Professor T. Komatsu of Nagaoka University for his valuable comments on the manuscript.

[1] H. Hirashima, Y Watanabe, and T Yoshida, J Non-Cryst. Solids 95&96, 825 (1987)
[2] Y Sakurai and J Yamaki, J Electrochem Soc **132**, 512 (1985)
[3] H Sakata, M Amano, Y Kawashima, and T Dkamoto, J Ceram Soc Jpn **102**, 314 (1994)
[4] K K Som and B K Chaudhuri, Phys Rev B **41**, 1581 (1990)
[5] S Chatterjee, S Banerjee, S Mollah, and B K Chaudhuri, Phys Rev B **53**, 5942 (1996)
[6] T Komatsu R Stao, C Hirose K Matusita, and Y Matushita Jpn J Appl Phys, Part 2 **27**, L2293 (1988)
[7] Y Akamatsu, M Tatsumisago, N Tohge, S Tsuboi, and T Minami, Jpn J Appl Phys, Part 2 **27**, L1696 (1988)
[8] S Mollah, K K Som, K Bose, A K Chakraborty, and B K Chaudhuri Phys Rev B **46**, 11075 (1992)
[9] A A Bahgat and T M Kamel, Phys Rev B **63**, 012101 (2001)
[10] M E Lines, Phys Rev B **15**, 388 (1977)
[11] T Matsumoto, A Fukuda M Johno, Y Motoyama, T Yui S S Seomun and M Yamashita J Mater Chem **9** 2051 (1999)
[12] M Sadhukhan, D K Modak, and B K Chaudhuri, J Appl Phys **85** 3477 (1999)
[13] M Sadhukhan S Chakraborty D K Modak and B K Chaudhuri Phil los Mag B **74**, 139 (1996)
[14] D C Sinclair, T B Adams F D Morrison, and A R West Appl Phys Lett **80**, 2153 (2002)
[15] B K Chaudhuri, Chin J Phys (Taipei) **38**, 2 (2000)
[16] S Bhattacharya and B K Chaudhuri J Appl Phys **88** 5033 (2000)
[17] S Bhattacharya, D K Modak P K Pal and B K Chaudhuri Mater Chem Phys **68**, 239 (2001)
[18] S Chatterjee, S Bhattacharya, and B K Chaudhuri J Chem Phys **108** 2954 (1998)
[19] N F Mott, J Non-Cryst Solids **1**, 1 (1968)
[20] T Holstein, Appl Phys **8**, 325 (1959)
[21] V K Dhawan, A Mansingh, and M Sayer J Non-Cryst Solids **51** 87 (1982)
[22] I G Austin and N F Mott, Adv Phys **18** 41 (1969)
[23] V N Bogomolov, E K Kudinov and Y A Firsov, Sov Phys Solid State **9**, 3175 (1967)
[24] G N Greaves, J Non-Cryst Solids **11**, 427 (1973)
[25] J Schnakenberg, Phys Status Solidi **28**, 623 (1968)
[26] T Komatsu, M Nakakura, R Sato, J Khaled, and K Matusita, J Non-Cryst Solids **195**, 102 (1996)
[27] N Tohge, S Tsuboi, Y Akamatsu, M Tatsumisago, and T Minami, J Ceram Soc Jpn **97**, 334 (1989)
[28] H Zheng, R Xu, and J D Mackenzie, J Mater Res **4** 911 (1989)
[29] W H Dumbaugh, Phys Chem Glasses **27**, 119 (1986)
[30] R Sato, T Komatsu, and K Matusita, J Non-Cryst Solids **160** 180 (1993)
[31] H Mori, H Matsuno, and H Sakata, J Non-Cryst Solids **276** 78 (2000)
[32] H Mori, T Kitami, and H Sakata, J Ceram Soc Jpn **101** 347 (1993)
[33] T Szörényi, K Bali, and I Hevesi, J Non-Cryst Solids **70**, 297 (1985)
[34] L D Zhang, H F Zhang, G Z Wang, C M Mo and Y Zhang, Phys Status Solidi A **157**, 483 (1996)

Physica Scripta. T97, 160–162, 2002

X-ray Photoemission Spectroscopy of VN–PbO–TeO_2 Glasses

S. Mollah[1], K. Hirota[2] and H. Sakata[3]

[1]Department of Physics, Aligarh Muslim University, Aligarh-202002, India
[2]Department of Chemistry, Tokai University, 1117 Kitakaname, Hiratsuka, Kanagawa 259-1292, Japan
[3]Department of Applied Chemistry, Tokai University, 1117 Kitakaname, Hiratsuka, Kanagawa 259-1292, Japan

Received September 19, 2000; revised version received March 29, 2001; May 14, 2001

PACS Ref: 81.05 Kt, 79.60 Bm

Abstract

Oxynitride glasses in the system VN–PbO–TeO_2 with different compositions were fabricated and X-ray photoelectron spectroscopy (XPS) of these glasses were studied. The glasses were melted, using VN, PbO, and TeO_2 reagent chemicals, in flowing N_2 atmosphere at 750°C for 1 h, and the melt was then rapidly press quenched.

X-ray diffraction (XRD) and differential thermal analysis (DTA) indicated amorphous nature of these glasses. The XPS analysis revealed presence of VN, V^{4+}, V^{5+}, Pb^{2+}, Pb^{4+}, Te^{4+}, and Te in the glasses. The presence of VN containing 8–10 atomic percent (at.%) VN confirmed vanadium–lead–tellurous oxynitride glasses. These VN contents corresponded to an equivalent content of 1–2 at.% N in the glasses. Values of $Cv = [V^{4+}]/([V^{4+}] + [V^{5+}])$ were calculated from areas of separated XPS peaks corresponding to V^{4+} and V^{5+} for different glass compositions. Some redox reactions assumed in the glass melts explained qualitatively changes in the Cv value.

1. Introduction

Recently oxynitride glasses have been widely studied to investigate their preparation method, structure, and properties different from those of oxide glasses. Mulfinger [1] reported earlier that soda-lime-silica glasses melted with addition of 5 wt% (0.74 mol%) Si_3N_4 produced an oxynitride glass containing 1.2 wt% (0.17 at.%) N_2 in the glass. Later, oxynitride glasses in the system Y–Si–Al–O–N containing N_2 up to 7 at.% were fabricated [2]. Makishima *et al.* fabricated La–Si–O–N oxynitride glasses with N_2 up to 18.2 at.% by glass melting under 30 atm N_2 pressure [3]. Nitrogen in oxynitride glasses is bonded to Si [2,4,5], and increasing N_2 amount increased hardness of oxynitride glasses [2]. Studies on phosphorous oxynitride glasses were recently reported [6]. No works, however, are found on oxynitride glasses based on tellurite glass matrix.

It is known that transition metal oxide glasses, for example, vanadate glasses, are semiconducting glasses [7]. The conduction mechanism has been understood by the Mott–Austin small polaron hopping model [8]. Recent reports on vanadium tellurite glasses [9,10] also confirm the small polaron hopping conduction.

It is expected that when vanadium–tellurium–oxynitride glasses are fabricated their semiconducting properties are varied by possible structural changes due to nitriding. Since V_2O_5–PbO–TeO_2 semiconductive glasses have been prepared [11], we report in the present work fabrication of V–Pb–Te–O–N oxynitride glasses in the possible VN–PbO–TeO_2 system and results of their XPS investigations.

2. Experimental procedure

Glasses were prepared using VN (97.5%), PbO (99.9%) and TeO_2 (98.0%) reagent grade raw materials. PbO was added for stabilizing glasses. We prepared four glass samples with different glass compositions: VN:PbO:TeO_2 = 50:10:40 (mol%) (sample A), 40:10:50 (sample B), 30:10:60 (sample C) and 20:10:70 (sample D). After mixing raw materials of prescribed composition in air for 20 min in an agate mortar, the batch was melted in an electric furnace in flowing nitrogen gas atmosphere (flow rate: 50 ml/min) at 750°C for 1 h. The melt was then rapidly press-quenched between two flat copper blocks at room temperature. This quenching produced glass samples of 10 × 10 cm^2 size and about 1 mm thickness. The glass density of each sample was determined by the Gay–Lussac method using toluene at 293 K.

Characterization of the quenched glasses was made by X-ray diffraction (XRD) (Rigaku, RINT2000, Tokyo, Japan), TG-DTA (Rigaku, TAS300) and X-ray photoelectron spectroscopy (XPS) (ULVAC-PHI, Chigasaki, Japan). In XPS measurements, data were taken for all the glass samples after 10 s sputter-etching in argon, and carbon correction was made.

3. Results and discussion

Figure 1 shows X-ray diffractogram (CuKα) for a VN–PbO–TeO_2 glass for the samples A–D with different compositions (Table I). Broad humps at 2θ equal to ca. 27° are observed, which confirms the amorphous nature of these glasses. Thus we could obtain a series of glasses in the VN–PbO–TeO_2 system. DTA curves for these glasses indicated characteristic temperatures of glass. For the glass sample D, the glass transition temperature T_g was 289°C, the crystallization temperature, T_c = 389°C, and the melting temperature, T_m = 597°C. The value of T_g was almost unchanged for increasing VN content.

Figure 2(a)–(c) show XPS spectra for V, Pb, and Te element for glass A, VN:PbO:TeO_2 = 50:10:40 (mol%). Figure 2(a) indicates XPS spectra for V $2p_{3/2}$ of glass A, where the main peak is separated to a peak corresponding to V^{5+} with binding energy 517.56 eV and that to V^{4+} with binding energy of 516.41 eV, respectively. Together with these peaks, a peak due to VN with 514.60 eV is observed, suggesting presence of VN bonding in the glass network. Possible structural units of VN in the glass network may be =V=N–O or ≡V=N–O.

Figure 2(b) shows XPS spectra for Pb $4f_{7/2}$ of sample A, indicating a peak for Pb^{2+} with binding energy of 138.88 eV

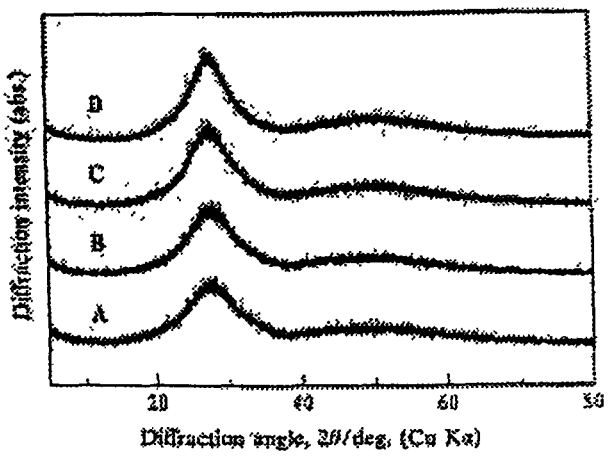

Fig. 1. X-ray diffraction patterns of VN–PbO–TeO_2 glasses. (A) VN:PbO:TeO_2 = 50:10:40 (mol%); (B) VN:PbO:TeO_2 = 40:10:50 (mol%); (C) VN:PbO:TeO_2 = 30:10.60 (mol%); D) VN:PbO:TeO_2 = 20:10:70 (mol%).

and one for Pb^{4+} with binding energy 138.55 eV, respectively. Thus we confirm presence of Pb^{2+} and Pb^{4+} ions in the glass matrix. Since PbO was used as a raw material the presence of Pb^{4+} ions means the oxidation of Pb^{2+} that was contained initially in the glass melts.

Figure 2(c) gives XPS spectra for Te $3d_{5/2}$ of glass A. This peak can be separated adequately to sub-peaks corresponding to Te^{4+} and Te of which the binding energy is 576.41 and 576.55 eV, respectively. Since TeO_2 was used as a raw material for the glass fabrication, the presence of Te in the glasses indicates a reducing action of TeO_2 during melting. The XPS spectra for the glasses B, C, and D were found to be similar to those above for glass A. Presence of O1s spectra for the samples was also confirmed.

Table I summarizes the XPS results for VN, V, Pb and Te ions obtained from Fig. 2 (a)–(c), which includes content (at.%) of each ion, ratio of atomic percent for the ion of the same kind but having different valencies, and, in particular, values of $Cv = [V^{4+}]/([V^{4+}] + [V^{5+}])$ relating to electric conduction of these glasses.

Figure 3(a)–(c) show relative atomic percent for V and Te ions with different valencies for the glasses A–D, calculated from the integrated area of each XPS peak. In Fig. 3(a) for VN = 50–20 mol% (TeO_2 = 40–70 mol%) approximately fixed content of VN is present in the glasses. With increasing TeO_2 content the relative concentration of V^{4+} decreases but that of V^{5+} increases. This indicates a fabrication of vanadium oxynitride glasses in the TeO_2 glass network, and is similar to the oxynitride glasses obtained by oxynitriding of SiO_2-based glass using AlN raw material [2].

The presence of V^{4+} and V^{5+} ions in the glasses suggests oxidation of V^{3+} in VN in the glass melts. This is favorable for preparing semiconducting glasses of which electric conduction are due to the valence exchange between V^{4+} and V^{5+} ions. Such semiconductive glasses containing transition metal ions have been extensively studied [7,12]. From the VN content listed in Table I it is confirmed that a 1–2 at.% N is equivalently involved in the glasses.

Figure 3(b) indicates relative atomic percent of Pb^{2+} and Pb^{4+} ions in the glasses, where the Pb^{4+} content decreased with increasing TeO_2 amount but the content of Pb^{2+} increased. This may be due to preferred oxidation of V ions by O_2 decomposed from TeO_2 as shown in Eq.(1), which decreases the amount of O_2 necessary for oxidizing PbO.

In Fig. 3(c) the concentration of Te^{4+} in the glasses increases with increasing TeO_2 content. But in contrast the Te content decreases with increasing TeO_2 (Fig. 3(c)) content. The increasing Te content for larger amount of VN accompanied with V^{4+} and V^{5+} contents (Fig. 3(a)) suggests a reducing reaction of TeO_2 which oxidizes V ions in the glasses on the glass melting.

Next we discuss redox reactions in the present glasses. From the presence of VN, V^{4+}, V^{5+}, Pb^{2+}, Pb^{4+}, Te^{4+} and Te ions in the glasses (Table I), the following redox reactions in the glass melts are assumed:

$$TeO_2 \rightarrow Te + O_2, \tag{1}$$

$$VN + O_2 \rightarrow VO_2 + \tfrac{1}{2}N_2, \tag{2}$$

$$VO_2 + \tfrac{1}{4}O_2 \rightarrow \tfrac{1}{2}V_2O_5, \tag{3}$$

$$PbO + \tfrac{1}{2}O_2 \rightarrow PbO_2. \tag{4}$$

For larger amounts of VN, the reaction (1) proceeds and causes the reactions (2) and (3), producing V^{4+} and V^{5+} ions, thus giving the large *Cv* value (0.710) as shown for glass A in Table I. Conversely, for larger amounts of TeO_2 (glass D) and lower amount of VN, the reaction (1) is not probable because amount of O_2 necessary for reactions (2) and (3) becomes the lower. This results in the low *Cv* value (0.653) (Table I). The PbO amount was relatively low (10 mol%) in these glasses, so conclusions about the contents of Pb^{2+} and Pb^{4+} are rather difficult.

4. Conclusions

Oxynitride glasses of the VN–PbO–TeO_2 system were prepared by the melt quenching method using VN, PbO, and TeO_2 raw materials melted in flowing N_2 atmosphere.

Table I. *XPS results of vanadium, lead and tellurium ions in the glasses.*

Nominal composition (mol%)				Results of composition (atomic %) from XPS data										
	VN	PbO	TeO_2	V (at.%)*	V^{5+}	V^{4+}	VN	*Cv*†	Pb (at.%)*	Pb^{2+}	Pb^{4+}	Te (at %)*	Te^{4+}	Te
(A)	50	10	40	24.09	26 64	65.11	8.25	0.710	5.31	24.90	75 10	11 51	65 60	34 40
(B)	40	10	50	17.97	29.62	60.92	9.47	0.673	4.64	31 58	68 42	20.57	75.65	24 35
(C)	30	10	60	12.81	30.36	60.57	8.89	0 666	5.84	39 45	60 55	22 80	85 7	14 30
(D)	20	10	70	7.06	31.26	58 64	10.10	0.653	4.46	45.80	52 50	39 09	95.53	4.47

* Total atomic (%) in the glasses. † $Cv = [V^{4+}]/([V^{4+}] + [V^{5+}])$.

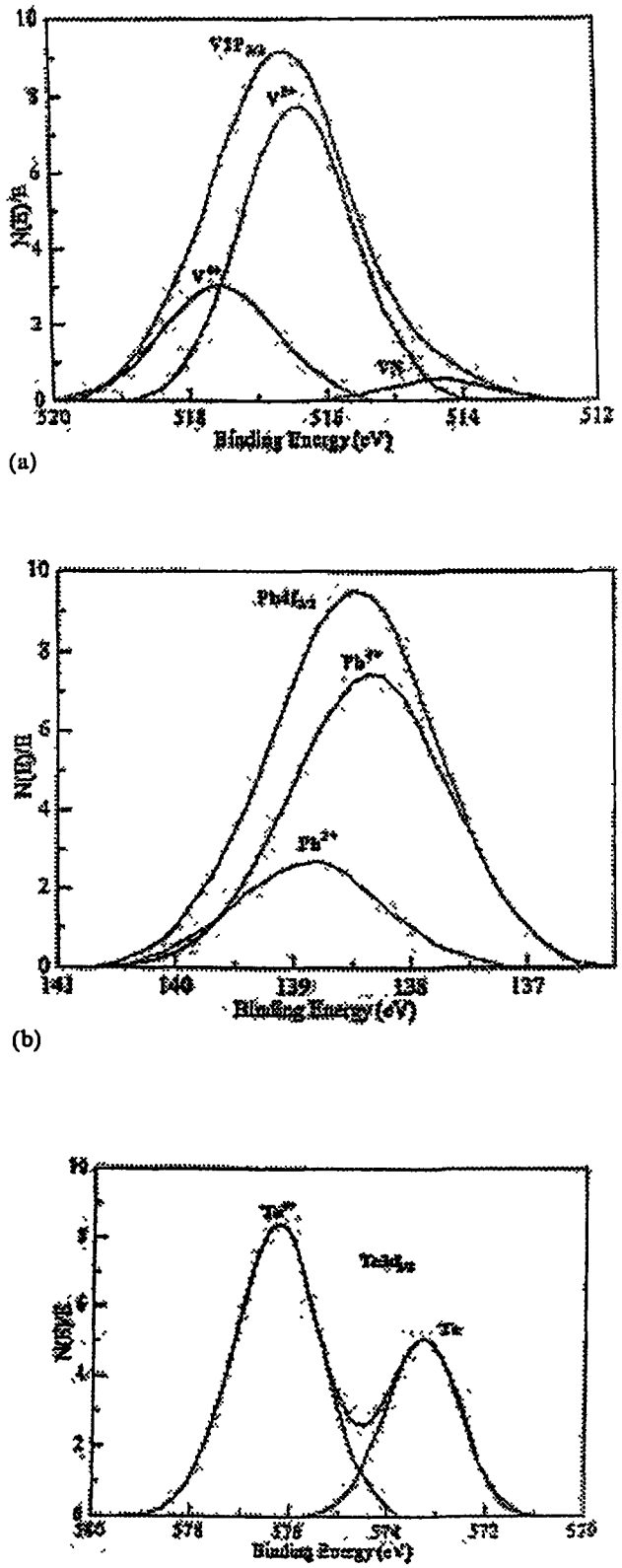

Fig. 2. (a) XPS spectra (V $2p_{3/2}$) of 50VN–10PbO–40TeO_2 (mol%) glass (b) XPS spectra (Pb $4f_{7/2}$) of 50VN–10PbO–40TeO_2 (mol%) glass. (c) XPS spectra (Te $3d_{5/2}$) of 50VN–10PbO–40TeO_2 (mol%) glass.

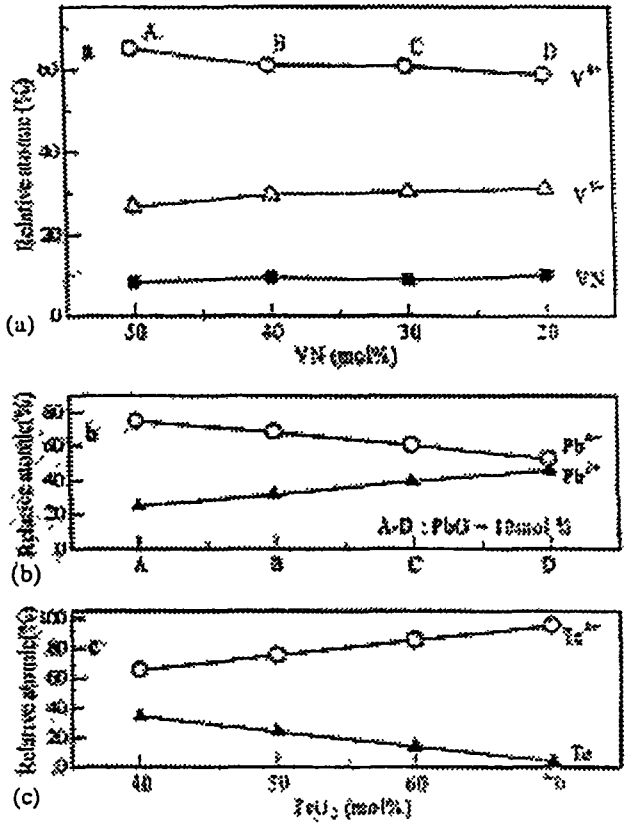

Fig 3 Relative atomic percent of (a) VN and V, (b) Pb and (c) Te ions in VN–PbO–TeO_2 glasses.

The XPS analysis revealed the presence of VN, V^{4+}, V^{5+}, Pb^{2+}, Pb^{4+}, Te^{4+} ions and Te in the glasses. The VN content in the glasses attained 8–10 at.%, and an equivalent 1–2 at.% N is involved. In these glasses the presence of =V=N–O or ≡V=N–O structual units was suggested.

From the presence of these metallic ions in the oxynitride glasses some re dox reactions in the glass melts were assumed to occur, which could explain qualitatively changes in the *Cv* ($[V^{4+}]/([V^{4+}] + [V^{5+}])$ value for the different glass compositions. Electric conduction of these oxynitride glasses will be reported elsewhere in the near future.

References

1. Mulfinger, H. O., J. Am. Ceram. Soc. 49, 462 (1966).
2. Lochman, R. E., J. Am. Ceram. Soc. 62, 491 (1979).
3. Makishima, A., Mitomo, M., Tanka, H., Li, N and Tsutumi, M., Yogyo-Kyokai-Shi 88, 701 (1980)
4. Sakka, S., J. Non-Cryst. Solids 181, 215 (1995)
5. Schneider, M., Gasparov, V. A., Richter, W., Deckwerth, M and Rüssel, C., J. Non-Cryst. Solids 215, 201 (1997).
6. Reidmeyer, M. R. and Day, D. E., J. Non-Cryst. Solids 181, 201 (1995)
7. Murawski, L., Chung, C. H. and Mackenzie, J D , J Non-Crest Solids 32, 91 (1979).
8. Austin, I. G and Mott, N. F , Adv. Phys 18, 41 (1969)
9. Mori, H , Kitami, T and Sakata, H., J Non-Crst Solids 168, 157 (1994).
10. Sega, K., Kuroda, Y and Sakata, H , J Mater. Sci 33, 1303 (1998)
11. Sakata, H , Amano, M. and Yagi, T., J Non-Cryst Solids 194, 198 (1996)
12. Sayer, M. and Mansingh, A., J. Non-Cryst Solids 58, 91 (1983).

Proc. Tenth Int. Workshop Phys. Semiconductor Devices, 1999

DC Conductivity of VN-PbO-TeO_2 Amorphous Semiconducting Glasses

S. Mollah

Department of Physics,
Aligarh Muslim University,
Aligarh

Temperature (80-450K) variation of dc conductivity of VN-PbO-TeO_2 glasses with different mol% of VN, PbO and TeO_2 have been reported. The glasses were prepared by usual melt cooling process from the melt at 750 °C to room temperature (25 °C) by quenching between two copper blocks. From XRD analysis, it is found that all the glasses are amorphous in nature. The glass transition temperatures (Tg) of the glasses are found to be from 268.80-302.33 °C from modulated differential scanning calorimetric (MDSC) analysis. DC conductivity of the glasses is found to vary from 1.875×10^{-6} to 7.431×10^{-9} $ohm^{-1}cm^{-1}$ at 360 K depending on the composition of the glasses. The carrier density determined was $0.45\text{-}2.1\times10^{21}$ cm^{-3}. The conduction was confirmed to be due to non-adiabatic small polaron hopping between vanadium ions. The materials show oxygen gas sensing property in ceramic form. DC conductivity of the glasses is found to decrease in oxygen atmosphere compared to air at a particular temperature.

INTRODUCTION

There are two types of ceramic gas sensors, viz. n-type and p-type. The well-known n-type gas sensors are ZnO [1], SnO_2 (Pd+) [2], WO [3] and ZnO:Ga [4]. Electrical conductivity of these sensors increases on the exposure to reducing gases at high temperature but that of p-type semiconductor such as CoO [5] increases on the exposure of oxidizing gases. Some glasses containing transition metal oxides e.g. V_2O_5-PbO-TeO_2 [6], V_2O_5-SnO-TeO_2 [7] and Fe_2O_3-Sb-TeO_2 [8] also exhibited oxygen gas sensing properties.

Recently there has been considerable interest in the study of semiconductive glasses with non-conventional glass former, tellurium oxide. It is expected that the highly conductive telluride glasses to be potential candidate for oxygen gas sensors. These gas sensors have wide application in medical, environmental, industrial and sanitation fields. Hardly any work has been done to exploit the gas-sensing behavior of semiconductive oxide glasses. To the author's knowledge, no work has been done on the transport properties of VN containing telluride glasses. This paper reports the temperature variation of dc conductivity of VN-PbO-TeO_2 glasses.

EXPERIMENTAL

Reagent grade VN, PbO and TeO_2 raw materials with purity 99.999% or

more were used to prepare the glass samples (Table-1).

Table-1: VN-PbO-TeO_2 glass samples

Glass samples	Nominal Composition (mol%)		
	VN	PbO	TeO_2
A	50	10	40
B	40	10	50
C	30	10	60
D	20	10	70
E	40	20	40
F	30	20	50

5 gm of raw material for each sample with appropriate weight of VN, PbO and TeO_2 were thoroughly mixed in agate mortar and sintered at 200 °C for 2h. Then it was again grinned and melted at 750 °C. Each melt was kept at this temperature for 1h. The glasses were prepared by usual melt cooling process from the melt at 750 °C to room temperature (25 °C) by rapid quenching between two highly polished copper blocks. This resulted the opaque black glasses with shining surfaces. X-ray diffraction (XRD) of the samples (in powder form) was taken by Rotofax 300 RU, Nigakumake, Japan, diffractometer at room temperature. Glass transition temperature (T_g) of the samples were determined from modulated differential scanning calorimetric (MDSC) analysis using DSC 2910, Modulated DSC, TA instruments. Dc conductivity of the glasses was measured by a two-probe method using programmable electrometer (Keithley-617) in the temperature range 80–450 K.

RESULTS AND DISCUSSION

Fig.1 shows the XRD pattern of the glass samples having only a broad hump at $2\theta \cong 30°$. The scattering wave vector k calculated from the relation $k=4\pi Sin\theta/\lambda$ gives the value of 2.11 A^{o-1} which is typical for amorphous material. This confirms the amorphous nature as well as the short-range order of the sample. T_g of the glasses were found to vary from 268.8 to 302.33 °C which is higher than those reported for telluride glasses [6]. Temperature variation of dc conductivity is shown in Fig.2, which shows the semiconducting behavior of the glasses. At a particular temperature, dc conductivity of A glass is maximum and that of F glass is minimum. At 360K, dc conductivity of the glasses is found to vary from 1.785×10-6 to 7.43×10-9 $ohm^{-1}cm^{-1}$. This large variation may be due to the variation of VN in the glasses.

Activation energy was calculated from $\sigma_{dc}=\sigma_o \exp(-2\alpha R) \exp(-W/KT)$, where σ_{dc} =dc conductivity, σ_o =pre-exponential factor=$\nu_{ph}e^2C(1-C)/KTR$, ν_{ph} being the optical phonon frequency, R the average V-V spacing, α the wave function decay constant, W=activation energy, K=Boltzman constant and T is the measuring temperature. W varies from .139 eV (for A glass) to .229 eV (for F glass) at 333K. The increase of W with the decrease of VN is consistent with the variation of dc conductivity. The Debye temperature, θ_D, (obtained from the slope of σ_{dc} Vs $10^3/T$ curve where it starts bending) varies from 285.7 to 400K.

The importance of tunneling term exp(-2αR) for the glasses could be understood by plotting $\log_{10}\sigma_{dc}$ against W at a fixed temperature. The temperature T_e estimated from the slope of such a plot would be close to the experimental temperature when the hopping is considered to be in the adiabatic regime. T_e would be very different from the experimental temperature if the hopping is considered to be in the non-adiabatic regime. The temperatures estimated from such plots for T=250 and 400K are found as 406 and 675K respectively. Thus the higher values of T_e from the corresponding experimental temperatures suggest non-adiabatic polaron hopping conduction in these glasses like Bi-Sr-Ca-Cu-O glasses [9]. The adiabatic small polaron hopping conduction is reported for V_2O_5 containing tellurite glasses [6]. This may be due to smaller vanadium ionic radius in V_2O_5 compared to VN. At a particular temperature, dc conductivity of the glasses is found to decrease in oxygen atmosphere compared to air.

CONCLUSION:

The glasses are amorphous in nature. DC conductivity of the glasses decreases with the decrease of VN content. These glasses can be used as oxygen gas sensors at higher temperature compared to other telluride glasses as these are having higher T_g. Further work is in progress on the measurement and analysis of other properties of these glasses.

ACKNOWLEDGEMENT

The author is grateful to Prof. H. Sakata, Tokai University, Japan for providing the samples. It is a great pleasure to acknowledge Prof. B. K. Chaudhuri, IACS, Calcutta for his keen interest in this work and giving the facility for measurement of transport properties. Facility provided by IUC, Indore for XRD and MDSC measurement is also acknowledged. This work is financially supported by UGC, Govt. of India from UGC Project (No.F. 10-31/98).

REFERENCES

1. T. Seiyama, A. Kato, K. Fujiishi and M. Nagatani, Anal. Chem., 34 (1962)1502.
2. S. Kanefusa, M. Nitta and M. Haradome, J. Chem Soc. Jpn. (1980) 1591.
3. A. Akiyama, J. Tamaki, N. Miura and N. Yamazoe, Chem. Lett. (1991) 1611.
4. S. Matsushima, D. Akeda, K. Kobayashi and G. Okada, Chem. Lett (1992) 323.
5. E. M. Logothesis, K. Park, A. H. Meitzler and K. R. Laud, Appl. Phys. Lett. 26 (1975) 209.
6. H. Sakata, M. Amano and T. Yagi, J. Non-Cryst Solids 194 (1996) 198.
7. H. Mori and H. Sakata, J. Mater. Sci. 32 (1997) 5243.
8. S. Chakraborty, H. Satou and H. Sakata, 82 (1997) 5520.
9. S. Mollah, K.K. Som, K. Bose, A.K. Chakraborty and B.K. Chaudhuri, Phys. Rev. B 46 (1992) 11075.

FIGURE CAPTIONS

Fig.1: X-ray diffraction pattern of the glasses showing amorphous nature
Fig.2: Thermal variation of dc conductivity (σ_{dc}) of the glasses

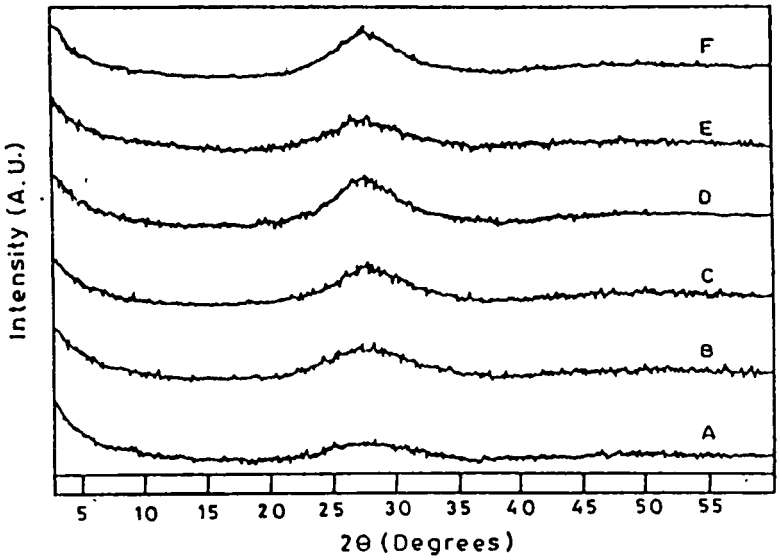
F
E
D
C
B
A
Intensity (A.U.)
5 10 15 20 25 30 35 40 45 50 55
2θ (Degrees)

Fig·1

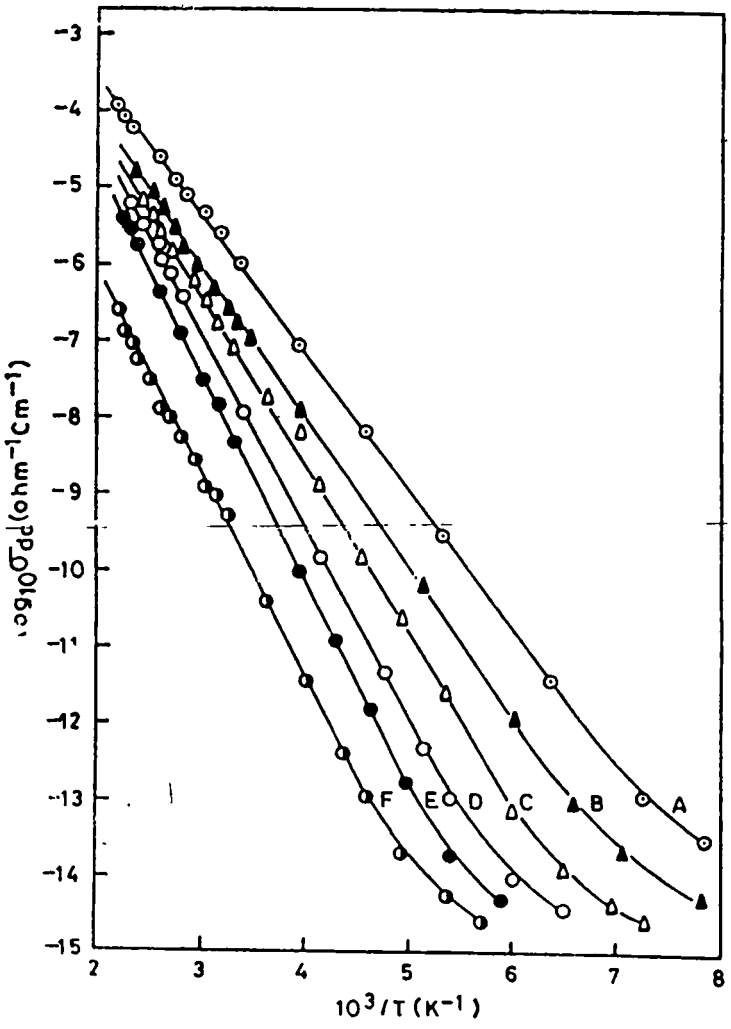
-3
-4
-5
-6
-7
-8
-9
-10
-11
-12
-13
-14
-15
F E D C B A
2 3 4 5 6 7 8
10³/T (K⁻¹)

ELSEVIER

Journal of Alloys and Compounds 326 (2001) 47–49

Journal of ALLOYS AND COMPOUNDS

www.elsevier.com/locate/jallcom

Electron paramagnetic resonance of Fe^{3+} ions in Bi_2O_3–PbO–Fe_2O_3 glasses

C. Prakash, Shahid Husain, R.J. Singh, S. Mollah*

Department of Physics, Aligarh Muslim University, Aligarh 202002, India

Received 23 June 2000; received in revised form 14 January 2001; accepted 15 January 2001

Abstract

The room temperature EPR study of Fe^{3+} ions in Bi_2O_3–PbO–Fe_2O_3 glasses has been carried out for different molar percentages of Fe_2O_3. Spectra recorded at different molar strengths of Fe_2O_3 in the glass differ from one another. In each spectrum, there is more than one line. 'g' values of all the lines in each spectrum have been determined. Explanation of the origin of each spectral line has been attempted. On the measurement of the density of glasses, it was found that when the concentration of Fe_2O_3 was increased at the cost of PbO concentration, the overall density decreased. It was also observed that the d.c. conductivity of the glasses increases with the increase of Fe_2O_3 content.

Keywords: EPR; Fe^{3+} ion; Glass; Density; Conductivity

1. Introduction

Due to multifarious practical applications, glasses have been the subject of wide range studies. To the authors' knowledge, there has been no report on the EPR and electrical conductivity of Bi_2O_3–PbO–Fe_2O_3 glasses. It was thought worthwhile to investigate the EPR of these systems to understand the behavior of Fe^{3+} ions and their site symmetries and measure electrical conductivity of these systems to understand the mechanism of electrical conduction. The density of these systems with different molar percentages of Fe_2O_3 was also measured to understand whether chemical reaction had taken place or not on the introduction of Fe_2O_3 in the Bi_2O_3–PbO glass.

2. Experimental

Analytical reagent-grade Fe_2O_3, PbO and Bi_2O_3 with 99.9% purity are used as the raw materials to prepare the glasses. With stoichiometric ratios of the compounds, the raw materials were mixed and ground in an agate mortar for 2 h. The mixture was kept at 500°C to evaporate the moisture (if any) for 2 h, cooled and again ground. Finally it was melted in an alumina crucible at 1100°C in an electric furnace for 2 h and the glasses were prepared by rapidly quenching the melt between two highly polished copper blocks from the melting temperature to room temperature in air. This gave opaque glasses with shining surfaces. In the preparation of the glasses, the molar percentage of Bi_2O_3 was always kept at 40% and the rest 60% was divided between PbO and Fe_2O_3. The samples are named (and hereafter will be referred to) as A, B, C, D, E, F and G as shown in Table 1. A part of the glass was used for EPR study and a part of it was used for d.c. conductivity measurements. The density of the glasses was measured by Archimedes' principle using water as the immersion liquid.

The EPR spectra of the samples were recorded at room temperature, on a Jeol (JES-RE2X) ESR spectrometer

Table 1
Composition and density of Bi_2O_3–PbO–Fe_2O_3 glasses

Samples	Composition (mol%)			Measured density (g/cc)	Expected density (g/cc)
	Bi_2O_3	PbO	Fe_2O_3		
A	40	59	1	6.5454	8.3318
B	40	57	3	6.5441	8.2754
C	40	55	5	6.4839	8.2190
D	40	50	10	5.9583	8.0780
E	40	30	30	–	7.5140
F	40	20	40	–	7.2320
G	40	10	50	–	6.9500

*Corresponding author. Tel.: +91-571-701-001; fax: +91-571-701-001.

E-mail address: smollah@rediffmail.com (S. Mollah).

0925-8388/01/$ – see front matter
PII: S0925-8388(01)01224-5

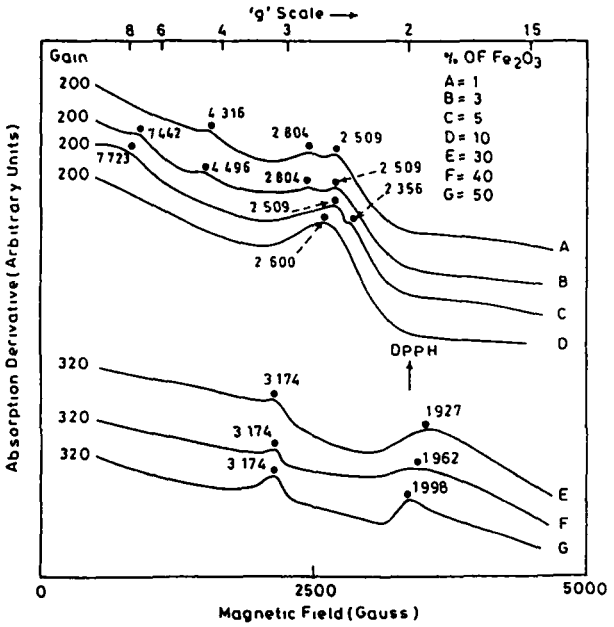

Fig 1 Absorption derivative versus magnetic field curves for Bi_2O_3–PbO–Fe_2O_3 glasses Compositions of Fe_2O_3 in different glasses are (A) 1%, (B) 3%, (C) 5%, (D) 10%, (E) 30%, (F) 40%, and (G) 50% The position of the DPPH signal with $g=2\,0036$ is shown by an arrow As the full absorption derivative curve is not observed, the g values correspond to the peak positions

working at x-band with 100 kHz field modulation D c conductivity measurement was done in the temperature range of 573–680 K The samples were pressed tightly between two platinum electrodes and the measurements were done using a Keithley Digital Multimeter (Model 2000) Silver wires were used for connections

3. Results and discussions

The EPR spectra of the Bi_2O_3–PbO–Fe_2O_3 glass of different compositions are shown in Fig 1 In these systems, only the Fe ions are EPR probe The g values of different signals in the EPR spectra for different compositions of the glasses are shown in Table 2 In the spectra (Fig 1), there are five distinct regions of g values

Table 2
The g values of different signals in the EPR spectra for different compositions of the glasses

Samples	g values					
A		4 316		2 804	2 509	
B	7442	4 496		2 804	2 509	
C	7 723				2 509	2 356
D				2 600		
B			3 174			1 927
F			3 174			1 962
G			3 174			1 998

(Table 2) In glass, the lines with g values of approximately 6 2 and 4 2 have been observed by the earlier workers [1] and have been attributed to Fe^{3+} ions with rather large crystal field splitting The two sets of lines with g values in the range 7 442–7 723 obtained in B and C and in the range 4 316–4 496 obtained in A and B may be the characteristic lines of Fe^{3+} ions in the glass A line of $g\approx2$ is usually observed in glasses and is attributed to predominantly octahedral surrounding of Fe^{3+} ions Lines occurring in the range of 2 356–2 804 in A, B, C, D and in the range of 1 927–1 998 in E, F G may belong to this origin with Fe^{3+} ions in different site symmetries or Fe ions entering into the cluster formation The two close signals in the range of 2 356–2 804 observed in A B, C may represent the $g_{\parallel}$ and $g_{\perp}$ components of one signal As the Fe^{3+} content is higher in D compared to A, B, C, the signal has not been resolved As the concentration of Fe^{3+} ion is much higher in E, F, G compared to A, B, C, D the same signal might have shifted to $g=3\,174$ in E, F, G due to different type of cluster formation Marked difference in the EPR spectra of A, B, C, D from E, F, G may be due to the fact that at lower concentrations, Fe^{3+} ion may behave as foreign impurity but at higher concentrations, it becomes a component of glass

The electrical conductivity of these glasses was measured to understand the mechanism of electrical conduction Fig 2 shows the log σ versus $1/T$ graph for different compositions It shows that the electrical conductivity increases with Fe^{3+} ion concentration Conductivity increases with temperature, showing an overall semi-conducting nature of the material Mechanism of conductivity is polaronic in nature Polaronic conductivity is less than

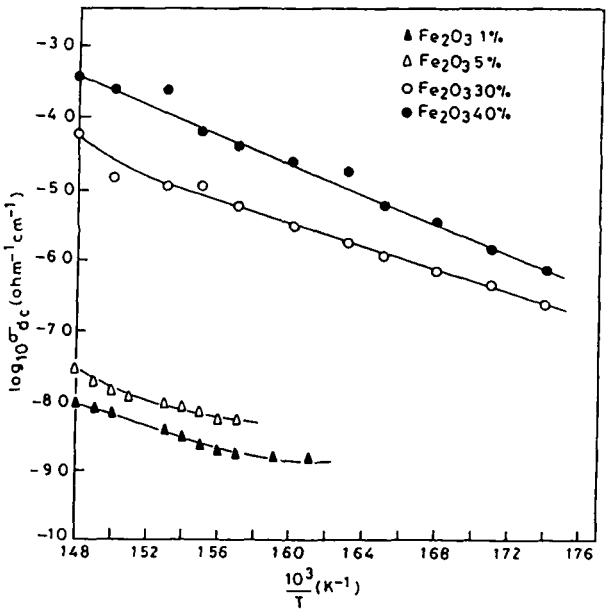

Fig 2 Inverse temperature variation of d c conductivity of Bi O_3–PbO–Fe O_3 glasses Starting from bottom Fe O_3=1 5 30 and 40%

electronic conductivity as the effective mass and mobility of polaron are, respectively, higher and lower than those of free electron. There are three possible models [2,3]; (a) band conduction, (b) phonon-assisted conduction or conduction by hopping; and (c) variable range hopping. The phonon-assisted hopping (polaronic conductivity) (b) seems to be the most probable because the $\log \sigma$ versus $1/T$ plot in Fig. 2 seems to be quite close to linear as required in (b). The deviation may indicate small contribution from other mechanisms including ionic conductivity. As the conductivity depends upon the Fe^{3+} concentration, hopping sites may be mediated by Pb^{2+} and Bi^{3+} sites.

The density of some prepared compounds were measured (Table 1). It was observed that their densities are different from what is expected (Table 1) if the substances would have been simply the physical mixture of three ingredients used in the composition. For a physical mixture, the expected density has been calculated by using the formula, $d = c_1d_1 + c_2d_2 + c_3d_3$ where c values represent relative ratios of components and d values their densities. The measured and expected densities (Table 1) are different. It shows that the chemical reaction has taken place and glass has been formed It was also observed that the measured density decreased when the concentration of Fe_2O_3 was increased at the cost of PbO concentration in the glass. The reason may be that the density of PbO is higher than that of Fe_2O_3

Acknowledgements

We are grateful to UGC, Govt. of India, for its financial support from the project (No.F. 10-31/98).

References

[1] T Castner, G S Newell, W C Holton, G P Slichter, J Chem Phys 32 (1960) 668.
[2] J. Zarzycki, in Glasses and Vitreous State, Cambridge University Press, Cambridge 1991.
[3] S Mollah, K K. Som, K Bose, A.K Chakraborty, B K Chaudhuri, Phys Rev B 46 (1992) 11075

Proc. Eleventh Int. Workshop Phys. Semiconductor Devices, 2001

Preparation and Characterization of Bi_2O_3-PbO-R (R=Fe_2O_3, MnO_2, CuO and V_2O_5) Semiconducting Oxide Glasses.

C. Prakash, Arfat Firdous and S. Mollah

Department of Physics, Aligarh Muslim University, Aligarh-202002, India.

A series of Bi_2O_3-PbO-R (R=Fe_2O_3, MnO_2, CuO and V_2O_5) glasses have been prepared from the respective melts to room temperature by rapidly quenching between two highly polished copper blocks. Bi_2O_3 was kept fixed (40 mol%) for all the glasses. The remaining 60 mol% was varied between PbO and R. PbO was kept between 59.9 to 50.0 mol% whereas R was varied between 0.1 to 10.0 mol%. Dc conductivity of all the glasses was measured at the temperature range (400-700K). The conductivity was found due to small polaron hopping conduction in the non-adiabatic region. At 650K, the conductivity of 1mol% R was found to be maximum (~10^{-7} $ohm^{-1}cm^{-1}$) for R=MnO_2 and minimum (~10^{-9} $ohm^{-1}cm^{-1}$) for R=Fe_2O_3. The 'g' values calculated from Electron Paramagnetic Resonance (EPR) signal varies from sample to sample. For all the samples one of 'g' values obtained nearly 2.0 whereas for R=Fe_2O_3 sample 'g' values of 4.3, 7.4 are also observed.

INTRODUCTION

The structural and transport properties of oxide glasses containing transition metal ions (TMI) have been studying with increasing interest. The fascinating transport properties in these glasses arise due to the presence of TMI in more than one valancy state. Strong electron-phonon interaction in these glasses forms small polarons and the electrical conduction is due to the hopping of these polarons between the two valance states of the TMI [1].

Electron paramagnetic resonance (EPR) has been successfully employed to obtain information about the glassy network through the use of TMI dopants. EPR and optical absorption studies have been made for Fe^{3+} ions in alkali-cadmium borosulphate glasses [2]. EPR and magnetic susceptibility measurements were performed on Fe_2O_3-TeO_2-B_2O_3-PbO glass [3]. Recently we have reported the EPR of Fe^{3+} ions in Bi_2O_3-PbO-Fe_2O_3 glass [4]. The 'g' values of different signals in the EPR spectra for different concentration of Fe^{3+} ions were having some new values not observed earlier. Thus our intention was to study the EPR signal of the glasses prepared with MnO_2, CuO and V_2O_5 in exchange of Fe_2O_3 in the same glass matrix (Bi_2O_3-PbO). This paper repots the dc conductivity and EPR of Bi_2O_3-PbO-R (R=Fe_2O_3, MnO_2, CuO and V_2O_5) glasses.

EXPERIMENTAL

Bi_2O_3-PbO-R (R=Fe_2O_3, MnO_2, CuO and V_2O_5) containing 40 mol% Bi_2O_3, 50-59.9 mol% PbO and 10-0.1 mol% R glasses are prepared. Glasses containing 1, 3, 5, 10, 30, 40, and 50 mol.% of Fe_2O_3 are symbolized as A, B, C, D, E, F, and G respectively [4]. Analytical reagent grade Bi_2O_3, PbO, Fe_2O_3, MnO_2, CuO and V_2O_5 with 99.9% purity are used as the raw materials to prepare the glasses. According to the stoitiometric ratio of the samples, the raw materials were mixed and grinned in an agate mortar for one hour. The mixture was kept at 500 °C to evaporate the moisture (if any) for two hours, cooled and again grinned. Finally it was melted in an alumna crucible at 1000-1100 °C in an electric furnace for one hour and the glasses were prepared by rapidly quenching the melt between two highly polished copper blocks from the melting temperature to room temperature in air. This gave the opaque glasses with shining surfaces. The samples were then annealed at 100 °C to reveal the micro-cracks (if any) at the time of glass formation. Parts of the glasses were used for EPR measurement and the remaining parts were utilized for dc conductivity measurements. Density of the glasses was measured by Archimedes' principle using water as the immersion liquid.

For electrical measurements, both polished surfaces of samples were coated with silver paste. The silver coated samples were heat treated at 100 °C for the stabilization of the electrodes. DC conductivity of the samples was measured at the temperature range (400-700K) using the Keithley Digital Multimeter (Model 2000). Sufficient time was given at each temperature during measurement to obtain the stabilized value. The EPR spectra of the samples were recorded at room temperature, in X band (9.4 GHz) and 100 kHz field with a Geol type equipment.

RESULTS AND DISCUSSION

Amorphous nature of the glasses is confirmed from the XRD spectra, which shows only a broad hump at $2\theta=30°$. The density of the glasses containing 10 mol.% R vary from 5.958 to 6.524 g cm^{-3} being minimum for Fe_2O_3 and maximum for CuO (Table 1). For same R (Fe_2O_3), the density of glasses increases with the decrease of R [4]. The same behavior is also observed for glasses with other transition metal oxides (CuO, MnO_2, and V_2O_5). This result is consistent with the increasing concentration of heavier PbO and decreasing R. The calculated expected density also shows the same trend (Table 1) which confirms the proper mixing of the raw materials at the time of glass formation. Apparent molar volume (V_o^*) occupied by one gm-atom of oxygen in these glasses is calculated from the relation $V_o^* = M/(n\rho)$, where M is the molecular weight calculated from the composition, n is the number of oxygen atoms in one formula unit, ρ is the density of the glasses. It is observed that V_o^* varies from 26.03 to 26.89 (Table 1) for 10 mol% of R in the glass matrix. Thus the random topology of the glasses change with the change of R content. The transition metal ion (TMI) concentration (N) in the glasses vary from 11.17×10^{21} to 12.30×10^{21} cm^{-3} (Table 1). DC conductivity of the glasses increases with the increase

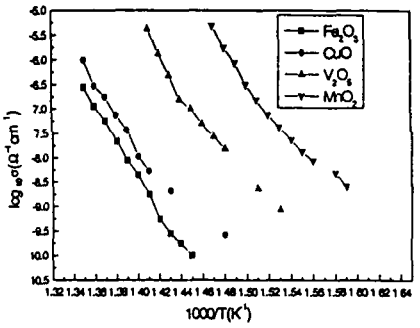

Fig.1 Inverse temperature variation of dc conductivity of $40Bi_2O_3$-59PbO-1R glasses.

of mol.% of R for all the four types of glasses [4]. Figure 1 shows the variation of dc conductivity with inverse temperature for 1mol% of R. Dc conductivity increases with the increase of temperature showing the semiconducting behavior of the glasses. At any temperature, the maximum conductivity is found for R= MnO_2 whereas minimum is observed for R= Fe_2O_3 (Figure 1).

The same behavior is also observed for other mol% of R. The activation energy and other parameters of the glasses confirm that the small polaron hopping (SPH) is the most probable transport mechanism in these glasses for dc conduction.

Table 1: Some important parameters of $40Bi_2O_3$-50PbO-10R glasses.

Sl.No.	Component R	Measured Density (gm/cc)	Expected Density (gm/cc)	N (cm^{-3})	V_o^* ($cm^3g^{-1}atom^{-1}$)
1.	Fe_2O_3	5.958	8.078	11.17×10^{21}	26.94
2.	MnO_2	6.408	8.397	12.17×10^{21}	26.03
3.	CuO	6.524	8.534	12.29×10^{21}	26.24
4.	V_2O_5	6.382	8.231	12.30×10^{21}	26.89

EPR spectra of Bi_2O_3-PbO-Fe_2O_3 glasses are reported in our recent paper [4]. The EPR spectra of the Bi_2O_3-PbO-Fe_2O_3 glass in different compositions are shown in Fig.1. In these systems, only the Fe ions are EPR probe. The g-values of different signals in the EPR spectra are shown in Fig.2. In these systems, only the Fe ions are EPR probe. The g-values of different signals in the EPR spectra for different compositions of the glasses are shown in Table 2.

Table 2: The g-values of different signals in the EPR spectra for different mol.% of Fe_2O_3 in the glasses

Samples	'g' values
A	4.316 2.804 2.509
B	7.442 4.496 2.804 2.509
C	7.723 2.509 2.356
D	2.600
E	3.174 1.927
F	3.174 1.962
G	3.174 1.998

In the spectra (Fig.2), there are five distinct regions of g-values (Table 2). The lines with g-values of approximately 6.2 and 4.2 have been observed by the earlier workers [5] and have been attributed to Fe^{3+} ions with rather large crystal field splitting. The two sets of lines with g-values in the range 7.442-7.723 obtained in B and C and in the range 4.316-4.496 obtained in A and B may be the characteristic lines of Fe^{3+} ions in the glass. A line of $g \approx 2$ is usually observed in glasses and is attributed to predominantly octahedral surrounding of Fe^{3+} ions. Lines occurring in the range of 2.356-2.804 in A, B, C, D and in the range of 1.927-1.998 in E, F, G may belong to this origin with Fe^{3+} ions in different site symmetries or Fe^{3+} ions entering into the cluster formation.

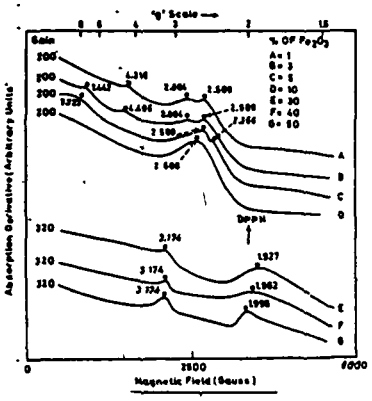

Fig.2 Absorption derivative Vs. magnetic field curves for Bi_2O_3-PbO-Fe_2O_3 glasses

The two close signals in the range of 2.356-2.804 observed in A, B, C may represent the g_{η} and $g_{\perp}$ components of one signal. As the Fe^{3+} content is higher in D compared to A, B, C; the signal has not been resolved. As the concentration of Fe^{3+} ion is much higher in E, F, G compared to A, B, C, D the same signal might have shifted to g=3.174 in E, F, G due to different type of cluster formation. Marked differences in the EPR spectra of A, B, C, D from E, F, G may be due to the fact that at higher concentrations, it becomes a component of glass.

The 'g' values of the EPR spectra of glasses containing CuO, MnO_2 and V_2O_5 are found to be nearly 2 varying slightly from sample to sample. This is attributed to predominantly octahedral surrounding of Cu, Mn and V ions.

CONCLUSION

The dc conductivity at any temperature is maximum for MnO_2 and minimum for Fe_2O_3 for same mol.%. The conduction in the glasses is due to small polaron hopping among TMIs. The measured and expected densities of the glasses confirm the proper mixing of the raw materials. The room temperature (300K) EPR lines of Fe^{3+} ions in Fe_2O_3 containing glasses are found for the magnetic field corresponding to several g values as listed in Table 2. But $g \approx 2$ for other glasses having R as CuO, V_2O_5 and MnO_2 are observed.

REFERENCES

1. Mott, N. F., J. Non-Cryst. Solids **1** (1968) 1.
2. Rao, A. S., Reddy, R. R., Rao, T.V.R. and Rao, J.L., Solid State Commun. **96** (1995) 701.
3. Ardelean, I., Poteanu, M., Filips, S., Simon, V., and Gyorffy, G., Solid State Commun. **102** (1997) 341.
4. Prakash, C., Husain, S., Singh, R. J., and Mollah, S., J. Alloys and Compounds, **326** (2001) 47.
5. Castnar, T., Newell, G. S., Holton, W. C., and Slichter, G.P, J. Chem. Phys. **32** (1960) 668.

PHYSICAL REVIEW B VOLUME 51, NUMBER 24 15 JUNE 1995-II

ac conductivity of glassy $Bi_{4-n}Pb_nSr_3Ca_3Cu_4O_x$ semiconductors (with $n = 0.0$, 0.1, 0.5, and 1.0): Precursors for high-T_c superconductors

S. Mollah,* K. K. Som, S. Chakraborty, A. K. Bera, S. Chatterjee, S. Banerjee, and B. K. Chaudhuri
Solid State Physics Department, Indian Association for the Cultivation of Science, Calcutta 700 032, India
(Received 9 August 1994; revised manuscript received 7 February 1995)

Experimental results are reported for the temperature- (T= 77–450 K) and frequency- ($\omega = 10^2$–10^4 Hz) dependent (ac) conductivities (σ_{ac}) of Pb-doped $Bi_{4-n}Pb_nSr_3Ca_3Cu_4O_x$ (n =0, 0.1, 0.5, and 1.0) semiconducting glasses. All these glasses show small clusters or grains of different sizes arising due to the phase separation as observed from the scanning electron microscopic study. The ac conductivities of these glasses follow the well-known relation $\sigma_{ac}(\omega) = A(T)\omega^s$. In these glasses the electron-phonon interaction is strong enough to form small polarons and electrical conduction occurs by a small-polaron hopping mechanism. Like Li-doped $Bi_4Sr_3Ca_3Cu_3O_x$ glasses, the exponents of all the present Pb-doped glasses are found to be a little higher than unity (1.1–1.2) in the low-temperature regime where $\sigma_{ac}(\omega)$ also shows little nonlinear variation with temperature. Similar values of s (≥ 1) have also been reported in the literature for glassy nonoxide semiconductors. The experimental ac conductivity data have been analyzed with different theoretical models based on quantum-mechanical tunneling through the barrier and classical hopping over the barrier mechanisms. The correlated barrier hopping (CBH) model is found to be most appropriate for these glasses, explaining the behavior of both $\sigma_{ac}(\omega, T)$ and its exponent s (except in the region where $s > 1$). Other models, such as the quantum-mechanical tunneling model and the overlapping large-polaron tunneling model, are found to be inadequate to explain the general behavior of both temperature- and frequency-dependent σ_{ac} and s. The extended-pair approximation model and the percolation theoretical model are also found to fit the ac-conductivity data of these glasses (with $s \leq 1$). However, the fitting with the CBH model appears to be better. All the Pb-doped glasses are also found to be good precursors for superconductors with T_c between 110 and 115 K in their crystalline phases obtained by annealing for optimum time of 24 h at 840 °C. The thermoelectric powers of these superconductors are positive (hole-type superconductors).

I. INTRODUCTION

The electrical properties of transition-metal-oxide (TMO) glasses with V_2O_5, Fe_2O_3, CuO, etc., and suitable glass formers (such as B_2O_3, P_2O_5, and GeO_2) have been elaborately studied[1–10] because of their probable technological applications in switching and memory devices.[11–13] The strong electron-phonon interaction in the TMO glasses, responsible[1,14] for the small-polaron formation and the dc electrical conduction in such semiconducting oxide glasses, occurs by small polarons hopping between transition-metal ions of different valence states[5–13] ($V^{4+} \rightarrow V^{5+}$, $Cu^{+} \rightarrow Cu^{2+}$, etc.). At low frequencies and temperatures the frequency-dependent ac conductivities of many TMO glasses showed an almost linear frequency dependence (with frequency exponent $s \leq 1$).[2,6,15,16] However, there is an apparent controversy over the temperature dependence of $\sigma_{ac}(\omega, T)$ and the exponent s. In some non-transition-metal-oxide glasses both temperature-dependent and temperature-independent ac conductivities have been reported[17,18] even at frequencies as low as 1 kHz. Various theoretical models were used[2,6,15,16] to explain the frequency dependence of ac conductivity of many binary vanadate, tungstate, or other similar glassy oxide semiconductors. However, few investigations of the ac conductivities of the multicomponent copper containing Bi-Sr-Ca-Cu-O oxide glasses has been made so far.

Recently, some of these glasses, such as Bi-Sr-Ca-Cu-O and Bi-(Li or Pb)-Sr-Ca-Cu-O, have been found[19,24] to be very good precursors for high-T_c superconductors. From these semiconducting glassy precursors high-T_c wires or tapes could also be made.[23] Among all these types of glasses, the $Bi_4Sr_3Ca_3Cu_4O_x$ (hereafter denoted by [4334]) glass composition is especially important as they are easily converted to the superconducting $Bi_2Sr_2Ca_2Cu_3O_x$ phase[25] with the highest-T_c value ($\gtrsim 110$ K) by slowly annealing the glass (well above the glass transition temperature T_g shown in Table I). By this annealing process the glasses become crystalline (also called glass ceramics) and oxygenated. Most of the previous studies on such systems have been confined to the investigations of the superconducting and related properties in the glass-ceramic (GC) phases. The occurrence of superconductivity close to insulator to metal transitions supported the conjecture that superconductivity might be due to the condensation of bipolarons.[26] Experimental evidences of polaron-hopping conduction is also found in a large number of cuprates.[27,28] Like TMO glasses, the small-polaron hopping mechanism is also responsible for the conduction mechanism in the Bi-Sr-Ca-Cu-O–type glasses[22–24] in their semiconducting phases. The Pb-doped Bi-Sr-Ca-Cu-O glassy system of our present investigation is especially interesting because the annealed crystalline phases of these

0163-1829/95/51(24)/17512(9)/$06.00

glasses have large T_c values and large volume fractions of the high-T_c phases compared to those of the corresponding undoped system.[29,30] Furthermore, unlike many oxide glasses, the Pb- or the Li-doped Bi-Sr-Ca-Cu-O glasses contain no glass former oxide.[24,31] The presence of Li and Pb reduces the annealing temperature for making superconducting glass ceramics to be less than that required for the undoped system. These glasses also show phase separation unlike many binary or ternary TMO glasses. Therefore, it is interesting to investigate the electrical and other properties of these glasses and also to compare their properties with those of other TMO glasses,[1-10] which do not become superconductors in their respective crystalline phases. All other TMO glasses are nonsuperconductors in their GC phases. Such studies on glassy systems are important for an in-depth understanding of the mechanism for the appearance of superconductivity in their crystalline phases.

In the present paper the Pb-doped $Bi_{4-n}Pb_nSr_3Ca_3Cu_4O_x$ semiconducting glasses prepared by a fast-quenching technique have been characterized and the results of frequency- and temperature-dependent ac-conductivity measurements have been reported. Different theoretical models have been applied to find the most suitable one explaining the ac-conductivity data of these special types of glasses showing some distinct features such as large values of glass transition temperature (T_g), Debye temperatures (θ_D), and strong electron-phonon interaction, compared to those of many binary or ternary TMO glasses. The presence of BiO_3/BiO_6-type structural units is another characteristic feature of both Li- and Pb-doped Bi-Sr-Ca-Cu-O glasses (as observed from infrared spectra). It has been shown that the Pb-doped glasses, when annealed at about 840 °C for an optimum time of 24 h, become high-T_c superconductors.

The remaining part of the paper is organized as follows. Section II deals with the preparation and characterizations of these glasses. In Sec. III the results of our measurements of ac conductivity are presented and in Sec. IV various theoretical models used to fit the frequency- and temperature-dependent ac conductivity data have been discussed. The paper ends with a brief conclusion. Since the electrical properties of the $Bi_{4-n}Pb_nSr_3Ca_3Cu_4O_x$ glass with $n=0$ have already been discussed in Ref. 22 we do not show the ac-conductivity data of this glass again in this paper.

II. EXPERIMENT

A. Sample preparation and characterization

The $Bi_{4-n}Pb_nSr_3Ca_3Cu_4O_x$ glasses (abbreviated as PBY) are denoted as PBY-0, PBY-1, PBY-2, and PBY-3 for $n=0$, 0.1, 0.5, and 1.0, respectively. They are prepared by rapidly quenching the respective melts as discussed earlier.[22,24] Accurately weighted PbO, Bi_2O_3, $SrCO_3$, $CaCO_3$, and CuO powders (all of purity 99.99% or better) for each composition were well mixed and preheated at about 500 °C for 5 h in a platinum crucible. Preheating is essential for keeping the correct Pb concentration in the glassy phase. The glass samples prepared without preheating show a low (~50 K) superconducting transition temperature (T_c) in their GC phases. The preheated sample is then cooled to room temperature, reground, melted at (1100±10 °C) for 2 h and then shaken frequently to ensure proper mixing and homogeneity. The glass plates (1–1.5 mm thick) are then made by rapidly quenching the melts between two highly polished copper blocks. Wire or tape can also be drawn from this molten glass. The x-ray diffraction (using the Philips x-ray diffractometer, Model PW 1710) pattern shows a broad peak, which is characteristic of an amorphous material (Fig. 1). However, the scanning electron micrographs of the as-quenched samples (studied with the Hitachi Model 415A), shown in Fig. 2, indicate phase separation with small clusters (5–25 μm in size) or grains (Fig. 2) of different densities and conductivities. Similar phase separation has also been observed earlier in the $Pb_{0.32}Bi_{1.68}Sr_2Ca_2Cu_3O_x$ (Refs. 28 and 30) and $Bi_4Sr_3Ca_3Cu_4O_x$ (Refs. 29 and 31) glasses, which are also good precursors for high-T_c superconductors. The P_2O_5-CaO-CuO-type copper containing glasses also showed similar phase separation.[7] This phase separation appears to have a major influence on the properties of the glasses.[31] The glass transition temperatures (T_g) measured with Shimadzu thermal analyzer (Model DT30) at the heating rate of 10 °C/min are found to be higher (Table I) than the usual vanadate-type semiconducting oxide TMO glasses, but these T_g values are comparable to those of other glassy precursors for high-T_c superconductors (Li-doped or undoped Bi-Sr-Ca-Cu-O systems,[23] for instances). The metallic compositions of the glasses were estimated by energy dispersive x-ray analysis (using the Hitachi Model H-600) and remain within ±3% of the corresponding theoretical (mixing) values.[32] Infrared (ir) absorption studies of the samples at ambient temperature as shown (Fig. 3) indicate features identical to those of the Li-doped Bi-Sr-Ca-Cu-O glasses.[23] The fundamental

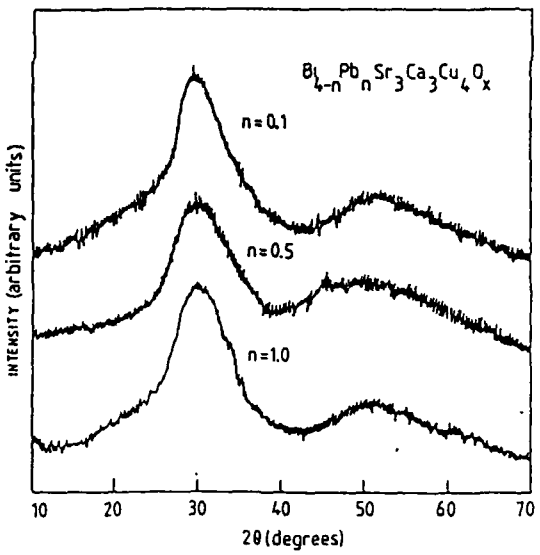

FIG. 1. X-ray powder diffraction patterns of $Bi_{4-n}Pb_nSr_3Ca_3Cu_4O_x$ glasses showing amorphous character

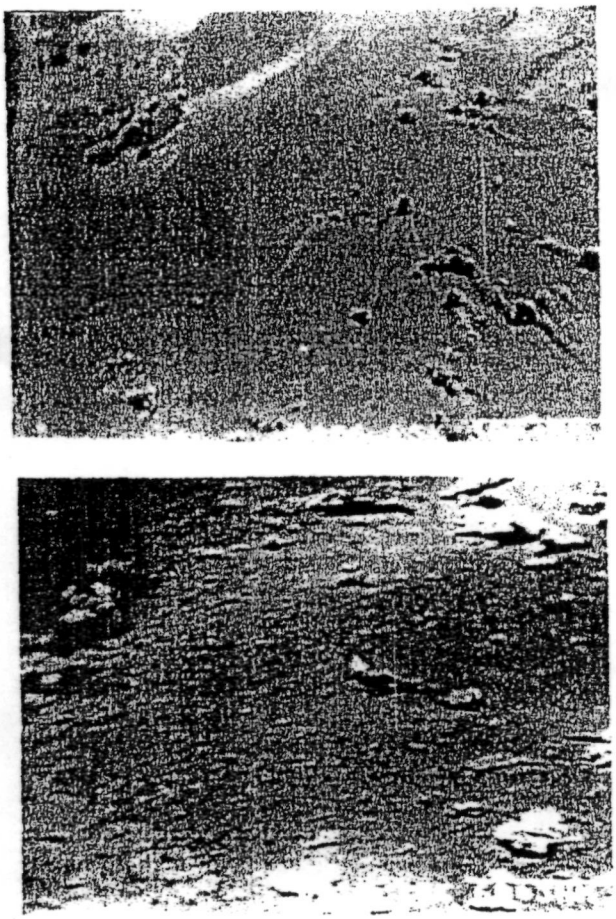

FIG. 2. Scanning electron micrographs of samples showing phase separated clusters or grains embedded in the glass matrix that had formed during quenching the melt: (a) $Bi_{3.5}Pb_{0.5}Sr_3Ca_3Cu_4O_x$ and (b) $Bi_3Pb_{1.0}Sr_3Ca_3Cu_4O_x$. [In (a) 20 mm=300 μm and in (b) 20 mm=60 μm.] Phase separations are also observed in the $Bi_4Sr_3Ca_3Cu_4O_x$ glass and in other similar glasses (Refs. 30 and 31).

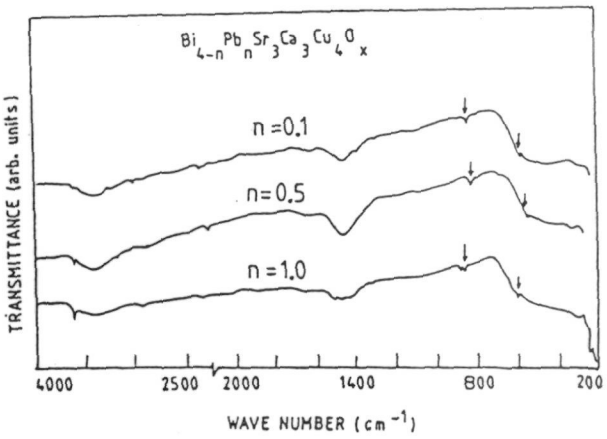

FIG. 3. Infrared spectra of glassy $Bi_{4-n}Pb_nSr_3Ca_3Cu_4O_x$ semiconductors showing the presence of BiO_3/BiO_6 groups in the frequency range of 540–620 cm^{-1}, a characteristic feature of these glassy precursors for high-T_c superconductors.

peaks between 540 and 620 cm^{-1} in the spectra (Fig. 3) indicate the presence of BiO_3/BiO_6 structural units. A detailed analysis of the ir data is planned for a future work. All the Bi-Pb-Sr-Ca-Cu-O glasses are also annealed at 840 °C for 24 h in air and then slowly cooled to room temperature, which make them superconducting. The superconducting transition temperatures of all the annealed samples have also been measured by the four-probe method showing T_c between 110 and 115 K (Table I). Thermoelectric powers of all the annealed (GC) samples are measured by the usual method.

B. ac conductivity of the PBY glasses

The ac conductivity (σ_{ac}) of the glasses has been measured over the frequency range 0.1–10 kHz and the temperature range 77–450 K, similar to our earlier work[23] with a low-temperature cryostatic arrangement and tem-

TABLE I. Some important parameters of $Bi_{4-n}Pb_nSr_3Ca_3Cu_4O_x$ with n =0.0 (PBY-0), 0.1 (PBY-1), 0.5 (PBY-2), and 1.0 (PBY-3), respectively.

Parameters \ Samples	PBY-0	PBY-1	PBY-2	PBY-3
n	0.0	0.1	0.5	1.0
Density ($g\,cm^{-3}$)	5.82±0.1	7.00±0.1	6.90±0.1	6.76±0.1
T_g (°C)	426.0±2	415.0±2	408.0±2	402.0±2
N (10^{21} cm^{-3})[a]	8.32	9.75	9.64	9.47
θ_D (K)[b]	428±5	420±5	412±5	408±5
ν_{ph}(10^{12} Hz)[b]	9.80	8.75	8.58	8.50
T_{c0} (K)[c]	65±1	73±1	75±1	80±1

[a]Obtained from the fitting of the dc conductivity of the glasses (Ref. 22).

[b]Calculated from the temperature ($\theta_D/2$), where the linearity of the $\ln\sigma_{dc}$ vs $1000/T$ curve breaks (Ref. 22) [σ_{dc} is the dc conductivity of the glass (Ref. 22)] and the phonon frequency ν_{ph} is calculated from the relation $k_B\theta_D = h\nu$.

[c]T_{c0} is the superconducting transition temperature (at zero resistance) of the glass-ceramic sample obtained by annealing the glass at 840 °C for 24 h and T_{c0} is the corresponding zero resistance temperature. For all the glass ceramics, T_c values are almost the same (110–115 K), as shown in Fig. 8.

perature controller. The Kiethly electrometer (Model 617) has been used to measure the resistance. The sample was in good contact with two polished and cleaned brass electrodes. Before electrical measurements the samples were annealed around 200 °C (well below glass transition temperature) to stabilize the contacts and also to remove mechanical stresses. Gold electrodes were deposited on the polished sample surfaces by the vacuum evaporation technique to serve as the conductive layers for the electrical measurements. The ac conductivity and dielectric loss (ε'') of the samples were obtained by measuring the conductance and capacitance of the samples using a Gen Rad 1615A capacitance bridge with the audio oscillator Model 1311A, the tuned amplifier Model 1232A, and a null detector. The temperature measurements were made with an accuracy of ±0.5 K or better. The ac conductivity for the present glasses are obtained from the relation[33,34]

$$\sigma_{ac}(\omega)=\sigma_t(\omega)-\sigma_{dc}\,, \tag{1}$$

where σ_{dc} and $\sigma_t(\omega)$ are the dc and the total frequency-dependent conductivities, respectively.

In many amorphous semiconductors and insulators the ac-conductivity data follow the relation[33]

$$\sigma_{ac}(\omega)=A\omega^s\,, \tag{2}$$

where A is a constant dependent on temperature and s is the frequency exponent, generally less than or equal to 1. To exhibit this behavior, the loss mechanism[34] should have a very wide range of possible relaxation times (τ). In particular, a nearly linear frequency dependence of $\sigma_{ac}(\omega)$ is predicted if the distribution of relaxation times $G(\tau)$ is inversely proportional to $\tau=\tau_0\exp(\xi)$, where ξ is a variable and τ_0 is a characteristic relaxation time almost equal to the inverse phonon frequency (ν_{ph}^{-1}) obtained from the dc-conductivity data.[24]

III. RESULTS AND DISCUSSION

The temperature-dependent σ_{dc} and $\sigma_t(\omega)$ conductivities of a typical $Bi_{3.5}Pb_{0.5}Sr_3Ca_3Cu_4O_x$ glass is shown in Fig. 4(a). The inverse temperature dependence of $\sigma_{ac}(\omega)$ of this glass obtained by using Eq. (1) is shown in Fig. 4(b). These figures indicate, similar to other amorphous semiconductors, that the temperature dependence of $\sigma_t(\omega)$ is much less at low temperatures, whereas at higher temperatures $\sigma_t(\omega)$ depends strongly on temperature with a relatively small frequency dependence. Ultimately, the measured conductivity at all frequencies appears to coincide with σ_{dc} at a higher temperature. The identical behavior is also observed for other compositions of the PBY glasses. However, the only difference is the temperature at which the measured conductivity becomes equal to the dc conductivity.

The thermal variation of $\sigma_{ac}(\omega)$ of the $Bi_{4-n}Pb_nSr_3Ca_3Cu_4O_x$ glasses at a fixed frequency of 5 kHz (Fig. 5) also looks similar to those of the usual TMO glasses,[1-6] which are not precursors for superconductors. But in their glassy phases the electrical conductivities (both ac and dc) of these TMO glasses are higher than

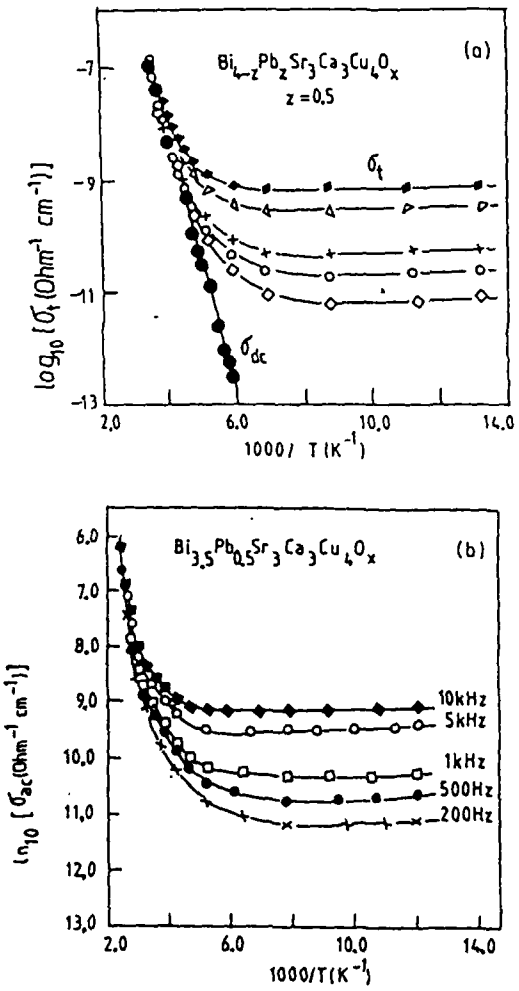

FIG. 4. (a) Temperature dependence of σ_{dc} and $\sigma_t(\omega)$ for a typical $Bi_{3.5}Pb_{0.5}Sr_3Ca_3Cu_4O_x$ glass at 10 kHz (■), 5 kHz (△), 1 kHz (+), 500 Hz (○), and 200 Hz (□). Solid lines are a guide for the eye. (b) Inverse temperature dependence of $\sigma_{ac}(\omega)$ of the $Bi_{3.5}Pb_{0.5}Sr_3Ca_3Cu_4O_x$ glass at 10 kHz (■), 5 kHz (○), 1 kHz (□), 500 Hz (●), and 200 Hz (×). Solid lines are a guide for the eye.

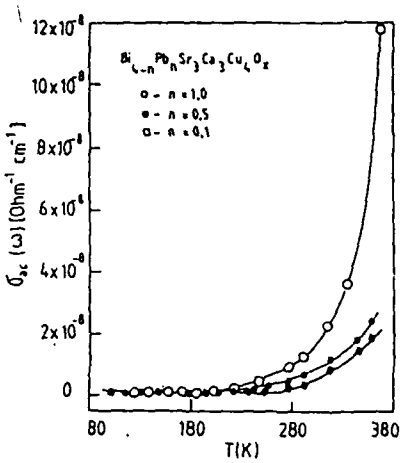

FIG. 5. Thermal variation of $\sigma_{ac}(\omega)$ of the $Bi_{4-n}Pb_nSr_3Ca_3Cu_4O_x$ glasses at a fixed frequency of 5 kHz (the solid line is a guide for the eye).

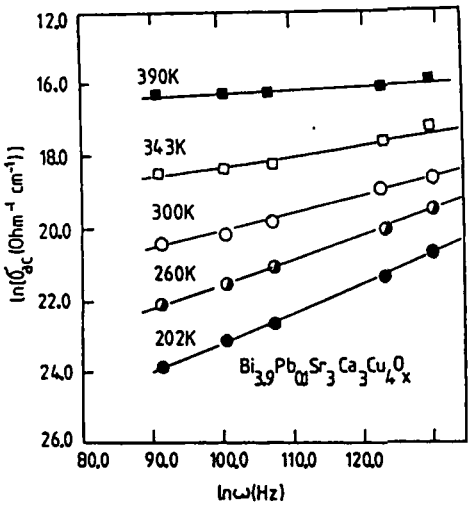

FIG. 6. Frequency dependence of ac conductivity of one of the PBY glasses ($Bi_{3.9}Pb_{0.1}Sr_3Ca_3Cu_4O_x$) for different fixed temperatures. Straight lines are obtained by a least-squares fitting. The slopes of the lines give the values of the exponent s (Fig. 7).

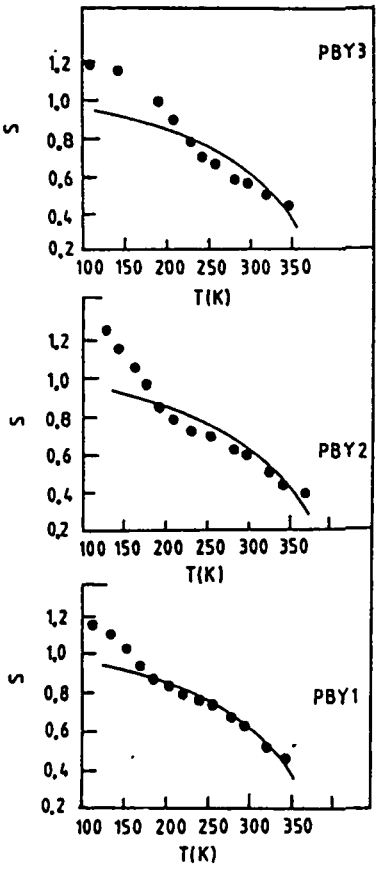

FIG. 7. Temperature dependence of the frequency exponent s with temperature indicating $s > 1$ below 200 K. Solid line, theoretical curve with the CBH model; closed circles, experimental points for the $Bi_{4-n}Pb_nSr_3Ca_3Cu_4O_x$ glasses with $n = 0.1$ (PBY-1), $n = 0.5$ (PBY-2), and $n = 1$ (PBY-3), respectively.

those of the Li- or Pb-doped Bi-Sr-Ca-Cu-O glasses.[24] From Fig. 5 one also finds that the ac conductivity increases with an increase of Pb concentration in the glasses. The corresponding frequency dependences of ac conductivity for different fixed temperatures, shown in Fig. 6 for a typical $Bi_{3.9}Pb_{0.1}Sr_3Ca_3Cu_4O_x$ glass, follows Eq. (2) quite well. Other PBY glasses behave similarly. The solid curves in Fig. 6 are the straight-line fitting obtained by the least-squares fitting method. The estimated frequency exponent s obtained from the slopes of Fig. 6 is shown in Fig. 7 as a function of temperature. In line with other TMO glasses,[1-6] the exponent decreases with an increase of temperature. No appreciable frequency dependence of s is observed for any of the present PBY glasses.[24] However, one of the most significant features of these glasses, unlike vanadate or many other TMO glasses (where $s \geq 1$ within the frequency range of our present investigation), is that the exponents s for all the PBY glasses become slightly greater than 1 below a certain temperature around 200 K (Fig. 7). This temperature depends on the Pb concentration in the glasses. This behavior of ac conductivity in the low-temperature region is common in the Li-doped and -undoped $Bi_4Sr_3Ca_3Cu_4O_y$ glasses.[23] There are also several examples of transition-metal oxide (for instance, $CuO\text{-}P_2O_5$ glass[10]) and chalcogenide glasses[35,36] showing $s > 1$ in the high-frequency ($\geq 10^6$ Hz) limit.

The thermal variations of electrical resistivities of some

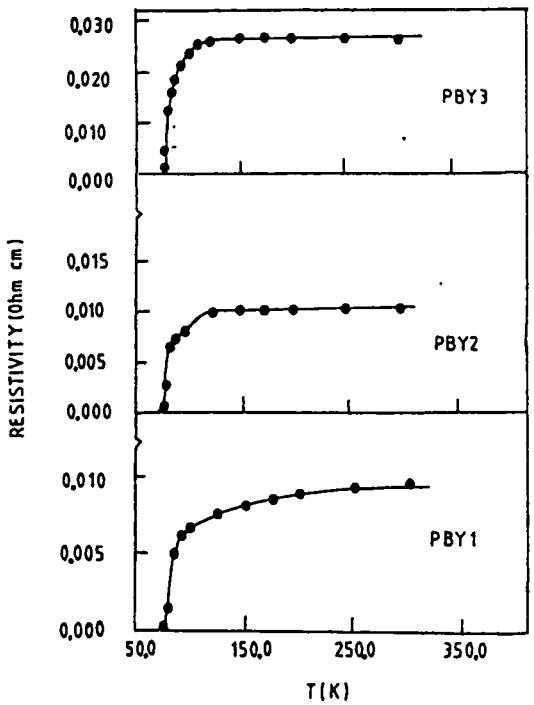

FIG. 8. Temperature dependence of resistivity of the PBY glass ceramics (annealed at 840 °C for 24 h and then slow furnace cooling to room temperature) showing the superconducting behavior of the glass ceramics. This figure also indicates that the glasses under investigation are good precursors for high-T_c superconductors. PBY-1, $Bi_{3.9}Pb_{0.1}Sr_3Ca_3Cu_4O_x$; PBY-2, $Bi_{3.5}Pb_{0.5}Sr_3Ca_3Cu_4O_x$; and PBY-3, $Bi_3Pb_1Sr_3Ca_3Cu_4O_x$.

of the glass ceramics (obtained by annealing them at 840 °C for a minimum time of 24 h) as shown in Fig. 8 indicate superconducting behavior. The superconducting transition temperature T_c and zero resistance temperature T_{c0} depend on the Pb concentration (Fig. 8 and Table I). These results indicate that the PBY glasses are good precursors for high-T_c superconductors. Measurements of the thermoelectric power of all the superconducting PBY glass-ceramic samples are found to be positive, indicating that these are hole-type superconductors.[37]

IV. THEORETICAL FITTING OF ac-CONDUCTIVITY DATA WITH DIFFERENT THEORETICAL MODELS

There are many theoretical models to fit the ac-conductivity data of semiconducting glasses. For convenience, we discuss below the models used by us to fit the experimental ac-conductivity data of the $Bi_{4-n}Pb_nSr_3Ca_3Cu_4O_y$ glasses.

Several authors[14,38–42] have developed, within the pair approximation, the ac conductivity for single-electron motion undergoing quantum-mechanical tunneling (QMT) and obtained the expression for $\sigma_{ac}(\omega)$ as

$$\sigma_{ac}(\omega)=Ce^2k_BT\alpha^{-1}[N(E_F)]^2\omega R_\omega^4 , \quad (3)$$

where C is the numerical constant taken as $\pi^4/24$ (cf. Refs. 35 and 39), $N(E_F)$ is the density of states at the Fermi level, α^{-1} is the special decay parameter for the localized wave function, k_B is Boltzmann's constant, T is the absolute temperature, e is the electronic charge, and R_ω is the hopping distance at frequency ω given by

$$R_\omega=(2\alpha)^{-1}\ln(1/\omega\tau_0) , \quad (4)$$

where τ_0 is the characteristic relaxation time. From the plot of $\sigma_{ac}(\omega)$ vs T (Fig. 9) for the Pb-doped glasses, it is found that $\sigma_{ac}(\omega)$ varies nonlinearly even in the low-temperature region. Moreover, the values of $\sigma_{ac}(\omega)$ show little tendency to increase in this temperature region (below 200 K), as shown in Fig. 9. This type of variation of $\sigma_{ac}(\omega)$ with temperature and frequency is inconsistent with that of the QMT model. At higher temperature, $\sigma_{ac}(\omega)$ starts to deviate more sharply from linearity (Fig. 9). Therefore, the QMT model fails to explain the temperature and frequency dependence of the ac conductivity of the PBY glasses. Even the frequency exponent s derived from this model, viz.,

$$s=1-4/\ln(1/\omega\tau_0) , \quad (5)$$

is temperature independent [Eq. (5)], which is in contrast to the experimental observation (Fig. 7) where s decreases with an increase of temperature.

Another model, called the overlapping large polaron tunneling (OLPT) model, was proposed by Long[38] where the large-polaron wells at two sites overlap, thereby reducing the polaron hopping energy.[14,43] This gives

$$W_h=W_{h0}(1-r_p/R), \quad (6)$$

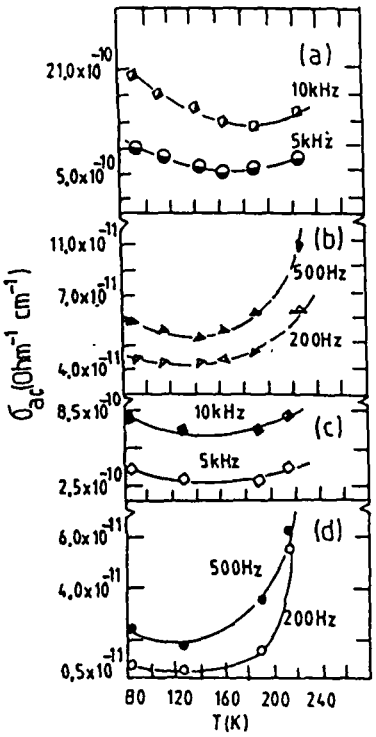

FIG. 9. Thermal variation of $\sigma_{ac}(\omega)$ showing nonlinear variation of σ_{ac} with temperature (the low-temperature region is drawn in extended scale) and a slight increase of σ_{ac} in the low-temperature region. The exponent s starts to increase at a temperature where σ_{ac} also starts to increase around 200 K. (a) and (b) $Bi_3Pb_1Sr_3Ca_3Cu_4O_x$ glass and (c) and (d) $Bi_{3.5}Pb_{0.5}Sr_3Ca_3Cu_4O_x$ glass. Solid lines are a guide for the eye.

where W_h is the polaron hopping energy, r_p is the polaron radius, R is the intersite separation, and $W_{h0}=e^2/4\varepsilon_p r_p$, where ε_p is the effective dielectric constant and R and r_p can be obtained from the fit of density and dc conductivity data,[24] respectively. Assuming R to be a random variable, the ac conductivity for this model has the form[38]

$$\sigma_{ac}(\omega)=[\pi^4/12]e^2(k_BT)^2[N(E_F)]^2 \times\omega R_\omega^4/(2\alpha k_BT+W_{h0}r_p/R_\omega^2) , \quad (7)$$

where $R'_\omega=2\alpha R_\omega$, $r'_p=2\alpha r_p$, and $\beta=1/k_BT$. Then the exponent s in the OLPT model can be evaluated from

$$(R'_\omega)^2+[\beta W_{h0}+\ln(\omega\tau_0)]R'_\omega-\beta W_{h0}r'_p=0 ,$$

where $R'_\omega=2\alpha R_\omega$, $r'_p=2\alpha r_p$, and $\beta=1/k_BT$. Then the exponent s in the OLPT model can be evaluated from

$$s=1-[4+6\beta W_{h0}r'_p/R'^2_\omega]/[R'_\omega(1+\beta W_{h0}r'_p/R'^2_\omega)^2] . \quad (8)$$

Equation (8) indicates that the frequency exponent s should be both temperature and frequency dependent. Furthermore, s is expected to decrease from unity with an increase of temperature. For large values of r'_p, s con-

tinues to decrease with an increase in temperature, eventually tending to the value of s predicted by the QMT model of nonpolaron forming carriers, whereas for small values of r_p', s exhibits a minimum[38] at a certain temperature and subsequently increases with temperature in a fashion similar to the case of the small-polaron QMT model.

However, the OLPT model also predicts the frequency dependence of s [cf. Eq. (8)]. A detailed analysis shows that in the low-temperature regions ($k_BT/W_h < 0.04$ –0.05), s should increase with frequency. In the samples of our present investigation any frequency dependence of s was not observed.

The other type of process, proposed for the relaxation mechanism, is the classical hopping over a barrier model (HOB), where the random variable is $\xi = W/k_BT$. For the case of atomic motion an expression is obtained[38,44] for ac conductivity, viz.,

$$\sigma_{ac}(\omega) = (\pi\eta/3)[(Np^2k_BT/W_0\Delta_0)\omega \tanh(\Delta_0/2k_BT)] , \tag{9}$$

where η is the mean-field correction term, N is the number of pair states per unit volume, p is the dipole moment associated with the transition, and it is assumed that every difference between sites Δ is randomly distributed in the range $0 < \Delta < \Delta_0$ and the barrier height is randomly distributed in the range $0 < W < W_0$. For the simple HOB model [cf. Eq. (9)], the frequency exponent of $\sigma_{ac}(\omega)$ is predicted to be unity and it is also independent of temperature and frequency. Even for the case of atomic tunneling, an expression similar to Eq. (9) is obtained[45] with $s = 1$, if the dipole moment is uncorrelated with the tunneling distance.[38] Therefore, the HOB model does not fit the present glass system.

Another pair-approximation-type model for ac conduction, which correlates the relaxation variables W with the intersite spacing R, was developed initially by Pike[46] for single-electron hopping and expanded by Elliott[47] for two-electron hopping simultaneously. For neighboring sites at a separation R, the Coulomb wells overlap, resulting in a lowering of the effective barriers from W_M to a value W, which for the case of two-electron transmissions is given by[10] $W = W_M - (2e^2/\pi\varepsilon_0\varepsilon R)$, where ε is the dielectric constant of the material and ε_0 that of the free space. The ac conductivity in this model, termed as correlated barrier hopping (CBH) model[38,43] in the narrow-band limit ($\Delta_0 \ll k_BT$) is expressed as

$$\sigma_{ac}(\omega) = \pi^3N^2\varepsilon\varepsilon_0\omega R_\omega^6/24 , \tag{10}$$

where N is the concentration of the pair sites. The hopping distance R_ω and the frequency exponent in this model are given by

$$R_\omega = 2e^2/\pi\varepsilon\varepsilon_0[W_M + k_BT\ln(\omega\tau_0)] , \tag{11}$$

and

$$1 - s = 6k_BT/[W_M + k_BT\ln(\omega\tau_0)] . \tag{12}$$

The CBH model therefore predicts a temperature dependence of s that reaches unity as $T \to 0$ K, in marked contrast to the QMT or simple HOB mechanism discussed above. So the CBH model appears to be applicable to the PBY glasses. The theoretical fitting of the temperature dependence of $\sigma_{ac}(\omega)$ with the CBH model [Eq. (10)] as shown in Fig. 10 for a typical $Bi_{3.9}Pb_{0.1}Sr_3Ca_3Cu_4O_x$ glass ensures that this model is the most appropriate one to explain the overall behavior of the ac conductivity of the PBY glasses. The best-fit parameters, viz., relaxation time (τ_0) and N, are shown in Table II. The relaxation frequency $\nu_0 = 1/\tau_0$ obtained from fitting the experimental data with this model are also consistent with those derived from the dc-conductivity data,[24] also shown in Table II for comparison. The values of N obtained from fitting Eq. (10) are also very close to those calculated from the density of the glasses (Table I). The values of W_M obtained from fitting the experimental values of s with Eq. (12) are close to twice the value of high-temperature activation energy for dc conduction.

In the low-temperature region (below 200 K), the theoretical fitting of the experimental values of s with the CBH model [Eq. (12)] is, however, poor (Fig. 7). This might be due to, e.g., inhomogeneity of the materials or the presence of more conducting regions or grains. The best-fitting parameters with the CBH model are also shown in Table II.

It is to be noted that in a slightly modified[34] CBH model the expression for s can be written as $s = 1 - 6k_BT/[W_M + k_BT\ln(\omega\tau_0)] + T/8T_g$. This indicates that, depending on the values of W_M and T_g, s might be greater than one. But in this situation both s and $\sigma_{ac}(\omega)$ should be an increasing function of temperature, which is not, however, supported by our experimental results. Elliott,[34] however, showed that a phononless photon-assisted electronic transition could lead to a superlinear frequency dependence of $\sigma_{ac}(\omega)$ with $s = 2 - 4/\ln(2I/\hbar\omega)$, where I is the overlap integral; this expression is also valid for very high frequency ($\hbar\omega \gg k_BT$), which is far beyond the frequency range of

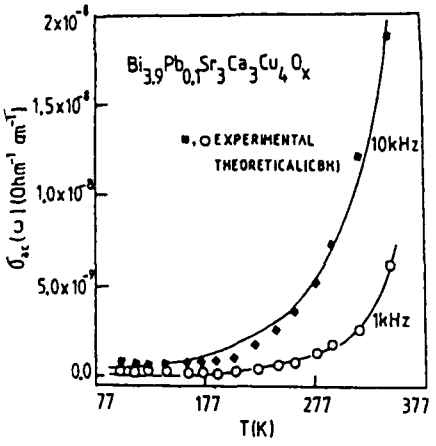

FIG. 10. Theoretical fitting (solid lines) of ac conductivity of a typical $Bi_{3.9}Pb_{0.1}Sr_3Ca_3Cu_4O_x$ (PBY1) glass with the CBH model [Eq. (10)]. The fitting parameters for the glasses are shown in Table III. Fitting is poor in the low-temperature region where conductivity shows little increase with a decrease of temperature.

TABLE II. Model parameters obtained by fitting the experimental ac-conductivity data of the $Bi_{4-n}Pb_nSr_3Ca_3Cu_4O_x$ glasses for $n=0$ (PBY-0), $n=0.1$ (PBY-1), $n=0.5$ (PBY-2), and $n=1.0$ (PBY-3) with the CBH model.

Parameters \ Samples	PBY-0		PBY-1		PBY-2		PBY-3	
Frequency (kHz)	10	1	10	1	10	1	10	1
W_M (eV)[a]	0.86	0.84	0.85	0.85	0.84	0.86	0.86	0.85
τ_0 (10^{-13} sec)[a]	1.21	2.11	1.71	1.29	1.75	1.36	3.63	4.23
N (10^{20} cm^{-3})[a]	1.84	1.11	2.71	2.65	2.43	0.44	3.88	3.53
W_M (eV)[b]	0.89	0.81	0.89	0.81	0.87	0.88	0.89	0.89
τ_0 (10^{-13} sec)[b]	1.00	2.45	1.00	1.82	1.10	1.65	3.20	3.10

[a]Obtained from the fitting of the σ_{ac} versus T curve (Fig. 10).
[b]Obtained from the fitting of the s versus T curve (Fig. 7).

our present investigation.

Other than the pair-approximation-type model discussed above, ac-conductivity data of the glassy semiconductor can also be fitted with other theoretical models, viz., the random-walk-type,[48] the extended pair-approximation-type,[49] and percolation theories.[50,51] Bryksin[48] showed that the entire frequency interval could be divided into four regions, each characterized by specific mechanism of the clusters in which hopping of the carrier takes place. Here dispersion of every level on the states is not taken into account. From Bryksin's model one also finds that $\mathrm{Re}[\sigma_{ac}(\omega)]-\sigma_{ac}(0)\sim\omega^s$, where s initially equals 2 and then sharply decreases. Such a behavior of s is not visualized for any of the Pb- (or Li-) doped Bi-Sr-Ca-Cu-O glasses of our present interest.

It is interesting to point out that the extended pair-approximation-type model used by Summerfield and Butcher[49] and the percolation theoretical models[50,51] can also be used to fit the present ac-conductivity data explaining most of the characteristic features of these glasses (particularly with $s \leq 1$), similar to the CBH model. However, in the frequency and temperature range of our investigation, the CBH model appears most appropriate to analyze the ac-conductivity data of the $Bi_{4-n}Pb_nSr_3Ca_3Cu_4O_x$-type glassy precursors for high-T_c superconductors. In this paper we therefore concentrate our attention mainly on the CBH model. This model has also been used earlier for the analysis of ac-conductivity data of similar Li-doped $Bi_4Sr_3Ca_3Cu_4O_x$ (Ref. 21) and many transition-metal-oxide glasses with success.

The values of s becoming larger than one appears to be a characteristic property of the glasses under investigation. A similar behavior of s (≥ 1 in the low-frequency range) observed in the semiconducting Cd-As-Si glassy system was confirmed[36] as a bulk property that did not depend on the contact potential or the thickness of these glassy samples.

We infer that the large value of s (>1) shown by the Pb-doped glasses of our present investigation is not due to contact resistance or other reasons, as suggested by Street, Donies, and Yoffe,[52] Cleach,[53] and Zvyagin.[50] We also measured (following the procedure used by Kocka and Kristofik[36]) conductivities of the same glassy samples with different thickness. The electrical conductivity and its exponents are found to be independent of the thickness of the samples. The measured conductivity is also found not to be influenced either by the gold contact layer or by the finite resistance of the leads. Thus the value of s becoming larger than unity is an inherent property of the present Pb-doped Bi-Sr-Ca-Cu-O glass, similar to amorphous Cd-As-Si-type semiconductors.[36] This seems to be a very interesting result because, except for amorphous Se (where $s=1.05$), s is less than unity in most other amorphous solids.

As mentioned in Sec. II, the presence of the clusters of different densities and conductivities is considered to be responsible for the low-temperature superlinear behavior of ac conductivities of the $Bi_{4-n}Pb_nSr_3Ca_3Cu_4O_x$ glasses. Sometimes such clusters were also found to be responsible for the metal-insulator transitions in some noncrystalline semiconductors.[54] Gilbert and Adkins[55] attempted to explain the superlinear behavior (with $s>1$) of ac conductivity of amorphous germanium films by considering the presence of more conducting regions in the glass. In the glassy precursors for high-T_c superconductors, in particular, such conducting regions are formed during glass formation by quenching the melt at room temperature. It is plausible that some of these clusters become more conductive in the low-temperature region, increasing the total ac conductivity of the bulk glass. The little increase of conductivity of the semiconducting PBY glasses in the low-temperature region (where the exponent s also starts to become more than one and ac conductivity indicates superlinear behavior), as shown in Fig. 9 (where low-temperature ac-conductivity data have been plotted in an extended scale), supports this conjecture. One may overlook this increase of σ_{ac} in the low-temperature region unless the data are very accurate.

Finally, it might be concluded that the properties of the Pb-doped glassy precursors for high-T_c superconductors depend largely on the microstructure of the glasses, unlike usual TMO glasses, which do not become glass-ceramic superconductors. More elaborate microstructural studies (e.g., formation of nanocrystals, phase separations, glass network structure) of these glasses for different annealing time and temperature would also be interesting.

ACKNOWLEDGMENTS

S.M. and B.K.C. are grateful to the Council of Scientific and Industrial Research and Department of Science and Technology for financial grants. The XRD, SEM, EDAX, IR, and DTA facilities provided by the Departments of Materials Science, Inorganic and Organic Chemistry are gratefully acknowledged. The authors are grateful to Professor J. Baram, Ben-Gurion University of the Negev, Israel, for his suggestion and comments on the paper.

*Present address: Department of Materials Engineering, Ben-Gurion University of the Negev, Beer Sheva 84105, Israel.

[1]N. F. Mott, J. Non-Cryst. Solids 1, 1 (1968).
[2]A. Mansingh, R. P. Tandon, and J. K. Valid, Phys. Rev. B 21, 429 (1980).
[3]L. Murawski, C. H. Chung, and J. D. MacKenzie, J. Non-Cryst. Solids 32, 91 (1979).
[4]A. P. Schmid, J. Appl. Phys. 39, 3140 (1968).
[5]M. Sayer and A. Mansingh, Phys. Rev. B 6, 4629 (1972).
[6]B. K. Chaudhuri, K. Chaudhuri, and K. K. Som, J. Phys. Chem. Solids 50, 1149 (1989).
[7]A. Duran, J. R. Jurado, and J. M. Fernandez Nararro, J. Non-Cryst. Solids 78, 333 (1986).
[8]A. Ghosh and D. Chakravorty, J. Phys. Condens. Matter 2, 931 (1990).
[9]C. F. Drake, I. F. Scanlan, and A. Engel, Phys. Status Solidi 32, 193 (1969).
[10]M. A. Hassan, C. A. Hogarth, and G. R. Moridi, Phys. Status Solidi A 101, 537 (1987).
[11]H. Hirashima, Y. Watanabe, and T. Yoshida, J. Non-Cryst. Solids 95&96, 825 (1987).
[12]H. Gahlman and R. Bruckner, J. Non-Cryst. Solids 13, 355 (1974).
[13]S. Nakamura and N. Ichinose, J. Non-Cryst. Solids 95&96, 849 (1987).
[14]I. G. Austin and N. F. Mott, Adv. Phys. 18, 41 (1969).
[15]L. Murawski, Philos. Mag. B 50, L69 (1984).
[16]A. Mansingh, J. K. Valid, and R. P. Tandon, J. Phys. C 8, 1023 (1875).
[17]H. K. Rokadat, Solid State Commun. 7, 1507 (1969); J. T. Polano and G. G. Roberts, Philos. Mag. 25, 117 (1972).
[18]H. Segawa, J. Phys. Soc. Jpn. 36, 1087 (1974).
[19]H. Zheng and J. D. Mackenzie, Phys. Rev. B 38, 7166 (1988); K. B. R. Varma, K. J. Rao, and C. N. R. Rao, Appl. Phys. Lett. 54, 69 (1989); M. Tatsumisago and C. A. Angels, *ibid.* 55, 600 (1989); 55, 2268 (1989).
[20]T. Komatsu, K. Imai, K. Matsusita, M. Takata, Y. Iwai, A. Kowakami, Y. Kaneko, and T. Yamashita, Jpn. J. Appl. Phys. 26, L1148 (1987).
[21]S. Mollah, K. K. Som, K. Bose, A. K. Chakraborty, and B. K. Chaudhuri, Phys. Rev. B 46, 11 075 (1992).
[22]K. K. Som and B. K. Chaudhuri, Phys. Rev. B 41, 1581 (1990).
[23]S. Mollah, K. K. Som, K. Bose, and B. K. Chaudhuri, J. Appl. Phys. 74, 931 (1993); S. Mollah, A. K. Chakraborty, S. Chakraborty, K. K. Som, and B. K. Chaudhuri, J. Non-Cryst. Solids 165, 192 (1994).
[24]S. Mollah, Ph.D thesis, Jadavpur University, Calcutta, 1993 (unpublished).
[25]R. C. Beaker, W. M. Hurng, and H. Steinfink, Appl. Phys. Lett. 54, 371 (1989).
[26]D. Emin, Phys. Rev. Lett. 72, 1052 (1994), and (unpublished).
[27]D. Mihailovic, C. M. Foster, K. Voss, and A. Heeger, Phys. Rev. B 42, 7889 (1990).
[28]P. Lunkenheimer, M. Resch, A. Loidi, and Y. Hihaka, Phys Rev. Lett. 69, 498 (1992).
[29]M. Tatsumisago, S. Tsuboi, N. Tohge, and T. Minami, J. Non-Cryst. Solids 124, 167 (1990).
[30]A. Aruchamy, S. J. Kim, D. P. Birnic, and D. R. Uhlmann, J. Non-Cryst. Solids 160, 60 (1993); N. P. Bansal, J. Appl. Phys. 68, 1143 (1990).
[31]K. K. Som and B. K. Chaudhuri, Ind. J. Phys. 66A, 37 (1992).
[32]S. Mollah, S. Chatterjee, S. Chakraborty, and B. K. Chaudhuri, Philos. Mag. (to be published).
[33]N. F. Mott and E. A. Davis, *Electronic Processes in Non-Crystalline Materials*, 2nd ed. (Clarendon, Oxford, 1979), p. 225.
[34]S. R. Elliott, Adv. Phys. 36, 135 (1987).
[35]M. Kitao, M. Senda, Y. Tanao, and S. Yamada, J. Non-Cryst. Solids 127, 36 (1991); K. Hirata, M. Kitao, and S. Yamada, J. Phys. Soc. Jpn. 52, 1317 (1983).
[36]J. Kocka and J. Kristofik, Phys. Status Solidi A 45, 559 (1978).
[37]S. Chatterjee, S. Banerjee, and B. K. Chaudhuri (unpublished).
[38]A. R. Long, Adv. Phys. 31, 553 (1982).
[39]M. Pollak, Philos. Mag. 23, 519 (1971).
[40]H. Böttger and V. V. Bryksin, Phys. Status Solidi B 78, 415 (1976).
[41]P. N. Butcher and K. J. Hayhden, in *Proceedings of the Seventh International Conference on Amorphous and Liquid Semiconductors*, edited by W. E. Spear (CICL, Edinburgh, 1977), p. 234.
[42]A. L. Efros, Philos. Mag. B 43, 829 (1981).
[43]M. Pollak, Phys. Rev. 138, 1822 (1965).
[44]M. Pollak and G. E. Pike, Phys. Rev. Lett. 28, 1449 (1972).
[45]G. Frossati, R. Maynard, R. Rummal, and D. Thoulouse, J. Phys. (Paris) Lett. 38, L15 (1977).
[46]G. E. Pike, Phys. Rev. B 6, 1572 (1972).
[47]S. R. Elliott, Philos. Mag. B 36, 1291 (1977).
[48]V. V. Bryksin, Fiz. Tverd. Tela (Leningrad) 22, 2441 (1980) [Sov. Phys. Solid State 22, 1421 (1980)].
[49]S. Summerfield and P. N. Butcher, J. Phys. C 15, 7003 (1982); 16, 295 (1983).
[50]I. P. Zvyagin, Phys. Status Solidi B 97, 143 (1980).
[51]H. Böttger, V. V. Bryksin, and G. Yu Yashin, J. Phys. C 12, 2797 (1979); 12, 3951 (1979).
[52]R. A. Street, G. Davies, and A. D. Yoffe, J. Non-Cryst. Solids 5, 276 (1971).
[53]X. Le Cleach, Solid State Commun. 21, 309 (1977).
[54]M. Mostafa and G. Olivier, Solid State Commun. 70, 489 (1989).
[55]M. H. Gilbert and C. J. Adkins, Philos. Mag. 34, 143 (1976).

PHILOSOPHICAL MAGAZINE B, 1995, VOL. 71, NO. 2, 151–162

Dielectric properties of semiconducting $Bi_{4-n}Pb_nSr_3Ca_3Cu_4O_x$ ($0 \leqslant n \leqslant 1$) glasses: precursors for high-T_c superconductors

By S. MOLLAH†, S. CHATTERJEE, S. CHAKRABORTY and B. K. CHAUDHURI

Solid State Physics Department, Indian Association for the Cultivation of Science, Calcutta-700 032, India

[*Received 24 December 1993‡ and accepted 21 June 1994*]

ABSTRACT

The dielectric constant (ε') and loss (ε'') for Pb-doped $Bi_{4-n}Pb_nSr_3Ca_3Cu_4O_x$ ($n = 0{\cdot}0$, $0{\cdot}1$, $0{\cdot}5$ and $1{\cdot}0$) glasses, which become high-T_c superconducting oxides in their glass-ceramic phases, have been measured at different temperatures (80–450 K) and frequencies (200–10 000 Hz) ranges. Though the temperature variations of ε' and ε'' of these Pb-doped glasses do not show any peak within the frequency range of our investigation, the imaginary parts (M'') of the dielectric modulus (M^*) show peaks that indicate Debye-type dielectric relaxation behaviour with a distribution of relaxation times, as suggested by the behaviour of the Cole–Cole plots. This property of ε' and ε'' is found to be common to all the multicomponent Bi–Sr–Ca–Cu–O type glasses, which become high-T_c superconductors in their corresponding crystalline phases. The relaxation behaviour is thermally activated in nature. These glasses are also very suitable for drawing wires which become superconductors in their glass-ceramic phases.

§ 1. INTRODUCTION

Transition-metal oxide (TMO) glasses, such as $Bi_4Sr_3Ca_3Cu_4O_x$ (hereafter denoted by [4:3:3:4]), have been found (Baker, Hurng and Steinfink 1989, Moriuchi, Kawai, Mitsui and Kawai 1990, Som and Chaudhuri 1990, Zheng, Colby and MacKenzie 1991, Mollah, Som, Bose, Chakraborty and Chaudhuri 1992, Som, Mollah, Bose and Chaudhuri 1992) to show superconducting properties in their glass-ceramic (GC) or crystalline phases. The [4:3:3:4] glass in particular has been much investigated because it is a precursor glass for a single-phase $Bi_2Sr_2CaCu_2O_8$ superconductor (Baker *et al.* 1989). Other alkali-metal-doped Bi–Sr–Ca–Cu–O glasses, with lower softening points and a higher superconducting transition temperature T_c in their GC phases, have also been studied (Moriuchi *et al.* 1990, Mollah *et al.* 1992). Like Li-doped glasses, Pb-doped glasses are also very interesting because of their superconducting behaviour in the ceramic phases which are obtained by properly annealing the glasses at higher temperatures (around 850°C). Furthermore, these glasses can easily be drawn into wires from their melts. Since the composition of these glasses can be varied, it is possible to find appropriate compositions to make wires/tapes from the corresponding glass phases. These wires/tapes can also be made superconducting by properly annealing them at higher temperatures (below the melting point). Therefore, it is of interest to study dielectric and other properties of these glassy precursors for high-T_c superconductors and to compare their properties with those of other TMO glasses (Mott and Davis 1979)

† Present address: Materials Engineering Department, Ben-Gurion University, Israel.
‡ Received in final form 9 June 1994.

0141–8637/95 $10·00

which are not precursors for superconductors. Detailed electrical properties (a.c. and d.c. conductivities) of similar glasses doped with Li, such as $Bi_4Sr_3Ca_{3-z}Li_zCu_4O_x$ ($z = 0{\cdot}0, 0{\cdot}1, 0{\cdot}5, 1{\cdot}0$) glasses, have recently been studied by Mollah *et al.* (1992) and Mollah, Som, Bose and Chaudhuri (1993), and it has been shown that all these glasses are semiconductors in their glassy phases with a d.c. conductivity that decreases with increase of Li conduction. On the contrary, the d.c. conductivity of the Pb-doped [4:3:3:4] glasses increases with the increase of Pb concentration (Mollah 1993), a behaviour that is considered to arise from the contribution of holes.

In the present paper we report some interesting dielectric properties of the Pb-doped $Bi_{4-n}Sr_3Ca_3Pb_nCu_4O_x$ glasses (hereafter referred to as PBY0, PBY1, PBY2 and PBY3 glasses, respectively, for $n = 0{\cdot}0$, $0{\cdot}1$, $0{\cdot}5$ and $1{\cdot}0$). It has been shown that the temperature- and frequency-dependent dielectric properties of these glasses show features not generally observed in many TMO glasses such as V_2O_5–Bi_2O_3, Fe_2O_3–Bi_2O_3, V_2O_5–P_2O_5 (Sayer, Mansingh, Reyes and Rosenblatt 1971, Mansingh, Vaid and Tandon 1975, Mansingh, Dhawan and Sayer 1983, Chaudhuri, Chaudhuri and Som 1989) which are, however, non-superconductors in their GC phases.

§ 2. Experimental

Glasses have been prepared with the starting oxide materials PbO, Bi_2O_3, CuO, $SrCO_3$ and $CaCO_3$ (each of purity 99·9% or better) by the technique reported earlier (Mollah *et al.* 1992, Som *et al.* 1992). Since the copper content of these glasses changes with melt temperature, as well as with the duration of melting (Som 1990), each was kept in their liquid state at 1100°C for 2 h (following a preheating of the oxide mixture at 500°C for 5 h and regrinding), after which the liquid was quickly quenched between two copper blocks kept at room temperature. Here we should mention that the preheating is necessary for making glassy precursors for high-T_c superconductors. The calculated copper contents of the glasses, as shown in the table, compare well with those obtained from chemical analysis and are similar to those reported in earlier work (Som *et al.* 1992). The amorphous character of all the samples was confirmed by X-ray diffraction (using a Philips X-ray generator model PW 1130 coupled with a diffractometer model PW 1710) and scanning electron microscopy with a Hitachi model 415A (Mollah 1993). X-ray diffraction patterns of some of the Pb-doped glasses are shown in fig. 1.

The density of the glasses was measured by the Archimedes' principle using carbon tetrachloride as the immersion liquid. The mean of five independent measurements for each sample was taken as the value of density. Thermogravimetric analysis (TGA) of the glass samples was made with a Shimadzu DT-30 thermal analyser. The glass transition temperature T_g of the samples was determined from differential scanning calorimetric (DSC) studies using a Perkin–Elmer DSC-7. The temperature- and frequency-dependent dielectric constant ε' was measured by a capacitance bridge (GR model 1615A) along with the frequency-dependent total conductivity in a low-temperature cryostat using an arrangement similar to that in our earlier work (Mollah *et al.* 1993, Som, Mollah, Bose and Chaudhuri 1993). The imaginary part of the dielectric constant ε'' was calculated from the experimental a.c. conductivity data as discussed below. To show that these Pb-doped glasses are good precursors for high-T_c superconductors, they are annealed at 840°C for 24 h in air and then slowly furnace-cooled. The resistivity of the furnace-cooled samples (glass-ceramics) thus obtained was measured by a standard four-probe technique using an APD cryocooler with Helium Compressor [HC-2D] attached to a temperature controller.

Some important parameters for the $Bi_{4-n}Pb_nSr_3Ca_3Cu_4O_x$ (PBY) glasses ($z = 0{\cdot}0$, $0{\cdot}1$, $0{\cdot}5$ and $1{\cdot}0$).

	Sample			
	PBY0	PBY1	PBY2	PBY3
Values of n	0	0·1	0·5	1·0
Cu content (wt%)	14·69 ± 0·02	14·70 ± 0·02	14·74 ± 0·02	14·78 ± 0·02
Density (g/cm^3)	5·82 ± 0·05	7·00 ± 0·05	6·90 ± 0·05	6·76 ± 0·05
T_g (°C)†	426 ± 5	415 ± 5	408 ± 5	402 ± 5
T_{c0} (K)‡	70·0 ± 1·0	72·0 ± 1·0	73·5 ± 1·0	78·5 ± 1·0
θ_D (K)§	428 ± 5	420 ± 5	412 ± 5	408 ± 5
ν_r (Hz)¶	$9{\cdot}80 \times 10^{12}$	$8{\cdot}75 \times 10^{12}$	$8{\cdot}58 \times 10^{12}$	$8{\cdot}50 \times 10^{12}$
W_r (eV)	0·544 ± 0·01	0·512 ± 0·01	0·580 ± 0·01	0·443 ± 0·01

† Obtained from DSC studies. Since T_g depends on various factors like thermal history, annealing rate, etc., we studied the DSC of the as quenched glass samples with a heating rate of 10°C/min for all samples.

‡ Obtained from the resistivity measurements of the respective glass-ceramic phases which were obtained by annealing the glasses at 840°C for 24 h in air. Further increment of T_{c0} is possible with the improvement of annealing conditions (time, temperature, oxygen pressure, etc.).

§ Calculated from the $\log_{10}(\sigma_{d.c.})$ versus $10^3/T$ plots.

¶ Obtained from the d.c. conductivity versus $10^3/T$ data of the glasses.

Fig. 1

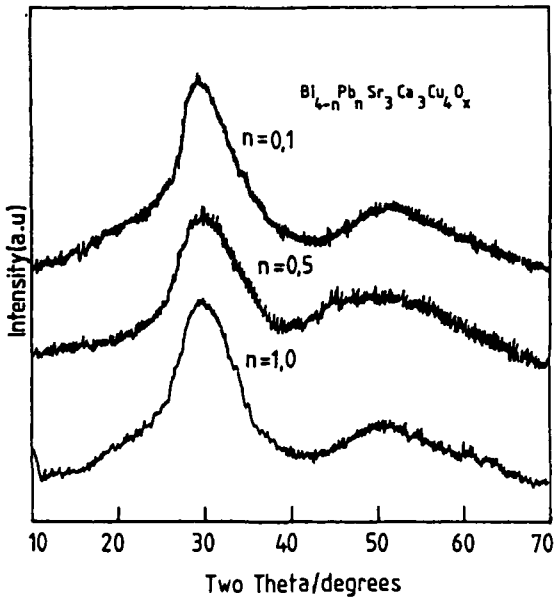

X-ray diffraction pattern of some Pb-doped glasses, indicating amorphous character of the glasses.

§ 3. Experimental results

The total copper concentrations of the glasses obtained by chemical analysis do not vary appreciably, as shown in the table. The theoretical values of the oxygen content x in the $Bi_{4-n}Sr_3Ca_3Pb_nCu_4O_x$ (hereafter referred to as PBY) samples are 16·00, 15·95, 15·75 and 15·50 for $n = 0{\cdot}0$, 0·1, 0·5 and 1·0, respectively. With increase of Pb (or decrease of Bi) in the PBY glasses, the values of x, as observed from thermogravimetric analysis, change slightly ($\pm$ 5% from the corresponding theoretical values (Som 1990, Mollah 1993). The densities of the Pb-doped glasses are larger than the undoped [4:3:3:4] glass (see the table). It is interesting to mention here that the density of the Li-doped $Bi_4Sr_3Ca_{3-z}Li_zCu_4O_x$ ($z = 0{\cdot}1$) glass is slightly lower than that of the undoped [4:3:3:4] glass (Mollah, Chakraborty, Chakraborty, Som and Chaudhuri 1994). Some other important parameters of the glasses are shown in the table. It is worth mentioning that these glasses are highly viscous and wires and tapes can easily be drawn from their respective melts. Some wires drawn by pulling the melt of such glasses are shown in fig. 2. These wires can be made superconducting by annealing them around 800–850°C for 24–48 h in air. The thermal variation of electrical resistivity ρ of a typical Pb-doped PBY3 ceramic (with $z = 1{\cdot}0$) obtained by annealing at 840°C for 24 h is shown in fig. 3, indicating superconducting behaviour. Similar ρ versus T curves are also obtained for the other Pb-doped glasses. The superconducting transition temperatures T_{c0} (zero resistance) for all the glass-ceramics are given in the table for the sake of completeness.

3.1. *Temperature and frequency variations of* ε'

The variations with temperature of the dielectric constants ε' and ε'' of the PBY3 glass samples at different measuring frequencies are shown in figs 4 (*a*) and (*b*), respectively. As shown, no peak in the ε' (or ε'') versus T plot is observed and this is also the case for all the glasses studied. The solid lines in fig. 4 and in other figures discussed below are guides for the eyes. The values of ε' varies slowly with temperature up to a certain temperature T_θ (say) which differs for different compositions. Here T_θ is the temperature where the value of ε' starts to increase abruptly with increase of temperature and lies between 250 and 300 K. T_θ is found to be almost equal to half the Debye temperature θ_D of the respective glasses. The values of θ_D as shown in the table were calculated from the d.c. conductivity $\sigma_{d.c.}$ data (from the temperature where the linearity of $\log(\sigma_{d.c.})$ versus $10^3/T$ plots breaks down (Schnakenberg 1968). Above T_θ the values of ε' for all the glasses increase rapidly with increase of temperature. This increase is sharper for lower measuring frequencies. The variation of ε' with frequency for all the PBY glasses at a fixed temperature of 333 K (shown in fig. 5 (*a*)) indicates that, at this fixed temperature, the values of ε' are not linear with the concentration of Pb in the glasses. The frequency dependence of one of the glass samples (with $n = 1{\cdot}0$) at different fixed temperatures, as shown in fig. 5 (*b*), indicates that the values of ε' decrease with the increase of frequency. This decrease of ε' is sharper at higher temperatures. Figure 5 (*b*) also shows that the values of ε' are lower for lower temperatures. All the other samples with different Pb concentrations behave in the same manner. This type of behaviour is similar to those of many other TMO glasses (Chaudhuri *et al.* 1989, Sayer *et al.* 1971, Mansingh *et al.* 1983) which, however, do not become superconductors in their crystalline phases. Unlike these TMO glasses, the present PBY glasses as well as the undoped $Bi_4Sr_3Ca_3Cu_yO_x$ ($y = 0$–5) glasses (Som *et al* 1993, Mollah *et al.* 1994) all become superconductors (in their crystalline phases)

Fig. 2

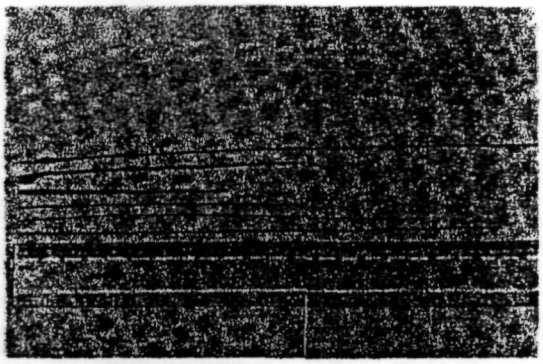

Typical Pb-doped ($Bi_{3.5}Pb_{0.5}Sr_3Ca_3Cu_4O_x$) glass wires drawn from the melt. Similar wires can also be made from the other Pb-doped glasses.

Fig. 3

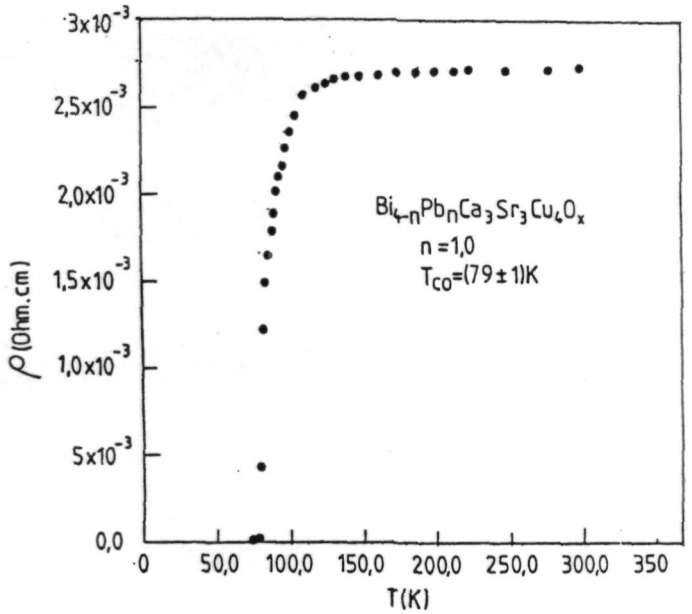

Thermal variation of the resistivity of a typical glass-ceramic obtained by annealing $Bi_3Pb_1Sr_3Ca_3Cu_4O_x$ glass at 840°C for 24 h in air. Other Pb-doped glasses, annealed similarly, also become superconductors. The corresponding T_{c0} (zero resistance) values are shown in the table.

Fig. 4

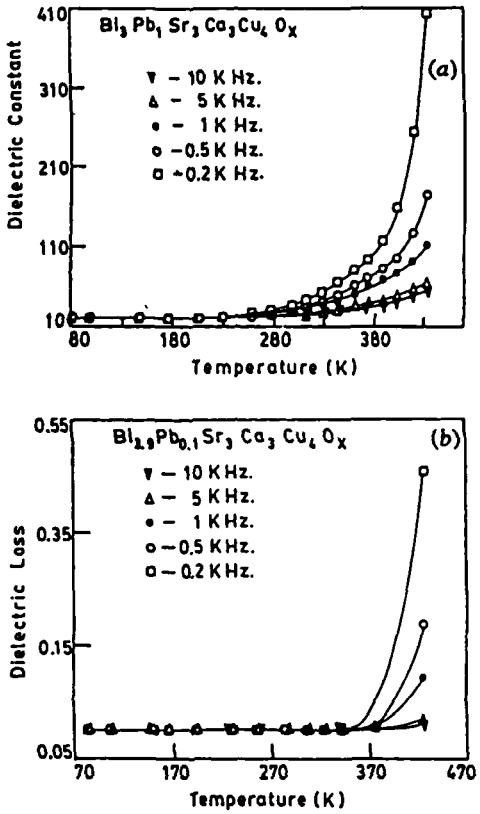

(*a*) Thermal variation of the dielectric constant ε' of $Bi_3Pb_1Sr_3Ca_3Cu_4O_x$ glass. (*b*) Thermal variation ε'' for $Bi_{2.9}Pb_{0.1}Sr_3Ca_3Cu_4O_x$ glass at different measuring frequencies, showing no peak within the temperature and frequency ranges of our investigation.

and do not show any peak within the temperature and frequency ranges of our investigations.

3.2. *Temperature and frequency variation of* ε''

The dielectric loss ε'' has been calculated from the relation $\varepsilon''(\omega) = \sigma_{a.c.}(\omega)/\varepsilon_0\omega$ (where $\sigma_{a.c.}(\omega)$ is the real part of the a.c. conductivity and ε_0 is the permittivity of free space). Figure 4 (*b*) shows that the values of ε'' are more or less temperature-independent up to a certain temperature T_θ (mentioned earlier) above which they start to rise rapidly. This temperature T_θ is higher for higher frequencies. It is interesting to note that both ε' and ε'' of the Pb-doped glasses do not show any peak when plotted as a function of temperature (figs 4 (*a*) and (*b*)). This behaviour of ε'' for the PBY glasses is also different from that of many other semiconducting TMO glasses mentioned above. However, ε'' for the [4:3:3:4] glass showed a peak around 360 K (Mollah *et al.* 1994). This behaviour distinguishes the undoped [4:3:3:4] glass from the corresponding Pb-doped glasses. It was also shown earlier (Som *et al.* 1993) that $Bi_4Sr_3Ca_3Cu_yO_x$ glasses with more than 35 mol% of CuO do not show peaks in the temperature variation of the dielectric loss. The Bi–Sr–Ca–Cu–O glasses with higher concentrations of CuO (more than 35 mol% CuO) and the present Pb-doped glasses, as well as Li-doped glasses,

Fig. 5

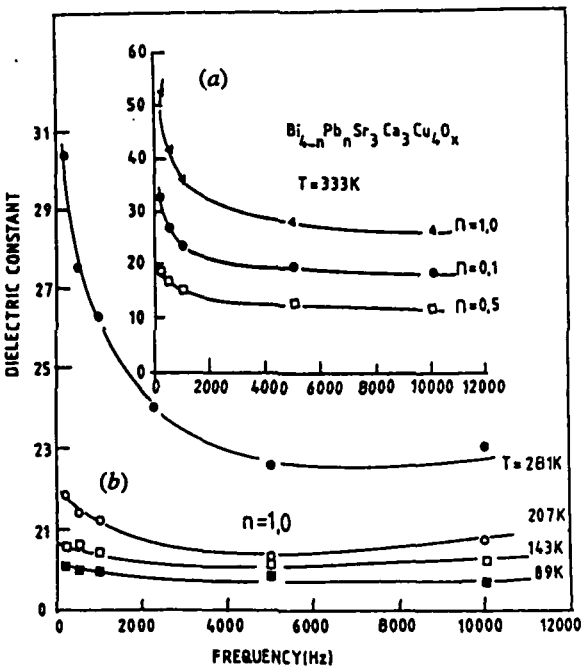

(*a*) Frequency dependence of ε' at a fixed temperature of 333 K for different $Bi_{4-n}Pb_nSr_3Ca_3Cu_4O_x$ glasses with $n = 0{\cdot}1$, $0{\cdot}5$ and $1{\cdot}0$. (*b*) Frequency dependence of ε' for a typical Pb-doped glass (with $n = 1{\cdot}0$) at different fixed temperatures.

indicate similar behaviour of ($\varepsilon' - T$) and ($\varepsilon'' - T$) plots without showing any peak. Both Li-doped and Pb-doped Bi–Sr–Ca–Cu–O glasses show similar variations of ε' and ε'' with temperature and frequency. However, the d.c. conductivity of the Pb-doped glasses is higher than those of the Li-doped glasses (Mollah *et al.* 1993).

The frequency variations of ε'' at a fixed temperature of 333 K (say) for different Pb-doped glass samples are shown in fig. 6 (*a*). The similar plot of fig. 6 (*b*) is drawn for a fixed concentration ($n = 1{\cdot}0$) and for different fixed temperatures. None of the curves in figs 6 (*a*) and (*b*) exhibits a peak.

§ 4. Discussion

Since no peak is observed in the temperature variations of ε' or ε'' for different fixed frequencies, it is difficult to understand the behaviour of relaxation times in these glasses. However, it appears from the study of dielectric modulus M^*, discussed below, that these glasses follow Debye-type dielectric relaxation process with relaxation frequency f_c ($= \frac{1}{2}\pi\tau$, τ being the relaxation time).

The dielectric loss peak is expected to be observed around the temperature where the d.c. conductivity approaches the total frequency-dependent conductivity in the higher temperature region (Sayer *et al.* 1971). Erroneous results are often produced (Mansingh 1980) by subtracting the two nearly equal quantities (total conductivity and d.c. conductivity) to obtain the value of the dielectric loss, ε'' ($= (\sigma_{tot}(\omega) - \sigma_{d.c.})/\omega\varepsilon_0$, where $\sigma_{tot}(\omega)$ is the total measured frequency-dependent conductivity and $\sigma_{d.c.}$ is d.c. conductivity) in this higher temperature region. For this reason a well-defined

Fig. 6

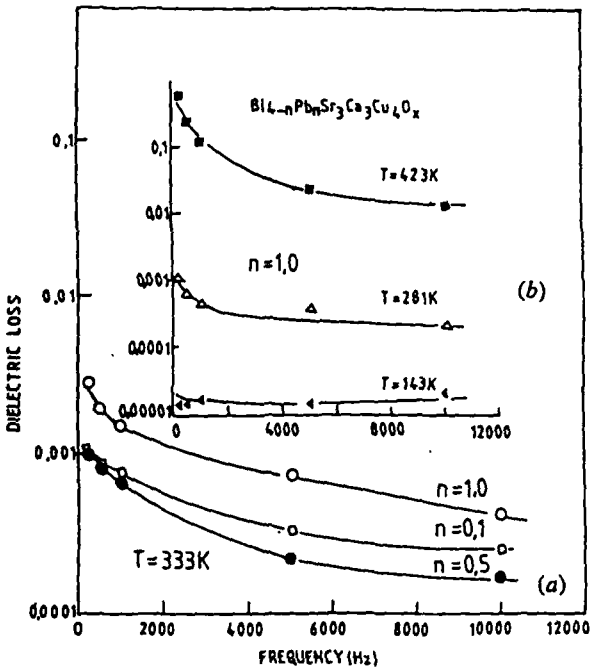

(*a*) Frequency variations of ε'' at a fixed temperature (333 K) for different $Bi_{4-n}Pb_nSr_3Ca_3Cu_4O_x$ glasses. (*b*) Frequency variations of ε'' for a typical Pb-doped glass (with $n = 1{\cdot}0$) at different fixed temperatures.

peak in the plot of ε'' versus temperature may not be observed in some cases, as, for example, in the present PBY-type glasses. It is thus not possible to use conventional methods of estimating the relaxation frequency and determining the nature of the dispersion. Another approach using the dielectric modulus has therefore been adopted.

The dielectric modulus is calculated (Macedo, Moynihan and Bose 1972) from $M^* = M' + iM'' = 1/\varepsilon^*$. The real and imaginary parts of the dielectric modulus are related to the real (ε') and imaginary (ε'') parts of the dielectric constant ε^* by $M' = \varepsilon'/[(\varepsilon')^2 + (\varepsilon'')^2]$ and $M'' = \varepsilon''/[(\varepsilon')^2 + (\varepsilon'')^2]$. The dielectric modulus M^* provides important information particularly when the contribution of d.c. conductivity is large. A plot of M'' versus temperature should give a peak at the temperature where the dielectric relaxation frequency is equal to the measuring frequency. For a typical PBY glass (with $n = 0{\cdot}5$), we have plotted M' as a function of temperature for different fixed frequencies (fig. 7 (*a*)). Similar behaviour is also observed for other compositions of the PBY glasses. It is observed that at a low temperature M' tends to a constant value for all frequencies. This behaviour indicates the thermally activated nature of the carriers. To demonstrate the dielectric dispersion, the imaginary part M'' has also been calculated and is plotted as a function of temperature (fig. 7 (*b*)) at different fixed frequencies. Figure 7 (*b*) shows peaks which shift to the higher-temperature side for higher frequencies. A similar nature of the temperature and frequency variation of M'' is also observed for other compositions. The peak position in the variation of M'' as a function of temperature (fig. 7 (*b*)) gives the temperature at which the measuring frequency is equal to the relaxation frequency $f_c = \nu_r \exp(-W_r/k_BT)$, where ν_r is the

Fig. 7

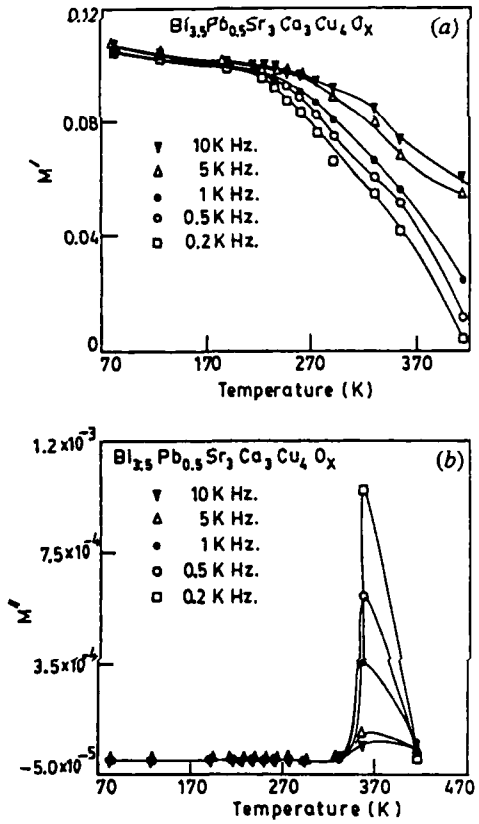

Thermal variation of (*a*) M', and (*b*) M'' of the $Bi_{3.5}Pb_{0.5}Sr_3Ca_3Cu_4O_x$ glass with $z = 0.1$ for different frequencies.

Fig. 8

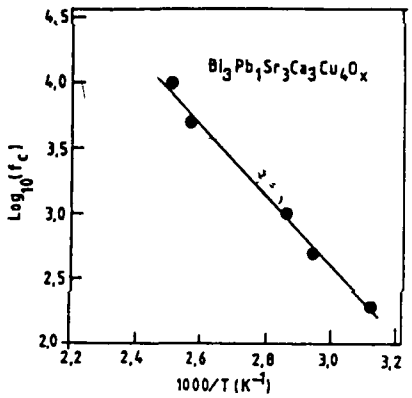

Variation of f_c with inverse temperature for different glasses with $n = 1.0$.

Fig. 9

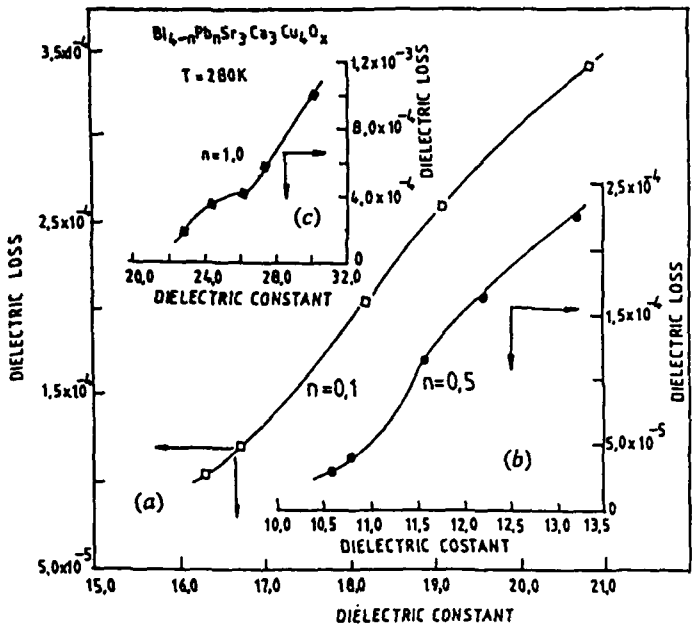

Cole–Cole plots for different PBY glasses with (*a*) $n = 0{\cdot}1$, (*b*) 0·5, and (*c*) 1·0, at a fixed temperature of 280 K.

Fig. 10

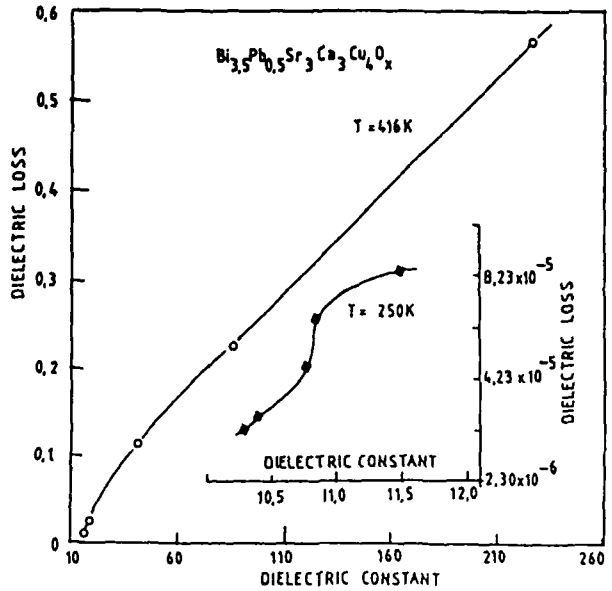

Cole–Cole plots for a typical PBY glass (with $n = 0{\cdot}5$) at different fixed temperatures.

characteristic phonon frequency calculated from the d.c. conductivity data (Mollah 1993) and W_r is the activation energy for conductivity relaxation. The values of ν_r and W_r obtained from the plots of $\log f_c$ versus $10^3/T$ (fig. 8) are very close to those obtained from the d.c. conductivity data (Mollah 1993) of the corresponding glasses (see the table). The nature of this plot (fig. 8) is very similar to the variation with inverse temperature of the d.c. conductivity (Mollah 1993) of the PBY glasses, which suggests that the relaxation mechanism is thermally activated in nature similar to the d.c. conductivity. It is interesting to note that, like the PBY glasses, all the Li-doped and undoped $Bi_4Sr_3Ca_3Cu_yO_x$ ($y = 0$–5) glasses also showed peaks (Som *et al.* 1993, Mollah *et al.* 1994) in the (M'' – T) plots, indicating Debye-type relaxation behaviour.

A plot of ε'' versus ε' (Cole and Cole 1941) gives important information about the distribution of relaxation time. The slope of the arc at $\varepsilon'' = 0$ is a measure of the extent of the distribution of relaxation times. According to Cole and Cole (1941), the complex dielectric constant ε^* is given by $\varepsilon^* = \varepsilon_\infty + (\varepsilon_s - \varepsilon_\infty)/[1 + (i\omega\tau_m)^{1-\beta}]$, where τ_m is the mean relaxation time, ε_s and ε_∞ are the static and high-frequency dielectric constants, respectively, and β is an empirical parameter lying between 0 and 1. For $\beta = 0$, one has a single relaxation time, and $\beta = 1$ corresponds to an infinite distribution of relaxation times. To check this, we have plotted ε'' versus ε' at a fixed temperature ($T = 280$ K) and at different frequencies for samples of all the PBY glasses as shown in fig. 9. The corresponding plots obtained for different temperatures for a typical PBY glass ($n = 0{\cdot}5$) is shown in fig. 10. The slopes of the plots (figs 9 and 10) give the value of $\bar{\beta} = (1 - \beta)\pi/2$. The values of β obtained from the slopes of figs 9 and 10 are found to be greater than zero, indicating a distribution of relaxation times for these glasses. However, the semicircular nature of the curves as suggested by Cole and Cole (1941) is not found for the PBY-type glasses that become high-T_c superconductors in their crystalline phases. Similar behaviour is also exhibited by all the Li-doped [4:3:3:4] glasses studied earlier (Mollah *et al.* 1994). The large value of high-frequency capacitance or d.c. conductivity of the glasses may be responsible for such a behaviour (Grant 1957).

§ 5. Summary and Conclusions

We have measured the temperature- and frequency-dependent dielectric behaviour of the Pb-doped $Bi_{4-n}Sr_3Ca_3Pb_nCu_4O_x$ ($n = 0{\cdot}1$, $0{\cdot}5$ and $1{\cdot}0$) glasses. None of these Pb-doped or other similar glasses, such as Li-doped Bi–Sr–Ca–Cu–O (Mollah *et al.* 1994), show any peak in the temperature (80–450 K) or frequency (200–10 000 Hz) ranges of our investigations. Furthermore, all the Pb-containing glasses exhibit Debye-type dielectric relaxation behaviour with a distribution of relaxation times. The relaxation process is predominantly thermally activated similar to the d.c. conductivities of these glasses. Finally, it is concluded that all the glass samples are good precursors for high-T_c superconductors and would be very suitable for drawing glass wires/tapes which could be made superconducting by properly annealing them between 800 and 850°C (as shown in fig. 2 for a typical glass sample).

Acknowledgments

Dr S. Mollah is grateful to the Council of Scientific and Industrial Research (CSIR), Government of India, for providing a research fellowship. Partial support from the Department of Science and Technology (DST) is also gratefully acknowledged.

References

BAKER, R. C., HURNG, W. M., and STEINFINK, H., 1989, *Appl. Phys. Lett.*, **54**, 371.

CHAUDHURI, B. K., CHAUDHURI, K., and SOM, K. K., 1989, *J. Phys. Chem. Solid*, **50**, 1137, 1148.

COLE, K. S., and COLE, R. H., 1941, *J. chem. Phys.*, **9**, 341.

GRANT, F. A., 1957, *J. appl. Phys.*, **29**, 176.

MACEDO, P. B., MOYNIHAN, C. T., and BOSE, R., 1972, *J. Phys. Chem. Glasses*, **13**, 171.

MANSINGH, A., 1980, *Bull. Mater. Sci.* (India), **2**, 325.

MANSINGH, A., DHAWAN, V. K., and SAYER, M., 1983, *Phil. Mag.* B, **48**, 215.

MANSINGH, A., VAID, J. K., and TANDON, P., 1975, *J. Phys.* C, **8**, 1023.

MOLLAH, S., 1993, PhD thesis, Jadavpur University, Calcutta, India.

MOLLAH, S., CHAKRABORTY, A. K., CHAKRABORTY, S., SOM, K. K., and CHAUDHURI, B. K., 1994, *J. non-crystalline Solids*, **167**, 192.

MOLLAH, S., SOM, K. K., BOSE, K., CHAKRABORTY, A., and CHAUDHURI, B. K., 1992, *Phys. Rev.* B, **48**, 11075.

MOLLAH, S., SOM, K. K., BOSE, K., and CHAUDHURI, B. K., 1993, *J. appl. Phys.*, **74**, 931.

MORIUCHI, T., KAWAI, T., MITSUI, K., and KAWAI, S., 1990, *Physica* C, **168**, 309.

MOTT, N. F., and DAVIS, E. A., 1979, *Electronic Processes in Non-Crystalline Materials*, 2nd Edn (Oxford: Clarendon).

SAYER, M., MANSINGH, A., REYES, J. M., and ROSENBLATT, G., 1971, *J. appl. Phys.*, **42**, 2857.

SCHNAKENBERG, J., 1968, *Phys. Stat. Sol.*, **28**, 623.

SOM, K. K., 1990, PhD thesis, Jadavpur University, Calcutta, India.

SOM, K. K., and CHAUDHURI, B. K., 1990, *Phys. Rev.* B, **41**, 1581.

SOM, K. K., MOLLAH, S., BOSE, K., and CHAUDHURI, B. K., 1992, *Phys. Rev.* B, **45**, 1655; 1993, *Ibid.*, **47**, 534.

ZHENG, H., COLBY, M. W., and MACKENZIE, J. D., 1991, *J. non-crystalline Solids*, **127**, 143.

PHYSICAL REVIEW B VOLUME 49, NUMBER 21 1 JUNE 1994-I

Anomalous dielectric relaxation behavior of K-doped amorphous $Ba_{1-x}K_xBiO_{3-\delta}$ ($x=0$–0.75) oxides

S. Mollah, A. K. Bera, S. Chakraborty, and B. K. Chaudhuri
Solid State Physics Department, Indian Association for the Cultivation of Science, Calcutta-700032, India
(Received 26 July 1993; revised manuscript received 22 November 1993)

In this paper we report the dielectric properties of $Ba_{1-x}K_xBiO_{3-\delta}$ ($x=0$, 0.2, 0.4, 0.625, and 0.75) glasses at different temperatures (80–450 K) and frequencies (1–10 kHz). Distinct anomalies (large increases) in the dielectric constant (ε') and dielectric loss (ε'') are observed for all the glasses between 297 and 320 K. A similar anomaly showing a change from semiconducting to metallic behavior is also observed in the electrical conductivities around the same temperature region. The anomalies observed around this temperature are considered to be associated with the orientational motion of the BiO_3 or BiO_6 structural units present in the glasses. Such motions might give rise to structural instability and different kinds of phase transitions including a superconducting transition in the crystalline phases.

I. INTRODUCTION

The $Ba_{1-x}K_xBiO_{3-\delta}$ (BKB) and $BaBi_{1-x}Pb_xO_{3-\delta}$ (BBP) type noncopper oxides have been greatly studied[1–3] because of their superconducting behavior at relatively higher temperatures[3] (at 30 K for BKB with $x=0.4$). Recently, several other oxide glasses like $Bi_4Sr_3Ca_3Cu_4O_y$ (Bi-4:3:3:4) etc., have been found[4] to be good precursors for high-T_c superconductors. While making an attempt to prepare BKB and BBP superconductors from their respective glassy phases, we noticed that only BKB forms glasses with different concentrations of potassium (K) or other alkali metals. Since BKB and BBP oxides show both metal-insulator and superconducting transitions[5,6] in their respective ceramic phases, it is interesting to study and compare the semiconducting behavior of the BKB glasses with that of the Bi-4:3:3:4 type glasses, which also show superconducting transitions in their respective glass-ceramic (crystalline) phases.

In the present paper we report the interesting anomalous nature of the dielectric constant (ε') and dielectric loss (ε'') observed in the BKB and $BaBiO_{3-\delta}$ (without K) glasses. The said anomaly, also observed in the dc conductivity, is considered to be associated with the motion of BiO_3 or BiO_6-type structural units already existing in the glasses. It is also pointed out that such an ionic or molecular motion is responsible for lattice distortion leading to interesting ferroelectric, metal-insulator, or even superconducting behavior.

II. EXPERIMENTAL

The $Ba_{1-x}K_xBiO_{3-\delta}$ glasses ($BaBiO_{3-\delta}$, $Ba_{0.8}K_{0.2}BiO_{3-\delta}$, $Ba_{0.6}K_{0.4}BiO_{3-\delta}$, $Ba_{0.375}K_{0.625}BiO_{3-\delta}$, and $Ba_{0.25}K_{0.75}BiO_{3-\delta}$) were prepared by the quick-quenching method discussed earlier.[7] Appropriate amounts of $BaCO_3$, K_2CO_3, and Bi_2O_3, all of purity 99.99% (or better), were well mixed for each composition and then first sintered at 500 °C for 10 h. The sintered sample was melted at 1200 °C for 1 h (for each sample). The melt thus obtained was quickly quenched between two steel blocks at room temperature. The amorphous character of all the dark brown glasses (except the $BaBiO_{3-\delta}$ glass which is light yellow) was tested by x-ray-diffraction (XRD) (Philips model PW 1710) and scanning electron microscopic (Hitachi model 415A) studies. The XRD patterns of some of the glasses, indicating their amorphous character, are shown in Fig. 1(a). The infrared (ir) absorption spectra [Fig. 1(b)] with KBr indicate almost identical features with those of the Bi-4:3:3:4-type glasses[8] containing Bi as discussed earlier, along with some new peaks.[9] The most prominent ir absorption peaks are indicated in Fig. 1(b). The fundamental peaks around 540–620 and 470 cm^{-1} correspond to

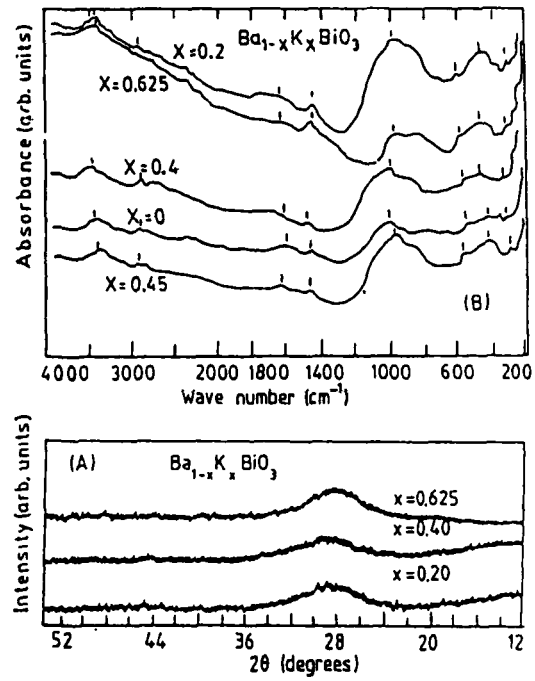

FIG. 1. X-ray powder diffraction patterns (a) and infrared absorption spectra (b) of some $Ba_{1-x}K_xBiO_{3-\delta}$ glasses.

0163-1829/94/49(21)/15017(6)/$06.00

TABLE I. Some important parameters for the $Ba_{1-x}K_xBiO_{3-\delta}$ glasses.

Samples	$BaBiO_{3-\delta}$	$Ba_{0.8}K_{0.2}BiO_{3-\delta}$	$Ba_{0.6}K_{0.4}BiO_{3-\delta}$	$Ba_{0.375}K_{0.625}BiO_{3-\delta}$	$Ba_{0.25}Bi_{0.75}BiO_{3-}$
Values of x	0.0	0.20	0.40	0.625	0.75
Density (g/cm^3)[a]	8.55	6.95	4.65	5.28	6.30
T_g (°C)	344±2	342±2	341±2	338±2	335±2
T_p (K)	313±1	312±1	309±1	297±1	(~300)

[a]Error in the determination of density lies within ±5%.

the presence of BiO_3 and BiO_6 structural units as discussed earlier.[8] Densities (ρ) of the glasses (measured by Archimedes' method with carbon tetrachloride as an immersion liquid) first decrease with increase of K content show a minimum around $x=0.4$ (Table I) and then increase with further increase of K content. This behavior is analogous to the "germanate anomaly" observed in the Na_2O-GeO_2 glasses.[10] An estimation of the glass transition temperature (T_g) and oxygen content are made, respectively, from differential thermal analysis and thermogravimetric analysis. The oxygen content of the glasses are found to be 2–3% less than the corresponding theoretical values. Some important parameters of the glasses are shown in Table I. The chemically estimated metal compositions, as shown in Table II, are found to be a little less than the corresponding theoretical values. This is primarily due to evaporation losses. The properties of the BKB glasses are assumed to be not affected by this small loss of metal ions. The dielectric constants of the well-shaped glass plates with sputtered gold electrodes were measured by a bridge (GR model 1615A) as in our earlier work.[7] The gold-plated samples were annealed at 200 °C for 2 h for good contact of the electrodes as well as for the removal of voids and microcracks, if any. To confirm the anomaly observed in the temperature-dependent dielectric constant curve (Fig. 2), we also measured dc conductivity (σ_{dc}) of the BKB glasses (Figs. 2 and 3) as a function of temperature, following the procedure discussed earlier.[7] The Ohmic character was confirmed from the I-V characteristic curves for all the glasses.

III. EXPERIMENTAL RESULTS

The thermal variations of dielectric constant (ε') at different frequencies for the $BaBiO_{3-\delta}$ and $Ba_{0.375}K_{0.625}KBiO_{3-\delta}$ glasses [shown in Figs. 2(a) and 2(b)] exhibit sharp peaks around 300 K. The peak temperature (T_p say) slightly varies with K concentrations as shown in Table I. Other glass compositions also show similar behavior. It is interesting to note that a similar anomaly has also been observed in the temperature-dependent dc conductivity (σ_{dc}) as shown in Figs. 2(c) and 3 for some of the glasses in our investigation. Below the peak temperature T_p, ε' increases with increase of temperature whereas above T_p it decreases first and then again increases linearly with increase of temperature. In many transition-metal oxide (TMO) glasses[11,12] and also in the Bi-4:3:3:4-type glassy[8] precursors for high-T_c superconductors, ε' increases very slowly with temperature in the low-temperature region; but above a certain temperature it increases very sharply with increase of temperature, which is not observed in the BKB and $BaBiO_{3-\delta}$ glasses. Furthermore, the peaks observed in ε'-T plots of some TMO glasses[11,12] mentioned above indicate Debye-type dielectric relaxation behavior. But unlike BKB glasses the TMO glasses, in general, do not show any peak in dc conductivity. As shown in Figs. 2(c) and 3(a) the thermal variation of dc conductivity indicates metallic behavior above T_p (decrease of conductivity with increase of temperature), which is similar to a metal-insulator-like transition. At lower temperature (below T_p), σ_{dc} remains almost temperature independent [Fig. 3(a)]. These are the very special features of the BKB-type glasses.

Figure 4(a) shows the nonlinear variation of ε' with frequency for a typical $Ba_{0.375}K_{0.625}BiO_{3-\delta}$ glass. The corresponding variations of ε' for different glasses at a fixed temperature of 343 K are shown in Fig. 4(b). This type of nonlinear variation of dielectric constant with frequency is also uncommon in many TMO glasses studied earlier.[8,11,12]

The dielectric loss (ε'') of the BKB glass was calculated from the ac conductivity $\sigma_{ac}(\omega)$ data, as discussed earlier,[8] using the relation $\varepsilon''(\omega)=\sigma_{ac}(\omega)/(\varepsilon_0\omega)$ (where ε_0 is the permittivity in vacuum and ω is the measuring angu-

TABLE II. Theoretically and chemically (in parentheses) determined wt % of K, Bi, and Ba.

Sample	K (wt %)[a]	Bi (wt %)[a]	Ba (wt %)[a]
$BaBiO_{3-\delta}$	0.0 (0.0)	52.99 (49.76)	34.83 (33.00)
$Ba_{0.8}K_{0.2}BiO_{3-\delta}$	2.08 (2.01)	55.77 (53.69)	29.32 (30.30)
$Ba_{0.6}K_{0.4}BiO_{3-\delta}$	4.40 (3.08)	58.86 (56.99)	23.21 (22.10)
$Ba_{0.375}K_{0.625}BiO_{3-\delta}$	6.99 (6.77)	62.31 (61.00)	16.38 (15.47)
$Ba_{0.25}K_{0.75}BiO_{3-\delta}$	8.78 (8.22)	67.04 (65.18)	13.21 (10.70)

[a]Error in the determination of wt % lies within ±5%.

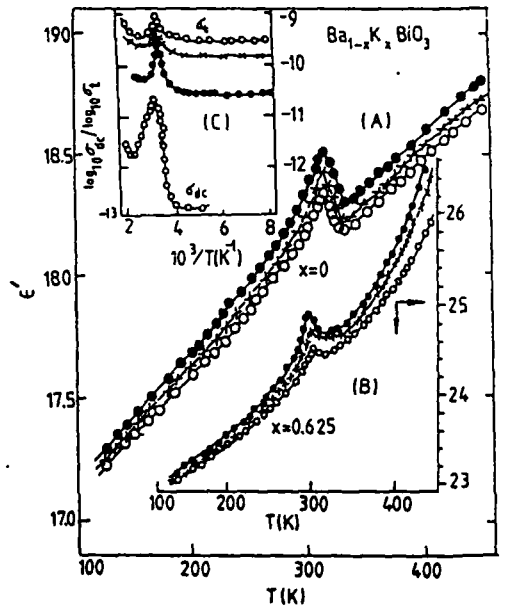

FIG. 2. Thermal variations of the dielectric constant (ε′) of some $Ba_{1-x}K_xBiO_{3-\delta}$ glasses with $x=0$ (a) and $x=0.625$ (b) at different frequencies 10 (○), 5 (×), and 1 (●) kHz, respectively. (c) Variations of $\log_{10}(\sigma_{dc})$ and $\log_{10}(\sigma_t)$ as a function of inverse temperature (where σ_{dc}=dc conductivity and σ_t=total frequency-dependent conductivity) of the typical $BaBiO_{3-\delta}$ glass at 10 (○), 5 (×), and 1 (●) kHz.

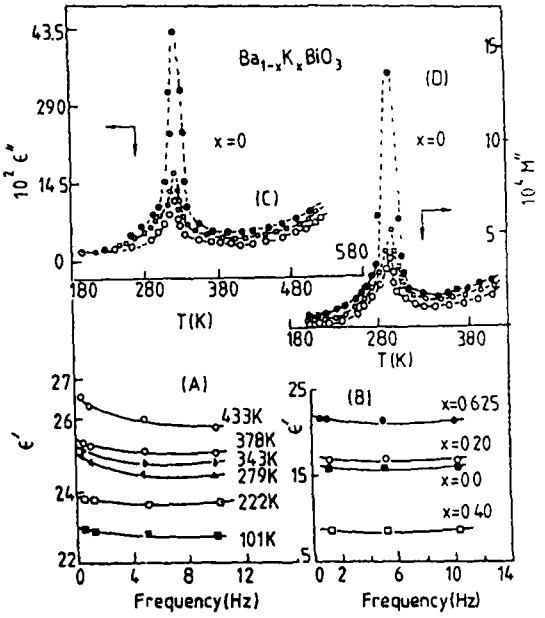

FIG. 4. (a) Frequency-dependent dielectric constant (ε′) at different temperatures of the $Ba_{0.375}K_{0.675}BiO_{3-\delta}$ glass and (b) at different potassium concentrations (for a fixed temperature of 343 K) of the $Ba_{1-x}K_xBiO_{3-\delta}$ glasses. (c) Thermal variation of the imaginary part of the dielectric constant (ε″) and (d) dielectric modulus (M'') of the $BaBiO_{3-\delta}$ glass at 10 (○), 5 (□), and 1 (●) kHz.

lar frequency). For the $BaBiO_{3-\delta}$ glass, the temperature variation of ε″ [Fig. 4(c)] indicates the presence of a sharp peak around T_p where ε′ and the dc conductivity also showed peaks [Figs. 2(c) and 3(a)]. A similar plot for another glass $Ba_{0.375}K_{0.625}BiO_{3-\delta}$ shown in Fig. 5(a) indicates two sharp peaks; the first peak around T_p resembles

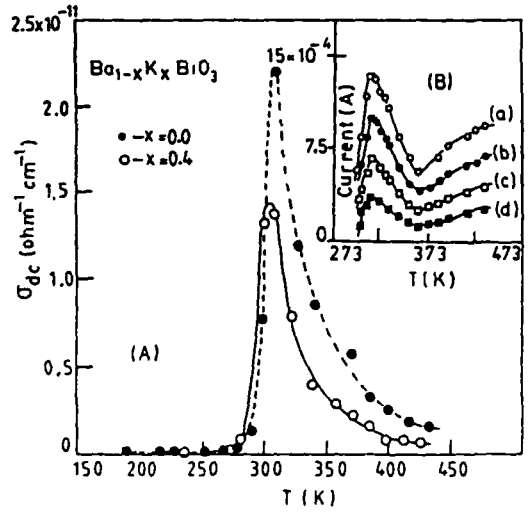

FIG. 3. (a) Thermal variations of dc conductivity of the $BaBiO_{3-\delta}$ and $Ba_{0.6}K_{0.4}BiO_{3-\delta}$ glasses; (b) Variation of the thermally stimulated depolarization current (TSDC) of the $Ba_{0.6}K_{0.4}BiO_{3-\delta}$ glass for different applied voltages a 250, b 200, c 150, and d 100 V.

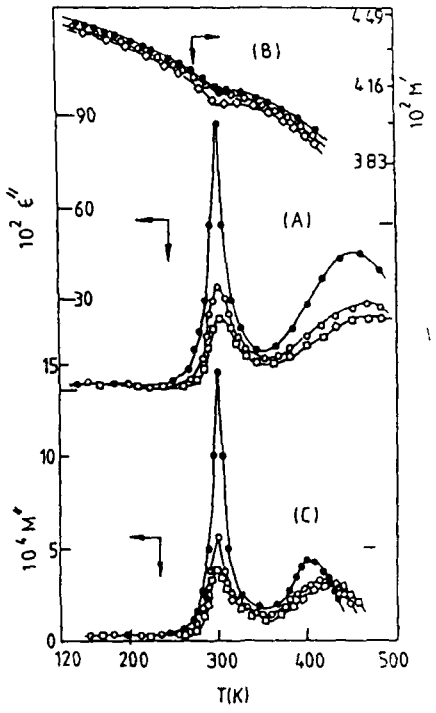

FIG. 5. Thermal variation of the imaginary part of the (a) the dielectric constant (ε″), (b) the real part of the dielectric modulus (M') and (c) the imaginary part of the dielectric modulus (M'') at 10 (□), 5 (○), and 1 (●) kHz of the $Ba_{0.375}K_{0.675}BiO_{3-\delta}$ glass.

the first anomaly observed in the ε' versus T plot [Fig. 2(b)], and the other relatively broad peak appearing at a higher temperature is the dielectric anomaly associated with Debye-type relaxation with a relaxation frequency $f_c = 1/2\pi\tau$ (where τ is the relaxation time). All the other BKB glasses show the second peak. For the $BaBiO_{3-\delta}$ glass, the second peak is not prominent [Fig. 4(c)] and it might appear at a higher temperature beyond the temperature range of our investigations. Both ε' and ε'' increase with increase of K content in the glasses. The peaks observed in the ε'-T, ε''-T, and σ_{dc}-T curves for the BKB glasses are considered to be associated with origins other than the Debye characteristic peak observed in many TMO glasses. To show the Debye-type relaxation behavior, it is sometimes (where ε'' vs T curves do not show the Debye peak) important to study the temperature-dependent dielectric modulus, as discussed below.

Using the experimental values of ε' and ε'', the real $[M' = \varepsilon'/[(\varepsilon')^2+(\varepsilon'')^2]]$ and the imaginary $[M'' = \varepsilon''/[(\varepsilon')^2+(\varepsilon'')^2]]$ parts of the dielectric modulus (M^*) are calculated.[13] The thermal variation of M' for a typical $Ba_{0.375}K_{0.675}BiO_{3-\delta}$ glass shown in Fig. 5(b) indicates a small anomaly around T_p. The corresponding variations of M'' with temperature for the $BaBiO_{3-\delta}$ and $Ba_{0.375}K_{0.675}BiO_{3-\delta}$ glasses are shown, respectively, in Figs. 4(d) and 5(c) both of which indicate sharp peaks around the respective T_p values (Table I). Other glasses also show similar behavior. Except for the $BaBiO_{3-\delta}$ glass [Fig. 4(d)], a second maximum is also observed in the M''-T plots [Fig. 5(c)]. The peak position of the second maximum shifts to the higher-temperature region with increase of frequency [Fig. 5(c)]; this is a characteristic feature of Debye-type relaxation behavior of the BKB glasses in the regions for $T > T_p$. For the $BaBiO_{3-\delta}$ glass, the second maximum in the M''-T curve is not observed within the temperature range of our investigation. The first peak height in the ε''-T and M''-T plots is also found to decrease with increase of measuring frequency. The second higher-temperature peak position of the M'' versus T curves gives the temperature at which the measuring frequency is equal to the relaxation frequency f_c [$= \nu_c \exp(-W_c/k_BT)$, where W_c is the activation energy for conductivity relaxation, and k_B is the Boltzmann constant]. Since the behavior of f_c plotted as a function of $1/T$ (for $T > T_p$) is almost similar to the temperature-dependent dc conductivity (σ_{dc}), a thermally activated dielectric relaxation mechanism is indicated above T_p.

To find information about the relaxation times, we also plotted $\varepsilon''(\omega)$ versus $\varepsilon'(\omega)$ (known as a Cole-Cole plot[14]) at a fixed temperature of 255 K, as shown in Fig. 6 for some typical glass compositions. The semicircular nature of the curves as suggested by Cole and Cole[14] is not very prominent for these glasses. This is also true for the Bi-4:3:3:4 glasses studied earlier.[8] As suggested by Grant[15] this might be due to the large value of the high-frequency capacitance or dc conductivity of these glasses. A similar nature of the Cole-Cole plot has recently been observed in polymeric semiconductors.[16] Due to the lack of a fit of

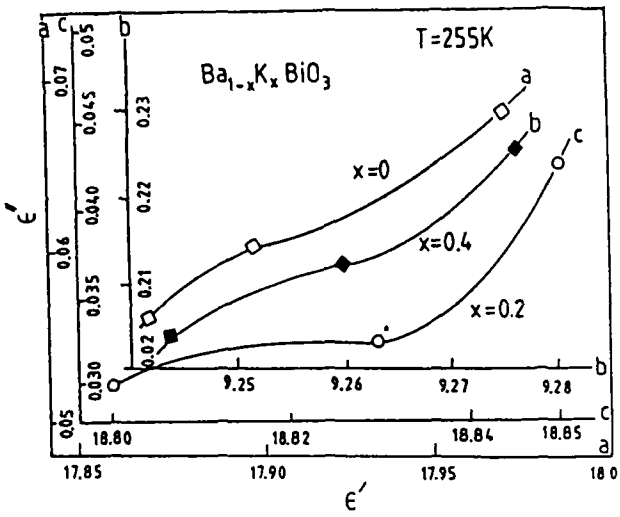

FIG. 6. Variation of the imaginary part (ε'') as a function of the real part (ε') of the dielectric constant for three different BKB glasses at a fixed temperature (255 K).

the experimental data to a pure semicircular Cole-Cole plot and because of the limited frequency range of our measurements, it is difficult to determine accurately the value for β [the slope of the Cole-Cole plot at $\varepsilon'' = 0$ gives the value of $(1-\beta)\pi/2$]. However, from Fig. 6 it is clear that the values of β for different BKB glasses are greater than zero but less than 1. This indicates that the BKB glasses have a distribution of relaxation times similar to the Bi-4:3:3:4 glasses,[8] becoming superconducting in their glass-ceramic phases.

IV. DISCUSSION

The large dielectric peak observed in the BKB glasses between 300 and 320 K is found to be not due to the appearance of spontaneous polarization, as in the case of ferroelectric materials.[17] There are examples[18] of large dielectric anomalies in crystals without ferroelectric or antiferroelectric transitions. The large anomalies in the dielectric constants, and loss factors as well as in the dc conductivity of the $BaBiO_{3-\delta}$ and BKB glasses are considered to be associated with the orientations of the BiO_6 octahedra or the BiO_3 tetrahedral units[8] around T_p. The presence of such structural units has already been indicated from the ir spectra [Fig. 1(b)] of these glasses. Since Bi can exist in two valence states Bi^{3+} and Bi^{5+}, a change from the low-valence state to the higher-valence state is also possible. However, it is also observed[10] from thermally stimulated depolarization measurements that thermally stimulated depolarization currents (TSDC) plotted as a function of temperature show peaks around T_p. This type of anomaly in the TSDC versus temperature curves, as shown in Fig. 3(b) for a typical $Ba_{0.6}K_{0.4}O_{3-\delta}$ glass, also indicates the probable dipolar orientation in these glasses.[19]

It should be pointed out that such an anomaly around T_p has not been observed in the ceramic BKB or

$BaBiO_{3-\delta}$ samples. At higher temperatures both $BaBi_{1-x}$, $Pb_xPb_xO_{3-\delta}$ and $Ba_{1-x}K_xBiO_{3-\delta}$ exhibit, for all x, the ideal cubic perovskite structure.[20,21] They also undergo a variety of structural phase transitions as a function of x. The various low-temperature phases represent only small distortions from the ideal phase. For $x=1$, a charge-density-wave instability of Pb or K leads to semiconducting behavior.[22,23] With increase of Pb or K concentration,[23] the semiconducting energy gap decreases and semimetallic behavior results for $x<0.4$. It is seen from Fig. 3(a) that, even in the glassy phase, a decrease of dc conductivity with increase of temperature (metallic or semimetallic behavior above T_p) is observed. We believe that the rotational or orientational motion of the BiO_3 structural units mentioned above gives rise to structural instability in the glass network (as in ferroelectric crystals) in the presence of strong electron-phonon interaction in such a system.

As for BKB glasses, large dielectric constants have also been reported in La_2CuO_4,[24] and in the high-temperature phase of polycrystalline $YBa_2Cu_3O_x$,[25] associated with structural instability. Ferroelectrics generally exhibit a large dielectric constant (ε') both above and below (but near) their Curie point T_f. It was shown by Testardi *et al.*[25] that the large dielectric constants observed in La_2CuO_4 or in the high-temperature phase of $YBa_2Cu_3O_x$ are not precisely due to true ferroelectricity, but to incipient ferroelectricity or some other causes. Frohlich[26] pointed out that the conditions $\varepsilon' \to \infty$ and $\omega_T \to 0$ for $T > T_f$ would lead to an insulator-(semiconductor-) to-metallic transition on cooling if the system retained linear response, or a ferroelectric transition in the event of nonlinear response. Similar arguments appear to be true even for the BKB system. Recently Bussmann-Holder *et al.*[21] also suggested the possibility of a common origin of ferroelectricity and superconductivity for the $BaBi_{1-x}Pb_xO_{3-\delta}$-type oxides.

Kristoffel and Konsin[27,28] also showed the importance of such structural instability arising from strong electron-phonon interactions. Not only is the application of such a model to elucidate the mechanism of superconductivity justified, but their structural similarity to the ferroelectric perovskites also, shown by the fact that these systems exhibit high static dielectric constants,[29] suggests that an important role is played by the electron-phonon interaction. The unusual local anisotropy of the nonlinear electron-phonon interaction (arising from such orientational motion of some of the ions or groups in the lattice) admits the reduction of a three-dimensional system to pseudo-one-dimensional systems as only one axis is lattice-dynamically relevant for the evolution of the polar state [e.g., [100] in ABO_3 (Ref. 30)]. The basic assumption of the underlying model is that in superconductors the same nonlinear electron-phonon coupling plays an essential role, thus again admitting the application of a one-dimensional model. It can be shown[21,27] that the lattice distortion and also the semiconducting energy gap decrease with increase of temperature (from low temperature) as in the theory of superconductivity and the Peierls transition.[30] Jorgensen *et al.*[31] also considered lattice instability to explain superconductivity in $La_{2-x}Ba_xCuO_4$. The nonsuperconducting La_2CuO_4, which has an orthorhombic structure, exhibits semiconducting behavior. The orthorhombic distortion is proposed to result from a Peierls $2k_F$ instability or a soft zone-boundary phonon mode. The role of Ba is to suppress the instability and stabilize a higher-symmetry tetragonal structure, which is metallic or superconducting.

Thus it appears that the strong electron-phonon interaction in BKB- or in BBP-type oxides might give rise to many types of transitions including superconducting[21] transitions. From knowledge of the existing theoretical models,[21,26,27] the nonlinear behavior of the conductivity and large dielectric constant can be phenomenologically explained. In the BKB system the rotational motion of the active ions (BiO_3 or BiO_6) plays an important role for strong electron-phonon interaction and lattice distortion. The elaborate calculation which has already been carried out by Bussmann-Holder *et al.*[21,32] for the $BaBi_{1-x}Pb_xO_{3-\delta}$-type oxides elucidated interesting features of superconductivity and ferroelectricity.

ACKNOWLEDGMENTS

The authors are grateful to the Department of Science and Technology (DST) and also to the Council of Scientific and Industrial Research (CSIR), Government of India, for financial assistance to do the work.

[1] R. J. Cava, B. Batlogg, J. J. Krajewski, R. Farrow, L. W. Rupp, A. E. White, K. Short, W. F. Peck, and T. Kometani, Nature 332, 814 (1988).

[2] D. G. Hinks, B. Dabrowski, J. D. Jorgensen, A. W. Michel, D. R. Richards, S. Pei, and D. Shi, Nature 333, 836 (1988).

[3] R. Kuentzler, C. Hornick, Y. Dossmann, S. Wegner, R. El Farsi, and M. Drillon, Physica C 184, 316 (1991).

[4] T. Kawai, T. Horiuchi, K. Mitsu, K. Ogura, S. Tanaka, and S. Kawai, Physica C 161, 561 (1989); H. Zheng, M. W. Colby, and J. D. Mackenzie, J. Non-Cryst. Solids, 127, 143 (1991).

[5] L. F. Mattheiss and D. R. Hamann, Phys. Rev. B 28, 4227 (1983); L. F. Mattheiss, Jpn. J. Appl. Phys. 24, Suppl. 2, 6 (1985).

[6] T. M. Rice and L. Sneddon, Phys. Rev. Lett. 47, 681 (1981).

[7] S. Mollah, K. K. Som, K. Bose, A. K. Chakravorty, and B. K. Chaudhuri, Phys. Rev. B 46, 11 075 (1992); S. Mollah, K. K. Som, K. Bose, and B. K. Chaudhuri, J. Appl. Phys. 74, 931 (1993).

[8] K. K. Som, S. Mollah, K. Bose, and B. K. Chaudhuri, Phys. Rev. B 45, 1165 (1992); 47, 534 (1993).

[9] S. Mollah, A. K. Bera, and B. K. Chaudhuri (unpublished).

[10] G. S. Henderson and M. E. Fleet, J. Non-Cryst. Solids 134, 259 (1991).

[11] A. Mansingh, V. K. Dhawan, and M. Sayer, Philos. Mag. B

48, 215 (1983).
[12]A. Mansingh, J. K. Vaid, and R. P. Tandon, J. Phys. C 8, 1023 (1975).
[13]P. B. Macedo, C. T. Moynighan, and R. Bose, Phys. Chem. Glasses 13, 171 (1972).
[14]K. S. Cole and R. H. Cole, J. Chem. Phys. 9, 341 (1941).
[15]F. A. Grant, J. Appl. Phys. 29, 76 (1958).
[16]N. Afanasev, L. V. Mukaeva, M. G. Voronkov, and T. G. Ermakova, Dokl. Akad. Nauk SSSR 320, 856 (1991) [Sov. Phys. Dokl. 36, 694 (1991)].
[17]M. E. Lines and A. M. Glass, *Principles and Applications of Ferroelectric and Related Materials* (Clarendon, Oxford, 1977).
[18]R. Pepinsky, in *Physics of Electronic Ceramics,* edited by L. L. Hench and D. B. Dove (Dekker, New York, 1972), Pt. B, p. 567.
[19]J. Laudat and F. Laudat, Z. Phys. Chem. 178, 211 (1991); J. van Turnhout, in *Electrets,* edited by G. M. Sessler, Topics in Applied Physics Vol. 33 (Springer-Verlag, New York, 1980), p. 81.
[20]A. W. Sleight, J. J. Gibson, and P. E. Biessted, Solid State Commun. 17, 27 (1975).
[21]A. Bussmann-Holder, H. Buttner, A. Simon, and V. Waas, Z. Phys. B 79, 445 (1990), and references therein.
[22]D. E. Cox and A. W. Sleight, Acta. Crystallogr. Sect. B 34, 1 (1979); A. Chaillout, A. Santoro, J. P. Remeika, A. S. Cooper, G. P. Espinosa, and M. Marezio, Solid State Commun. 65, 1363 (1988).
[23]T. D. Thanh, A. Koma, and S. Tanaka, J. Appl. Phys. 22, 205 (1980); S. Tajima, S. Uchida, A. Kasaki, M. Takagi, K. Kitazawa, S. Takeda, and A. Katsui, Phys. Rev. B 32, 6302 (1985); S. Tajima, S. Uchida, S. Masaki, H. Takaji, K. K. Tazawa, S. Tanaka, and S. Sagai, *ibid.* 36, 1696 (1988).
[24]D. Reagor, E. Abrens, S. W. Cheong, A. Migliori, and Z. Fisk, Phys. Rev. Lett. 62, 2048 (1989).
[25]L. R. Testardi, W. G. Moulton, H. Mathias, H. K. Ng, and C. M. Rey, Phys. Rev. B 37, 2324 (1988).
[26]H. Frohlich, in *Ferroelectricity,* edited by E. Weller (Elsevier, New York, 1967), p. 9.
[27]N. N. Kristoffel and P. Konsin, Phys. Status Solidi 28, 731 (1968).
[28]P. Konsin, Phys. Status Solidi 76, 487 (1976).
[29]Y. N. Venevtsev, V. V. Bogatko, M. V. Plotnikova, and S. J. Rieman, Ferroelectrics 56, 61 (1984).
[30]L. N. Bulaevskii, Usp. Fiz. Nauk 115, 263 (1974) [Sov. Phys. Usp. 18, 131 (1975)]; 116, 449 (1975) [18, 514 (1975)].
[31]J. D. Jorgensen, H. B. Schuttler, D. G. Hinks, D. W. Capone, H. K. Zhang, and M. B. Brodsky, Phys. Rev. Lett. 58, 1024 (1987).
[32]A. Bussmann-Holder, H. Bilz, and G. Benedek, Phys. Rev. B 39, 4840 (1989).

High dielectric constants in $BaTiO_3$ doped $90V_2O_5$–$10Bi_2O_3$ oxide glasses obeying Debye-type dielectric relaxation behavior

Sahana Chakraborty, A. K. Bera, S. Mollah, and B. K. Chaudhuri
Solid State Physics Department, Indian Association for the Cultivation of Science, Calcutta 700 032, India

(Received 16 August 1993; accepted 5 April 1994)

$BaTiO_3$ doped $90V_2O_5$–$10Bi_2O_3$ (VB) oxide glasses show a larger dielectric constant (10^2–10^4) compared to that of the base glass VB ($\sim 10^2$). The VB glass with 15 wt. % $BaTiO_3$ shows the largest dielectric constant, and all the glasses show a Debye-type dielectric relaxation behavior. The increase in dielectric constant appears to be mainly due to the formation of microcrystalline clusters of $BaTiO_3$ (1.8–8 μm, depending on the $BaTiO_3$ concentration present in the base glass). Other than the dilution effect with $BaTiO_3$, the glass-former oxide Bi_2O_3 also influences the dielectric behavior of $BaTiO_3$ doped VB glasses.

Ceramics and glasses with large dielectric constants are very important for technological applications.[1] Semiconducting barium titanate grains separated from each other by insulating layers have also been used to develop barrier layer capacitors.[2] In the present communication we have reported that the $BaTiO_3$ doped V_2O_5–Bi_2O_3 glasses have very larger dielectric constants with Debye-type dielectric relaxation behavior.

The starting base glass $90V_2O_5$–$10Bi_2O_3$ (VB) and the (VB + $x BaTiO_3$) glasses (VBBT) with x = 5, 10, 15, 20, 30, and 40 wt. % of VB (termed, respectively, VBB5, VBB10, VBB15, VBB20, VBB30, and VBB40) are prepared by a quick quenching method similar to our earlier work.[3] High purity (99.9%) V_2O_5, Bi_2O_3, and $BaTiO_3$ (particle size 1.8–2 μm) are mixed together in appropriate proportions and heated at 900° to 1100 °C (depending on $BaTiO_3$ concentrations) for 2 h and then quenched to room temperature between two copper plates. The glass plates are cut, polished, and gold plated by sputtering before dielectric and electrical measurements. The amorphous character of the samples was studied by x-ray diffraction (Philips, Model PW 1710). The scanning electron microscopic studies (Model 415A, Hitachi, Japan) of three different glasses (VBB5, VBB15, and VBB20), shown in Fig. 1, indicate the presence of small clusters/particles of microcrystalline $BaTiO_3$ embedded in the glass matrix. These particle sizes of the clusters vary from 1.8–8 μm, depending on the concentration of $BaTiO_3$ in the base glass. The glass-transition temperatures (T_g) (measured with a Shimadzu thermal analyzer, Model DT-30) of the samples are shown in Table I along with some other important parameters. The composition of the metal ions in the glasses tested by EDX studies (Model 3600-0388, KEVWX International, USA) was found to fall within ±5 wt. % of the corresponding theoretical values. Dielectric constants (ε') and dielectric losses (ε'') of the glasses were measured by the Gen-Rad type 1615A capacitance bridge technique.[3]

Temperature (100–480 K) and frequency 100 Hz to 10 kHz) dependencies of both ε' and ε'' have been measured for all VBBT and VB glasses. The thermal variations of ε' and ε'' for the base glass (VB) shown in Fig. 2 indicate broad peaks. The peak height decreases with the increase of frequency. Variations of ε' with frequency for all the VBBT glasses at three different temperatures (360 K, 300 K, and 110 K) are shown in Figs. 3(a), 3(b), and 3(c), respectively. The frequency dependence of the imaginary part of the dielectric constants (ε'') of all the glasses at a fixed temperature is also shown in Fig. 3(d). It is observed from Fig. 3 that the dielectric constants of the VBBT glasses do not increase consistently with the increase of $BaTiO_3$ concentration. At lower frequencies (below 3 kHz) and at a temperature of 300 K (or above), the dielectric constant of the VBB15 glass is the highest (with respect to other VBBT glasses) and is comparable with that of pure $BaTiO_3$ oxide. It is also observed from Figs. 3(a)–3(c) that with the increase in frequency ε' decreases at all temperatures, and at low temperature (110 K and below) ε' is almost independent of frequency (particularly at higher frequencies). The dielectric constants of the VBBT glasses are also larger than those of many other transition metal oxide (TMO) glasses such as Bi_2O_3–V_2O_5,[4,5] Bi_2O_3–Fe_2O_3,[6] etc.

Unlike VB glasses, the (ε'–T) plots of the VBBT glasses do not show (up to 480 K) sharp peaks, as shown in Fig. 4(a) for the typical VBB15 glass. The values of dielectric loss ε'' for the VB and VBBT glasses are obtained, as usual, from the ac conductivity data using the relation,[3,6] $\omega\varepsilon_0\varepsilon'' = \sigma(\text{total}) - \sigma_{dc}$, where σ(total) is the measured total conductivity, σ_{dc} is the dc conductivity, ω is the measuring angular frequency, and

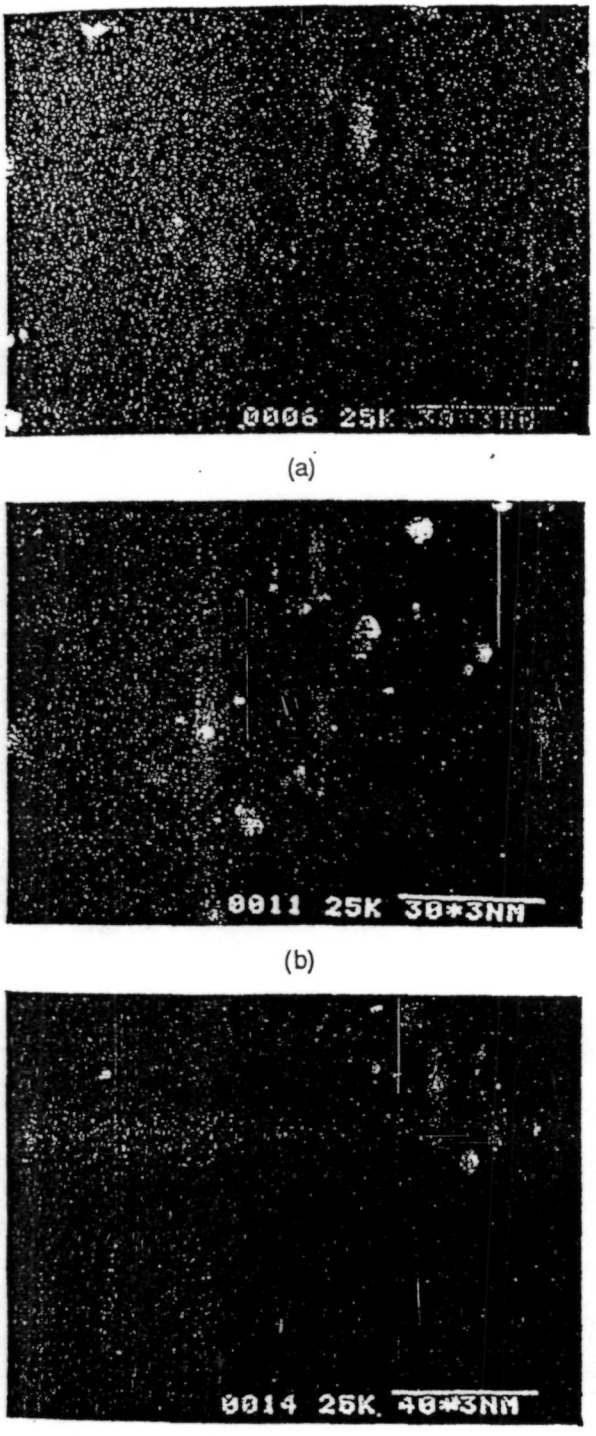

FIG. 1. Scanning electron micrographs of three typical glasses, (a) VBB5, (b) VBB15, and (c) VBB20, showing glassy character with microcrystalline clusters of $BaTiO_3$. [In (a) and (b) 20 mm = 30 μm, and in (c) 20 mm = 40 μm.]

ϵ_0 is the free space permittivity. Unlike the base glass VB, no peak in the dielectric loss curve of VBBT glasses exists within the temperature range of our investigation. Figure 4(b) shows the (ε''–T) curves of the VBB15 glass at different frequencies. Similar behavior [as in Fig. 4(b)] is also exhibited by other VBBT glasses. Such peaks in the VBBT glasses may, however, appear at much higher temperatures (above 480 K). The appearance of such a peak in the base glass VB, as shown in Fig. 2(b), is an indication of the Debye-type dielectric dispersion characterized by a relaxation frequency f_0 ($f_0 = 1/2\pi\tau_0$, where τ_0 is the dielectric relaxation time). The thermal variations of tan δ (where tan $\delta = \varepsilon''/\varepsilon'$) for the typical VBB15 glass are, however, very large and exhibit peaks [Fig. 5(a)] that shift to a higher temperature region with the increase of frequency.

To show dielectric dispersion behavior more clearly (for the VBBT-type glasses where the ε'–T or ε''–T curves do not show clear peaks), it is interesting to

TABLE I. Some parameters of the $(90V_2O_5-10Bi_2O_3) + x BaTiO_3$ glasses.

x wt. %	Glass-making temperature (°C)	ρ (g/cm^3)[a]	T_g (°C)
5	900	4.11	234 ± 2
10	900	4.20	246 ± 2
15	1000	4.29	250 ± 2
20	1000	4.38	275 ± 2
30	1100	4.56	286 ± 2
40	1100	4.78	...

[a]Maximum error in the measurement of density (ρ) is ±5%.

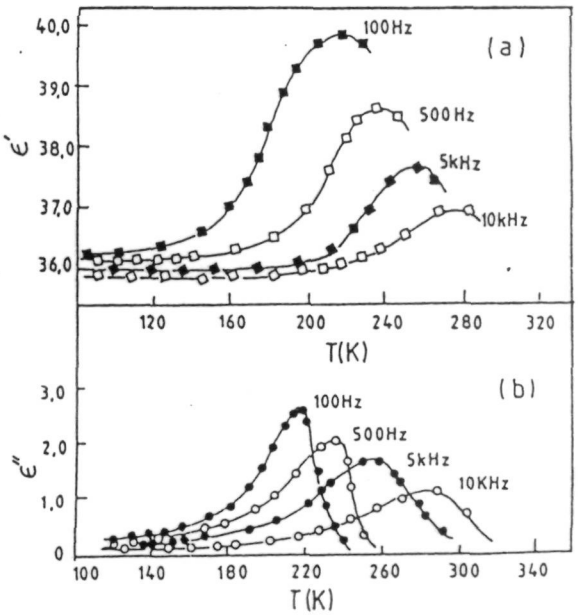

FIG. 2. Thermal variations of (a) dielectric constant $\varepsilon'(\omega)$ and (b) dielectric loss $\varepsilon''(\omega)$ of the $90V_2O_5-10Bi_2O_3$ (VB) glass at different frequencies.

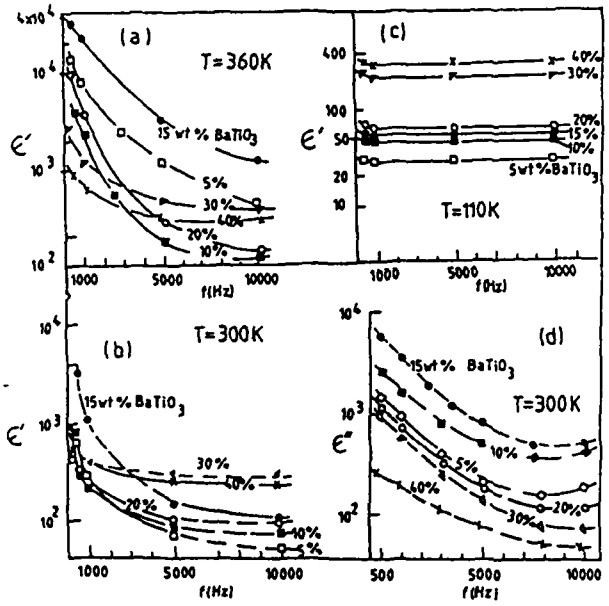

FIG. 3. The frequency dependences of dielectric constants (ε') of the VBBT glasses at different temperatures: (a) 360 K, (b) 300 K, and (c) 110 K. (d) Variations of dielectric loss (ε'') of the VBBT glasses with frequency at a fixed temperature (300 K).

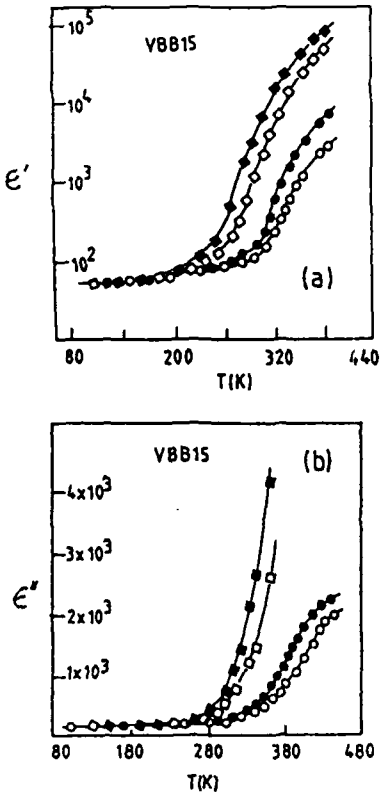

FIG. 4. Thermal variations of (a) dielectric constant $\varepsilon'(\omega)$ and (b) dielectric loss $\varepsilon''(\omega)$ of the VBB15 glass at 500 Hz (■), 1 kHz (□), 5 kHz (●), and 10 kHz (○).

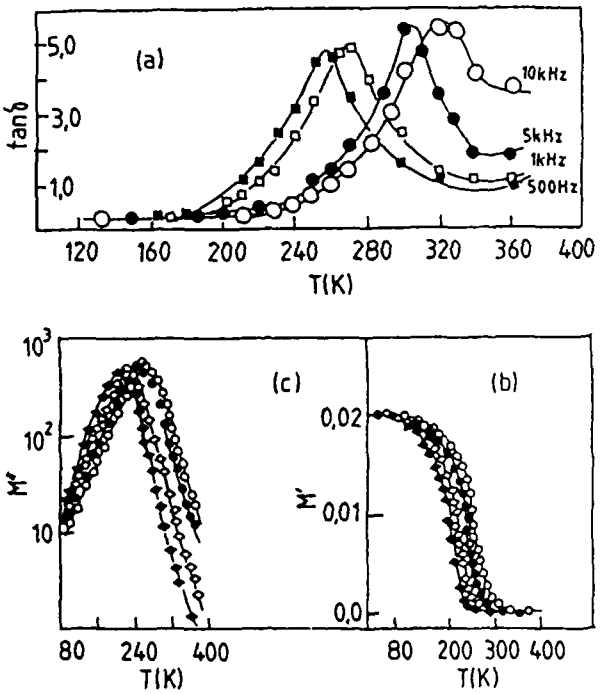

FIG. 5. (a) Temperature dependence of tan δ (tan $\delta = \varepsilon''/\varepsilon'$). (b) Real ($M'$) and (c) imaginary ($M''$) parts of the dielectric modulus of the VBB15 glass at 500 Hz (■), 1 kHz (□), 5 kHz (●), and 10 kHz (○).

plot the real (M') and the imaginary (M'') parts of the dielectric modulus[7] of the glasses. Both M' and M'' are related to dielectric constants as $M' = [\varepsilon'/(\varepsilon')^2 + (\varepsilon'')^2]$ and $M'' = [\varepsilon''/(\varepsilon')^2 + (\varepsilon'')^2]$. Thermal variations of both M' and M'' show peaks for all the VBB15 type glasses. The variations of M' and M'' with temperature, for the typical VBB15 glass, are shown in Figs. 5(b) and 5(c), respectively. At high temperature M' tends to reach a constant value, which shifts to a higher temperature region for higher frequencies. This behavior indicates the thermally activated nature of the dielectric constant in the VBBT glasses. The M'' vs T curve [Fig. 5(c)] shows peaks that also shift to higher temperatures for higher frequencies. The peak positions of M'' give the temperature at which measuring frequency (ω) is equal to the relaxation frequency $f_c = \nu_c \exp(-W_c/k_B T)$, where W_c is the activation energy of conductivity relaxation. The f_c vs T^{-1} curves for the VBBT type glasses are found to be very similar to the temperature dependent dc conductivity curve of the same glasses, suggesting that both dc conductivity and relaxation mechanism are thermally activated in nature.[5]

We also attempted to find the nature of the dielectric relaxation behavior of the VBBT glasses from the Cole–Cole plot[8] at a fixed temperature and different frequencies, as shown in Fig. 6. The slopes of these curves at a fixed temperature (say, 300 K) increase with

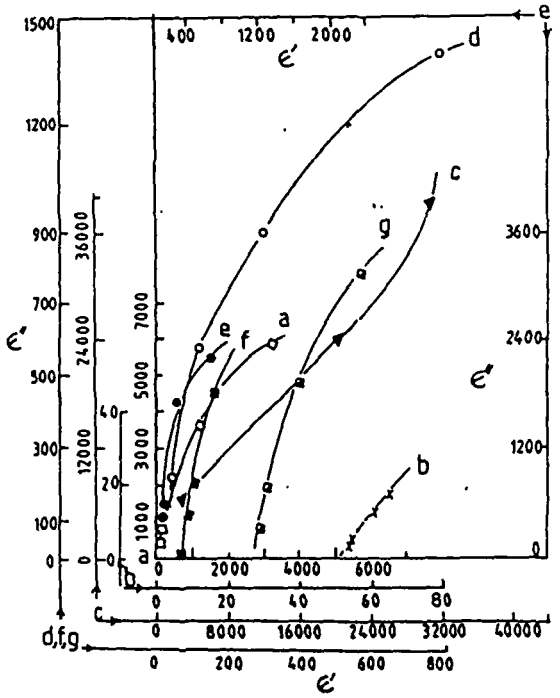

FIG. 6. Cole–Cole plots of VBB15 glass at 300 K (a), 180 K (b), and 360 K (c); VBB5 glass at 300 K (d), VBB10 glass at 300 K (e), VBB20 glass at 300 K (f), and VBB30 glass at 300 K (g).

the increase of $BaTiO_3$ concentration. This means that the distribution of relaxation times becomes sharper with the increase of $BaTiO_3$ concentration. This behavior is not very common in the transition metal oxide glasses. Moreover, the semicircular nature of the curves as suggested by Cole and Cole[8] is not well visualized in these glasses. This might, however, be due to large values of high frequency capacitance or dc conductivity of these glasses as suggested by Grant.[9]

Finally it is concluded that the dielectric constants of all the VBBT glasses are much higher than the undoped V_2O_5–Bi_2O_3 and similar TMO glasses[4–6] mentioned above. This increase is primarily due to the formation of small microcrystalline clusters of $BaTiO_3$ (1.8–8 μm sizes) in the glasses as observed from the SEM micrographs (Fig. 1). The particle sizes are larger and well separated for the glasses containing lower concentrations of $BaTiO_3$. The increase of ϵ' is consistent with the increase of $BaTiO_3$ up to 15 wt.% of $BaTiO_3$, and then it decreases with further increase of $BaTiO_3$ in the base glass. Here the glass-former oxide (Bi_2O_3) appears to play an important role. In support of this we find that $90V_2O_5$–$10P_2O_5$ + $x$$BaTiO_3$ glasses do not show[10] such large dielectric constants as in the present VBBT glasses.

Though the tan δ values of the VBBT glasses are very large and not suitable for use as capacitor materials, it was found that the addition of about 1–2 wt.% of Ag powder (1.5–1.8 μm particle sizes) reduces the tan δ value of the VBB15 glass by about 20–30%. Therefore, the VBBT glasses show the interesting and unusual nature of heterogeneous transport that distinguishes them from many TMO glasses.

ACKNOWLEDGMENT

One of the authors (Miss Sahana Chakraborty) is grateful to the University Grants Commission, India, for providing her a research fellowship.

REFERENCES

1. M.E. Lines and A.M. Glass, *Principles and Applications of Ferroelectrics and Related Materials* (Clarendon Press, Oxford, 1979).
2. R. Wernicke, in *Grain Boundary Phenomena in Electronic Ceramics*, edited by L.H. Lavirison (The American Ceramic Society Inc., Westerville, OH, 1981), Vol. 1, p. 261.
3. K.K. Som, S. Molah, K. Bose, and B.K. Chaudhuri, Phys Rev B 47, 534 (1993).
4. A. Ghosh and B.K. Chaudhuri, *Key Engineering Materials*, edited by A.K. Bhatnagar (Trans Tech Publications, Bay Village, OH, 1986), Vol. 15, p. 515.
5. M. Sayer and A. Mansingh, Phys. Rev. B 6, 4629 (1972)
6. B.K. Chaudhuri, K. Chaudhuri, and K.K. Som, J. Phys. Chem. Solids 50, 1149 (1990).
7. P.B. Macedo, C.T. Moynihan, and R. Bose, Phys. Chem. Glasses 13, 171 (1972).
8. K.S. Cole and R.H. Cole, J. Chem. Phys. 9, 341 (1941).
9. F.A. Grant, J. Appl. Phys. 29, 76 (1957).
10. S. Chakraborty, S. Mollah, A.K. Bera, and B.K. Chaudhuri, unpublished.

ELSEVIER

Journal of Non-Crystalline Solids 167 (1994) 192–198

JOURNAL OF NON-CRYSTALLINE SOLIDS

Study of dielectric relaxation behaviour in Li-doped semiconducting Bi–Sr–Ca–Cu–O glasses

S. Mollah, A.K. Chakraborty, S. Chakraborty, K.K. Som, B.K. Chaudhuri *

Solid State Physics Department, Indian Association for the Cultivation of Science, Calcutta 700 032, India

(Received 25 November 1992; revised manuscript received 17 July 1993)

Abstract

The temperature- (80–450 K) and frequency- (50–10^4 Hz) dependent dielectric constant, ϵ', and loss, ϵ'', for Li-doped $Bi_4Sr_3Ca_{3-z}Li_zCu_4O_x$ ($z = 0.0$, 0.1, 0.5 and 1.0) glasses, which become high T_c superconducting oxides in their crystalline phases, have been measured. Unlike many other semiconducting transition metal oxide glasses, the temperature variations of ϵ' and ϵ'' of the Li-doped glasses do not have a peak within the frequency range of the investigations. However, the imaginary (M'') parts of the dielectric modulus, M^*, have peaks indicating Debye-type dielectric relaxation behaviour with a distribution of relaxation times. The relaxation behaviour is thermally activated.

1. Introduction

The transition metal oxide (TMO) glasses are important for many technological applications [1–3]. Some of these glasses might also be used [4] for first protonic switching. Recently, a special type of TMO glasses with compositions such as $Bi_4Sr_3Ca_3Cu_4O_x$ have been prepared [5–10] and show superconductivity in their crystalline phases. The $Bi_4Sr_3Ca_3Cu_4O_x$ [4:3:3:4] glass, in particular, has been well investigated because it is a glass from which a single phase $Bi_2Sr_2CaCu_2O_8$ (2:2:1:2) superconductor can be prepared [10]. Another alkali-metal-doped Bi–Sr–Ca–Cu–O glass system with lower glass melting temperature and higher superconducting transition temperature, T_c, in their crystalline phases have also been reported [7,9]. Electrical properties of these Li-doped $Bi_4Sr_3Ca_{3-z}Li_zCu_4O_x$ glasses have recently been investigated by us [7] and it has been shown that these Li-doped glasses are precursors for high T_c superconductors.

In the present paper, we report dielectric behaviour of these Li-doped $Bi_4Sr_3Ca_{3-z}Li_zCu_4O_x$ glasses (hereafter referred to as LIY0, LIY1, LIY2 and LIY3 glasses, respectively, for $z = 0.0$, 0.1, 0.5 and 1.0). It has also been shown that the temperature- and frequency-dependent dielectric properties of these Li-doped [4:3:3:4] glasses, which are superconductors in their crystalline phases, show some uncommon features not generally observed in many transition metal oxide glasses (such as V_2O_5–Bi_2O_3, Fe_2O_3–Bi_2O_3,

* Corresponding author. Tel: +91-33 46 9371. Telefax: +91-33 473 2805. Telex: (021)5501 ICAS IN.

SSDI 0022-3093(93)E0242-Z

V_2O_5–P_2O_5 [13–16], etc.) which are not superconductors in their respective crystalline phases.

2. Experimental

Detailed methods of preparation of these LIY glasses by a quick quenching technique from their respective liquid states have been discussed [7,8]. Since the copper contents of these glasses change with melting temperature as well as with duration of melting [11], each glass specimen was kept in its liquid state at 1200°C for 1 h and then the liquid was quickly quenched between two copper blocks at room temperature. The total copper contents of the glasses as shown in Table 1 are obtained from chemical analysis similar to our earlier work [8]. The amorphous state of all the samples was confirmed by X-ray diffraction (Philips X-ray generator model PW 1130 coupled with a diffractometer model PW 1710) and scanning electron microscopy (Hitachi model 415A) [7,17]. The densities of samples were measured by Archimedes' principle using carbon tetrachloride as the immersion liquid. The mean of five independent measurements with each sample was taken as the value of density. Thermogravimetric analysis (TGA) of the glass samples was carried out with a thermal analyzer (Shimadzu DT-30 (Japan)) three times for each sample. The glass transition temperature, T_g, was determined from the mean value of T_g obtained for two samples of each composition using a differential scanning calorimeter (DSC) (Perkin–Elmer DSC-7). The dielectric constant, ϵ', was measured by a capacitance bridge (GR Model 1615A) in a low temperature cryostat [5,11–13]. The temperature and frequency dependences of ϵ' and ac conductivities, $\sigma_{ac}(\omega)$, of the $Bi_4Sr_3Ca_{3-z}Li_zCu_4O_x$ samples were measured simultaneously using this bridge technique. The imaginary parts of dielectric constant, ϵ'', were calculated from the ac conductivity data as discussed below.

3. Results

Some of the important parameters of the glasses are shown in Table 1. Total copper concentrations of the glasses obtained by chemical analysis do not vary appreciably as shown in Table 1. The theoretical values of oxygen content, x, in the $Bi_4Sr_3Ca_{3-z}Li_zCu_4O_x$ samples are 16.00, 15.95, 15.75 and 15.50 for $z = 0.0$, 0.1, 0.5, and 1.0, respectively. With increase of Li (or decrease of Ca) in the LIY glasses, the values of x, obtained from thermogravimetric analysis, change ($\pm 5\%$ from the corresponding theoretical values [11,17]). The glass samples containing oxygen greater than the above limit were not measured. The densities of the Li-doped samples (except for the LIY1 sample) are larger than the undoped [4:3:3:4] samples (Table 1).

The ac conductivity, $\sigma_{ac}(\omega)$, of these samples can be fitted [18] with the relation $\sigma_{ac}(\omega) = A\omega^s$ (where A slowly varies with temperature and s is

Table 1
Some important parameters for the $Bi_4Sr_3Ca_{3-z}Li_zCu_4O_x$ [LIY] glasses ($z = 0.0$, 0.1, 0.5 and 1.0)

Sample	z	Cu content (±0.02 wt%)	Density (±0.05 g/cm³)	T_g [a] (±5°C)	T_c [b] (±1.0 K)	θ_D [c] (±5 K)	ν_r (Hz)	W_r (±0.01 eV)
LIY0	0	15.90	5.88	426	84.0	428	–	–
LIY1	0.1	15.60	5.82	405	86.0	510	3.00×10^{10}	0.52
LIY2	0.5	15.55	6.02	400	88.5	500	3.40×10^{9}	0.46
LIY3	1.0	15.65	6.59	380	89.5	490	3.20×10^{10}	0.55

T_g, glass transition temperature; T_c, superconducting transition temperature; θ_D, Debye temperature; ν_r, characteristic phonon energy; W_r, activation energy for conductivity relaxation.

[a] Obtained from DSC studies. Since T_g depends on various factors such as thermal history, annealing rate, etc., we studied DSC of the as quenched glass samples with heating rate of 10°C/min for all samples.

[b] Obtained from the resistivity measurements of the respective glass-ceramic phases which was obtained by annealing the glass at 850°C for 48 h in air.

[c] Calculated from the dependence of $\log_{10}(\sigma_{dc})$ on $10^3/T$.

the frequency exponent, generally less than unity). Here, we assume A is a constant.

The temperature dependence of ϵ' and ϵ'' for one of the Li-doped glass samples is shown in Figs. 1(A) and 1(B), respectively. Similar temperature dependence is also observed for other compositions.

3.1. Variation of ϵ' with temperature and frequency

Fig. 1(A) shows the temperature dependence of dielectric constants, ϵ', for a typical Li-doped (LIY1) glass sample at different measuring frequencies. No peak in ϵ' as a function of T is observed for any of these glass samples. (It should be noted that the solid lines in Fig. 1 and in other figures discussed below are guides for the eye.) ϵ' varies slowly with temperature to a temperature, T_Θ, where T_Θ is a function of composition of the samples. For the three compositions, T_Θ ranges from 240 to 270 K. T_Θ is the temperature at

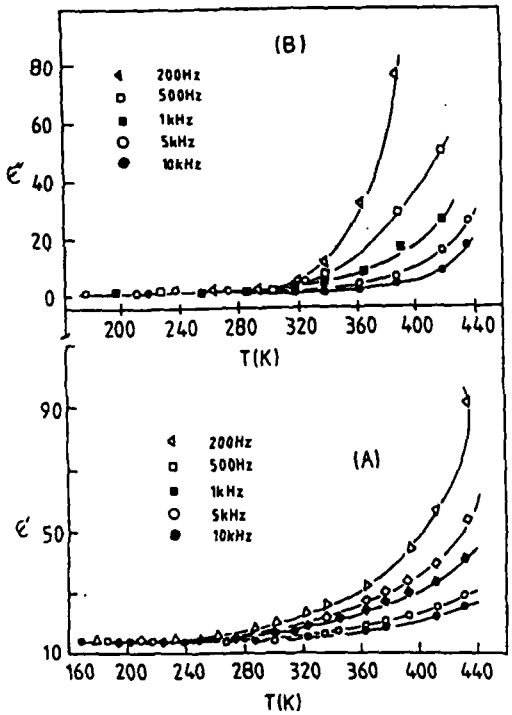

Fig. 1. (A) Thermal variation of dielectric constant, ϵ', of $Bi_4Sr_3Ca_{3-z}Li_zCu_4O_x$ sample with $z = 0.1$ at different frequencies. (B) Temperature dependence of ϵ'' for $Bi_4Sr_3Ca_{3-z}Li_zCu_4O_x$ sample with $z = 0.5$ at different frequencies. Lines are guides for the eye.

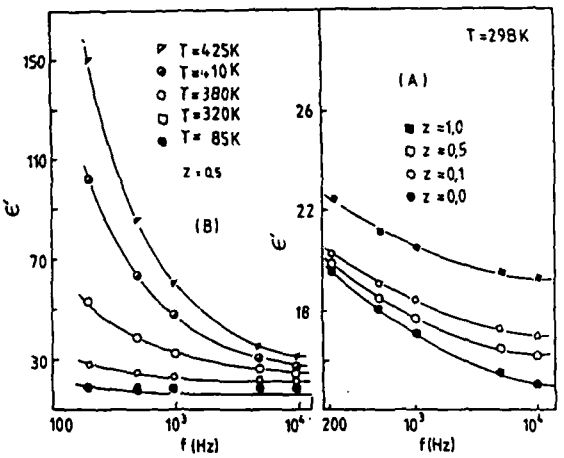

Fig. 2. (A) Frequency dependence of ϵ' at a fixed temperature of 298 K for different $Bi_4Sr_3Ca_{3-z}Li_zCu_4O_x$ samples with $z = 0.0$, 0.1, 0.5 and 1.0. (B) Frequency dependence of ϵ' for a typical Li-doped sample $Bi_4Sr_3Ca_{2.5}Li_{0.5}Cu_4O_x$ at different temperatures.

which the value of ϵ' begins to increase from an approximately constant value at temperatures $< T_\Theta$. T_Θ is equal approximately to half of the Debye temperature, Θ_D, of the respective samples. The values of Θ_D as shown in Table 1 are calculated from the dc conductivity, σ_{dc}, data [7] (from knowledge of the temperature at which the linear dependence of $\log(\sigma_{dc})$ on $10^3/T$ ends [19]). Above this temperature (T_Θ), the values of ϵ', for samples of all the compositions, increase with increase of temperature. The variation of ϵ' with frequency for all the LIY samples (shown in Fig. 2(A)) at a temperature of 298 K indicates that at this temperature values of ϵ' are larger for the samples with larger Li concentration. Frequency dependence of one of the glass samples with $z = 0.5$ at different temperatures, as shown in Fig. 2(B), indicates that the values of ϵ' decrease with increase of frequency. The rate of this decrease of ϵ' is larger at higher temperatures. The other samples with different Li concentrations have a similar temperature dependence. This type of dependence is also similar to those of many TMO glasses [13–16].

3.2. Variation of ϵ'' with temperature and frequency

The dielectric loss, ϵ'', has been calculated from the relation $\epsilon''(\omega) = \sigma_{ac}(\omega)/\epsilon_0\omega$ (where

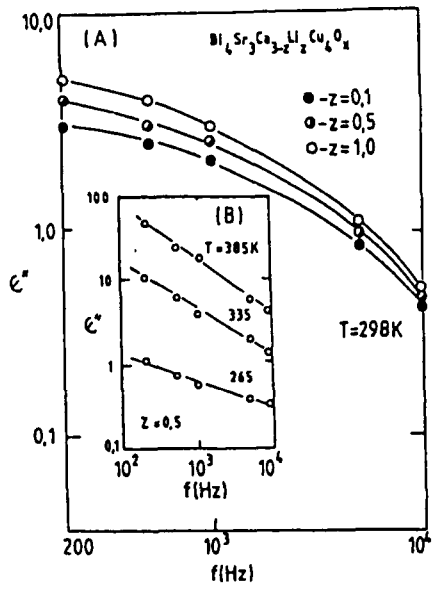

Fig. 3. (A) Frequency variations of ϵ'' at a temperature (298 K) for samples of different $Bi_4Sr_3Ca_{3-z}Li_zCu_4O_x$ glasses. (B) Frequency variations of ϵ'' for a sample of a typical Li-doped glass (with $z = 0.5$) at different temperatures.

$\sigma_{ac}(\omega)$ is the real part of the ac conductivity and ϵ_0 is the permittivity of free space). Fig. 1(B) shows that the temperature dependence of ϵ'' is similar to that of ϵ' (as shown in Fig. 1(A)). Dielectric constants, ϵ', and dielectric losses ϵ'', of the LIY glasses do not have maxima when plotted as a function of temperature (Figs. 1(A) and 1(B)).

The frequency variations of ϵ'' at a temperature of 298 K for different LIY glass samples are shown in Fig. 3(A). A similar plot shown in Fig. 3(B) is for the sample with $z = 0.5$ and for different temperatures. No maxima are evident in the data in Figs. 3(A) and 3(B).

4. Discussion

Unlike many TMO glasses [13–16], the present LIY glass samples as well as the undoped $Bi_4Sr_3Ca_3Cu_yO_x$ ($y = 0$–5) glass samples [12], all becoming superconductors in their crystalline phases, do not have a maximum in the temperature variation of ϵ' within the temperature and frequency ranges of our investigations. Here, it is interesting to note that another series of glassy precursors for high T_c superconductors, Pb-doped $Bi_{4-z}Pb_zSr_3Ca_3Cu_4O_x$ ($z = 0$–1.0) glasses [17], do not have maxima in the frequency and thermal dependences of dielectric constant.

The temperature variation of ϵ'' for the LIY samples differs from that of the other semiconducting TMO glasses mentioned above [13,16]. However, the temperature dependent dielectric loss, ϵ'', for the undoped samples of the [4:3:3:4] sample had a maximum around 360 K (Fig. 4). This behaviour distinguishes the undoped [4:3:3:4] sample from the corresponding Li-doped samples. It was also shown earlier [12] that the $Bi_4Sr_3Ca_3Cu_yO_x$ glasses with more than 35 mol% CuO do not have maxima in the dielectric loss. The Bi–Sr–Ca–Cu–O glasses with higher concentrations of CuO (> 35 mol% CuO) and the present Li-doped glasses have a similar behaviour of ϵ' on T and ϵ'' on T without maxima. Similarly the Pb-doped $Bi_{4-z}Pb_zSr_3Ca_3Cu_4O_x$ ($z =$ 0–0.1) samples also do not have maxima in their ϵ' (T) and ϵ'' (T) between 80 and 450 K [17]. Both Li-doped and Pb-doped Bi–Sr–Ca–Cu–O samples have similar variations of ϵ' and ϵ'' with temperature and frequency.

Since the differences in the oxygen content of the Li-doped samples is small, the sample-depen-

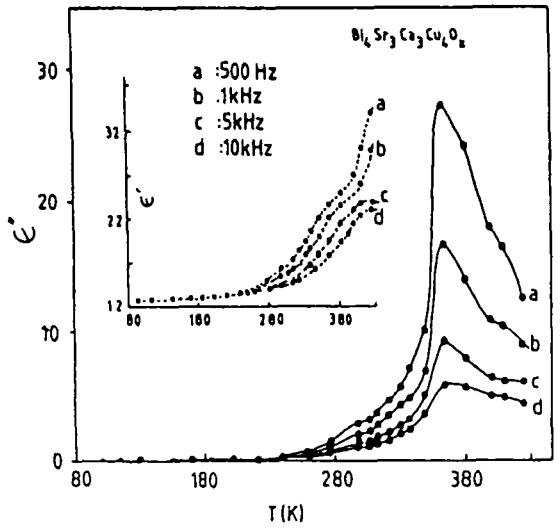

Fig. 4. Thermal variation of ϵ'' for the $Bi_4Sr_3Ca_3Cu_4O_x$ base glass sample with different frequencies. The inset shows the thermal variation of ϵ' for the same sample.

dent changes observed in the dielectric properties of the Li-doped samples are assumed to be primarily due to variations in z (i.e., Li content). Although no maxima are observed in the temperature dependence of ϵ' or ϵ'' for a fixed frequency, these samples have a Debye-type dielectric relaxation process with relaxation frequency f_c ($= \frac{1}{2}\pi\tau$, τ being the relaxation time) [20]. This relaxation process can be more clearly resolved from the calculation of dielectric modulus, M^*, as discussed below.

It is also to be noticed that a dielectric loss peak is expected around the temperature at which the dc conductivity approaches the total frequency-dependent conductivity in the higher temperature region [21]. The errors in the difference of two nearly equal quantities (total conductivity and ac conductivity) [22] are large. The dielectric loss, ϵ'' ($= (\sigma_{tot}(\omega) - \sigma_{dc})/\omega\epsilon_0$, where $\sigma_{tot}(\omega)$ is the total measured frequency-dependent conductivity), in this higher temperature region is an example. For this reason, a well resolved maxima in the temperature dependence of ϵ'' may not be observed in the dielectric properties of the LIY-type samples. It is, therefore, difficult to use conventional methods of estimating the relaxation frequency and magnitude of the dispersion. Therefore, another approach has been adopted.

Following Macedo et al. [23], the dielectric modulus is calculated from $M^* = M' + iM'' = 1/\epsilon^*$. The real and the imaginary parts of dielectric modulus are related to the real, ϵ', and imaginary, ϵ'', parts of dielectric constant, ϵ^*, as $M' = \epsilon'/[(\epsilon')^2 + (\epsilon'')^2]$ and $M'' = \epsilon''/[(\epsilon')^2 + (\epsilon'')^2]$. The dielectric modulus, M^*, provides important information particularly when the dc conductivity is large compared with the ac conductivity. A plot of M'' versus temperature should give a maximum at the temperature for which the dielectric relaxation frequency is equal to the measuring frequency. For a typical LIY sample (with $z = 0.1$), we have plotted M' as a function of temperature for different frequencies (Fig. 5). A similar temperature dependence is also observed for other LIY compositions. We observed that, at lower temperature, M' tends to a constant value for all frequencies. This temperature dependence of M' indicates that the dielectric

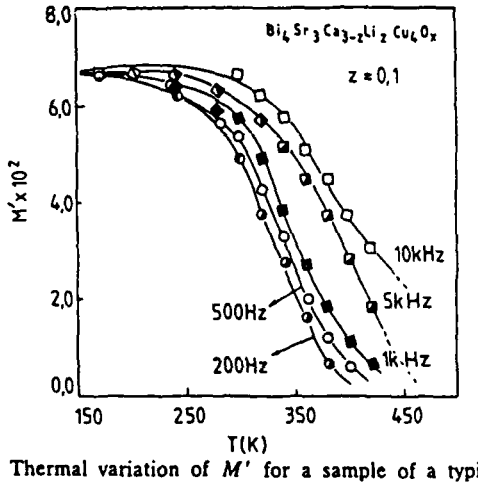

Fig. 5. Thermal variation of M' for a sample of a typical $Bi_4Sr_3Ca_{3-z}Li_zCu_4O_x$ glass, with $z = 0.1$, for different frequencies.

constant of samples of the LIY glasses is thermally activated. In order to demonstrate the dielectric dispersion, the imaginary part, M'', was also calculated and plotted in Fig. 6 as a function of temperature at different frequencies. The data in Fig. 6 show maxima which shift to higher temperature for higher frequencies. Similar dependence of the temperature and frequency variation of M'' is also observed for other LIY compositions. The position of the maximum in the variation of M'' as a function of temperature (Fig. 6) gives the temperature at which the measuring frequency is equal to the relaxation frequency, $f_c = \nu_r \exp(-W_r/k_BT)$ (where ν_r is the characteristic phonon frequency and W_r is the activation energy for conductivity relaxation). The values of both ν_r and W_r are obtained from the plots of log f_c versus $10^3/T$ (Fig. 7) as shown in Table 1. The values of ν_r and W_r are found to be less than those obtained from the dc conductivity data [7], also observed in V_2O_5–TeO_2 glasses [14]. However, the nature of this plot (Fig. 7) is similar to the variation of dc conductivity [7] of the LIY glasses with temperature, which indicates that the relaxation mechanism is thermally activated similar to the dc conductivity. It is interesting to note that, like LIY samples, all the $Bi_4Sr_3Ca_3Cu_yO_x$ glasses ($y = 0$–5) also have maxima [12] in the (M''–T) plots, indicating Debye-type relaxation behaviour.

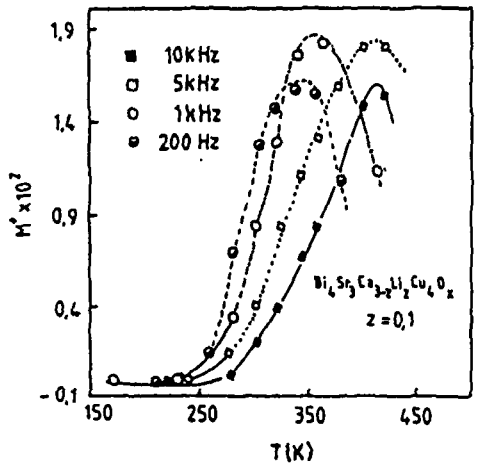

Fig. 6. Thermal variation of M'' for a typical $Bi_4Sr_3Ca_{3-z}Li_zCu_4O_x$ sample with $z = 0.1$ for different frequencies.

A method of displaying Debye type relaxation is by drawing a Cole–Cole plot [24]. Cole and Cole [24] suggested that ϵ'' as a function of ϵ' gives important information about the distribution of relaxation times. The slope of the arc at $\epsilon'' = 0$ is a measure of the extent of distribution of relaxation times. According to Cole and Cole [24], the complex dielectric constant, ϵ^*, is given by $\epsilon^* = \epsilon_\infty + (\epsilon_s - \epsilon_\infty)/[1 + (i\omega\tau_m)^{1-\beta}]$ where τ_m is the mean relaxation time, β is an emperical parameter lying between 0 and 1, and ϵ_s and ϵ_∞ are the static and high frequency dielectric constants, respectively. The slope of the Cole–Cole plot at $\epsilon'' = 0$ gives the value of $(1-\beta)\pi/2$. For $\beta = 0$, it leads to a single relaxation time, while $\beta = 1$ corresponds to an infinite distribution of relaxation times. We have plotted ϵ'' versus ϵ' at a temperature ($T = 265$ K) and at different frequencies for samples of all the LIY glasses as shown in Fig. 8. The corresponding plots obtained for three different temperatures for a typical LIY glass ($z = 0.1$) is shown in Fig. 9. The data do not fit a semi-circular curve, suggested by Cole and Cole [24]. According to Grant [25], the large value of high frequency capacitance or dc conductivity of the glasses is responsible for such a dependence. Due to the lack of a fit of the data to a pure semi-circular curve of the Cole–Cole plots and because of the limited frequency range of our measurements, it is difficult to determine a value for β. However, from Figs. 8 and 9, it is evident that β for different glasses is greater than zero but less than 1 and almost the same for all glass compositions and at all temperatures (except in the low temperature region where σ_{ac} approaches σ_{dc}). From this deduction we suggest that these Li-doped [4:3:3:4] samples have a distribution of relaxation times.

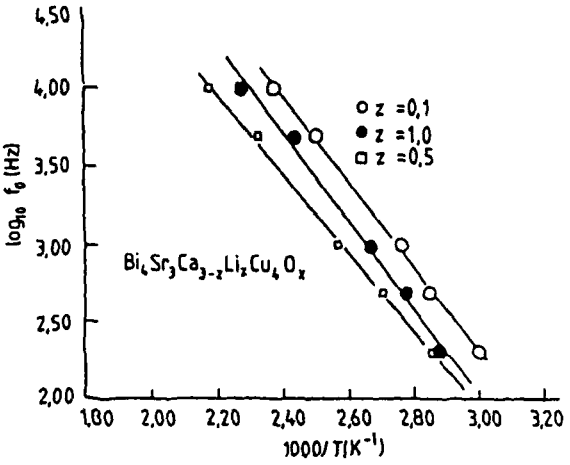

Fig. 7. Variation of f_c with inverse temperature for different samples with $z = 0.1$, 0.5 and 1.0.

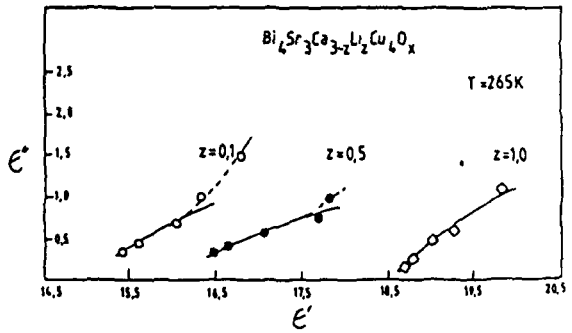

Fig. 8. Cole–Cole plots for samples of different LIY glasses with $z = 0.1$, 0.5 and 1.0 at a fixed temperature of 265 K.

The small decrease of density in the LIY1 sample compared with the [4:3:3:4] glass may be due to various causes such as changes of microstructures. We note that these glasses are viscous and wires and tapes could be easily drawn from the liquids. One such wire is shown in Fig. 10. These wires can be made superconducting by annealing at 800°C for 48 h in air. Superconduct-

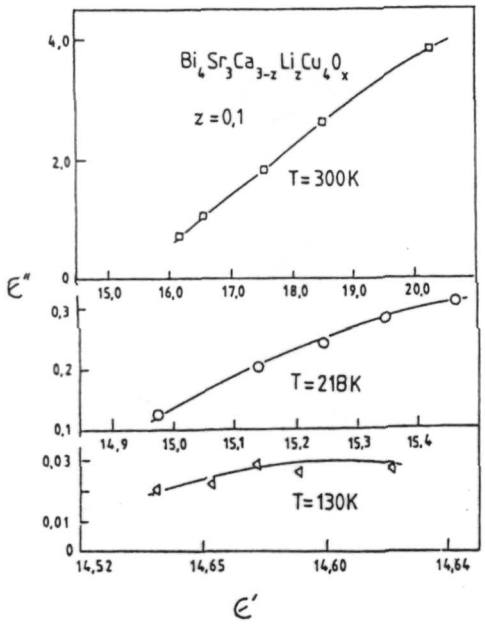

Fig. 9. Cole–Cole plots for a typical LIY sample ($z = 0.1$) at different fixed temperatures.

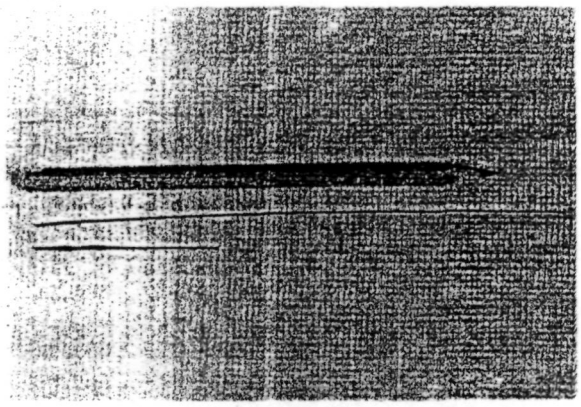

Fig. 10. Photograph of the LIY3 glass wires drawn from the melt.

ing transition temperatures for some glass-ceramics is shown in Table 1 for the sake of completeness.

5. Conclusion

The Li-containing glasses exhibit Debye-type dielectric relaxation behaviour with a distribution of relaxation times. The relaxation process is predominantly thermally activated similar to the dc conductivities of these glasses.

S.M. is grateful to the Council of Scientific and Industrial Research (CSIR), Government of India, for providing a research fellowship.

References

[1] S. Nakamura and N. Ichinose, J. Non-Cryst. Solids 95&96 (1987) 849.
[2] H. Hirashima, Y. Watanabe and T. Yoshida, J. Non-Cryst. Solids 95&96 (1987) 825.
[3] A. Ghosh, J. Appl. Phys. 64 (1988) 2652.
[4] M.E. Lines, J. Appl. Phys. 69 (1991) 6876.
[5] K.K. Som and B.K. Chaudhuri, Phys. Rev. B41 (1990) 1581.
[6] H. Zheng, M.W. Colby and J.D. Mackenzie, J. Non-Cryst. Solids 127 (1991) 143.
[7] S. Mollah, K.K. Som, K. Bose, A. Chakravorty and B.K. Chaudhuri, Phys. Rev. B46 (1992) 11075.
[8] K.K. Som, S. Mollah, K. Bose and B.K. Chaudhuri, Phys. Rev. B45 (1992) 1655.
[9] T. Moriuchi, T. Kawai, K. Mitsui, K. Orura and S. Kawai, Physica C168 (1990) 309.
[10] R.C. Baker, W.M. Hurng and H. Steinfink, Appl. Phys. Lett. 54 (1989) 371.
[11] K.K. Som, PhD thesis, Jadavpur University, Calcutta (1990).
[12] K.K. Som, S. Mollah, K. Bose and B.K. Chaudhuri, Phys. Rev. B47 (1993) 534.
[13] B.K. Chaudhuri, K. Chaudhuri and K.K. Som, J. Phys. Chem. Solids 50 (1989) 1137, 1148.
[14] A. Mansingh, V.K. Dhawan and M. Sayer, Philos. Mag. B48 (1983) 215.
[15] M. Sayer, A. Mansingh, J.M. Reyes and G. Rosenblatt, J. Appl. Phys. 42 (1971) 2857.
[16] A. Mansingh, J.K. Vaid and R.P. Tandon, J. Phys. C8 (1975) 1023.
[17] S. Mollah, PhD thesis, Jadavpur University, Calcutta (1993).
[18] A.R. Long, Adv. Phys. 31 (1982) 553.
[19] J. Schnakenberg, Phys. Status Solidi 28 (1968) 623; E. Gorham-Bergeron and D. Emin, Phys. Rev. B15 (1977) 3667.
[20] M. Sayer and A. Mansingh, Phys. Chem. Glasses 23 (1982) 83.
[21] M. Sayer and A. Mansingh, Phys. Rev. B6 (1972) 4629.
[22] A. Mansingh, Bull. Mater. Sci. (India) 2 (1980) 325.
[23] P.B. Macedo, C.T. Moynihan and R. Bose, J. Phys. Chem. Glasses 13 (1972) 171.
[24] K.S. Cole and R.H. Cole, J. Chem. Phys. 9 (1941) 341.
[25] F.A. Grant, J. Appl. Phys. 29 (1957) 176.

ac conductivity in $Bi_4Sr_3Ca_3Cu_yO_x$ ($y=0$–5) and $Bi_4Sr_3Ca_{3-z}Li_zCu_4O_x$ ($z=0.1$–1.0) semiconducting oxide glasses

S. Mollah, K. K. Som, K. Bose, and B. K. Chaudhuri
Solid State Physics Department, Indian Association for the Cultivation of Science, Calcutta-700 032, India

(Received 7 August 1992; accepted for publication 26 March 1993)

Semiconducting oxides such as $Bi_4Sr_3Ca_3Cu_yO_x$ ($y=0$–5) and $Bi_4Sr_3Ca_{3-z}Li_zCu_4O_x$ ($z=0.1$, 0.5, and 1.0), many of which become superconductors in their glass-ceramic phases, have been studied over the wide temperature (77–450 K) and frequency (100–10^4 Hz) ranges. The universal power-law behavior [exponent $s<1$ in $\sigma(\omega)=\sigma_0+A\omega^s$] is found to be valid for most of these glasses. Little deviation from this limiting behavior is also observed for some glass compositions in the low-temperature and high-frequency regions. The correlated barrier hopping model based on the pair approximation is found to be more appropriate for explaining the frequency- and temperature-dependent ac conductivity data. The random walk type of model, on the other hand, is found to be valid for a limited range of temperature.

I. INTRODUCTION

Transition-metal-oxide (TMO) glasses are becoming very important for many of their technological applications, viz., switching and memory devices,[1] cathode ray tube materials,[2] ferrites,[3] fast photonic switching,[4] etc. Recently TMO glasses such as Y-Ba-Cu-O (Ref. 5) and (Bi,Pb)-Sr-Ca-Cu-O (Refs. 6 and 7) with various compositions have been prepared which become high-temperature superconducting oxides (HITSO) in their respective glass-ceramic (GC) phases. It was reported earlier[8] that the Bi-Sr-Ca-Cu-O-type glasses show higher values of glass transition temperature T_g, Debye temperature θ_D, electrical resistance, etc. compared to other TMO glasses. Furthermore, the addition of alkali metal ions in the Bi-Sr-Ca-Cu-O-based oxide reduces the glass melting temperature and also increases[8] the superconducting transition temperatures T_c.

In the present article we report the results of the frequency and temperature-dependent ac conductivity $[\sigma_{ac}(\omega,T)]$ measurements in several lithium-doped and undoped $Bi_4Sr_3Ca_3Cu_4O_x$ oxide glasses becoming HITSO in their GC phases. The basic $Bi_4Sr_3Ca_3Cu_4O_x$ glass is the precursor material for preparing single-phase $Bi_2Sr_2Ca_1Cu_2O_8$ superconductor.[7] We have also provided evidence that both the frequency and the temperature dependencies of σ_{ac} in these glasses can be well described in the light of the correlated barrier hopping (CBH) model of the pair approximation type. The random free-energy barrier model[9] based on random-walk-type models[9,10] used in percolation theory, on the other hand, fits the ac conductivity data for a limited range of temperature.

II. EXPERIMENTAL RESULTS

The detailed method of preparation and characterization of these two series of glasses, viz., $Bi_4Sr_3Ca_3Cu_yO_x$ or [Y] glasses (with $y=0$–5) and $Bi_4Sr_3Cu_{3-z}Li_zCu_4O_x$ or [LIY] glasses (with $z=0.1$, 0.5 and 1.0) has already been discussed.[8] Here the square brackets denote nomenclature of the glasses. In brief, all these glasses were made from high-purity (99.99%) metallic oxides by quick quenching from their respective melts (all samples melted at 1100 °C for 2 h). For electrical measurements, disk-shaped samples of 10.0 mm diameter and 1.0 mm thickness were cut, polished, and gold coated on both the faces by sputtering. The gold-coated samples were again annealed at 200 °C for 2 h for good contact of the electrodes with the glass surface. The ac conductivity data were obtained[11–13] with a General Radio (model GR-1615A) capacitance bridge which measures equivalent parallel conductance and capacitance of the sample in a three-terminal arrangement within the low-temperature cryostat. Scanning electron microscopy (SEM) and x-ray powder-diffraction studies indicated the amorphous character of all the glasses.[8,12] Some characteristic parameters of the glasses, such as the glass transition temperature T_g, density ρ, total copper ion concentration N, and superconducting transition temperature T_c of the corresponding glass ceramics are shown in Tables I and II, respectively, for the [Y] and [LIY] glasses.

The logarithm of total measured frequency-dependent conductivities $[\sigma_t(\omega)]$ as a function of inverse temperature along with the dc conductivity for a typical [Y] (viz., $Bi_4Sr_3Ca_3Cu_4O_x$) and some [LIY] glasses is shown in Fig. 1. The general behavior of the $\sigma_t(\omega)$ vs $10^3/T$ curves for both [Y] and [LIY] glasses is very similar to those of the other TMO glasses.[13–15] It is further observed that the temperature variation of $\sigma_t(\omega)$ is much slower than that of the dc conductivity in the low-temperature region. At higher temperature, on the other hand, the temperature dependence of $\sigma_t(\omega)$ becomes much stronger and ultimately the measured conductivities at all frequencies coincide with the dc conductivity σ_{dc}. The actual values of $\sigma_{ac}(\omega)$ as shown in Fig. 2 were calculated by subtracting the measured dc conductivity data from the measured total frequency-dependent conductivity $\sigma_t(\omega)$ such that $\sigma_{ac}(\omega)=\sigma_t(\omega)-\sigma_{dc}$ which is applicable for all TMO glasses including the base glass $Bi_4Sr_4Ca_3Cu_4O_x$ studied earlier.[11,12]

The variation of σ_{ac} with Cu and Li concentrations at different fixed temperatures and frequencies is shown in

 0021-8979/93/74(2)/931/7/$6.00

TABLE I. Some important parameters for the $Bi_4Sr_3Ca_3Cu_yO_x$ [Y] glasses.

Sample	Y1	Y2	Y3	Y4	Y5	Y6	Y7	Y8
Value of y	0	1	2	3	3.5	4	4.5	5
Starting Cu content (wt %)[a]	0	4.26	8.09	11.56	13.17	14.70	16.17	17.57
Final Cu content (wt %)[b]	0	4.63	8.21	11.64	14.05	15.90	17.22	18.08
Density ρ ($g\,cm^{-3}$)	5.97	5.95	5.93	5.92	5.89	5.88	5.88	5.86
$C=Cu^{1+}/Cu_{total}$	...	0.79	0.75	0.70	0.75	0.78	0.80	0.79
T_g (°C)[c]	408	402	422	422	440	426	446	431
T_c (K)[d]	...	...	...	70	79	85	85.5	76

[a]Calculated concentration of the copper atom used at the time of preparation of the glasses.
[b]Obtained from atomic absorption spectroscopy.
[c]Glass-transition temperature as obtained from differential thermal analysis (DTA) studies of the glass samples.
[d]Superconducting transition temperature of the glass ceramics obtained from the four-probe resistivity measurements.

Fig. 3. The ac conductivities for both the glasses increases with Cu and Li concentrations.

III. THEORETICAL DISCUSSION

Like many amorphous semiconductors and insulators, the ac conductivities of the [Y] and [LIY] glasses at a fixed temperature is found to obey the universal dynamic response,[16,17]

$$\sigma_{ac}(\omega,T)=A(T)\omega^s, \tag{1}$$

where $A(T)$ is a constant generally dependent on temperature and s is the frequency exponent and generally lies in the range $0<s<1$.

The plots of $\log \sigma_{ac}(\omega)$ as a function of $\log(\omega)$ at various temperatures as shown in Fig. 4 for the [Y] and [LIY] glasses indicate that the slopes of the curves at a particular temperature remain almost constant over the entire frequency range of our measurements. Therefore, the values of s do not change much with change in frequency. However, at the high-temperature region Fig. 4 shows a slight increase of the slope, hence an increase of the values of s with the increase of measuring frequency. The frequency exponent s was calculated from the slopes of the $\log \sigma_{ac}(\omega)$ vs $\log(\omega)$ curves (Fig. 4). The variation of s with temperature for some [Y] glasses, viz., $Bi_4Sr_3Ca_3Cu_4O_x$ and $Bi_4Sr_3Ca_3Cu_3O_x$, are shown in Fig. 5. Similarly the variation of s for the [LIY] glasses are shown in Fig. 6. The frequency exponent s is found to decrease considerably with the increase of temperature in all the [Y] and [LIY] glasses and for low frequency the values of s tends to 1. This limiting value of s is visualized for all the glasses. However, it is observed from Figs. 5 (for [Y] glasses) and 6 (for [LIY] glasses) that slightly higher values of s (>1) also exist for some of the glass compositions. This behavior of s is also observed in many other TMO glasses.[13–15]

To explain the temperature and frequency dependencies of $\sigma_{ac}(\omega,T)$ and its frequency exponent s, theoretical models of the pair approximation type (PAT), viz., the quantum-mechanical tunneling (QMT) model,[18] corre-

TABLE II. Some important parameters for the $Bi_4Sr_3Ca_{3-x}Li_xCu_4O_x$ [LIY] glasses. The meaning of the parameters is the same as in Table I.

Sample	LIY0	LIY1	LIY2	LIY3
Values of z	0	0.1	0.5	1.0
T_g (°C)	426	405	399	372
Density ρ ($g\,cm^{-3}$)	5.88	5.82	6.02	6.59
T_c (K)	85	86.0	88.5	89.5

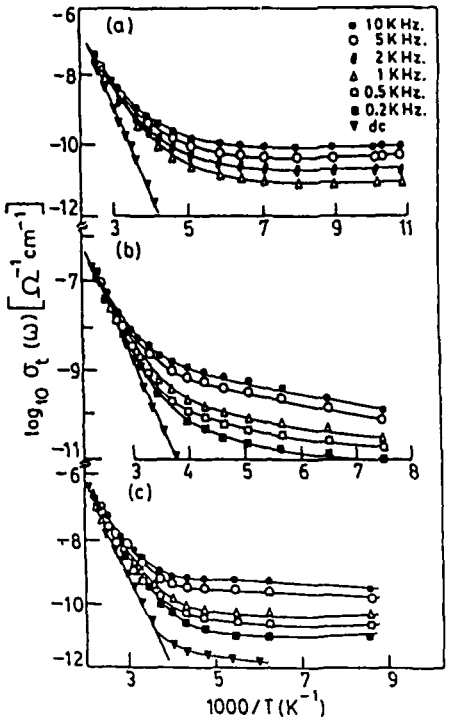

FIG. 1. Variation of dc conductivities and total frequency-dependent ac conductivities of the (a) $Bi_4Sr_3Ca_3Cu_4O_x$, (b) $Bi_4Sr_3Ca_{2.9}Li_{0.1}Cu_4O_x$, and (c) $Bi_4Sr_3Ca_{2.0}Li_{1.0}Cu_4O_x$ glasses at different frequencies

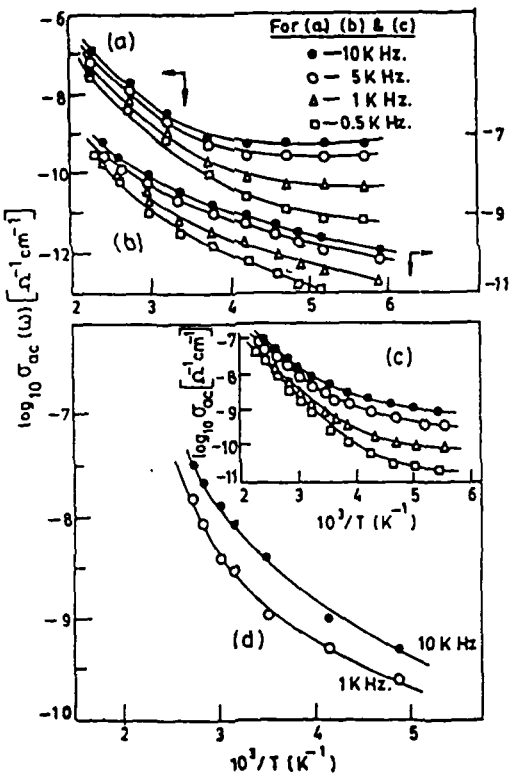

FIG. 2. Thermal variation of actual ac conductivities of the (a) $Bi_4Sr_3Ca_2Li_1Cu_4O_x$, (b) $Bi_4Sr_3Ca_{2.9}Li_{0.1}Cu_4O_x$, (c) $Bi_4Sr_3Ca_{2.5}Li_{0.5}Cu_4O_x$, and (d) $Bi_4Sr_3Ca_3Cu_4O_x$ glasses at different frequencies.

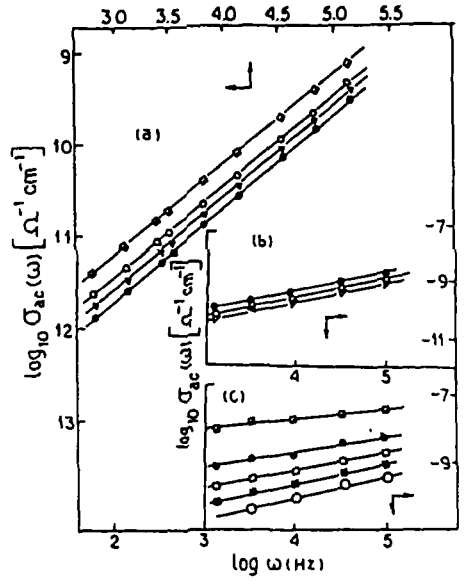

FIG. 4. Variation of ac conductivities of the [Y] and [LIY] glasses with frequencies at different fixed temperatures: (a) $Bi_4Sr_3Ca_3Cu_3O_x$ (●), $Bi_4Sr_3Ca_3Cu_4O_x$ (◁), $Bi_4Sr_3Ca_3Cu_{4.5}O_x$ (○), and $Bi_4Sr_3Ca_3Cu_5O_x$ (◪) glasses at 100 K; (b) $Bi_4Sr_3Ca_2Li_1Cu_4O_x$ (●), $Bi_4Sr_3Ca_{2.5}Li_{0.5}Cu_4O_x$ (○), and the $Bi_4Sr_3Ca_{2.9}Li_{0.1}Cu_4O_x$ glasses (▷) at 250 K; (c) for the $Bi_4Sr_3Ca_{2.9}Li_{0.1}Cu_4O_x$ glass at 385 K (◪), 295 K (●), 240 K (□), 204 K (■), and 170 K (○).

lated barrier hopping (CBH) model,[19] overlapping large polaron tunneling (OLPT) model,[20] small polaron tunneling (SPT) model,[21] etc., have been applied by different scientists. There is another group of scientists who used

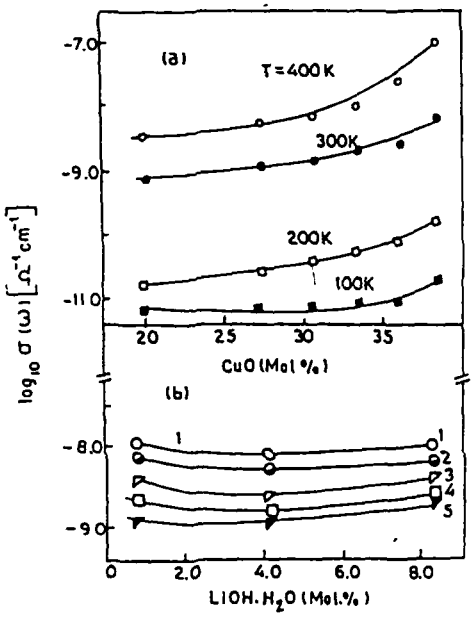

FIG. 3. Variation of $\sigma_{ac}(\omega)$ with CuO and $LiOH \cdot H_2O$ concentrations of (a) [Y] glasses at 1 kHz for different temperatures, and (b) [LIY] glasses at 350 K for different frequencies: (1) 10 kHz; (2) 5 kHz; (3) 1 kHz; (4) 500 Hz; and (5) 200 Hz.

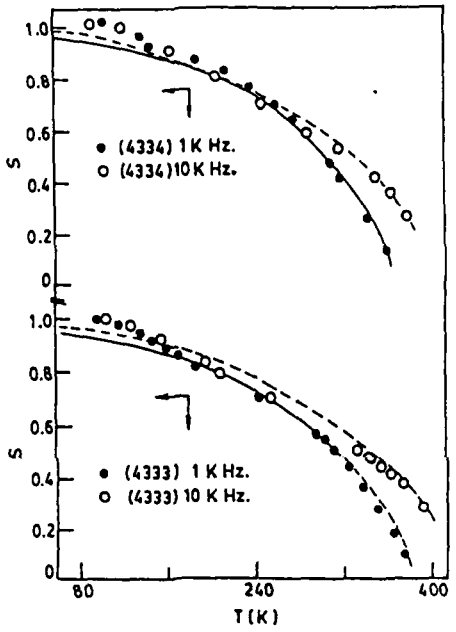

FIG. 5. Temperature dependencies of the exponent (s) for the $Bi_4Sr_3Ca_3Cu_4O_x$ (4334) and $Bi_4Sr_3Ca_3Cu_3O_x$ (4333) glasses at 1 and 10 kHz. The parameters obtained from the best-fit curves (solid and dashed lines) using the CBH model are given in Table III.

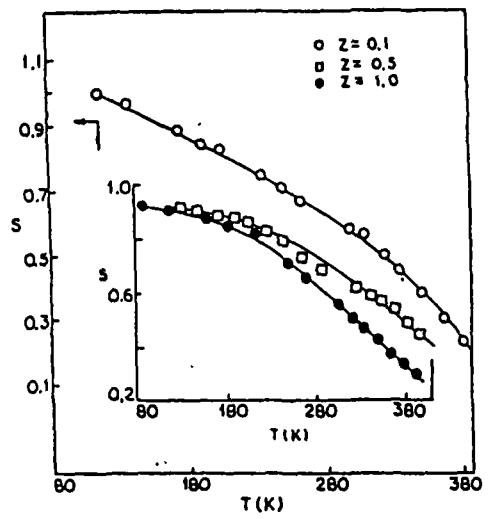

FIG. 6. Thermal dependencies of the exponent (s) for the $Bi_4Sr_3Ca_{2.9}Li_{0.1}Cu_4O_x$ glass (○), $Bi_4Sr_3Ca_{2.5}Li_{0.5}Cu_4O_x$ glass (□), and $Bi_4Sr_3Ca_2Li_1Cu_4O_x$ glass (●) at 1 kHz. The parameters obtained from the best-fit curves (solid lines) using the CBH model [Eq. (7)] are shown in Table IV.

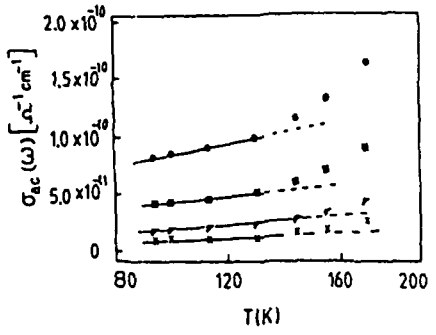

FIG. 7. Thermal variation of ac conductivities of the $Bi_4Sr_3Ca_3Cu_4O_x$ glass at various frequencies: (●) 10 kHz, (■) 5 kHz, (▼) 2 kHz, and (×) 1 kHz. The solid lines are best-fit curves using the QMT model (the model parameters are shown in Table III).

random-walk-type[9,10] (RWT) models for explaining $\sigma(\omega,T)$ data. A general discussion on the applicability of the PAT models has been made earlier.[12]

For the present glass systems a comparative investigation of both type of models (PAT and RWT) have been made. We shall concentrate first on the vastly used pair-approximation-type QMT and the CBH models which appear to be more appropriate than any other existing models. The QMT model predicts a linear temperature dependence of $\sigma_{ac}(\omega)$ and a temperature-independent s which is given by

$$s=1+4/\ln(\omega\tau_0), \tag{2}$$

where ω is the angular frequency of measurement and τ_0 is the characteristic relaxation time of the carrier. For a typical value of $\tau_0=10^{-13}$ s and $\omega/2\pi=10^4$ Hz, one obtains a value of $s=0.81$. However, it is clearly observed from Figs. 5 and 6 that the frequency exponent s decreases markedly with the increase of temperature at all fixed frequencies for the [Y] and [LIY] glasses. Furthermore, the QMT model predicts a linear temperature dependence of $\sigma_{ac}(\omega)$; but, the temperature variation of $\sigma_{ac}(\omega)$ (as shown in Fig. 2 for $Bi_4Sr_3Ca_3Cu_4O_x$ and Li-doped glasses) indicates a sharper increase of $\sigma_{ac}(\omega)$ with the rise of temperature, particularly in the high-temperature regime. However, in the low-temperature region $\sigma_{ac}(\omega)$ appears to increase linearly with temperature [i.e., $\sigma_{ac}(\omega)=T^n$ with $n=1$] as shown in Fig. 7 for the $Bi_4Sr_3Ca_3Cu_4O_x$ glass. For the Li-doped [LIY] glasses the values of $\sigma_{ac}(\omega)$ in the low-temperature range (below 120 K) are very small compared to the [Y] glasses. We have also attempted to fit the experimental values of $\sigma_{ac}(\omega,T)$ with Eq. (3) (below) for the ac conductivity in the QMT model, viz.,

$$\sigma_{ac}(\omega,T)=A_0e^2k_BT\alpha^{-1}[N(E_F)]^2\omega R_\omega^4, \tag{3}$$

where k_B is the Boltzmann constant, e is the electronic charge, T is the absolute temperature, α is the wave function decay constant, $N(E_F)$ is the density of states at the Fermi level, and $N=k_BTN(E_F)$ is the number actually contributing to the ac loss. The constant A_0 is a temperature-independent factor. R_ω is the characteristic tunneling distance and is given by

$$R_\omega=(1/2\alpha)\ln(1/\omega\tau_0). \tag{4}$$

The values of the parameters obtained from the least-squares fitting in the linear region (below 130 K) of the curves for the [Y] and [LIY] glasses are shown in Table III. The values of $N(E_F)$ thus obtained for the [Y] glasses are in the range of 1.39×10^{20}–3.29×10^{20} and for [LIY] glasses they are in the range of 1.89×10^{20}–$3.60\times10,^{20}$ which seems to be quite reasonable for the present glass systems. Therefore, the QMT model appears to be consistent with the behavior of ac conductivity in the low-temperature region only but completely fails to interpret the observed temperature dependence of the frequency exponent s.

The temperature-dependent frequency exponent can also be obtained within the framework of QMT model by assuming that the carriers form nonoverlapping small polarons. In this case the frequency exponent is predicted to increase with the increase of temperature. In [Y] and [LIY]

TABLE III. Values of $N(E_F)$ obtained from the QMT model for the [LIY] or $Bi_4Sr_3Ca_{3-z}Li_zCu_4O_x$ (4:3:3−z:z:4) and [Y] or $Bi_4Sr_3Ca_3Cu_y$ (4:3:3:y) glasses.

Sample	Glass composition (Bi:Sr:Ca:Li:Cu)	Frequency (kHz)	$N(E_F)$ (10^{20} eV^{-1} cm^{-3})
LIY1	(4:3:2.9:0.1:4)	1.0 (10.0)	2.50 (3.10)
LIY2	(4:3:2.5.0.5:4)	1.0 (10.0)	2.96 (3.54)
LIY3	(4:3:2:1:4)	1.0 (10.0)	2.71 (3 60)
Y3	(4:3:3:0:2)	1.0 (10.0)	1.39 (1.47)
Y4	(4:3:3:0:3)	1.0 (10.0)	1.46 (1 65)
Y5	(4.3:3:0:3.5)	1.0 (10.0)	1.69 (1.90)
Y6	(4:3:3:0:4)	1.0 (10.0)	1.89 (2.28)
Y7	(4:3:3:0:4.5)	1.0 (10.0)	1.90 (2.28)
Y8	(4:3:3:0:5)	1.0 (10.0)	2.74 (3 29)

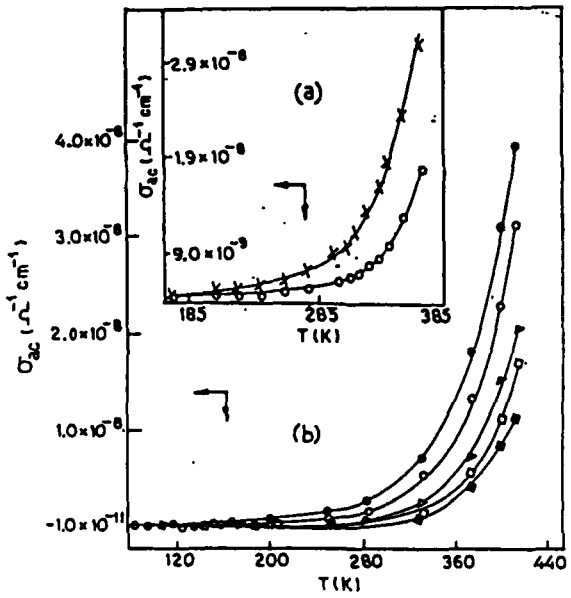

FIG. 8. Thermal variation of $\sigma_{ac}(\omega)$ for different frequencies: (a) $Bi_4Sr_3Ca_3Cu_4O_x$ glass at two different frequenices at 10 kHz (×) and 1 kHz (○); (b) $Bi_4Sr_3Ca_{2.5}Li_{0.5}Cu_4O_x$ at 10 kHz (●), 5 kHz (○), 1 kHz (◁), 500 Hz (□), and 200 Hz (■). The solid lines are best-fit curves using the CBH model (the model parameters are shown in Table IV).

glasses, however, the frequency exponent decrease, with the increase of temperature (Figs. 5 and 6).

Another interesting and competitive model predicting the correct temperature and frequency dependencies of the exponent is the correlated barrier hopping (CBH) model. In this model it is assumed that the charge carriers hop between defect centers over the potential barrier separating them. The barrier height W is correlated with the separation R of the defect centers. This model was proposed by Pike[19] for single electron hopping and extended by Elliott[19,22] for the case of two electrons hopping simultaneously. The ac conductivity in this CBH model, in the narrow-band limit, is given by[22]

$$\sigma_{ac}(\omega)=\frac{\pi^3}{24}N^2\epsilon_0\epsilon\omega R_\omega^6 \tag{5}$$

where N is the total number of carriers actually contributing to the ac loss, ϵ_0 is the free-space permittivity, R_ω is the hopping distance, and ϵ is the dielectric constant of the medium (sample). The hopping distance R_ω is given by

$$R_\omega=[e^2/\pi\epsilon_0\epsilon]/[W_M+k_BT\ln(\omega\tau_0)], \tag{6}$$

and the frequency exponent s is obtained from the relation

$$s=1-\frac{6k_BT}{[W_M+kT\ln(\omega\tau_0)]}, \tag{7}$$

where W_M is the energy required to remove the electron completely from the site to the excited state. Therefore, in the CBH model the exponent s is temperature dependent (s increasing toward unity as $T\to0$) which is in marked contrast to that of the QMT model.[18]

TABLE IV. Parameters for the [LIY] and [Y] glasses obtained from the CBH model [relaxation time τ_0 is calculated (a) from fitting of s vs temperature using Eq. (7), and (b) from fitting the σ_{ac} vs temperature curves using Eq. (5)].

Sample	Measuring frequency (kHz)	W_M (eV)	Relaxation time τ_0 (10^{13} s) (a)	(b)	N (10^{20} cm^{-3})
LIY1	1.0	0.853	3.23	2.90	6 77
	10.0	0.853	···	1.36	3 13
LIY2	1.0	0.828	9.46	1.93	3.02
	10.0	0.828	···	2.00	2 20
LIY3	1.0	0.826	4.09	1.40	4 38
	10.0	0.826	···	1.93	3 00
Y3	1.0	0.960	0.64	0.38	1 29
	10.0	0.960	0.23	0.21	1 37
Y4	1.0	0.900	0.50	0.45	1.41
	10.0	0.900	0.14	1.40	1 53
Y5	1.0	0.870	1.90	0.83	1.65
	10.0	0.870	1.12	0.64	1.68
Y6	1.0	0.850	3.20	0.21	1.80
	10.0	0.850	2.40	0.10	1.00
Y7	1.0	0.840	3.19	0.78	2.59
	10.0	0.830	2.26	1.20	2 10
Y8	1.0	0.820	3.34	1.06	2.42
	10.0	0.820	2.10	2.90	2.60

A critical test of the CBH model comes from the temperature dependence of $\sigma_{ac}(\omega)$ and its frequency exponent s. In Fig. 8 we have plotted the experimental $[\sigma_{ac}(\omega)-T]$ curves for typical $Bi_4Sr_3Ca_3Cu_4O_x$ and $Bi_4Sr_3Ca_{2.5}Li_{0.5}Cu_4O_x$ glasses along with the corresponding theoretical curves obeying Eq. (5). The reasonably good fitting of the experimental and theoretical (solid lines) curves indicates that for explaining the ac conductivity data of [Y] and [LIY] glasses, the CBH model is the most appropriate one. For multicomponent glasses such as [Y], [LIY], etc., the random-walk-type model according to Dyre[9] and Bryksin[10] is found to be not successful to explain ac conductivity data for a wide range of temperature and frequency as discussed below. However, the CBH model [Eq. (7)] clearly explains the thermal variation of s (Figs. 5 and 6) for some [Y] and [LIY] glasses. The little discrepancy existing between the theoretical and the experimental values as observed from Figs. 5 and 6 might be due to the correlation between the barrier height and the hopping length R_ω.

The CBH model [Eq. (7)], however, predicts an upper bound of s equal to 1 as $T\to0$, but the CBH or any other existing model cannot explain the higher values of s (>1) observed in some glasses. The values of the parameters W_M and τ_0, etc. obtained from the best fitting of the experimental data with the CBH model for [Y] and [LIY] glasses are listed in Table IV. The values of W_M are somewhat less than the predicted value of twice the activation energy (as obtained from the dc conductivity data), while the values

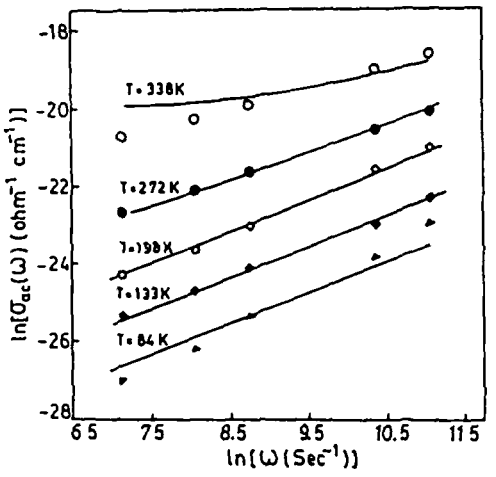

FIG. 9 Variation of $\ln[\sigma_{ac}(\omega)]$ with $\ln(\omega)$ for the $Bi_4Sr_3Ca_{2.5}Li_{0.5}Cu_4O_x$ glass at different temperatures The solid lines are the best-fit curves using Dyre's model [Eq (8)] The model parameters are shown in Table V

TABLE V. Model parameters obtained from best fitting of the ac conductivity data with Dyre's model [Eq (8)] for two $Bi_4Sr_3Ca_{3-z}Li_zCu_4O_x$ or [LIY] glasses

	$Bi_4Sr_3Ca_{2.5}Li_{0.5}Cu_4O_x$			$Bi_4Sr_3Ca_2Li_1Cu_4O_x$		
Sample	T (K)	τ (s)	$\Delta\epsilon^a$	T (K)	τ (s)	$\Delta\epsilon^a$
	84	1.413	0 479	84	0 193	0 654
	133	3 250	1 835	117	0 179	0 809
	154	3.688	3 124	160	0.139	1 177
	177	4 019	4 726	182	0 147	1 494
	198	3.500	6 139	230	0 143	2 665
	218	2 651	7 294	264	0 125	6 363
	236	0.898	7.805	299	1.28×10^{-2}	10 843
	272	$6\,62\times10^{-2}$	8 857	330	$3\,38\times10^{-3}$	16 224
	306	$4\,94\times10^{-3}$	8 361	361	1.19×10^{-3}	26 881
	324	$1\,40\times10^{-3}$	7 189	390	$2\,04\times10^{-4}$	20 736
	338	$4\,35\times10^{-4}$	5 403	412	$5\,09\times10^{-5}$	14 372
	369	$6\,07\times10^{-5}$	3 428	The fit is poor above 400 K		

The fit is poor above 380 K

$^a\Delta\epsilon=\epsilon(0)-\epsilon(\infty)$

of τ_0 and hence $\nu_0(=1/\tau_0)$ are in reasonably good agreement with those obtained from the dc conductivity data and are nearly equal to the values obtained for other semiconducting TMO glasses. Using the same values of W_M and τ_0 from Table IV we have calculated the values of the hopping length R_ω from Eq. (6). Putting these values of R_ω and ϵ from our experimental dielectric constant data[12] in Eq. (5) we find the values of N (shown in Table IV) which are in good agreement with those shown in Table III.

The RWT models such as the random free-energy barrier model of Dyre[9] and effective-medium method of Bryksin[10] can also be used to fit the ac conductivity data. A somewhat arbitrary method is used by Bryksin[10] for formulating the concept of bonds between nearest neighbors Furthermore, according to Bryksin[10] in the relation $\mathrm{Re}[\sigma(\omega)]-\sigma(0)\sim\omega^{s'}$, s' is initially equal to two then sharply decreases, then slowly grows and approaches unity, and then decreases again with the increase of frequency. Such behavior is not indicated by our experimental data. The predicted ω^2 dependence at low frequencies is possibly beyond the lowest frequency of our measurement. The random free-energy barrier model used by Dyre,[9] on the other hand, is very interesting and is found to fit our data quite well for a limited range of temperatures. According to Dyre[9] the expression for frequency-dependent ac conductivity is given by

$$\sigma_{ac}(\omega)=\frac{\sigma(0)\omega\tau\tan^{-1}(\omega\tau)}{\{[\tan^{-1}(\omega\tau)]^2+[\ln(1+\omega^2\tau^2)^{1/2}]^2\}}. \quad (8)$$

Equation (8) is very simple with only one unknown parameter (τ) which is temperature dependent and is also related to $\epsilon(0)$ and $\epsilon(\infty)$ through dc conductivity $\sigma(0)$ as $\epsilon_0\Delta\epsilon=\sigma(0)\tau/2$, where $\Delta\epsilon=\epsilon(0)-\epsilon(\infty)$. We tried to fit the ac conductivity data for the [LIY] glasses with Eq (8) For a typical [LIY] glass (viz , $Bi_4Sr_3Ca_{2.5}Li_{0.5}Cu_4O_x$) the best fit curve with Eq (8) is shown in Fig 9 where $\ln\sigma(\omega)$ is plotted against $\ln(\omega)$ for different fixed temperatures. It is found from Fig. 9 that the fitting of the experimental data with theory [Eq. (8), solid line] is quite good for intermediate temperatures between 350 and 125 K (for the $z=0.5$ glass). Above and below this range fitting with Dyre's model is poor. For the other [LIY] glass with $z=1\,0$ the corresponding fitting with Eq. (8) is also poor above 400 K. Similar is the case with other glass compositions. The fitting parameter τ and calculated value of $\Delta\epsilon$ for two [LIY] glasses with $z=0.5$ and 1.0 are shown in Table V. Here we also mention that from the fitting parameters shown in Table V we do not find the Curie-law-type behavior, viz., $\Delta\epsilon\propto T^{-1}$, as suggested by Dyre.[9] More elaborate investigation with such RWT models will be published elsewhere; however, it is clear that even the RWT model is not sufficient to explain the exact variation of the frequency exponent s becoming greater than one for some glasses. Compared to the random-walk-type model the PAT model, such as CBH, gives more elaborate information about the characteristic features of the [Y]- and [LIY]-type multicomponent glasses of our investigation.

IV. SUMMARY AND CONCLUSION

To summerize, the ac conductivities of the Bi-Sr-Ca-Cu-O-based glasses which become superconductors in their respective glass-ceramic phases (see Table I) are found to obey the universal relation $\sigma_{ac}(\omega)=A\omega^s$ with $0<s<1$ for most of the glasses. Some of the glass compositions, however, indicate values of s larger than one The pair-approximation-type correlated barrier hopping (CBH) model is found to be the best model representing this universal behavior of the exponent s tending to 1 as well as the overall temperature dependence of $\sigma_{ac}(\omega,T)$ of these glasses The similar QMT model apparently explains the low-temperature ac conductivity data but completely fails to predict the temperature dependence of the frequency exponent s even at low temperature On the other hand, the random free-energy barrier model[9] of random walk type can also explain the ac conductivity data in the intermedi-

ate temperature range. For very high and very low temperatures this theory fails; however, both the RWT model and the PAT model explain the above-mentioned limiting behavior of the exponent s. The values of s slightly greater than one as observed for some of the [LIY] glasses in the low-temperature region remain unexplained with these models (both PAT and RWT). For most of the $Bi_4Sr_3Ca_3Cu_yO_x$ glasses the values of the exponent are very close or equal to unity at low temperature depending on the copper concentration. Recently we also noticed larger values of s for the $Bi_{4-y}Pb_ySr_3Ca_3Cu_4O_x$ ($y=0.1$, 0.5, and 1.0) glass.[23] Some scattered reports showing very large values of the exponent ($s=2$) for TMO glasses also are found in the literature.[24,25] However, it was pointed out by Long[20] that the larger values of s (>1) might be due to the effect of contact resistance,[26] formation of barrier capacitance at the electrodes,[27] etc, but this criterion is not enough to explain the large value of exponent[28] s. A critical analysis of frequency and temperature dependencies of the exponent s becoming greater than one is still necessary.

ACKNOWLEDGMENTS

The authors are grateful to the Council of Scientific and Industrial Research (CSIR) and the Department of Science and Technology for financial assistance to complete the work.

[1] H. Hirashima, Y. Watanabe, and T. Yoshida, J. Non-Cryst. Solids 95 & 96, 825 (1987).
[2] Y. Sakuri and J. Yamaki, J. Electrochem. Soc. 132, 512 (1985).
[3] S. Nakamura and N. Ichinose, J. Non-Cryst. Solids 95 & 96, 849 (1987).
[4] M. E. Lines, J. Appl. Phys. 69, 6876 (1991).
[5] T. Komatsu, K. Imai, K. Matusita, M. Takata, Y. Iwai, A. Kawakami, Y. Kaneko, and T. Yamashita, Jpn. J. Appl. Phys. 26, L1148 (1987).
[6] D. Shi, M. Blank, M. Patel, D. G. Hinks, A. W. Mitchell, K. Vandervoort, and H. Claus, Physica C 156, 882 (1988); T. Komatsu, R. Sato, and K. Matusuita, Appl. Phys. Lett. 54, 170 (1990); K. B. R. Varma, K. J. Rao, and C. N. R. Rao, *ibid.* 54, 69 (1989).
[7] R. C. Baker, W. M. Hurng, and H. Steinfink, Appl. Phys. Lett. 54, 371 (1989).
[8] K. K. Som, S. Mollah, K. Bose, and B. K. Chaudhuri, Phys. Rev. B 45, 1655 (1992); S. Mollah, K. K. Som, K. Bose, A. K. Chakraborty, and B. K. Chaudhuri, *ibid.* 46, 11 075 (1992).
[9] J. C. Dyre, J. Appl. Phys. 64, 2456 (1988).
[10] V. V. Bryksin, Sov. Phys. Solid State 22, 1421 (1980).
[11] K. K. Som and B. K. Chaudhuri, Phys. Rev. B 41, 1581 (1990).
[12] K. K. Som, Ph.D. thesis, Jadavpur University, Calcutta, 1991.
[13] B. K. Chaudhuri, K. Chaudhuri, and K. K. Som, J. Phys. Chem. Solids 50, 1155 (1989).
[14] A. Ghosh and B. K. Chaudhuri, J. Non-Cryst. Solids 83, 151 (1986).
[15] M. Sayer, A. Mansingh, J. M. Reyes, and G. Rosenblatt, J. Appl. Phys. 42, 2857 (1971).
[16] A. K. Jonscher, J. Non-Cryst. Solids 8-10, 293 (1972).
[17] W. K. Lee, J. F. Liu, and S. Walker, Phys. Rev. Lett. 67, 1559 (1991).
[18] M. Pollak and T. H. Geballe, Phys. Rev. 122, 1742 (1961); M. Pollak, Philos. Mag. 23, 519 (1971); P. N. Butcher and K. J. Hayden, *ibid.* 36, 657 (1977); A. L. Efros, Philos. Mag. B 43, 829 (1981).
[19] G. E. Pike, Phys. Rev. B 6, 1572 (1972); S. R. Elliott, Philos. Mag. 36, 1291 (1977).
[20] A. R. Long, Adv. Phys. 31, 553 (1982); A. R. Long, W. Balkan, W. R. Hogg, and R. P. Ferrier, Philos. Mag. B 45, 497 (1982).
[21] D. Emin and T. Holstein, Ann. Phys. (NY) 53, 439 (1969).
[22] S. R. Elliott, Adv. Phys. 36, 135 (1987).
[23] B. K. Chaudhuri, S. Mollah, K. K. Som, and A. Bera (unpublished).
[24] G. S. Linsley, A. E. Owen, and G. M. Hayatte, J. Non-Cryst. Solids 4, 208 (1970).
[25] M. A. Hassan, C. A. Hogarth, and G. R. Moridi, Phys. Status Solidi A 101, 537 (1987).
[26] R. A. Street, G. R. Davis, and A. D. Yoffe, J. Non-Cryst. Solids 5, 276 (1971); A. I. Lakatos and M. Abkowitz, Phys. Rev. B 3, 1791 (1971).
[27] J. G. Simmons, G. S. Nadkarni, and M. C. Lancaster, J. Appl. Phys. 41, 538 (1970).
[28] All the theoretical models such as CBH, QMT, small polaron tunneling, overlapping large polaron tunneling, etc. give the upper bound of s as 1.0. However, in a slightly modified CBH model [S. R. Elliott, Philos. Mag. B 38, 325 (1979)] considering the effect of glass transition the frequency exponent s is given by $s=1-\{6k_BT/[W_M+k_BT\ln(\omega\tau_0)]\}+T/8T_g$. In principle this model can give a value of s greater than 1.0 depending on the values of W_M and T_g. In such a situation, however, s would be an increasing function of temperature and also $\sigma_{ac}(\omega)$ would be a decreasing function of temperature. This type of variation of s and $\sigma_{ac}(\omega)$ with temperature is not supported by any experimental evidence. With a slightly different approach Elliott [Ref. 22] has shown that a phononless photon-assisted electronic transition can lead to a superlinear frequency dependence of $\sigma_{ac}(\omega)$ and the frequency exponent s can be expressed as $s=2-[4/\ln(2I_0/\hbar\omega)]$ which is valid for high frequency ($\hbar\omega>k_BT$), where I_0 is the overlap integral. For a reasonable value of the $I_0\simeq 5$–10 eV and $\omega=10^6$ Hz one finds $s=1.83$. It should be noted here that for some of the [LIY] (this article), and also for Pb-doped $Bi_{4-y}Pb_yCa_3Sr_3Cu_4O_x$ ($y=0.1$, 0.5, and 1) glasses (unpublished) we find values of s slightly greater than one in low-temperature regions.

PHYSICAL REVIEW B VOLUME 47, NUMBER 1 1 JANUARY 1993-I

Debye-type dielectric behavior of Bi-Sr-Ca-Cu-O-based transition-metal oxide glasses: Precursors for oxide superconductors

K. K. Som, S. Mollah, K. Bose, and B. K. Chaudhuri
Solid State Physics Department, Indian Association for the Cultivation of Science, Calcutta-700 032, India
(Received 27 April 1992; revised manuscript received 23 July 1992)

Detailed measurements of the frequency- (50 Hz to 10 kHz) and temperature- (80–450 K) dependent dielectric constant (ϵ') and dielectric loss (ϵ'') have been performed for the $Bi_4Sr_3Ca_3Cu_yO_x$ ($y=0$ to 5) glasses. Some of these glasses become high-temperature superconducting oxides in their respective glass-ceramic phases. The dielectric properties of these glasses are found to follow a Debye-type relaxation behavior with relaxation frequency f_c [$=\nu_c \exp(-W_c/k_BT)$]. The relaxation behavior is thermally activated in nature similar to the dc electrical-conduction process of these glasses observed in our earlier investigation.

In a series of papers,[1–5] a special type of transition-metal oxide (TMO) glasses such as $Bi_4Sr_3Ca_3Cu_4O_x$[4:3:3:4] has been shown to become high-temperature superconducting oxides (HTSO) in their respective glass-ceramic (GC) phases. This particular glass composition is a precursor for single-phase $Bi_2Sr_2CaCu_2O_8$ (2:2:1:2) superconductor.[1] Such precursors may be applicable[3,4] to the fabrication of superconducting wires, films, tapes, etc. Recently alkali-metal-doped Bi-Sr-Ca-Cu-O glass ceramic (GC) showing increase of superconducting transition temperature (T_c) and lowering of glass melting and ceramic sintering temperatures have been studied.[6,7]

The purpose of this paper is to report the temperature- and frequency-dependent dielectric properties of the [4:3:3:y] glasses with $y=0-5$. It is also our motivation to find from these studies if there is any unusual behavior of these glasses compared to those of other TMO glasses, which do not become superconductors in their GC phases.

Details of the preparation of such glasses have already been discussed in our earlier papers.[2,3,5] Some characteristic parameters of these glasses are shown in Table I for comparison.

The dielectric constant was measured by a capacitance bridge (General Radio Model 1615A) along with low-temperature cryostatic arrangements similar to our earlier works.[3,8] The eight glass samples studied are G1($y=0$), G2($y=1$), G3($y=2$), G4($y=3$), G5($y=3.5$), G6($y=4$), G7($y=4.5$), and G8($y=5$). The temperature and frequency variations of dielectric constant (ϵ') and ac conductivity of these glasses were measured simultaneously using the above-mentioned bridge. Like many amorphous semiconductors and insulators,[8] the ac conductivity (σ_{ac}) of the Bi-Sr-Ca-Cu-O glass at a fixed temperature is found to follow an equation of the form[9] $\sigma_{ac}(\omega)=A\omega^s$ [where A is a constant slowly varying with temperature (T), and s is the frequency exponent generally less than unity], which indicates that the loss mechanism should have a distribution of relaxation times in-

TABLE I. Some important parameters for the $Bi_4Sr_3Ca_3Cu_yO_x$ (4:3:3:y) glasses (T_g and T_{cr} denote glass transition and crystallization temperatures, respectively).

Sample	G1	G2	G3	G4	G5	G6	G7	G8
Values of y	0	1	2	3	3.5	4	4.5	5
Starting Cu content (wt%)	0	4.26	8.09	11.56	13.17	14.70	16.17	17.57
Final Cu content (wt%)[a]	0	4.63	8.21	11.64	14.06	15.90	17.22	18.08
T_g (°C)	408	402	422	423	440	426	446	431
T_c (K)[b]				70	79	85	85.5	76
τ_0 (10^{-13} sec) at 1 kHz		(c)	0.64	0.50	1.90	3.20	3.19	3.34
		(d)	0.38	0.45	0.83	0.21	0.78	1.06
τ_0 (10^{-13} sec) at 10 kHz		(c)	0.23	0.14	1.12	2.40	2.26	2.10
		(d)	0.21	1.40	0.64	0.10	1.20	2.90

[a]Obtained from atomic absorption spectroscopy.
[b]Superconducting transition temperatures of the glass ceramics.
[c]From fitting of the s vs T curves (Ref. 11).
[d]From fitting of the $\sigma_{ac}(\omega)$ vs T curves (Ref. 11).

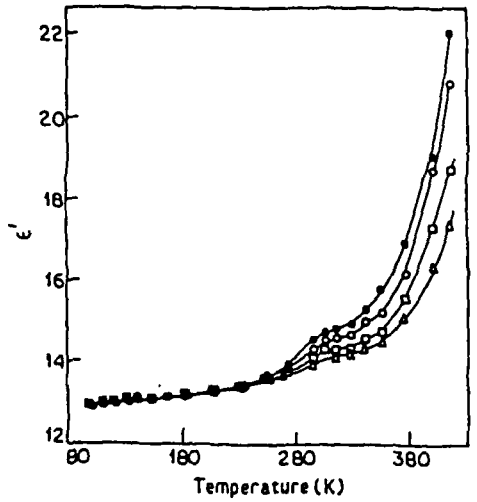

FIG. 1. Thermal variation of dielectric constant (ϵ') for G4 glass at (●) 1 kHz, (○) 2 kHz, (□) 5 kHz, and (△) 10 kHz.

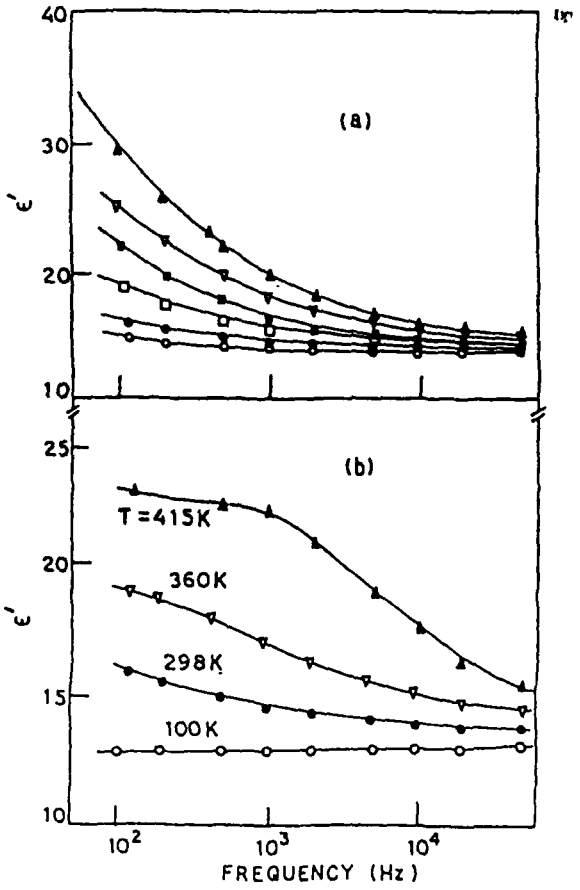

FIG. 2. (a) Frequency variation of dielectric constant of different glass samples at 298 K; (○) G3, (●) G4, (□) G5, (■) G6, (▽) G7, and (▲) G8 glasses. (b) Frequency dependence of dielectric constant at different temperatures for the G4 glass.

stead of a single relaxation time. This behavior is also visualized from the temperature- and frequency-dependent dielectric constant (ϵ') and dielectric loss (ϵ'') data discussed in this paper.

The temperature variation of ϵ' for a typical glass sample G4 at different fixed frequencies is shown in Fig. 1. All the other glasses of this series behave in a similar fashion. The dielectric constant varies slowly with increasing temperature up to about 300 K and then the magnitude of ϵ' increases sharply with further increase of temperature. This increase is sharper for lower measuring frequency. Some transition-metal vanadate glasses[8,10] showed peaks in the $\epsilon'-T$ curves that was considered[10] to be a characteristic feature of Debye-type dielectric relaxation in these glasses. Though such peaks have not been observed in the present glass samples, a Debye-type dielectric dispersion becomes evident from the thermal variation of dielectric loss (ϵ'') of these glasses (to be discussed later).

The frequency dependence of ϵ' for some glasses at a fixed temperature of 298 K shown in Fig. 2(a) is similar to that observed in the TMO glasses. For a typical glass G4 the frequency dependences of ϵ' at different temperatures are shown in Fig. 2(b). The value of ϵ' is found to increase with the increase of CuO concentration in the glasses.

The dielectric loss ϵ'' as mentioned above has been calculated from the ac conductivity [$\sigma_{ac}(\omega)$] data using the relation $\epsilon''=\sigma_{ac}(\omega)/\epsilon_0(\omega)$ (where ϵ_0 is the permittivity of

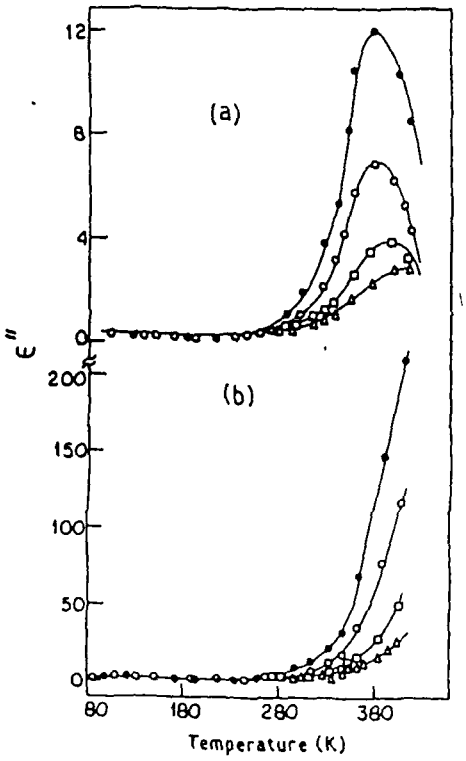

FIG. 3. Temperature variation of dielectric loss (ϵ'') of (a) G4 glass, and (b) G8 glass at (●) 1 kHz, (○) 2 kHz, (□) 5 kHz, and (△) 10 kHz.

free space). The temperature dependence of dielectric loss for two glasses G4 and G8 is shown in Fig. 3. The glass samples for low concentration of CuO (33.33 mol% or less) show a peak in the dielectric loss that shifts to higher temperature for higher frequencies (with lower values of ϵ''). This behavior strongly suggests a Debye-type dielectric relaxation process with a relaxation frequency $f\,(=1/2\pi\tau_0$, where τ_0 is the characteristic relaxation time shown in Table I).[11] The two glasses G7 and G8 with higher CuO concentrations do not, however, show a peak in the dielectric loss [see, for example, Fig. 3(b) for G8]. This might be due to shifting which is beyond the temperature range of our investigation. The frequency variations of ϵ'' for some glasses at 298 K as shown in Fig. 4(a) do not show any peak. The corresponding curves for a typical glass G3 at different temperatures are shown in Fig. 4(b). Like dielectric constant ϵ', dielectric loss ϵ'' also increases with the increase of CuO concentrations in the glasses.

Attempts to treat the dielectric constant data with the modulus approach[12] were made to show dielectric dispersion in the glasses. The dielectric modulus is defined as $M^*=M'+iM''=1/\epsilon^*$. The real (M') and imaginary (M'') parts of dielectric modulus are related to ϵ' and ϵ'' as

$$M'=\epsilon'/[(\epsilon')^2+(\epsilon'')^2]$$

and

$$M''=\epsilon''/[(\epsilon')^2+(\epsilon'')^2]\,.$$

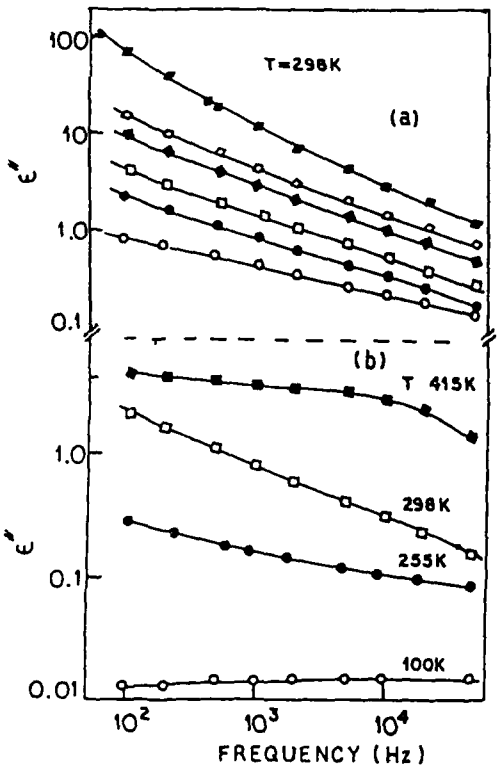

FIG. 4. (a) Frequency variation of dielectric loss (ϵ'') for different glass samples; (○) G3, (●) G4, (□) G5, (■) G6, (◇) G7, and (◆) G8. (b) Frequency dependence of dielectric loss (ϵ'') at different temperatures for the G4 glass.

The temperature dependence of M' for a typical glass (G6) for four fixed frequencies is shown in Fig. 5(a). These curves are almost similar to those of semiconducting V_2O_5-TeO_2 glasses.[10] At high temperatures, M' tends to reach a constant value that shifts to the higher-temperature region for higher frequencies. This behavior indicates thermally activated nature of the dielectric constant in the 4:3:3:y glasses. In order to demonstrate the dielectric dispersion, the imaginary part M'' was also calculated and plotted in Fig. 5(b) (for glass G8) as a function of temperature. The peaks in Fig. 5(b) shift to the higher-temperature side for higher frequencies. A similar nature is also observed for other glasses. The peak position of M'' gives the temperature at which the measuring frequency is equal to the relaxation frequency f_c $[=\nu_c\exp(-W_c/k_BT)$, where W_c is the activation energy for conductivity relaxation]. It is interesting to note that the f_c versus T^{-1} curves for these glasses is very similar to the temperature variation of dc conductivity of the same glasses[5,11] suggesting that both dc conductivity and the relaxation mechanism are thermally activated in nature.

Information about the distribution of relaxation times are obtained from the plot of $\epsilon''(\omega,T)$ versus $\epsilon'(\omega,T)$ (commonly known as Cole-Cole[13] plot) at different fixed temperatures and various frequencies (Fig. 6). The slopes

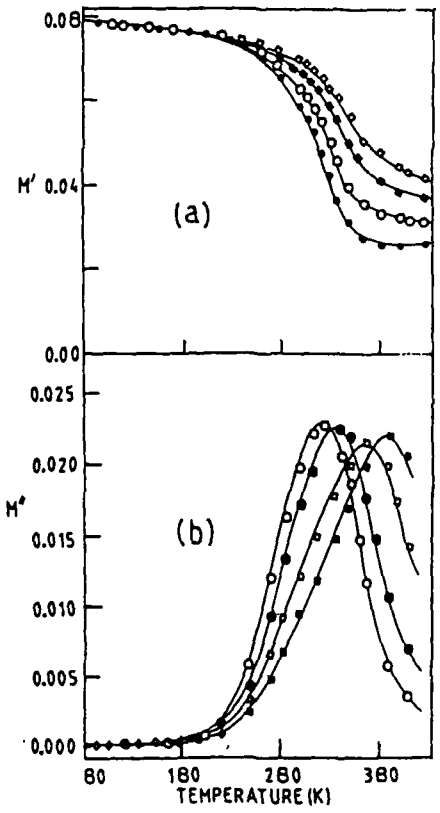

FIG. 5. (a) Temperature dependence of the real part of dielectric modulus, $M'[=\epsilon'/[(\epsilon')^2+(\epsilon'')^2]]$ for the G6 glass; (●) 1 kHz, (○) 2 kHz, (■) 5 kHz, and (□) 10 kHz. (b) Temperature dependence of $M''[=\epsilon'/[(\epsilon')^2+(\epsilon'')^2]]$ for the G8 glass, (○) 1 kHz, (●) 2 kHz, (□) 5 kHz, and (■) 10 kHz.

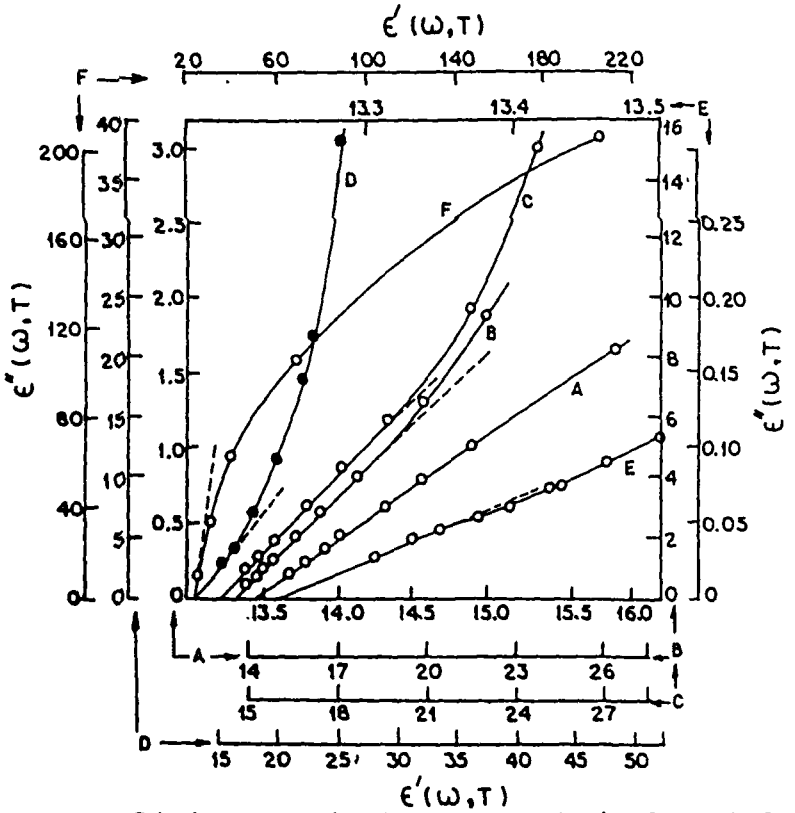

FIG. 6. Some representative Cole-Cole plots at some selected temperatures and various frequencies for the G4 (A), G6 (B), G7 (C), G8 (D) glasses at 298 K, and G7 glass at 174 K (E) and 405 K (F).

of these curves at a fixed temperature (say, 298 K) increase, which means that the distribution of relaxation times becomes sharper with the increase of CuO (or TMO) concentration in the glasses. The distribution also becomes sharper with increasing temperature for a particular glass sample. This behavior is very uncommon among TMO glasses. However, the semicircular nature of the curves as suggested by Cole and Cole[13] is not prominent for the present glasses. This might be due to the large value of high-frequency capacitance or dc conductivity of these glasses as suggested by Grant.[14]

Finally, we conclude from the dielectric constant and dielectric loss data that all the $Bi_4Sr_3Ca_3Cu_yO_x$ glasses becoming HTSO in their glass-ceramic phases (Table I) exhibit Debye-type dielectric behavior with a distribution of relaxation times. It is also revealed from the experimental data that the relaxation process is thermally activated similar to the dc conductivity of these glasses.[5,11] Results of detailed studies of the microstructural properties of these glasses and the superconducting properties of the corresponding glass ceramics will be given elsewhere.

Financial support for this work was provided by the Council of Scientific and Industrial Research (CSIR) and (DST), Government of India.

[1]R. C. Baker, W. M. Hurng, and H. Steinfink, Appl. Phys. Lett. 54, 371 (1989).
[2]K. K. Som, S. Mollah, K. Bose, and B. K. Chaudhuri, Phys. Rev. B 45, 1655 (1992).
[3]K. K. Som and B. K. Chaudhuri, Phys. Rev. B 41, 1581 (1990).
[4]H. Zhang, M. W. Colby, and J. D. Mackenzie, J. Non-Cryst. Solids 127, 143 (1991).
[5]S. Mollah, K. K. Som, K. Bose, A. Chakravorty, and B. K. Chaudhuri, Phys. Rev. B 46, 11 075 (1992).
[6]T. Moriuchi, T. Kawai, K. Mitsui, K. Orura, and S. Kawai, Physica C 168, 309 (1990).
[7]S. X. Dou, H. K. Liu, W. M. Wu, W. X. Wang, C. C. Sorrel, R. Winn, and N. Savvides, Physica C 172, 295 (1990).
[8]B. K. Chaudhuri, K. Chaudhuri, and K. K. Som, J. Phys. Chem. Solids 50, 1137 (1989); 50, 1148 (1989); A. Ghosh and B. K. Chaudhuri, J. Non-Cryst. Solids 83, 151 (1986).
[9]W. K. Lee, J. F. Liu, and A. S. Nowick, Phys. Rev. Lett. 67, 1559 (1991).
[10]A. Mansingh, V. K. Dhawan, and M. Sayer, Philos. Mag B 48, 215 (1983); M. Sayer, A. Mansingh, J. M. Reyes, and G. Rosenblatt, J. Appl. Phys. 42, 2857 (1971).
[11]K. K. Som, Ph.D. thesis, Jadavpur University, 1990.
[12]P. B. Macedo, C. T. Moynihan, and R. Bose, Phys. Chem Glasses 13, 171 (1972).
[13]K. S. Cole and R. H. Cole, J. Chem. Phys. 9, 341 (1941).
[14]F. A. Grant, J. Appl. Phys. 29, 76 (1957).

PHYSICAL REVIEW B VOLUME 45, NUMBER 4 15 JANUARY 1992-II

Nonlinear physical properties of amorphous $Bi_4Sr_3Ca_3Cu_yO_x$ semiconducting oxides with y between 0 and 5

K. K. Som, S. Molla, K. Bose, and B. K. Chaudhuri
Solid State Physics Department, Indian Association for the Cultivation of Science, Calcutta 700 032, India
(Received 15 May 1991; revised manuscript received 1 August 1991)

We report the nonlinear behavior of the CuO-concentration-dependent density (ρ), mean molar oxygen volume (V_0^*), and electrical conductivities (both ac and dc) of the $Bi_4Sr_3Ca_3Cu_yO_x$ ($y=0-5$) semiconducting oxide glasses. Infrared-spectroscopic data and mean molar oxygen volume (V_0^*) in these glasses indicate a change of (BiO_6) octahedral structural unit to pyramidal (BiO_3) structural unit with a change of CuO content in the glasses. However, no direct x-ray structural data of these glasses are found to show evidence of such changes. The nonlinearity is associated with the nonlinear variation of the ratio of $[Cu^+]/[Cu(total)]$ in the glasses depending on CuO concentrations, melting temperatures of the glasses, etc.

Recently, high-temperature superconducting oxides (HTSO's) obtained from $Bi_4Sr_3Ca_3Cu_4O_x$ (4:3:3:4) semiconducting oxide glasses (SOG) have been extensively studied.[1-7] This is because that starting with this glass composition it is found convenient to make a single phase[4] HTSO with superconducting transition temperature $T_c \sim 85$ K. Furthermore, it is also found advantageous to make wires, tapes, or thick films from the glass matrix[8-10] and then to convert them to the HTSO phases by annealing them at high temperatures (above the glass transition temperature T_g). The HTSO materials obtained from these glasses are also highly dense and homogeneous. Therefore, elaborate investigations of various properties of these glasses for different concentrations of the transition-metal (Cu) ions (TMI) as well as glass former oxide (Bi_2O_3) have been undertaken in our laboratory.

In the present paper we report the room-temperature behavior of electrical conductivities (both ac and dc) and infrared-spectroscopic studies of the ($Bi_4Sr_3Ca_3Cu_yO_x$) or (4:3:3:y) glasses with different concentrations of TMI with $y=0-5$.

The general method of preparation of the (4:3:3:y) glasses is the same as discussed earlier.[2,7,11] The starting materials, viz., CuO, $BaCO_3$, $SrCO_3$, and Bi_2O_3 (each of purity 99.99% procured from E. Merck, Aldrich, and Sigma) in appropriate proportion (according to the desired compositions) are well mixed and melted at 1200 °C for 1 h and then quickly quenched to room temperature by pressing the hot melt between two polished copper blocks. Since the ionic states of copper TMI might change depending on the melting temperature and time for which the melt was kept inside the furnace, each glass was melted at the same temperature for the same fixed time as mentioned above.

The x-ray diffraction patterns for all the glasses with Cu $K\alpha$ radiation showed broad peaks with maxima between $2\theta=26°$ and 30° as shown in Fig. 1. The concentrations of the Cu^{2+} ions in the glasses were obtained from the magnetic susceptibility measurements similar to our earlier work.[12] The small paramagnetism of the glasses[11] is considered to be solely due to the Cu^{2+} ions. The total copper ions present in the glasses (Cu_t) were calculated from the atomic absorption spectroscopic method and also from the chemical analysis. The total copper ions in the glasses are assumed to be composed of Cu^{1+} and Cu^{2+}. Some of the important parameters of the glasses studied are shown in Table I.

The densities of the glasses were measured by Archimedes's principle using carbon tetrachloride and microbalance with an accuracy of ± 0.01. The mean molar oxygen volume (V_0^*) was also calculated from the relation[13]

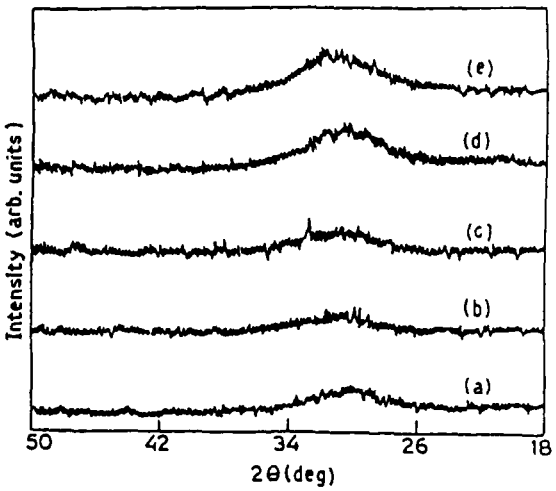

FIG. 1. X-ray diffraction patterns of some of the (4 3 3 y) glasses, (a) (4:3:3:1), (b) (4:3:3:2), (c) (4:3:3:3), (d) (4:3:3:4), and (e) (4:3:3:5) glass.

TABLE I. Some important physical parameters of (4:3:3:y) glasses. T_{cr} is crystallization temperature.

Values of y	0	1	2	3	3.5	4	4.5	5
Starting Cu content (wt %)	0	4.26	8.09	11.56	13.17	14.70	16.17	17.57
Final Cu content (wt %)	0	4.63	8.21	11.64	14.05	15.90	17.22	18.08
$[Cu^+]/[Cu(total)]$		0.79	0.75	0.70	0.75	0.78	0.80	0.79
T_g (°C)	408	402	422	422	440	426	446	431
T_{cr} (°C)	505	512	534	495	555	532	532	491
Θ (K)[a]			484	452	444	428	420	400
			(480)	(444)	(424)	(412)	(396)	(388)
σ_{dc} (Ω^{-1} cm^{-1}) at 300 K		1.03×10^{-12}	2.42×10^{-12}	9.00×10^{-11}	2.05×10^{-10}	7.70×10^{-10}	1.70×10^{-9}	3.90×10^{-9}
T_c (zero) (K)				70	79	85	85.5	76

[a]Calculated from $\ln\sigma_{dc}$ vs $1/T$ curves. Values within parentheses were obtained from the $\ln(\sigma_{dc}T)$ vs $1/T$ curves (see Ref. 2).

$$V_0^* = \frac{\text{molecular weight}}{\text{density} \times \text{no. of oxygen units in one formula unit}} . \quad (1)$$

The variations of density ρ and mean molar volume V_0^* with CuO concentrations are shown in Fig. 2. It appears that there is some nonlinearity in both the curves around 25–30 mol % of CuO. This nonlinearity corresponds closely to the theoretical (4:3:3:4) composition. This glass composition, in its glass-ceramic phase, gives rise to a sharp superconducting transition around 85 K and shows single phase character.[3,5] Similar anomalous behavior of density was also observed in some other ternary vanadate glasses studied earlier.[14] The density of the (4:3:3:y) glass varies from 5.97 to 5.86 g/cm^3 for a change of CuO concentration from 0 to 38.5 mol %. The nonlinear variation of (V_0^*) also suggests that the geometry and topology of the random network of the glasses change with CuO concentrations. This is also suggested from the fact that the superconducting transition temperatures T_c (zero) of the corresponding glass-ceramics (with $y=3-5$) change with the corresponding change of CuO concentrations[20] (see Table I). The nonlinearities mentioned above are also reflected in the dc and ac conductivities of the (4:3:3:y) glasses measured with different concentrations of TMI as discussed below.

The dc and ac conductivities (σ) of these glasses were measured similarly to our earlier work.[2,14] The general trend of variation of (σ_{dc}) with temperature (between 77 and 450 K) is almost same for all the (4:3:3:y) glass compositions as that of the (4:3:3:4) glass.[2] The concentration dependence of dc conductivity (σ_{dc}) and activation energy (W) of some of the (4:3:3:y) glasses for two fixed temperatures (300 and 410 K) are shown in Fig. 3. It appears

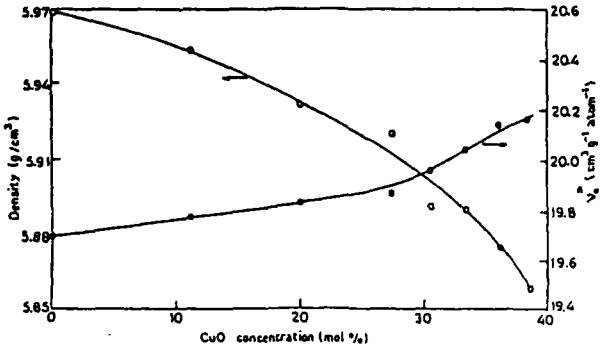

FIG. 2. Density and apparent molar volume of oxygen (V_0^*) vs concentration of CuO in the (4:3:3:y) glasses. The density of each glass was measured four times and the mean density value was plotted in the curve. Each glass sample of a particular composition was prepared three times and the density values of the glasses were found to vary by not more than ±5% from one sample to another of the same composition.

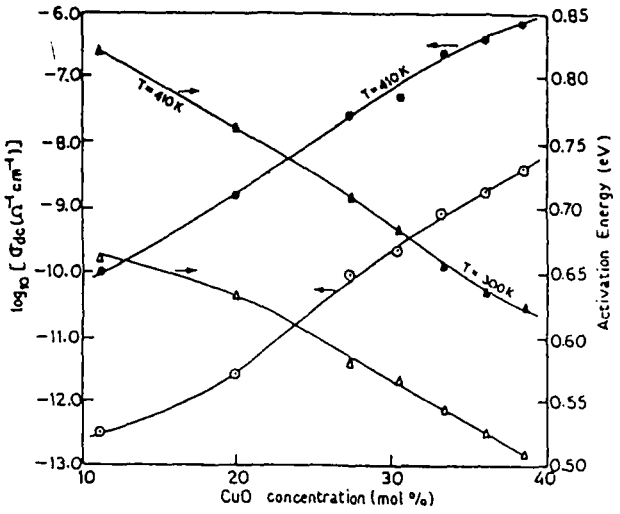

FIG. 3. Concentration (mol % of CuO) dependences of dc conductivity and activation energy at 300 and 410 K.

from this figure that there is some anomalous variation of (σ_{dc}) around the same concentrations (25–30 mol % of CuO), where (ρ) and ($V_0^{\bullet\bullet}$) showed nonlinearities. It is further observed from this figure that (σ_{dc}) at any fixed temperature increases with an increase of CuO concentrations and this increase with an increase of CuO (mol %) is more rapid above ~25 mol % of CuO. The nature of all the curves for different fixed temperatures is the same. The activation energy at higher temperature (above $\Theta/2$, Θ being the Debye temperature) decreases with the increase of CuO concentrations (Fig. 3). The magnitude of (σ_{dc}) at any temperature is found to be lower in all the (4:3:3:y) glasses having higher values of activation energies. It is also observed that the present (4:3:3:y) glass system shows higher room-temperature resistivities compared to many other (TMO) glasses like (P_2O_5-V_2O_5),[15] (Bi_2O_3-V_2O_5),[16] (Bi_2O_3-Fe_2O),[17] (CaO-P_2O_5CuO),[18] etc.

We have also measured the ac conductivities of the (4:3:3:y) glasses for a fixed frequency (1 kHz) with different concentrations of CuO as shown in Fig. 4. The ac conductivities of these glasses also show a quasilinear variation starting the nonlinearity around 25–30 mol % of CuO, similar to other properties of these glasses mentioned above. Here we should also mention that the glass prepared with $y=0$ in the series (4:3:3:y) is transparent and insulator. The (4:3:3:y) glasses with $y<2$ are practically insulators and they do not even become superconductors in their glass-ceramic phases within the temperature range of our observation (80 K).

For some structural information we have also studied the infrared (ir) absorptions for all the (4:3:3:y) glasses as discussed below. The ir spectra of all the powder glasses with KBr were taken in the frequency range of 200 to 4000 cm^{-1} at room temperature (~298 K) as shown in Fig. 5. The important absorption peaks and bands are shown in Table II. The main features observed from the above spectra are as follows.

(i) All the glass samples exhibit a weak water band around 3440 cm^{-1} and an -OH stretching peak near 2920 cm^{-1}. These peaks might be due to the little hygroscopic nature of the powdered glass samples. It has been observed that in the glass samples with lower concentration of CuO (i.e., higher concentration of the glass former oxide Bi_2O_3), the glass powder absorbs moisture and become gradually discolored, indicating the effect of moisture absorption.

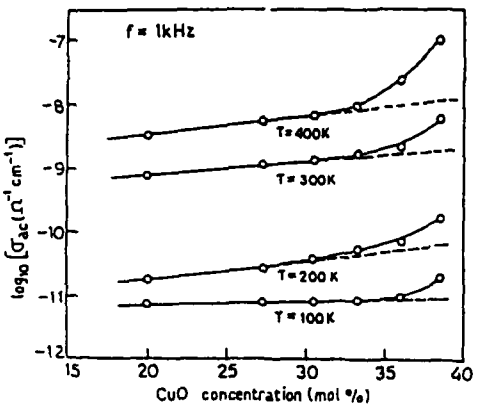

FIG. 4. Concentration (mol % of CuO) dependences of ac conductivity at 1 kHz.

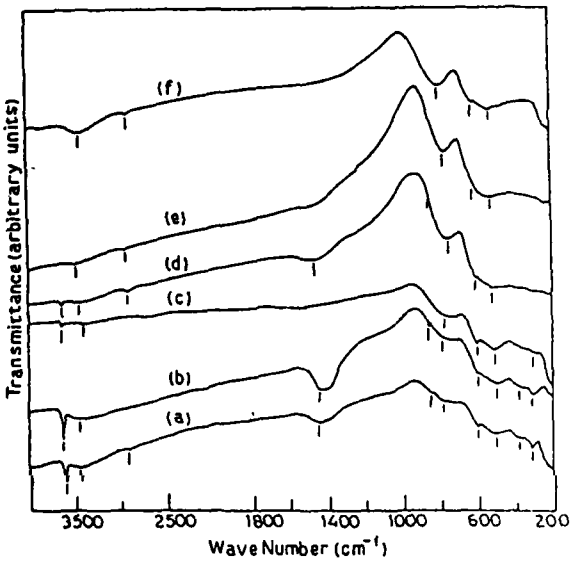

FIG. 5. Infrared-absorption spectra of some of the (4:3:3:y) glasses, (a) (4:3:3:0), (b) (4:3:3:1), (c) (4:3:3:2), (d) (4:3:3:3), (e) (4:3:3:4), and (f) (4:3:3:5) glass.

(ii) All the glass samples exhibit three major absorption peaks near 765–790 cm^{-1}, 600–610 cm^{-1}, and 505–510 cm^{-1}. There is possibly another absorption peak near 310 cm^{-1} in some of these glasses. The absorption peak near 600–610 cm^{-1} is very weak in all the glasses.

(iii) The hydroxyl ion OH^{1-} is characterized by a sharp band at 3500–3700 cm^{-1}. In general, the hydroxyl (-OH) stretching band is sharper and at a higher frequency than the -OH stretching band of water. The observed sharp absorption peak at 3620 cm^{-1} in some of the glasses may be due to the formation of metal hydroxides resulting from the absorbed water by the glass samples. $Ca(OH)_2$ has a stretching frequency[19] of 3644 cm^{-1} which is close to the peak frequency at 3600 cm^{-1} exhibited by some glass samples.

(iv) The very weak absorption bands at 860 and 1450 cm^{-1} observed in some glasses may be due to the presence of some $CaCO_3$ or $SrCO_3$ in nanocrystalline phases not detectable with x-ray study. The concentration of these crystalline phases is so small in the amorphous matrix that they do not affect the electrical properties studied. This is confirmed from the fact that the same glass samples prepared in different lots under the same conditions show almost identical electrical and other physical properties. The electrical resistivities of these glasses, for example, at a fixed temperature (300 K) was found to differ only by about 5%, which might be attributed to the change of degree of amorphousness in the samples. Furthermore, the amount of oxygen absorbed by these glasses during preparation might also differ causing a change of resistivities. The nature of the thermal variation of resistivity, however, remains the same as shown in

TABLE II. Infrared-absorption peaks and bands of the (4:3:3:y) glasses.

Glass samples	Peak positions (cm^{-1})									
(4:4:3:0)	3620	3440		1450	860	790	600	510	380	310
(4:3:3:1)	3620	3420		1400	860	780	600	510	380	310
(4:3:3:2)	3620	3440		1450		780	600	510	380	310
(4:3:3:3)	3620	3440	2920	1460	860	750	610	510		310
(4:3:3:4)		3440	2920			765	605	505		
(4:3:3:5)		3440	2920			780	610	508		

Figs. 3 and 4.

Crystalline Bi_2O_3 has absorption peaks[20] at 1400, 610, 525, 450, 395, and 360 cm^{-1}. The absorption peaks around 1400 and 395 cm^{-1} appearing in crystalline Bi_2O_3 are related in the glasses with a high concentration of Bi_2O_3 (or low concentration of CuO), although the peaks at 395 cm^{-1} shift to a lower frequency at 380 cm^{-1}. However, these peaks seem to have disappeared in the glasses with increasing CuO concentrations. The absorption peaks appearing at 610 and 525 cm^{-1} in the crystalline Bi_2O_3 are also related in all the glass samples with a little shift towards the lower frequency (600–610 cm^{-1} and 505–510 cm^{-1}, respectively). A strong absorption band around 765–790 cm^{-1} also appears in all the glasses. Moreover, although some of the characteristic peaks of the crystalline Bi_2O_3 disappear in the glasses containing higher concentrations of CuO, no new absorption peaks or bands appear in the glasses with the increase of CuO concentrations.

From the above considerations it is reasonable to assume that the structure of the Bi-Sr-Ca-Cu-O glasses are primarily determined by the Bi_2O_3 structure. Copper structural units do no change significantly with the increase of CuO content in the (4:3:3:y) glasses. As the Cu structural units remain almost unchanged in the glasses, the characteristic phonon frequency (ν_{ph}) is not expected to change much with CuO concentrations. This is also further supported by the temperature-dependent variations of conductivities for different CuO concentrations,[10,20] more details of which will be published elsewhere.

As suggested by Zheng, Xu, and Mackenzie,[5] the bismuth ions remain as $[BiO_3]$ octahedra with coordination number 6 or may also be present as $[BiO_3]$ pyramidal units in the presence of polarizing cations in the glass network. The $[BiO_3]$ pyramidal units have four fundamental infrared vibrations. They are as follows: ν_1, a totally symmetric-stretch vibration (840 cm^{-1}); ν_2, a totally symmetric bond-bending vibration (470 cm^{-1}); ν_3, a doubly degenerate stretching vibration (540–620 cm^{-1}); and ν_4, a doubly degenerate bond-bending vibration (350 cm^{-1}). The $[BiO_6]$ units have only two infrared-active fundamental vibrations (ν_2 and ν_3) (Ref. 19) and the peak positions shift to longer wavelengths because of a weaker polarizing effect. It has already been pointed out[4,5,21] that one of the indications of the $[BiO_3]$ pyramidal units is the 640 cm^{-1} vibration band in these glasses as shown in Fig. 5.

In some of the glasses with low CuO concentrations and higher Bi_2O_3 and (Ca-Sr-O) concentrations only weak absorption peaks near 860 and 310 cm^{-1} are present. In all the other glasses with higher CuO content these two peaks totally disappear. The other two fundamental peaks around 540–620 and 470 cm^{-1}, corresponding to both $[BiO_3]$ and $[BiO_6]$ structural units, are present in all the glasses.

From the above infrared spectra (Fig. 5) of the (4:3:3:y) glasses, it appears that the glass network is mainly made up of $[BiO_6]$ octahedral structural units. Some of the glasses with low CuO concentrations (less than 20 mol % of CuO) show some evidences of the presence of a small number of $[BiO_3]$ pyramidal structural units. Zheng, Colby, and Mackenzie[4] and Zheng, Xu, and Mackenzie[5] suggested that the presence of these $[BiO_3]$ units in the (Ca-Sr-O) and Bi_2O_3 containing (or low CuO content) glasses may be caused by the polarizing effect of Ca^{2+} and Sr^{2+} cations. The presence of these polarizing cations may also reduce the coordination number of bismuth from 6 to 3 and hence a transition from the octahedral $[BiO_6]$ structural units to the pyramidal $[BiO_3]$ structural units is also possible, depending on the CuO concentrations in the glass (i.e., TMI concentrations). However, no such evidence of the change of the structural unit is available from x-ray diffractograms (Fig. 1) of these glasses with different "y" values. This also indicates that there is no long-range order in the as-quenched glasses. However, the change of slope of (V_0^*) with CuO concentration (Fig. 2) might be due to structural change or the phase-separation effect in the glasses. This was also pointed out in Refs. 18(a) and 18(b) in V_2O_5-P_2O_5 glasses.

This change of coordination number possible with a change of CuO and/or Bi_2O_3 concentrations is supposed to be responsible for the nonlinear variations of some of the basic physical properties of the glasses around (20–30 mol %). It has already been mentioned that nonlinear variations of density (ρ), T_g, and electrical conductivities have also been observed in some other ternary oxide glasses,[14] viz., V_2O_5-P_2O_5-M, with $M = Bi_2O_3$, Sb_2O_3, and GeO_2. For these glasses it has been shown that nonlinear variations of the physical properties as mentioned above are really associated with the nonlinear change of the ionic ratio of V^{5+} and V^{4+} ions in the vanadate glasses. These nonlinear or quasilinear variations of density, molar oxygen volume, T_g, electrical conductivities, etc., of ternary or quaternary oxide glasses might be an incipient behavior of these glasses. Similar properties[22] have also

been noticed in the other series, viz., ($Bi_ySr_3Ca_3Cu_4O_x$) or (y:3:3:4) glasses (with $y=2.5-5$). The ($Bi_{3.5}Sr_3Ca_3Cu_4O_x$) glass of this series is of particular importance since only this very glass can be drawn in the form of long wires or filaments very easily like vanadate glasses. More about this (y:3:3:4) series will be discussed elsewhere.

One of the authors (S.M.) is grateful to CSIR for partial support. Thanks are also due to Professor S. P. Sengupta and Professor N. Raychowdhury for allowing the authors to use the x-ray diffractometer and DTA apparatus of their respective laboratories.

[1]H. Zheng and J. D. Mackenzie, Phys. Rev. B 38, 7166 (1989).
[2]K. K. Som and B. K. Chaudhuri, Phys. Rev. B 41, 1581 (1990).
[3]R. C. Baker, W. H. Hurng, and H. Steinfink, Appl. Phys. Lett. 54, 371 (1989).
[4]H. Zheng, M. W. Colby, and J. D. Mackenzie, J. Non-Cryst. Solids 127, 143 (1991).
[5]H. Zheng, R. Xu, and J. D. Mackenzie, J. Mater. Res. 4, 911 (1989).
[6]J. M. Tarascon, Y. Le Page, P. Barboux, B. G. Bagley, L. H. Greene, W. R. McKinnon, G. W. Hull, M. Giroud, and D. M. Hwang, Phys. Rev. B 37, 9382 (1988).
[7]B. K. Chaudhuri, K. K. Som, and S. P. Sengupta, J. Mater. Sci. Lett. 8, 520 (1989).
[8]H. Zheng, Y. Hu, and J. D. Mackenzie, Appl. Phys. Lett. (to be published).
[9]S. E. Lebeau, J. Righi, J. E. Ostenson, S. C. Sanders, and D. K. Finnemore, Appl. Phys. Lett. 55, 292 (1989).
[10]B. K. Chaudhuri and K. K. Som, Bull. Mater. Sci. (India) 14, 1093 (1991).
[11]K. K. Som, A. K. Ghoshal, and B. K. Chaudhuri, J. Mater. Sci. Lett. 8, 749 (1989).
[12]K. K. Som and B. K. Chaudhuri, J. Mater. Sci. 26, 1223 (1991).
[13]S. Glasstone, *The Elements of Physical Chemistry* (MacMillan, London, 1955), p. 146.
[14]K. K. Som and B. K. Chaudhuri, J. Mater. Sci. 26, 1228 (1991).
[15]M. Sayer and A. Mansingh, Phys. Rev. B 6, 4629 (1972); A. P. Schmid, J. Appl. Phys. 39, 3140 (1968).
[16]A. Ghosh and B. K. Chaudhuri, J. Non-Cryst. Solids 83, 151 (1986).
[17]B. K. Chaudhuri, K. Chaudhuri, and K. K. Som, J. Phys. Chem. Solids 50, 1137 (1989).
[18](a) C. F. Drake, I. F. Scanlan, and A. Engel, Phys. Status Solidi 32, 193 (1969); (b) C. F. Drake, J. A. Stephen, and B. Yates, J. Non-Cryst. Solids 28, 61 (1986).
[19]K. Nakamoto, *Infrared Spectra of Inorganic and Coordination Compounds* (Wiley, New York, 1963).
[20]K. K. Som, Ph.D. thesis, Jadavpur University, Calcutta, 1990.
[21]A. Bishay and C. Maghrabi, Phys. Chem. Glasses 10, 1 (1969).
[22]S. Molla, K. Bose, K. K. Som, and B. K. Chaudhuri (unpublished).

PHYSICAL REVIEW B VOLUME 46, NUMBER 17 1 NOVEMBER 1992-I

Nonadiabatic small-polaron hopping conduction in Li-doped and undoped $Bi_4Sr_3Ca_3Cu_yO_x$ ($0 \le y \le 5$)

S. Mollah, K. K. Som, K. Bose, A. K. Chakravorty, and B. K. Chaudhuri
Solid State Physics Department, Indian Association for the Cultivation of Science, Calcutta 700 032, India
(Received 7 January 1992; revised manuscript received 4 May 1992)

Detailed experimental results of temperature- and CuO-concentration-dependent dc conductivities of semiconducting $Bi_4Sr_3Ca_3Cu_yO_x$ ($y=0$ to 5) and Li-doped $Bi_4Sr_3Ca_{3-z}Li_zCu_4O_x$ ($z=0.1$, 0.5, and 1.0) glasses are reported. The variation of activation energy with glass compositions dominates the conductivity. Unlike many glasses with transition-metal ions, a strong preexponential factor containing the "small-polaron" tunneling term $[\exp(-2\alpha R)]$ is observed. Nonadiabatic small-polaron hopping mechanism is found to be appropriate for explaining the conductivity data of both glass systems. Addition of alkali-metal ions decreases the conductivities and causes appreciable change of some model parameters obtained from least-squares fittings of the experimental data. The overall thermal behavior of the electrical conductivities of the glasses, however, remains unaltered. This indicates that small (less than 10 wt.%) amount of Li or other alkali-metal ions in these glasses acts as a flux to keep the oxygen content fixed in the corresponding glass-ceramic (superconducting) phases. This in turn helps increase the superconducting transition temperature of the glass ceramics and also lower the sintering and melting temperatures of the glasses.

I. INTRODUCTION

The study of transition-metal oxide glasses are of particular importance for many technological applications.[1] Recently several transition-metal oxide glasses, such as $YBa_2Cu_3O_x$,[2] (Bi,Pb)-Sr-Ca-Cu-O,[3] etc., have been discovered, which become superconductors in their glass-ceramic phases. These glasses with transition-metal ions (TMI) are very useful precursor materials for making high-temperature superconducting oxide wires, tapes, or thick films.[4] The room-temperature electrical conductivities of these glasses are, however, two to three orders of magnitude lower than those of iron, vanadium, or other TMI glasses.[5,6] The glasses of our present investigation, such as $Bi_4Ca_3Sr_3Cu_yO_x$ (hereafter referred to as 4:3:3:y, glasses) have already been found[7,8] to show interesting nonlinear variations of glass transition temperature (T_g), density (ρ), mean molar oxygen volume (V_0^*), etc., as a function of CuO or Bi_2O_3 concentrations. The 4:3:3:4 glass is especially important as it acts as a precursor for making single phase $Bi_2Sr_2Ca_1Cu_2O_8$ (2:2:1:2) superconductors with T_c between 80 and 84 K.[9] It has also been reported[10–13] that addition of some alkaline oxides in this system improves the superconducting behavior of the glass ceramics (increase of T_c) and also lowers the ceramic sintering temperature. However, detailed investigation of the electrical properties of both Li-doped and undoped Bi-Sr-Ca-Cu-O glasses for different CuO concentrations has not yet been reported.

Since the superconducting behavior of the present glass ceramics depends on the CuO concentrations,[7,8] our plan is to study the CuO- and Li-concentration-dependent electrical and other properties of the $Bi_4Ca_3Sr_3Cu_yO_x$ (with $y=0$–5) and $Bi_4Sr_3Ca_{3-z}Li_zCu_4O_x$ (with $z=0.1$, 0.5, and 1.0) glasses, respectively. An attempt has also been made to study the effects of Li ions on the superconducting transition temperatures (T_c) of the corresponding Li-doped 4:3:(3−z):4 glass ceramics. Such studies would elucidate the differences in the properties of these and other transition-metal oxide (TMO) glasses, which do not become superconductors in their glass-ceramic phases. Furthermore, the model parameters like Debye temperature, electron-phonon interaction constant, polaron radius, etc., obtained from the electrical conductivities of these glasses might be useful to a deeper understanding of the mechanism of superconductivity in the corresponding glass ceramics.

In Sec. II we have discussed in brief the preparation and characterization of the glasses. In Sec. III results of dc conductivities of both 4:3:3:y and Li-doped 4:3:(3−z):4 glasses have been discussed with small-polaron hopping models. The different model parameters calculated for both the glass systems are reported. Finally, the paper ends with a conclusion in Sec. IV.

II. PREPARATION AND CHARACTERIZATION OF THE GLASSES

The method of preparation of the $Bi_4Ca_3Sr_3Cu_yO_x$ glasses have already been discussed earlier.[7,8,14] A similar method has also been used to prepare the lithium-doped 4:3:(3−z):4, or $Bi_4Sr_3Ca_{3-z}Li_zCu_4O_x$, glasses. Three Li-doped 4:3:(3−z):4 glass samples studied are for $z=0.1$ (sample No. 9), 0.5 (sample No. 10), and 1.0 (sample No. 11). The oxide materials, viz., Bi_2O_3, $CaCO_3$, $SrCO_3$, CuO, and $LiOH\cdot H_2O$ used for the preparation of the glasses are of 99.99% purity. Since the ratio $C=[Cu^{1+}]/[Cu(\text{total})]$ depends on the glass making temperature, all the glasses were made by quick quenching from their respective melts at 1200 °C to room tempera-

ture (303 K). Each melt was kept at this temperature for one hour. The amorphous character of these glasses were confirmed by x-ray diffraction (Philips, Model PW 1050/1051) and scanning electron microscopic (Hitachi, Model S-415A) studies as before.[7,14] The scattering wave vector k calculated from the relation $k = 4\pi \sin\theta/\lambda$ gives a value of 2.11 $Å^{-1}$, which is typical for an amorphous material. Annealing the samples up to 200 °C for 2 h did not induce any crystallinity. Figure 1 shows the differential thermal analysis (DTA) (Shimadzu DT-30) curves of different glasses. Each curve shows an endothermic peak around 400–425 °C that corresponds to the glass transition temperature (T_g). Most of the TMO glasses, however, show lower (around 350 °C) T_g values. We did not observe, unlike Zheng and co-workers,[4] a systematic variation of T_g with CuO concentration as shown in Table I. There are number of exothermic crystallization peaks followed by endothermic glass transition peaks some of which are only prominent (Fig. 1). The difference ($T_{cr} - T_g$) between crystallization temperature (T_{cr}) and T_g for the 4:3:3:y glasses vary from 60 °C to 115 °C (Table I) indicating that the glasses are fairly stable. Some important parameters obtained from DTA (for determining T_g and T_{cr}), density measurement, atomic absorption, and chemical analysis are shown in Tables I and II, respectively, for the 4:3:3:y and Li-doped 4:3:(3−z):4 glasses. Slightly higher values of the final wt% of Cu than the corresponding starting value (Table I) is considered to be mainly due to the loss of oxygen from the melt. However, evaporation loss of Bi_2O_3, in particular, should also be taken into account. It is further observed from Table I that a majority of the copper atoms exist in the glasses as Cu^{1+} ions. Addition of Li ions does not appreciably change the value of Cu concentration in the Li-doped 4:3:(3−z):4 glasses. Little increase in the T_g values of the Li-doped 4:3:(3−z):4 glasses than those of the corresponding base glass, viz., $Bi_4Sr_3Ca_3Cu_4O_x$ (4:3:3:4, for which $z = 0$) is also noticed from Table II.

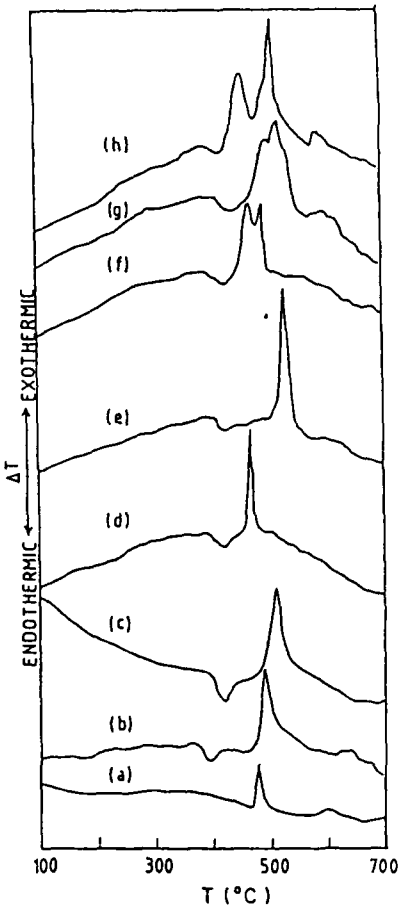

FIG. 1. DTA curves of $Bi_4Sr_3Ca_3Cu_yO_x$ glasses with (a) $y = 0$, (b) $y = 1$, (c) $y = 2$, (d) $y = 3$, (e) $y = 3.5$, (f) $y = 4$, (g) $y = 4.5$, and (h) $y = 5$.

III. RESULTS AND DISCUSSION

Figure 2(a) shows the logarithm of dc conductivity (σ_{dc}) of the $Bi_4Sr_3Ca_3Cu_yO_x$ glasses for different y (CuO

TABLE I. Some important parameters for the $Bi_4Sr_3Ca_3Cu_yO_x$ glasses.

Sample	No. 1	No. 2	No. 3	No. 4	No. 5	No. 6	No. 7	No. 8
Values of y	0	1	2	3	3.5	4	4.5	5
Starting Cu content (wt%)	0	4.26	8.09	11.56	13.17	14.70	16.17	17.57
Final Cu content (wt%)[a]	0	4.63	8.21	11.64	14.05	15.90	17.22	18.08
Density (ρ) (g cm^{-3})	5.97	5.95	5.93	5.92	5.89	5.89	5.88	5.86
N (10^{21} cm^{-3})		2.61	4.61	6.53	7.84	8.87	9.59	10.04
$C = [Cu^+/Cu(total)]$		0.79	0.75	0.70	0.75	0.78	0.80	0.79
R (Å)		7.26	6.01	5.35	5.03	4.83	4.71	4.64
r_p (Å)		2.93	2.42	2.16	2.03	1.95	1.90	1.87
T_g (°C)	408	402	422	422	440	426	446	431
$T_{cr} - T_g$ (°C)	97	110	112	73	115	106	86	60
T_c (K)[b]				70	79	85	85.5	76

[a]Obtained from atomic absorption spectroscopy.
[b]Superconducting transition temperature of the glass ceramics obtained from resistivity measurement.

TABLE II. Some important parameters for the $Bi_4Sr_3Ca_{3-z}Cu_4Li_zO_x$ glasses.

Sample	No. 9	No. 10	No. 11
Values of z	0.1	0.5	1.0
Density (ρ) ($g\ cm^{-3}$)	5.82	6.02	6.59
N ($10^{21}\ cm^{-3}$)	8.24	8.62	9.54
R (Å)	4.95	4.88	4.71
r_p (Å)	1.99	1.96	1.89
T_g (°C)	428	433	436
T_c (K)[a]	86.0	88.5	89.5

[a]Superconducting transition temperature of the glass ceramics obtained from resistivity measurement.

concentration) values as a function of $10^3/T$ (T is the absolute temperature). The slopes of the curves change slightly with T in the high-temperature region indicating slow variation of activation energy (W). The corresponding dc conductivity curves for lithium-doped $Bi_4Sr_3Ca_{3-z}Li_zCu_4O_x$ samples are shown in Fig. 3(a). The nature of the curves (with $z=0.1$, 0.5, and 1.0) are almost similar to those of the pure 4:3:3:y glasses shown in Fig. 2(a). However, the magnitude of dc conductivity at any temperature (say at room temperature) is lower in the Li-doped 4:3:(3−z):4 glasses. A plot of excess conductivity $\Delta\sigma_{dc}$ [$=\sigma_{dc}$ (undoped 4:3:3:4 glasses) $-\sigma_{dc}$ (Li-doped 4:3:(3−z):4 glasses)] as a function of temperature for different Li concentrations (shown in Fig. 4) distinguishes the low- and high-temperature regions of the thermal variations of σ_{dc}. The low-temperature conductivities are almost independent of temperature in the Li-doped glasses. Below a certain temperature, which varies from 240 to 200 K (for different 4:3:3:y glasses) the change of slopes are more pronounced in the glasses with higher values of y having higher conductivity at low temperature. Such a behavior of σ_{dc} is typical for "small-polaron" hopping conduction in transition-metal oxide glasses.[15] The variation of conductivity and activation energy W with y are shown in Fig. 5, which indicates that at any fixed temperature, σ_{dc} increases with increasing CuO concentration. This increase is, however, nonlinear,[7,8] unlike iron-bismuth,[6] vanadate,[5] or Cu-Te-O-type[16] glasses. The magnitude of activation energy at higher temperatures (above $\Theta_D/2$, Θ_D being the Debye temperature) decreases with the increase of CuO content in the glasses. Similar variation of σ_{dc} and W are also observed for Li-doped 4:3:(3−z):4 glasses as shown in Fig. 5.

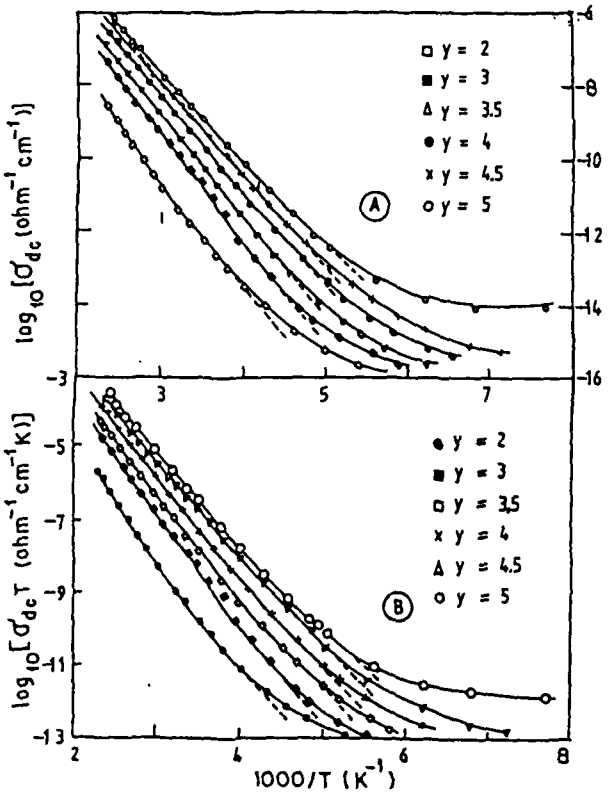

FIG. 2. (a) Thermal variation of dc conductivity (σ_{dc}) of different $Bi_4Sr_3Ca_3Cu_yO_x$ glasses. (b) Variation of $\log_{10}[(\sigma_{dc}T)]$ vs $10^3/T$ curves for different 4:3:3:y glasses.

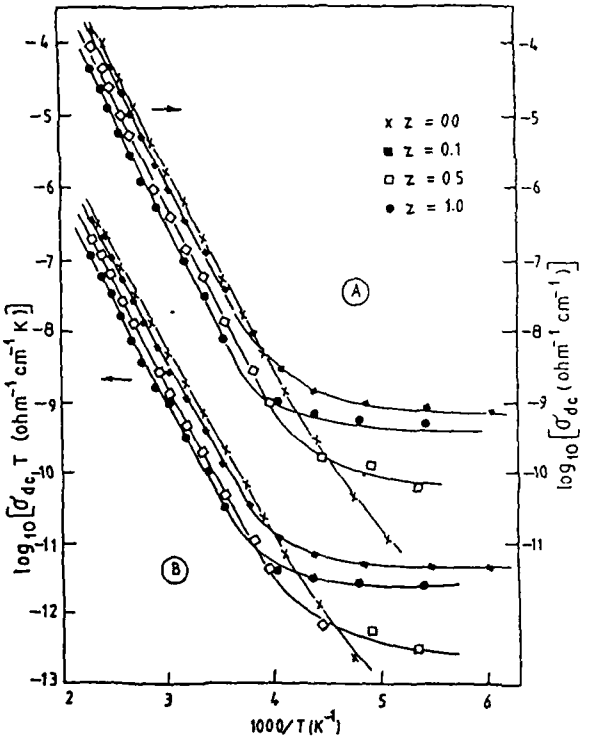

FIG. 3. (a) Thermal variation of dc conductivity (σ_{dc}) of different $Bi_4Sr_3Ca_{3-z}Li_zCu_4O_x$ glasses. (b) Variation of $\log_{10}[(\sigma_{dc}T)]$ vs $10^3/T$ curves for different 4:3:3:y glasses.

Using a polaron hopping mechanism, the experimental conductivity data of these glasses could be explained[14,17] with an equation (in the nonadiabatic approximation) of the form[15]

$$\sigma_{dc}=\sigma_0\exp(-2\alpha R)\exp(-W/k_BT)\ , \qquad (1)$$

where $\sigma_0 = \nu_{ph} e^2 C(1-C)/k_B TR$, ν_{ph} is the optical phonon frequency, R is the average Cu-Cu spacing, k_B is Boltzmann's constant, and α is the wave-function decay constant. The activation energy W can be written as[15]

$$W = \begin{cases} W_h + W_d/2 , & (\text{for } T > \Theta_D/2) \\ W_d , & (\text{for } T < \Theta_D/4) , \end{cases} \quad (2)$$

where W_h and W_d are, respectively, the polaron hopping energy and disorder energy arising from the energy difference of the neighboring sites.

The presence of T^{-1} term in the preexponential factor of Eq. (1) suggests that a plot of $\log_{10}(\sigma_{dc}T)$ as a function of T^{-1} would be more appropriate to distinguish between the high- and the low-temperature region. Figures 2(b) and 3(b) show such curves, respectively, for the 4:3:3:y and Li-doped 4:3:(3−z):4 glasses. The values of Θ_D determined from the departure from the linearity of these curves are shown in Table III. The values of Θ_D calculated for the Li-doped 4:3:(3−z):4 glasses are higher than those of the 4:3:3:y glasses. The values of phonon frequency (ν_{ph}) calculated from different curves in Figs. 2 and 3 are in good agreement as shown in Table III. The values of ν_{ph} calculated from the infrared spectra corresponding to the characteristic absorption band[7,17] at 505–510 cm^{-1} is 1.53×10^{13} Hz, which is slightly higher but almost constant for all the glass samples studied (Table III). Both ν_{ph} and Θ_D of the Li-doped 4:3:(3−z):4 glasses are higher than those of the pure 4:3:3:y glasses. The higher values of Θ_D and ν_{ph} are found to give higher values of T_c in the Li-doped superconducting glass ceramics.

The dc conductivity of semiconducting TMO glasses, such as 4:3:3:y and Li-doped 4:3:(3−z):4 can be explained by considering hopping of polarons (electrons) between localized states. The values of different parameters like W, α, r_p (polaron radius), W_h, C, etc., as calculated from the σ_{dc} values following Eqs. (1) and (2) are shown in Tables I–IV. The value of W_h is calculated from the relation

$$W_h = W_p/2 = (e^2/4\epsilon_p)(r_p^{-1} - R^{-1}) , \quad (3)$$

where r_p is the polaron radius and ϵ_p is the effective dielectric constant ($\epsilon_p = \epsilon_\infty = n^2$, n is the refractive index of the glass). Since dielectric constant[17] of the 4:3:3:y glasses do not change much with CuO concentrations, the value of n, for all the 4:3:3:y glasses, is taken to be equal to 1.995, which was determined from the measurements of Brewster's angle.[14,17] W_h obtained from the slopes of the curves of Figs. 2 and 3 at two fixed temperatures (300 and 410 K) are shown in Table IV. The disorder energy (W_d) is calculated from the Miller-Abrahams theory.[18] The difference between W and W_h arises from the disorder term $W_d/2$ [Eq. (2)]. The values of W_d cal-

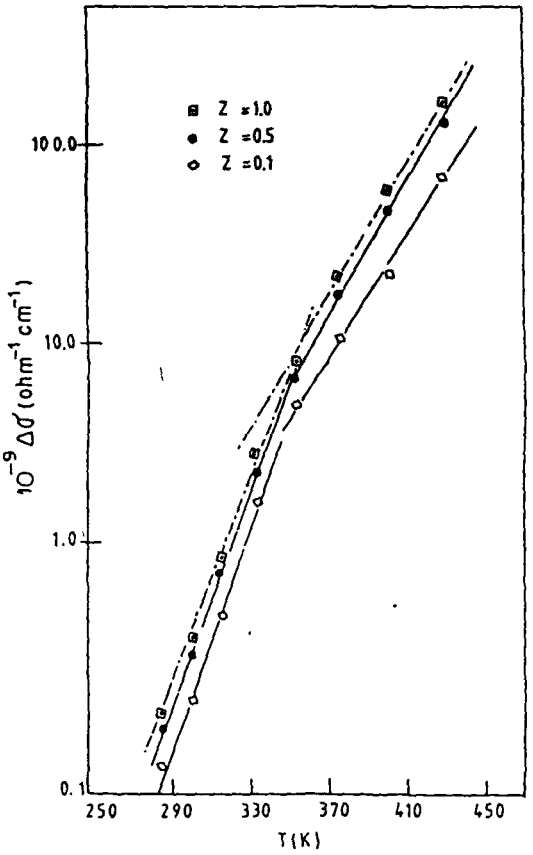

FIG. 4. Variation of excess conductivity $\Delta\sigma_{dc} = \sigma_{dc}$ (for 4:3:3:4 base glass) $-\sigma_{dc}$ (for the Li-doped 4:3:(3−z):4 glass).

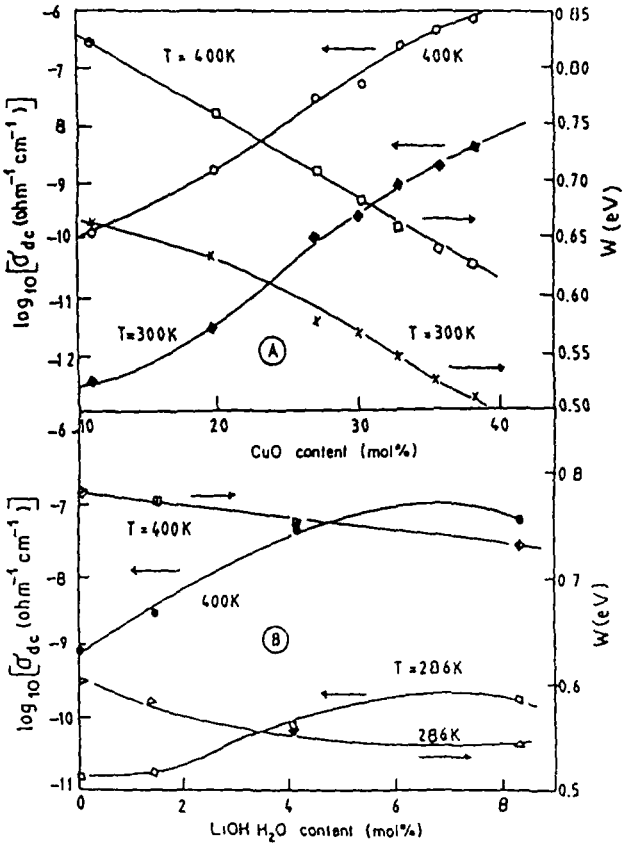

FIG. 5. Variation of dc conductivity (σ_{dc}) and activation energy (W) with Cu (a) and Li (b) concentrations in the 4:3:3:y and Li-doped 4:3:(3−z).4 glasses, respectively, at two different fixed temperatures.

TABLE III. Some important parameters for the 4:3:3:y and Li-doped 4:3:(3−z):4 glasses obtained from the dc conductivity data.

	Debye temperature Θ_D (K)		Phonon frequency ν_{ph} (Hz)		
Sample	(a)	(b)	(a)	(b)	(c)
No. 3	484	480	1.01×10^{13}	1.00×10^{13}	1.11×10^{13}
No. 4	452	444	9.41×10^{12}	9.25×10^{12}	9.89×10^{12}
No. 5	444	424	9.25×10^{12}	8.83×10^{12}	9.31×10^{12}
No. 6	428	412	8.91×10^{12}	8.58×10^{12}	8.93×10^{12}
No. 7	420	396	8.75×10^{12}	8.25×10^{12}	8.70×10^{12}
No. 8	400	388	8.33×10^{12}	8.08×10^{12}	8.58×10^{12}
(Li-doped) No. 9	510		1.06×10^{13}		
(Li-doped) No. 10	500		1.04×10^{13}		
(Li-doped) No. 11	490		1.03×10^{13}		

[a]Calculated from the $\log_{10}(\sigma_{dc})$ versus $10^3/T$ curve [Figs. 2(a) and 3(a)].
[b]Obtained from the $\log_{10}(\sigma_{dc}T)$ versus $10^3/T$ curve [Fig. 2(b)].
[c]Obtained from the intercept of the $\log_{10}[\sigma_0/C(1-C)]$ versus R curve [Fig. 6(a)].

culated[18] from $W_d=0.3e^2/\epsilon_s R$ (where ϵ_s is the static dielectric constant) varies from 0.062 to 0.029 eV for the 4:3:3:y glasses. It is found that the disorder energy decreases with increase of CuO concentrations. This is also true for the other TMO glasses. We notice from Table IV that the values of ΔW ($=W-W_h$, at 300 K, say) vary in the range of 0.48–0.22 eV, which is much higher than the theoretically calculated values of $W_d/2$. Similar results have also been reported for the Fe_2O_3-Bi_2O_3 and vanadate glasses.[5,6] Since the C values [the ratio $[Cu^{1+}]/[Cu(total)]$] do not change much (see Table I) in the 4:3:3:y glasses for different CuO contents, this discrepancy in activation energy might be described as the effect of the partial charge of the cations of the glass forming oxides (Bi_2O_3, CaO, etc.).[19]

The importance of the tunneling term $[\exp(-2\alpha R)]$ in Eq. (1) for the glasses could be understood[20] by plotting $\log_{10}\sigma_{dc}$ against W at a fixed temperature. The temperature T_e estimated from the slope of such a plot would be close to the experimental temperature when the hopping is considered to be in the adiabatic regime.[20] On the other hand, T_e would be very different from the experimental temperature if the hopping is considered to be in the nonadiabatic regime. Such a plot for two fixed temperatures ($T=300$ and 410 K) is shown in Fig. 6(a). The temperatures estimated from the slopes of the curves are 195 and 260 K, respectively. Similarly for the Li-doped 4:3:(3−z):4 glasses such a plot for two fixed temperatures (286 and 400 K) the corresponding T_e values estimated are 647 and 915 K, respectively. Thus, the higher values of T_e from the corresponding experimental temperatures suggest nonadiabatic polaron hopping conduction in the 4:3:3:y and Li-doped 4:3:(3−z):4 glasses. The nonadiabatic hopping character is also supported from the validity of Holstein's condition[21] as discussed below.

For adiabatic hopping the polaron bandwidth J should satisfy the following condition,[21] viz.,

$$J>H\ , \tag{4}$$

where

TABLE IV. Some electrical parameters of the 4:3:3:y and Li-doped 4:3:(3−z):4 obtained from the conductivity data.

	σ_{dc} (Ω^{-1}cm^{-1})		W (eV)		W_h[a]	ΔW	W_d[b]
Sample	at 300 K	at 410 K	300 K	410 K	(eV)	(eV)	(eV)
No. 2	1.03×10^{-12}	8.70×10^{-10}	0.660	0.820	0.18	0.480	0.062
No. 3	2.42×10^{-12}	1.50×10^{-9}	0.634	0.760	0.22	0.414	0.043
No. 4	9.00×10^{-11}	2.53×10^{-8}	0.580	0.709	0.25	0.330	0.050
No. 5	2.05×10^{-10}	4.71×10^{-8}	0.568	0.684	0.26	0.308	0.030
No. 6	7.70×10^{-10}	2.31×10^{-7}	0.544	0.656	0.28	0.264	0.029
No. 7	1.70×10^{-9}	3.80×10^{-7}	0.526	0.637	0.28	0.246	0.037
No. 8	3.90×10^{-9}	6.95×10^{-7}	0.510	0.625	0.29	0.220	0.029
(Li-doped) No. 9	4.29×10^{-10}	1.46×10^{-7}	0.561	0.643	0.28	0.281	0.029
(Li-doped) No. 10	2.15×10^{-10}	8.57×10^{-8}	0.588	0.664	0.29	0.298	0.029
(Li-doped) No. 11	1.25×10^{-10}	4.29×10^{-8}	0.591	0.682	0.30	0.291	0.030

[a]Calculated from Eq. (3) assuming $\epsilon_p=\epsilon_\infty=n^2$ (with $n=1.995$).
[b]Calculated from $W_d=0.03e^2/\epsilon_s R$. The values of ϵ_s were estimated from the experimental dielectric constant data of the samples (Ref. 17).

$$H=(2k_BTW_h/\pi)^{1/4}(\hbar\omega_{ph}/\pi)^{1/2}\ .$$

Similarly for nonadiabatic hopping one has $J<H$. The condition for the formation of small polaron is $J<W_h/3$. An estimation of J can be made from the approximate relation

$$J\approx e^3[N(E_F)]^{1/2}/\epsilon_p^{3/2}\ . \tag{5}$$

The right-hand side of Eq. (4) gives a value of 0.03–0.04 eV. From Eq. (5) one finds $J=0.02$ eV for a value of $N(E_F)=10^{20}$ eV^{-1} cm^{-3} [$N(E_F)$ is the density of states at the Fermi level obtained from the ac conductivity data of the 4:3:3:y glasses[17]]. The condition for small-polaron formation ($J<W_h/3$) is also satisfied. The estimated value of J obtained from Eq. (5) is slightly less than the right-hand side of Eq. (4), which indicates that the small-polaron hopping occurs in the nonadiabatic regime. Nonadiabatic hopping conduction in the present glass systems is also supported from other facts as illustrated below.

The wave-function decay constant (α) can be obtained experimentally from the slope of $\log_{10}[\sigma_0/C(1-C)]$ versus R curve [Fig. 6(a)]. Murawski and Gzowski[22] have shown that $\log_{10}\sigma_0$ is a linear function of R in iron-phosphate glasses and σ_0 [Eq. (1)] should be divided by $[C(1-C)]$ as the value of C may vary for different glass compositions. From the slope of the linear curve [Fig. 6(a)] the value of α is found to be 0.67 Å^{-1}. This value of α is well within the limit suggested by Austin and Garbett[23] and also satisfies the requirement for applying small-polaron theory, viz., $\alpha^{-1}<r_p<R$. Murawski, Chung, and Mackenzie[24] have shown that the value of α ranges from 0.4–4 Å^{-1} for a series of TMO glasses. The values of α can also be calculated from Eq. (1) by inserting the values of N, R, and C from Tables I and II and assuming a reasonable value of $\nu_{ph}=10^{13}$ Hz. We have already estimated from IR spectra a value of $\nu_{ph}=1.53\times10^{13}$ Hz for the 4:3:3:y-type glasses. The values of $\nu_{ph}\exp(-2\alpha R)$ calculated from the conductivity data is shown in Table V. It is noticed from Table V that the values of $\nu_{ph}\exp(-2\alpha R)$ varying from 2.92×10^9 to 1.69×10^{10} Hz are much less than the corresponding values of the TMO glasses obeying adiabatic hopping conduction. This also suggests that the nonadiabatic conduction mechanism is valid for the 4:3:3:y and Li-doped 4:3:(3−z):4 glasses. The values of ν_{ph} have also been calculated from the conductivity data assuming $\alpha=0.67$ Å^{-1} as obtained from the slope of Fig. 6(a) and using the values of R, N, and C from Table I. These values of ν_{ph} (shown in Table V) are little less than those obtained from the IR absorption spectra. The IR spectra, as mentioned above, gives more or less constant values of ν_{ph} for all 4:3:3:y glasses, whereas the values of ν_{ph} obtained from the conductivity data of the glasses decreases with the increase of CuO concentrations of the glasses. The values of ν_{ph} calculated from Θ_D values (Table III) also show this trend of variation of ν_{ph} (see Table III).

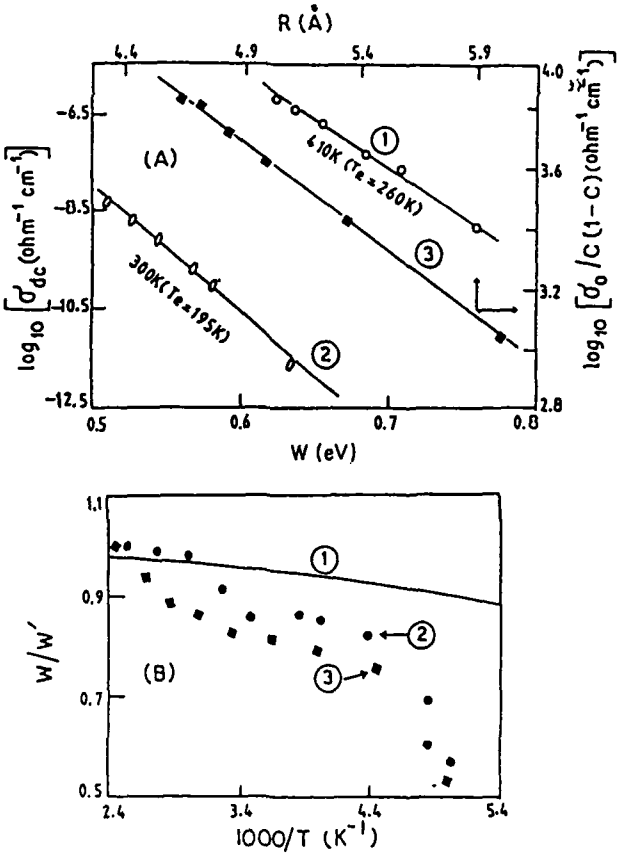

FIG. 6. (a) Plot of $\log_{10}(\sigma_{dc})$ vs activation energy (W) for the 4:3:3:y glasses at two fixed experimental temperatures, 410 K (1) and 300 K (2). The temperatures T_e within the parentheses are obtained from the slopes of the curves; variation of $\log_{10}[\sigma_0/C(1-C)]$ with R (mean separation between Cu sites) for the 4:3:3:y glasses (3). (b) Plot of W/W' vs $10^3/T$ for the $Bi_4Sr_3Ca_3Cu_4O_x$ (3) and $Bi_4Sr_3Ca_{3-z}Li_zCu_4O_x$ (for $z=1.0$ only) (2) glasses. The theoretical curve (1) is obtained from Eq. (7).

The values of small-polaron coupling constant (γ_p), which is a measure of electron-phonon interaction in the glasses, can be estimated from the relation[15] $\gamma_p=2W_h/h\nu_{ph}$. Using the values of W_h from Table IV and $\nu_{ph}=10^{13}$ Hz, the calculated values of γ_p listed in Table V are found to vary from 8.69 to 14 for the 4:3:3:y-type glasses. Austin and Mott[15] suggested that a value of $\gamma_p>4$ usually indicates strong electron-phonon interaction in solids. From the values of γ_p, we have evaluated the effective mass (m_p) of the polaron in the glasses using the relation[15]

$$m_p=(h/2JR^2)\exp(\gamma_p)=m^*\exp(\gamma_p)\ , \tag{6}$$

where m^* is the rigid-lattice effective mass. The calculated values of γ_p and m_p/m^* are found to be quite large indicating strong electron-phonon interaction in these glasses, which also supports the formation of small polarons in them.[25] The values of m_p/m^* for the Li-doped 4:3:(3−z):4 glasses are a little bit higher (see Table V) than those of the Li-free glasses.

Schnakenberg[26] suggested that with the lowering of temperature the multiphonon processes are replaced by a single phonon (optical) process and the activation energy for conduction should follow the relation

TABLE V. Some electrical parameters characterizing the 4:3:3:y and Li-doped 4:3:(3−z):4 glasses.

Sample	$\nu_{ph}\exp(-2\alpha R)$ (Hz)	ν_{ph}^{a} (Hz)	α^{b} (Å^{-1})	α^{c} (Å^{-1})	$\gamma_p^{d}=2W_h/\hbar\omega_{ph}$	$m_p/m^*=\exp(\gamma_p)$
No. 2	2.92×10^{9}	1.34×10^{13}	0.47	0.98	8.69	5.9×10^{3}
No. 3	4.00×10^{9}	1.25×10^{13}	0.46	0.92	10.62	4.1×10^{4}
No. 4	7.78×10^{9}	1.01×10^{13}	0.45	1.23	12.07	1.7×10^{5}
No. 5	1.13×10^{10}	9.57×10^{12}	0.45	0.99	12.56	2.8×10^{5}
No. 6	1.38×10^{10}	8.88×10^{12}	0.44	0.97	13.52	7.5×10^{5}
No. 7	1.64×10^{10}	8.94×10^{12}	0.44	0.75	13.52	7.5×10^{5}
No. 8	1.69×10^{10}	8.40×10^{12}	0.44	0.87	14.00	1.2×10^{6}
(Li-doped) No. 9	3.28×10^{10}	1.06×10^{13}	0.58		13.61	8.1×10^{5}
(Li-doped) No. 10	2.20×10^{10}	1.04×10^{13}	0.63		13.81	1.0×10^{6}
(Li-doped) No. 11	1.15×10^{10}	1.02×10^{13}	0.71		14.29	1.6×10^{6}

[a]Calculated from $\nu_{ph}\exp(-2\alpha R)$ assuming $\alpha=0.67$ Å^{-1} as obtained from the slope of $\log_{10}[\sigma_0/C(1-C)]$ versus R curve [Fig. 6(a)].
[b]Calculated from the values of $\nu_{ph}\exp(-2\alpha R)$ assuming $\nu_{ph}=10^{13}$ Hz.
[c]Obtained from the slope of $\log_{10}(\sigma_{dc}T^{1/2})$ versus $T^{-1/4}$ curve (Fig. 7).
[d]Assuming $\omega_{ph}/2\pi=10^{13}$ Hz.

$$W/W'=\tanh(\hbar\omega_{ph}/4k_BT)/(\hbar\omega_{ph}/4k_BT)\ , \tag{7}$$

where W' is the high-temperature activation energy. In Fig. 6(b), the experimental as well as theoretical values of W/W' for one typical glass sample ($Bi_4Sr_3Ca_3Cu_4O_x$) are plotted as a function of temperature. All the other members of the 4:3:3:y glasses also behave almost similarly. It is observed from Fig. 6(b) that both the experimental and theoretical values of W/W' decrease with the decrease of temperature but the quantitative fit is rather poor. Almost similar is the case with Li-doped glasses [Fig. 6(b)]. It should be mentioned here that the fall in activation energy with temperature is quite consistent in the light of polaron hopping model of dc conductivity.

At sufficiently low temperature where the polaron binding energy is small and static disorder energy of the glass plays a dominant role in the conduction process, Mott's $T^{-1/4}$ analysis for the variable range hopping (VRH) can in general be applied for the TMO glasses. But for the 4:3:3:y and Li-doped 4:3:(3−z):4 glasses sufficient data at low temperature is not available due to experimental limitations and very high resistivity of the samples. An attempt to verify the applicability of this law gives unacceptably large values of α and W_d. In an alternative way, Greaves[27] suggested a variable range hopping conduction in the intermediate temperature range and derived an expression for the conductivity as

$$\sigma_{dc}T^{1/2}=L\exp(-B/T^{1/4})\ , \tag{8}$$

where B and L are constants. The slope (B) of $\log_{10}(\sigma_{dc}T^{1/2})$, versus $T^{-1/4}$ curve is given by

$$B=2.1[\alpha^3/k_BN(E_F)]^{1/4}=2.4[W_d(\alpha R)^3/K_B]^{1/4}\ . \tag{9}$$

Figure 7 shows the plot of $\log_{10}(\alpha_{dc}T^{1/2})$ as a function of $T^{-1/4}$ for some of the 4:3:3:y and Li-doped 4:3:(3−z):4

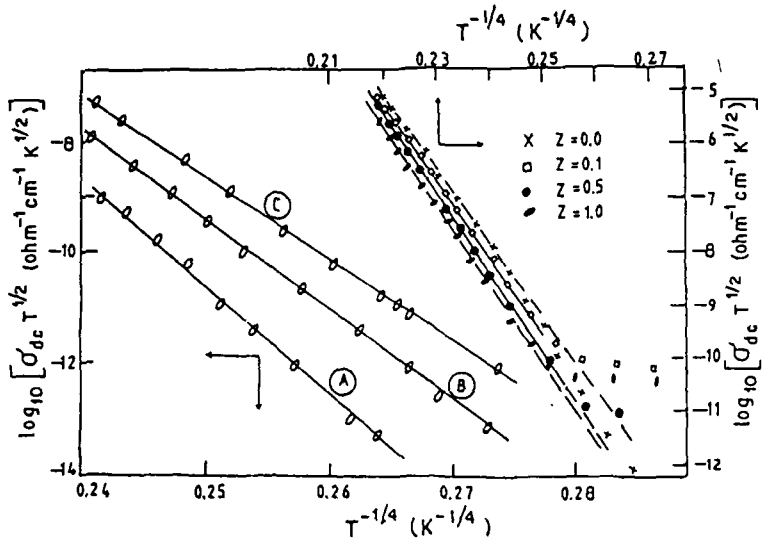

FIG. 7. Plot of $\log_{10}[(\sigma_{dc}T^{1/2})]$ vs $T^{-1/4}$ for the $Bi_4Sr_3Ca_3Cu_yO_x$ [$y=3$ (A), $y=4$ (B), $y=5$ (C)] and $Bi_4Sr_3Ca_{3-z}Li_zCu_4O_x$ glasses.

glasses. Other members also follow similar behavior. From the slopes (B) of the curves the values of α and W_d have been calculated using Eq. (9). The calculated values of α from Greaves' $T^{-1/4}$ plot shown in Table V are higher than those obtained from the dc conductivity data at higher temperatures but still they are well within the limit suggested by Austin and Garbett.[23] The calculated values of W_d from Eq. (9) are unacceptably large. This type of large value of W_d was also reported for the vanadate[28] and Bi_2O_3-Fe_2O_3 glasses.[6]

IV. CONCLUSION

The dc conductivities of the Li-doped 4:3:(3−z):4 glasses are lower than those of the undoped 4:3:3:y glasses. Electrical conduction in both the glasses are found to be, due to hopping of small polarons between localized sites and the hopping process occurs, unlike many other TMO glasses, in the nonadiabatic regime. In the high-temperature region the activation energy W decreases slowly with the decrease of temperature and the conduction process is dominated by the thermally activated nearest-neighbor hopping of small polarons. In the intermediate- and low-temperature regions the VRH conduction appears to be more appropriate. The fitting of the experimental conductivity data with Greaves' relation[27] [Eq. (8)] at intermediate temperature shows qualitative agreement but the quantitative fit is not very good. An attempt to fit the low-temperature conductivity data of some glasses with Mott's VRH (Refs. 15 and 25) gives unacceptably large values of the disorder energy W_d and wave-function decay constant α.

Partial replacement of Ca by Li is found to increase the superconducting transition temperatures (T_c) by 4–5 K in the corresponding glass ceramics (see Table II). Since the electrical conductivities of both 4:3:3:y and Li-doped 4:3(3−z):4 glasses behave similarly it appears that Li or another alkali metal acts as a flux in the glass matrix to lower the melting point of the glasses and finally to increase the superconducting T_c by reducing the possibility of oxygen loss in the glass ceramics. Recent experimental results on alkali-metal doped superconducting ceramics[29] indicate that Li gets some preferred position in the Cu sites in the three-dimensional lattice. Addition of Li has, however, little effect on the overall microstructural behavior of the Li-doped 4:3:(3−z):4 glasses, which is also indicated from the similar nature of the temperature dependent electrical and other properties of 4:3:3:y and Li-doped 4:3:(3−z):4 glasses.

Finally, it would be worthwhile to point out that the theoretical discussion made in this paper could also be extended for explaining the conductivity of polymers and ionic conductors.

ACKNOWLEDGMENTS

The authors are grateful to Professor S. P. Sengupta, Dr. B. Banerjee, Professor G. V. Subbarao for their help. This work was supported by Department of Science and Technology (DST) and Council of Scientific and Industrial Research (CSIR), government of India.

[1]Y. Sakuri and J. Yamaki, J. Electrochem. Soc. 132, 512 (1985); H. Hirashima, Y. Watanabe, and T. Yoshida, J. Non-Cryst. Solids 95&96, 825 (1987); S. Nakamura and N. Ichinose, *ibid.* 95&96, 849 (1987).

[2]T. Komatsu, K. Imai, K. Matusita, M. Tanaka, Y. Iwai, A. Kawakami, Y. Kaneko, and T. Yamashita, Jpn. J. Appl. Phys. 26, L1148 (1987); A. Bailey, G. Alvarez, G. J. Russel, and K. N. R. Taylor, Bull. Mater. Sci. (India) 14, 111 (1991); M. Miijak, E. Babic, A. Hamzic, G. Bratinas, and Z. Marohnic, Supercond. Sci. Technol. 1, 141 (1988).

[3]E. V. Sampathkumaran and R. Vijayaraghavan, Bull. Mater. Sci. (India) 14, 297 (1991); T. Komatsu, R. Sato, and K. Matusita, Appl. Phys. Lett. 54, 170 (1990); K. B. R. Varma, K. J. Rao, and C. N. R. Rao, Appl. Phys. Lett. 54, 69 (1989); H. Zheng and J. D. Mackenzie, Phys. Rev. B 38, 7166 (1989); M. Tatsumisago, C. A. Angell, Y. Akamatsu, S. Tsuboi, N. Tohge, and T. Minami, Appl. Phys. Lett. 55, 600 (1989).

[4]H. Zheng, M. W. Colby, and J. D. Mackenzie, J. Non-Cryst. Solids 127, 143 (1991); K. B. R. Varma, G. N. Subbana, T. V. Ramakrishnan, and C. N. R. Rao, J. Appl. Phys. 55, 75 (1989); B. K. Chaudhuri and K. K. Som, Bull. Mater. Sci. 14, 1093 (1991); S. E. LeBeau, J. Righi, J. E. Osttenson, S. C. Sanders, and K. K. Finnemore, Appl. Phys. Lett. 55, 292 (1989).

[5]A. Ghosh and B. K. Chaudhuri, J. Non-Cryst. Solids 83, 151 (1986).

[6]B. K. Chaudhuri, K. Chaudhuri, and K. K. Som, J. Phys. Chem. Solids 50, 1137 (1989); C. H. Chung and J. D. Mackenzie, J. Non-Cryst. Solids 42, 357 (1980).

[7]K. K. Som, S. Mollah, K. Bose, and B. K. Chaudhuri, Phys. Rev. B 45, 1655 (1992).

[8]S. Mollah, K. Bose, K. K. Som, and B. K. Chaudhuri, J. Mater. Sci. Lett. (to be published).

[9]R. C. Baker, W. H. Hurg, and H. Steinfink, Appl. Phys. Lett. 54, 371 (1989).

[10]R. Horiuchi, T. Kawai, K. Mitsui, K. Ogura, and S. Kawai, Physica C 168, 309 (1990).

[11]T. Kawai, T. Horiuchi, K. Mitsui, K. Ogura, S. Takagi, and S. Kawai, Physica C 161, 561 (1989).

[12]S. X. Dau, H. K. Liu, W. M. Wu, W. X. Wamg, C. C. Sorrel, R. Winn, and N. Savvides in *Advances in Superconductivity-III Proceedings of the 3rd International Symposium on Superconductivity (ISS, 1990), Japan*, edited by K. Kajimura and H. Hayakawa (Springer-Verlag, Berlin, 1991), p. 431.

[13]S. V. Suryanaryana, B. G. Krishna, R. Gundakaram, and S. V. Reddy, Bull. Mater. Sci. (India) 14, 303 (1991); I. Matsubara, H. Tanigawa, T. Ogura, H. Yamashita, M. Kinoshita, and T. Kawai, Physica C 167, 503 (1990).

[14]K. K. Som and B. K. Chaudhuri, Phys. Rev. B 41, 1581 (1990).

[15]N. F. Mott, J. Non-Cryst. Solids 1, 1 (1968); I. G. Austin and N. F. Mott, Adv. Phys. 18, 41 (1969).

[16]A. Ghosh, J. Phys.: Condens. Matter 1, 7819 (1989).

[17]K. K. Som, Ph. D. thesis, Jadavpur University, 1991.

[18]A. Miller and E. Abrahams, Phys. Rev. 120, 745 (1960); J. O. Isard, J. Non-Cryst. Solids 42, 371 (1980).

[19]C. H. Chung, J. D. Mackenzie, and L. Murawski, Rev. Chem. Min. 16, 308 (1964).

[20]M. Sayer and A. Mansingh, Phys. Rev. B 6, 4629 (1972).

[21]T. Holstein, Ann. Phys. (NY) 8, 325 343 (1959).

[22]L. Murawski and O. Gzowski, Phys. Status Solidi (a) 19, K125 (1973).

[23]I. G. Austin and E. S. Garbett, in *Electronic and Structural Properties of Amorphous Semiconductors*, edited by P. G. LeComber and J. Mort (Academic, London, 1973), p. 393.

[24]L. Murawski, C. H. Chung, and J. D. Mackenzie, J. Non-Cryst. Solids 32, 91 (1979).

[25]N. F. Mott and E. A. Davis, *Electronic Processes in Non-Crystalline Materials*, 2nd Ed. (Clarendon, Oxford, 1979).

[26]J. Schnakenberg, Phys. Status Solidi 28, 623 (1968).

[27]G. N. Greaves, J. Non-Cryst. Solids 11, 427 (1973); 51, 87 (1982).

[28]V. K. Dhawan, A. Mansingh, and M. Sayer, J. Non-Cryst. Solids 51, 87 (1982).

[29]P. S. Mukherjee, A. Simon, M. S. Sharma, and A. D. Damodaran, Solid State Commun. 81, 253 (1992); M. Ausloos, C. Laurent, H. W. Vanderschueren, A. Rulmont, and P. Tarte, *ibid.* 68, 539 (1988).

Concentration-dependent physical properties of $Bi_zCa_3Sr_3Cu_4O_x$ oxides glasses with $z = 1–5$

S. MOLLA, K. BOSE, K. K. SOM, B. K. CHAUDHURI
Solid State Physics Department, Indian Association for the Cultivation of Science, Calcutta 7000 32, India

The $Bi_4Ca_3Sr_3Cu_4O_x$ or [4:3:3:4] glasses have recently been well studied in their superconducting and glassy phases [1–8]. These glasses can be used as the precursor materials for making superconducting wires, films [6,7], etc. High-temperature superconducting oxide (HITSO) materials obtained from these glasses are also found to be very dense as well as homogeneous [4]. Therefore, proper characterizations of these glasses with different concentrations of transition-metal (Cu) ions (viz. $Bi_4Ca_3Sr_3Cu_yO_x$, hereafter referred to as [Y] glasses) as well as with different glass former oxide (viz. $Bi_2Ca_3Sr_3Cu_4O_x$, hereafter referred to as [Z] glasses) would be highly interesting. From these studies one might also point out the differences in the physical properties of these and other similar transition-metal oxide glasses (TMO) which do not become superconductors in their glass-ceramic (GC) phases.

Furthermore, it is well known that there is a possible influence of phase separation effects on the electrical properties of the semiconducting oxide glasses [9, 10] which might also influence the appearance of the HITSO phases in the glasses in this investigation. The density and the apparent molar volume (V_O^*) of oxygen were found to give important information about the phase separation and homogeneity of these glasses.

Non-linear variations in density (ρ), glass-transition temperature (T_g), electrical conductivity (σ), etc., with the corresponding variation of transition-metal ion (TMI) concentrations in the [Y] glasses have already been reported [11]. In this letter we report the variation in ρ, T_g and room-temperature d.c. conductivities of the [Z] glasses for different Bi_2O_3 concentrations. Attempts have also been made to calculate the V_O^* of oxygen, knowing the densities and other parameters of the glasses.

The general method of preparation of these glasses ([Y] and [Z]) was the same as discussed in [3, 11]. The starting materials, viz. Bi_2O_3, CuO, $CaCO_3$ and $SrCO_3$ (each of purity 99.99% as procured from Merck, Aldrich and Sigma), in appropriate proportions (with $y = 2$, 2.5, 3, 3.5, 4, 4.5 and 5) were melted separately in crystalline alumina crucibles, all compositions at 1200 °C, for 1 h each and were then quickly quenched at room temperature by pressing the melt between two polished copper blocks. Since the TMI concentrations (Cu^+/Cu^{2+}) change [11] with glass-making temperature (T_M) as well as with the duration for which the glass is kept inside the furnace (t_F) we kept T_M and t_F fixed for all of the glasses.

The X-ray diffractions patterns (Philips PW 1050/51 coupled with a PW 1130 generator) with CuK_α radiation showed broad peaks between $2\theta = 20–30°$ for all of the glasses, as shown in our earlier work [3, 11, 12]. The amorphous character of the glasses was also examined by scanning electron microscopy (Hitachi, model S-415A). The concentrations of the Cu^{2+} ions were obtained from magnetic susceptibility measurements [12] and the total copper ions (assumed to be composed of Cu^+ and Cu^{2+}), Cu_t, present in the glasses was obtained by the atomic absorption spectroscopic technique as shown in Table I. The small paramagnetism of the [Y] and [Z] glasses is considered to be solely due to the presence of Cu^{2+} ions in the glasses.

The room-temperature (300 K) magnetic susceptibility (χ) of the [Z] glasses as a function of the Bi_2O_3 concentration is shown in Fig. 1. A change of slope of the $\chi–T$ curve around $z = 4$ is observed in this figure. The T_g of all these [Z] glasses were obtained from differential thermal analysis (Shimadzu DT-30) curves. The variation of T_g with Bi_2O_3 concentration (z) was found to be non-linear with a change of slope around $z = 4$ (Fig. 1). This non-linear behaviour was also reflected in other physical properties (density, mean molar volume of oxygen, d.c. conductivity, etc.) as discussed below.

The densities of the glasses were measured by the Archimedes method, using a microbalance and carbon tetrachloride, with an accuracy of $\pm 0.02\ g\,cm^{-3}$. The variation of densities of the [Z] glasses with Bi_2O_3 concentration as shown in Fig. 2 is almost continuous below 20 mol % Bi_2O_3 and shows a non-linear behaviour between 20 and 30 mol % Bi_2O_3. At around the same concentration

TABLE I Some important parameters of the $Bi_zCa_3Sr_3Cu_4O_x$ glasses

	z					
	2	2.5	3	3.5	4	5
Melting temperature (°C) (kept for 1 h)	1200	1200	1200	1200	1200	1200
Starting Bi_2O_3 (wt%)	46.80	52.30	56.85	60.60	63.72	68.70
Final Bi_2O_3 (wt%)[a]	45.00	49.80	54.10	58.10	60.58	65.82
$C = Cu^+/Cu_t$	0.71	0.75	0.74	0.73	0.78	0.76
T_c(zero) (K)[b]			70	75	85	78

[a]Obtained from chemical analysis and atomic absorption spectroscopy. Maximum error in the measurement was within ±5%.
[b]Measured by the four-probe method with GC samples.

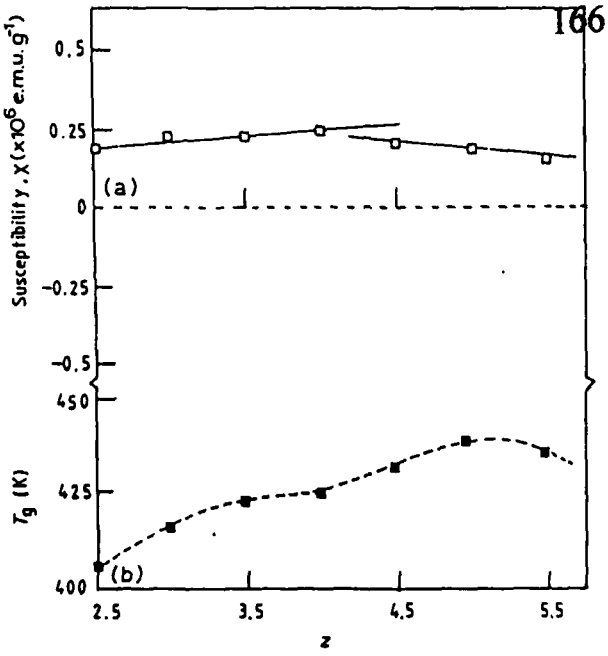

Figure 1 (a) Variations of d.c. magnetic susceptibilities and (b) glass transition temperature (T_g) of the $Bi_xSr_3Ca_3Cu_4O_x$ glasses with z at 300 K.

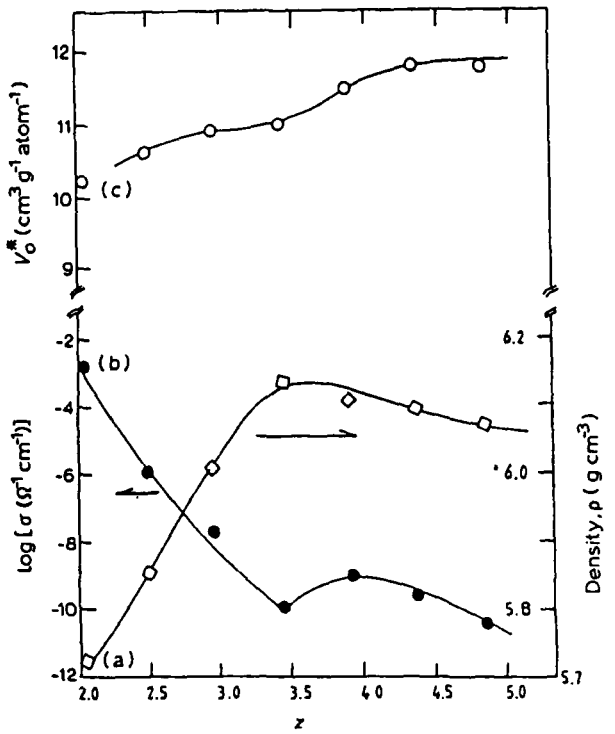

Figure 2 Variations of (a) density, (b) d.c. electrical conductivities and (c) mean molar volume oxygen (V_o^*) in the $Bi_xSr_3Ca_3Cu_4O_x$ glasses with z at 300 K.

of CuO the density of the [Y] glasses showed anomalous behaviour [11]. It appears that for both the [Y] and [Z] glasses the non-linearity starts around the glass composition $Bi_4Ca_3Sr_3Cu_4O_x$ [4:3:3:4]. This is the most stable glass composition in the two series ([Y] and [Z] glasses) which becomes a highly homogeneous superconductor with a sharp superconducting transition around $T_c = 85$ K [5, 11, 12].

It is often advantageous to express the relationship between the density of an oxide glass and its composition in terms of the apparent molar volume (V_o^*) occupied by 1 g-atom oxygen. The values of V_o^* calculated [11, 13] for the [Z] glasses are shown in Fig. 2 as a function of z. The variations of V_o^* with concentration are also found to be non-linear (Fig. 2), indicating that the geometry and topology of the random network change with the concentration. This is also supported from the fact that the T_c of these glasses (with $z = 3$–5) in their GC phases change with z (see Table I). However, the main characteristic features and the semiconducting properties of these glasses with different values of z are found to be similar [3, 11, 12].

The observed variations of ρ with CuO [11] or Bi_2O_3 in the [Y] and [Z] glasses appear to distinguish these glasses from many other TMO glasses [14–17] containing V_2O_5, Fe_2O_3 and CuO. To justify our argument we have plotted in Fig. 3 the variations in densities of some of these TMO glasses which do not become superconductors in their GC phases. The densities of thesee glasses appear to increase with the corresponding increase of TMI as shown in Fig. 3.

As with ρ and T_g, the values of the electrical conductivities (σ) or the [Y] glasses are also found to show non-linear variations with the Bi_2O_3 concentration. The values of conductivities of these glasses

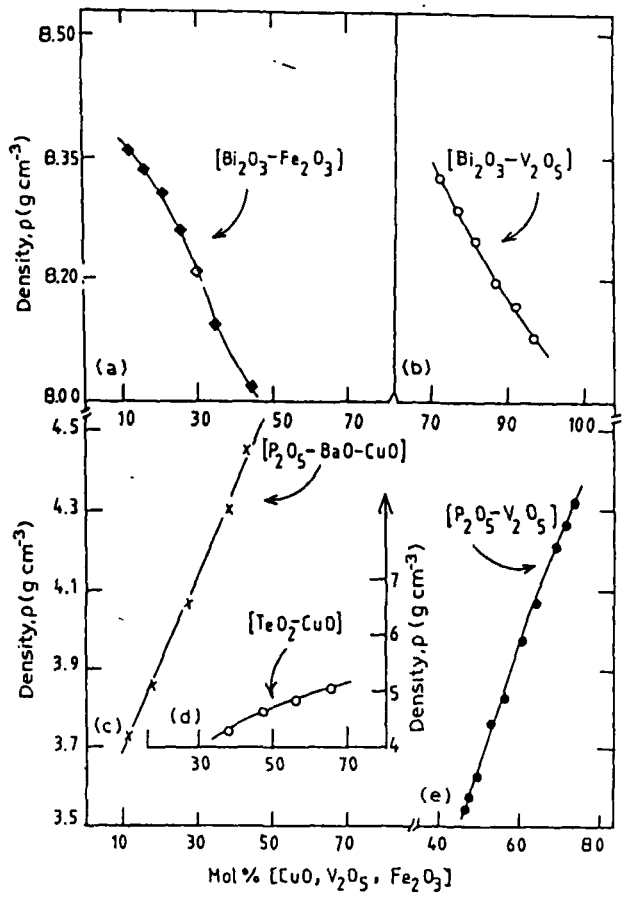

Figure 3 Variations of densities of different TMO glasses (which do not become superconductors in their GC phases) with transition-metal ions [14–17].

as a function of z are also shown in Fig. 2. This maximum is also visualized from Fig. 2b around 25–30 mol % Bi_2O_3.

Finally, it may be concluded that, unlike many

TMO glasses, some of the glasses of this class becoming superconductors in their GC phases, show some interesting non-linear variations in ρ, T_g, σ, etc., when plotted as a function of TMI (as in [11]) or glass former oxide (such as Bi_2O_3) concentrations (as reported here). The densities of both the [X] and [Y] glasses also change quite appreciably under heat treatment for several hours. Variations in densities of two such glasses, viz. [4:3:3:4] and [5:3:3:4], with different annealing time (at 300 and 800 °C) are shown in Fig. 4. With the increase of annealing time and temperature the values of the density of the glasses are increased. This is due to the large amount of oxygen intake by the system with the appearance of the crystalline GC phases which ultimately become HITSO materials.

The non-linear variation of the V_o^* of oxygen with CuO or Bi_2O_3 concentration indicates a small change of slope. This again suggests either a composition dependent structural change or phase separation behaviour in these glasses. For higher concentrations of the [Y] glasses ($y > 4$) some phase separation effects have been observed by scanning electron microscopy studies [10] which will be discussed elsewhere.

From CuO-dependent infrared studies of the [Y] glasses [5, 7, 11] a change of $[Bi_2O_3]$ octahedral structural units to $[BiO_3]$ polyhedral structural units is also found with change of CuO concentration in the [Y] glasses. The anomalous variations of ρ, T_g, V_o^* and other physical properties of these [Y] and [Z] glasses with concentration might also be associated with such a change of octahedral to polyhedral structural units. This is in turn also related to the anomalous change in the cationic ratio Cu^+/Cu^{2+} in the glasses with change of CuO or Bi_2O_3 concentration. Such anomalous changes of ionic concentrations have also been reported earlier in some vanadate glasses [18]. It should be pointed out here that the melting temperature as well as the duration for which the melt is kept inside the furnace also affect the ratio of the copper cations. This might be taken into consideration to maintain the desired cationic ratio in the glass necessary for the appearance of appropriate superconducting phase in the corresponding GC. It would be relevant to point out that for the $Bi_{3.5}Ca_3Sr_3Cu_4O_x$ [3.5:3:3:4] glass, for instance, if prepared at two melting temperatures (say 1200 °C and 1300–1400 °C, respectively) one finds two types of glasses: a highly brittle phase (becoming a high-temperature superconductor in its ceramic phase as shown in Table I) and a very viscous phase (from the higher-temperature melting glass) which can be drawn into the forms of long wires from the melt as shown in Fig. 5. The wires thus prepared become conducting in their CG phases but they do not show zero resistance down to 70 K within the limit of the present low-temperature investigation. More-elaborate work characterizing these glasses would be interesting.

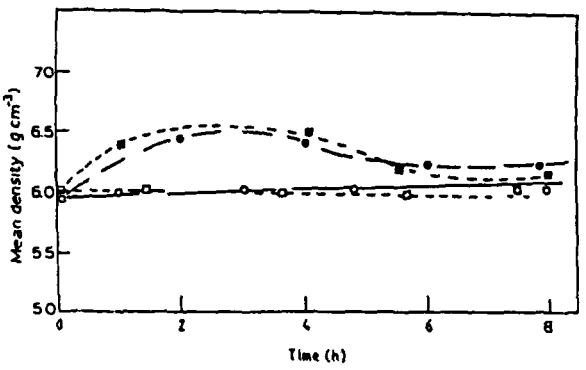

Figure 4 Variation of mean density of some samples of (circles) $Bi_4Ca_3Sr_3Cu_4O_x$ and (squares) $Bi_3Ca_3Sr_3Cu_4O_x$ glasses with different annealing time at (○, □) 300 and (●, ■) 800 °C.

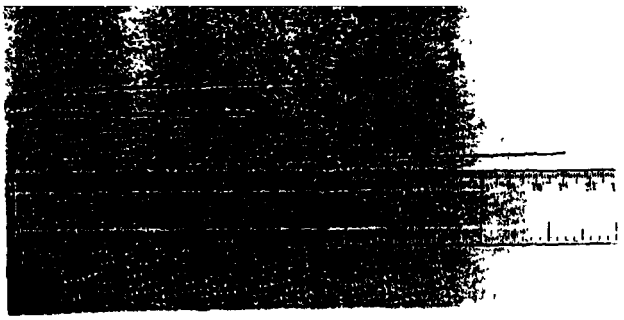

Figure 5 $Bi_{3.5}Sr_3Ca_3Cu_4O_x$ glass wires/fibres drawn by pulling the molten glass.

Acknowledgement

One of the authors (S. M.) is grateful to the CSIR, India, for financial assistance to complete the work. The authors are also grateful to Professor V. G. Subba Rao, Indian Institute of Technology, Madras, for providing some oxides used in this work.

References

1. J. M. TARASCON, Y. LE PAGE, P. BARBOUX, B. G BAGLEY, L. H. GREENE, W. R. McINNON, G. W. HULL, M. GIROUD and D. M. HWANG, *Phys. Rev.* B37 (1988) 9382.
2. H. ZHENG and J. D. MACKENZIE, *ibid.* B38 (1989) 7166.
3. K. K. SOM and B. K. CHAUDHURI, *ibid.* B41 (1990) 1591.
4. R. C. BAKER, W. H. HURNG and H. STEINFINK, *Appl. Phys. Lett.* 54 (1989) 371.
5. H. ZHENG, M. W. COLBY and J. D. MACKENZIE, *J. Non-Cryst. Solids* 127 (1991) 143.
6. S. E. LEBAU, I. RIGHT, J. E. OSTENSON, S. C. SANDERS and D. K. FINNEMORE, *Appl. Phys. Lett.* 55 (1989) 292.
7. H. ZHENG, R. XU and J. D. MACKENZIE, *J. Mater. Res.* 4 (1989) 911.
8. B. K. CHAUDHURI and K. K. SOM, *Bull Mater. Sci (India)* 14 (1991) 1093.
9. T. N. KENNEDY and J. D. MACKENZIE, *Phys. Chem. Glasses* 8 (1967) 169.
10. K. K. SOM, PhD thesis, Jadavpur University (1991)

11. K. K. SOM, S. MOLLA, K. BOSE and B. K. CHAUDHURI, *Phys. Rev.* **B45** (1992).
12. B. K. CHAUDHURI, K. K. SOM and S. P. SENGUPTA, *J. Mater. Sci. Lett.* **8** (1989) 520.
13. S. GLASSTONE, in "The elements of physical chemistry" (Macmillan, London, 1955) p. 147.
14. M. SAYER and A. MANSINGH, *Phys. Rev.* **B6** (1972) 4629.
15. A. GHOSH and B. K. CHAUDHURI, *J. Non-Cryst. Solids* **83** (1986) 151.
16. B. K. CHAUDHURI, K. CHAUDHURI and K. K. SOM, *Phys. Chem. Solids* **50** (1989) 1137.
17. C. F. DRAKE, I. F. SCANLAN and A. ENGEL, *Phys Status Solidi* **32** (1969) 193.
18. K. K. SOM and B. K. CHAUDHURI, *J. Mater. Sci.* 26 (1991) 1236.

Received 11 September 1991
and accepted 7 January 1992

Chapter-II

Chapter-II

This chapter contains the reprints on superconducting materials. Structural and transport properties of Pb–Bi–Sr–Ca–Cu–O (PbBiSCCO) superconductors containing 10, 25 or 30 wt.% Ag or AgCu or AgIn are included here. The thermoelectric power (TEP) of $Bi_{4-n}Pb_nSr_3Ca_3Cu_4O_x$ (n = 0-1) and the reprints on $YBa_2Cu_3O_x$ and ($YBa_2Cu_3O_x$ –Ag) superconductors are included here. The effect of hydrostatic pressure (P) up to 17 kbar on the superconducting transition temperature (T_C) of the intermetallic non-oxide perovskite superconductor MgC_xNi_3 (x = 1-1.5) and the magnetic field dependence of low temperature specific heat of spinel oxide superconductor $LiTi_2O_4$ are attached here. The book article on Bi-based glass-ceramic superconductor and the review articles on $MgCNi_3$ and MgB_2 are also given here. The Topical Review on $MgCNi_3$ in J. Phys.: Condens. Matter 16 (2004) R1237-R1276 has been widely accepted and downloaded for more than 250 times within 27 days of from its date of publication. This is done for top 10% of J. Phys.: Condens. Matter articles as informed by the editor of this journal.

Transformation of high T_C superconducting phase in $Bi_{2-x}Pb_xSr_2Ca_2Cu_{3-y}A_yO_\delta$ (A = K, Na ; x = 0.1-0.3 ; y = 0.1-0.3) to the ferroelectric phase by K and Na doping

Soma Mukherjee[1], S Mollah[2], H. D. Yang[2], and B. K. Chaudhuri[1]

[1]*Department of Solid State Physics, Indian Association for the Cultivation of Science, Jadavpur, Kolkata – 700 032, India.*

[2]*Department of Physics, National Sun Yat Sen University, Kaohsiung 804, Taiwan, ROC*

The $Bi_{4-y}Pb_ySr_3Ca_3Cu_4O_\delta$ forms homogeneous glass which becomes superconductor around T_c (~ 80 K) in the ceramic phase obtained by annealing the glass around 1113 K. Partial substitution of Cu by alkali metal like K and Na in this multicomponent glassy precursor for high T_c superconductor viz. $Bi_{2-x}Pb_xSr_2Ca_2Cu_{3-y}A_yO_\delta$ (A = K, Na ; x = 0.1-0.3 ; y = 0.1-0.3) is found to destroy superconductivity of the corresponding annealed ceramic phase. The destruction of superconductivity is due to the appearance of nanocrystalline phase in the Na and K doped glasses. Interestingly, this nanocrystal dispersed glasses show ferroelectric (FE) behavior with FE transition between 500 and 550 K (depending both on x and y concentration). Nanoparticles/clusters (~ 10-50 nm size) embedded in the glassy precursors in the alkali doped glass is confirmed from the transmission electron micrographs. Both the as-quenched glasses (with and without the alkali metal A) show semiconducting behavior with non-adiabatic small polaron hopping mechanism, though their dielectric behavior is different. Present investigation indicates that superconducting behavior is suppressed by the precipitation of ferroelectric nanoparticles in the alkali metal doped glassy system. Though magnetism and superconductivity might coexist, ferroelectricity and superconductivity cannot be observed in the same sample.

PACS No. : 61.43.Fs, 61.46.+w, 77.80.-e

*Corresponding author: email: sspbkc@rediffmail.com

I. INTRODUCTION

It is well known that Bi based transition metal oxide glasses like $Bi_4Sr_3Ca_3Cu_4O_x$, $Bi_2Sr_2Ca_2Cu_3O_x$, $Bi_{4-y}Pb_ySr_3Ca_3Cu_4O_x$ etc. (referred to as SG glass) are very good precursors for high T_c superconductors [1-2]. These glasses become superconductors (mostly 2223/2212 type) [1-4] by annealing them around 840^0C for about 24h. It is a long-standing problem whether FE transition with spontaneous polarization is possible in pure homogeneous inorganic oxide glassy system. Lines [5] considered theoretically the possibility of FE phase in pure glass. But ferroelectricity has so far not been observed in pure glassy system even though FE ordering has been observed in liquid crystalline medium [6] where some kind of molecular order is present. So the appearance of ferroelectricity in the homogeneous single-phase $Bi_{1.8}Pb_{0.3}Sr_2Ca_2Cu_{2.8}K_{0.2}O_\delta$ type glass (FG glass) reported by Bahgat et al [7] is not beyond question.

In this paper, microstructural, transport and dielectric properties of the alkali metal glass have been studied and the results have been compared with those of the corresponding alkali metal free SG glasses, which are good precursors for high T_c superconductor. The alkali metal containing glasses showing FE behavior are not homogeneous single-phase glass but they are all glass-nanocrystal composites (GNC). Moreover, the annealed alkali metal doped glasses are not superconductors.

II. EXPERMENTAL

$Bi_{2-x}Pb_xSr_2Ca_2Cu_{3-y}A_yO_\delta$ (A= K, Na; x = 0.0-0.3, y=0.1-0.3) glasses showing FE behavior are prepared by partially replacing Cu with K and Na in a typical Bi-based glassy precursor for high T_c superconductor (SG) viz. $Bi_{2-x}Pb_xSr_2Ca_2Cu_3O_y$. The $Bi_{2-x}Pb_xSr_2Ca_2Cu_{2.8}K_{0.2}O_\delta$ type FG glasses, termed as Pb0K2, Pb1K2, Pb2K2, respectively, for A=K; x = 0.0, 0.1, 0.2; Pb3K2 (FG) for $Bi_{1.8}Pb_{0.3}Sr_2Ca_2Cu_{2.8}K_{0.2}O_\delta$ and Pb0Na2, Pb2Na2 and Pb3Na3 for A=Na; x = 0.0, 0.2; y=0.2 and x=0.3, y=0.3 are prepared by a similar method as discussed in our earlier papers [1,4,8]. Differential thermal analysis (DTA) at a heating rate of 10 °C/min from room temperature to 900 °C was made to find the glass transition (T_g) and crystallization (T_x) temperatures. A small endothermic peak was also observed from the DTA curves varying between 500 and 530K depending on Pb concentrations (x = 0.1-0.3). The transmission electron micrographs of the said FG type glasses were obtained by Hitachi Model H600 with

fine glass powder on carbon grids. The conductivity and dielectric constant of the samples from 80-450K was measured similar to our earlier work [1,4,9]. The temperature was measured with a nanovoltmeter (Keithley 181) within an accuracy of 0.5K.

III. RESULTS AND DISCUSSION

X-ray diffraction (XRD) analysis using CuK_α radiation confirmed the amorphous state of all the melt-quenched glasses. The values of the glass transition (T_g) and crystallization temperature (T_x) of the FG glasses obtained from the DTA trace are shown in Table-I. Figure 1a shows the TEM micrograph of a typical ferroelectric glass (Pb3K2), which clearly indicates the presence of microcrystals/clusters (10-50 nm size). The large cluster of a selected region of (a) is shown in Fig. 1b. The TEM micrographs clearly indicate that these FG glasses are not pure single-phase homogeneous glasses. They are glass-nanocomposites (GNC). These nanoparticles are considered to be responsible for the ferroelectric behavior of alkali metal containing glasses.

Interestingly, the alkali metal free SG glass becomes superconductor [8] by annealing around 840 ^{0}C. Figure 2a shows the thermal variation of resistivity of the annealed FG glass and Fig. 2b demonstrates the same for the annealed SG glass showing its superconducting nature. Therefore, presence of alkali metals and hence the appearance of ferroelectricity suppresses superconducting behavior of the annealed FG glass sample. Like SG glasses, the high temperature conductivity data of both the FG and SG glasses can be well fitted with small polaron hopping model [10] viz.

$$\sigma = \upsilon_{ph}\left(\frac{Ne^2R^2}{kT}\right)C(1-C)\exp(-2\alpha R)\exp\left(-\frac{W}{kT}\right) \qquad (1)$$

where symbols have their usual meanings [1,8]. The values of C for all the glasses were estimated from the room temperature magnetic susceptibility and density data (Table -I). The activation energy W arises from the electron-lattice interaction and/or the static disorder. Figure 3a shows the plot of log σ_{dc} versus T^{-1} for various compositions of Pb and a fixed composition of K and similar curves were also obtained for the Na doped glasses. Bi-based precursor glasses (SG) studied earlier [1,8] shown in Fig. 3b also shows similar behavior. Figure 3c shows the thermal variation of conductivity for a typical Na doped glass (Pb3Na3). The values of W of FG type glasses are, however, comparable to those of other SG glasses like $Bi_4Sr_3Ca_3Cu_4O_x$, $(Bi_{4-x}Pb_x)Sr_3Ca_3(Cu_{4-y}A_y)O_x$ (A = Cr, Mn, Fe) [1,8,11]. It is also noted that both concentrations and average particle/cluster sizes of the Pb0K2, Pb1K2, Pb2K2 glasses are smaller than those of the Pb3K2 (or FG) glass. A phase separation seems to occur around this particular concentration (Pb3K2) of the FG glasses showing lower value of conductivity with larger grain/cluster size (~50 nm average grain/cluster size). The values of Debye temperature θ_D, estimated from Fig. 3a (from the point where the change of slope occurred) are little less (Table-I) than those of other binary or ternary transition metal oxide (TMO) or SG glassy precursors [1,8]. All the parameters fitting the high temperature ($T>\theta_D/2$) conductivity data (Fig. 3a) with Eq. 1 are shown in Table-I.

Using Holstein's condition [12] it has been found that the FG glasses follow the non-adiabatic small polaron hopping conduction mechanism similar to that of the SG glasses. The hopping distance, R, and polaron radius r_p (estimated from the equation [13,14] $r_p = \frac{1}{2}\left(\frac{\pi}{6N}\right)^{1/3}$ shown Table-I) of the FG glasses are also comparable to those of other Bi-based SG glasses mentioned above [1-4,11] and satisfies the condition [15] ($r_p < R$) required for the small polaron hopping conduction mechanism.

Dielectric constant of the Bi-based glassy precursor for high T_c superconductors (SG glasses) did not show any ferroelectricity [1-4]. Figure 4a shows the variation of the dielectric constant of a typical FG glass Pb3K2 as a function of temperature for different frequencies 0.1, 0.12, 1.0, 10, 100 kHz. The appearance of small broad peak in the (ε'-T) curve (Fig.5a) around 600K along with the large peak for every frequency indicates the presence of the relaxation mode in the glass. Figure 4b shows the same for the Pb1K2 glass. Figure 4c shows the thermal variation of dielectric constant for a typical Na doped glass Pb3Na3. The ε' (real part of dielectric constant) values of the K-doped glasses are little larger than those of the Na-doped glasses as well as the Bi-based multicomponent SG glasses [1-4]. This is due to the presence of large number of nanocrystalline phases in the K-doped glasses with higher dielectric constants (lower conductivity). The dielectric constant data of the FG glass follow the Curie-Weiss relation, $\varepsilon' = C/(T-T_0)$, where C is the Curie Constant. T_0 is the extrapolated intersection of the high temperature part of the plot with the temperature axis as shown in Fig 5a with two different frequencies. Similar ferroelectric behavior

was observed with the other K and Na doped samples of different concentrations (not shown here). The observed transition temperature T_0 = 466K is close to the value 470 K observed by Bahgat et al [7] for similar sample. The order of the transition is identified by finding the ratio of the slopes $\partial(1/\varepsilon')/\partial T$ (in Fig.5a) below and above T_{cf}. The value of this ratio (= -2.63) indicates that the transition is of first order type, which is also confirmed from the value of T_0, (< Curie temperature T_{cf}). Interestingly, for any of the alkali metal free superconducting precursor glasses (SG glasses) becoming superconductor by annealing, the plot of $1/\varepsilon'$ vs. T shown in Fig. 5b for a typical SG glass $Bi_{3.9}Pb_{0.1}Sr_3Ca_3Cu_4O_x$ does not at all match with that of FG glass showing ferroelectric behavior (Fig. 5a). Detailed analysis of the dielectric properties of other SG glasses without showing FE behavior has already been made earlier [1,4].

IV. CONCLUSION

In conclusion (i) the glassy precursors for high T_c superconductors (SG glasses) show ferroelectric behavior when Cu is partially substituted by alkali metal like K or Na. (ii) These K or Na containing FG glasses showing ferroelectric transition are glass nanocrystal composite rather than single phase homogeneous glass. (iii) Ferroelectricity in these glasses is due to the presence of ferroelectric nanocrystalline particles/clusters embedded in the glass matrix. (iv) Superconducting behavior is suppressed by alkali metal (like K or Na) doping in the Cu site in the annealed FG glasses, which modifies the network structure of SG glass. (v) Ferroelectricty in pure single-phase glass has not yet been observed. This suggest that coexistence of ferroelectricity and superconductivity in the same material is yet to be explored.

ACKNOWLEDGEMENT

The author S. Mukherjee is grateful to the Council of Scientific and Industrial Research (CSIR) and Department of Science & Technology (DST), Govt. of India for the financial support.

Table-I Some parameters for the $Bi_{2-x}Pb_xSr_2Ca_2Cu_{2.8}K_{0.2}O_\delta$ (x = 0.0, 0.1, 0.2), $Bi_{1.8}Pb_{0.3}Sr_2Ca_2Cu_{2.8}K_{0.2}O_\delta$ (Pb3K2) and $Bi_{2-x}Pb_xSr_2Ca_2Cu_{3-y}Na_yO_\delta$ (x = 0.0,0.2,0.3; y = 0.2,0.3) FG glasses. T_g, T_x, density, and θ_D are obtained from the experimental data. Other parameters are obtained from the best fitting.

Parameter	Pb0K2	Pb1K2	Pb2K2	Pb3K2	Pb0Na2	Pb2Na2	Pb3Na3
T_g (°C)	340 ±5	350±5	360±5	400±5	330±5	350±5	380±5
T_x (°C)	400± 5	405± 5	410±5	430±5	410±5	420±5	440±5
Density (g cm^{-3})	5.39±0.02	5.34±0.02	5.32±0.02	5.28±0.02	5.45±0.02	5.39±0.02	5.51±0.02
N (10^{21} cm^{-3})	9.017	8.932	8.899	8.821	9.022	8.798	8.655
R (Å)	4.805	4.820	4.826	4.839	4.789	4.825	4.854
C	0.777	0.8532	0.737	0.773	0.789	0.756	0.781
r_p (Å)	1.936	1.942	1.945	1.950	1.940	1.949	1.955
θ_D (K)	365	418	360	348	370	365	368
ν_{ph} (10^{12} Hz)[a]	7.6	8.72	7.51	7.26	7.89	6.78	6.45
α ($Å^{-1}$)[a]	0.551	1.075	1.652	2.137	0.653	1.742	1.987
W (eV)[a]	0.2519	0.124	0.122	0.101	0.236	0.131	0.125

a) indicates the parameters obtained from the Mott's Eq.1.

REFERENCES

[1] K. K. Som and B. K. Chaudhuri, Phys. Rev. B **41**, 1581 (1990).
[2] T. Komatsu, R. Stao, C. Hirose, K. Matusita, and Y. Matushita, Jpn. J. Appl. Phys. **27**, L2293 (1988).
[3] Y. Akamatsu, M. Tatsumisago, N. Tohge, S. Tsuboi, and T. Minami, Jpn. J. Appl. Phys. **27**, L1696 (1988).
[4] S. Mollah, K. K. Som, K. Bose, A. K. Chakraborty, and B. K. Chaudhuri, Phys. Rev. B **46**, 11075 (1992)
[5] M. E. Lines, Phys. Rev. B **15**, 388 (1977).
[6] T. Matsumoto, A. Fukuda, M. Johno, Y. Motoyama, T. Yui, S. S. Seomun, and M. Yamashita, J. Mater. Chem. **9**, 2051 (1999).
[7] A. A. Bahgat and T. M. Kamel, Phys. Rev. B **63**, 012101 (2001).
[8] B. K. Chaudhuri, Chinese J. Phys. **38**, 2 (2000).
[9] M. Sadhukhan, D. K. Modak, and B.K. Chaudhuri, J. Appl. Phys. **85**, 3477 (1999).
[10] N. F. Mott, J. Non-Cryst. Solids **1**, 1 (1968).
[11] S. Chatterjee, S. Bhattacharya, and B. K. Chaudhuri, J. Chem. Phys. **108**, 2954 (1998).
[12] T. Holstein, Ann. Phys. (NY) **8**, 325 (1959).
[13] I. G. Austin and N. F. Mott, Adv. Phys. **18**, 41 (1969).
[14] V.N. Bogomolov, E.K. Kudinov, and Y.A. Firsov, Sov. Phys. Solid State **9**, 3175 (1967).
[15] G. N. Greaves, J. Non-Cryst. Solids **11**, 427 (1973).

FIGURE CAPTIONS

Fig. 1. Transmission Electron Micrographs (TEM) for (a) the as quenched $Bi_{1.8}Pb_{0.3}Sr_2Ca_2Cu_{2.8}K_{0.2}O_\delta$ glass and (b) large cluster of the selected region of (a).

Fig. 2. Thermal variation of the resistivity of (a) annealed $Bi_{1.8}Pb_{0.3}Sr_2Ca_2Cu_{2.8}K_{0.2}O_\delta$ (FG glass) which is a nonsuperconductor and (b) $Bi_{3.9}Pb_{0.1}Sr_3Ca_3Cu_4O_x$ (SG glass) showing superconducting behavior.

Fig. 3. (a) Variation of log σ_{dc} vs. 1000/T for (a) $Bi_{2-x}Pb_xSr_2Ca_2Cu_{2.8}K_{0.2}O_\delta$ (b) $Bi_{3.9}Pb_{0.1}Sr_3Ca_3Cu_4O_x$ (SG glass) and (c) $Bi_{1.7}Pb_{0.3}Sr_2Ca_2Cu_{2.7}Na_{0.3}O_\delta$ glasses. The solid lines are the best fit with Eq. 1.

Fig. 4. Temperature variation of dielectric constant ε' for FG glasses (a) $Bi_{1.8}Pb_{0.3}Sr_2Ca_2Cu_{2.8}K_{0.2}O_\delta$ (Pb3K2) (b) $Bi_{1.9}Pb_{0.1}Sr_2Ca_2Cu_{2.8}K_{0.2}O_\delta$ (Pb1K2) and (c) $Bi_{1.7}Pb_{0.3}Sr_2Ca_2Cu_{2.7}Na_{0.3}O_\delta$ (Pb3Na3) for different frequencies.

Fig. 5. Plot of $1/\varepsilon'$ vs. T for (a) $Bi_{1.8}Pb_{0.3}Sr_2Ca_2Cu_{2.8}K_{0.2}O_\delta$ (FG glass) glass showing FE transition and (b) $Bi_{3.9}Pb_{0.1}Sr_3Ca_3Cu_4O_x$ (SG glass) showing no FE transition.

INSTITUTE OF PHYSICS PUBLISHING JOURNAL OF PHYSICS CONDENSED MATTER

J Phys.: Condens Matter 16 (2004) R1237–R1276 PII S0953-8984(04)81247-5

TOPICAL REVIEW

The physics of the non-oxide perovskite superconductor $MgCNi_3$

S Mollah

Department of Physics, Aligarh Muslim University, Aligarh 202002, India

E-mail s mollahm@lycos com and smollah@rediffmail com

Received 26 May 2004, in final form 29 July 2004
Published 15 October 2004
Online at stacks iop.org/JPhysCM/16/R1237
doi:10.1088/0953-8984/16/43/R01

Abstract

The present review article discusses the physics of the non-oxide perovskite superconductor $MgCNi_3$ on the basis of theoretical and experimental results available on the material up to July 2004. It was discovered following on from the breakthrough of the finding of the MgB_2 superconductor at the beginning of 2001, which has subsequently been intensively studied; however, less attention has been paid to it due to its much lower superconducting transition temperature, T_c (~8 K), as compared to that of MgB_2 ($T_c \sim 39$ K) But it has many interesting properties which need to be focused on to obtain an understanding of its complicated physics. Energy band calculations show that the density of states (DOS) at the Fermi level, $N(E_F)$, is dominated by Ni d states and there is a von Hove singularity in the DOS just below E_F (<50–120 meV) It is surprising that the conduction electrons in it are derived from partially filled Ni d states, which typically lead to ferromagnetism in metallic Ni and many Ni-based binary alloys. MgC_xNi_3 has a simple cubic perovskite structure with space group $Pm\bar{3}m$ and the lattice parameter a is ~3.812 Å for $x \sim 0.97$ at ambient temperature and pressure. However, the $Ni_6(O_6)$ octahedron is locally distorted from those expected in the perfect cubic $Pm\bar{3}m$ form The carbon atom of $MgCNi_3$ at the body centre is surrounded by six Ni atoms at the face centred positions and eight Mg atoms at the cube corners The carriers in it are of electron type in the normal state, although theoretically they were predicted to be of hole type. T_c increases with increase of x in MgC_xNi_3, but generally decreases with Ni site doping with Co, Fe, Mn, Cu etc Theoretically, the DOS peak should be greatly reduced by doping at the Mg or Ni site, which accounts for the reduced T_c The T_c is found to increase with increase of the external pressure (P) at a rate of $dT_c/dP \sim 0.0155$ K kbar^{-1}, which is the same as that for the intermetallic RNi_2B_2C (R = rare earth) superconductors but about one order lower than that for MgB_2. The $T_c(P)$ result focuses our attention on the feature that $N(E_F)$ should increase with pressure due to the broadening of the energy level Also, a controversial magnetoresistance

is reported. It has been observed that the electronic contribution is slightly higher than the lattice one in the normal state thermal conductivity. Specific heat and tunnelling spectroscopic studies indicate that this is an s-wave BCS-type weak/moderate coupling type-II superconductor, but this needs further confirmation as the penetration depth distinctly exhibits a non-s-wave BCS low temperature behaviour which theoretically suggests a d-wave superconductor.

Contents

1. Introduction

Since the discovery of the new intermetallic non-oxide perovskite superconductor $MgCNi_3$ by He *et al* [1], following on from that of MgB_2 [2], extensive experimental [3–48] and theoretical [47–69] studies have been carried out on it. It has a perovskite structure [1] like that of $CaTiO_3$ with equivalence of Ca to Mg, Ti to C and O to Ni. Its structure is also like that of the 30 K non-cuprate oxide cubic superconductor [1] $Ba_{1-x}K_xBiO_3$. The high proportion of Ni in this compound suggests that magnetic interactions may play a dominant role in explanations of its superconductivity. In fact, the density of states (DOS) in the vicinity of the Fermi level is dominated by the Ni d states [49–54], though it is not large enough to induce magnetic instability [51] but is associated with the superconducting properties [53]. Ni K-edge x-ray absorption measurements [16] reveal that the $Ni_6(O_6)$ octahedra are locally distorted from those expected for the perfect cubic $Pm\bar{3}m$ form and electronic states in the vicinity of the Fermi level are mostly derived from the Ni d states and are degenerate. Experimental

investigation and theoretical computation reveal that there is a von Hove singularity (vHs) of the DOS just below E_F (<50–120 meV) [15, 54]. These bands are very narrow as they cannot disperse about the many points of high symmetry in the simple cubic Brillouin zone [50]. The degeneracy in the structure can be lifted by small perturbations such as electron–phonon (e–ph) interactions and lowering of the symmetry from cubic through Peierls-type transitions. The ^{13}C NMR investigation on this material [3] suggests that the electronic states reach modestly mass enhanced Fermi-liquid-like states prior to the superconducting transition. Evident structural inhomogeneity was detected by Li *et al* [7], with the appearance of regular superconducting domains of average size ~4 nm. The temperature dependence of the structural parameters revealed by neutron diffraction study shows that there are no unusual changes in these [5] near T_c. The covalent character of the Ni–C bond implies that although most of the amplitude of the electron wavefunction resides on the Ni d, there might be spatial distribution of charge and spin governed by the Ni–C hybridization and Coulomb and e–ph interactions [70]. Lattice distortion associated with charge density waves (CDW) and long range antiferromagnetic (AF) ordering consistent with spin density waves (SDW) are not revealed in $MgCNi_3$ [1, 5]. Single-phase perovskite structure in MgC_xNi_3 is found [12] only in a narrow range of carbon content ($0.88 < x < 1.0$). The doping of the Ni site with Cu and Co decreases T_c significantly [6, 10]. Rosner *et al* [54] have suggested that $MgCNi_3$ is near a ferromagnetic instability that can be reached by hole doping on the Mg site (if 12% Mg is replaced by Na or Li, i.e., 0.04 hole/Ni) and the effective carriers are Ni-derived holes of very high band mass although the Hall coefficient and thermoelectric power data show that the carriers in this superconductor are electrons [4, 7]. Shein *et al* [53] have shown theoretically the deterioration of the superconducting characteristics of $MgCNi_3$ that occurs upon hole doping in $MgC_{1-x}Ni_3$ compositions. No magnetic solution is found for $MgCNi_2Co$ and $MgCNiCo_2$ [56]. This indicates that the hole doping does not produce a magnetic instability which could be responsible for pair breaking [56]. The decline of the superconductivity upon electron doping ($MgCNi_{3-x}Cu_x$) is due to the filling of antibonding states and a sharp drop in DOS at the Fermi level, $N(E_F)$ [53]. Thus there are many interesting properties of this non-oxide perovskite superconductor. The present review discusses the synthesis of $MgCNi_3$ along with its electronic, magnetic, thermal, mechanical and optical properties in the light of experimental findings and theoretical computations.

2. Synthesis of $MgCNi_3$

2.1. Polycrystalline bulk

MgC_xNi_3 samples with $x = 0.9$–1.5 were prepared by He *et al* [1] using as raw materials Mg flakes, fine Ni powder and glassy spherical carbon powder. The starting materials were properly mixed and pressed into pellets. The pellets were placed into Ta foil, put in an alumina boat and fired in a quartz tube furnace in a mixed gas (95% Ar and 5% H_2) environment. The samples were heat treated at 600 °C for 1/2 h and this was followed by treatment for 1 h at 900 °C. Then these were cooled, ground, pressed and heated at 900 °C for one more hour. Owing to the volatility of Mg, 20% excess of its stoichiometric ratio was added to the initial mixture. The preparation procedures of other groups are almost the same as that of He *et al* [1], as shown in table 1. Although most of the groups used Mg flakes, Ni powder and glassy C powder as raw materials with the final heat treatment temperature as 900 °C and Ta foil for wrapping or positioning the sample, there is a lot of variation as regards the starting mixture of raw materials, the final heat treatment time and the annealing environment (table 1). For example, Li *et al* [4, 7] prepared a sample with nominal formula $Mg_{1.2}C_{1.4}Ni_3$ in a stainless steel reactor under

Table 1. Summary of different recipes for the synthesis of $Mg_xC_yNi_3$ superconductor. Mg flakes, Ni powder and glassy C powder are used as the starting raw materials. Only the final heat treatment time, temperature and environment are shown. Ta foil was used by different groups either to wrap the sample or to place the sample on.

x	y	Annealing time (h)	Annealing temperature (°C)	Annealing environment	References
1.0	0.9–1.5	2	900	95% Ar + 5% H_2	[1]
1.2	1.4	2	900	Ar	[4, 7]
1.0–1.3	0.7–1.55	2	900	95% Ar + 5% H_2	[8]
1.0	1.0	3	900	Vacuum	[13]
1.2	1.45	2	900	Vacuum	[15]
1	1.45	8	900	Ar	[19]
1.0	1.0	3	900	Vacuum	[23]
1.2	1.6	—	900	Ar	[24]
0.5–1.55	1.0	4–30	850–1000	Vacuum	[28, 47]
0.75–1.55	0.85–1.45	4–30	850–1000	Vacuum	[28, 47]

an Ar atmosphere in a glove box. A heat treatment like that of He *et al* [1] in a tube furnace under Ar resulted in dense samples of length 7 mm and width 2 mm. Lin *et al* [13] started with the appropriate stoichiometric ratio, but added 20% excess of Mg over its stoichiometric ratio and the final pellets were annealed at 900 °C for 3 h in an evacuated quartz tube. The nominal composition of $MgC_{1.45}Ni_3$ was sintered at 900 °C for 8 h in flowing argon [19]. Kim *et al* [15] mixed powder with the nominal composition $Mg_{1.2}C_{1.45}Ni_3$. This was heated at 900 °C for 2 h and quenched. Afterwards, they [15] put the sample in a high pressure cell and annealed it under a pressure of 3 GPa at 900 °C for 1/2 h to get a dense sample for photoemission spectroscopy (PES) and x-ray absorption spectroscopy (XAS) studies. Bulk alloy samples of $Mg_xC_yNi_3$ ($1.0 < x < 1.3, 0.7 < y < 1.55$) were prepared by Li *et al* [8] using the conventional method [1]. Despite the fact that most of the groups used the final annealing temperature of 900 °C (table 1), there are some reports of synthesis with a temperature of 850–1000 °C [28, 47]. Non-superconducting α-MgC_xNi_3 and superconducting β-MgC_xNi_3 phases are found in the MgC_xNi_3 system for $x < 1.0$ and $x > 1.0$ [28] respectively, depending on the annealing temperature. Non-superconducting α-MgC_xNi_3 with $x < 1.0$ was prepared at a temperature lower than 965 °C. However, superconducting β-MgC_xNi_3 exists for $x > 1.0$, prepared at a temperature of 900–985 °C, and for $x < 1.0$, prepared at a temperature higher than 965 °C. MgC_xNi_3 ($x = 0.5$–1.55) and $Mg_xC_yNi_3$ ($x = 0.75$–1.55, $y = 0.85$, 1.0 and 1.45) systems were synthesized in an evacuated quartz tube placed in a box furnace and heated to the designed temperature (850–1000 °C) for 4–30 h; this was followed by furnace cooling to room temperature [28, 47]. In addition to being obtained by the conventional method [1], $MgCNi_3$ was synthesized from the Mg, Ni and graphite powders by mechanical alloying (MA), in which the preliminary condition for the formation of $MgCNi_3$ was the advance formation of Mg_2Ni [25]. $Mg_xC_yNi_3$ was prepared in two steps [26]; no evidence of Mg loss due to volatilization or of unreacted C was found at the end of the preparation. A new and feasible way to prepare $MgCNi_3$ under ambient conditions by ball milling (BM) Mg, Ni powder and paraffin or graphite was presented by Ouyang *et al* [44]. It was found that paraffin was partially dissociated during ball milling, which resulted in free carbon and hydrogen being incorporated within the Mg–Ni alloy powder in increasing amounts with increasing milling time. Recently, formation of transition metal boride and carbide perovskites related to superconducting $MgCNi_3$ in the ternary systems AXM_3 (A = Mg, Ca, Sc, Y, Lu, Zr, Nb; X = B; M = Ni, Ru, Rh, Pd, Pt) was reported by Schaak *et al* [27].

Table 2. Summary of different recipes for the preparation of $Mg_xC_yNi_{3-z}M_z$ (M = doping element) superconductor from Mg flakes, Ni powder, glassy C powder and M metallic powder. The final heat treatment temperature was 900 °C for all cases except those of [10] and [33]. Ta foil was used by different groups either to wrap the sample or to place the sample on.

x	y	z	M	Time (h)[a]	Atmosphere[a]	Excess Mg (%)	Excess C (%)	Max. T_c (K)	References
1 2	1.5	0.03–0.75	Co	2	95% Ar + 5% H_2	20	50	6.6	[6]
1 0	1.0	0.03–0.09	Cu	2	95% Ar + 5% H_2	20	50	6.5	[6]
1 0	1.45	0–3.0	Co	5	Vacuum	20	—	7.5	[10][b]
1 0	1.0	0.05–0.30	Fe	2	92% Ar + 8% H_2	20	50	8.5	[18]
1 0	1.0	0.05–0.40	Co	2	92% Ar + 8% H_2	20	50	7.7	[18]
1 0	1.0	—	Ag	2	Vacuum	—	—	6.6	[21]
1.2	1.5	0–0.05	Mn	7	Ar	—	—	—	[33][b]

[a] Final heat treatment time and atmosphere.
[b] The final heat treatment temperature is 950 °C.

2.2. *Chemical doping in $MgCNi_3$ polycrystalline bulk*

Chemical doping and diffusion of metallic particles in $MgCNi_3$ have been reported by several groups [6, 10, 18, 21, 33, 34, 36–38, 41]. The recipes for the syntheses by some groups are summarized in table 2. Most of the groups doped at the Ni site. However, the effect of doping at the Mg site is also studied [38, 41]. The preparation technique is over all conventional types [1]. Excess Mg and C in initial mixtures are found to be favourable for obtaining single-phase samples (table 2). $Mg_xC_yNi_{3-z}M_z$ (z = 0.05–0.30 and M = Fe, Co) were prepared [18] following the procedure of He *et al* [1] using the starting materials Mg, Ni, Fe, Co and amorphous carbon. Mg and C were taken with respectively 20% and 50% excess to get the required stoichiometry in the final sample. The final heat treatment atmosphere was also a little different (tables 1 and 2) to that of He *et al* [1]. $Mg_xC_yNi_{3-z}M_z$ (M = Cu, z = 0.03–0.09; M = Co, z = 0.03–0.75) samples were synthesized by Hayward *et al* [6] using the initial stoichiometry of $Mg_{1.2}C_{1.5}Ni_{3-x}M_x$. Ren *et al* [10] prepared Co doped (z = 0–3.0) samples in vacuum at a higher temperature (950 °C). Mn doped samples with x = 1.2, y = 1.5 and z = 0–0.5 (table 2) were synthesized at a slightly higher temperature with a higher heat treatment time in Ar [33]. Complete and partial replacement of Mg by Zn was carried out and $ZnCNi_3$ and $(Mg_{0.85}Zn_{0.15})CNi_3$ were prepared from the nominal compositions $Zn_{1.2}C_{1.3}Ni_3$ and $(MgZn)_{1.2}C_{1.3}Ni_3$, respectively, under a high purity Ar atmosphere [38, 41]. The pellets were reacted for 1 h at 900 °C, rapidly quenched to room temperature, then treated again for 2 h at 1000 °C. Excess Zn and C were used to compensate for the Zn evaporation during the reaction and to ensure full C incorporation, respectively. Ag diffused $MgCNi_3$ was synthesized by Liu *et al* [21] using stoichiometric $MgCNi_3$ pellets and a highly pure thin piece of Ag. These were wrapped in a Ta foil, sealed in a quartz tube, sintered at 900 °C for 2 h and cooled down to room temperature.

2.3. *Thin film*

So far, there has been only one report on the preparation of $MgCNi_3$ as a thin film [20]. The metastable intermetallic CNi_3 precursor films were deposited onto sapphire substrates by electron beam evaporation of CNi_3 targets. High purity graphite and nickel were used as the buttons, with initial composition $CNi_{3.25}$, to avoid the loss of Ni during the melting process. The films were grown with a typical growth rate ~0.1 nm s^{-1} in a vacuum of 2 μTorr at room temperature and were handled in air. The adherent and pristine CNi_3 films were subsequently

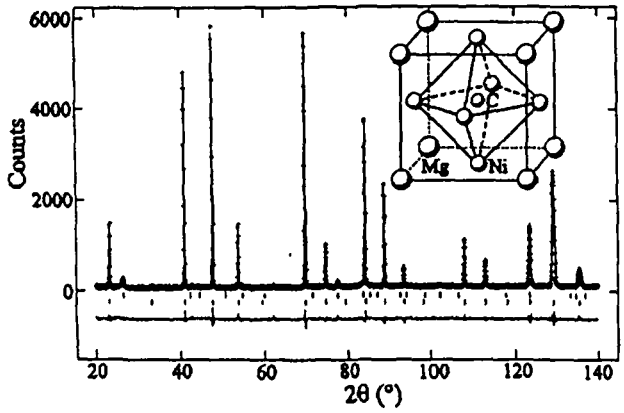

Figure 1. The powder neutron diffraction pattern at ambient temperature for $MgC_{1.25}Ni_3$; the inset shows the crystal structure of $MgCNi_3$ [1].

exposed to Mg vapour at 700 °C by sealing in a quartz tube in vacuum with 0.1 g of Mg metal. The entire quartz tube was rapidly quenched after heating for 20 min leading to the $MgCNi_3$ thin film formation.

It should be noted that although polycrystalline $MgCNi_3$ has been extensively studied in the form of bulk or thin film, it has not yet been investigated in the form of single crystal or wires/tapes. Thus there is immense scope for research focusing on the changes of properties (if any) in the above-mentioned form compared to those of the polycrystalline bulk and thin films.

3. The spectroscopic characterization and structure of $MgCNi_3$

This intermetallic $MgCNi_3$ superconductor is found to possess the classical cubic perovskite structure with the space group $Pm\bar{3}m$ and the lattice constant $a \sim 3.81221$ Å at 295 K [1, 5, 14, 21, 29]. Its neutron diffraction pattern and the atomic positions of the unit cell are shown in figure 1. From neutron diffraction study, it is found [1, 5] that the formula for the superconducting phase is $MgC_{0.96}Ni_3$ for the nominal composition $MgC_{1.25}Ni_3$. This is due to the small amount of unreacted graphite found in the sample [1, 5]. The C site occupancy is also found to be 0.960(8), by Ren *et al* [10]. The positions of the atoms are: Mg 1a (0, 0, 0); C 1b (0.5, 0.5, 0.5); Ni 3c (0, 0.5, 0.5), respectively with temperature factors 0.90(3), 0.54(4) and 0.75(1) $Å^2$ [1, 5]. Figure 2 shows the x-ray diffraction (XRD) spectrum of $MgCNi_3$ with unreacted Ni peaks. $Mg_xC_yNi_3$ ($1.0 < x < 1.3$, $1.0 < y < 1.55$) samples reveal evident structural inhomogeneity [8]. Regular domains, with an average size as small as ~4 nm, appear commonly in the superconducting phase [8]. This structural phenomenon is qualitatively explained in terms of the perovskite cubic structure of $MgCNi_3$, modulated locally by the variable stoichiometry on the C sites. The presence of the local C deficiency can be a dominant factor affecting the crystal structure and superconductivity. Single-phase perovskite structure is found only in a narrow range of carbon content, $0.88 < x < 1.0$, in MgC_xNi_3 [12]. The introduction of carbon vacancies has significant effects on the positions of the Ni atoms. No evidence for long range magnetic ordering is observed by means of neutron diffraction for carbon stoichiometries within the perovskite phase stability range [12]. No homogeneous region with changeable content of Mg exists in $Mg_xC_yNi_3$ ($x = 0.75$–1.55 and $y = 0.85$–1.45) systems [28]. The electronic structure of $MgC_{1-x}Ni_3$ obtained by x-ray photoemission spectroscopy (XPS) and x-ray absorption spectroscopy (XAS) shows that the overall band structure is in reasonable agreement with band structure calculations, including

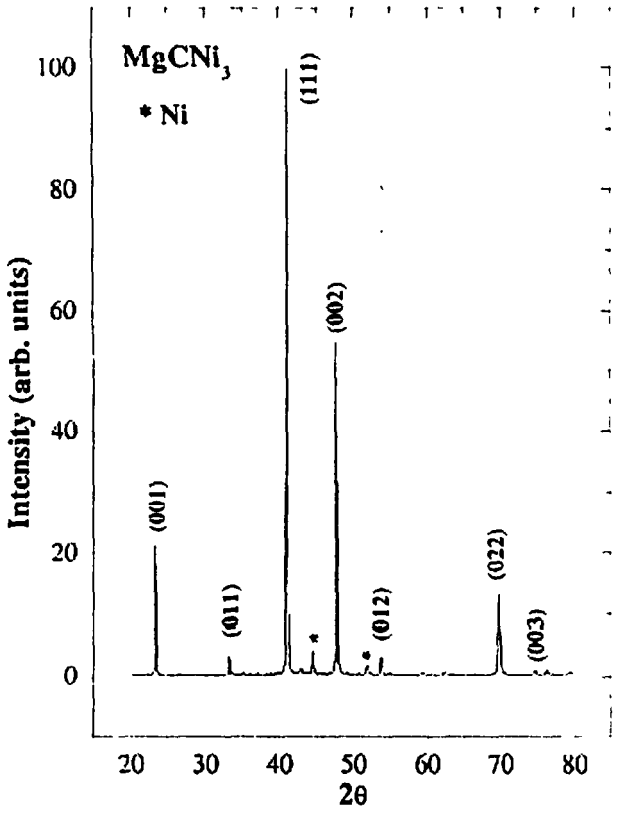

Figure 2. The x-ray diffraction pattern of pristine $MgCNi_3$. The lines marked with an asterisk correspond to unreacted Ni [18].

the existence of a von Hove singularity (vHs) near E_F [15]. However, the sharp vHs peak predicted theoretically near E_F [54] is substantially suppressed. As for the Ni core level and absorption spectrum, there exist satellites of Ni 2p which have a slightly larger energy separation and reduced intensity compared to the case for Ni metal [15]. These facts indicate that correlation effects among Ni d electrons may be important for understanding various physical properties. The onset of local distortions can be closely related to the removal of the degeneracy in the electronic states dominated by the Ni d bands [16]. The validity of the band structure calculations is confirmed by x-ray emission (C Kα, Ni $L_{2,3}$ and Co $L_{2,3}$) and x-ray photoelectron spectra [56].

In the $MgC_{1.45}Ni_{3-x}Co_x$ system [10], the lattice parameter decreases slightly with increasing x (figure 3). Thus, Shein *et al* [56] have used the same lattice parameter for all Co doped $MgCNi_3$ compounds because the changes in the lattice parameter from $MgC_{1.45}Ni_3$ to $MgC_{1.45}Co_3$ are found to be negligible [10]. Kumary *et al* [18] also find no significant changes of lattice parameter upon partial replacement of Ni with Fe or Co. It should be noted that *in situ* high pressure energy dispersive x-ray diffraction has also revealed that the structure of $MgCNi_3$ is stable under a pressure of ~22 GPa [30]. Therefore, the chemical and the external pressure have the same effect on the lattice parameter [10, 15, 18, 30]. It decreases by only about 1% with Ag diffusion [21]. The XRD spectrum of Ag–$MgCNi_3$ also exhibits a series of Ag crystal peaks [21] corresponding to the known cubic structure with the lattice parameter 4.1065 Å. The XRD results show that a small amount of Ag is substituted at Ni sites, and much of the Ag is in vacancy sites of the Ag diffused $MgCNi_3$ [21]. Actually, the

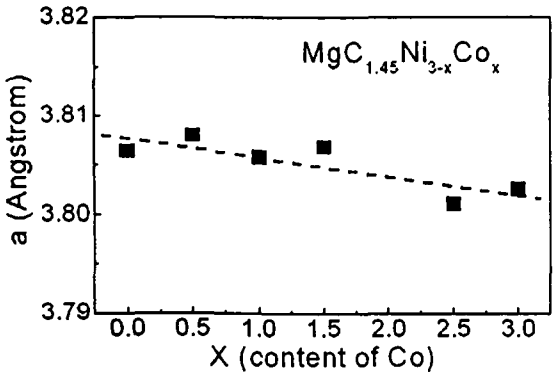

Figure 3. Lattice parameter versus x for the nominal composition $MgC_{1.45}Ni_{3-x}Co_x$ [10].

Ag is mostly located at the grain boundaries. The volume fraction of Ag on the surface of the samples is estimated at about 7.7% from XRD studies [21]. Raman spectroscopy reveals that Ag–$MgCNi_3$ has a special Raman peak at around 842.1 cm^{-1} compared to that of C [21]. The surface properties of Ag–$MgCNi_3$ have been studied using Raman scattering spectra and x-ray photoemission spectra (XPS) [21]. The coexistence of metal magnesium and magnesium oxide in the surface areas of Ag–$MgCNi_3$ is consistent with the results obtained from transmission electron microscopic (TEM) analysis.

Huang *et al* [5] report the structural parameters of superconducting MgC_xNi_3 ($x = 0.96$, $T_c = 7.3$ K) as a function of temperature, from 2–295 K, as determined by neutron powder diffraction profile refinement. It is established that the compound has the perovskite structure over the whole temperature range and no structural or long range magnetic ordering transitions are observed [5]. There are no unusual changes of the structural parameters near T_c [5]. This is also confirmed by the Ni K-edge x-ray absorption fine structure (EXAFS) over the temperature range of 3–300 K, which exhibits no anomaly near $T_c \sim 7$ K [16]. However, the symmetry of Ni_6 octahedra below the temperature $T^* \sim 70$ K is lower than cubic $Pm\bar{3}m$ [16]. Both the uniform spin susceptibility and the spin fluctuations show a strong enhancement with decreasing temperature and saturate below ~50 and 20 K, respectively, as observed from ^{13}C nuclear magnetic resonance (NMR) characterization [3]. The lattice parameter a and the Debye–Waller factors for the individual atoms decrease smoothly with decreasing temperature. The lattice parameter a_T at any temperature T can be fitted with [5]

$$a_T = a_0 + \alpha T + \beta T^2, \tag{1}$$

where $a_0 = 3.8066$ is the value of a at $T = 0$ K; α (=3.7985×10^{-6}) and β (=5.3493×10^{-8}) are the polynomial coefficients. The thermal expansion of the model parameter cannot be fitted, unlike that for MgB_2 superconductor, with a model where the behaviour is dominated by a single phonon energy [52], which is expected as the strongly bonded network of light atoms (B) present in MgB_2 is absent in $MgCNi_3$. Thus there is the trend of decreasing lattice parameter with decrease of the temperature and increase of the Co doping [5, 10] although the effect of Co doping is negligible.

4. Electrical properties

4.1. The critical temperature (T_c)

The critical temperature (T_c) of a superconductor is determined as the average of the onset and end point temperatures. The upper part of figure 4 shows the temperature variation

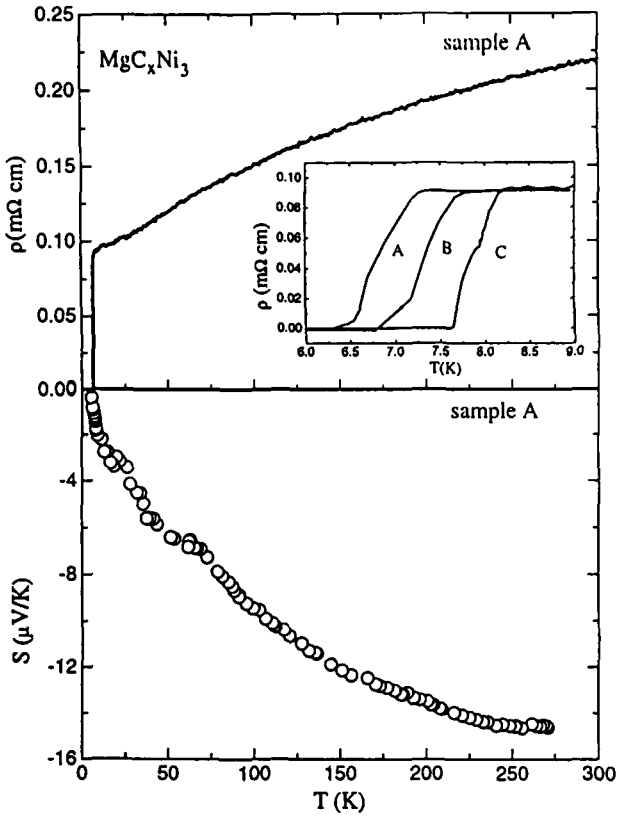

Figure 4. The temperature (T) variation of the resistivity (ρ) and the thermoelectric power (S) for sample A ($MgCNi_3$) at ambient pressure. The inset shows the resistivity (ρ) for the three MgC_xNi_3 samples with $x = 1.0$ (A), $x = 1.25$ (B) and $x = 1.5$ (C) near T_c [17].

of the resistivity for MgC_xNi_3 samples for $x = 1$ (A), 1.25 (B) and 1.5 (C). He *et al* [1] observe T_c from resistivity measurements for a sample with nominal composition $MgC_{1.5}Ni_3$ as 8.4 K with the onset temperature as 8.5 K and a 90%–10% transition width at 0.1 K. The T_c onset of the same sample is found from magnetization measurements as 7.4 K, whereas that from specific heat (C) studies is 6.1 K. Differences among the values of T_c derived from resistivity, magnetization and specific heat measurements are also found by several other groups [4, 7, 13, 17]. Different values of T_c being obtained by different techniques is also a well known fact for other intermetallic and oxide superconductors; they mainly depend on the sample homogeneity and transition width. Young *et al* [20] report on the T_c of $MgCNi_3$ thin films with thickness 7.5–60 nm (figure 5). Films thicker than ~40 nm have $T_c \sim 8$ K, which is comparable to that of polycrystalline bulk samples. T_c decreases with decrease of the film thickness as shown in figure 5, becoming the minimum for the film with thickness 7.5 nm [20]. It should be mentioned that Artini *et al* [31] observe double superconductive transitions, with one ~10 K higher than that (~8 K) reported by others [1, 4, 7, 13, 17] and a second one at ~6 K. In the following, the internal (chemical) and external pressure effects on the T_c of $MgCNi_3$ have been discussed.

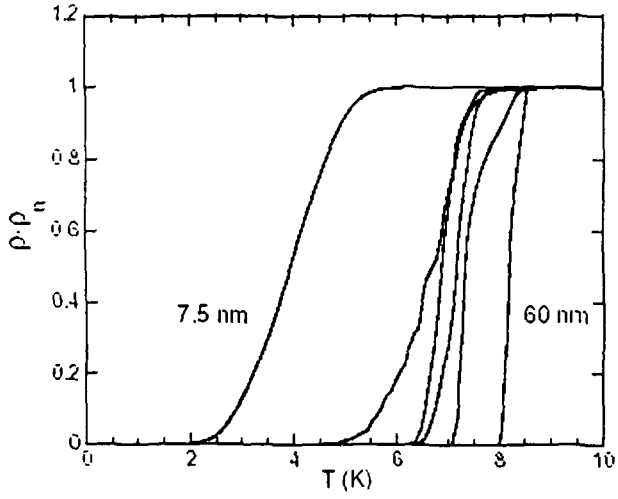

Figure 5. The temperature dependence of the resistivity for $MgCNi_3$ films with different thicknesses. The curves correspond from left to right to $MgCNi_3$ layer thicknesses of 7.5, 15, 20, 30, 45 and 60 nm [20].

4.1.1. The internal pressure (chemical doping) effect. The T_c of MgC_xNi_3 is sensitive to the carbon content as shown in table 3. The T_c varies from 6.4 to 8.4 K depending on the value of x (table 3). MgC_xNi_3 ($x = 1.0$–1.5) samples reveal an increase of T_c [17] with increase of x (figure 4). The highest T_c corresponds to $x \sim 1.45$–1.5 and decreases with further increase of x [1, 10, 11, 17, 19, 48]. The T_c is found to decrease systematically with decreasing carbon concentration [12] from the stoichiometric value. It is concluded from theoretical calculations that the absence of superconductivity for non-stoichiometric compositions $MgC_{1-x}Ni_3$ is due to the transition of the system to the magnetic state [53]. Excess of Mg and C in the initial material mixture is favourable for improving T_c and for obtaining single-phase samples [1, 10]. The T_c of $MgC_{1.45-x}B_xNi_3$ decreases with increase of x up to 0.10 and then it becomes non-superconducting for $x = 0.15$–0.20 [10]. The T_c of Ag–$MgCNi_3$ (~6.6 K) is lower than that of pure $MgCNi_3$ [21]. The complete replacement of Mg by Zn in $ZnCNi_3$ causes it to become paramagnetic without the onset of superconductivity down to ~2 K [38].

Doping at the Ni site with Co, Fe, Mn, Cu etc also causes a decrease of T_c (table 2)—except the initial increase with Fe doping [18]. Calculation of the expected electronic DOS suggests that electron (Cu) and hole (Co) doping should have different effects on T_c [6]. However, the T_c of $MgCNi_{3-z}Cu_z$ decreases systematically from 7 to 6 K for $z = 0.1$ [6]. It is also observed by other groups that both electron (Cu) and hole (Co, Fe and Mn) doping quench the superconductivity of $MgCNi_2T$ (T = Co, Fe, Mn and Cu) [36, 37]. Consequently, comparing with the hole (Co) doping, we see that there is not much difference between Cu and Co doping, which is opposite to what observed by Hayward *et al* [6]. As the metallic doping at the Ni site finally leads to non-superconducting phases, the maximum T_c of $Mg_xC_yNi_{3-z}M_z$ (M = metal) for lower metallic doping concentrations (z) is shown in table 2. The T_c of $MgC_{1.45}Ni_{3-z}Co_z$ decreases gradually with increasing z [10]. A small superconducting transition is observed for the sample with $z = 1.5$, which indicates that the superconducting volume fraction decreases upon substitution of Co for Ni. This is inconsistent with the finding of [6], where z above 0.03 completely suppresses the superconductivity. Kumary *et al* [18] also monitored the decrease of T_c with increase of the Co content. No magnetic solution was found for $MgCNi_2Co$ and $MgCNiCo_2$ [56]. This indicates that the hole doping does not produce the magnetic instability which could be responsible for pair breaking [56]. Again, no long range magnetic ordering is observed in the magnetic susceptibility of $MgCNi_{3-z}Co_z$ [6]. The Co doping of $MgCNi_3$ is

Table 3. Some important characteristic parameters of MgC_xNi_3.

Parameters[a]	Values of parameters								
x	1.0	1.0	1.5	1.6	1.0	1.0	1.4	1.0	1.0
T_c (K)	7.63	6.4	8.4	6.8	7.3	7	8	8	6.7
$H_{c2}(0)$ (T)	14.4	11.5	12.8	11.0	16	11.8	15	14	—
$H_c(0)$ (T)	0.19	0.29	—	0.18	0.6	—	—	—	—
$H_{c1}(0)$ (mT)	10	—	—	11.3	12.6	—	—	—	—
$\xi_{GL}(0)$ (Å)	46	56	50	54.7	45	—	47	50	—
$\lambda_{GL}(0)$ (Å)	2480	1800	—	2370	2300	—	—	—	—
$\kappa(0)$	54	—	66	43.3	51	—	—	—	—
γ_n (mJ K^{-2} (mol Ni)$^{-1}$)	10.03	11.2	10	10.5	—	11.3	—	—	9.8
θ_D (K)	284	287	—	292	—	351	206	—	256
n (10^{22} cm^{-3})	—	—	—	—	—	—	1.0	4.2	—
λ	—	0.83	0.77	0.84	—	0.66	1.4	—	0.79
$\Delta C/\gamma_n T_c$	2.1	1.97	1.9	2.09	—	1.7	—	—	—
$2\Delta/k_B T_c$	4.4	$\geqslant 4$	—	3.75	—	~5	—	—	—
Δ (meV)	1.5	1.1	—	1.1	—	1.5	—	—	—
References	[9]	[13, 14]	[1, 11]	[48]	[23]	[47]	[4, 7]	[20]	[38]

[a] The symbols are explained in the text.

accompanied by a reduction of the DOS at the Fermi level, which seems to be responsible for the reduced superconductivity in the $MgCNi_{3-z}Co_z$ system [56]. An increase followed by a decrease of T_c is observed if Ni is replaced by Fe [18]. The maximum T_c is found by monitoring when the Fe concentration is 0.05. The authors of [18] argue that the spin fluctuation effect would be less for Fe substituted compounds as compared to that for Co substituted ones for low concentration of doping. The detected variation of T_c is explained in terms of the competition between an increase in T_c due to increase in the DOS and a decrease in spin fluctuation [18]. Conversely, Alzamora *et al* [34] find that the Fe doping in $MgC(Ni_{1-x}Fe_x)_3$ ($0 \leqslant x \leqslant 1.0$) quickly reduces T_c, completely destroying the superconducting state for $x \sim 0.04$. It is confirmed that Co and Fe dopants in $MgCNi_3$ behave as a source of d band holes [36, 37] and the suppression of superconductivity occurs faster for the Fe doped compared to the Co doped case, which is in contrast to the finding of Kumary *et al* [18]. So the above discussion suggests that doped Co and Fe do not act as magnetic impurities in $MgCNi_3$. On the contrary, the rapid loss of superconductivity for Co replacement of Ni is argued to be consistent with magnetic quenching of the superconductivity [6]. It is also suggested that Co is a very strong magnetic impurity rather than a source of hole doping [6], which is opposite to the observation of other groups [6, 18, 36, 37, 53, 56]. Again, the establishment of an ordered magnetic state is observed for Fe concentration ($z \geqslant 0.3$) far above the concentration for which the superconducting state has completely disappeared [34]. In addition, Das and Kremer [33] observe a rapid suppression of the superconductivity (~−21 K/at.% Mn) in Mn substituted $MgCNi_3$. Doping with only 0.3 at.% of Mn completely destroys the superconductivity in $MgCNi_{3-z}Mn_z$ via pair breaking effects due to moment formation for Mn [33]. This is consistent with the observation of Ren *et al* [10] who find that the suppression effect is smaller for Co than for Mn, when replacing Ni. Thus the doping effect needs further investigation to settle the controversies.

4.1.2. The external pressure effect. High pressure (P) plays an important role as regards the T_c of the intermetallic superconductors [71–77]. The P can change the electronic structure, phonon frequencies and electron–phonon coupling, affecting the T_c. Isotropic pressure will not affect too much the electronic structure but anisotropic compression will cause large

Table 4. The superconducting transition temperature T_c (determined from the mid-point of the resistive transition for MgC_xNi_3) at ambient pressure, dT_c/dP and $d\ln T_c/dP$ for some metallic as well as some intermetallic superconductors.

Sample composition	T_c (K)	dT_c/dP (10^{-2} K kbar^{-1})	$d\ln T_c/dP$ (10^{-3} kbar^{-1})	References
MgB_2	38.6	−8.0	−2.07	[72]
MgB_2	37.5	−16.0	−4.26	[73]
$LuNi_2B_2C$	15.9	+1.88	+1.18	[75]
V	5.3	+1.0	+1.88	[81]
Ta	4.3	−0.26	−0.60	[82]
$MgCNi_3$	7.69	~−1.0	~−1.30	[18][a]
$MgCNi_3$	7.69	~+0.75	~+0.97	[18][b]
MgC_xNi_3 (A)	6.9	+1.55	+2.24	[17]
MgC_xNi_3 (B)	7.4	+1.34	+1.81	[17]
MgC_xNi_3 (C)	7.9	+1.52	+1.92	[17]

[a] Below the pressure of 17 kbar.
[b] Above the pressure of 17 kbar.

pressure induced changes due to the change of bonding strength in different crystallographic directions [71]. Yang *et al* [17] have measured the hydrostatic pressure dependent ac magnetic susceptibility (χ_{ac}) of MgC_xNi_3 using the piston–cylinder self-clamped technique [78]. The hydrostatic pressure environment around the sample is generated inside a Teflon cell with 3M Fluroinert FC-77 as the pressure-transmitting medium [17]. The pressure is determined by using a Sn manometer situated near the sample in the same Teflon cell [17]. On the other hand, a high pressure resistance measurement has been carried out [18] for pristine $MgCNi_3$ using a pressure locked, opposed Bridgman anvil apparatus [79] using the four-probe method. A superconducting Pb manometer is used for the pressure calibration [18].

An initial decrease in T_c of $MgCNi_3$ with $dT_c/dP \sim -1.0 \times 10^{-2}$ K kbar^{-1} up to a pressure of ~17 kbar (table 4) followed by an increase is observed on application of external pressure, from resistivity measurements [18]. The decrease in T_c for small applied pressures is explained in terms of the decrease in the DOS at the Fermi level. The subsequent increase in T_c with pressure is argued to be due to a lattice softening or a structural phase transition, consistent with the band structure calculations. It is conjectured that suppression of spin fluctuations by pressure may also be responsible for the observed increase in T_c at higher pressures [18]. However, Yang *et al* [17] observe an increase of T_c with pressure from ac susceptibility measurements on three MgC_xNi_3 (for $x = 1.0$, 1.25 and 1.5) samples, which is in contradiction to the low pressure result of Kumary *et al* [18]. The temperature variation of the ac magnetic susceptibility (χ_{ac}) for different MgC_xNi_3 samples under pressure (0–17 kbar) is shown in figure 6. The T_c (mid-point) for the sample with $x = 1.0$ (sample A) increases from 6.56 to 6.79 K with increase of the pressure from ambient to 14.80 kbar, as illustrated in figure 7, at the rate of $dT_c/dP \sim 0.015$ K kbar^{-1}. A similar trend of the pressure effect on T_c for other samples [17] is also observed (table 4). This rate is slightly higher than that (~0.0075 K kbar^{-1}) observed by Kumary *et al* [18] at pressures above 17 kbar. To give a clear idea of the pressure effect on T_c for other intermetallic and metallic superconductors such as MgB_2, $LuNi_2B_2C$, Ta and V [71–77, 80–82], some of the results are listed in table 4. Yang *et al* [17] explain the increase of T_c with pressure as follows.

The change of T_c with the unit cell volume (V) can be given by [71, 75]

$$(V/T_c)(dT_c/dV) = d\ln T_c/d\ln V = -(B/T_c)(dT_c/dP), \tag{2}$$

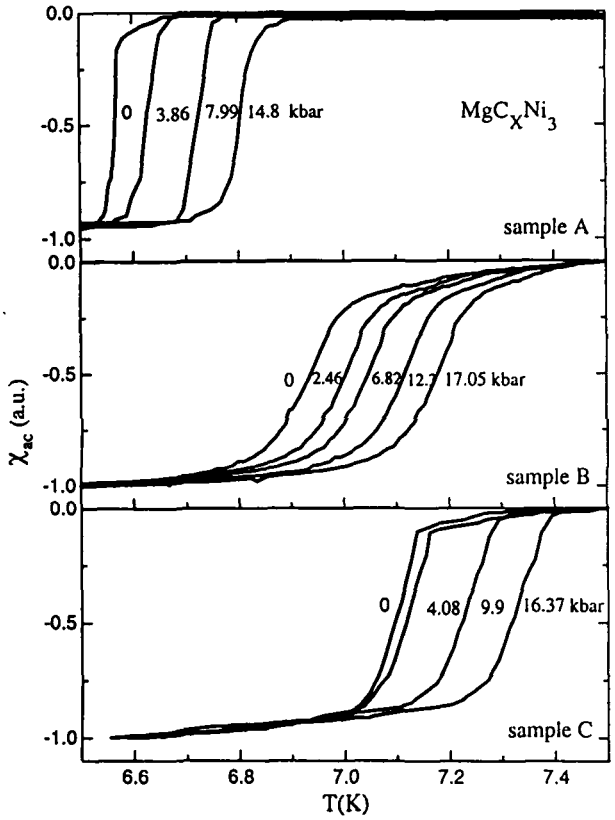

Figure 6. The variation of the ac magnetic susceptibility (χ_{ac}) of MgC_xNi_3 samples with $x = 1.0$ (A), 1.25 (B) and 1.5 (C) near T_c at various pressures (P) [17].

where B is the bulk modulus of the superconductor. Using the calculated value of B for MgC_xNi_3, 1510 kbar [18], and taking the dT_c/dP and T_c obtained from table 4, the $d \ln T_c/d \ln V$ values were found from equation (2); they vary from -3.18 to -2.58. These values are of the same order of magnitude for MgB_2 superconductor (+4.16), but with the opposite sign [71].

Since the DOS is sufficiently large in MgC_xNi_3 to produce strong electron–phonon coupling [51] and is supported by the thermoelectric power (S) data, the T_c can be expressed by the McMillan formula [80] as

$$T_c = (\theta_D/1.45) \exp\{-1.04(1+\lambda)/[\lambda - \mu^*(1+0.62\lambda)]\}, \quad (3)$$

where μ^* is the Coulomb pseudopotential and θ_D is the Debye temperature. λ is the electron–phonon coupling constant and is given by

$$\lambda = N(E_F)\langle I^2\rangle/M\langle\omega^2\rangle, \quad (4)$$

where $N(E_F)$ is the DOS at the Fermi level, $\langle I^2\rangle$ is the square averaged electronic matrix element for electron–phonon interaction, M is the ionic mass and $\langle\omega^2\rangle$ is the square averaged phonon frequency. It appears from equation (3) that the change of λ and θ_D caused by pressure will determine the sign of dT_c/dP. It is well established that the pressure induces lattice stiffening and generally reduces the T_c [75, 76]. However, the DOS effect can either

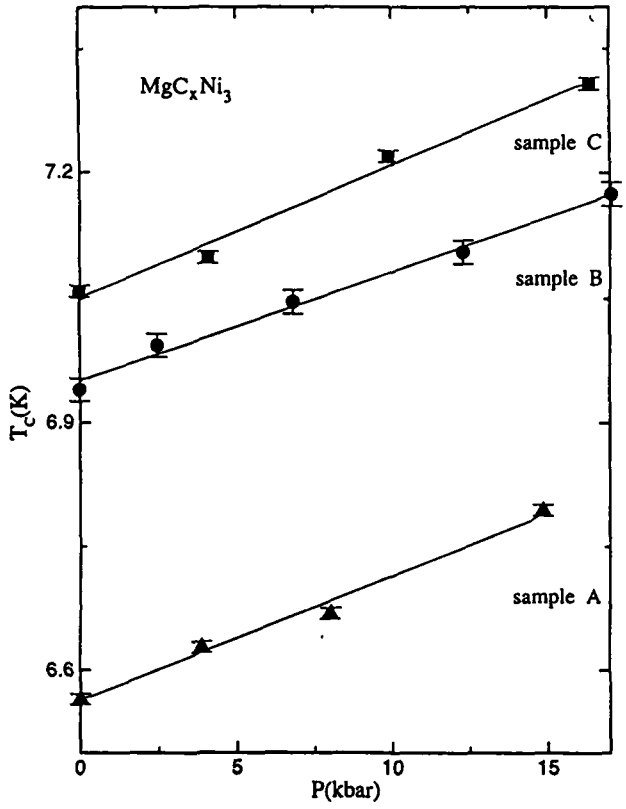

Figure 7. The pressure (P) dependence of the superconducting transition temperature (T_c) of MgC_xNi_3 samples with $x = 1.0$ (A), 1.25 (B) and 1.5 (C) [17].

enhance or reduce the T_c by, respectively, increasing or decreasing $N(E_F)$ on application of pressure [75, 76]. The dependence of T_c on θ_D is complicated as it appears both in the linear and in the exponent (being connected with $\langle\omega^2\rangle$ in equation (4)) terms of equation (3). Again, the change of exponent λ in equation (3) will be more effective than that of the linear term θ_D in determining T_c. Therefore, the positive dT_c/dP for MgC_xNi_3 possibly originates from the increase of $N(E_F)$ and consequently the enhancement of the electron–phonon coupling constant λ (equations (4)) if μ^* and $\langle I^2\rangle$ are less pressure dependent [17]. In addition, the P causes not only a shifting of the E_F but also a broadening of the energy bands. This broadening of the energy bands may also increase the $N(E_F)$. The computation of some important parameters such as $d\ln N(E_F)/dP$ and $d\ln\omega/dP$ of MgC_xNi_3 may be useful for quantitative analysis of the pressure dependent T_c data.

Yang *et al* [17] have also argued that the reduction of spin fluctuation with P may also be one of the reasons for the positive pressure effect on the T_c of MgC_xNi_3. Generally, the deficiency of carbon compared with the optimum value decreases the T_c [1, 8]. Non-stoichiometry of carbon (if any) may also affect the energy bands of the sample and alter the position of E_F compared to that expected from theoretical energy band calculations [49–54] for stoichiometric $MgCNi_3$. As the dT_c/dP is not changed much with carbon content, this suggests that the carbon deficiency does not significantly affect the pressure effect on T_c of MgC_xNi_3 [17]. The controversial results of Yang *et al* [17] as compared with those of Kumary *et al* [18] may be due to the reduction of grain boundary effects caused by pressure. Yang *et al* [17] claim that once the pressure applied is high enough (~17 kbar) to overcome the

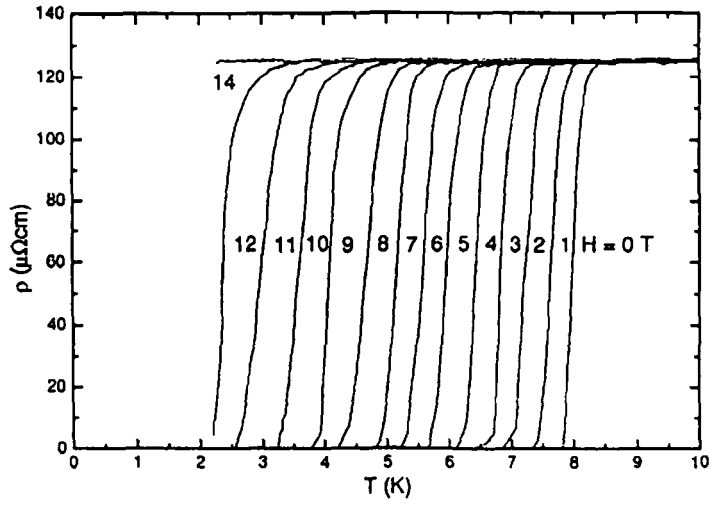

Figure 8. Resistivity versus temperature curves of $MgCNi_3$ at different fixed magnetic fields (H) [4].

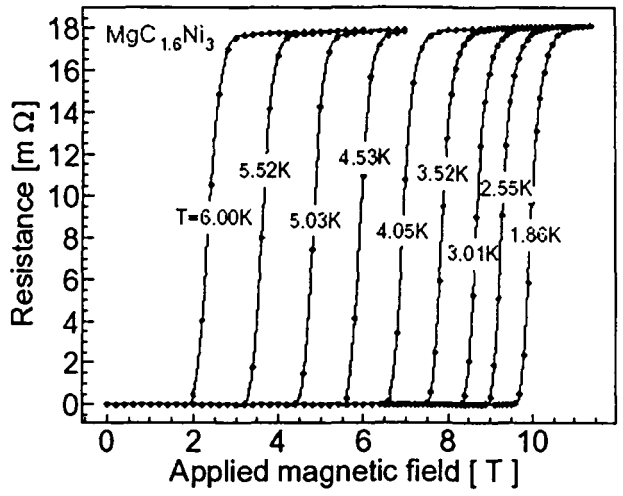

Figure 9. The field dependence of the resistivity of $MgC_{1.6}Ni_3$ measured at several fixed temperatures [48].

grain boundary effect, the bulk superconductivity dominates and the positive dT_c/dP is found the same as the observation of Kumary *et al* [18] using resistivity measurements. It should be mentioned that the effect of irradiation pressure on T_c is just opposite to that of hydraulic pressure [17, 32]. It has been found that the T_c of $MgCNi_3$ decreases from 6.5 to 2.9 K upon disordering induced by irradiation from a nuclear reactor and is completely restored after annealing at a temperature of 600 °C [32].

5. Magnetic properties

5.1. Critical fields (H_{c1} and H_{c2})

The upper critical field $H_{c2}(0)$ of $MgCNi_3$ is determined both from the specific heat (C) and from the resistivity (ρ) data [1, 4, 7, 9, 11–14, 20, 23, 47, 48, 83]. The results derived from ρ are nearly identical to those determined from the anomaly in C. Figure 8 shows the temperature

Table 5. Comparison between $MgCNi_3$, $Nb_{0.5}Ti_{0.5}$ and Nb. The parameters of $MgCNi_3$ are similar to those of $Nb_{0.5}Ti_{0.5}$ and Nb [13].

	$MgCNi_3$	$Nb_{0.5}Ti_{0.5}$	Nb
T_c (K)	6.4	9.3	9.2
$\Delta C/\gamma_n T_c$	1.97	~1.9	1.87
$\ln(\theta_D/T_c)$	3.79	3.23	3.40
$2\Delta/k_B T_c$	$\geqslant 4$	3.9	3.80
H_{c2} (T)	11.5	14.2	~0.2
θ_D (K)	287	236	275
γ_n (mJ mol^{-1} K^{-2})	33.6 (11.2/Ni)	10.7	7.79

variation of ρ in different magnetic fields (H) up to 14 T [4]. The magnetic field dependence of the resistivity of $MgC_{1.6}Ni_3$ measured at several temperatures is illustrated in figure 9 [48]. The T_c decreases with increase of the magnetic field and finally becomes non-superconducting (figures 8 and 9). A magnetic field of 8 T leads to about 50% suppression of T_c and a complete suppression takes place at 14 T [4, 14]. The width $\Delta H = H_{90} - H_{10}$, with H_{90} and H_{10} being respectively the field values where 90% and 10% of the normal state resistivity is observed, remains constant at ~0.6 T down to low temperature (figure 9). This indicates that $MgCNi_3$ has a small anisotropy in H_{c2}, as the strongly anisotropic superconductor shows a gradual broadening of the superconducting transition with decrease of the temperature [48]. The slopes $(dH_{c2}/dT)_{T_c}$ derived from the linear fits of both the C and the ρ data for $0.8 \leqslant (T/T_c) < 1$ are very close to each other [14]. The values of $(dH_{c2}/dT)_{T_c}$ are found as 2.96 ± 0.08 and 2.88 ± 0.03 T K^{-1} respectively from C and ρ measurements [13, 14]. Neglecting the spin–orbit interaction and the spin paramagnetic term in $MgCNi_3$, the relation

$$H_{c2}(0) \approx 0.69 T_c (dH_{c2}/dT)_{T_c} \tag{5}$$

leads to $H_{c2}(0) \sim 13.2 \pm 0.7$ T [14]. Similarly, $H_{c2}(0) = 14.8$ T is estimated from equation (5) by Mao *et al* [9]. As the spin–orbit and the spin paramagnetic effect are not taken into account, the value of $H_{c2}(0)$ is significantly overestimated [13]. It is found that the physical properties of $MgCNi_3$ [13] are very similar to those of $Nb_{0.5}Ti_{0.5}$ (table 5). Thus Lin *et al* [13] conclude that the two compounds may have similar relations between $H_{c2}(0)$ and $(dH_{c2}/dT)_{T_c}$. Again, $H_{c2}(0) \approx 0.59 T_c (dH_{c2}/dT)_{T_c}$ for $Ni_{0.5}Ti_{0.5}$ [13]. Following this relation, it is found that $H_{c2}(0) = 11.2 \pm 0.6$ T for $MgCNi_3$ [13]. The values of $H_{c2}(0)$ obtained by different groups vary from 11 to 16 T (table 3). The H_{c2} versus T curve of $MgCNi_3$ is shown in figure 10 [4]. Downward curvature in figure 10 indicates the conventional superconductivity in $MgCNi_3$. It is contended [16, 48] that $MgCNi_3$ has a Werthamer–Helfand–Hohenberg-like [84] temperature dependence of $H_{c2}(T)$ and follows the quadratic relationship

$$H_{c2}(0) = 0.0237(1 + \lambda)^{2.2} T_c^2 / (10^5 \times v_F^2), \tag{6}$$

with v_F as the bare Fermi velocity, which points to an effective predominant single-band behaviour near the quasi-clean limit [85]. It is also found that the value of $H_{c2}(0)$ is the same as that obtained from the Werthamer–Helfand–Hohenberg formula [84] if the spin paramagnetic effect and the spin–orbit interaction are taken into account by utilizing the relation $\gamma(H) \propto H$ and the value of $d\gamma/dH$ [13, 14] as discussed later. It is observed that the critical field behaviour of 60 nm thin film [20] is comparable to that of sintered $MgCNi_3$ powders. Films thicker than ~40 nm have an upper critical field $H_{c2} \sim 13$ T, which is comparable to that of polycrystalline bulks [16, 20, 48].

The Pauli limiting field $H_P(0) = 1.84 \times 10^4 T_c$ is expected within the weak coupling BCS theory [86]. The $H_{c2}(0)$ [9] obtained from Werthamer–Helfand–Hohenberg theory [84]

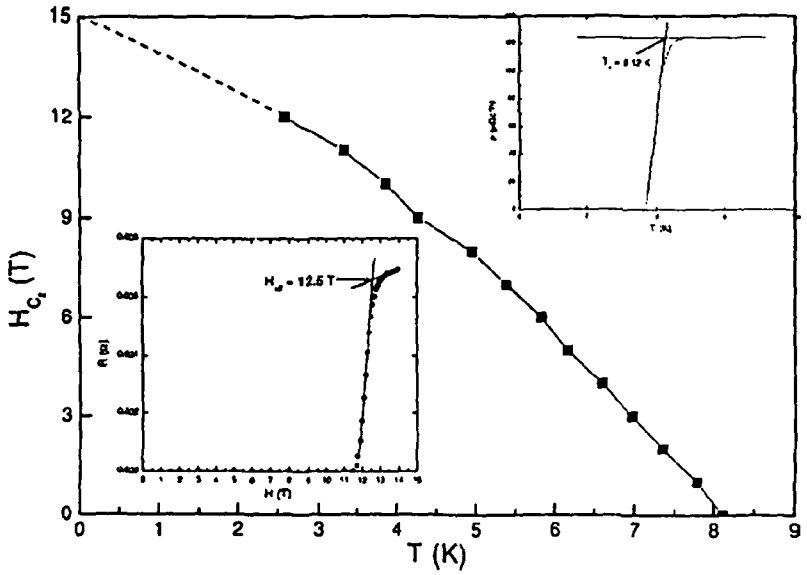

Figure 10. The upper critical field H_{c2} of $MgCNi_3$ as a function of temperature. The upper inset shows the temperature dependence of the sample resistivity at zero magnetic field. The lower inset shows the magnetic field dependence of the resistance at a temperature of 2.3 K [4].

is higher than $H_P(0)$, suggesting that pair breaking effects due to the Zeeman energy in $MgCNi_3$ are slight. For type-II superconductors, $H_P(0)$ should satisfy the relation [87] $H_{c2}(0) \leqslant H_P(0)$. Taking $T_c = 6.4$–8 K (table 3), $H_P(0)$ is estimated as ~11.7–14.72 T. Thus $H_P(0)$ for $MgCNi_3$ is of the order of its $H_{c2}(0)$ (table 3), indicating type-II superconductivity. The thermodynamic critical field $H_c(0) \sim 0.18$–0.6 T, Ginzburg–London (GL) coherence length $\xi_{GL}(0) \sim 45$–56 Å, penetration depth $\lambda_{GL}(0) \sim 1800$–2480 Å and lower critical field $H_{c1}(0) \sim 10$–12.6 mT (table 3) are generally estimated from the following relations [88, 89]:

$$H_c(0) = 4.23\gamma_n^{1/2}T_c \text{ Oe}, \tag{7}$$

$$\xi_{GL}(0) = \{\Phi_0/[2\pi H_{c2}(0)]\}^{1/2} \text{ Å}, \tag{8}$$

$$\lambda_{GL}(0) = 6.42 \times 10^5(\rho_{res}/T_c)^{1/2} \text{ Å}, \tag{9}$$

$$H_{c1}(0) = H_c(0)(2^{1/2}\kappa)^{-1} \ln\kappa \text{ Oe}, \tag{10}$$

where the fluxon $\Phi_0 \approx 2.0678 \times 10^9$ Oe Å^2 and $\kappa(0)$ $[=\lambda_{GL}(0)/\xi_{GL}(0)] \sim 43.3$–66. All the parameters obtained for $MgCNi_3$, $\xi_{GL}(0)$, $\lambda_{GL}(0)$ and $\kappa(0)$, also satisfy the conditions for type-II superconductivity [89].

5.2. *The critical current density (J_c)*

Figure 11(a) shows the critical current density (J_c) of $MgC_{1.5}Ni_3$ [11] at different temperatures (1.8–6.5 K). Assuming that the current flows through the entire sample, Cooley *et al* [11] calculate that $J_c = 3\Delta M/d$, taking the applied magnetic field perpendicular to the thin square prism, where ΔM is the full width of the magnetization and d is the width of the sample. The calculation shows that $J_c \sim 10^3$–10^4 A cm^{-2} at 4.2 K. Taking into consideration the presence of carbon in grain colonies, inferred from microstructural analysis [11], the modified J_c $(=16\Delta M/3\pi a)$, with the critical state of a sphere of diameter $2a = 10$ μm,

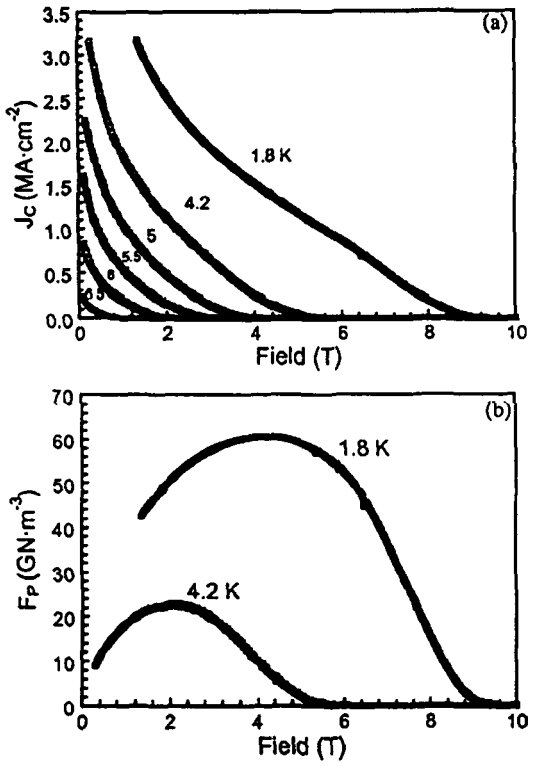

Figure 11. (a) The critical current density (J_c) at 1.8–6.5 K, assuming that magnetization current loops flow around grain colonies with diameter 10 μm. (b) The bulk pinning force (F_P) at 1.8 and 4.2 K derived from the $J_c(H)$ data using a scaling length of 10 μm colony size [11].

gives a very high $J_c \sim 1.8 \times 10^6$ A cm^{-2} at 1 T and 4.2 K. Again the pinning force, $F_P(H) = \mu_0 H \times J_c(H, T)$, derived from J_c is significantly higher for the latter assumption (figure 11(b)). The peak value is found as 23.5 GN m^{-3} at 4.2 K, which is greater than that of the Nb–48% Ti superconductor with the higher irreversibility field at 4.2 K [90]. Cooley *et al* [11] argue that the Ginzburg–Landau (GL) parameter, $\kappa(0) = 66$, of $MgCNi_3$ (table 3) suggests that the pinning force per flux line $J_c \times \phi_0 \sim 2 \times 10^{-5}$ N m^{-1} is about 10% of the flux line tension $\mu_0 H_{c2}^2 \pi \xi_{GL}/2\kappa^2 \sim 1.5 \times 10^{-4}$ N m^{-1}, taking $\phi_0 = 2 \times 10^{-15}$ Wb as the flux quantum. This strong pinning is within the single-vortex pinning regime where it plastically deforms the flux line lattice [11]. The high value of F_P at 1.8 K (figure 11(b)) suggests core pinning in $MgCNi_3$ [11]. The low field pinning characteristic can be exceeded by incorporating nanoprecipitates in $MgCNi_3$ [35]. However, too many precipitates within the grain boundaries can block uniform current flow between grains. The bulk pinning force $F_P(H)$ is comparable to that of other strong flux pinning superconductors, such as Nb–N, Nb–Ti and Nb_3Sn, all of which have higher critical temperatures [11]. While $F_P(H)$ indicates the expected grain boundary pinning mechanism just below $T_c \sim 7.2$ K, a systematic change to a core pinning mechanism is indicated by a shift of the $F_P(H)$ curve peak to higher (reduced) field with decreasing temperature. The lack of temperature scaling of $F_P(H)$ suggests the presence of pinning sites at a nanometre scale inside the grains, smaller than the diameter of the fluxon cores $2\xi_{GL}(T)$ at high temperature, which become effective when the coherence length $\xi_{GL}(T)$ approaches the nanostructural scale with decreasing temperature. It is concluded that no other fine grained bulk intermetallic superconductor exhibits a similar change from grain boundary to core pinning with decreasing temperature, suggesting that the arrangement of pinning sites in $MgCNi_3$ is

unique [11]. These results also indicate that strong flux pinning might be combined with a technologically useful upper critical field if variants of $MgCNi_3$ with higher T_c can be found.

5.3. The normal state magnetoresistance (MR)

Normal state magnetoresistance (MR) is an important tool for getting further insight into the charge transport mechanism, since it is more sensitive to the change in the charge carrier scattering rate $1/\tau$, the effective mass m^* and the geometry of the Fermi surface. The MR is given by $\Delta\rho/\rho_0 = [\rho(H) - \rho_0]/\rho_0$ where $\rho(H)$ and ρ_0 are respectively the resistivities with and without a magnetic field H. Since the charge carrier scattering rate, $1/\tau$, is proportional to ρ_0, the MR depends only on H/ρ_0. Kohler's rule for conventional superconductors is given by [91]

$$\mathrm{MR} = \Delta\rho/\rho_0 = f(H\tau) = F(H/\rho_0) \quad . \tag{11}$$

where f and F are universal functions. In the low field limit, $\Delta\rho(T) = A(H/\rho_0)^2$ as MR quadratically depends on H, where A is a constant. The resistance of $MgCNi_3$ increases with magnetic field (figure 12) showing a positive magnetoresistance [7]. It is also comparable to that of a normal metal [91]. However, the MR of $MgCNi_3$ is much smaller than that for the borocarbide superconductors [7]. It is found that the normal state transverse MR of $MgCNi_3$ is always positive and monotonically decreases with increasing temperature (figure 12). The data above 50 K follow Kohler's rule, although those below 50 K do not. This electronic crossover at 50 K is also observed in NMR data [3], which may be associated with this deviation of MR from Kohler's rule below 50 K. Here it should be mentioned that Das and Kremer [33] observe a negative MR at 2 K and followed by a $\sim H^2$ dependence for $MgCNi_{2.97}Mn_{0.03}$ samples. The authors of [33] argue that the negative MR is from partial alignment of impurity spins reducing the spin flip scattering. They [33] also show a correlation between MR and M^2 indicating the Kondo effect [92]. This can be described by the relation

$$\Delta R = R(H, T) - R(0, T) = [3\pi^2 mcVJ^2M^2]/[E_F e^2 h] \tag{12}$$

where m and e are respectively the charge and mass of an electron, V is the atomic volume, J is the s–d exchange constant, c is the atomic concentration of impurities, E_F is the Fermi energy, h is Planck's constant and M is the magnetization in μ_B/atom. ΔR versus M^2 indeed satisfies the above relation (equation (12)) for $MgCNi_{2.97}Mn_{0.03}$ samples [33].

5.4. The Hall effect

Hall effect measurements are used to get a direct idea of the type of the carriers (namely electrons or holes) in a material. They can also give the number of carriers per unit volume (n). The Hall coefficient (R_H) of $MgCNi_3$ at a magnetic field of 10 T is almost constant up to a temperature of 140 K (figure 13) and beyond that the magnitude decreases with increase of the temperature [4]. The inset of figure 13 shows the increase of the Hall voltage (V_H) measured at 100 K with increase of the magnetic field in the opposite direction. R_H of $MgCNi_3$ is negative for the whole temperature range, which definitely indicates that the carriers in $MgCNi_3$ are of electron type, as supported by the thermoelectric power data [7, 17, 39]. At $T = 100$ K, $R_H = -6.1 \times 10^{-10}$ m^3 C^{-1} and the carrier density (n) was 1.0×10^{22} cm^{-3}, which is comparable with the theoretically calculated [50] value (1.3×10^{22} cm^{-3}) and that for perovskite (Ba, K)BiO_3, but less than that for the metallic binary MgB_2. However, the value of n for $MgCNi_3$ thin film [20] is found to be 4.2×10^{22} cm^{-3} (table 3) which is about four times higher than that of the bulk sample [4] although the superconducting properties of bulk and thin film samples are almost the same. Again the R_H depends on temperature, which is not observed

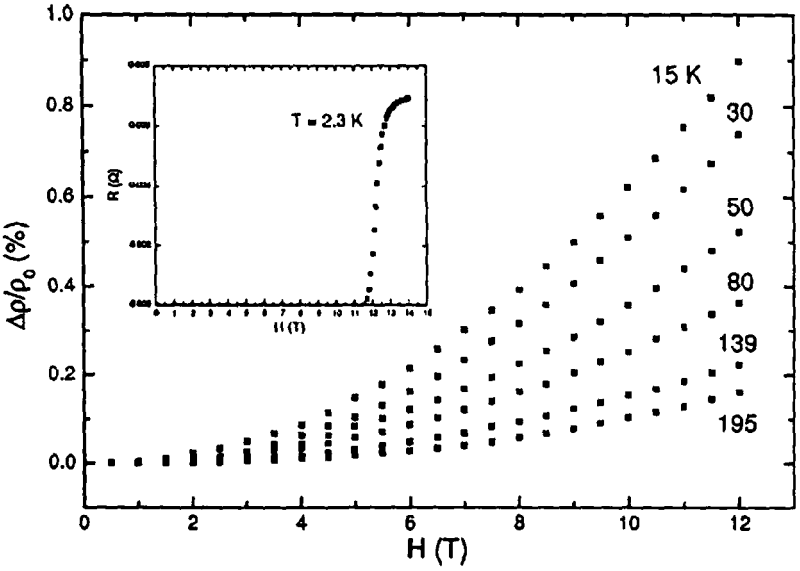

Figure 12. The magnetoresistance of $MgCNi_3$ as a function of the magnetic field at various temperatures. The inset shows the magnetic field dependence of the resistance at 2.3 K [7].

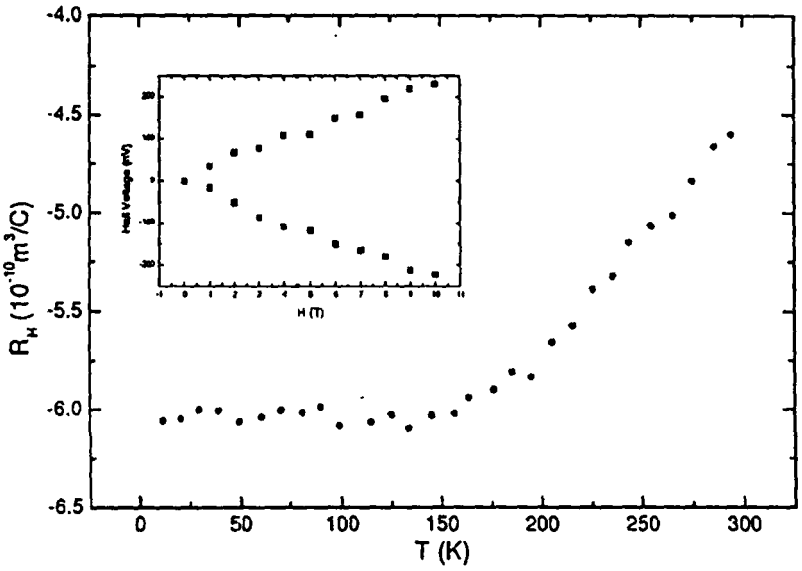

Figure 13. The temperature variation of the Hall coefficient (R_H) measured at a magnetic field of 10 T. The inset shows the Hall voltage measured at 100 K for two opposite directions of the applied field up to 10 T [4].

for conventional superconductors. Moreover, it is temperature independent between T_c and 140 K. Above 140 K, the magnitude of R_H decreases with increase of the temperature [39]. The temperature variation of R_H is also observed in non-cuprate $Ba_{1-x}K_xO_3$ and copper-based

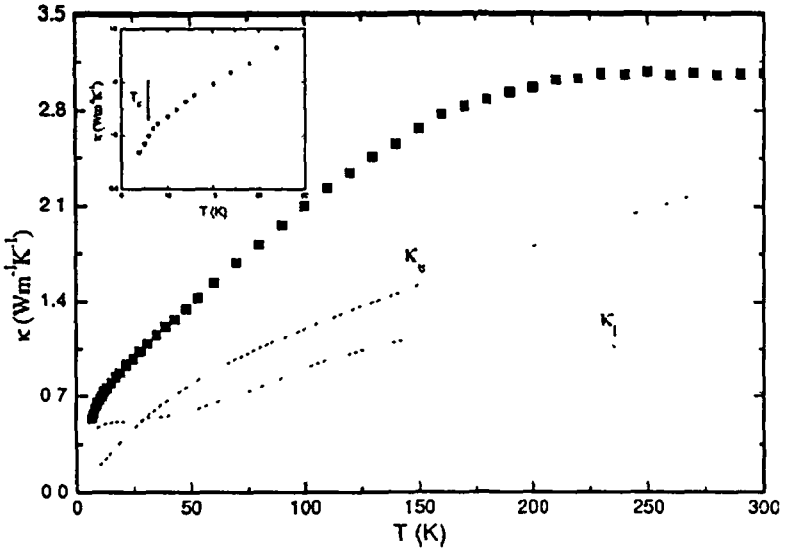

Figure 14. The temperature variation of the thermal conductivity of $MgCNi_3$ The dashed curves represent the electronic contribution k_e and the lattice contribution k_l The inset shows the change of slope at $T_c = 8$ K [7]

superconductors [93, 94]. The thermal dependence of R_H in $MgCNi_3$ may be explained as due to magnetic excitations of the electrons supplied by Ni d states [49–54]. But interestingly the non-cuprate $Ba_{1-x}K_xO_3$ has the same temperature behaviour [93] of R_H, which needs further investigation.

6. Thermal properties

6.1. The thermal conductivity (k)

The temperature variation of the thermal conductivity (k) of $MgCNi_3$ (figure 14) shows that it is nearly constant above 210 K [7]. It is of the order of that for intermetallics, larger than that of borocarbides [95] and smaller than that of MgB_2 [96]. A change of slope in the thermal variation of k is observed at T_c (figure 14). The total thermal conductivity $k = k_e + k_l$ where k_e and k_l are respectively the electronic and lattice contributions in k. The electronic contribution can be obtained from the Wiedemann–Franz law [97]

$$k_e(T) = L_0 T/\rho(T) \tag{13}$$

where L_0 is the Lorentz number, ρ is the resistivity and T is the absolute temperature Then the lattice contribution is achieved from the total thermal conductivity. The electrons contribute a large fraction to the thermal conductivity in the normal state because of the non-localization of the mutual effect of electrons [61]. Analysis of the electronic thermal conductivity indicates that the scattering by impurities prevails in the electronic thermal resistance It has been observed [7] that the electronic contribution is slightly higher than the lattice contribution in the normal state (figure 14). It has also been found from thermal conductivity that the scattering of electrons by static imperfections of the crystal becomes dominant near T_c [7] However, the spin fluctuations are increased with decrease of the temperature [3] and the scattering of electrons with spin fluctuations decreases the thermal conductivity at low temperatures

6.2. *The thermoelectric power (TEP)*

The lower part of figure 4 shows the thermoelectric power (S) of the MgC_xNi_3 sample [17] with $x = 1.0$ (sample A). The temperature dependence of S is negative, confirming the carriers to be of electron type, which is consistent with other published results [4, 7, 39] and inconsistent with the theoretical predictions [50]. The absolute value of $S(275\ K) \sim 9.5$–$14\ \mu V\ K^{-1}$ for this sample decreases with decreasing temperature and is a characteristic of metallic transport in the normal state [7, 17]. The magnitude of S at room temperature (RT) is higher than that associated with free electron or conventional metals but of the same order as that for RNi_2B_2C (R = rare earth) superconductors [7]. There are generally diffusion and phonon drag contributions to S. The former contribution is proportional to temperature (T) while the latter one falls both at low and high temperature, respectively due to the freezing out of the phonons and phonon–phonon scattering. No phonon drag peak is observed in S of $MgCNi_3$ from room temperature down to 10 K [7]. A different type of contribution to S is found compared to the borocarbide case; it may be due to the three-dimensional (3D) and non-layered nature of $MgCNi_3$. Li *et al* [7] observe a nonlinear temperature dependence of S below 150 K, which is explained by the electron–phonon interaction renormalization effects. The nonlinear temperature dependence of S [7, 39] seems to suggest that the enhancement of the electron–phonon interaction plays an important role in the superconductivity of $MgCNi_3$ like in the chevrel phase compounds [98] $Cu_{1.8}Mo_6S_{8-y}Se_y$ and $Cu_{1.8}Mo_6S_{8-y}Te_y$. An electronic crossover occurs at about 50 K, resulting in the abnormal behaviour of S below 50 K [39].

The electron–phonon interaction renormalization effect may show a low temperature 'knee' in $S(T)$ and may be written as [98]

$$S/T = (S_b/T)[1 + \lambda(T)] \tag{14}$$

where $\lambda(T)$ is the electron–phonon mass enhancement parameter which is maximum at $T = 0$ but becomes very small near room temperature [7] and S_b is the bare S without any renormalization effect. Li *et al* [7] observe a change of curvature in the S/T versus T curve near 50 K, as is also observed by Singer *et al* [3] from NMR investigation, which may be associated with the electronic crossover at 50 K prior to the superconducting transition. Li *et al* [7] estimate the value of $\lambda(0)$ from S data as ~ 1.4, which is much higher than that (~ 0.66–0.84; table 3) calculated from low temperature specific heat (C) data [1, 9, 13, 38, 47, 48] (discussed later). This suggests that there may be a mechanism other than the electron–phonon interaction for the mass enhancement. $MgCNi_3$ has a strong spin fluctuations [3, 13] which may be lessened with decreasing temperature. The larger value of $\lambda(0)$ obtained from S data compared to that obtained from C data may be arising from spin fluctuations. Thus the modified S is of the form

$$S/T = (S_b/T)[1 + \lambda(T) + \lambda_{sf}] \tag{15}$$

where λ_{sf} is the mass enhancement parameter due to spin fluctuations. The λ_{sf} term can explain the discrepancy between the values of $\lambda(0)$ obtained from S and C data [1, 3, 7, 13].

6.3. *The specific heat (C)*

The specific heat (C), a thermodynamic bulk property, unlike resistivity and magnetization, of $MgCNi_3$ has been intensively studied by several groups [1, 13, 24, 38, 48]. Figure 15 shows the low temperature specific heat $C(T, H)$ of $MgCNi_3$ with $H = 0$ and 8 T as C/T versus T^2 [13]. The superconducting anomaly observed by Lin *et al* [13] at $H = 0$ is much sharper than that observed by He *et al* [1], indicating the high quality of the sample of the former group. The C data are discussed on a qualitative level in terms of effective single- and

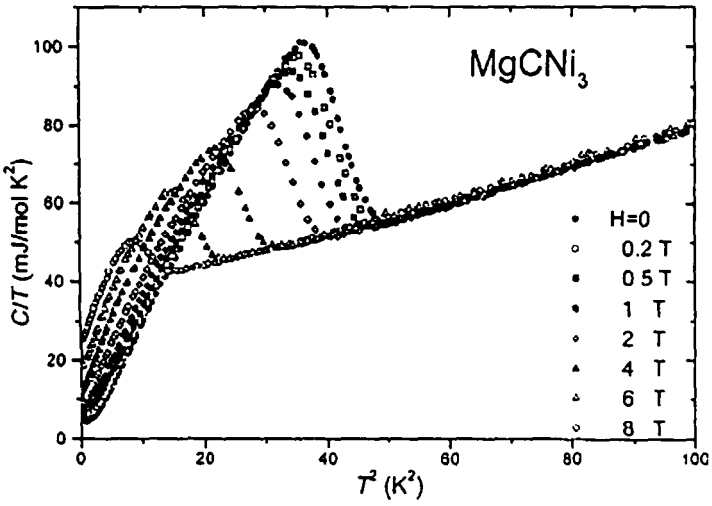

Figure 15. $C(T, H)/T$ versus T^2 for $MgCNi_3$ for $H = 0$–8 T [13].

multi-band models [24, 48] based on an orbital assignment of the disjoint Fermi surface sheets (FSS) derived from LDA full-potential electronic structure calculations. It is noted that C/T shows an upturn at very low temperatures [1, 13] and disappears in high field, which is a demonstration of a paramagnetic contribution such as a Schottky anomaly. The normal state specific heat, $C_n(T) = \gamma_n T + C_{lattice}(T)$, was extracted from $H = 8$ T data by Lin *et al* [13] between 4 and 10 K using

$$C(T, H = 8\text{ T}) = \gamma_n T + C_{lattice}(T) + nC_{Schottky}(g\,\mu H/k_B T), \tag{16}$$

where the third term is a two-level Schottky anomaly. $C_{lattice}(T) = \beta T^3 + \delta T^5$ represents the phonon contribution and $\gamma_n T$, the electronic contribution with γ_n as the coefficient of the electronic specific heat in the normal state. It was found by several groups that $\gamma_n = 9.8$–11.2 mJ K^{-2} (mol Ni)$^{-1}$ (table 3). The value of γ_n increases with increasing Mn concentration in $MgCNi_{3-z}Mn_z$ samples [33]. This observation indicates that the reduction in T_c with addition of Mn is due to the pair breaking interaction, which is of magnetic origin and not electronic [33]. This value of γ_n, with the electron–phonon coupling constant λ discussed below, requires a higher band $N(E_F)$ than most of those reported from calculations [49–51, 54–57]. It is found that for MgC_xNi_3, the γ_n of the superconducting sample ($x \sim 1$) in the normal state is twice than that of the sample in the non-superconducting state ($x \sim 0.85$) [47]. Comparison of the measured γ_n and the calculated electronic DOS shows that the effective mass renormalization changes remarkably as the carbon concentration alters. The Debye temperature (θ_D) derived from the relation

$$\beta = 1.944 \times 10^6 \times n/\theta_D^3, \tag{17}$$

where n is the number of atoms per formula unit and takes the value 5 for $MgCNi_3$, varies from 206 to 351 K (table 3) and is much lower than that (450 K) of Ni. These values are also lower than the calculated $\theta_D \sim 440$ K of $MgCNi_3$ obtained by using the Rietveld refinement method based on the powder XRD data [29]. However, these are close to that estimated by considering the softening of the Ni lattice [51], which can enhance the electron–phonon interaction. The concentration of paramagnetic centres can be estimated to be of the order of 10^{-3}, consistent with that assessed from the magnitude of the low temperature upturn. With a dominant content of Ni in this compound, this number is understandable and the paramagnetic contribution is indeed observed in the magnetization measurements, too [23].

The characteristics of the superconducting phase transition in $MgCNi_3$ can be analysed using the relation

$$\Delta C(T) = C(T, H = 0\,\mathrm{T}) - C_n(T). \tag{18}$$

The resultant $\Delta C(T)/T$ versus T at $H = 0$ is shown in figure 16(a), where the inset illustrates the conservation of entropy $S = \int_0^{T_c} \frac{\delta C}{T}\,dT$ around the transition. This conservation of entropy is essential for a second-order (such as the superconducting–normal) phase transition. It is worth noting that $\Delta C(T)/T$ for $MgCNi_3$ is qualitatively different from that of Sr_2RuO_4, which is considered as a p-wave superconductor [99]. By the conservation of entropy around the transition, the dimensionless specific heat jump at T_c is $\Delta C/\gamma_n T_c = 1.7$–$2.1$ (table 3), as shown in figure 16(b) [13], which is greater than the typical weak coupling value (~1.43). Thus $\Delta C(T)/T$ is well fitted by the BCS model, as shown in figure 16(a) by the solid curve [13] with $2\Delta/k_B T_c \sim 4.0$, where Δ is the superconducting energy gap. The values of $2\Delta/k_B T_c$ observed by different groups vary from 3.75–5.0 (table 3). This is higher than the weak coupling value (~3.52). Consequently, the superconductivity in $MgCNi_3$ can be explained by the moderate coupling BCS framework.

The electronic specific heat in the superconducting state is given by $C_{es}(T) = C(T) - C_{lattice}(T)$. A logarithmic plot of $C_{es}(T)/\gamma_n T_c$ versus T_c/T (figure 17) shows that the fitting of data (as demonstrated by the solid line) within the range 2 to 4.5 K leads to [13] the relation

$$C_{es}(T)/\gamma_n T_c = A \exp[(-aT_c/T)], \tag{19}$$

with $A = 7.96$ and $a = 1.46$. However, the BCS theory predicts $C_{es}(T)/\gamma_n T_c = 8.5 \times \exp[(-1.44T_c/T)]$ for this temperature fitting range in the weak coupling limit [80]. Therefore, the values of both the coefficient and the prefactor are in the ranges for typical moderate coupling BCS fully gapped superconductors. Lin *et al* [13] argue that since the magnetic contribution will make C_{es} overestimated at low temperatures, the value of 1.46 in the exponent is probably slightly underestimated. This is in contrast to the case for MgB_2 [100], for which $C_{es} \propto \exp(-0.38T_c/T)$. This small coefficient in the exponent for MgB_2 is usually attributed to a multi-gap order parameter.

The electron–phonon coupling constant $\lambda \sim 0.66$–0.84 (table 3) is estimated from the relation [101]

$$\Delta C/\gamma_n T_c = 1.43 + 0.942\lambda^2 - 0.195\lambda^3. \tag{20}$$

According to McMillan model [80], the value of λ for weak coupling is $\lambda \ll 1$, for weak and intermediate coupling $\lambda < 1$ and for strong coupling $\lambda > 1$. Therefore, the present λ values suggest that $MgCNi_3$ is a moderate coupling superconductor.

The field dependences of $C(T, H)/T$ and $\delta C(T, H)$ ($\equiv C(T, H) - C_n(T)$)$/T$ are shown in figures 18(a) and (b), respectively. It is noticed that the conservation of entropy (the areas above and below zero of C/T are equivalent around the superconducting transition) is fundamentally satisfied for all fields studied. $\gamma(H)$ is expected to be proportional to H for a gapped superconductor [102]. For nodal superconductivity, the relation between $\gamma(H)$ and H is expected to be $\gamma(H) \propto H^{1/2}$ [103]. Actually, $\gamma(H)$ for high temperature cuprate superconductors has been intensively studied in this context [103, 104]. Lin *et al* [13] find that $\gamma(H)$ follows a straight line passing through the origin, which suggests that $\delta\gamma \propto H$. At $T = 2$ K, the magnetic contribution is not so significant as that at 0.6 K; thus [105, 106]

$$C_{es}(T, H) \approx C_{es}(T, H = 0) + \gamma(H)T. \tag{21}$$

This approximation neglects the temperature dependence of Δ. However, since Δ varies slowly below $T_c/2$, information on $\gamma(H)$ can still be deduced in this way consistently, as we will see from $d\gamma/dH$. $\delta C/T$ data for all fields are shown as the solid circles (figure 18). As seen in

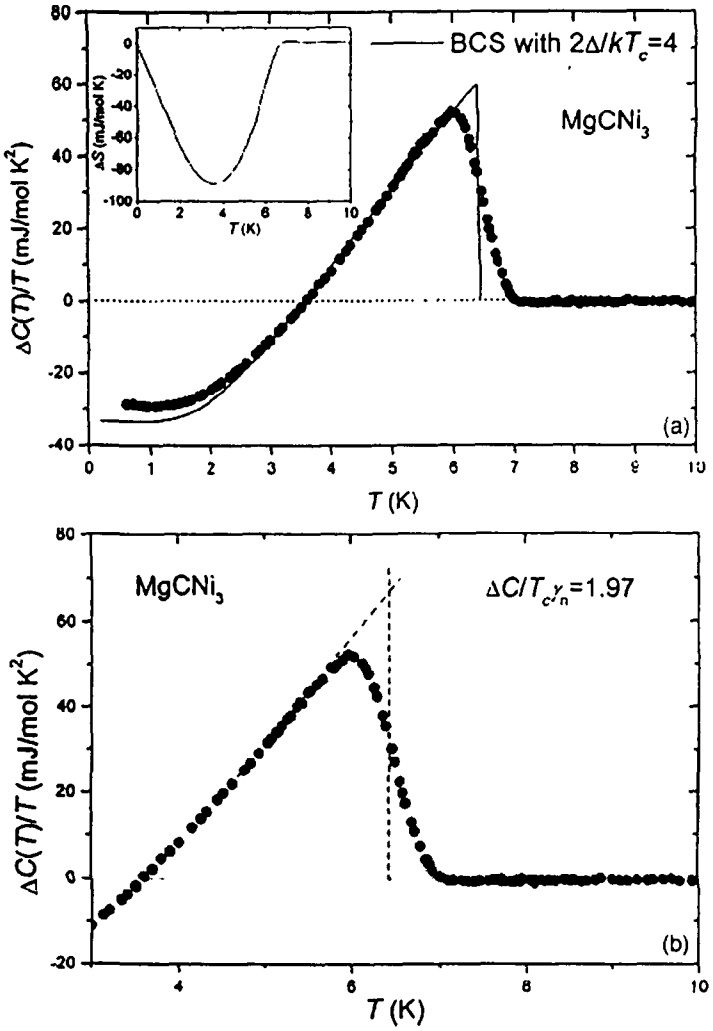

Figure 16. (a) $\Delta C(T)/T$ versus T. The data are presented as the solid circles. The solid curve is the BCS $\Delta C(T)/T$ with $2\Delta/kT_c = 4$. The deviation at low temperatures from the solid curve is due to the magnetic contribution of a small amount of paramagnetic centres in the sample. Inset: the entropy difference ΔS obtained by integration of $\Delta C(T)/T$ according to the data above 3 K and the solid curve below 3 K. (b) The dashed lines are determined from the conservation of entropy around the anomaly, to estimate $\Delta C/T_c$ at T_c [13].

figure 18(b), all high field data can be well described by the straight line, indicating again a linear H dependence of γ [13]. Data below $H = 1$ T begin to deviate from the linear behaviour due to flux line interactions at low H, as nicely demonstrated in [106]. The straight line passes through the origin in figure 18(a), which implies that the flux line interactions are relatively insignificant compared to the core contribution at very low temperatures. This trend is also observed in [106]. The slopes $d\gamma/dH$ in figures 18(a) and (b) are 2.91 ± 0.05 and 3.15 ± 0.08 mJ mol^{-1} K^{-2} T^{-1}, respectively. These two close values derived from different methods suggest that the relation $\delta\gamma \propto H$ is genuine [13]. On the other hand, one may try to fit the data in figure 18(b) with

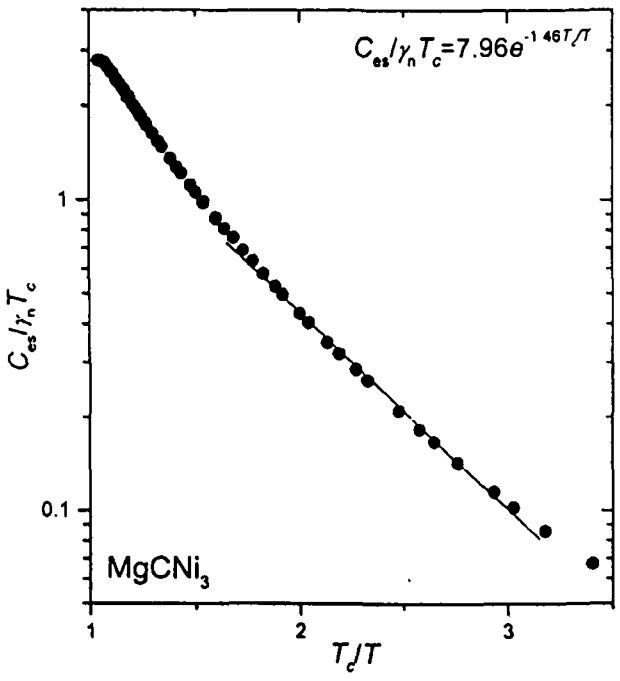

Figure 17. C_{es} for $MgCNi_3$ in the superconducting state is plotted on a logarithmic scale versus T_c/T. The straight line is the fit from 2–4.5 K [13].

$\delta\gamma(H) \propto H^{1/2}$. The results are represented by the dashed curve in figure 18(b). Apparently, the data cannot be well described in this manner, in contrast to the nice $\delta\gamma(H) \propto H^{1/2}$ relation found for cuprates [107, 108]. In principle, it is possible to obtain $\gamma(H)$ in low fields by subtracting the paramagnetic contribution $C_m(T, H)$ from $C(T, H)$. There have been attempts to obtain $\gamma(H)$ by taking $C_m(T, H)$ in the form of a Schottky anomaly [13, 22]. It is found that the derived $\gamma(H)$ can differ depending on the details of the fitting. This implies that the Schottky anomaly cannot totally account for the magnetic contribution at low temperatures. The results are fascinating but inconclusive [13, 22]. Consequently, the field dependence of $\gamma(H)$ suggests that $MgCNi_3$ is an s-wave superconductor in nature.

7. Mechanical properties

The mechanical relaxation properties of $MgC_{1-x}Ni_3$ with $x = 0$ (superconducting) and 0.2 (non-superconducting) were measured by Yao *et al* [40]. The internal friction (Q) and modulus (Y) of the mechanical relaxation spectra were measured for rectangular bars in the clamped–free flexural vibration mode using frequency modulation acoustic attenuation (FMAA-I) equipment [40]. The schematic set-up of the equipment is shown in the inset of figure 19. The mechanical relaxation spectra of a superconducting $MgCNi_3$ sample show two internal friction peaks (at 300 K labelled as P1 and 125 K, as P2) as shown in figure 19, whereas for the non-superconducting one, the position of P1 shifts to 250 K, while P2 is almost completely depressed [40]. Thus the peak P2 may be thermally activated. It is found from the Arrhenius relation

$$2\pi f_p = \nu_0 \exp(-W/T_p) \tag{22}$$

where f_p is the resonant frequency, T_p is the peak temperature and $\nu_0 = 2.9 \times 10^9$ Hz that the value of the activation energy (W) is 0.13 eV. It is observed that the peak position

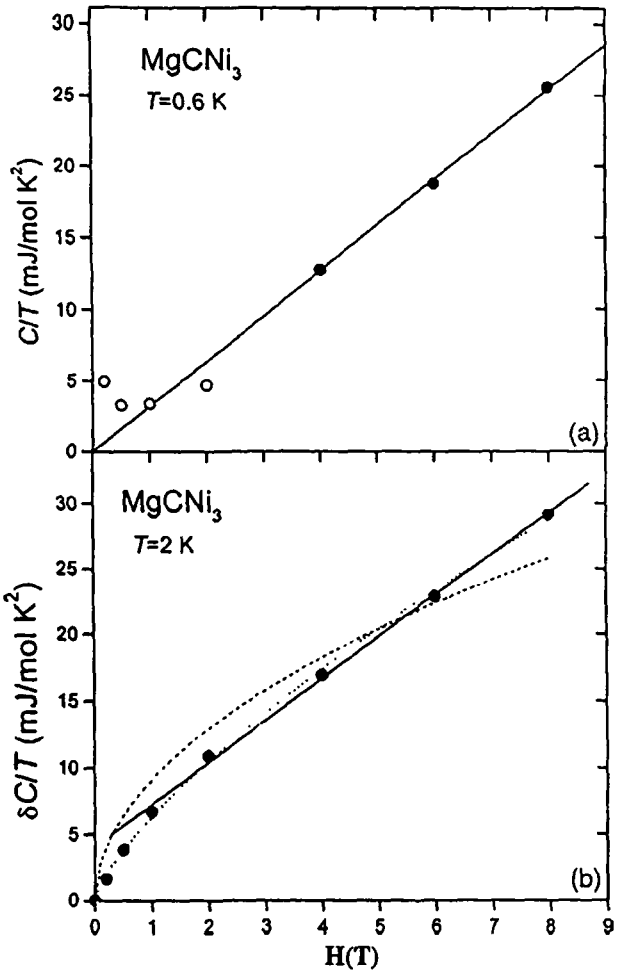

Figure 18. The magnetic field dependence of (a) C/T at $T = 0.6$ K and (b) $\delta C/T$ at $T = 2$ K. The straight lines are linear fits of the data for $H \geqslant 4$ T, implying $\delta\gamma \propto H$. The open circles in (a) represent C/T data corrected with the Schottky term (see the text). In (b), the fitting range is from 1 to 8 T. Data below $H = 1$ T deviate from the linear behaviour due to flux line interactions at low H. The fits with $\delta\gamma(H) \propto H^{1/2}$ and $\delta\gamma(H) \propto H^n$ are also shown, by the dashed and dotted curves, respectively, in (b) for comparison. The latter leads to $n = 0.73$ [13].

of P2 shifts towards higher temperature for higher measuring frequency [40]. The relative changes of the modulus ($\Delta Y/Y$) for the two samples are also shown in figure 19, where $\Delta Y/Y = (f^2 - f_0^2)/f^2$ with f the resonant frequency and f_0 the resonant frequency at 81 K. No clear softening (local minimum) is observed (figure 19), confirming that there is no lattice instability, and this is supported by XRD data [5] which show that the lattice parameter and the Debye–Waller factors for individual atoms decrease smoothly with decreasing temperature, and no unusual change of the structure parameters occurs near T_c. It is to be noted here that although the structure of $MgCNi_3$ is similar to that of $Ba_{1-x}K_xBiO_3$ [1], the latter has a lattice instability [40]. The prediction of Debye theory for the inverse internal friction (Q^{-1}),

$$Q^{-1} = \Delta\omega\tau/T(1 + \omega^2\tau^2), \tag{23}$$

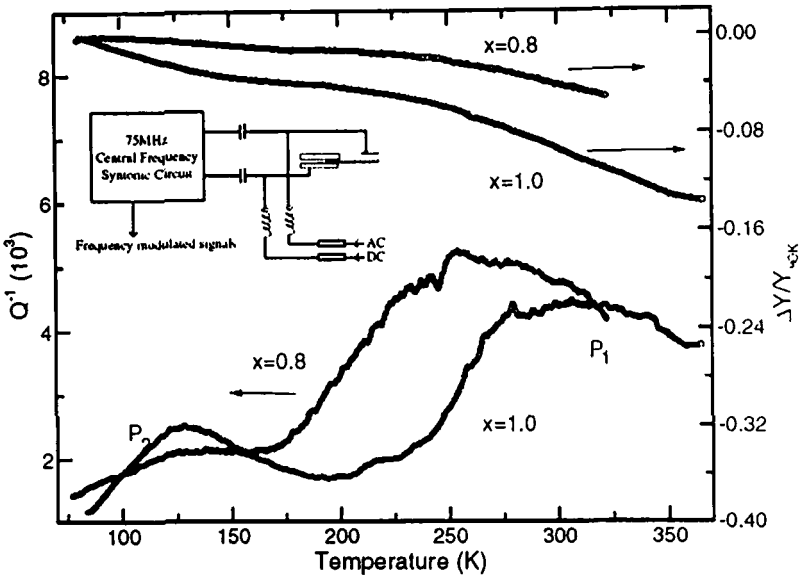

Figure 19. The inverse internal friction (Q^{-1}) and reduced modulus ($\Delta Y/Y_{80K}$) of the mechanical relaxation spectra of the superconducting and non-superconducting $MgC_{1-x}Ni_3$ samples in the temperature range 77–300 K. The inset shows a schematic plot of the frequency modulation acoustic attenuation (FMAA-I) equipment [40].

is compared with the P2 peak, where Δ is the relaxation strength, $\omega = 2\pi f$ and $\tau = \nu^{-1}\exp(W/T_p)$. It is found that the prediction is much narrower than the experimental findings [40]. Thus the Cole–Cole law [109]

$$Q^{-1} = (\Delta/T)\,\mathrm{Im}[1/(1+\{i\omega\tau\}^{\alpha})] \tag{24}$$

is used to fit the experimental data. It is found that $\alpha = 0.52$, indicating the existence of a strong correlation between the relaxation units. There are generally two phases in $MgC_{1-x}Ni_3$, namely non-superconducting α-$MgC_{1-x}Ni_3$ and superconducting β-$MgC_{1-x}Ni_3$ phases [28]. Due to the smaller lattice parameters of the α-$MgC_{1-x}Ni_3$ phase, the off-centre configurations would be suppressed, which is consistent with the depression of the P2 peak for the non-superconducting sample. Yao *et al* [40] propose an explanation relating P2 to carbon atom jumping among the off-centre positions. And further they predict that the behaviour of carbon atoms may correspond to the normal state crossovers around 150 and 50 K observed by many other experimental findings [3, 4, 7, 39].

8. The energy gap of $MgCNi_3$ and the type of superconductivity

Unlike the case for the MgB_2 superconductor which shows two energy gaps [100, 110], a clear gap feature corresponding to the bulk phase T_c is observed for $MgCNi_3$ [9, 19]. The superconducting energy gap Δ is found to be ~1.5 meV by Mao *et al* [9] and ~1.1–1.15 meV by Kinoda *et al* [19], from the tunnelling spectra of $MgCNi_3$. These values of Δ are found to be consistent with the one calculated from the specific heat and other data (table 3). The tunnelling spectroscopy and specific heat studies show that $2\Delta/k_BT_c$ for $MgCNi_3$ varies from 3.75 to 5 (table 3), which is higher than the typical weak coupling BCS value (~3.52) as discussed earlier. The electron–phonon coupling constant $\lambda = 0.66$–0.84 (table 3) indicates

moderate coupling superconductivity in $MgCNi_3$. The values of the Ginzburg–London (GL) coherence length $\xi_{GL}(0) \sim 45$–56 Å, penetration depth $\lambda_{GL}(0) \sim 1800$–$2480$ Å and $\kappa(0)$ $(=\lambda_{GL}(0)/\xi_{GL}(0)) \sim 43.3$–$66$ (table 3) argue for type-II superconductivity [89] in it. Thus, from the above discussions, it can be concluded that $MgCNi_3$ is a BCS s-wave, moderate coupling, type-II, single-gap superconductor. However, this is still controversial as discussed below.

The electron tunnelling spectroscopy results and theoretically estimated superconducting parameters support a BCS s-wave pairing in $MgCNi_3$ in the weak coupling regime [19, 43, 49, 51]. The nuclear spin–lattice relaxation rate $(1/T_1)$ displays behaviour typical of isotropic s-wave superconductivity [3] with a coherence peak below T_c. The properties of Ag diffused Ag–$MgCNi_3$ and Zn doped $(Mg_{0.85}Zn_{0.15})CNi_3$ can be interpreted properly via the conventional BCS phonon mechanism [21, 41]. The difference between the low temperature specific heats of isostructural $MgCNi_3$ and $ZnCNi_3$ with similar carrier densities can be understood within the BCS framework [38].

Waelte *et al* [48] derive $\lambda = 0.84$ from the McMillan formula [80] (equation (3)), although the specific heat data show $\lambda \sim 1.45$ which is identical to the value ~ 1.75 calculated by Ignatov *et al* [66]. Therefore, Waelte *et al* [48] conclude that strong electron–phonon coupling is present in $MgCNi_3$, which is supported by Tan *et al* [65]. The s- and p-wave scenarios are observed from the calculated DOS of different Fermi surface sheets [48]. The large mass renormalization for the superconducting sample and the low T_c (~ 7 K) indicate that more than one kind of boson mediated electron–electron interaction exists in MgC_xNi_3 [47]. The penetration depth exhibits distinctly a non-s-wave BCS low temperature behaviour, instead of showing quadratic temperature dependence, suggestive of a nodal order parameter [42]. Mao *et al* [9] interpret the observed zero-bias conductance peak (ZBCP) as caused by Andreev bound states which result from a possible unconventional non-s-wave pairing state in $MgCNi_3$. On this basis, of the simultaneous appearance of two conductance dips, they suggest strong coupling superconductivity in $MgCNi_3$. However, Naidyuk [45] shows that the current transport through these junctions is determined by thermal effects due to the huge normal state resistivity of $MgCNi_3$. Therefore no conclusion can be drawn about the possible unconventional pairing or strong coupling superconductivity in $MgCNi_3$ [45]. Again, Mao *et al* [46] argue, on the basis of specific heat rather than tunnelling data, that strong coupling superconductivity is suggested. Here it should be mentioned that comparing only $2\Delta/k_BT_c \sim 4.4$ with the weak coupling value of 3.52, Mao *et al* [9] suggest that $MgCNi_3$ is a strong coupling superconductor although another criterion for it, i.e. $\lambda > 1$ [80], is not satisfied.

9. Theoretical studies

The theoretical calculations on doped and undoped $MgCNi_3$ were performed by different methods as discussed below. Some of the important theoretically calculated parameters such as ΔE $(=E_{FM} - E_{PM})$, where E_{FM} and E_{PM} are respectively the energies of the ferromagnetic and paramagnetic states, the DOS at the Fermi level $N(E_F)$ and the magnetization (M) of pure and doped $MgCNi_3$ are shown in table 6. The DOS of the components of $MgCNi_3$ along with the total DOS [49] are displayed in figure 20. The electronic density of states, $N(E)$, of $MgCNi_3$ calculated within the local density approximation (LDA), along with the d contribution inside the Ni spheres, via the radius 2.04 a_0 obtained by the general potential linearized augmented plane wave (LAPW) method [50], is demonstrated in figure 21. The lower panel of figure 21 is an expanded view near the Fermi level, E_F. It is found that the band structure is dominated by a Ni 3d-derived DOS peak [49, 50] just below the Fermi energy (figures 20 and 21). The $N(E_F)$ of pure $MgCNi_3$ varies from 1.8 to 5.34 states eV^{-1}/fu (table 6). This variation in $N(E_F)$

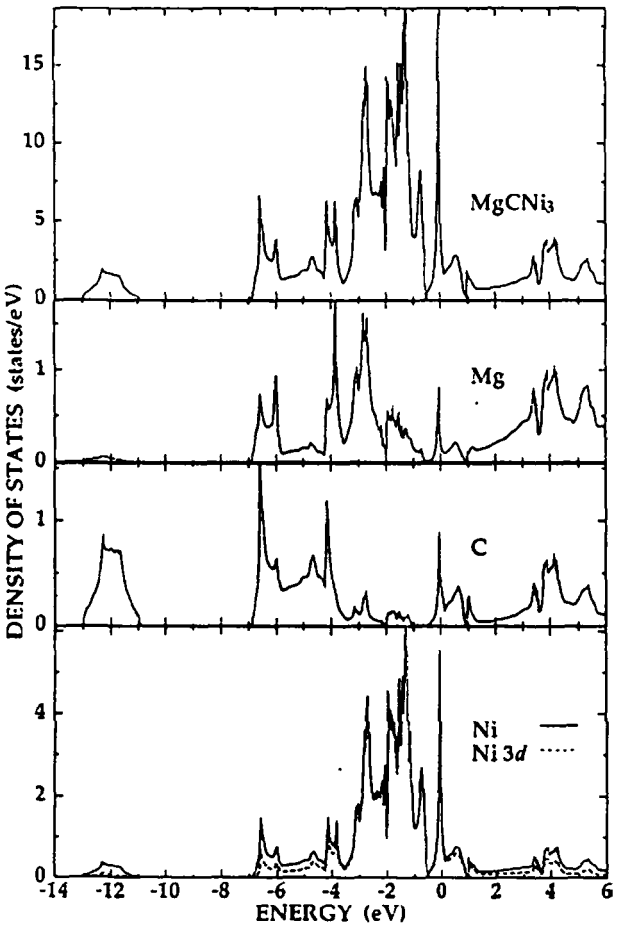

Figure 20. The total and atomic site-projected densities of states (DOS) of $MgCNi_3$ [49].

may arise from the different approximations made by different groups [49, 52, 53, 56, 57]. The linearized muffin-tin orbital (LMTO) method [51], the self-consistent spin-polarized full-potential linear muffin-tin orbital (FP-LMTO) method [53] and the self-consistent tight-binding linear muffin-tin orbital (TB-LMTO) method [52] also show that the E_F for $MgCNi_3$ is located in the slope descending from a sharp peak originating from Ni 3d states. This leads to a moderate Stoner enhancement, placing $MgCNi_3$ in the range where spin fluctuations may noticeably affect the transport, specific heat and superconductivity, providing a mechanism for reconciling various measures of the electron phonon (e–ph) coupling constant λ. Strong e–ph interactions are found for the octahedral rotation mode and may exist for other bond angle bending modes. Several other groups [51–53, 56, 58, 64] indicate that the DOS peak just below the Fermi level provides the superconducting properties of this compound. Wan *et al* [64] argue that the DOS peak is strongly correlated with various instabilities. After including the strong electron–electron (e–e) correlation effects on the Ni 3d state via the on-site Coulomb interaction correction, the DOS is greatly redistributed and the peak just below E_F disappears [64]. Shim *et al* [49] accomplish a correspondence of the peak to the π^* antibonding states of Ni 3d and C 2p but with a predominant Ni 3d character. The results calculated from density functional theory and the LDA also show that the conduction bands in this compound are derived from

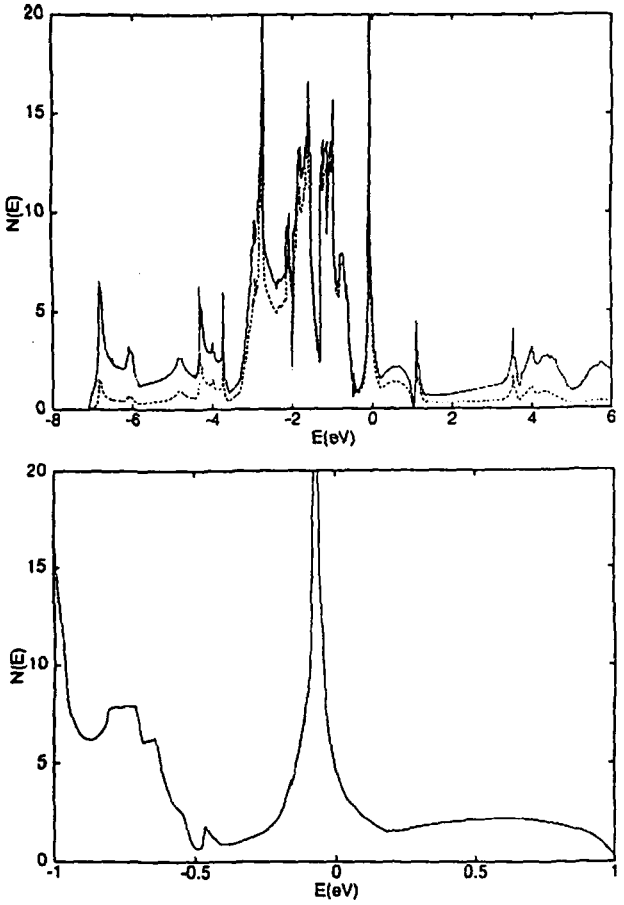

Figure 21. *The electronic density of states, $N(E)$, of $MgCNi_3$ calculated within the local density approximation* (upper limit). The dashed curve is the d contribution within the Ni spheres with radius 2.04 a_0 obtained by the general potential linearized augmented plane wave (LAPW) method. The lower panel is an expanded view near the Fermi level, E_F [50].

Ni 3d and C 2p states [65]. Tan *et al* [67] also find that the conduction bands in this compound are derived from Ni 3d and C 2p states. The top valence states have essentially Ni 3d character and the C 2p states occupy the region from 4.0 to 7.0 eV below the Fermi energy. The E_F locates just at the slope step of the sharply structured Ni $3d_{yz+zx}$ and $3d_{3z^2-r^2}$ peaks. Optical conductivity in the energy range 0–12 eV is also contributed by the Ni 3d to Ni 4s and C 2p transitions [65]. The optical properties of $MgCNi_3$ have been calculated using the full-potential linearized augmented plane wave (FLAPW) method within the generalized gradient approximation scheme for the exchange–correlation potential [68]. The dielectric function, reflectivity, optical absorption coefficient, optical conductivity, energy loss function, refractive index and extinction coefficient are calculated [68] to fully elucidate the optical properties of $MgCNi_3$. The calculation [68] predicts a large reflectivity and small extinction coefficient in the low energy region, as shown in figure 22. The absorption coefficient and optical conductivity are very small at low energy [68]. All these computed results need experimental verification. Wan *et al* [64] find that $MgCNi_3$ is a metal from electronic structure calculations using the local

Table 6. Some important theoretically calculated parameters for pure and doped $MgCNi_3$. Here $\Delta E = E_{FM} - E_{PM}$; E_{FM} and E_{PM} are respectively the energies of the ferromagnetic and paramagnetic states. M is the magnetization and $N(E_F)$ is in states eV^{-1}/fu.

	Parameters				
Composition	ΔE (meV)	$N(E_F)$	M (μ_B)	Model used[a]	References
$MgCNi_3$	0.2	1.8	—	FLAPW	[57]
$MgCNi_3$	—	5.34	—	LDA-LMTO	[49]
$MgCNi_3$	—	5.26	—	TB-LMTO	[52]
$MgCNi_3$	—	4.65	—	FP-LMTO	[53, 56]
$MgCNi_3$	—	4.99	—	LAPW	[53]
$MgCNi_2Co$	0.2	1.2	—	FLAPW	[57]
$MgCNi_2Co$	—	3.65	—	FP-LMTO	[56]
$MgCNiCo_2$	0.0	0.7	—	FLAPW	[57]
$MgCNi_2Fe$	0.0	0.5	—	FLAPW	[57]
$MgCNiFe_2$	−271.6	2.9	0.08(Ni)	FLAPW	[57]
MgC(FeCoNi)	−60.6	2.6	0.97(Fe)	FLAPW	[57]
$MgCNi_{2.84}Co_{0.16}$	−1.0	4.6	0.646(Co)	LDA	[58]
$MgCNi_{2.92}Co_{0.083}$	−1.8	6.5	0.638(Co)	LDA	[58]
$MgCNi_{2.95}Mn_{0.042}$	—	—	1.06(Mn)	TB-LMTO	[58]
$MgCCo_3$	−30.4	2.0	0.39(Co)	FLAPW	[57]
$MgCFe_3$	−379.1	3.4	1.42(Fe)	FLAPW	[57]
$MgBNi_3$	—	4.79	—	LDA-LMTO	[49]
$MgNNi_3$	—	3.63	—	LDA-LMTO	[49]
$ScBNi_3$	—	2.59	—	FP-LMTO	[53]
$InBNi_3$	—	1.47	—	FP-LMTO	[53]

[a] The abbreviations for the models are explained in section 9.

spin density approximation (LSDA) of the density functional theory, using the self-consistent FLAPW method. The magnetic moment on the Ni ion is only 0.014 μ_B. The magnetic moment on the Ni ion increases when electron–electron (e–e) correlation effects are considered and becomes 0.66 μ_B [64]. The ΔE of pure $MgCNi_3$ is ~0.2 meV (table 6). It is observed that the Fermi surface contains nearly cancelling hole and electron sheets [52] that give an unusual behaviour of transport quantities, particularly the thermoelectric power. The prominent nesting feature is observed in the Γ-centred electron Fermi surface of an octahedral cage-like shape that originates from the 19th band [50].

Ignatov *et al* [66] have calculated a large coupling constant $\lambda = 1.75$ which is much higher than the experimentally observed values, ~0.66–0.84 (table 3), but comparable to those (~1.4–1.45) obtained by others [7, 48]. The theoretical Sommerfeld constant $\gamma_{cal} \sim 4.45$ mJ K^{-2} (mol Ni)$^{-1}$ [66] is lower than the experimental values ~9.8–11.2 mJ K^{-2} (mol Ni)$^{-1}$ (table 3). On the basis of BCS strong coupling theory and first-principles calculation, the Debye frequency (ω_D) for $MgCNi_3$ is estimated to be 87 cm^{-1} approximately.

The surface electronic structures of $MgCNi_3$(001) with both MgNi terminated and CNi terminated surfaces are investigated using the all-electron FLAPW method within the generalized gradient approximation to density functional theory [55]. It is found that the calculated work function of the MgNi terminated surface (~4.17 eV) is lower than that of the CNi terminated surface (~5.16 eV). The total numbers of electrons in the surface layer of the MgNi terminated surface and the CNi terminated surface are respectively greatly and slightly reduced with respect to the centre layer values [55]. The number of Ni(S) d electrons

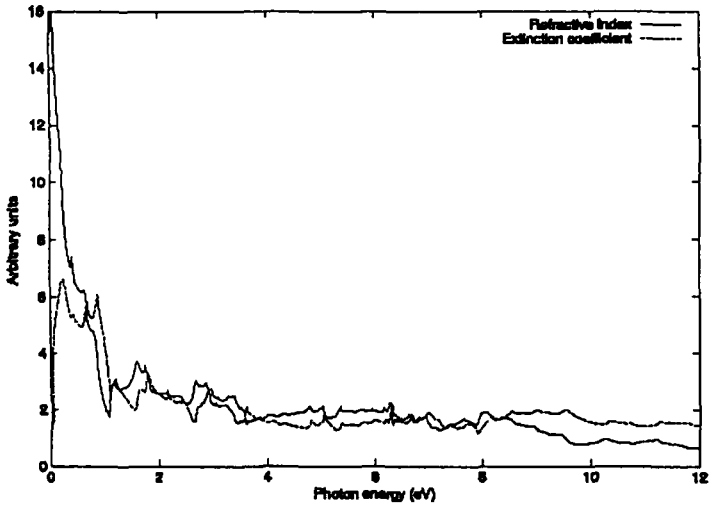

Figure 22. The calculated refractive index and extinction coefficient of $MgCNi_3$ [68].

for the MgNi terminated surface is calculated to be 0.08 electrons more than that for the CNi terminated surface. The layer-projected *l*-decomposed local DOS shows that the difference in the number of Ni(S) d electrons is due to the strong C p and Ni d hybridization at the surface layer of the CNi terminated surface. The peak just below E_F for bulk $MgCNi_3$ is broadened substantially at the Ni(S) CNi terminated surface, while that peak survives at the Ni(S) MgNi terminated surface [55]. By analysing the charge density for a very narrow energy window just below E_F, such considerable modifications of the DOS peak at the CNi terminated surface are distinguished as being due to the broken local symmetry of the CNi layer at the surface [55]. It is considered that the behaviour of the modification of the peak near E_F resembles the p band hole doping through C site substitution and this is supported by the stability against ferromagnetism determined from total-energy calculations [55].

The possibility of superconductivity is discussed for the intermetallics $ScBNi_3$, $InBNi_3$, $MgCCo_3$ and $MgCCu_3$ which are isostructural with $MgCNi_3$ [49]. Electronic structures of the $MgCNi_{3-z}M_z$ (M = Co, Cu; $z = 0, 0.5, 1.0$) system have been calculated using the TB-LMTO method [52]. Electron (Cu) and hole (Co) doping of $MgCNi_3$ reconstructs its band structure but does not lead to magnetic order, although the DOS initially increases with increase of the Co concentration (figure 23). However, investigation of the electronic structures and magnetism of $MgCNi_{3-z}T_z$ compounds ($z = 0, 1, 2$ and 3; T = Co and Fe) via first-principles all-electron FLAPW calculations within the local spin density approximation reveals that the suppression of superconductivity occurs faster for the Fe doped case than for the Co doped one with increase of z and ferromagnetic transitions occur when $z \geqslant 2$ for the Co doped cases, while the Fe doped cases become ferromagnetic before $z = 2$ [47]. From the calculated DOS, it is found that $MgCNi_3$ becomes paramagnetic and then ferromagnetic as the number of minority spin d band holes are increased via Co and Fe doping at Ni sites. The effects on the electronic structure and magnetic properties of the Ni site substitution in $MgCNi_{3-z}Co_z$ are studied by using density functional calculations [58]. Co doping results in the onset of ferromagnetism at $z = 0.083$. However, the slightly energy gain as well as small magnetic moment per atom indicate weak itinerant ferromagnetism [58]. Cu doping can be well accounted for by the rigid band model, which reduces the DOS at the Fermi level and the T_c [58]. Co doping of $MgCNi_3$ is accompanied by a reduction of the DOS at the Fermi level, which seems to be responsible for the reduced superconductivity in the $MgCNi_{1-z}Co_z$ system [56]. No magnetic solution is

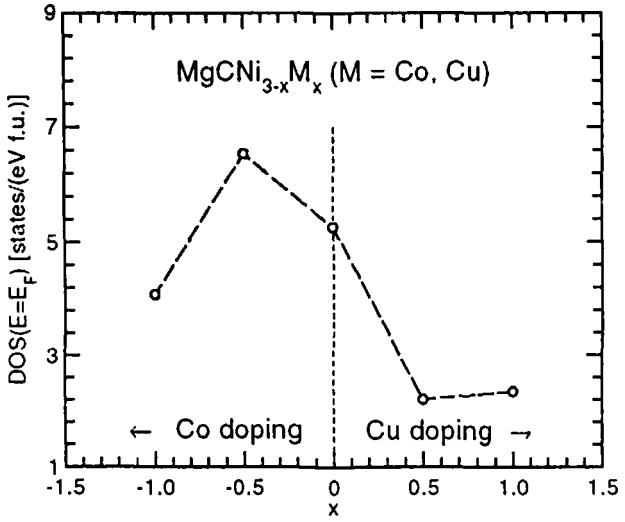

Figure 23. The density of states (DOS) at $E = E_F$ for $MgCNi_{3-x}M_x$ (M = Co, Cu) plotted as a function of the impurity concentration, x [52].

(This figure is in colour only in the electronic version)

found for $MgCNi_2Co$ and $MgCNiCo_2$ [56]. This indicates that hole doping does not produce the magnetic instability which could be responsible for pair breaking [56]. Starting from a first-principles electronic structure calculation for $MgCNi_3$ and using a simple Hartree–Fock approximation, Granada *et al* [59] compute the magnetic moment of transition impurities T in the dilute limit of $MgC(Ni_{1-z}T_z)_3$ with T = Co, Fe, Mn, Cr and V. The computation shows that Co impurities are non-magnetic and for the remaining ones at least a small moment exists. Rosner *et al* [54] observe an unusual quasi-two-dimensional heavy band mass von Hove singularity (vHs) very near the Fermi energy for $MgCNi_3$. It is pointed out [54] that this compound is strongly exchange enhanced and unstable against ferromagnetism upon hole doping with ~12% Mg → Na or Li (i.e., 0.04 hole/Ni). An essentially infinite mass along the M–Γ line accounts for the two dimensionality of this vHs [54]. Thus this compound provides new opportunities to probe the ferromagnetic critical point as well as introducing the novelties of 2D behaviour into a 3D system. It is concluded that experimental studies on the change of T_c with concentration might indicate, for non-magnetic impurities, a d-wave behaviour of these superconductors [59].

Replacement of C by B or N greatly reduces the DOS peak [49] near E_F (figure 24). The $N(E_F)$ of $MgBNi_3$ (~4.79 states eV^{-1}/fu) is much higher than that (~3.63 states eV^{-1}/fu) of $MgNNi_3$ (table 6). The replacement of Mg in $MgBNi_3$ by In or Sc reduces the $N(E_F)$ even more (table 6). The total or partial replacement of Ni in $MgCNi_3$ by Co or Fe also greatly diminishes $N(E_F)$, as shown in table 6, except for $MgCNi_{2.92}Co_{0.083}$ where a higher value (~6.5 states eV^{-1}/fu) is obtained. The magnetic moment (M) of doped $MgCNi_3$ calculated by several groups is shown in table 6. Depending on the doping element, i.e. Co, Fe, Mn etc, the value of M differs. ΔE for some doped and undoped $MgCNi_3$ samples is shown in table 6. A hypothetical system, MgC(FeCoNi), has been found to be ferromagnetic with magnetic moments of 0.97, 0.24 and 0.03 μ_B for Fe, Co and Ni, respectively; these are roughly proportional to the number of d band holes of minority spin (table 6). The role of the transition metal dopants [57] in the magnetism may be understood from the site-projected spin-polarized

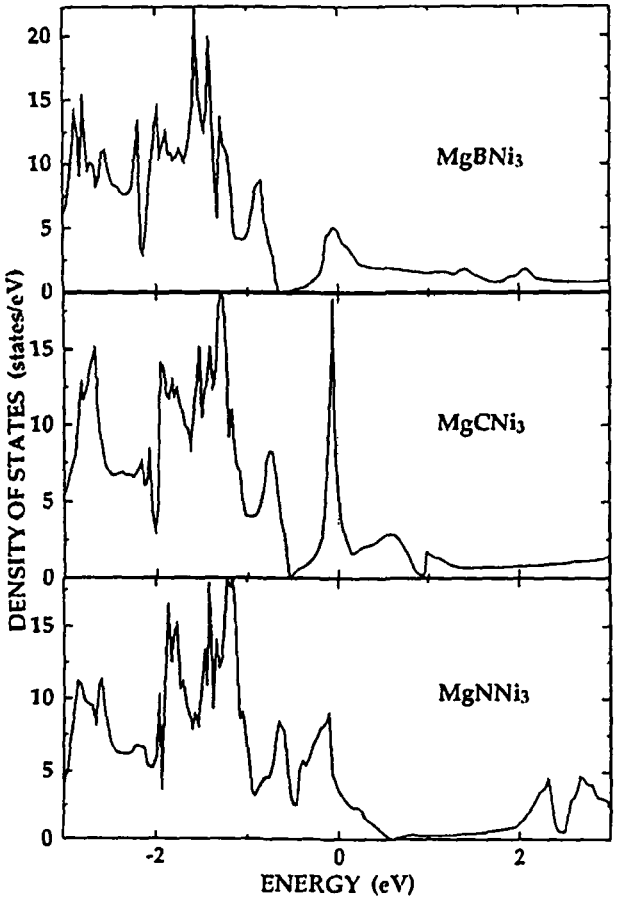

Figure 24. The density of states of $MgXNi_3$ (X = B, C, N) [49].

DOS of hypothetical MgC(FeCoNi). The majority spin d bands are seen to be nearly filled for all transition metal atoms. On the other hand, the location of E_F is shifted to the top of the minority spin d band as we move from Fe to Ni, which is again understood as behaviour typical of metallic ferromagnetism. It also confirms that Co and Fe doping in $MgCNi_3$ provide a source of minority spin d band holes rather than magnetic scattering centres that quench superconductivity. In addition, their locations and the widths of the main peaks of the minority spin d bands are seen to be rather independent of each other, but the shape of the Fe d bands is modified from that in the bcc phase [57]. This again confirms the independence of the magnetic moments of the face centred transition metal atoms. The strong ferromagnetic spin fluctuation in $MgCNi_{3-z}Co_z$ leads to quenched bulk superconductivity, while the Mn atom forms a local magnetic moment of 1.06 μ_B at $z = 0.042$ which suppresses superconductivity more seriously than Co does in the low doping case [58]. There is a large variation of ΔE (−379.1–0.2 meV) according to the difference in composition.

A two-band model [18, 24, 48] provides a consistent interpretation of the temperature dependence of the normal state resistance and the Hall constant. The thermoelectric power also needs to be explained by a multi-band model [48]. Although the band structure calculations suggest an increase in T_c upon partial replacement of Ni with Fe and Co, the Co substitution quenches the superconductivity and Fe substitution leads to an increase followed by a decrease

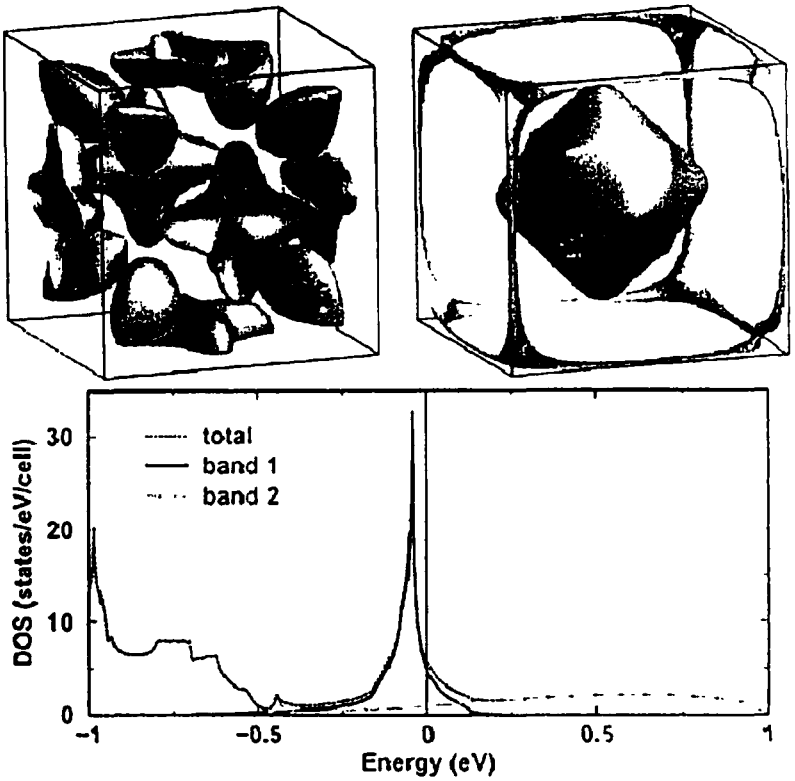

Figure 25. The two Fermi surface sheets of $MgCNi_3$ and the corresponding band resolved density of states near E_F. Band 1 corresponds to the Fermi surface sheet in the top right panel and band 2 corresponds to that of the top left panel [24].

in T_c [18]. The DOS of the two bands along with those of their Fermi surface sheets are shown in figure 25. A multi-band superconductor [111, 112] with a conventional phonon mechanism can develop an unconventional state with a non-trivial order parameter phase relation between the individual bands. It is proposed [69] that such a state can explain the experimentally found [9] s-wave pairing symmetry and unconventional superconductivity in $MgCNi_3$. It has been shown [69] that such a state gives rise to Andreev bound states and to spontaneous currents, at surfaces and around impurities, which can explain the zero-bias features observed in quasi-particle tunnelling [9].

10. Conclusions

The following conclusions can be drawn as regards the physics of $MgCNi_3$.

(1) It has a simple cubic perovskite structure [1] like the 30 K oxide non-cuprate superconductor $Ba_{1-x}K_xBiO_3$ with space group $Pm\bar{3}m$ and the lattice parameter a is ~3.812 Å.

(2) The Ni K-edge x-ray absorption study [16] suggests that the $Ni_6(O_6)$ octahedra are locally distorted from those expected in the perfect cubic $Pm\bar{3}m$ form.

(3) It is found [5] that the compound has the perovskite structure over the temperature range (2–295 K) and no structural or long range magnetic ordering transitions are observed. Its structure is also stable under a pressure of ~22 GPa [30].

(4) A high proportion of Ni in this compound indicates that the magnetic interactions may play a dominant role as regards its superconductivity.

(5) The superconducting transition temperature T_c of MgC_xNi_3 is sensitive to the carbon content increasing with x and $x \sim 1.45$–1.5 corresponds to the highest T_c [10, 12, 17, 56]. However, doping at the Mg and Ni sites decreases the T_c [6, 18, 33, 56] sharply.

(6) The external pressure increases the T_c of MgC_xNi_3 [17, 18] at the same rate as for other intermetallic superconductors but at a rate one order lower than that for MgB_2 and the pressure effect on T_c is independent of the C content.

(7) The ^{13}C NMR investigation on this material [3] implies that the electronic states reach a modestly mass enhanced Fermi-liquid-like state prior to the superconducting transition.

(8) Normal state NMR properties of $MgCNi_3$ are irregular [3] and analogous to those observed for the exotic superconductor Sr_2RuO_4.

(9) The change from grain boundary to core pinning by intragranular nanoparticles near T_c suggests [11] that the arrangement of pinning sites in $MgCNi_3$ is unique.

(10) Hall coefficient and thermoelectric power data [4, 7] on $MgCNi_3$ show that the carriers in this compound are electrons, in contrast to those of MgB_2. However, He *et al* [1] suggest that the holes in Ni d states might be responsible for the electrical conduction in this material in an electronic analogy to the holes in the O p states in perovskite oxide superconductors. The constant scattering approximation also shows that the thermoelectric power is hole type [50] above 10 K.

(11) It has been suggested [54] that $MgCNi_3$ is near a ferromagnetic instability and can be reached by hole doping at the Mg site (if 12% Mg is replaced by Na or Li, i.e., 0.04 hole/Ni).

(12) Energy band calculations [49–60] illustrate that the density of states (DOS) of the Fermi level (E_F) is dominated by Ni 3d states and there is a von Hove singularity (vHs) of the DOS [15, 54] just below the E_F (<50–120 meV). Nevertheless, photoemission and x-ray absorption studies [15] show that the sharp vHs peak theoretically predicted near E_F is substantially suppressed, which may be due to electron–electron and electron–phonon interactions.

(13) Both positive and negative magnetoresistances are reported [7, 16, 33], which needs further clarification.

(14) It has been observed [7] that the electronic contribution is slightly higher than the lattice one in the normal state thermal conductivity.

(15) $MgCNi_3$ is a single-gap superconductor in contrast to MgB_2 [100, 110] and the value of the superconducting gap (Δ) is estimated to be 1.1–1.5 meV [9, 13, 19, 47, 48], from tunnelling spectroscopy and specific heat data.

(16) The nuclear spin–lattice relaxation rate ($1/T_1$) displays the typical behaviour of isotropic s-wave superconductivity [3] for $MgCNi_3$ with a coherence peak below T_c. However, the field dependent specific heat and resistivity results imply that it is a moderate coupling, type-II, s-wave BCS superconductor [1, 11, 13, 14, 38, 47, 48]; this is supported by tunnelling and other experiments as well as theoretical calculations [19, 21, 49, 51, 67]. Again, the penetration depth distinctly exhibits a non-s-wave BCS low temperature behaviour [42], instead of showing a quadratic temperature dependence, suggestive of a nodal order parameter. It is also theoretically suggested that it is a d-wave superconductor [59]. Thus the nature of the superconductivity in $MgCNi_3$ is still controversial and needs more efforts to clarify it.

11. Future scope of work

(1) The single-crystal or wires/tapes form of $MgCNi_3$ should be studied to allow focusing on the changes of properties (if any) compared to those of the polycrystalline bulk and thin films.
(2) The nature of the superconductivity in $MgCNi_3$ should be clarified.
(3) The computation of some important parameters such as $d \ln N(E_F)/dP$ and $d \ln \omega/dP$ for MgC_xNi_3 may be useful for quantitative analysis of pressure dependent T_c data
(4) The calculated optical properties should be experimentally verified.
(5) Intensive theoretical studies are needed to clarify the controversies over the type of the superconductivity and normal state magnetoresistance of $MgCNi_3$

Acknowledgments

The author is grateful to his colleagues for their constant encouragement, support and constructive suggestions.

References

[1] He T *et al* 2001 *Nature* **411** 54
[2] Nagamatsu J, Nakagawa N, Muranaka T, Zenaitani Y and Akimitsu J 2001 *Nature* **410** 63
[3] Singer P M, Imai T, He T, Hayward M A and Cava R J 2001 *Phys Rev Lett* **87** 257601
[4] Li S Y *et al* 2001 *Phys Rev.* B **64** 132505
[5] Huang Q, He T, Regan K A, Rogado N, Hayward M, Hass M K, Inumaru K and Cava R J 2001 *Physica* C **363** 215
[6] Hayward M A, Hass M K, Ramirez A P, He T, Regan K A, Rogado N, Inumaru K and Cava R J 2001 *Solid State Commun* **119** 491
[7] Li S Y *et al* 2002 *Phys Rev.* B **65** 064534
[8] Li J Q, Wu L J, Li L and Zhu Y 2002 *Phys Rev* B **65** 052506
[9] Mao Z Q, Rosario M M, Nelson K D, Wu K, Deac I G, Schiffer P, Liu Y, He T, Regan K A and Cava R J 2003 *Phys Rev* B **67** 094502
[10] Ren Z A, Che G C, Jia S L, Chen H, Ni Y M and Zhao Z X 2001 *Preprint* cond-mat/0105366
Ren Z A, Che G C, Jia S L, Chen H, Ni Y M and Zhao Z X 2001 *Sci China* A **44** 1205
[11] Cooley L D, Song X, Jiang J, Larbalestier D C, He T, Regan K A and Cava R J 2002 *Phys Rev* B **65** 214518
[12] Amos T G, Huang Q, Lynn J W, He T and Cava R J 2002 *Solid State Commun* **121** 73
[13] Lin J-Y, Ho P L, Huang H L, Lin P H, Zhang Y-L, Yu R-C, Jin C-Q and Yang H D 2003 *Phys Rev* B **67** 052501
[14] Lin J-Y, Lin P H, Ho P L, Huang H L, Zhang Y-L, Yu R-C, Jin C-Q and Yang H D 2002 *J Supercond* **15** 485
[15] Kim J H, Ahn J S, Kim J, Park M-S, Lee S I, Choi E J and Oh S-J 2002 *Phys Rev* B **66** 172507
[16] Ignatov A Y, Dieng L M, Tyson T A, He T and Cava R J 2003 *Phys Rev* B **67** 064509
[17] Yang H D, Mollah S, Huang W L, Ho P L, Huang H L, Liu C-J, Lin J-Y, Zhang Y-L, Yu R-C and Jin C-Q 2003 *Phys. Rev.* B **68** 092507
[18] Kumary T G, Janaki J, Mani A, Jaya S M, Sastry V S, Hariharan Y, Radhakrishnan T S and Valsakumar M C 2002 *Phys. Rev.* B **66** 064510
[19] Kinoda G, Nishiyama M, Zhao Y, Murakami M, Koshizuka N and Hasegawa T 2001 *Japan J Appl Phys* **40** L1365
[20] Young D P, Moldovan M, Craig D D, Adams P W and Chan J Y 2003 *Phys Rev* B **68** 020501
[21] Liu F M, Li J Q, Dong C, Wang T M, Zhou Y Q and Chen H 2002 *Supercond Sci Technol* **15** 1316
[22] Lin J-Y, Yang H D and Jin C-Q 2003 *Physica* C **388/389** 559
[23] Jin C Q, Zhang Y L, Liu Z X, Li F Y, Yu W and Yu R C 2003 *Physica* C **388/389** 561
[24] Rosner H *et al* 2003 *Physica* C **388/389** 563
[25] Wang H, Ouyang L Z, Zeng M Q and Zhu M 2004 *Scr Mater* **50** 1471
[26] Ferretti M, Ciccarelli C, Magnone E, Rubino S, Parodi N and Martinelli A 2004 *Mater Res Bull* **39** 647
[27] Schaak R E, Avdeev M, Lee W L, Lawes L G, Zandbergen H W, Jorgensen J D, Ong N P, Ramirez A P and Cava R J 2004 *J Solid State Chem.* **177** 1244

[28] Ren Z A, Che G C, Jia S L, Chen H, Ni Y M, Liu G D and Zhao Z X 2002 *Physica* C **371** 1
[29] Wei Z F, Chen X L, Che G C, Wang F M, Li W C and He M 2002 *Chin Phys Lett* **19** 249
[30] Zhang Y L, Li F Y, Chen L C, Liu J, Yu R C, Liu Z X, Yu W and Jin C Q 2003 *Chin Sci Bull* **48** 2287
[31] Artuni C, Costa G A, Magnone E, Cimberle M R and Masini R 2003 *Int J Mod Phys* B **17** 819
[32] Kar'kin A E, Goshchitskii B N, Kurmaev E Z, Ren J A and Che G C 2003 *Phys Met Metallogr* **95** 324
[33] Das A and Kremer R K 2003 *Phys Rev* B **68** 064503
[34] Alzamora M, Sanchez D R, Cindra M and Baggio-Saitovitch E M 2002 *Braz. J Phys* **32** 755
[35] Cooley L, Song X Y and Larbalestier D 2003 *IEEE Trans Appl Supercond* **13** 3280
[36] Chen L, Li H and Mei L M 2004 *J. Mater Sci Technol* **20** 203
[37] Chen L and Li H 2004 *Acta Phys Sin* **53** 922
[38] Park M S, Giim J S, Park S H, Lee Y W, Lee S I and Choi E J 2004 *Supercond Sci Technol* **17** 274
[39] Wang C H, Mo W Q, Li S Y, Yu M, Fan R, Ruan K Q, Yang H S, Cao L Z and Chen X H 2002 *Acta Phys Sin* **51** 1816
[40] Yao Y X, Ying X N, Huang Y N, Wang Y N, Ren Z A, Che G C, Wen H H, Zhao Z X and Ding J W 2004 *Supercond. Sci. Technol* **17** 608
[41] Park S H, Lee Y W, Giim J, Jung S H, Ri H C and Choi E J 2004 *Physica* C **400** 160
[42] Prozorov R, Snezhko A, He T and Cava R J 2003 *Phys Rev* B **68** 180502
[43] Shan L, Tao H J, Gao H, Li Z Z, Ren Z A, Che G C and Wen H H 2003 *Phys Rev* B **68** 144510
[44] Ouyang L Z, Wang H, Peng C H, Zeng M Q, Chung C Y and Zhu M 2004 *Mater Lett* **58** 2203
[45] Naidyuk Y G 2004 *Phys. Rev.* B **69** 136501
[46] Mao Z Q, Rosario M M, Nelson K D, Wu K, Deac I G, Schiffer P, Liu Y, He T, Regan K A and Cava R J 2004 *Phys. Rev.* B **69** 136502
[47] Shan L, Xia K, Liu Z Y, Wen H H, Ren Z A, Che G C and Zhao Z X 2003 *Phys Rev* B **68** 024523
[48] Waelte A, Fuchs G, Mueller K-H, Handstein A, Nenkov K, Narozhnyi V N, Drechsler S-L, Shulga S, Schultz L and Rosner H 2004 *Preprint* cond-mat/0402421
[49] Shim J H, Kwon S K and Min B I 2001 *Phys. Rev.* B **64** 180510
[50] Singh D J and Mazin I I 2001 *Phys. Rev.* B **64** 140507
[51] Dugdale S B and Jarlborg T 2001 *Phys. Rev.* B **64** 100508
[52] Szajek A 2001 *J. Phys.: Condens. Matter* **13** L595
[53] Shein I R, Ivanovskii A L and Medvedeva N I 2001 *JETP Lett* **74** 122
[54] Rosner H, Weht R, Johannes M D, Pickett W E and Tosatti E 2002 *Phys Rev Lett* **88** 027001
[55] Kim I G, Lee J I and Freeman A J 2002 *Phys. Rev.* B **66** 174512
[56] Shein I R, Ivanovskii A L, Kurmaev E Z, Moewes A, Chiuzbian S, Finkelstein L D, Neumann M, Ren Z A and Che G C 2002 *Phys. Rev.* B **66** 024520
[57] Kim I G, Lee J I and Freeman A J 2002 *Phys. Rev.* B **65** 064525
[58] Wang J L, Xu Y, Zeng Z, Zheng Q Q and Lin H Q 2002 *J Appl Phys* **91** 8504
[59] Granada C M, Silva C M D and Gomes A A 2002 *Solid State Commun* **122** 269
[60] Shein I R and Ivanovskii A L 2002 *J. Struct. Chem.* **43** 168
[61] Wu B M, Li B, Yang D S, Zheng W H, Li S Y, Gao L Z and Chen X H 2003 *Acta Phys Sin* **52** 3150
[62] Liu S, Shen R, Zheng Z M and Xing D Y 2003 *Chin Phys Lett* **20** 284
[63] Heid R, Renker B, Schober H, Adelmann P, Ernst D and Bohnen K P 2004 *Phys Rev* B **69** 092511
[64] Wan X G, Weng H M and Dong J M 2002 *Chin. Phys. Lett* **19** 1522
[65] Tan M Q, Tao X M, Xu X J, He J H and Ye G X 2003 *Acta Phys Sin* **52** 463
[66] Ignatov A Y, Savrasov S Y and Tyson T A 2003 *Phys. Rev* B **68** 220504
[67] Tan M Q, Tao X M, Xu X J, He J H and Ye G X 2003 *Physica* B **337** 95
[68] Okoye C M I 2003 *J. Phys.: Condens. Matter* **15** 833
[69] Voelker K and Sigrist M 2003 *Preprint* cond-mat/0208367
[70] Yonemitsu K, Bishop A R and Lorenzana J 1993 *Phys. Rev* B **47** 8065
[71] Schilling J S, Jorgensen J D, Hinks D G, Deemyad S, Hamlin J, Looney C W and Tomita T 2001 *Studies of High Temperature Superconductors* vol 38, ed A V Narlikar (New York: Nova Science) p 321
[72] Monteverde M, Nunez-Regueiro M, Rogado N, Regan K A, Hayward M A, He T, Loureiro S M and Cava R J 2001 *Science* **292** 75
[73] Lorenz B, Meng R L and Chu C W 2001 *Phys Rev* B **64** 012507
[74] Sato E, Taknenobu T, Ito T, Iwasa Y, Prassides K and Arima T 2001 *J Phys Condens Matter* **13** L267
[75] Schmidt H and Braun H F 1994 *Physica* C **229** 315
[76] Alleno E, Neumeier J J, Thompson J D, Canfield P C and Cho B K 1995 *Physica* C **242** 169
[77] Meenakshi S, Vijaykumar V, Rao R S, Godwal B K, Sikka S K, Ravindran P, Hossain Z, Nagarjan R, Gupta L C and Vijayaraghavan R 1998 *Phys Rev.* B **58** 3377

[78] Weng S S, Hong I P, Chang C F, Tsay H L, Chatterjee S, Yang H D and Lin J-Y 1999 *Phys Rev* B **59** 11205
[79] Mani A, Bharathi A, Sastry V S, Hariharan Y and Radhakrishnan T S 2001 *ICEC18 Proc 18th Int Conf on Cryogenic Engineering* ed K G Narayankhedkar (New Delhi Narosa Publishing House) p 615
[80] McMillan W L 1968 *Phys Rev* **167** 331
[81] Ishizuka M, Iketani M and Endo S 2000 *Phys Rev* B **61** 3823
[82] Jennings L D and Swenson C A 1958 *Phys Rev* **112** 31
[83] Lin J-Y and Yang H D 2004 *Superconductivity Research at the Leading Edge* ed P S Lewis (New York Nova Science) pp 111–30
[84] Werthamer N R, Helfand E and Hohenberg P C 1966 *Phys Rev* 147 295
[85] Shulga S V and Drechsler S-L 2002 *J Low Temp Phys* **129** 93
[86] Clogston A M 1962 *Phys Rev Lett* **9** 266
[87] Chandrasekhar B S 1962 *Appl Phys Lett* **1** 7
[88] Orlando T P, McNiff E J J, Foner S and Beasley M R 1979 *Phys Rev* B **19** 4545
[89] Kittel C 1996 *Introduction to Solid State Physics* 7th edn (New York Wiley)
[90] Meingast C and Larbalestier D C 1989 *J Appl Phys* **66** 5971
[91] Pippard A B 1989 *Magnetoresistance in Metals* (Cambridge Cambridge University Press)
[92] Heeger A 1969 *Solid State Physics* vol 23 (New York Academic) p 283
[93] Affronte M, Marcus J and Escribe-Filippini C 1993 *Solid State Commun* **85** 501
[94] Anderson P W 1991 *Phys Rev Lett* **67** 2092
[95] Sera M, Kobayash S, Hiroi M, Kobayashi N, Takeya H and Kadouaki K 1996 *Phys Rev* B **54** 3062
[96] Bauer E, Paul C, Berger S, Majumdar S, Michor H, Giovannini M, Saccone A and Bianconi A 2001 *J Phys Condens Matter* **13** L487
[97] Berman R 1976 *Thermal Conduction in Solids* (London Oxford University Press)
[98] Kaiser A B 1987 *Phys Rev* B **35** 4677
[99] Nishizaki S, Maeno Y and Mao Z 2000 *J Phys Soc Japan* **69** 572
[100] Yang H D, Lin J-Y, Li H H, Hsu F H, Liu C-J, Li S-C, Yu R-C and Jin C-Q 2001 *Phys Rev Lett* **87** 167003
[101] Kresin V Z and Parkhomenko V P 1975 *Sov Phys —Solid State* **16** 2180
[102] Caroli C, Gennes P G D and Matricon J 1964 *Phys Lett* **9** 307
[103] Volovik G E 1993 *JETP Lett* **58** 469
[104] For a brief review, see Yang H D and Lin J Y 2001 *J Phys Chem Solids* **62** 1861
[105] Ramirez A P 1996 *Phys Lett.* A **211** 59
[106] Sonier J E, Hundley M F and Brill J W 1999 *Phys Rev Lett* **82** 4914
[107] Chen S J, Chang C F, Tsay H L, Yang H D and Lin J-Y 1998 *Phys Rev* B **58** 14753
[108] Chang C F, Lin J-Y and Yang H D 2000 *Phys Rev* B **61** 14350
[109] Cole K S and Cole R H 1941 *J Chem. Phys* **9** 311
[110] Mollah S, Yang H D and Chaudhuri B K 2003 *Ind J Phys* A **77** 9
[111] Suhl H, Matthias B T and Walker L R 1959 *Phys Rev Lett* **3** 552
[112] Agterberg D F, Barzykin V and Gor'kov L P 1999 *Phys Rev* B **60** 14868

PHYSICAL REVIEW B 70, 054519 (2004)

Magnetic field dependence of low-temperature specific heat of the spinel oxide superconductor $LiTi_2O_4$

C. P. Sun,[1] J.-Y. Lin,[2] S. Mollah,[1,*] P. L. Ho,[1] H. D. Yang,[1,†] F. C. Hsu,[3] Y. C. Liao,[4,5] and M. K. Wu[5,6]
[1]*Department of Physics, National Sun Yat Sen University, Kaohsiung 804, Taiwan, Republic of China*
[2]*Institute of Physics, National Chiao-Tung University, Hsin-chu 300, Taiwan, Republic of China*
[3]*Department of Materials Science and Engineering, National Tsing Hwa University, Hsin-chu 300, Taiwan, Republic of China*
[4]*Materials Science Center, National Tsing Hwa University, Hsin-chu 300, Taiwan, Republic of China*
[5]*Department of Physics, National Tsing Hwa University, Hsin-chu 300, Taiwan, Republic of China*
[6]*Institute of Physics, Academia Sinica, Taipei 100, Taiwan, Republic of China*
(Received 11 March 2004; revised manuscript received 17 May 2004; published 31 August 2004)

Magnetic field dependence of low temperature specific heat of spinel oxide superconductor $LiTi_2O_4$ has been elaborately investigated. In the normal state, the obtained electronic coefficient of specific heat γ_n = 19.15 mJ/mol K^2, the Debye temperature Θ_D = 657 K and some other parameters are compared with those reported earlier. The superconducting transition at $T_c \sim 11.4$ K is very sharp ($\Delta T_c \sim 0.3$ K) and the estimated $\delta C/\gamma_n T_c$ is ~1.78. In the superconducting state, the best fit of data leads to the electronic specific heat $C_{es}/\gamma_n T_c = 9.87 \exp(-1.58\, T_c/T)$ without field and $\gamma(H) \propto H^{0.95}$ with fields. In addition, $H_{c2}(0) \sim 11.7$ T, $H_c(0) \sim 0.32$ T, $\xi_{GL}(0) \sim 55$ Å, $\lambda_{GL}(0) \sim 1600$ Å, and $H_{c1}(0) \sim 26$ mT are estimated from the Werthamer-Helfand-Hohenberg (WHH) theory or other relevant relations. All results from the present study indicate that $LiTi_2O_4$ can be well described by a typical type-II, BCS-like, moderate coupling, and fully gapped superconductor in the dirty limit. It is further suggested that $LiTi_2O_4$ is a moderately electron-electron correlated system.

DOI: 10.1103/PhysRevB.70.054519 PACS number(s): 74.25.Bt, 74.25.Ha

I. INTRODUCTION

$LiTi_2O_4$ is unique among oxide superconductors in many respects like its chemistry, crystal structure and superconducting properties.[1–11] In the normal spinel-like structure (space group $Fd3m$) of $LiTi_2O_4$, the Li and Ti atoms are, respectively, at the positions of tetrahedral (8a) and octahedral (16d) sites. The resistivity and magnetic susceptibility data[1] of $LiTi_2O_4$ showed the $T_c \sim 10-12$ K. The disappearance of superconductivity in $Li_{1+x}Ti_{2-x}O_4$ for $x > 0.15$ was concluded to be due to grain boundary effects.[1,7] It has attracted a lot of attention due to at least having the following physical significances related to the present studies. For example, it is the only spinel oxide superconductor ($T_c \sim 12$ K) so far to our knowledge. Also, it is the rare oxide superconductor showing a sharp superconducting anomaly[2–4] in specific heat (C) in contrast to an unpronounced one in polycrystalline $BaPb_{1-x}Bi_xO_3$ with a comparable $T_c \sim 12$ K.[12] The upper critical field $H_{c2}(0)$ of $LiTi_2O_4$ reported by several groups varied from 2 to 32.8 T.[3,7] Issues like whether the superconductivity in $LiTi_2O_4$ can be well explained in the framework of BCS theory based upon the electron-phonon (e-ph) interactions and the role of the electron-electron (e-e) interactions have not been totally clarified.[9] Some theoretical predictions showed that $LiTi_2O_4$ was a strong coupling BCS superconductor while the low temperature specific heat and magnetic susceptibility data implied for the conditions for weak coupling d-band superconductivity.[1–4,10] Furthermore, there has been a very recently revived debate on Anderson's resonating valance bond (RVB)-type ground state as the possible origin of superconductivity in cuprates.[13,14] Since the Ti sub-lattice of the spinel structure allows a high degree of frustration, the RVB ground state is probable in the $LiTi_2O_4$ spinel.[10]

In fact, the specific heat (C), a thermodynamic bulk property unlike resistivity and magnetization, of $LiTi_2O_4$, has been elaborately studied by some groups[2–4] in the absence of a magnetic field (H). Though some of the derived parameters (listed in Table I) agree quite well with each other, some of them differ significantly and lead to incompatible descriptions for the nature of superconductivity. These controversies especially warrant a comprehensive revisit of superconductivity in $LiTi_2O_4$. In addition, the recent intensive investigations of its isostructural compounds $LiMn_2O_4$ (Ref. 15) and LiV_2O_4 (Refs. 4 and 16) exhibiting, respectively, high-voltage electrolyte and $3d$ heavy fermion behavior also tempt us to study the crucial role of $3d$ metals in the spinel oxide structure. In particular, it is interesting to study the evolution from $3d$ superconductivity to a $3d$ heavy fermion in $Li(Ti_{1-x}V_x)_2O_4$.[17] In this report, we thus provide the detailed magnetic field (up to 8 T) dependence of the low temperature specific heat on $LiTi_2O_4$, which has never been reported in the literature earlier and is crucial to the determination of superconducting properties, to explore its pairing mechanism of superconductivity.

II. EXPERIMENTAL METHODS

The preparation and characterization of polycrystalline $LiTi_2O_4$ used in this low temperature specific heat measurement were described elsewhere.[8] Highly pure Li_2CO_3 and TiO_2 were mixed in an appropriate ratio, calcined in a quartz tube under a pure oxygen atmosphere for 20 h at 750°C,

TABLE I. Some important parameters of $LiTi_2O_4$ obtained from the present and earlier investigations.

Parameters	Ref. 2	Ref. 3	Ref. 4	Present work
T_c (K)	11.7	12.4	11.8	11.4±0.3
ΔT_c (K)	1.2	0.32	0.2	0.3
γ_n (mJ/mol K^2)	21.4	21.98	17.9	19.15±0.20
$N(E_F)$ (states/eV atom)	0.97	0.76	0.82	0.70±0.01
β (mJ/mol K^4)	0.043	0.089	0.040	0.048±0.002
Θ_D (K)	685	535	700	657±33
$\delta C/\gamma_n T_c$	1.59	1.57	1.75	1.78
$2\Delta/k_B T_c$	–	~3.8	–	~4.0
Δ (meV)	–	–	–	1.97
λ	0.64	0.71	0.63	0.65
$H_{c2}(0)$ (T)	–	>2	–	11.0±0.5
$H_c(0)$ (T)	–	–	–	0.327±0.003
$H_{c1}(0)$ (mT)	–	20-25	–	26.3±0.3
$H_p(0)$ (T)	–	–	–	21.0±0.4
l (Å)				32
$\xi_{GL}(0)$ (Å)	–	–	–	55±3
$\lambda_{GL}(0)$ (Å)	–	–	–	1600±50
κ	–	–	–	29±1

leading to the formation of $Li_2Ti_2O_5$. Then it was mixed with a proper amount of Ti_2O_3, grounded thoroughly, pressed into pellets, and sintered at 880°C for 24 h under a dynamic vacuum with pressure less than 10^{-4} Torr. Basically, to obtain a pure $LiTi_2O_4$ phase, one needs to add ~15% more of Li than nominal composition due to its volatility. Powder x-ray diffraction (XRD) data obtained by SIEMENS D5000 diffractometer using $CuK\alpha$ radiation showed that $Li_{1+x}Ti_2O_4$ exhibited a Ti_2O_3 impurity phase for $x=0$ and the pure $LiTi_2O_4$ phase was obtained for $0.1 \leqslant x \leqslant 0.15$ (Ref. 8) which was used for this specific heat measurement. The low temperature specific heat $C(T,H)$ was measured with a ^{3}He heat-pulsed thermal relaxation calorimeter[18] in the temperature range from 0.6 to 20 K under different magnetic fields (0–8 T). The precision of the measurement in this temperature range is about 1%. To test the accuracy of the field dependence of specific heat, $C(T,H)$ of a standard copper sample was measured at $H=0$, 1, and 8 T, respectively. The scatter of data in different magnetic fields was within 3%. T_c(~11.4 K) obtained from specific heat data is consistent with that measured by resistivity on the same sample.[8]

III. RESULTS AND DISCUSSION

Figure 1 shows the low temperature specific heat $C(T,H)$ of $LiTi_2O_4$ with $H=0$ and 8 T as C/T vs T^2. The normal state specific heat in the absence of a magnetic field,

$$C_n(T) = \gamma_n T + C_{lattice}(T), \quad (1)$$

is extracted from $H=8$ T data between 8 and 20 K, where $\gamma_n T$ is the electronic term due to free charge carriers and $C_{lattice}(T)=\beta T^3+\alpha T^5$ is representing the phonon contribution which is assumed to be independent of the magnetic field. It is found that $\gamma_n=19.15\pm0.20$(mJ/mol K^2), $\beta=0.048\pm0.002$(mJ/mol K^4), and $\alpha=0.00012\pm0.00005$(mJ/mol K^6) give the best fitting (solid line in Fig. 1) to the experimental data. It is noted that if we take $C_{lattice}(T)=\beta T^3+\alpha T^5+DT^7$, the best fit occurs at a negative value of $D(=-2.8\pm0.5\times10^{-7}$ mJ/mol K^8) which is unreasonable. On the other hand, $C_{lattice}(T)=\beta T^3$ gives a much higher rms value compared to $C_{lattice}(T)=\beta T^3+\alpha T^5$. The enhancement of γ_n by the electron-phonon interaction is given by[19]

$$\gamma_n = (1/3)k_B\pi^2 N(E_F)(1+\lambda), \quad (2)$$

where $N(E_F)$ is the band structure density of states at the Fermi level, k_B is the Boltzmann constant, and λ is the electron-phonon interaction constant. Taking $\lambda=0.65$ as obtained from low temperature specific heat data (discussed later), the calculated value of $N(E_F)$ for the present sample

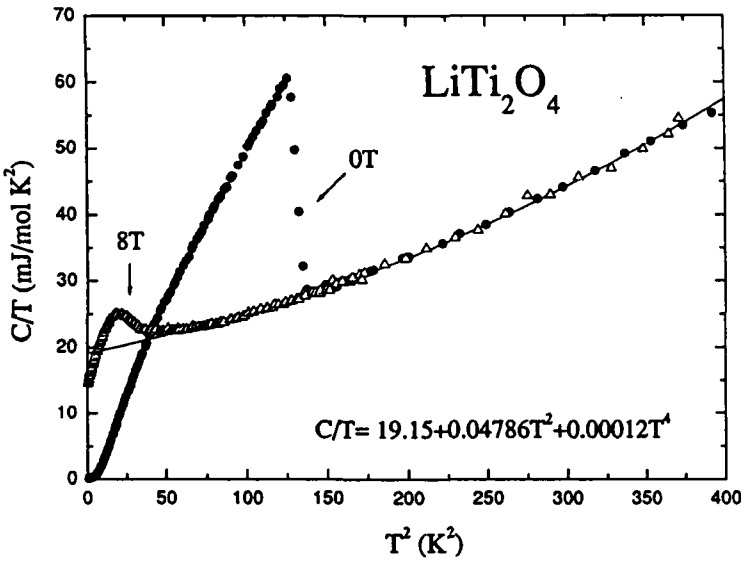

FIG. 1. $C(T,H)/T$ vs T^2 of $LiTi_2O_4$ without and with a magnetic field of 8 T. The solid line is the best fit of $C_n(T)/T=\gamma_n+\beta T^2+\alpha T^4$ to the $H=8$ T data between 8 and 20 K.

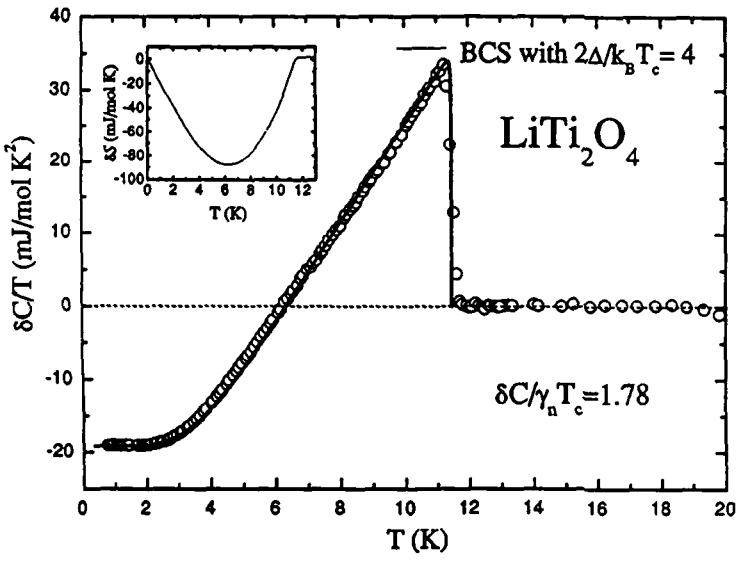

FIG. 2. Plot of $\delta C(T)/T$ vs T with $\delta C(T) = C(T) - C_n(T)$. The solid line is the BCS fitting with $2\Delta/k_BT_c=4$. The inset shows the entropy conservation around the transition temperature.

is ~0.70 states/eV atom. This is lower than that (~0.97 states/eV atom) perceived by McCallum *et al.*[2] from susceptibility data which would not satisfy the transition temperature from the McMillan equation.[19] However, the authors[2] indicated that the reduction of $N(E_F)$ by 15% (orbital contribution and/or exchange enhancement to total susceptibility) would explain it. The reduced $N(E_F)$ is in close agreement with the present investigation. The Debye temperature $\Theta_D=657\pm33$ K is derived by using the relation

$$\beta = 1.944 \times 10^6 \times n/\Theta_D^3, \quad (3)$$

where n is the number of atoms per formula unit and takes 7 for $LiTi_2O_4$. This is somewhat higher than those experimentally obtained and theoretically predicted values[3,11] (~575 K) but closer to those (685–700 K) reported by the group of Johnston.[2,4] The values of γ_n, $N(E_F)$, and Θ_D are listed in Table I along with some other parameters for a comparison with reported results.

The characteristics of superconducting phase transition in $LiTi_2O_4$ can be analyzed using the relation

$$\delta C(T) = C(T, H=0\ \mathrm{T}) - C_n(T). \quad (4)$$

The resultant $\delta C(T)/T$ vs T is shown in Fig. 2, where the inset illustrates the conservation of entropy $S=\int_0^{T_c}(\delta C/T)dT$ around the transition. This conservation of entropy is essential for a second order, such as superconducting-normal, phase transition. In this case, failure to include the αT^5 term in Eq. (1) will not totally satisfy this requirement.[2] In fact, this requirement may be used to testify the justification of the values of γ_n and Θ_D. The dimensionless specific-heat jump at T_c is $\delta C/\gamma_n T_c=1.78$ as indicated in Fig. 2 which is greater than the typical weak coupling value (~1.43). Thus $\delta C(T)/T$ is well fitted to the BCS model as shown in Fig. 2 by the solid line with a little higher $2\Delta/k_BT_c$(~4.0), where Δ is the superconducting energy gap instead of the weak coupling value (~3.52). This value of $2\Delta/k_BT_c$~4 (i.e., Δ = 1.97 meV) is consistent with 3.8 in Ref. 3 and the reference therein where the tunneling experiments yielded the value of 4.0. Consequently, *the superconductivity in $LiTi_2O_4$ can be explained by the moderate coupling BCS framework though the early low temperature specific heat and theoretical calculations, respectively, indicated weak and strong coupling.*[2–4,10,11]

The electronic specific heat in the superconducting state is given by $C_{es}(T)=C(T)-C_{lattice}(T)$. A plot of logarithmic $C_{es}(T)/\gamma_nT_c$ vs T_c/T (Fig. 3) shows that the fitting of data (as demonstrated by the solid line) within $T_c/T=2$ to 5 and fol-

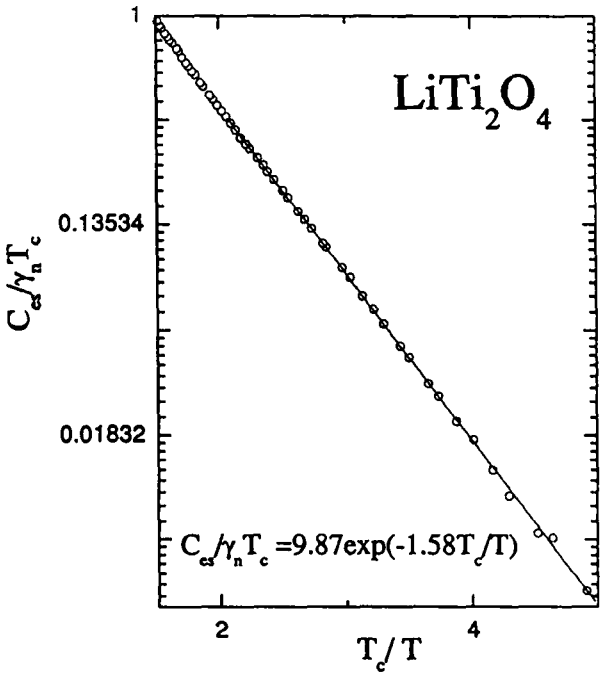

FIG. 3. Logarithmic C_{es}/γ_nT_c vs T_c/T of $LiTi_2O_4$ in the superconducting state. The solid line is the linear fit to the data for T_c/T between 2 and 5.

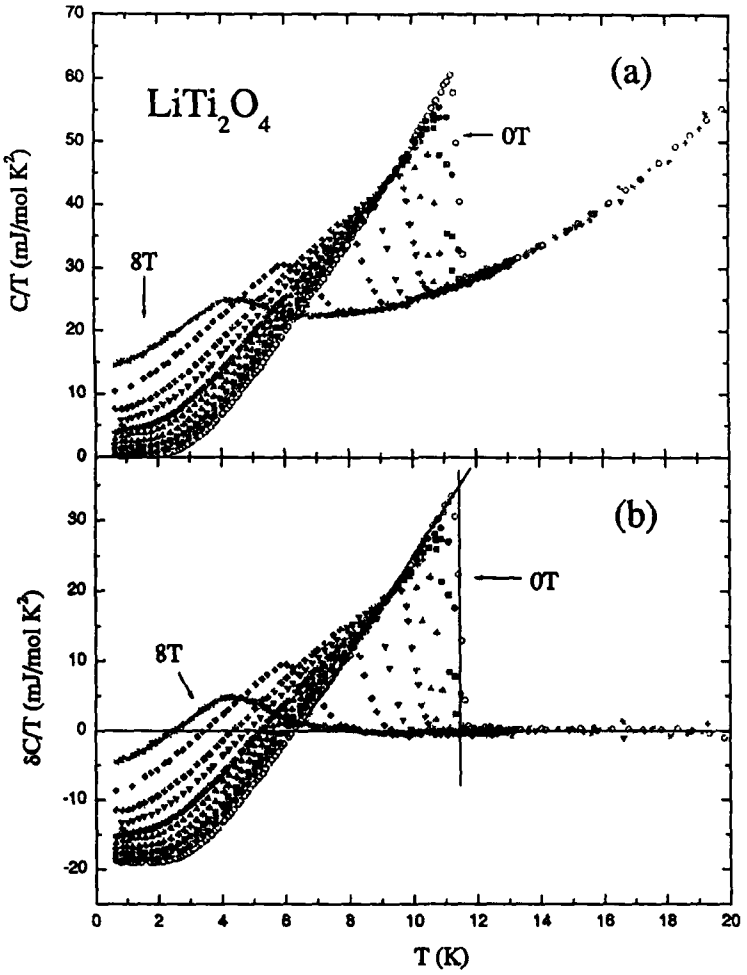

FIG 4 (a) $C(T,H)/T$ vs T and (b) $\delta C(T,H)/T$ vs T under various magnetic fields The entropy around the superconducting transition is conserved even in magnetic fields

lows the relation $C_{es}(T)/\gamma_n T_c = A \exp[(-aT_c/T)]$ with A =9.87 and a=1 58. However, the BCS theory predicts $C_{es}(T)/\gamma_n T_c$=8.5 exp[(−1.44T_c/T)] for this temperature fitting range in the weak coupling limit [2] Therefore, both the values of the coefficient and prefactor are in the range of typical moderate coupling BCS fully gapped superconductors

The electron-phonon coupling constant λ is estimated to be ~0 65 (Table I) using the relation[20]

$$\delta C/\gamma_n T_c = 1\ 43 + 0\ 942\lambda^2 - 0\ 195\lambda^3 \qquad (5)$$

According to McMillan model,[19] for weak coupling $\lambda \ll 1$, for weak and intermediate coupling $\lambda < 1$, and for strong coupling $\lambda > 1$ Therefore, the present λ value suggests that $LiTi_2O_4$ is a moderate coupling superconductor rather than a weak coupling one [2-4] Nevertheless, the value of λ is much lower than that (~1 8) of the theoretical predictions (indicating strong coupling superconductivity in $LiTi_2O_4$) which may be due to the spin fluctuation effect [10,11] Taking Θ_D =657 K, λ=0 65, and observed T_c~11 4 K, the Coulomb repulsion parameter μ^* ~0 13 can be obtained from the McMillan formula,[19]

$$T_c = (\Theta_D/1\ 45) \times \exp\{-1\ 04(1+\lambda)/[\lambda - \mu^*(1+0\ 62\lambda)]\} \qquad (6)$$

The value of μ^* is the same as transition metals,[19] and is in the range of those reported earlier[2,3] confirming the BCS-type d-band superconductivity in $LiTi_2O_4$

The magnetic field dependence of $C(T,H)/T$ and $\delta C(T,H)(\equiv C(T,H) - C_n(T))/T$ were plotted in Figs 4(a) and 4(b), respectively It is noticed that the conservation of entropy (the area above and below zero of C/T are equivalent around the superconducting transition) is fundamentally satisfied for all studied magnetic fields This implies that the sample is of good quality without detectable impurities (particularly magnetic field dependent nonsuperconducting phases) The dissimilar example has been observed in $Ba_{1-x}K_xBiO_3$ (Ref 21) due to defects and the inhomogeneity of the sample Figure 5 demonstrates the magnetic field dependence of very low temperature (≤5 K) specific heat as C/T vs T^2 The coefficient of electronic specific heat $\gamma(H)$ with various fields has been estimated from the linear extrapolation of data below 2 K down to 0 K In order to investigate the low energy vortex excitation under magnetic fields, the variation of $\gamma(H)$ with H is shown in Fig 6 The

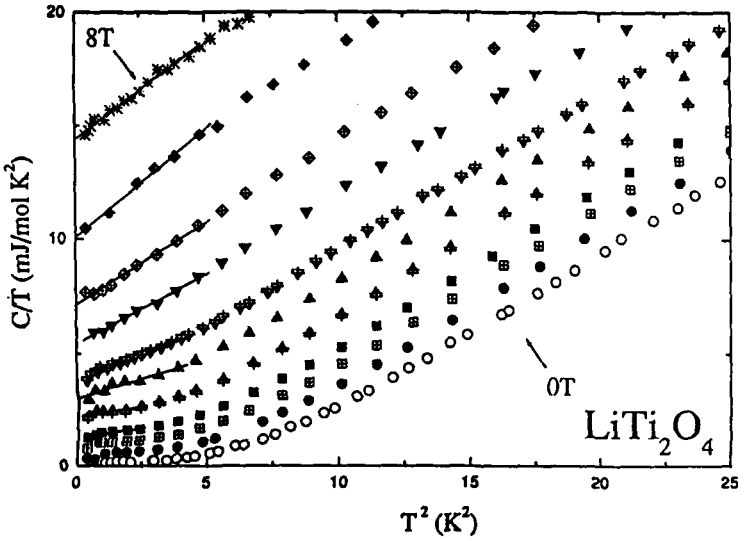

FIG. 5. C/T vs T^2 at very low temperature ($\lesssim$5 K) under different magnetic fields. $\gamma(H)$ has been estimated from the linear extrapolation of data down to 0 K.

best fit leads to $\gamma(H) \sim H^{0.95}$ as indicated by the solid line. Clearly, $\gamma(H)$ follows an H dependence which is very close to be linear, especially for $H \geq 1$ T. The slight deviation in low H could be due to the vortex-vortex interaction as discussed in Refs. 22 and 23. The value of $H_{c2}(T=0)$ estimated from Fig. 6 using linear extrapolation of $\gamma(H)$ for $H \geq 1$ T to $\gamma_n \sim 19.15$ mJ/mol K^2 is $H_{c2}(T=0) = 11.0 \pm 0.5$ T. It is noted that a pronounced nonlinearity of $\gamma(H)$, seen in UPt_3,[24] $CeRu_2$,[25] and $NbSe_2$,[26] at low magnetic fields, is not obvious in the present $LiTi_2O_4$. Theoretically, $\gamma(H)$ is expected to be proportional to H for a conventional s-wave superconductor.[27] However, $\gamma(H) \propto H^{0.5}$ is predicted for a nodal superconductivity.[28] In fact, $\gamma(H)$ of cuprate superconductors

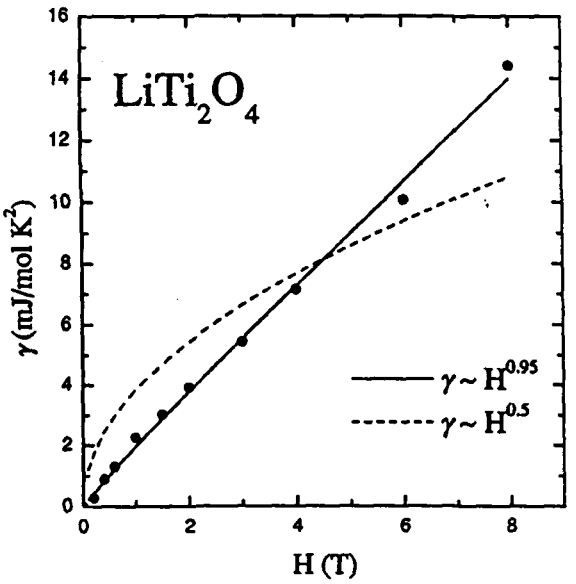

FIG. 6. Magnetic field dependence of electronic specific heat coefficient $\gamma(H)$ derived from the linear extrapolation of data using C/T vs T^2 plot (Fig. 5) for various magnetic fields below 2 K.

has been extensively studied in this context.[29] Consequently, the magnetic field dependence of $\gamma(H)$ suggests that $LiTi_2O_4$ is an s-wave superconductor in nature.

Figure 7 shows the temperature variation of upper critical field $H_{c2}(T)$ as obtained from Fig. 4 where the solid line is the theoretical fitting based on negligible spin paramagnetic and spin-orbital effect by using the Werthamer-Helfand-Hohenberg (WHH) theory.[30] The error bar in $T_c(H)$ is determined by the sharpness of the superconducting transition as shown in the inset of Fig. 7 for a particular magnetic field of 6 T. The same procedure is also followed for other magnetic fields. The best fit results in $(dH_c/dT_c)_{T=T_c} = 1.45 \pm 0.03$(T/K) and consequently $H_{c2}(0) = 11.7 \pm 0.4$ T (Table I). It is noted that the value of $H_{c2}(0)$ estimated from WHH theory is consistent with the value (11.0±0.5 T) obtained from Fig. 6. This consistency implies that the spin-orbital interaction in $LiTi_2O_4$ is negligible as considered for the fitting of the data with WHH theory. The small spin-orbital interaction is actually expected since Ti is one of the lightest transition elements. However, the $H_{c2}(0)$ of present sample is much higher than that (~2 T) predicted by Heintz *et al.*[3] but lower than that (~32.8 T) reported by Harrison *et al.*[7] For type-II superconductors, the Pauli limiting field $H_p(0) = 1.84 \times 10^4 T_c$ should satisfy the relation[31] $H_{c2}(0) \leq H_p(0)$. Though Harrison *et al.*[7] concluded $LiTi_2O_4$ to be an extreme type-II superconductor, their reported value of $H_{c2}(0)$ did not satisfy the above condition. Our estimated value of $H_p(0) \sim 21$ T (Table I) is higher than $H_{c2}(0) \sim 11.7$ T, confirming the typical type-II superconductivity in $LiTi_2O_4$.

To determine the following important parameters of $LiTi_2O_4$, the residual resistivity $\rho_{res} \sim 6.9 \times 10^{-5}$ Ω cm was calculated from the formula[32]

$$[-dH_{c2}/dT]_{T=T_c} = 4.48 \times 10^4 \gamma_n \rho_{res}. \quad (7)$$

It is noted that the calculated ρ_{res}, though much lower than the measured value ($\sim 5.3 \times 10^{-2}$ Ω cm) from the resistivity data (not shown), is in the same order of magnitude as that

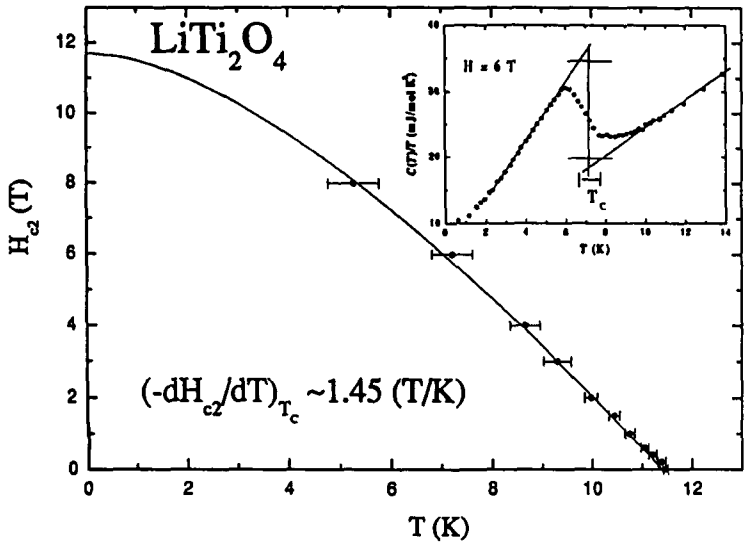

FIG 7 Temperature variation of upper critical field $H_{c2}(T)$ of $LiTi_2O_4$ obtained from Fig 4 where the solid line indicates the fitting of data with WHH theory by which $H_{c2}(0) \sim 11.7$ T is estimated The inset shows the example of how the error bar of $T_c(H)$ is determined by the sharpness of the superconducting transition for H =6 T data

reported in Ref. 7. However, the measured value is consistent with that reported by Johnston *et al.*[1] This large discrepancy between the measured and calculated ρ_{res} indicates that the studied sample exhibits a lot of grain boundaries which highly affect its electrical transport properties. The single crystalline $LiTi_2O_4$ may be indispensable for solving the puzzles of the transport properties. Thermodynamic critical field $H_c(0) \sim 0.320 \pm 0.003$ T, Ginzburg-London (GL) coherence length $\xi_{GL}(0) \sim 55 \pm 3$ Å, penetration depth $\lambda_{GL}(0) \sim 1600 \pm 50$ Å, and lower critical field $H_{c1}(0) \sim 26.0 \pm 0.3$ mT (Table I) are estimated from the following relations[32,33] in the dirty limit by using $\gamma_n \sim 4570$ erg/cm^3 K^2 (converted from $\gamma_n \sim 19.15$ mJ/mol K^2), $\rho_{res} \sim 6.9 \times 10^{-5}$ Ω cm [calculated from Eq. (7)] and $H_{c2}(0) \sim 11.7$ T,

$$H_c(0) = 4.23 \gamma_n^{1/2} T_c \text{ Oe}, \tag{8}$$

$$\xi_{GL}(0) = \{\Phi_0/[2\pi H_{c2}(0)]\}^{1/2} \text{ Å}, \tag{9}$$

$$\lambda_{GL}(0) = 6.42 \times 10^5 (\rho_{res}/T_c)^{1/2} \text{ Å}, \tag{10}$$

$$H_{c1}(0) = H_c(0)(2^{1/2}\kappa)^{-1} \ln \kappa \text{ Oe}, \tag{11}$$

where the fluxon $\Phi_0 \approx 2.0678 \times 10^9$ Oe Å^2 and $\kappa [= \lambda_{GL}(0)/\xi_{GL}(0)] \sim 29 \pm 1$. The values of $\xi_{GL}(0)$ and $\lambda_{GL}(0)$ are, respectively, higher and lower than those [$\xi_{GL}(0) \sim 25.9$ Å and $\lambda_{GL}(0) \sim 2730$ Å] reported by Harrison *et al.*[7] Furthermore, $H_{c1}(0)$ is in the range of the values achieved from[3] the M-H curve (~20 mT) and the fitting of $H_{c1}(T) = H_{c1}(0)(T_c - T)$ plot (~25 mT). All the obtained parameters $\xi_{GL}(0)$, $\lambda_{GL}(0)$, and κ of $LiTi_2O_4$ further satisfy the conditions for type-II superconductivity.[33]

All the above estimation of the parameters assumes the dirty limit superconductivity in $LiTi_2O_4$. Consequently, it is of interest to estimate the value of mean free path l below T_c, which should be smaller than that of $\xi_{GL}(0)$ in the dirty limit The band structure calculations indicate that the Fermi level of $LiTi_2O_4$ in the partially filled conduction band lies in an electronic structure which is not too far from the free-electron-like one with a mass renormalization factor[10,11] By the free electron model with $\rho_{res} = 6.9 \times 10^{-5}$ Ω cm and the carrier concentration $n = 1.35 \times 110^{23}$ cm^{-3} (Ref 7), the estimated $l = 32$ Å is indeed shorter than $\xi_{GL}(0)$ Therefore, the

TABLE II. A comparison of several important parameters for particular transition-metal oxide superconductors

Superconductors	$LiTi_2O_4$	$BaPb_{0.75}Bi_{0.25}O_3$	$Ba_{0.6}K_{0.4}BiO_3$	$La_{1.84}Sr_{0.16}CuO_4$	Sr_2RuO_4
Crystal structure	Spinel cubic	Perovskite cubic	Perovskite cubic	Layered-perovskite	Layered-perovskite
T_c (K)	11.4±0.3	11.7	30	38	1 48
γ_n (mJ/mol K^2)	19.15±0.20	1.6	0.9	0 77	37 5
$N(E_F)$ (states/eV atom)	0.70±0.01	0.14	0 32±0 07	–	–
Θ_D (K)	657±33	195	346	389	–
$\delta C/\gamma_n T_c$	1.97	–	–	–	0 74±0 02
$2\Delta/k_B T_c$	~4	–	3.5±0.1	–	–
λ	0.65	1.45	0.6–0.8	–	–
Pairing state	*s*-wave	*s*-wave	*s*-wave	*d*-wave	*p*-wave?
Reference	This work	12	21, 34	35, 36	37

above analysis using Eqs. (7)–(11) in the dirty limit regime is self-consistent. In addition, the issue of the mass renormalization factor in the previous literature[10,11] was actually unsolved. A large $\lambda_{tot}=1.8$ was inferred implying a strong electron-electron interaction with unknown origin.[11] One can express $\lambda_{tot}=\lambda+\lambda_e$, where λ is the electron-phonon coupling constant and λ_e manifests the interactions due to the possible spin fluctuations and other electron-electron interactions If we rewrite Eq. (2) as $\gamma_n=(1/3)k_B\pi^2N(E_F)(1+\lambda_{tot})$ and assume the theoretical $N(E_F)=0.46$ states/eV atom as achieved from the band structure calculations,[10,11] then $\lambda_{tot}=1$ 53 can be obtained from the $\gamma_n=19$ 15(mJ/mol K^2) of present specific heat data. Therefore, the resultant $\lambda_e=\lambda_{tot}-\lambda=1.53-0.65=0.88$ suggests a moderate electron-electron interaction in $LiTi_2O_4$, and is more consistent with a Stoner enhancement factor $(1-S)^{-1}\sim 2$, which was derived from the magnetic susceptibility $\chi=\mu_B^2N(E_F)/(1-S)$.[1,11]

Finally, it may be interesting to look over the existing transition-metal oxide superconductors, such as, $BaPb_{0.75}Bi_{0.25}O_3$ (Ref. 12), $Ba_{0.6}K_{0.4}BiO_3$ (Refs. 21 and 34), $La_{1.84}Sr_{0.16}CuO_4$ (Refs. 35 and 36) and Sr_2RuO_4 (Ref. 37) for comparison. Some of the important parameters along with those of our studied $LiTi_2O_4$ are summarized in Table II. One would find that the T_c of these superconductors does not strongly correlate with their structure, γ_n, $N(E_F)$, Θ_D, and the electron-phonon coupling constant λ. It is also evident that the superconductivity of each material occurs at only very narrow transition-metal composition. A small amount of metal substitution or a little off-stoichiometry for transition metal will dramatically suppress the superconductivity. Thus, the electronic properties of the transition metals Ti, Bi, Cu, and Ru must play a unique role on the occurrence of superconductivity. In addition, the superconducting pairing state of these superconductors varies from s-wave, d-wave to possible p-wave symmetry (Table II). Accordingly, theoretical calculations and experimental probes on the energy bands need to be done for clarifying these points. Moreover, three more transition-metal oxide superconductors $Cd_2Re_2O_7$ ($T_c\sim 1$ K, Ref. 38), $Na_{0.35}CoO_2\cdot 1.3H_2O$ ($T_c\sim 5$ K, Ref. 39) and KOs_2O_6 ($T_c\sim 9$ K, Ref. 40) were reported most recently and also have attracted much attention due to their novel normal- and superconducting-state features It is no doubt that the understanding of nature of superconductivity in transition-metal oxide superconductors will still challenge the scientists in the fields of condensed matter physics

IV. SUMMARY

In summary, the low temperature specific heat of $LiTi_2O_4$ in magnetic fields is presented. Based on the present measurements and relevant theoretical relations, the normal- and superconducting-state parameters including electronic specific heat coefficient $\gamma_n=19$ 15 mJ/mol K^2, Debye temperature $\Theta_D=657$ K, $\delta C/\gamma_nT_c\sim 1$ 78, superconducting energy gap $\Delta\sim 1.97$ meV, electron-phonon coupling constant $\lambda\sim 0.65$, upper critical field $H_{c2}(0)\sim 11$ 7 T, thermodynamic critical field $H_c(0)\sim 0.32$ T, coherence length $\xi_{GL}(0)\sim 55$ Å, penetration depth $\lambda_{GL}(0)\sim 1600$ Å, and lower critical field $H_{c1}(0)\sim 26$ mT are evaluated and compared with some of those reported. Combining the results $C_{es}(T)/\gamma_nT_c=9.87\exp(-1.58T_c/T)$ and $\gamma(H)\propto H^{0.95}$, we conclude that $LiTi_2O_4$ is a typical BCS-like, fully gapped, and moderate-coupling type-II superconductor in the dirty limit. The analysis also suggests that $LiTi_2O_4$ is a moderately electron-electron correlated system.

ACKNOWLEDGMENTS

This work was supported by National Science Council of Republic of China under contracts No NSC 92-2112-M-110-017 and No NSC 92-2112-M-009-032

*Corresponding author Electronic address yang@mail.phys.nsysu.edu.tw

†Permanent address: Department of Physics, Aligarh Muslim University, Aligarh-202002, India

[1] D. C. Johnston, J. Low Temp. Phys. 25, 145 (1976).

[2] R. W. McCallum, D. C. Johnston, C. A. Luengo, and M. B Maple, J. Low Temp. Phys 25, 177 (1976).

[3] J. M. Heintz, M. Drillon, R. Kuentzler, Y. Dossmann, J. P. Kappler, O. Durmeyer, and F Gautier, Z. Phys. B: Condens. Matter 76, 303 (1989).

[4] D C Johnston, C. A. Swenson, and S. Kondo, Phys. Rev. B 59, 2627 (1999).

[5] D. P. Tunstall, J R. M. Todd, S. Arumugam, G. Dai, M. Dalton, and P. P. Edwards, Phys Rev B 50, 16 541 (1994)

[6] E. G Moshopoulou, J Am Ceram Soc. 82, 3317 (1999)

[7] M R Harrison, P P Edwards, and J. B Goodenough, J Solid State Chem 54, 136 (1984), Philos Mag. B 52, 679 (1985)

[8] F C Xu, Y C Liao, M J Wang, C T Wu, K F Chiu, and M K Wu, J Low Temp Phys 131, 569 (2003)

[9] O. Durmeyer, J P Kappler, E Beaurepaire, J M Heintz, and M Drillon, J Phys : Condens Matter 2, 6127 (1990).

[10] S Satpathy and R. M. Martin, Phys Rev B 36, 7269 (1987)

[11] S. Massidda, J. Yu, and A J. Freeman, Phys. Rev B 38, 11 352 (1988).

[12] T. Itoh, K. Kitazawa, and S Tanaka, J. Phys. Soc. Jpn. 53, 2668 (1984).

[13] P W. Anderson, P A. Lee, M Randeria, T. M Rice, N Trivedi, and F. C. Zhang, cond-mat/0311467 (unpublished).

[14] C. M. Varma, cond-mat/0312385 (unpublished)

[15] D. Guyomard and J. M Tarascon, Solid State Ionics 69, 222 (1994), S Shi, C Ouyang, D S Wang, L Chen, and X Huang, Solid State Commun 126, 531 (2003)

[16] S Kondo, D C Johnston, C A Swenson, F Borsa, A V Mahajan, L. L Miller, T Gu, A I Goldman, M B Maple, D A Gajewski, E J Freeman, N R Dilley, R P Dickey, J Merrin, K Kojima, G M Luke, Y J Uemura, O Chmaissem, and J D Jorgensen, Phys Rev Lett 78, 3729 (1997)

[17] C P Sun and H D Yang (unpublished)

[18]H. D. Yang, J.-Y. Lin, H. H. Li, F. H. Hsu, C.-J. Liu, S.-C. Li, R.-C. Yu, and C.-Q. Jin, Phys. Rev. Lett. **87**, 167003 (2001).
[19]W. L. McMillan, Phys. Rev. **167**, 331 (1968).
[20]V. Z. Kresin and V. P. Parkhomenko, Sov. Phys. Solid State **16**, 2180 (1975).
[21]B. F. Woodfield, D. A. Wright, R. A. Fisher, and N. E. Phillips, Phys. Rev. Lett. **83**, 4622 (1999).
[22]J.-Y. Lin, P. L. Ho, H. L. Huang, P. H. Lin, Y.-L. Zhang, R.-C. Yu, C.-Q. Jin, and H. D. Yang, Phys. Rev. B **67**, 052501 (2003).
[23]A. P. Ramirez, Phys. Lett. A **211**, 59 (1996).
[24]A. P. Ramirez, N. Stücheli, and E. Bucher, Phys. Rev. Lett. **74**, 1218 (1995).
[25]M. Hedo, Y. Inada, E. Yamamoto, Y. Haga, Y. Onuki, Y. Aoki, T. D. Matsuda, H. Sato, and S. Takahashi, J. Phys. Soc. Jpn. **67**, 272 (1998).
[26]J. E. Sonier, M. F. Hundley, J. D. Thompson, and J. W. Brill, Phys. Rev. Lett. **82**, 4914 (1999).
[27]C. Caroli, P. G. de Gennes, and J. Matricon, Phys. Lett. **9**, 307 (1964).
[28]G. E. Volovik, JETP Lett. **58**, 469 (1993).
[29]H. D. Yang and J.-Y. Lin, J. Phys. Chem. Solids **62**, 1861 (2001).
[30]N. R. Werthamer, E. Helfand, and P. C. Hohenberg, Phys. Rev. **147**, 295 (1966).
[31]B. S. Chandrasekhar, Appl. Phys. Lett. **1**, 7 (1962).
[32]T. P. Orlando, E. J. McNiff, Jr., S. Foner, and M. R. Beasley, Phys. Rev. B **19**, 4545 (1979).
[33]C. Kittel, *Introduction to Solid State Physics*, 7th ed. (Wiley, New York, 1996).
[34]B. Batlogg, R. J. Cava, L. W. Rupp, Jr., A. M. Mujsce, J. J. Krajewski, J. P. Remeika, W. F. Peck, Jr., A. S. Cooper, and G. P. Espinosa, Phys. Rev. Lett. **61**, 1670 (1988).
[35]S. J. Chen, C. F. Chang, H. L. Tsay, H. D. Yang, and J.-Y. Lin, Phys. Rev. B **58**, R14 753 (1998).
[36]A. Junod, in *Studies of High Temperature Superconductors*, edited by A. V. Narlikar (Nova Science, Commack, NY, 1996), Vol. 19, p. 1.
[37]S. Nishizaki, Y. Maeno, and Z. Mao, J. Phys. Soc. Jpn. **69**, 572 (2000).
[38]M. Hanawa, Y. Muraoka, T. Tayama, T. Sakakibara, J. Yamaura, and Z. Hiroi, Phys. Rev. Lett. **87**, 187001 (2001).
[39]K. Takada, H. Sakurai, E. Takayama-Muromachi, F. Izumi, R. A. Dilanian, and T. Sasaki, Nature (London) **422**, 53 (2003).
[40]S. Yonezawa, Y. Muraoka, Y. Matsushita, and Z. Hiroi, J. Phys.: Condens. Matter **16**, L9 (2004).

PHYSICAL REVIEW B 68, 092507 (2003)

Pressure effects on the transition temperature of superconducting MgC_xNi_3

H. D. Yang,[1,*] S. Mollah,[1,†] W. L. Huang,[1] P. L. Ho,[1] H. L. Huang,[1] C.-J. Liu,[2] J.-Y. Lin,[3] Y.-L. Zhang,[4] R.-C. Yu,[4] and C.-Q. Jin[4]

[1]*Department of Physics, National Sun Yat Sen University, Kaohsiung 804, Taiwan, Republic of China*

[2]*Department of Physics, National Changhua University of Education, Changhua 500, Taiwan, Republic of China*

[3]*Institute of Physics, National Chiao Tung University, Hsinchu 300, Taiwan, Republic of China*

[4]*Institute of Physics, Center for Condensed Matter Physics and Beijing High Pressure Research Center, Chinese Academy of Sciences, P.O. Box 603, Beijing 100080, People's Republic of China*

(Received 22 April 2003; revised manuscript received 27 June 2003; published 22 September 2003)

The effect of hydrostatic pressure (P) up to 17 kbar on the superconducting transition temperature (T_C) of the newly discovered intermetallic nonoxide perovskite superconductor MgC_xNi_3 has been reported. T_C is found to increase with increasing P at a rate of $dT_C/dP \sim 0.0134$ to 0.0155 K/kbar depending on the value of carbon content x. The absolute value of dT_C/dP for MgC_xNi_3 is about the same as that of intermetallic RNi_2B_2C (R denotes rare earth) and metallic superconductors but about one order of magnitude smaller than that of the most recently and intensively studied superconductor MgB_2. However, the $d \ln T_C/dP \sim 0.001\,81$ to $0.002\,24\ \text{kbar}^{-1}$ and the rate of change of T_C with unit cell volume (V), $d \ln T_C/d \ln V \sim -3.18$ to -2.58 of MgC_xNi_3 are having the comparable magnitude to that of MgB_2 with opposite sign. The increase of T_C with P in MgC_xNi_3 can be explained in the framework of density of states (DOS) effect.

DOI: 10.1103/PhysRevB.68.092507 PACS number(s): 74.62.Fj, 74.25.Fy, 74.25.Ha

Soon after the discovery of a record high-T_C ($\sim$39 K) intermetallic noncuprate superconductor MgB_2,[1] a new intermetallic nonoxide superconductor $MgCNi_3$ was found[2] to undergo a superconducting transition at $T_C \sim 8$ K. Though the T_C of $MgCNi_3$ is much lower than that of MgB_2, it still attracts a lot of attention due to at least having the following physical significance related to the present studies. (1) It has a perovskite structure as does the 30 K oxide noncuprate superconductor $Ba_{1-x}K_xBiO_3$.[2] (2) A high proportion of Ni in this compound indicates that the magnetic interactions may play a dominant role in understanding its superconductivity. (3) Its normal state NMR properties are irregular[3] and analogous to that observed in the exotic superconductor Sr_2RuO_4. (4) A typical isotropic s-wave superconductivity[3] is displayed by the nuclear spin-lattice relaxation rate ($1/T_1$) with a coherence peak below T_C. (5) The change from grain boundary to core pinning by intragranular nanoparticles near T_C proposes that the arrangement of pinning sites in $MgCNi_3$ is unique.[4] (6) The Hall coefficient and thermoelectric power data[5,6] show that the carriers in this compound are electrons in contrast to MgB_2. (7) Energy band calculations[7–9] demonstrate that the density of states (DOS) of the Fermi level (E_F) is dominated by Ni d states and there is a von Hove singularity (vHS) of the DOS just below ($<$50 meV) the E_F.[8] Moreover, the photoemission and x-ray absorption studies show that the sharp vHS peak theoretically predicted near E_F is substantially suppressed which may be due to electron-electron and electron-phonon interactions.[10]

It is well known that the high pressure (P) plays an important role on the T_C of the metallic and intermetallic superconductors.[11–19] In general, P can change the electronic structure, phonon frequencies, or electron-phonon coupling that affecting the T_C. Both positive and negative pressure derivatives, dT_C/dP, are observed in the metallic and intermetallic superconductors.[11–19] For example, simple s,p,d-metal superconductors[16] such as Sn, In, Ta, or Hg, and the intermetallic superconductor such as the recently discovered MgB_2 (Refs. 11–13) have shown decreasing T_C with increasing P. However, depending on the rare earth site of the quaternary borocarbides, RNi_2B_2C (R denotes rare earths), both an increase and decrease of T_C are observed with an increase of pressure.[14,15] In addition, the pressure can basically shift the Fermi level (E_F) towards higher energies[14,15] and thereby provide a probe on the slope of the DOS near E_F. Moreover, it can also modify the magnetic pair breaking effect and tune the competitive phenomena between superconductivity and spin fluctuations. From our magnetic field dependent resistivity and specific-heat studies,[20,21] it has been suggested that the $MgCNi_3$ is basically a typical BCS-like superconductor. In this report, we further present the pressure effects on the T_C of this exotic superconductor to testify the above-mentioned unique electronic and magnetic properties.

The details of MgC_xNi_3 sample preparation and characterization can be found in Refs. 2 and 22. With increasing the nominal carbon content, T_C was improved. Depending on the values of nominal carbon x, the samples with different T_C's are hereafter referred as A ($x=1.0$), B ($x=1.25$), and C ($x=1.5$). Electrical resistivity (ρ) of MgC_xNi_3 was measured by the standard four-probe method. Thermoelectric power (S) measurements were performed with steady state techniques. The hydrostatic pressure- (P) dependent ac magnetic susceptibility (χ_{ac}) data were taken by the piston cylinder self-clamped technique.[23] The hydrostatic pressure environment around the sample was generated inside a Teflon cell with 3M Fluroinert FC-77 as the pressure-transmitting medium. The pressure was determined by using a Sn manometer situated near the sample in the same Teflon cell. In each instance, the original value was reproduced within experimental error after the pressure released indicating complete reversibility of the pressure effect.

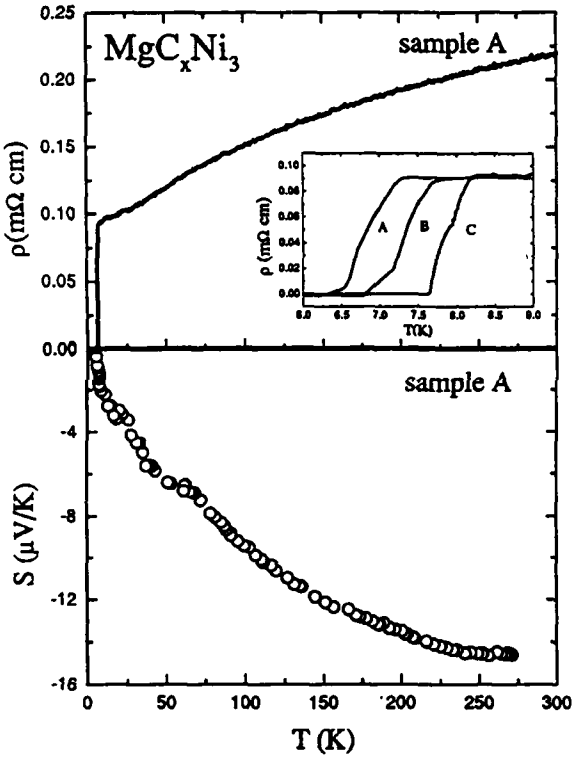

FIG. 1. Temperature (T) variation of resistivity (ρ) and thermoelectric power (S) for sample A at ambient pressure. The inset shows the resistivity (ρ) of the three samples A, B, and C near T_C.

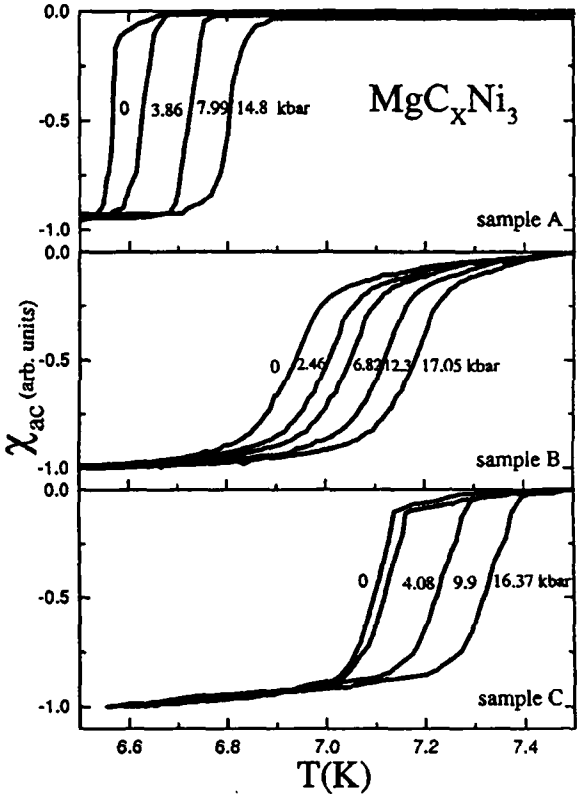

FIG. 2. Variation of ac magnetic susceptibility (χ_{ac}) of samples A, B, and C near T_C at various pressures (P).

Figure 1 shows the temperature dependence of resistivity (ρ) and thermoelectric power (S) for sample A. The inset of Fig. 1 displays the ρ of samples A, B, and C near T_C. The variation of ρ with temperature shows the same trend as reported in the literature[2,5,6,24,25] with $T_C \sim 7-8$ K, $\rho_{300\,K}/\rho_{10\,K} \sim 2.3$ and 90%-10% transition width ~ 0.2 K. The different values of T_C for three studied MgC_xNi_3 samples are mainly due to the carbon stoichiometry.[2,24] The temperature dependence of S is negative, confirming the carriers to be electron type, which is consistent with the published results.[5,6] The nonlinear temperature dependence of S seems to suggest that the enhancement of electron-phonon interaction plays an important role in the superconductivity of MgC_xNi_3 as in chevrel-phase compounds[26] $Cu_{1.8}Mo_6S_{8-y}Se_y$ and $Cu_{1.8}Mo_6S_{8-y}Te_y$.

Temperature variation of ac magnetic susceptibility (χ_{ac}) of samples A, B, and C under pressure (0–17 kbar) is shown in Fig. 2. At ambient pressure, T_C (~ 6.5 K) of sample A is the same as that obtained from specific heat[21] but a little lower than that from the resistivity data (Fig. 1). The T_C (midpoint) for sample A increases from 6.56 to 6.79 K with an increase of pressure from ambient to 14.80 kbar as shown in Fig. 3, having the rate of $dT_C/dP \sim 0.015$ K/kbar and $d\ln T_C/dP\ [=(1/T_C)(dT_C/dP)] \sim 0.002\ \text{kbar}^{-1}$. The similar trend of pressure effect on T_C for samples B and C is also shown in Figs. 2 and 3. The positive values of dT_C/dP and $d\ln T_C/dP$ for these three samples are listed in Table I. It is noted that these values of $d\ln T_C/dP$ (Table I) for MgC_xNi_3 lie in the range of $\sim 0.001-0.008\ \text{kbar}^{-1}$ of conventional superconductors.[27]

For a clear and detailed idea of the pressure effect on the T_C of other metallic and intermetallic superconductors, some of them are also listed in Table I for comparison. The decrease and increase of T_C are observed, respectively, in metallic superconductors Ta and V with an analogous magnitude of dT_C/dP and $d\ln T_C/dP$ as MgC_xNi_3 (Table I). It is explained by the decrease of the electron-phonon coupling constant in Ta and by the suppression of spin fluctuations as well as the increase of electron-phonon coupling in V.[16–18] The magnitude of positive dT_C/dP for electron-carrier MgC_xNi_3 is about the same as that of its three-dimensional analog $LuNi_2B_2C$ superconductor, and the latter has been interpreted by an increase of the DOS with P.[14] However, the negative dT_C/dP and $d\ln T_C/dP$ for hole-carrier MgB_2 may be either from a decrease of the DOS (Ref. 12) or by a lattice stiffening.[13]

The change of T_C with the unit cell volume (V) can be given by[11,14]

$$(V/T_C)(dT_C/dV) = d\ln T_C/d\ln V = -(B/T_C)(dT_C/dP), \quad (1)$$

where B is the bulk modulus of the superconductor. Using the calculated value of B for MgC_xNi_3 as 1510 kbar (Ref. 25) and taking the obtained dT_C/dP and T_C from Table I, the $d\ln T_C/d\ln V$ values are found from Eq. (1), respec-

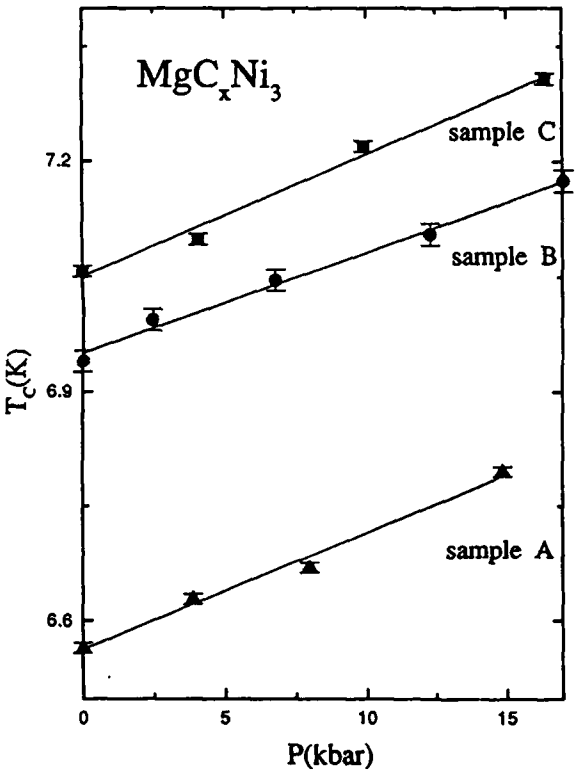

FIG. 3. Pressure (P) dependence of superconducting transition temperature (T_C) of samples A, B, and C.

tively, for samples A, B, and C as -3.18, -2.58, and -2.76. These values are of the same order of magnitude in the MgB_2 superconductor ($+4.16$) with opposite sign.[11]

Since the DOS is sufficiently large in MgC_xNi_3, produces strong electron-phonon coupling[9] and is supported by its S data, the T_C can be expressed by the McMillan formula[28] as

$$T_C=(\theta_D/1.45)\exp\{-1.04(1+\lambda)/[1-\mu^*(1+0.62\lambda)]\}, \quad (2)$$

where, μ^* is the Coulomb pseudopotential and θ_D is the Debye temperature. λ is the electron-phonon coupling constant and is given by

$$\lambda=N(E_F)\langle I^2\rangle/M\langle\omega^2\rangle, \quad (3)$$

where $N(E_F)$ is the DOS at the Fermi level, $\langle I^2\rangle$ is the square averaged electronic matrix element for electron-phonon interaction, M is the ionic mass, and $\langle\omega^2\rangle$ is the square averaged phonon frequency. It appears from Eq. (2) that the change of λ and θ_D by pressure will determine the sign of dT_C/dP. It is well established that the pressure induces the lattice stiffening and generally reduces the T_C.[14–17] However, the DOS effect can either enhance or reduce the T_C correspondingly by the increase or decrease of $N(E_F)$ due to applied pressure.[14,15] The dependence of T_C on θ_D is complicated as it appears both in the linear and exponent [being connected with $\langle\omega^2\rangle$ in Eq. (3)] terms of Eq. (2). Again, the change of exponent λ in Eq. (2) will be more effective than that of the linear term θ_D in determining T_C. θ_D generally increases by P amplifying the phonon frequency[19] as $\langle\omega^2\rangle=0.5\theta_D^2$ and thus may decrease λ [Eq. (3)], which in turn may reduce T_C [Eq. (2)]. Therefore, the positive dT_C/dP for MgC_xNi_3 possibly originates from the increase of $N(E_F)$ and consequently by the enhancement of electron-phonon coupling constant λ [Eqs. (3)] if μ^* and $\langle I^2\rangle$ are less pressure dependent. In addition, P causes not only a shifting of the E_F but also a broadening of the energy bands. This broadening of energy bands may also increase $N(E_F)$. Most recently, Louis and Iyakutti[19] have successfully calculated the pressure effects on T_C of vanadium (V). Similarly, the computation of some important parameters such as $d\ln N(E_F)/dP$ and $d\ln\omega/dP$ of MgC_xNi_3 may be useful for quantitative analysis of our data.

Even though it is unfavorable that strong spin fluctuations exist in MgC_xNi_3,[21] the marginal or unstable spin fluctuations suppressing T_C have not been totally ruled out.[8] In general, pressure reduces the spin fluctuations and increases T_C because the spin fluctuations and superconductivity are mutually competitive phenomena. This may also be one of the reasons for the positive pressure effect on T_C of MgC_xNi_3. Another considerable factor showing a positive dT_C/dP is the carbon stoichiometry in the sample. Generally, the deficiency of carbon from the optimum value decreases the T_C.[2,24] The nonstoichiometry of carbon (if any) may also affect the energy bands of the sample and alter the

TABLE I. The superconducting transition temperature T_C (determined from the midpoint of resistive transition for MgC_xNi_3) at ambient pressure, dT_C/dP, and $d\ln T_C/dP$ for some metallic as well as intermetallic superconductors.

Sample composition	T_C (K)	dT_C/dP (10^{-2} K/kbar)	$d\ln T_C/dP$ (10^{-3}/kbar)	Reference
MgB_2	38.6	−8.0	−2.07	12
MgB_2	37.5	−16.0	−4.26	13
$LuNi_2B_2C$	15.9	+1.88	+1.18	14
Ta	4.3	−0.26	−0.60	16
V	5.3	+1.0	+1.88	18, 19
MgC_xNi_3(A)	6.9	+1.55	+2.24	This work
MgC_xNi_3(B)	7.4	+1.34	+1.81	This work
MgC_xNi_3(C)	7.9	+1.52	+1.92	This work

position of E_F compared to that expected from theoretical energy band calculations[7–9] for stoichiometric $MgCNi_3$. The present investigations for three samples with different carbon content and T_C show almost the same positive value of dT_C/dP suggesting that the carbon deficiency does not significantly affect the pressure effect of MgC_xNi_3 on T_C. However, it is noted that Kumary *et al.*[25] recently found a decrease of T_C up to a pressure of 17 kbar and an increase of T_C beyond this pressure using resistivity measurements. It may be possible to briefly explain these controversial results as followings. (1) The T_C determined from the resistivity (transport property) is always higher than that from susceptibility and specific heat (bulk property) measurements.[2,20,21,25] This may suggest that a small amount of higher T_C phase existing in the grain boundaries[4] superconducts through percolation effects. (2) The negative dT_C/dP observed in Ref. 25 using resistivity measurements at low pressures may be due to the reduction of grain boundary effects by pressure. Once the pressure is applied high enough ($\sim$17 kbar) to overcome the grain boundary effect, the bulk superconductivity dominates and the positive dT_C/dP is found to be the same with our results using susceptibility measurements.

In summary, pressure increases T_C of three intermetallic, nonoxide, and perovskite electron-type superconductors MgC_xNi_3. The magnitude of change rate $d\ln T_C/dP$ in MgC_xNi_3 is about the same order as that in MgB_2 and RNi_2B_2C (R denotes rare earths), which lies in the range of that of conventional superconductors The positive value of dT_C/dP for three MgC_xNi_3 samples are almost the same and independent of various T_C resulting from different carbon *stoichiometry The present results of positive* dT_C/dP *of* MgC_xNi_3 can be explained mainly by the increase of density of states by pressure

This work was supported by National Science Council of Republic of China under Contract No NSC91-2112-M110-005 and NSC90-2112-M009-025.

*Corresponding author.
Email address: yang@mail.phys.nsysu.edu.tw
†Permanent address: Department of Physics, Aligarh Muslim University, Aligarh-202002, India.

[1] J. Nagamatsu, N. Nakagawa, T. Muranaka, Y. Zenaitani, and J Akimitsu, Nature (London) **410**, 63 (2001).
[2] T. He, Q. Huang, A. P. Ramirez, Y. Wang, K. A. Regan, N Rogado, M. A. Hayward, M. K. Hass, J. S. Slusky, K. Inumaru, H W. Zandbergen, N. P. Ong, and R. J. Cava, Nature (London) **411**, 54 (2001).
[3] P. M. Singer, T. Imai, T. He, M. A. Hayward, and R. J Cava, Phys. Rev. Lett. **87**, 257601 (2001).
[4] L. D. Cooley, X. Song, J. Jiang, D. C. Larbalestier, T He, K. A Regan, and R. J. Cava, Phys. Rev. B **65**, 214518 (2002).
[5] S. Y. Li, R. Fan, X. H. Chen, C. H. Wang, W. Q Mo, K Q Ruan, Y M. Xiong, X. G. Luo, H. T. Zhang, L. Li, Z Sun, and L Z Cao, Phys Rev. B **64**, 132505 (2001).
[6] S Y. Li, W Q. Mo, M. Yu, W. H. Zheng, C H. Wang, Y M Xiong, R. Fan, H. S. Yang, B. M. Wu, L Z. Cao, and X H Chen, Phys. Rev. B **65**, 064534 (2002).
[7] D J. Singh and I. I. Mazin, Phys. Rev. B **64**, 140507 (2001)
[8] H Rosner, R. Weht, M. D. Johannes, W. E. Pickett, and E. Tosatti, Phys. Rev. Lett. **88**, 027001 (2002).
[9] S B. Dugdale and T. Jarlborg, Phys. Rev. B **64**, 100508 (2001)
[10] J. H. Kim, J. S. Ahn, J. Kim, M. S. Park, S I Lee, E. J Choi, and S.-J Oh, Phys. Rev. B **66**, 172507 (2002).
[11] J. S. Schilling, J. D. Jorgensen, D. G. Hinks, S. Deemyad, J Hamlin, C. W. Looney, and T. Tomita, in *Studies of High Temperature Superconductors*, edited by A. V. Narlikar (Nova Science, New York, 2001), Vol. 38, p. 321.
[12] M. Monteverde, M. Nunez-Regueiro, N. Rogado, K A Regan, M A Hayward, T He, S M Loureiro, and R J Cava, Science **292**, 75 (2001)
[13] B Lorenz, R L Meng, and C W Chu, Phys Rev B **64**, 012507 (2001)
[14] H. Schmidt and H F Braun, Physica C **229**, 315 (1994)
[15] E Alleno, J J Neumeier, J D Thompson, P C Canfield, and B K. Cho, Physica C **242**, 169 (1995)
[16] L D. Jennings and C A Swenson, Phys Rev **112**, 31 (1958)
[17] V V Struzhkin, Y A Timofeev, R J Hemley, and H K Mao, Phys Rev Lett **79**, 4262 (1997)
[18] M Ishizuka, M Iketani, and S Endo, Phys Rev B **61**, 3823 (2000).
[19] C N. Louis and K. Iyakutti, Phys Rev B **67**, 094509 (2003)
[20] J -Y. Lin, P H Lin, P L Ho, H L Huang, Y-L Zhang, R -C Yu, C -Q Jin, and H D Yang, J Supercond **15**, 485 (2002)
[21] J -Y Lin, P L Ho, H L Huang, P H Lin, Y-L Zhang, R -C Yu, C -Q Jin, and H D Yang, Phys Rev B **67**, 052501 (2003)
[22] C Q Jin, Y L Zhang, Z X Liu, F Y Li, W Yu, and R C Yu, Physica C **388–389**, 561 (2003)
[23] S S Weng, I P Hong, C F Chang, H L Tsay, S Chatterjee, H D Yang, and J -Y Lin, Phys Rev B **59**, 11 205 (1999)
[24] J Q. Li, L J Wu, L Li, and Y Zhu, Phys Rev B **65**, 052506 (2002)
[25] T G Kumary, J Janaki, A Mani, S M Jaya, V S Sastry, Y Hariharan, T S Radhakrishnan, and M C Valsakumai, Phys Rev B **66**, 064510 (2002)
[26] A B Kaiser, Phys Rev B **35**, 4677 (1987)
[27] M Levy and J L Olsen, *Physics of High Pressures and Condensed Phase* (North-Holland, Amsterdam, 1964), Chap 13
[28] W L McMillan, Phys Rev **167**, 331 (1968)

Indian J. Phys. **77A** (1), 9-22 (2003)

IJP A
— an international journal

MgB_2 superconductor : a review

S Mollah,[1,2] H D Yang[1] and B K Chaudhuri[1,3]*

[1]Department of Physics, National Sun Yat Sen University, Kaohsiung, Taiwan 804, R O C

[2]Department of Physics, Aligarh Muslim University, Aligarh-202 002, India

[3]Department of Solid State Physics, Indian Association for the Cultivation of Science, Jadavpur, Kolkata -700 032, India

E-mail : sspbkc@mahendra.iacs.res.in

Received 5 November 2002, accepted 15 November 2002

Abstract : Synthesis, structure and properties of the most intensively studied newly discovered intermetallic binary superconductor MgB_2 have been reviewed up to October, 2002. Though this material was known since 1950s, it was recently discovered to be superconductive with a record high T_c ~ 40 K. The detection of this binary superconductor by a Japanese research group in January, 2001 initiated the basic research to find out other binary and ternary intermetallic superconductors like TaB_2, $BeB_{2.75}$, $MgCNi_3$ etc. It has a hexagonal unit cell with cell parameters a ~ 3.1432 Å and c ~ 3.5193 Å. MgB_2 bulk samples synthesized under high pressure (~3.5 GPa) and high temperature (~1000 °C) has density ~2.63 g/cm^3. The normal state carriers of MgB_2 are holes which have been established from the positive thermoelectric power and Hall coefficient measurements. The external pressure decreases the critical temperature (T_c) with dT_c/dP in the range of -1 to -2 K/GPa. The T_c decreases rapidly by the doping of Mn, Li, Co, C, Al, Ni and Fe but increases slightly by Zn doping. However, no significant change of T_c is observed by the doping of Si and Be. It is further noticed that the anisotropic ratio γ (= H_{c2}^{ab}/H_{c2}^{c}) ~1- 5 with lower critical field (H_{c1}) ~ 25-48 mT and upper critical field, $H_{c2}(0)$ ~ 40 T. The critical current density (J_c) of it is as high as 1.3×10^6 Acm^{-2} in the self-field and 9.4×10^4 Acm^{-2} in a magnetic field of 2 T at the temperature of 20 K. The most interesting feature of this superconductor is the appearance of two superconducting energy gaps one Δ_1 ~ 1.92 meV and the other at Δ_2 ~ 3.45 meV. From theoretical studies, it is found that MgB_2 superconductor has a minimum of the density of states (DOS) just above the Fermi level which can account for the decrease of T_c with the increase of pressure. This review mainly deals with experimental results obtained by different research groups working on this new superconductor. Since more new and interesting results are expected in near future, critical theoretical analysis of the existing experimental data has not been made. We hope to do this work in our next review on this subject.

Keywords : MgB_2, superconductivity, synthesis, structure, applications

PACS Nos. : 01.30.Rz, 74.25.Fy, 74.70.Ad, 74.25.Ha, 74.25.Bt, 74.62.Fj

PLAN OF THE ARTICLE

* Corresponding Author

1. Introduction

At the beginning of 2001, after the discovery of high T_c cuprate superconductors, researchers all over the world were stimulated by the discovery of another new superconductor MgB_2 [1] with critical temperature (T_c) around 39 K higher than (at least by a factor of two) the traditional theories predicted was possible. It introduced a new binary inter-metallic superconductor with three atoms per unit cell. It is cheap to manufacture, easy to work with, and will probably become the alloy of choice for the next generation of superconducting devices. This superconductor (SC) raises many interesting issues. Whether the behavior of this SC resembles to the high temperature copper oxide contained SC or low temperature metallic BCS type of SC has not yet been clearly understood. There are several fundamental questions about the mechanism of MgB_2 superconductor which are yet to be addressed. For examples, is MgB_2 a fully gapped superconductor or a multi-gap superconductor ? Is it a conventional s-wave superconductor ?

MgB_2 has a large critical current density ($J_c \sim 10^5$ Acm^{-2}) with upper critical field $H_{c2}(0) \sim 16$-18 T [2]. A high number density of flux pinning centers is crucial for obtaining $J_c \sim 10^5$ Acm^{-2} [3]. This high value of J_c confirms the absence of electromagnetic granularity [2] and the depairing current density $\sim 10^8$Acm^{-2} [3]. Simon *et al* [4] studied the conduction electron spin resonance (CESR) in fine powders of MgB_2 both in the superconducting and normal states. From CESR study, they suggested that MgB_2 is a strongly anisotropic superconductor with the upper critical field, H_{c2}, varying between 2 and 16 T The superconducting anisotropy in MgB_2 was again confirmed by Bud'ko *et al* [5] from magnetizaton data. It would be beneficial for the researchers to have a fruitful review of this rapidly growing new system of superconductor. This review may give sufficient idea for the new generation researchers to this field of intensive research interest

2. Synthesis of MgB_2

The MgB_2 superconductors have been prepared in the form of single crystal, polycrystalline bulk, thin film, and wires/tapes In the following we will discuss, in brief, about their different preparation techniques

2.1. Polycrystalline bulk :

The polycrystalline samples were prepared from powdered magnesium (Mg:99.9% pure) and powdered amorphous boron (B:99% pure) in a dry box [1]. The powders were mixed in an appropriate ratio of 1:2, ground and pressed into pellets The pellets were heated at 700 °C under a high argon pressure, 196 MPa, in a hot isostatic-pressing furnace for 10 hours Larbalestier *et al* [2] used Mg flakes instead of Mg powders They used different heat treatment history. The pellets were placed on Ta foil in alumina boat and fired in a tube furnace in mixed gas (95%Ar+5%H_2) for 1 hour at 600 °C, 1 hour at 800 °C and 1 hour at 900 °C This powder was lightly ground, pressed into pellets and fired again at 700 °C for one hour Part of the powder was hot pressed at 800 °C under a pressure of 10 kbar for 1 hour Polycrystalline bulk samples were synthesized [6, 7] under a pressure of 3 5 GPa at high temperature (1000 °C) Bulk materials were prepared by high pressure sintering using a cubic anvil press and the samples were heated up to 1250 °C [6] The samples were pressurized [8-10] at 3 GPa and sintered at 850-950 °C Porous and granular samples were prepared by slowly heating up to 950 °C in an evacuated sealed quartz tube ampoule in Ta [11]. Yang *et al* and Li *et al* [13] prepared the polycrystalline samples by high-pressure synthesis with pyrophyllite as the transmitting medium with pressure of 3-5 GPa and temperature ~1000°C for 15-30 min. They [12, 13] got almost pure sample with a little amount of MgO and B_2O High density nanocrystalline MgB_2 bulk superconductors with distinctly improved pinning were prepared by mechanical alloying of Mg and B powders at ambient temperatures followed by hot pressing [14]

2 2 Chemical doping in MgB_2 polycrystalline bulk

Aluminium (Al) doped samples were synthesized by direct reaction method with final heat treatment temperatures 900-950 °C with or without pressure with different heating times using Mg flakes, fine Al powder and amorphous boron powder [15]. $Mg_{1-x}Al_xB_x$ ($0 \le x \le 0.4$) was prepared by almost the same technique [16]. Li and Be doping were reported by other groups [17, 18]. Ti doped MgB_2 with an atomic ratio Mg Ti B = 1 – x x . 2 (x = 0–1) were prepared by Zhao *et al* [19] Hydrogen absorption was performed at 100 °C at a pressure of 20 bars-7 kbars and the hydrogen content was kept constant (3%/f u) [20]. MgB_2 superconductor synthesis with boron isotope will be available in [21]

2.3. Thin film .

The MgB_2 thin films of thickness 500 nm were synthesized by pulsed laser deposition (PLD) technique at room temperature onto (*111*) oriented single crystal $SrTiO_3$ substrates [3] The target MgB_2 was prepared by pressing and sintering [2] The deposition was done under 0.3 Pa of Ar The films were annealed at 750-850 °C for 15-30 minutes in evacuated niobium/quartz tube. Mg pellets were also included in each tube to prevent Mg loss Thin films with thickness 0 4 μm were fabricated on Al_2O_3

and $SrTiO_3$ substrates by two-step method [22]. Si (*100*) substrates were used by Blank *et al* [23] for the process of Mg-B films by PLD in an *in-situ* two- step process using multi-component targets. The MgB_2 target was mixed with 50% extra Mg powder to avoid the loss of Mg during the thin film deposition and special care was taken regarding the color of the plasma. The color of the plasma changed from green to blue depending on the argon pressure, laser fluencies and ablation time. The deposition temperature was varied from room temperature (~30 °C) to 300 °C. Growth of MgB_2 thin films by PLD is examined under *ex situ* and *in situ* processing condition [24]. In *ex situ* condition, B films (~1000 Å) were deposited at the rate of 0.035 Å/pulse on $SrTiO_3$ (*100*) or (*111*) substrates and reacted these in a sealed Ta tube with Mg vapor at 900 °C. The laser energy density and pulsed repetition rate were 1.5 J/cm^2 and 10 Hz, respectively, both *in situ* and *ex situ* conditions. The ambient was vacuum and the background pressure was below 10^{-7} Torr. The *in situ* deposition was also done by three different procedures *i.e.* (i) PLD from MgB_2 sintered target, (ii) PLD of multi-layers of MgB_2 and Mg followed by *in situ* annealing at high temperature and (iii) PLD of multi-layers of Mg and B followed by *in situ* high temperature annealing.

2.4. Wires/tapes :

The Fe or Cu (linked with an inner tube of Fe) tubes were filled with MgB_2 powder, drawn into wires, cold rolled to ribbons and sintered at 900 °C [25]. As magnesium in MgB_2 reacts with copper and silver, Jin *et al* [25] did not use these as cladding materials. But Grasso *et al* [26] used pure metallic tubes of Ag, Cu and Ni as sheath materials. The entire process of fabricating the metal-sheathed MgB_2 wires were the same as used in silver sheathed Bi-2223 wires/tapes [27-31]. The MgB_2 powder was packed inside tubes of various diameters (6-8 mm) and wall thickness (1-2 mm) with a pressure of 250 MPa using a hardened steel piston. The entire loading procedure was carried out in argon atmosphere with both ends of the tube tightly closed by tin plugs whereas for the preparation of Bi-2212 type superconducting wire, powders are loaded in Ag tubes in air [27-31]. The loaded tubes were then cold drawn into wires and finally rolled into tapes of thickness 180 μm [26]. The superconducting filling factor (fraction of total volume of conductor filled with superconductor) is an important parameter to control the micro-structural properties and J_c of the superconducting wires/tapes. It is found that more filling factor causes better micro-structural and transport properties. Grasso et al [26] found the filling factor as 20-30% of the whole conductor volume. Suo *et al* [32] used commercial MgB_2 powder as the precursor material and Ni or Fe as the sheath material. The outer diameters (o.d.) of the tubes were 8-12.7 mm and the inner diameters (i.d.) were 5-7 mm. The filling factor was found to be 20-28%. Pradhan *et al* [33] used Mg and B powders as raw material instead of MgB_2 superconductor [25, 26]. They filled the powder in Ta tube and the tube was inserted into Cu tube. After drawing and rolling, it was annealed at 900-950 °C. Tungsten sheathed 2 mm long wires with 15 μm i.d. and 180-200 μm o.d. were prepared by Prozorov *et al* [34]. Kumakura *et al* [35] used stainless steel and Cu-Ni tubes and commercially available MgB_2 powders for the fabrication of the wires/tapes. They carried out the packing process in air. They also fabricated multi-filamentary tapes using Cu-Ni tubes. They prepared 7-filament tapes using the wire of diameter 2 mm. The Cu-Ni sheathed wire was cut into seven pieces, bundled and inserted into another Cu-Ni tube of larger diameter, swaged, drawn and cold rolled into multi-filamentary tapes.

2.5. Single Crystal :

Though several groups have synthesized the polycrystalline MgB_2 bulk, thin films or wires/tapes, very few groups have produced the single crystal of this superconductor. Xu *et al* [36] grew single crystals using vapor transport method [37]. A total of 2 gm mass of Mg chips and a B chunk in a molar ratio of 1:1.9 were sealed in a molybdenum crucible (i.d.=10 mm and length = 60 mm) by the electron beam welding. The crucible was heated to 1400 °C at a rate of 200 °C/h, kept for 2 hours and slowly cooled down to 1000 °C with a cooling rate of 5 °C/h and finally to room temperature by switching off the furnace. More than 20 thin plate single crystals of maximum size 0.5×0.5×0.02 mm^3 were obtained from the inner surface of the crucible. Pradhan *et al* [7] extracted golden yellow colored shiny single crystalline platelet samples of dimension 250×100×40 μm^3.

3. Structure of MgB_2

Powder X-ray diffraction (XRD) pattern (Figure 1) shows that the MgB_2 superconductor has hexagonal unit cell with cell parameters $a = 3.1432 \pm 0.0315$ Å and $c = 3.5193 \pm 0.0323$ Å. [21]. MgB_2 remains strictly hexagonal up to the highest pressure applied on it and no structural transition is observed [38]. It possesses AlB_2-type structure (space group *p6/mmm*) and has a simple hexagonal lattice [39] of closed pack Mg layers alternating with graphite like B layers (Figure 2). The B atoms arranged at the corners of a hexagon with 3 nearest neighbor B

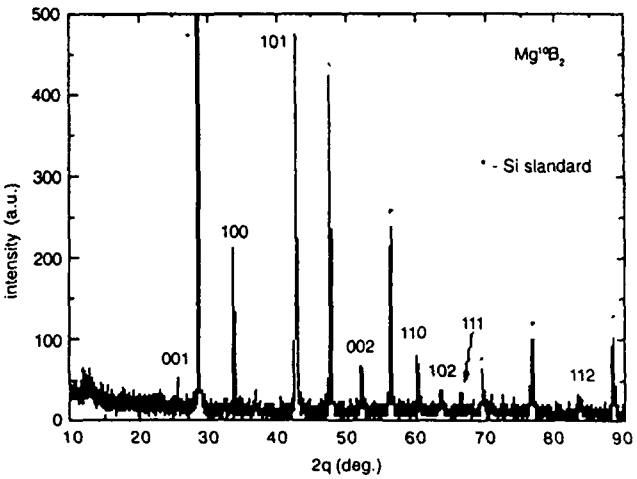

Figure1. Powder X-ray diffraction spectra of $Mg^{10}B_2$ using CuKα radiation indicating (*h,k,l*) values and Si standard (*) [21].

atoms in each plane. Mg atoms are located at the center of the B hexagon, midway between adjacent B layers. MgB_2 exhibits a strong anisotropy in the B-B lengths similar to graphite The distance of boron planes is much larger than the in-plane B-B distance. The values of unit cell parameters differ from those of

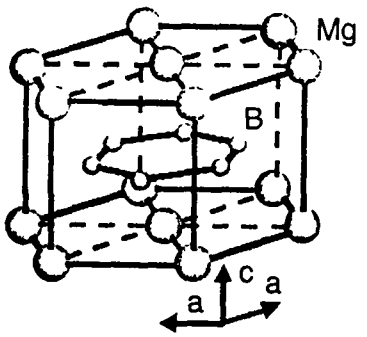

Figure 2. Crystal structure of MgB_2 graphite-type B layers separated by hexagonal close-packed layers of Mg [38]

Nagamatsu *et al* [1], where the reported values of the cell parameters are $a = 3.086$ Å and $c = 3.524$ Å. The *a*- and *c*- axes lattice constants determined from the (*101*) and (001) peaks for thin film are found to be 3.10 and 3.52 Å, respectively [22]. Both '*a*' and '*c*' lattice constants decrease with the increase of Al in Al doped magnesium diboride [16]. The cell parameters and the cell volume remained unchanged after hydrogenation of the sample [20]. X-ray procession photograph of single crystal revealed the lattice parameters as $a = 3\ 047$ Å and $c = 3\ 404$ Å [3] Small peaks corresponding to MgO was observed by Kumakura *et al* [35] in the XRD pattern. MgB_2 bulk samples synthesized under high pressure (3.5 GPa) and high temperature (1000 °C) has density ~2.63 g/cm^3 [7]. The in-plane lattice parameter '*a*' of $Mg_{1-x}Li_xB_2$ [17] decreases with x, while the lattice parameter '*c*' does not show obvious change. Precise structural information on the $Mg_{1-x}Al_xB_2$ superconductors in the vicinity of $x \approx 0.5$ was derived from high-resolution synchrotron x-ray powder diffraction measurements [40]. Margadonna *et al* [40] found that a hexagonal superstructure, accompanied by doubling of the *c* axis, ordering of Mg and Al in alternating layers, and a shift of the B layers towards Al by ~0.12 Å, was observed. The unusually large width of the (001/2) superlattice peak implied the presence of micro-strain broadening, arising from anisotropic stacking of Al and Mg layers and/or structural modulations within the *ab* plane. The ordered phase survived only over a limited range of compositions away from the optimum $x \approx 0.5$ doping level. Chemical bonding and electronic structure of MgB_2 were studied using self-consistent band-structure techniques [41]. Analysis of the transformation of the band structure showed that the band structure of MgB_2 is graphite like, with π bands falling deeper than that in ordinary graphite [41] These bands possess a typically delocalized and metallic, as opposed to covalent, character. The in-plane σ bands retain their two-dimensional (2D) covalent character, but exhibit metallic hole-type conductivity The coexistence of 2D covalent in-plane and three-dimensional (3D) metallic-type interlayer conducting bands is a unique feature of MgB_2 A comparative study of powder and bulk specimens of MgB_2 by electron spin resonance (ESR) verified the presence of intense conduction electron spin resonance (CESR) in the normal state [42] A low concentration paramagnetic center stemming from the initial amorphous boron powders along with traces of Fe impurities were identified in the ESR spectra Intense microwave absorption, that distorts CESR below T_c, was observed in fine powders implying enhanced microwave dissipation due to the viscous flux motion The porosity decreases and the connectivity increases with the increase of sintering temperature as evident from scanning electron micrographs (SEM) [43] unlike the high temperature Bi-Sr-Ca-Cu-O and Y-Ba-Cu-O type superconducting oxides Superconducting grains of hot pressed samples are well connected compared to that of the cold pressed one [8]

4. Properties of MgB_2

4.1. Critical temperature

Superconducting onset and end point transition temperatures as observed by Nagamatsu *et al* [1] from resistivity measurement are, respectively, 39 and 38 K as shown in Figure 3 Zero field cooling (ZFC) and field cooling (FC) at 10 Oe magnetic susceptibility measurements also support the onset temperature as 39 K (Figure 4) In the following, we shall discuss briefly the effect of different parameters on the superconducting transition temperature (T_C)

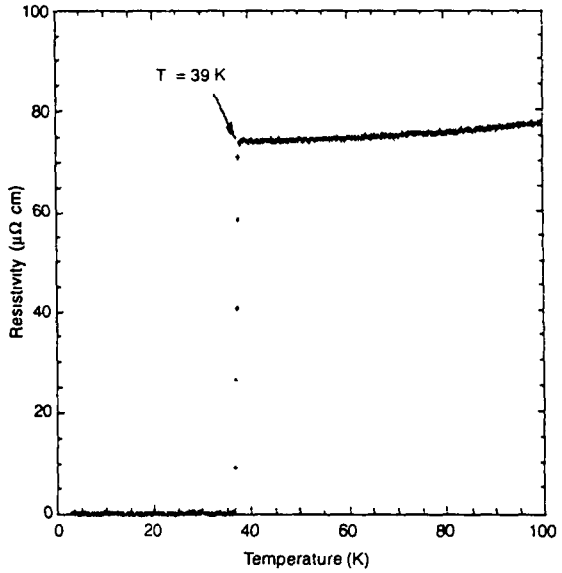

Figure 3 Variation of resistivity of MgB_2 under zero magnetic field [1]

(a) External pressure effect

It is found that the critical temperature, T_c decreases with the increase of pressure (Figure 5) as observed both from the

pressure dependent resistivity [15, 44] and magnetic susceptibility [45] measurements Monteverde *et al* [15] found that the rate of decrease of T_C as -0 8K/GPa up to a pressure of

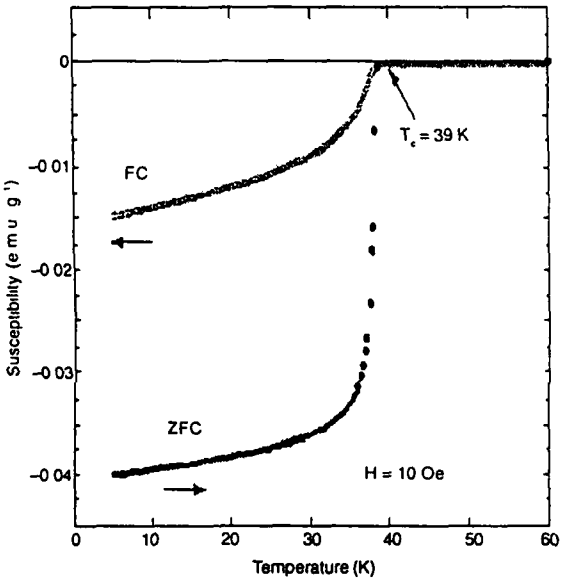

Figure 4 Magnetic susceptibility (χ) of MgB_2 as a function of temperature [1] ZFC and FC stand for zero field cooling and field cooling at 10 Oe respectively

7 GPa and then followed the purely quadratic equation, T_c = 38 6K – 0 0263 K/GPa x P^2 where P stands for pressure However, Saito *et al* [44] found the decrease of T_c quasi-linearly with applied pressure at a rate of -2 K/GPa which is some what larger than that derived from ac susceptibility measurement namely -1 6 K/GPa [45] It is found that T_c decreased linearly and reversibly under pressure at the rate $dT_c/dP \approx -1\ 11\pm0\ 02$ K/GPa [46] But the decrease of T_c from ac susceptibility measurement is in good qualitative agreement with the ensuing calculated value of -1 4 K/GPa within the BCS framework The value of $d\ln T_c/d\ln V$ = +4 16±0 08 [46] and is also between the known values of conventional *sp* and *d* superconductors The different values of the rate of decrease of T_c with the increase of pressure by various groups may be due to the use of different pressure transmitting media As the MgB_2 superconductor is anisotropic in nature, it may be sensitive to non-hydrostatic pressure components Another important point is the sample quality The samples used by various groups to study the pressure dependent T_c are different Thus the Mg non-stoichiometry in different samples may be an important factor for different behavior of pressure dependent T_c It is worthwhile to mention that the theoretical models [47, 48] based on holes predicted an increase of dT_c/dP as a result of decreasing in-plane B-B distance with increasing pressure which causes the hardening of phonon frequencies Thus the experimental results totally contradict the theoretical predictions and the main reason for the negative dT_c/dP is not an electronic effect It may be due to the strong enhancement of phonon frequency with pressure which has been directly observed by Raman spectroscopy [49]

(b) Internal pressure (chemical doping) and isotope effect

Doping effect on both the Mg and B sites of MgB_2 by suitable elements has been widely studied T_c is found to decrease at various rates with the doping of different elements though the doping of few elements showed either a small increase of it or remain unchanged The T_c decreases rapidly by the doping of Mn [50], Li [17], Co [50], C [51, 52], Al [16, 53], Ni [50] and Fe [50] But no significant decrease of T_c is observed by the doping of Si [54] and Be [18] However, doping of Zn [50] increases the T_c slightly (~1 K) Figure 6 shows the dependence of resistivity on the doping concentration (x) in $Mg_{1-x}Al_xB_2$ superconductor [53] It is found that the T_c is decreased with the increase of x From magnetization measurement, Slusky *et al* [16] found that the sample lost the superconducting property for x = 0 4 The structural and magnetic data taken together indicated that the disappearance of bulk superconductivity for x = 0 4 is due to a structural transition resulted in the partial collapse of the

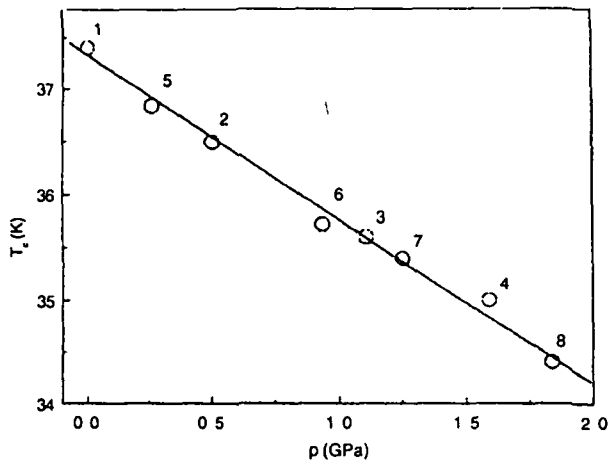

Figure 5 Pressure dependence of T_c from ac susceptibility measurement The numbers present the sequential order of the experimental runs [45]

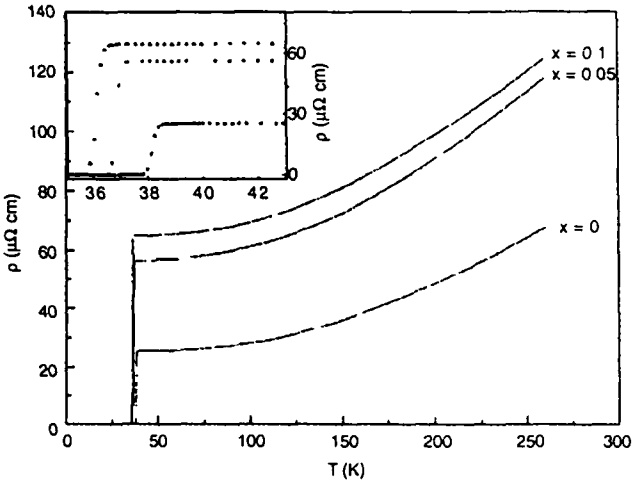

Figure 6 Resistivity of $Mg_{1-x}Al_xB_2$ The inset shows details near T_c [53]

separation between boron planes, not a change in the B-B distance. Though the T_c is decreased with the increase of Al doping in Mg site [16, 53], no such effect is observed by the doping of C in the B site [51]. The magnetization data (Figure 7) of the $MgB_{2-x}C_x$ ($x = 0 - 0.1$) samples [51] indicate the same T_c onset with or without carbon doping. The T_c of $Mg_{1-x}Li_xB_2$ decreases with increase of x and loss of superconductivity occurs for $x = 0.5$ [17]. However, the Be doped $Mg_{1-x}Be_xB_2$ (x=0.15, 0.30) system has the same $T_c = 39$ K as that of pure MgB_2, indicating that Be does not replace Mg atoms in the structure [18]. The boron isotope effect for MgB_2, reveals a 1.0 K higher T_c in $Mg^{10}B_2$ ($T_c \sim 40.2$ K) compared to that of $Mg^{11}B_2$ ($T_c \sim 39$ K) obtained from temperature dependent magnetization and specific heat study [21]. The higher T_c might imply exotic coupling mechanisms in the superconductor.

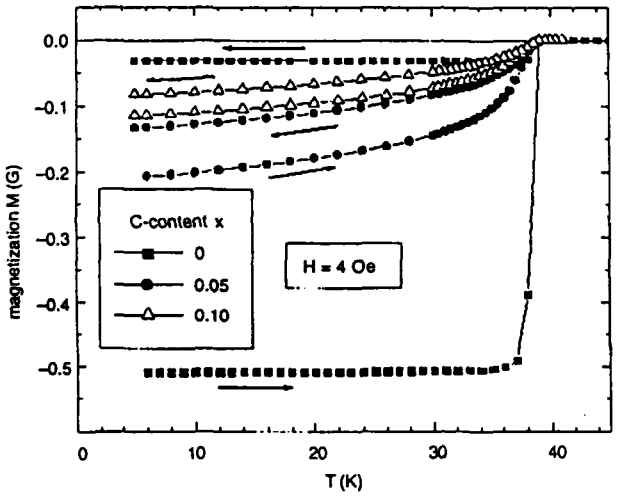

Figure 7. Temperature variation of magnetization (M) for $MgB_{2-x}C_x$ ($x = 0 - 0.1$) samples. The arrows indicate the ZFC and FC magnetization at a magnetic field of 4 Oe [51].

4.2. Magnetic properties :

Measurements of the magnetic moment in superconducting MgB_2 single crystals were reported by Zehetmayer *et al* [55]. The authors have calculated various fundamental parameters from the variation of magnetization with the applied magnetic field as discussed in section 4.3. The magnetic-field-dependent magnetization measurements on the MgB_2 superconductor were also reported by Dulcic *et al* [56] where the magnetic irreversibility in MgB_2 was concluded due to flux pinning or flux creep and three dimensional (3D) flux lattices melting. The magnetic susceptibility (Figure 8) of MgB_2 [56,57] showed the T_c value clearly around 40 K. From the damping of the muon precession signal, Panagopoulos *et al* [58] found the magnetic penetration depth (λ) at zero temperature to be ~ 85 nm. The low-temperature (< 20 K) penetration depth showed a T^2 dependence which is a strong evidence of unconventional superconducting pairing in MgB_2. Pissas *et al* [59] demonstrated the magnetic-field distribution of the pure vortex state in lightly doped $Mg_{1-x}Al_xB_2$ ($x \leq 0.025$) powder samples, by using ^{11}B nuclear magnetic resonance (NMR) in magnetic fields of 23.5 and 47 kOe. The magnetic-field distribution at $T = 5$ K was Al-doping dependent, revealing a considerable decrease of anisotropy in respect to pure MgB_2. The penetration depth λ

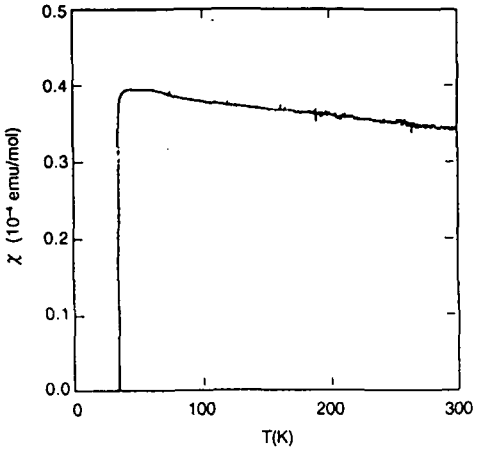

Figure 8. Temperature dependence of magnetic susceptibility (χ) of MgB_2 measured at $H = 1$T [57].

of MgB_2 was deduced both from the ac susceptibility χ and the magnetization M(H) of sorted powders [60]. The good agreement between the two sets of data without geometric correction for the grain orientation suggested MgB_2 to be an isotropic superconductor [60]. The magnetic susceptibility above T_c showed Pauli paramagnetism with a substantial T dependence [57]. The magnetic relaxation rate had very weak temperature dependence [61] below $1/2T_c$ showing a clear residual relaxation rate at 0 K, which could not be easily explained as due to thermally activated flux creep. Furthermore, the relaxation rate had strong field dependence. The flux dynamics of thin films was very similar to that of bulks although the relaxation rate in thin film was systematically higher than that of a bulk sample. All the results obtained from bulk and thin film suggested that the quantum effects, such as quantum fluctuation and tunneling, might dominate the flux dynamics. The magnetotransport data on dense wires of MgB_2 in applied magnetic fields (up to 18 T [62]) showed that the temperature and field dependencies of the electrical resistivity were consistent with MgB_2 behaving like a simple metal and following a generalized form of Kohler's rule. λ (T,H<130 Oe) showed a strong diamagnetic downturn below 10 K [34] which was completely suppressed by a dc magnetic field of 130 Oe. A theory for the proximity effect in the clean limit, together with an assumed distribution of the Mg layer thickness, qualitatively explained the field and temperature dependences of the data.

4.3. Critical fields (H_{c1} and H_{c2}) :

The lower critical field, $H_{c1}(0)$ of a well-shaped cylindrical dense sample was found to be 176 Oe [63]. The $\Delta\lambda\ (T) = \lambda\ (T) - \lambda(0)$ was found to be proportional to temperature T below 20 K.

However, from the isotropic s-wave BCS theory [63], $\Delta\lambda(T)/\lambda(0) \sim 3.3\,(T_c/T)^{1/2}\exp(-\Delta/k_BT)$ where Δ is the superconducting energy gap and k_B is the Boltzman constant. Thus the behavior of this superconductor is different from the isotropic s-wave superconductor and found to have anisotropic energy gap. It was found that a linear relation of $H_{c1}(T)$ also appeared in the whole temperature region below T_c. Furthermore, a finite slope of dH_{c1}/dT and $d\lambda(T)/dT$ remained down to the lowest temperature (2 K). The anisotropy ratio, γ decreased in a monotonic fashion [64] from 7 (at T = 1.8 K) to 4 (at T = 35 K) with increase of temperature. It was found that H_{c2} was linearly dependent on temperature near T_c and the dc irreversibility field exponent was ~1.4 [56]. H_{c2} of thin films obtained from measurement of the field dependence of the resistivity (Figure 9) was estimated to be more than 15 T at 20 K [65]. From figure 9, we see that the critical field H_{c2} increased with the decrease of temperature and the T_c decreased with the increase

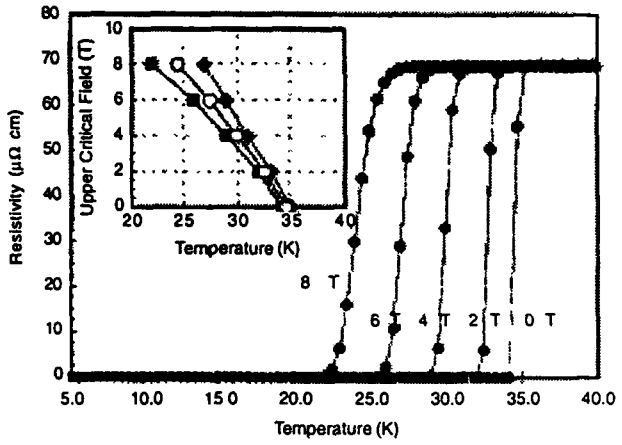

Figure 9. Resistivity *vs.* temperature for MgB_2 film [65] on c-plane sapphire substrate in different applied magnetic fileds (0-8T). The inset shows the upper critical field (H_{c2}) of the film. The onset temperature, temperature for maximum $d\rho/dT$ and end point temperature are indicated respectively by solid diamonds, open circles and solid squares.

of magnetic field. Zehetmayer *et al* [55] found from magnetic moment measurement that $\mu_0 H_{c2}^{c}(0) = 3.2$ T, $\mu_0 H_{c2}^{ab}(0) = 14.5$ T, $\gamma = H_{c2}^{ab}/H_{c2}^{c} = 4.6$, $\mu_0 H_c(0) = 0.28$ T, $\mu_0 H_{c1}^{ab}(0) = 22$ mT, $\mu_0 H_{c1}^{c}(0) = 63$ mT, $\lambda_{ab}(0) = 82$ nm, $\lambda_c(0) = 370$ nm, $\xi_{ab}(0) = 10.2$ nm, $\xi_c(0) = 2.3$ nm and Ginzburg-Landau (GL) parameter $\kappa(T_c) = \lambda/\xi = 4.7$, where γ is the anisotropy ratio and ξ is the coherence length. The H_{c2} of polycrystalline MgB_2 at 10 K was found to be 14 T [2]. But H_{c2} in polycrystalline MgB_2 was enhanced and the magnetic-field-induced broadening was significantly reduced with increasing grain size [7], probably due to reduced contamination at the grain boundaries. Single-crystalline MgB_2 exhibited [7] remarkable anisotropy of $H_{c2}(T)$ and irreversibility field $H^*(T)$ with anisotropy ratio $\gamma \sim 3\pm0.2$. The large broadening of the superconducting transition for the $H \| c$ direction indicated a significant suppression of $H^*(T)$ below H_{c2}^{c}, giving $H^{*c}(T) \sim 0.71\ H_{c2}^{c}(T)$. An accurate and complete $H_{c2}(T)$ curve determined [62] by using the electric transport measurement up to 18 T. $H_{c2}(T)$ indicated a linear variation with T over a wide range of temperature (7 K = T = 32 K) and had an upward curvature for T close to T_c [62]. These features are similar to those of other high GL (Ginzburg-Landau) parameter κ, clean limit, boron-bearing intermetallics superconductors, *viz.* YNi_2B_2C and $LuNi_2B_2C$ [62]. The bulk upper critical field $H_{c2}(T)$ of superconducting MgB_2 and its anisotropy were established [66] by analyzing experimental data on the temperature and magnetic-field dependences of the *ab*-plane thermal conductivity of a single-crystal sample in external magnetic fields, oriented both parallel (H_{c2}^{c}) and perpendicular (H_{c2}^{ab}) to the *c* axis of the hexagonal lattice. From numerical fits, the authors [66] deduced the anisotropy ratio $\gamma = 4.2$ at T = 0 K. Both the values and the temperature dependences of H_{c2}^{c} and H_{c2}^{ab} were distinctly different from the previously claimed values obtained from the measurements of the electrical resistivity. An irreversibility line strongly shifted towards higher magnetic fields resulting in $H_{irr}(T) \sim 0.8\ H_{c2}(T)$, whereas typically $H_{irr}(T) \sim 0.5\ H_{c2}(T)$ was observed for un-textured bulk samples [14]. These values exceeded from those of all other reported bulk samples and were in the range of values obtained for thin films.

4.4. Critical current density :

The nanocrystalline samples [14] revealed $J_c = 10^5$ Acm^{-2} at 20 K with 1 T magnetic field (Figure 10). The improved pinning of this material, which mainly consisted of spherical grains about 40–100 nm in size, was attributed to the large number of grain boundaries in the nanocrystalline state. The magnetic field and angular dependence of J_c at various temperatures between 32 and 38 K indicated pinning by point pinning centers and was in good agreement with the predictions of anisotropic Ginzburg-Landau model [67]. Anisotropy parameter (γ) of 2.55 was determined from the scaling behavior of J_c [67]. The J_c of Ti doped $Mg_{1-x}Ti_xB_2$ (x = 0–1) samples changed significantly with

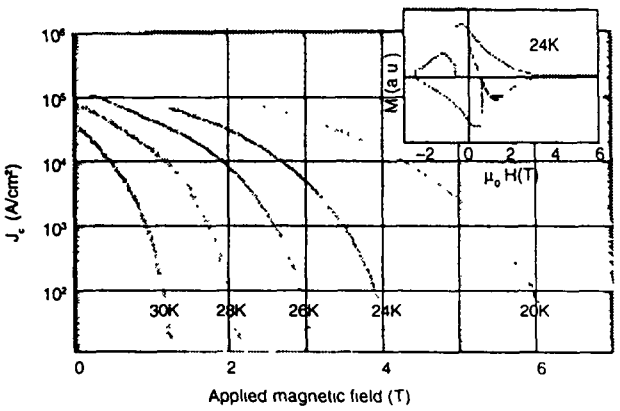

Figure 10. Critical current density (J_c) calculated from magnetization data [14] The inset shows the magnetization loop at 24 K (SQUID data) with two jumps at low magnetic fields

the doping level, and the best result achieved for x = 0.1 [19]. At 5 K, the J_c reached 2×10^6 Acm^{-2} in the self-field and 5×10^4 Acm^{-2} in 5 T field. At 20 K, the J_c was still as high as 1.3×10^6 Acm^{-2} in the self-field and 9.4×10^4 Acm^{-2} in a field of 2 T. It was further observed that partial melting occurred in the Ti-doped samples [19], resulting in an excellent grain connection and extremely high current density. In addition, some fine particles (with sizes from 10 to 100 nm) of the second phases induced by Ti doping were distributed in the MgB_2 matrix, and this played an important role in flux pinning enhancement. However, the shielding signal decreased monotonically with C content in $MgB_{2-x}C_x$ ($x = 0-0.1$) samples, which may be due to the carbon on the grain boundaries that isolated grains and prevented flow of super-currents on the perimeter [51].

4.5. Thermoelectric power :

Measurement of thermoelectric power (TEP) is an important tool to determine the type of carriers in the material. Sign of TEP are positive and negative respectively for the hole and electron type carriers. The TEP of MgB_2 is positive and decreases with the decrease of temperature [45]. Thus the carriers of this inter-metallic superconductor are hole-type. However, the TEP with a positive sign showed [57] a linear increase up to ~150 K but indicated a saturated behavior at higher temperatures, which suggested the existence of two types of charge carrier. Though the pressure decreases T_c [15, 44-46], the TEP value is found to increase with pressure [68] as evident from Figure 11. The results showed that the metallic hole carriers from σ bands are important to explain the temperature dependence of TEP. The decrease of T_c and increase of TEP with pressure [68] were explained by the two metallic bands (hole and electron bands) model. The density of states (DOS) of both the bands decreased with the increase of pressure but the electron band gave larger effect due to the anisotropic compressibility. As the DOS at the Fermi level, $N(E_F)$ decreases, the T_c will be decreased from that obtained from the Macmillan formula [69] and as the electrons are decreased more than holes, TEP will be increased because of the hole carrier superconductivity. The chemical pressure effect by doping of Al in MgB_2 also showed the increase of TEP with the increase of doping [53] though the doping decreases the T_c value [16].

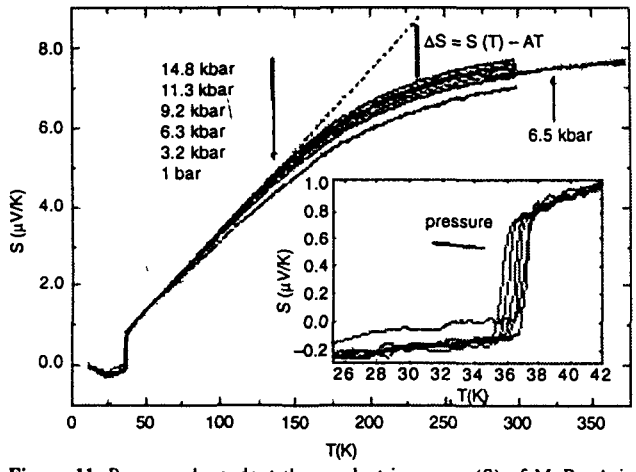

Figure 11. Pressure dependent thermoelectric power (S) of MgB_2. A is the slope of the linear-T dependence curve between T_c and 120 K [68]. The inset shows the magnified low temperature region.

4.6. Thermal conductivity :

Thermal conductivity (k) of single-crystalline hexagonal MgB_2 in normal state, superconducting state and in mixed state have been elaborately studied by Sologubenko *et al* [70] both in presence and absence of magnetic fields. The *ab*-plane thermal conductivity (k) as a function of magnetic field H with orientations both parallel and perpendicular to the c axis and at temperatures between 0.5 and 300 K has been investigated [70]. In the mixed state, $k(H)$ at constant temperatures, revealed features that were not typical for common type-II superconductors. A nonlinear temperature dependence of the electronic thermal conductivity was observed in the field-induced normal state at low temperatures. This behavior was at variance with the Wiedemann and Franz law, and suggested an unexpected instability of the electronic subsystem. The thermal conductivity (Figure 12) showed suppression below T_c without a clear anomaly at T_c which is considered to be as a result of the reduction of the normal charge carrier concentration below T_c [57].

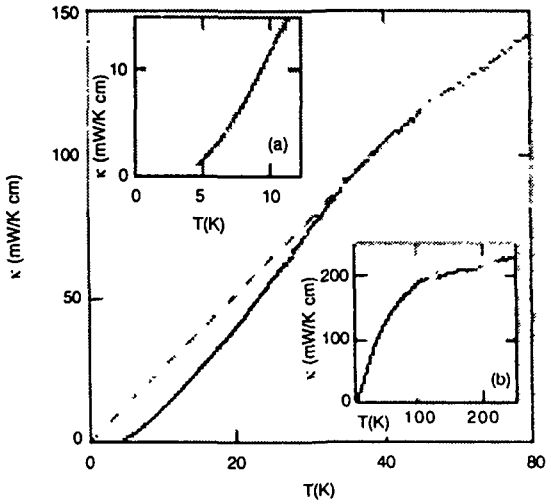

Figure 12. Temperature dependence of thermal conductivity (k) of MgB_2 below 60 K [57]. The dashed line is the guide to the eye The insets (a) and (b) show those upto 10 K and 250 K respectively.

4.7. Hall effect:

The mixed-state Hall resistivity ρ_{xy} and the longitudinal resistivity ρ_{xx} in superconducting MgB_2 thin films have been measured as a function of the magnetic field over a wide range of current densities from 10^2 to 10^4 Acm^{-2} [71]. A universal Hall scaling behavior was observed [71] with a constant exponent β of 2.0±0.1 in $\rho_{xy} = A\rho_{xx}^{\beta}$, which was independent of the magnetic field, the temperature, and the current density. This result was interpreted well within the context of theories. Jin *et al* [72] have investigated the temperature and magnetic field

dependence of the Hall coefficient (R_H) of two well-characterized superconducting MgB_2 films (T_{c0} = 38 K) both in the normal and superconducting states. Their results showed that the normal-state R_H value was positive (Figure 13) and increased with increasing temperature, independent of the applied magnetic field. They also found that $R_H^{-1} \propto T$(40–300 K) and the Hall angle θ_H followed cot $\theta_H \propto T^2$(100–300 K). As the sample was cooled below $T_c(H)$, R_H decreased rapidly with temperature and changed its sign before it reached zero. The position and magnitude at which R_H showed a minimum depending on the applied magnetic field [72].

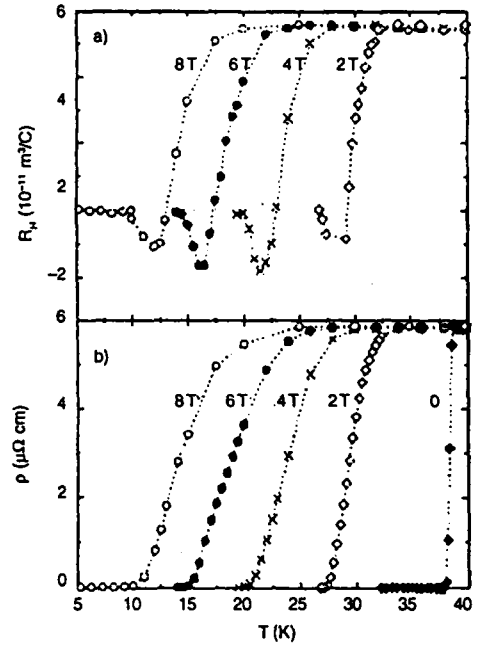

Figure 13. Temperature dependence of (a) R_H and (b) longitudinal resistivity of MgB_2 thin films [72] at different magnetic fields (0-8T).

4.8. Specific heat :

Yang *et al* [12] have measured the low-temperature specific heat $C(T)$ for polycrystalline MgB_2. Figure 14 shows the C *vs.* T and C/T *vs.* T curves for polycrystalline MgB_2 [12] at H=0 and 8T. Figure 15 shows the $\Delta C/T$ *vs.* temperature for polycrystalline MgB_2 [12] where $\Delta C = C(H) - C(8T)$. Together with the small specific heat jump $\Delta C/\gamma T_c = 1.09$, γ being the anisotropic parameter stated as the anisotropic s-wave or multicomponent order parameter, Yang *et al* [12] observed that the magnetic field dependence of anisotropic parameter $\gamma(H)$ was neither linear for a fully gapped s-wave superconductor nor $H^{1/2}$ dependent for nodal order parameter. Thus, the intriguing behavior of $\gamma(H)$ was associated with the intrinsic electronic properties other than flux pinning. Boron isotope effect was studied [21] on the C(T) of MgB_2. C(T) of MgB_2, in the temperature range between 3 and 220 K, were reported by Wälti *et al* [73]. Based on a modified Debye-Einstein model, the authors [73] have achieved a rather accurate account of the lattice contribution to the specific heat, separating the electronic contribution from the total measured specific heat. From their result for the electronic specific heat, they estimated the electron-phonon coupling constant ϕ to be of the order of 2, significantly enhanced compared to common weak-coupling values ≤ 0.4. Their data also indicated that a conventional, s-wave type BCS model could account for the electronic specific heat in the superconducting state of MgB2.

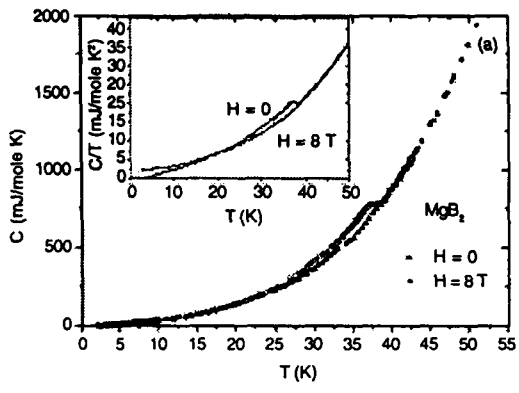

Figure 14. Temperature variation of specific heat of MgB_2 at H = 0 and 8 T [12]. The anomaly around 39 K manifests the bulk superconductivity. The inset shows C/T *vs.* T.

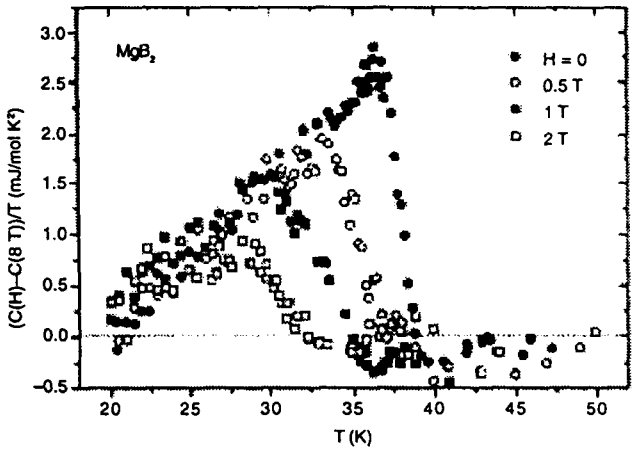

Figure15: Variation of $\Delta C/T = (C(H) - C(8T))/T$ with temperature at different magnetic fields (0-2T) for polycrystalline MgB_2 [12].

4.9. Optical properties :

X-ray emission and absorption spectra of the constituents of MgB_2 presented by Kurmaev *et al* [74] were in good agreement with the calculated X-ray spectra, taking dipole matrix elements into account. The comparison of X-ray emission spectra of graphite, AlB_2, and MgB_2 in the binding energy scale, supported the idea of charge transfer from σ to π bands, which creates holes at the top of the bonding σ bands and drives the high-T_c superconductivity in MgB_2. A c-axis oriented thin film and a high-density sintered pellet of MgB_2 have been studied by X-ray photoemission spectroscopy and the measured valence band was consistent with the calculated density of states [75]. Raman and infrared absorption spectra of $Mg_{1-x}Al_xB_2$ have been

studied by Postorino *et al* [76] for $0 \leq x \leq 0.5$ in the frequency range of the phonon spectrum. The data showed a remarkable dependence on the Al content and the suppression of the superconducting phase at high Al content was established from the spectra [76]. Goncharov *et al* [77] reported Raman spectra and synchrotron x-ray diffraction measurements of lattice parameters of polycrystalline MgB_2 under hydrostatic pressure up to 14.7 GPa. An anomalously broadened Raman band at 620 cm^{-1} was observed (Figure 16) that exhibited a large linear pressure shift of its frequency. Hlinka *et al* [78] presented a detailed Raman scattering study of the unusually broad E_{2g}

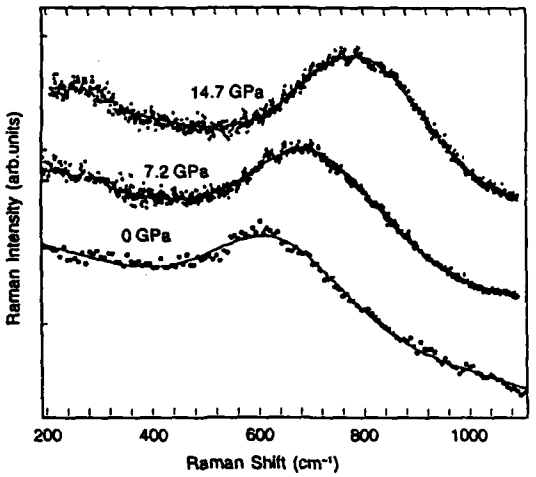

Figure16. Raman spectra of MgB_2 at elevated pressures (0-14.7 GPa). The excitation wave length was 514.5 nm [77].

phonon mode in MgB_2 crystal. It was shown by polarized Raman scattering on a few-micron-size crystallites with natural faces that the observed broad Raman feature obeyed the selection rules of an E_{2g} mode. Raman spectra on high quality polycrystalline superconducting MgB_2 wires revealed a very symmetric E_{2g} phonon line near 615 cm^{-1} with the room temperature line width of 260 cm^{-1} only. Microwave surface impedance measurements were carried out in applied magnetic fields up to 8 T [56]. The low-field data showed an absence of weak links in the superconducting state. By inverting the surface impedance data, the authors [56] found a vortex depinning frequency that decreased with increasing magnetic field, which was characteristic of collective pinning. Andreev reflection tunneling spectroscopy on MgB_2/PtIr point contacts has systematically been investigated [79] to find the superconducting energy gaps. By fitting the tunneling conductance to Blonder-Tinkham-Klapwijk (BTK) theory [80], *s*-wave superconducting gaps were resolved [79].

4.10. Mechanical properties :

Cordero *et al* [81] measured the complex dynamic elastic modulus of MgB_2 between 1.3 and 650 K at frequencies included between 5 and 70 kHz by anelastic spectroscopy. The Young's modulus presented an anomalous softening on cooling below 400 K and hysteresis between cooling and heating. Intense relaxation processes, however, could account for such anomalies, with maxima between 50 and 150 K. Additional intense relaxation processes were observed above room temperature, and their possible origin was discussed [81]. The influence of the highly anharmonic in-plane vibration modes of the B atoms on the elastic and anelastic properties of MgB_2 was discussed in detail [46]. MgB_2 yielded the bulk modulus B = 147.2 ± 0.7 GPa [46].

4.11. Acoustical properties :

Temperature dependent elastic constants and ultrasonic attenuation of polycrystalline MgB_2 were reported [82]. An electromagnetic acoustic resonance method detected the specimen's resonance frequencies, from which the authors [82] derived the elastic constants for nonporous MgB_2 using micromechanical calculation. The bulk and shear moduli extrapolated to 0 K were determined to be 96.6 GPa and 74.2 GPa, respectively, which gave the Debye temperature θ_D = 819 K and the electron-phonon coupling constant ϕ = 0.76–0.89 using McMillan formula [69]. In the temperature behavior of ultrasonic attenuation, two anomalous peaks were observed near 30 K [82].

4.12. Positron annihilation properties :

Pujari *et al* [83] reported results on two-detector coincidence Doppler and lifetime spectroscopic measurements as a function of temperature (12–300 K) in the MgB_2 superconductor. Coincidence Doppler measurements in Mg, B, and MgB_2 indicated that the positrons annihilate primarily in the boron sublattice in MgB_2. The positron lifetime in MgB_2 was seen to decrease at the onset of superconductivity. These results provided direct evidence of charge density fluctuations in the boron layer associated with the superconducting transition.

5. Energy gap of MgB_2 and type of superconductivity

The most arguable and controversial issue of MgB_2 superconductor since its discovery [1] is the superconducting energy gap and the type of superconductivity. Far-infrared reflectance of MgB_2 film has been measured by Fourier-transform spectroscopy for frequencies 10 $cm^{-1} < \nu < 4000$ cm^{-1} above and below the superconducting transition by Pimenov *et al* [84]. The data provided clear experimental evidence for the onset of a superconducting gap at 24 cm^{-1} at T = 5 K. On increasing the temperature, the gap energy is increased, contrary to what is expected in isotropic BCS superconductors. The small zero-temperature gap value and its unconventional increase on increasing temperature were explained by a highly anisotropic or multiple gap function. The distribution of the obtained gaps from Andreev reflection tunneling spectroscopy [79] unequivocally showed two groups: one centered at 9.8 meV and the other peaked at 2.8 meV with a gap ratio of 3.5. For two typical gaps Δ_1 = 1.92 meV and Δ_2 = 3.45 meV, their temperature-dependent behavior displayed that $\Delta_1(T)$ unambiguously persisted to the bulk T_c at 39 K, and $\Delta_2(T)$ closes

to 33 K. In Al-doped MgB_2, the result of nuclear-spin-lattice relaxation rate $1/T_1$, where T_1 is the spin-lattice relaxation time, in the superconducting state revealed that the size of the gap was not changed by substituting Al for Mg [85]. The reduction in T_c by Al doping was shown to be due to the decrease of the density of states at the Fermi level $N(E_F)$. According to the McMillan equation [69], an experimental relation between T_c and the relative change in $N(E_F)$ estimated a characteristic phonon frequency ω ~700 cm^{-1} and an electron-phonon coupling constant ϕ ~ 0.87. These results suggested that the high-T_c superconductivity in MgB_2 is mediated by the strong electron-phonon coupling with high-frequency phonons. Specific heat, $C(T)$ below 10 K vanished exponentially [12], which unambiguously indicated a fully opened superconducting energy gap. However, this gap was found to be too small to account for T_c of MgB_2 [12]. Removal of the Mg by chemical etching [34] from the surface of MgB_2 resulted in an exponential temperature dependence for penetration depth $\lambda(T,H)$ with an energy gap of $2\Delta(0)/T_c \approx 1.54$ [$\Delta(0) \approx 2.61$ meV]. The tunneling spectra [86] exhibited BCS-like gap structures, with gap parameters in the range of 5 to 7 meV, yielding a ratio of $2\Delta/k_BT_c$ ~3–4. This suggested that MgB_2 as a conventional BCS *s*-wave superconductor, either in the weak coupling or in the 'intermediate coupling' regime. The boron isotope effect in MgB_2 was consistent with the material being a phonon-mediated BCS superconductor [21]. The standard Ginzburg-Landau and London model relations led to a consistent data set and indicated that MgB_2 was a clean limit superconductor of intermediate coupling strength with very pronounced anisotropy effects [55]. The behavior of thermal conductivity [70] was not typical for common type-II superconductors and was attributed to be associated with the field-induced reduction of two superconducting energy gaps, significantly different in magnitude. It has been concluded [45] from pressure effect study that the electron-phonon interaction plays a significant role in the superconductivity of MgB_2. The results of pressure dependent study supported the emerging picture that MgB_2 is a BCS superconductor with electron-phonon pairing interaction [46]. Masui *et al* [87] extracted phonon contributions from the transport properties of MgB_2 single crystal. The temperature dependence of the in-plane resistivity was well explained by the Bloch-Grüneisen formula with the Debye temperature θ_D ~ 400 K, taking into account an additional contribution of the E_{2g} phonon mode (~890 K). From the thermoelectric power, the authors [87] found a phonon-drag peak around 70 K, which gave a consistent estimation of θ_D with the resistivity result. Thus from the above discussion, it seems that MgB_2 is a conventional BCS type *s*-wave superconductor with two energy gaps. But this is still controversial as some groups reported differently and needs to be clarified

6. Theoretical studies

Ravindran *et al* [88] have made electronic structure calculations for MgB_2 and closely related systems for understanding the unexpected superconducting behavior of MgB_2. Their calculated Debye temperature (θ_D) from the elastic properties indicated that the average phonon frequency (ν_{ph}) was very large in MgB_2 compared with those of other superconducting intermetallics and its exceptionally higher T_c can be explained through a BCS mechanism only if phonon softening occurs or the phonon modes are highly anisotropic. They [88] have found that Fermi energy E_F, in the closely related compound MgB_4, was lying in a pseudogap with a negligibly small density of states at E_F, which was not favorable for superconductivity The same authors [88] also calculated the single-crystal elastic constants for MgB_2 by the accurate full-potential method and derived the directional-dependent linear compressibility, Young's modulus, shear modulus, and relevant elastic properties from these results Ravindran *et al* [88] have observed large anisotropy in the elastic properties consistent with recent high-pressure findings Their calculated polarized optical dielectric tensor also showed highly anisotropic behavior even though it possessed isotropic transport property The mixed bonding character of MgB_2 has been verified from density of states (DOS), charge density, and crystal orbital Hamiltonian population analyses [88] The BCS 'electron-phonon' mechanism and the unconventional 'hole mechanism' have been proposed for the explanation of high temperature superconductivity observed in MgB_2 [48] The 'hole mechanism' predicted that T_c would drop rapidly to zero as holes are added, while the 'electron-phonon mechanism' appeared to predict increasing T_c for a substantial range of hole doping [48] The frequency and momentum dependent dielectric function $\varepsilon(q,\omega)$ as well as the energy loss function $\mathrm{Im}\left[\varepsilon^{-1}(q,\omega)\right]$ were calculated [89] by using the plane-wave pseudopotential method and the tight-binding version of the linear muffin-tin orbital method. Zhukov *et al* [89] found two plasmon modes dispersing at energies ~2–8 eV and ~18–22 eV. Both plasmon modes demonstrated clearly anisotropic behavior of both the peak position and the peak width The specific heat C and the electronic and phononic thermal conductivities k_e and k_{ph} were calculated [90] in the mixed state for magnetic fields H, near upper critical field H_{c2}, including the effects of supercurrent flow and Andreev scattering. The resulting function C(H) was nearly linear, while k_e(H) exhibited an upward curvature near H_{c2}. The slopes decreased with impurity scattering in agreement with the experimental data. The ratio of normal and superconducting state phonon relaxation times $\tau_n/\tau_s = g(\omega_0,H)$, where ω_0 is the phonon energy, smeared out around $\omega_0 = 2\Delta$ and tends to unity for increasing H This led to a rapid reduction of $k_{ph}(H)$ in MgB_2 for relatively small fields due to the rapid suppression of the smaller energy gap A model by Mazin *et al* [91] predicted strong suppression of T_c by interband impurity scattering and, presumably, a strong correlation between the T_c and the residual resistivity Mazin *et al* [91] argued that this fact could be understood if the band disparity of the electronic structure of both superconducting and normal states were taken into account Band structure calculations indicated that Mg was substantially ionized, and

the bands at the Fermi level derived mainly from B orbital [92]. Strong bonding with an ionic component and considerable metallic density of states (DOS) yielded a sizable electron-phonon coupling. Kortus *et al* [92] estimated high phonon frequencies in the range between 300 to 700 cm^{-1} which produced a high T_c consistent with experimental results. The DOS of MgB_2 and its constituents [92] are shown in Figure 17. Similar behavior of the DOS was also reported by Ravindran *et al* [88]. The DOS has a minimum [88, 92] just above the Fermi level (E_F) which can explain the decrease of T_C with the increase of pressure, as the pressure shifts the E_F to higher energies and T_c is directly proportional to $N(E_F)$ from Macmillan formula [69].

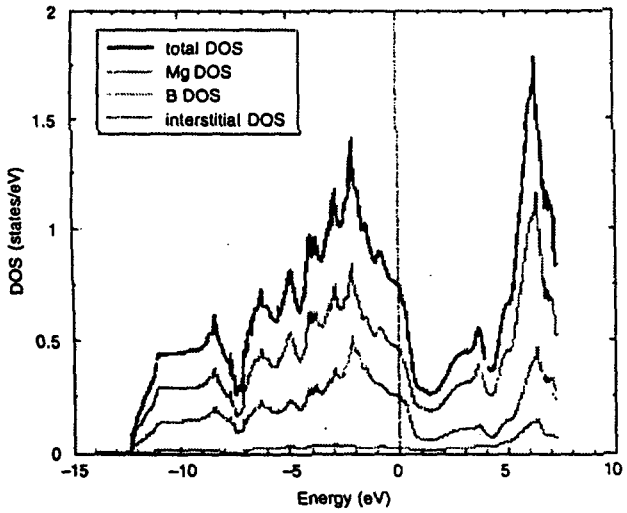

Figure 17. Total density of states (DOS) of MgB_2. The DOS of the constituents Mg and B as well as interstitial DOS are also presented [92]. DOS of MgB_2, Mg, B and interstitial are shown respectively from the top to bottom of the figure.

7. Application

Copper oxide based high temperature cuprate superconductors (HTSC) are limited in their use as their critical current density (J_c) is governed by many factors like size of the superconducting grains, intra and inter grain connectivity, texture of the superconducting grain *etc.* Though the wires/tapes made of HTSC can be operated above liquid nitrogen temperature (77 K), these are expensive due to the use of 70% silver for fabrication. MgB_2 offers the possibility of a new class of superconducting materials having low cost and high performance for magnetic and electronic applications. The advantages of MgB_2 are its lower anisotropy compared to that of HTSC, larger coherence lengths and comparatively cleaner grain boundaries to current flow. Its high T_c value, simple crystal structure, large coherence lengths, high critical current densities and fields promise that MgB_2 would be the most probable candidate for large scale applications and devices. Considering its higher T_c, J_c values and low cost compared to the existing metallic superconductor NbTi *etc.*, there is an immense possibility of MgB_2 to be emerging out as the next generation superconductor for technological applications. It would also provide higher operating temperature compared to the present Nb based electronics with higher device speed.

8. Conclusions

The preparation and characterization of MgB_2 superconductor in the form of bulk, thin film, single crystal and wires/tapes have been reviewed up to October, 2002. Its superconducting transition temperature (T_c) is ~ 40 K and anisotropic ratio γ ($=H_{c2}^{ab}/H_{c2}^{c}$) ~ 1- 5 with lower critical field (H_{c1}) ~ 25-48 mT and upper critical field, $H_{c2}(0)$ ~ 40 T. The critical current density (J_c) is as high as 1.3×10^6 Acm^{-2} in the self-field and 9.4×10^4 Acm^{-2} in a magnetic field of 2 T at the temperature of 20 K. The thermoelectric power and Hall coefficients are positive indicating hole-type carrier in MgB_2 in normal state. It has two superconducting energy gaps Δ_1 ~ 1.92 meV and Δ_2 ~ 3.45 meV. This superconductor has a minimum density of states (DOS) just above the Fermi level. The isotope effect on the superconducting properties, the linear T dependence of H_{c2} with a positive curvature near T_c and the shift of T_c to lower temperatures with increasing magnetic field indicate that it is a conventional *s*-wave BCS type superconductor. On the other hand, the quadratic temperature dependence of the penetration depth as well as the sign reversal of the Hall coefficient near T_c indicates an unconventional superconductivity like high-T_c cuprates. Intensive research is still going on to solve these basic controversies. Though the raw materials are cheap and easily affordable, the requirement of high pressure (> 3 GPa) to synthesize this superconductor makes it difficult to manufacture in an ordinary laboratory without having high pressure facility for material synthesis. However, this minor problem could be easily solved if MgB_2 with its doped family are found to replace the NbTi type liquid He- based superconductors.

Acknowledgment

This work was supported by National Science Council of Republic of China.

References

[1] J Nagamatsu, N Nakagawa, T Muranaka, Y Zenaitani and J Akimitsu *Nature* (London) **410** 63 (2001)

[2] D C Larbalestier, L D Cooley, M O Rikel, A A Polyanskii, J Jiang, S Patnaik, X Y Cai, D M Feldmann, A Gurevich, A A Squitieri, M T Naus, C B Eom, E E Hellstrom, R J Cava, K A Regan, N Rogado, M A Hayward, T He, J S Slusky, P Khalifah, K Inumaru and M Hass *Nature* (London) **410** 186 (2001)

[3] C B Eom, M K Lee, J H Choi, L J Belenky, X Song, L D Cooley, M T Naus, P Patnaik, J Jiang, M Rikel, A Polyanskii, A Gurevich, X Y Cai, S D Bu, S E Babcock, E E Hellstorm, D C Larbalestier, N Rogado, K A Regan, M A Hayward, T He, J S Slusky, K Inumaru, M K Hass and R J Cava *Nature* (London) **411** 558 (2001)

[4] F Simon, A Jánossy, T Fehér, and F Murányi, S Garaj, L Forró, C Petrovic, S L Bud'ko, G Lapertot, V G Kogan, and P C Canfield *Phys. Rev. Lett.* **87** 047002 (2001)

[5] S L Bud'ko, V G Kogan and P C Canfield *Phys. Rev.* B **64** 180506 (2001)

[6] Y Takano, H Takeya, H Fujii, H Kumakura, T Hatano, K Togano, H Kito and H Ihara *Appl Phys Lett* **78** 2914 (2001)

[7] A K Pradhan, Z X Shi, M Tokunaga, T Tamegai, Y Takano, K Togano, H Kito and H Ihara *Phys Rev* B **64** 212509 (2001)

[8] C U Jung, M S Park, W N Kang, M S Kim, S Y Lee and S -I Lee *Physica* C **353** 162 (2001)

[9] W N Kang, C U Jung, Kijoon H P Kim, Min-Seok Park, S Y Lee, Hyeong-Jin Kim, Eun-Mi Choi, Kyung Hee Kim, Mun-Seog Kim and Sung-Ik Lee *Appl Phys Lett* **79** 982 (2001)

[10] Mun-Seog Kim, C U Jung, Min-Seok Park, S Y Lee, Kijoon H P Kim, W N Kang and Sung-Ik Lee *Phys Rev* B **64** 012511 (2001)

[11] X H Chen, Y S Wang, Y Y Xue, R L Meng, Y Q Wang and C W Chu *Phys Rev* B **65** 024502 (2001)

[12] H D Yang, J-Y Lin, H H Li, F H Hsu, C J Liu, S -C Li, R -C Yu and C -Q Jin *Phys Rev Lett* **87** 167003 (2001)

[13] S C Li, J L Zhu, R C Yu, F Y Li, Z X Liu and Changquin Jin *Chin Phys* **10** 338 (2001)

[14] A Gümbel, J Eckert, G Fuchs, K Nenkov, K -H Müller and L Schultz *Appl Phys Lett* **80** 2725 (2002)

[15] M Monteverde, M Nunez-Regueiro, N Rogado, K A Regan, M A Hayward, T He, S M Loureiro and R J Cava *Science* **292** 75 (2001)

[16] J S Slusky, N Rogado, K A Regan, M A Hayward, P Khalifah, T He, K Inumaru, S M Loureiro, M K Haas, H W Zandbergen and R J Cava *Nature* **410** 343 (2001)

[17] Y G Zhao, X P Zhang, P T Qiao, H T Zhang, S L Jia, B S Cao M H Zhu, Z H Han, X L Wang and B L Gu Cond-Mat/**0103077** (2001)

[18] I Felner *Physica* C **353** 11 (2001)

[19] Y Zhao, Y Feng, C H Cheng, L Zhou, Y Wu, T Machi, Y Fudamoto, N Koshizuka and M Murakami *Appl Phys Lett* **79** 1154 (2001)

[20] A J Zaleski, W Iwasieczko, D Kaczorowski, H Drulis, M Tkacz, O J Zogal and J Klamut Low *Temp Phys* **27** 780 (2001)

[21] S L Bud'ko, G Lapertot, C Petrovic, C E Cunningham, N Anderson and P C Canfield *Phys Rev Lett* **86** 1877 (2001)

[22] W N Kang, H J Kim, E M Choi, C U Jung and S I Lee *Science* **292** 1521 (2001)

[23] D H A Blank, H Hilgenkamp, A Brinkman, D Mijatovic, G Rijnders and H Rogalla *Appl Phys Lett* **79** 394 (2001)

[24] S R Shinde, S B Ogale, R L Greene, T Venkatesan, P C Canfield, S L Bud'ko, G Lapertot and C Petrovic *Appl. Phys Lett* **79** 227 (2001)

[25] S Jin, H Mavoori, C Bower and R B V Dover *Nature* (London) **411** 563 (2001)

[26] G Grasso, A Malagoli, C Ferdeghini, S Roncallo, V Braccini, A S Siri and M R Cimberle *Appl Phys Lett* **79** 230 (2001)

[27] Y Yamada, B Obst and R Flukiger *Supercond. Sci Technol* **4** 165 (1991)

[28] G Grasso, A Perin, B Hensel and R Flukiger *Physica* C **217** 335 (1993)

[29] M Lelovic, P Krishnaraj, N G Eror and U Balachandran *Physica* C **242** 246 (1995)

[30] D C Larbalestier, X Y Cai, Y Feng, H Edelman, A Umezawa, G N Riley and W L Carter *Physica* C **221** 299 (1994)

[31] N V Vo, S X Dou and H K Liu *Physica* C **250** 139 (1995)

[32] H Suo, C Beneduce, M Dhalle, N Musolino, J Y Genound and R Flukiger *Appl Phys Lett* **79** 3116 (2001)

[33] A K Pradhan, Y Feng, Y Zhao, N Koshizuka, L Zhou, P X Zhang, X H Liu, P Ji, S J Du and C F Liu *Appl Phys Lett* **79** 1649 (2001)

[34] R Prozorov, R W Giannetta, S L Bud'ko and P C Canfield *Phys Rev* B **64** 180501 (2001)

[35] H Kumakura, A Matsumoto, H Fujii and K Togano *Appl Phys Lett* **79** 2435 (2001)

[36] M Xu, H Kitazawa, Y Takano, J Ye, K Nishida, H Abe, A Matsushita, N Tsujii and G Kido *Appl Phys Lett* **79** 2779 (2001)

[37] M M R Naslain, A Guette and M Barret *J Solid State Chem* **8** 68 (1973)

[38] C Buzea and T Yamashita *Supercond Sci Technol* **14** R115 (2001)

[39] P Ravindran, P Vajeeston, R Vidya, A Kjekshus and H Fjellvåg *Phys Rev* B **64** 224509 (2001)

[40] Serena Margadonna, Kosmas Prassides, Ioannis Arvanitidis Michael Pissas, Georgios Papavassiliou and Andrew N Fitch *Phys Rev* B **66** 014518 (2002)

[41] K D Belashchenko, M van Schilfgaarde and V P Antropov *Phys Rev* B **64** 092503 (2001)

[42] V Likodimos and M Pissas *Phys Rev* B **65** 172507 (2002)

[43] C U Jung, Min-Seok Park, W N Kang, Mun-Seog Kim, Kijoon H P Kim, S Y Lee and Sung-Ik Lee *Appl Phys Lett* **78** 4157 (2001)

[44] E Saito, T Taknenobu, T Ito, Y Iwasa, K Prassides and T Arnira *J Phys Condens Matter* **13** L267 (2001)

[45] B Lorenz, R L Meng and C W Chu *Phys Rev* B **64** 012507 (2001)

[46] T Tomita, J J Hamlin, J S Schilling, D G Hinks and J D Jorgensen *Phys Rev* B **64** 092505 (2001)

[47] J E Hirsch *Studies of High Temperature Superconductors* ed by A Narlikar, Nova Sci Pub , New York (2002)

[48] J E Hirsch and F Marsiglio *Phys Rev* B **64** 144523 (2001)

[49] Alexander F Goncharov, Viktor V Struzhkin, Eugene Gregoryanz Jingzhu Hu, Russell J Hemley, Ho-kwang Mao, G Lapertot S L Bud'ko and P C Canfield Cond-Mat/**0104042** (2002)

[50] Y Moritomo and Sh Xu Cond-Mat/**0104568** (2002)

[51] M Paranthaman, J R Thompson and D K Christen Cond Mat/ **0104086** (2002)

[52] T Takenobu, T Ito, Dam H Chi, K Prassides and Y Iwasa Cond-Mat/**0103241** (2002)

[53] B Lorenz, R L Meng, Y Y Xue, C W Chu *Phys Rev* B **64** 052513 (2001)

[54] M R Cimberle, M Novak, P Manfrinetti and A Palenzona, cond-mat/**0105212**

[55] M Zehetmayer, M Eisterer, J Jun, S M Kazakov, J Karpinski, A Wisniewski and H W Weber Phys Rev B **66** 052505 (2002)

[56] A Dulcic, D Paar, M Pozek, G V M Williams, S Krämer, C U Jung, Min-Seok Park and Sung-Ik Lee *Phys Rev* B **66** 014505 (2002)

[57] T Muranaka, J Akimitsu and M Sera *Phys Rev* B **64** 020505(R) (2001)

[58] C Panagopoulos, B D Rainford, T Xiang, C A Scott, M Kambara and I H Inoue *Phys Rev* B **64** 094514 (2001)

[59] M Pissas, G Papavassiliou, M Karayanni, M Fardis, I Maurin I Margiolaki, K Prassides and C Christides *Phys Rev* B **65** 184514 (2002)

[60] X H Chen, Y Y Xue, R L Meng and C W Chu *Phys Rev* B **64** 172501 (2001)

[61] H H Wen, S L Li, Z W Zhao, H Jin, Y M Ni W N Kang Hyeong Jin Kim, Eum-Mi Choi and Sung-Ik Lee *Phys Rev* B **64** 134505 (2001)

[62] S L Bud'ko, C Petrovic, G Lapertot, C E Cunningham P C Canfield, M H Jung and A H Lacerda *Phys Rev* B **63** 220503(R) (2001)

[63] S L Li, H H Wen Z W Zhao, Y M Ni, Z A Ren G C Che H P Yang, Z Y Liu and Z X Zhao *Phys Rev* B **64** 094522 (2001)

[64] Sergey L Bud'ko and Paul C Canfield *Phys Rev* B **65** 212501 (2002)

[65] W Jo, J -U Huh, T Ohnishi, A F Marshall, M R Beasley and R H Hammond *Appl Phys Lett* **80** 3563 (2002)

[66] A V Sologubenko, J Jun, S M Kazakov, J Karpinski and H R Ott *Phys Rev* B **65** 180505(R) (2002)

[67] Shashwati Sen, Ajay Singh, D K Aswal, S K Gupta, J V Yakhmi, V C Sahni, Eun-Mi Choi, Hyeong-Jin Kim, Kijoon H P Kim, Hyun Sook Lee, W N Kang and Sung-Ik Lee *Phys Rev* B **65** 214521 (2002)

[68] E S Choi, W Kang, J Y Kim, Min-Seok Park, C U Jung, Heon-Jung Kim and Sung-Ik Lee, Cond-Mat/0104454 (2002)

[69] W L McMillan *Phys Rev* **167** 331 (1968), P B Allen and R C Dynes *Phys Rev* B **12** 905 (1975)

[70] A V Sologubenko, J Jun, S M Kazakov, J Karpinski and H R Ott *Phys Rev* B **66** 014504 (2002)

[71] W N Kang, Hyeong-Jin Kim, Eun-Mi Choi, Heon Jung Kim, Kijoon H P Kim and Sung-Ik Lee *Phys Rev* B **65** 184520 (2002)

[72] R Jin, M Paranthaman, H Y Zhai, H M Christen, D K Christen and D Mandrus, *Phys Rev* B **64** 220506(R) (2001)

[73] Ch Wälti, E Felder, C Degen, G Wigger, R Monnier, B Delley and H R Ott *Phys Rev* B **64** 172515 (2001)

[74] E Z Kurmaev, I I Lyakhovskaya, J Kortus, A Moewes, N Miyata, M Demeter, M Neumann, M Yanagihara, M Watanabe, T Muranaka and J Akimitsu *Phys Rev* B **65** 134509 (2002)

[75] R P Vasquez, C U Jung, Min-Seok Park, Heon-Jung Kim, J Y Kim and Sung-Ik Lee *Phys Rev* B **64** 052510 (2001)

[76] P Postorino, A Congeduti, P Dore, A Nucara, A Bianconi, D Di Castro, S De Negri and A Saccone *Phys Rev* B **65** 020507(R) (2002)

[77] Alexander F Goncharov, Viktor V Struzhkin, Eugene Gregoryanz, Jingzhu Hu, Russell J Hemley, Ho-kwang Mao, G Lapertot, S L Bud'ko and P C Canfield *Phys Rev* B **64** 100509(R) (2001)

[78] J Hlinka, I Gregora, J Pokorny, A Plecenik, P Kus, L Satrapinsky and S Benacka *Phys Rev* B **64** 140503(R) (2001)

[79] Zhuang-Zhi Li, Hong-Jie Tao, Yi Xuan Zhi-An Ren, Guang-Can Che and Bai-Ru Zhao *Phys Rev* B **66** 064513 (2002)

[80] G E Blonder M Tinkham and T M Klapwijk *Phys Rev* B **25** 4515 (1982)

[81] F Cordero, R Cantelli, G Giunchi and S Ceresara *Phys Rev* B **64** 132503 (2001)

[82] T Ichitsubo, H Ogi, S Nishimura, T Seto M Hirao and H Inui *Phys Rev* B **66** 052514 (2002)

[83] P K Pujari, K Sudarshan A Goswami, S B Manohar, D K Aswal Ajay Singh, Shashwati Sen and S K Gupta *Phys Rev* B **66** 012518 (2002)

[84] A Pimenov, A Loidl and S I Krasnosvobodtsev *Phys Rev* B **65** 172502 (2002)

[85] H Kotegawa, K Ishida, Y Kitaoka, T Muranaka, N Nakagawa, H Takagiwa and J Akimitsu *Phys Rev* B **66** 064516 (2002)

[86] Amos Sharoni, Israel Felner and Oded Millo *Phys Rev* B **63** 220508(R) (2001)

[87] T Masui, K Yoshida, S Lee, A Yamamoto and S Tajima *Phys Rev* B **65** 214513 (2002)

[88] P Ravindran, P Vajeeston, R Vidya, A Kjekshus and H Fjellvåg *Phys Rev* B **64** 224509 (2001)

[89] V P Zhukov, V M Silkin, E V Chulkov and P M Echenique *Phys Rev* B **64** 180507(R) (2001)

[90] L Tewordt and D Fay *Phys Rev Lett* **89** 137003 (2002)

[91] I I Mazin, O K Andersen, O Jepsen, O V Dolgov, J Kortus, A A Golubov, A B Kuz'menko and D van der Marel *Phys Rev Lett* **89** 107002 (2002)

[92] J Kortus, I I Mazin, K D Belashchenko, V P Antropov and L L Boyer *Rev Lett* **86** 4656 (2001)

About the Reviewers

Dr S Mollah, Lecturer, Department of Physics, Aligarh Muslim University, India, is presently working as a Postdoctoral fellow in the Department of Physics, National Sun Yat Sen University, Kaohsiung, Taiwan Apart from his present position, he has worked as a postdoctoral fellow at different Research Institutes and Universities in India and abroad *viz* National Physical Laboratory, India, Toyohashi University of Technology Japan and Ben Gurion University of the Negev, Beer Sheva Israel He has published more than 30 research papers in different reputed international journals His present interest of research is High temperature superconductivity, Intermetallic superconductors, Colossal magnetoresistive (CMR) materials and Amorphous semiconductors

Dr H D Yang, Professor, Department of Physics, National Sun Yat Sen University, Kaohsiung, Taiwan, is the Director General of Department of Natural Sciences and Mathematics, National Science Council of R O C He obtained his Ph D (Physics) degree from Iowa State University, USA, in 1987 Apart from his present appointment, he also acted as the Chairman of the Department of Physics and as the Dean of College of Science of NSYSU He won the distinguished Teaching Award, Ministry of Education, R O C, distinguished Research Award, NSYSU, Excellent Research Award, National Science Council, R O C *etc* He is the member of Phi Tau Phi Scholastic honor Society American Physical Society and Chinese Physical Society Professor Yang worked on diferent fields of low temperature condensed matter physics *viz* Superconductivity, Magnetism and different novel materials of current interest He has more than one hundred publications in various international journals of physics *viz* Phys Rev Letters, Applied Phys Letters, J Applied Physics, *etc*

Prof B K Chaudhuri, Ph D , D Sc (Cal), is the Head of Solid State Physics Department, Indian Association for the Cultivation of Science, Kolkata, India He worked as a visiting Professor of National Sun Yat Sen University, Kaohsiung, Taiwan Formerly, he worked as visiting fellow J S P S (Japan) and AvH (Germany) He is the member of Physical Society, Japan and fellow of Indian Physical Society and Indian Cryogenic Council He was awarded Young Scientist Award, Indian National Science Academy for his excellent research work Prof Chaudhuri worked on different fields of Condensed Matter Physics like, superconductivity, CMR and Half-metallic compounds, ferroelectric liquid crystals, semiconducting properties of disordered materials and oxide glasses, structural phase transitions and photo-acoustic properties of solids He has published more than 250 research papers in different international journals and guided 25 Ph D students working on different branches of condensed matter physics (both theoretical and experimental)

ELSEVIER

January 2002
240

Materials Letters 52 (2002) 159–165

MATERIALS LETTERS

www.elsevier.com/locate/matlet

Critical temperatures and critical currents of PbBiSCCO–metal/alloy composites

S. Mollah *

Department of Physics, Aligarh Muslim University, Aligarh 202002, India

Received 10 April 2000; received in revised form 11 April 2001; accepted 15 April 2001

Abstract

Critical temperatures (T_c) and critical currents (I_c) of Pb–Bi–Sr–Ca–Cu–O (PbBiSCCO) superconductors containing 10, 25 or 30 wt.% Ag or AgCu or AgIn are reported. Specimens of 24-h annealed, 10 wt.% added metal/alloy composites show the highest critical currents, which is much higher than pure PbBiSCCO. Samples annealed for 24 h bestow better transport property than the 48-h annealed samples for the same composition. The connectivity effect of metal/alloy between superconducting grains can explain this finding. The I_c of AgIn composites is superior to AgCu but inferior to Ag composites. This finding is explained in terms of supercurrent transport properties.

Keywords: Superconductor; Silver; Silver–copper alloy; Silver–indium alloy; Critical temperatures; Critical currents

1. Introduction

Three superconducting phases have been identified in the Bi-based superconductor system. Their nominal compositions are approximately given by the general formula $Bi_2Sr_2Ca_{n-1}Cu_nO_{2n+4}$, where n is the number of CuO_2 layers [1]. The three phases are 2201 ($n=1$, $T_c \approx 20$K), 2212 ($n=2$, $T_c \approx 85$ K) and 2223 ($n=3$, $T_c \approx 110$ K). Bi-based superconductors are of distinct interest for practical application as these three phases maintain a more static oxygen stoichiometry ratio in air than yttrium-based superconductor ($YBa_2Cu_3O_{7-\delta}$) and they are less toxic than thallium-based superconductors (Tl–Ba–Ca–Cu–O). They do not need high oxygen pressure to synthesize. These are also easy to prepare and the raw materials are of low cost. But these superconductors are usually brittle and very difficult to prepare in the form of wires/tapes for practical use. To improve their ductility without impairing the critical current density (J_c), the bulk superconductor is processed as a composite material adding a high volume fraction of metal or alloy. In these composites, metal–superconductor interfaces are formed. These composites are considered as a dispersion of strongly superconducting granular islands embedded in a metallic matrix. The volume fraction of superconducting phases, the relative orientation of superconducting grains and the connection between them affects the J_c as well as weak links formed at metal–superconductor interfaces [1–3]. Low values of grain boundary J_c pose severe problems for large current applications of high-temperature superconductors and the enhancement of J_c is a key issue for

* Tel./fax: +91-571-401001.
E-mail addresses: smollah@rediffmail.com, pht23msm@amu.up.nic.in (S. Mollah).

00167-577X/02/$ - see front matter
PII: S0167-577X(01)00384-6

their further advancement. The transport properties are influenced both by the weak links and the coupling of the superconducting order parameters to Josephson junction [4]. In the composite material, each Josephson junction is of superconductor–normal–superconductor (SNS) type. The critical current (I_c) of SNS junctions determines the I_c of the whole composite. Several groups preparing the composite superconductor have already used Ag and their structural and transport properties have been contemplated. The effect of adding AgCu has already been reported by us [5]. To the author's knowledge, there is no report so far on the effect of AgIn addition on the micro-structural and transport properties of Bi-based superconductor. As silver does not have any poisonous effect on the properties of Bi-based high-temperature superconductors, it is ubiquitously used as the sheath material for devising superconducting wires/tapes in the powder-in-tube (PIT) method [6–9]. Substituting AgCu for Ag sheathing caused interfacial Cu segregation [10]. Extensive research is going on to explore whether any other metal/alloy can be used as sheathing material instead of Ag. Consequently, it is necessary to study the doping effect of different alloys on the micro-structural and transport properties of bulk Bi-based superconductors and compare with those of Ag doping for their practical use.

In this letter, a comparative study of the addition of 10–30 wt.% Ag, AgCu and AgIn on the micro-structural and transport properties of bulk Pb–Bi–Sr–Ca–Cu–O (hereafter referred as PbBiSCCO) superconductors is reported. The concentration of copper (Cu) and indium (In) in AgCu and AgIn alloys, respectively, has been preferred as 4 at.% according to the optimum measured wettability [11]. The possible influence of either interfacial processes or junction transport properties can determine the critical current of the composites.

2. Experimental

The composite materials were processed in the same way as reported earlier [5,12]. $Pb_{2.82}Bi_{1.926}Sr_{2.494}Ca_{2.424}Cu_{2.823}O_x$ powder, supplied by Hoechst (Germany), was used to prepare the PbBiSCCO–Ag/AgCu/AgIn composites. This powder was mixed with 10, 25 and 30 wt.% of Ag (1.7- to 3.3-mm size), AgCu and AgIn powders, respectively, for the preparation of PbBiSCCO–Ag, PbBiSCCO–AgCu and PbBiSCCO–AgIn composites. The size of Cu and In particles, respectively, in AgCu and AgIn alloy are in the range 30–60 μm. For each composite, the powders were thoroughly mixed and compacted in 1.5 mm thick pellets using a hydraulic press. Two series of samples were processed at different heat-treatment times. One series was heat-treated at 810 ± 5 °C for 24 h (hereafter referred to as series I) and the other was heat-treated at 810 ± 5 °C for 48 h (hereafter referred to as series II) in air, followed by furnace cooling. Heat treatment of the samples above 820 °C caused the partial melting of the pellets [5,12]. Here, it should be mentioned that according to literature, annealing at reduced oxygen

Table 1
Some important parameters of series I (24-h annealed) and series II (48-h annealed) composites

Sample	Wt.% of metal/alloy in the composite	T_c (K)	I_c (A)	J_c (A/cm^2)
Series I				
PbBiSCCO	0	113 6	16 5	183.3
PbBiSCCO/Ag	10	112.7	49 5	550 0
	25	113 4	47 0	522 2
	30	109 4	38 5	427 7
PbBiSCCO/	10	106.6	47 5	527 7
Ag–Cu	25	100.5	17 0	188 8
	30	95 5	6 0	66 6
PbBiSCCO/	10	108.5	48 5	538 8
Ag–In	25	105 0	40 0	444 4
	30	101 6	30 0	333 3
Series II				
PbBiSCCO	0	102 3	12 5	138 8
PbBiSCCO/Ag	10	107 7	6 0	66 6
	25	97 5	4 5	50 0
	30	97 5	2 0	22 2
PbBiSCCO/	10	98 0	5 3	58 8
Ag–Cu	25	90 8	4 0	44 4
	30	93 3	4 0	44 4
PbBiSCCO/	10	103 8	8 0	88 8
Ag–In	25	95 5	6 0	66 6
	30	95 5	5 0	55 5

partial pressure might give better results. Our primary aim was not to investigate the effect of annealing environment but that of different metal/alloy on the superconducting properties of PbBiSCCO–metal/alloy composites. So we annealed the samples *in air*. The pellets were cut into 9.0×6.0 mm^2 sizes and used for transport property measurement. The relative volume fractions (V) of superconductive (2201, 2212 and 2223) and impurity (Ca_2PbO_4) phases have been calculated by comparing the intensities (I) of the characteristic X-ray diffraction (XRD) peaks obtained by a PW 1050-70 diffractometer with CuKα radiation [3,5]. The relative volume fraction of 2223 phase is obtained using [2]

$$V_{2223} = I_{2223} \times 100/(I_{2223} + I_{2212} + I_{2201})$$

where the characteristic intensity peaks for each phase were aggregated separately and taken as I of that phase in the composite. The error on volume fraction of 2223 phase is $\pm 3\%$. The dispersion of superconductor grains into metallic matrix are confirmed by taking the back scattering images of the samples using Jeol 35C SEM with an EDAX attachment [5]. I_c and T_c of the samples were ascertained by a standard four-probe method maintaining the floating voltage condition as 1 μV cm^{-1}. T_c and I_c at five different places of the samples were measured which differed by $\pm 1\%$ from each other and taking the average. For T_c measurement, the resistance of the samples was ascertained at different temperatures ranging from room (300 K) to liquid nitrogen (77 K) temperature. The temperature at which the resistance started decreasing rapidly was taken as the T_c(onset) and at which the resistance became zero was taken as T_c(zero). T_c of the samples was taken as the average of T_c(onset) and T_c(zero). The I_c of the samples was measured by directly immersing these into liquid nitrogen to avoid the heating effect in zero magnetic fields. In the absence of any external magnetic field, the only magnetic field will be due to

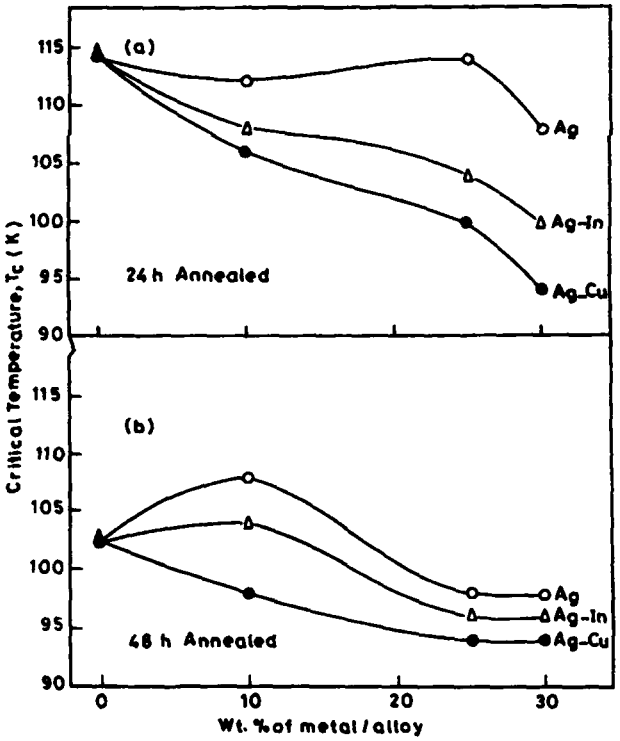

Fig. 1. (a) Variation of critical temperature (T_c) with added wt.% of metal/alloy in PbBiSCCO (series I) heat-treated at 810 ± 5 °C for 24 h. (b) Change of critical temperature (T_c) with added wt% of metal/alloy in PbBiSCCO (series II) heat-treated at 810 ± 5 °C for 48 h.

transport current. According to Silsbee's hypothesis [13], the I_c will be that current rate which will generate the critical magnetic field H_c at the surface of the superconductor. Thus, at I_c, the sample will relax its superconductive property and show resistance. Hence, I_c was taken as the current where the resistance of the samples started increasing from zero value. The samples were detected to be highly homogenous as the values of T_c and I_c did not change much at different positions.

3. Results

The T_c, I_c, and J_c of all composites are shown in Table 1. The critical temperatures (T_c) of series I and II PbBiSCCO superconducting composite pellets containing 0, 10, 25 and 30 wt.% Ag/AgCu/AgIn are shown in Fig. 1a and b, respectively. For series I samples, the T_c of the Ag added samples are superior to the corresponding wt.% added AgCu and AgIn samples (Table 1) but the pure PbBiSCCO shows the highest T_c (~ 114 K). PbBiSCCO–Ag composites with up to 25 wt.% Ag reveal nearly the same T_c as pure PbBiSCCO but this decreases above 25% Ag addition (Fig. 1a). However, the T_cs of the AgIn added composites are higher than AgCu added composites but lower than that of pure PbBiSCCO and PbBiSCCO–Ag composite (Table 1). The T_c of series II samples are inferior to the corresponding series I samples (for all the three composites and pure PbBiSCCO) [Table 1]. Among series II samples, the T_c of 10 wt.% Ag and AgIn added composites are higher than pure PbBiSCCO superconductor though that of PbBiSCCO–AgCu composites is always lower than pure PbBiSCCO (Fig. 1b).

The critical current (I_c) of series I samples with 10 wt.% added metal/alloy composite is above that of pure PbBiSCCO and 25–30 wt.% added metal/alloy composite (Fig. 2a). 10 wt.% Ag-added series I composite showed the highest I_c (~ 50A). The I_cs of PbBiSCCO–AgIn are inferior to PbBiSCCO–Ag but superior to PbBiSCCO–AgCu composites (Table 1). The I_c of series II samples is much lower than the corresponding series I samples. However, among the series II samples, the pure PbBiSCCO shows the

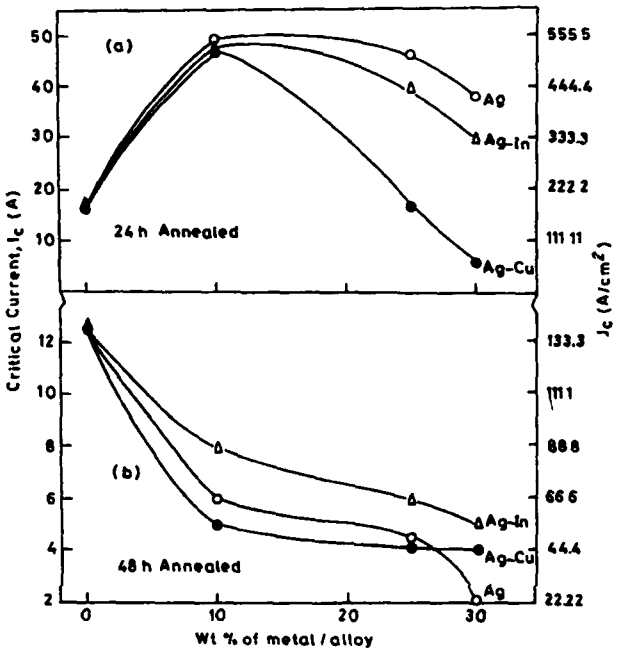

Fig. 2. (a) Dependence of I_c and J_c on added wt % of metal/alloy in PbBiSCCO (series I) heat-treated at 810 ± 5 °C for 24 h. (b) Dependence of I_c and J_c on added wt % of metal/alloy in PbBiSCCO (series II) heat-treated at 810 ± 5 °C for 48 h

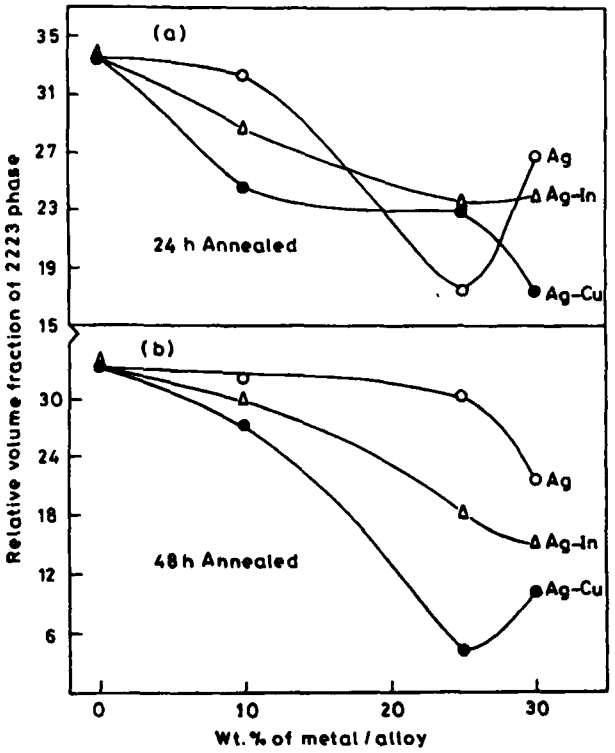

Fig. 3. Variation of relative volume fraction of the 2223 phase, obtained from XRD analysis with added wt.% metal/alloy in PbBiSCCO heat-treated at 810 ± 5 °C for 24 h (a) and 48 h (b).

maximum I_c (Fig. 2b). The estimated current densities (J_c) are given in Table 1. It has been established that the supercurrent flows within 5–10 μm under the surface of the superconducting sample specifically in PbBiSCCO–Ag wires/tapes [7,8]. But in J_c calculation, we have assumed that the current flows through the whole thickness (1.5 mm) of the composite giving rise to lower J_c values.

Significant compositional changes have not been detected in series I compared to series II samples. The superconducting grain size are found in the range 20.0–35.0 μm. Clustered silver with sizes of 12.0–25.0 μm are observed [5] in all composites. Silver clustering and overall area coverage are more pronounced in composites with 25–30 wt.% metal/alloy. Fig. 3a and b shows the relative volume fraction of 2223 phase of series I and II samples, respectively. There is no exact correlation among T_c, I_c, and 2223 phase (also true for 2201, 2212 and Ca_2PbO_4, which are not shown). In both series of samples, pure PbBiSCCO has the highest volume fraction of 2223 phase. Among the composites, the volume fraction of 2223 phase of PbBiSCCO–AgIn is higher than PbBiSCCO–AgCu but lower than PbBiSCCO–Ag (Fig. 3a and b). This is consistent with the higher values of T_c and I_c for AgIn-added composites compared to AgCu-added composites (Figs. 1 and 2).

4. Discussion

The decrease of T_c and I_c (as well as J_c) of series II compared to series I samples (Table 1) may be due to the prolonged exposure of the former to atmospheric oxygen [2,14]. There is a contradictory report on the role of Ag in the transport properties of PbBiSCCO–Ag composites [15,16]. But most of the groups noted the enhancement of T_c and I_c due to addition of Ag in PbBiSCCO superconductor. At

lower wt.% (i.e., ≤ 10 wt.%) of Ag, it acts as a good connector between the superconducting grains causing the enhancement of I_c [5] due to the proximity effect. But at higher wt.% of Ag addition, it probably acts as a normal metal performing as a weak link and barrier causing the decrease of I_c. It is a fact that I_c values depend not only on the amount (volume fraction) of the superconducting phases in the material, but also on their alignment and the extent of connectivity among bulk superconducting grains, which allows for higher unpinned super current to flow [17,18]. The role of Ag, AgIn and AgCu in critical current of the composites can be explained more clearly from the following argument.

The critical current density (J_c) below the critical temperature (T_c) for an SNS junction is inversely proportional to γ [4] where $\gamma = V_s/V_n$ (V_s and V_n being the Fermi velocities of the superconducting matrix and normal metal, respectively). But the Fermi velocity of the superconducting states of all composites is identical. Consequently, the value of γ varies with the variation of Fermi velocity in the normal state. Subsequently it is known that $V_{Cu} < V_{In} < V_{Ag}$ [19], and we can presume that $V_{AgCu} < V_{AgIn} < V_{Ag}$ and hence $\gamma_{Ag} < \gamma_{AgIn} < \gamma_{AgCu}$. The lower values of γ causes the higher values of J_c—in agreement with our study. Again, the tendency of oxide formation varies from metal to metal. Among Ag, Cu and In, copper has the highest whereas silver has the lowest tendency of oxide formation [19]. The oxidation behavior of indium is in between copper and silver [19]. Thus, the proportion of oxide layers among the superconducting grains will be highest for AgCu and lowest for Ag if wt.% doping of metal/alloy and annealing condition are the same. Therefore, the oxidation behavior of the different alloys is following the same direction as γ. Accordingly, the formation of oxide barriers is expected to be different for the different alloys used being maximum for AgCu and minimum for Ag. The transport property is inversely proportional to the amount of oxide layers' obstacle among the superconducting grains. Hence, it can be concluded that the J_c(PbBiSCCO–Ag) > J_c(PbBiSCCO–AgIn) > J_c(PbBiSCCO–AgCu). While the samples' size are the same, I_c(PbBiSCCO–Ag composites) > I_c(PbBiSCCO–AgIn composites) > I_c(PbBiSCCO–AgCu composites), consistent with our observation.

5. Conclusion

To conclude, the transport and micro-structural properties of the normal metal inclusions in SNS junctions seem to play a major role in the critical current density of the Ag or AgCu or AgIn added PbBiSCCO composites. This consequence appears to be more important than the superconductor–normal metal interface. According to the transport and micro-structural properties of the metal/alloy composites, it appears that Ag is the best one for utilizing as a sheathing material to fabricate PbBiSCCO superconductor wires/tapes in PIT method.

Acknowledgements

The author is grateful to the Israeli Ministry of Science for providing a fellowship that enabled him to perform part of the work in Ben Gurion University of the Negev, Israel. The author is also indebted to Prof. J.P. Srivastava, Prof. R. Dayal, Prof. S.K. Singh (Chairman, Department of Physics) and Prof. J.H. Naqvi (Dean, Faculty of Science), AMU, Aligarh, for their keen interest and encouragement. The financial support of UGC, Govt. of India, from the project (No. F. 10-31/98) is also gratefully acclaimed.

References

[1] J.M. Tarascon, W.R. Mckinnon, P. Barboux, D.M. Hwang, B.G. Bagley, L.H. Greene, G.W. Hull, Y. Lepage, N. Stoffel, M. Ground, Phys. Rev. B 38 (1988) 8885.
[2] S. Mollah, N. Froumin, J. Baram, in: A.V. Narlikar (Ed.), Studies of High Temperature Superconductors, vol. 16, Nova Scientific Publishers, New York, 1995, p. 155.
[3] Y. Massalkar, A.N. Sembira, J. Baram, J. Mater. Res. 8 (1993) 2445.
[4] A. Goulb, B. Horovitz, Phys. Rev. B 49 (1994) 4222.
[5] S. Mollah, N. Frumin, M. Polak, J. Baram, Mater. Lett. 27 (1996) 187.
[6] B.A. Glowacki, J. Jackiewicz, J. Appl. Phys. 75 (1994) 4222.
[7] M. Lelovic, P. Krishnaraj, N.G. Error, A.N. Iyer, U. Balachandran, Supercond. Sci. Technol. 6 (1996) 201;
M. Lelovic, P. Krishnaraj, N.G. Error, A.N. Iyer, U. Balachandran, Physica C 242 (1995) 246.

[8] F. Marti, G. Grasso, Y.B. Huang, R. Flukiger, Supercond. Sci. Technol. 11 (1998) 1251.
[9] Y.C. Guo, H.K. Liu, S.X. Dou, J. Am. Ceram. Soc. 83 (2000) (July).
[10] K. Nomura, T. Sasaoka, J. Sato, S. Kuma, H. Kumakura, K. Togano, N. Tomita, Appl. Phys. Lett. 64 (1994) 112.
[11] N. Frumin, J. Baram, M. Polak, Mater. Lett. 18 (1994) 176; Physica C 209 (1993) 315.
[12] S. Mollah, Proc. of SSP-DAE Symposium, held at IGCAR, Kalpakkam, India during 20–24 December, 1999.
[13] F.B. Silsbee, J. Wash. Acad. Sci. 6 (1916) 597.
[14] S.X. Dou, K.H. Song, H.K. Liu, C.C. Sorrell, Physica C 160 (1989) 533.
[15] Y.D. Chiu, T.S. Lei, C.H. Kao, J. Mater. Sci. 29 (1994) 2678.
[16] R. Yufang, Z. Zuoto, M. Jian, H. Ping, Solid State Commun. 75 (1990) 625.
[17] A.K. Sarkar, I. Maartense, T.L. Peterson, J. Mater. Res. 7 (1992) 1672.
[18] J. Mannhart, H. Bielefeldt, B. Goetz, H. Hilgenkamp, A. Schmehl, C.W. Schneider, R.R. Schulz, Philos. Mag. B 80 (2000) 827.
[19] C. Kittel, Introduction to Solid State Physics. Wiley, New York, 1967;
Handbok of Chemistry and Physics. 65th edn., CRC Press, Boca Raton, 1984–85.

Role of Normal Metal Inclusions in the Critical Current of PbBiSCCO–Ag/AgCu/AgIn Composites

S Mollah
Department of Physics, Aligarh Muslim University, Aligarh 202 002 India

Abstract

A comparative study of the addition of silver (Ag), silver–copper alloy (AgCu) and silver–indium alloy (AgIn) on the micro-structural and transport properties of bulk Pb–Bi–Sr–Ca–Cu–O (PbBiSCCO) superconductors is reported. The composites are prepared by the addition of 10, 25 and 30 wt% of Ag, AgCu and AgIn. Concentration of Cu and In in the AgCu and AgIn alloy respectively have been chosen as 4 at% according to the optimum measured wettability. The composites were heat-treated at 810 ± 5°C for 24h and 48h. 24h annealed samples show better transport and micro-structural properties compared to 48h annealed samples. Among all the composites, 10 wt% Ag added composites show the highest critical temperature (T_c) and critical current (I_c). No correlation was found for the different superconducting and impurity phases with T_c and I_c of the samples. The silver-added composites show better transport and micro-structural properties compared to same wt% AgCu or AgIn added composites. Thus, Ag is found to be the most suitable sheath material for fabricating the superconducting wires/tapes in powder-in-tube (PIT) method.

INTRODUCTION

Practical applications of bulk Bi-based high temperature superconductors require high critical current densities. These superconductors are usually brittle and it is very difficult to fabricate them in the form of wires/tapes for practical use. To improve their ductility, without imparing the critical current density (J_c), the superconductor is processed as a composite material adding a high volume fraction of metal or alloy. In these superconductors, metal–superconductor interfaces are formed. These composites are considered as a dispersion of strongly superconducting granular islands embedded in a metallic matrix. The volume fraction of superconducting phases, the relative orientation of superconducting grains and the connection among the grains affect the J_c as well as weak links formed at a metal–insulator superconductor interfaces. The transport properties are influenced both by the weak links and the coupling of the superconducting order parameters to Josephson junction. In the composite material, each Josephson junction is of the SNS (superconductor–normal–superconductor) type. The critical current of the whole composite is determined by the critical current of SNS junctions. Extensive research is going on to examine whether there is any alloy which can be used as sheathing material in exchange of Ag for fabrication the wires/tapes in PIT method.[1] Thus it is necessary to study the doping effect of different alloys on the micro-structural and transport properties of bulk Bi-based superconductors and compare with those of Ag doping for their practical use.

In this paper, a comparative study of the addition of 10–30 wt% Ag, AgCu and AgIn on the micro-structural and transport properties of bulk Pb–Bi–Sr–Ca–Cu–O (PbBiSCCO) superconductors is reported. The concentration of Cu and In in the AgCu and AgIn alloy respectively have been chosen as 4 at%.

EXPERIMENTAL DETAILS

The PbBiSCCO–Ag/AgCu/AgIn composite materials were prepared using $Pb_{2.82}Bi_{1.926}Sr_{2.494}Ca_{2.424}Cu_{2.823}O_x$ powder supplied by Hoechst, Germany. This powder was mixed with 10, 25 and 30 wt% of Ag (1.7 to 3.3 mm size), AgCu and AgIn powders. The size of Cu and In particles respectively in AgCu and AgIn alloy are in the range 30–60 μm. The composites were thoroughly mixed and compacted in 1.5 mm thick pellets using hydraulic press. These pellets were heat-treated at 810 ± 5° C for 24 and 48h in air, followed by furnace cooling. Heat-treatment of the samples above 820° C caused the partial melting of the pellets. The pellets were cut into 9.0 × 6.0 mm^2 size and used for transport property measurement. The relative volume fractions of superconductive (2201, 2212 and 2223) and of impurity (Ca_2PbO_4) phases have been calculated by comparing the intensities of the characteristic X-ray diffraction (XRD) peaks.[2] The dispersion of superconductor grains into metallic matrix are confirmed by taking the back scattering images of the samples.[2] The critical current (I_c) and critical temperature (T_c) of the samples were measured by a standard four probe method maintaining the floating voltage condition as 1 μVcm^{-1}.

RESULTS AND DISCUSSION

For the 24h heat treated samples, the T_c of the Ag added samples are higher than the corresponding wt% added AgCu and AgIn

samples. T_c of Ag added samples are nearly the same as non-added samples upto 25 wt% addition but decreases with farther addition of Ag. The T_c's of the AgIn added composites are higher than AgCu added composites but lower than that of pure PbBiSSSO. The T_c of 48h heat-treated samples are lower than those of 24h heat-treated samples (for all the three composites). However the T_c of the 10 wt% Ag and AgCu added samples are higher than the non-added PbBiSCCO superconductor.

The critical current (I_c) of the 10 wt% added metal/alloy are higher than the PbBiSCCO and 25–30 wt% added metal/alloy (Fig. 1a). I_c of the PbBiSCCO-AgIn composites are lower than the PbBiSCCO-Ag composites. I_c of 48h heat-treated samples are much lower than the 24h heat-treated samples (for same composition). However among the 48h heat-treated samples, the PbBiSCCO shows the maximum I_c (Fig. 1b).

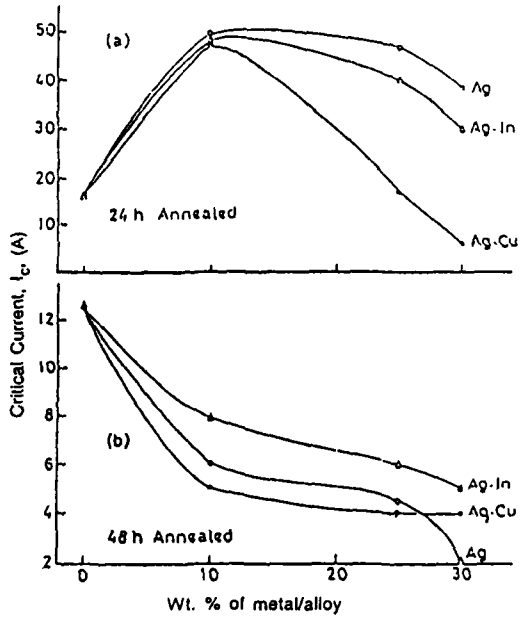

Fig. 1 Dependence of critical current (I_c) with added wt% of metal/alloy in PbBiSCCO heat-treated at 810 ± 5° C for (a) 24h and (b) 48h.

There is no exact corerelation between the T_c, I_c, and 2223 phase (true for 2201, 2212 and Ca_2PbO_4 also which are not shown). But the relative volume fraction of 2223 phase of AgIn added composites are higher than those of AgCu added composites. This is in agreement with the higher values of T_c and I_c for AgIn added composites compared to AgCu added composites.

The decrease of T_c and I_c for 48h heat-treated samples compared to those of 24h heat-treated samples may be due to the prolonged exposure of the former samples to atmospheric oxygen. For addition of lower wt% (i.e. ≥ 10 wt%) of Ag, probably it acts as a good connector among the superconducting grains causing the enhancement of I_c.[2] For higher wt% of Ag addition, it probably acts as a normal metal behaving as a weak link and causing the decrease of I_c. The role of AgIn and AgCu in critical current of the composites can be explained from the following discussion.

The critical current density (J_c) at temperatures below the critical temperature (T_c) for an SNS junction is given by[3]

$$J_c = A.\exp^{-vd/\xi_S}/(\pi T v)^2\gamma^3 d[1+K\{1+(\Delta/\pi T)^2\}^{1/2}] \quad (1)$$

where $t = T/T_c$, T and T_c are the measuring and critical temperatures of the sample respectively, $v = m_s/m_n$, with m_s and m_n the critical masses of the superconducting and normal states respectively, $\gamma = v_s/v_n$ with v_s and v_n the Fermi velocities of the superconducting matrix and normal metal respectively. $K = (1+\gamma^2/2\gamma)$, 'd' is the thickness of the normal metal, ξ_S is the coherence length in the superconducting state, D is an order parameter and 'A' is a constant. So the variation of J depends on the variation of γ since the other parameters are almost constant. As the Fermi velocity of the superconducting states of all composites is the same, the value of γ varies with the variation of Fermi velocity in the normal state. Since it is known that $v_{Cu} < v_{In} < v_{Ag}$[4], we can assume that $v_{AgCu} < v_{Ag}$, $v_{AgIn} < v_{Ag}$ and $v_{AgCu} < v_{AgIn}$. Thus the γ for AgCu is larger than that of Ag and AgCu. Similarly γ for AgIn is larger than Ag but smaller than AgCu. The higher values of γ causes the lower values of J_c according to eqn (1). So the I_c (PbBiSCCO-Ag composites) > I_c (PbBiSCCO-AgIn composites) > I_c (PbiSCCO-AgCu composites) observed in our systems are easily explained using eqn. (1).

CONCLUSION

To conclude, the normal metal inclusions in SNS junctions seem to play a major role in the critical current density of the Ag, AgCu or AgIn added composites. Among the three, Ag seems to be the best one as sheathing material for fabricating the PbBiSCCO superconductor wires/tapes in PIT method.

ACKNOWLEDGEMENT

The author is grateful to the Israeli Ministry of Science for providing a fellowship to perform part of the work in Ben-Gurion University of the Negev, Israel. The financial support of UGC, Govt. of India, from the project (No.F. 10-31/98) is also gratefully acknowledged.

REFERENCES

1 F Marti, G Grasso, Y B Huang and R Flukiger, *Supercond Sci Technol.*, 11 1251 (1998)

2 S Mollah, N Frumin, M Polak and J Baram, *Materials Letts.*, 27 187 (1996).

3 J M Tarascon, W R Mckinnon, P Barboux, D M Hwang, B G Bagley, L H Greene, G W Hull, Y Lepage, N Stoffel and M Ground, *Phys. Rev.*, B 38 8885 (1988).

4 C Kittel, *Introduction Solid State Physics*, 3rd Edition, John Wiley & Sons.

PHYSICAL REVIEW B VOLUME 53, NUMBER 9 1 MARCH 1996-I

Transport properties of Pb-doped $Bi_4Sr_3Ca_3Cu_4O_x$ semiconducting glasses and glass-ceramic superconductors

S. Chatterjee, S. Banerjee, S. Mollah, and B. K. Chaudhuri
Department of Solid State Physics, Materials Research Section, Indian Association for the Cultivation of Science, Calcutta-700 032, India
(Received 27 April 1995; revised manuscript received 7 August 1995)

Electrical conductivity and thermoelectric power (TEP) of the as-quenched and annealed (at 500 °C for 10 h and 840 °C for 24 h) $Bi_{4-n}Pb_nSr_3Ca_3Cu_4O_x$ ($x = 0$–1.0) glasses have been measured. The dc conductivity data of the as-quenched and the partially annealed (at 500 °C) glasses can be explained by considering the small-polaron hopping conduction mechanism which is found to change from the nonadiabatic to the adiabatic regime with annealing the glasses at 500 °C. This change over is due to the presence of microcrystals in the partially annealed glasses as observed from x-ray-diffraction and scanning electron microscopic studies. This adiabatic behavior is also visualized even for some as-quenched glasses having a very small amount of the more conducting microcrystalline phase. All the 840 °C annealed glasses are superconductors with T_c between 110 and 115 K. The Seebeck coefficient (S) of the partially annealed glass system is found to be positive and increases linearly with temperature. The S values of the corresponding glass-ceramic superconductors showing broad peaks around T_c. A change over in the values of S from positive (below $\sim$290 K) to negative (above $\sim$290 K) indicates the coexistence of both electrons and holes in these superconductors. The TEP data can be fitted with both the two-band model of Forro *et al.* [Solid State Commun. 73, 501 (1990)] and the Nagaosa-Lee model [Phys. Rev. Lett. 64, 2450 (1990)]. Therefore, the bosonic contribution in the transport properties of these superconductors, as suggested by the Nagaosa-Lee model, is supported.

I. INTRODUCTION

The glassy precursors for high-T_c superconductors like $Bi_{4-n}Pb_nSr_3Ca_3Cu_4O_x$ are very interesting because of several reasons. There is immense possibility of making superconducting wire/tapes, and thick films[1–3] for technological applications. Therefore, elaborate investigations of various physical properties of these special type of glassy and corresponding glass-ceramic (GC) phases are important. Among the possible coexisting phases in the Bi-Sr-Ca-Cu-O systems,[4,5] the 80 K phase forms more easily. This phase is also thermodynamically more stable. Partial substitution of Bi by Pb enhances the preparation of the nearly single phase (2223) superconductor ($T_c \sim 110$ K).[6,7] Endo *et al.*[8] proposed that Pb^{+2} substituted for Bi^{+3} as well as Sr defects act as hole donors. Since the valency of Pb is +2 and that of Bi is +3, one Pb atom can dope a hole to the system. Study of thermoelectric power of this system would be important to find the nature of the carriers (holes or electrons). As the Pb-doped (2223) phase has the high-T_c value ($\sim$115 K), it is interesting to process this phase via controlled crystallization of the corresponding glassy precursor phase.

Recently, several investigations of the superconducting behavior of the Pb-doped Bi-Sr-Ca-Cu-O system have been made.[9,10] But the comparative study of the semiconducting properties of the as-quenched and the corresponding partially annealed (with the appearance of micro crystals) glassy systems have not been made so far. Here it is interesting to point out that the appearance of microcrystals (more conducting crystalline phases) in the as-quenched glass (by partial annealing or produced during glass formation) changes the hopping conduction mechanism (nonadiabatic to adiabatic) along with other behavior. Furthermore, very little or no report has been made so far on the detailed thermoelectric powers of these glassy precursors and those of the corresponding glass-ceramic (GC) superconductors,

The purpose of the present paper is to study the effect of annealing time and temperature on the electrical conductivity and thermoelectric power (TEP) of the $Bi_{4-n}Pb_nSr_3Ca_3Cu_4O_x$ ($0.1 \leqslant n \leqslant 1.0$) glasses which are very good precursors of high-T_c superconductors. The $Bi_4Sr_3Ca_3Cu_4O_x$ or (4334) system has been chosen as the mother glassy phase because it is easily converted[11] to single phase $Bi_2Sr_2Ca_1Cu_2O_y$ or [2212] superconductor. Furthermore, transport properties of Li-doped $Bi_4Sr_3Ca_3Cu_4O_x$ glassy system have also been elaborately studied earlier[12,13] using small polaron hopping conduction mechanism. However, there is still a controversy over the true mechanism (adiabatic or nonadiabatic) of conduction in the glassy precursors of high-T_c superconductors. While the nonadiabatic small polaron hopping conduction mechanism is found to be valid for the Li-doped (4334) glasses.[12] Singh and Zacharias[14] argued that the polaron hopping mechanism is in the adiabatic regime in such glassy semiconductors. Therefore, the semiconducting behavior of the as-quenched Pb-doped $Bi_4Sr_3Ca_3Cu_4O_x$ (4334) glasses, behaving similarly to those of the corresponding Li-doped glasses,[12,15] has also been studied. From the present investigation, it would be visualized how the model parameters like Debye temperature, phonon frequency, conduction mechanism (nonadiabatic to adiabatic) and microstructure change in the Pb-doped (4334) glasses due to annealing.

Since the theoretical analysis of the experimental dc conductivity of the as-quenched Pb-doped (4334) glasses can be made similarly to that of the Li-doped (4334) glasses[12] (hereafter referred to as Ref. 1), we shall only briefly discuss the

0163-1829/96/53(9)/5942(11)/$10.00

results on dc conductivity data of the present as-quenched glasses for comparison with those of the partially annealed semiconducting glasses.

In Sec. II sample preparation and different techniques used have been discussed in short. Section III deals with the microstructural properties of the glasses and glass ceramics. Analysis of the dc conductivity data of the as-quenched, partially annealed glasses and the corresponding superconducting glass ceramics have also been made in this section. The thermoelectric power data of the glassy semiconductors and the corresponding glass-ceramic superconductors have been discussed in Sec. IV. The paper ends with a brief summary and conclusion in Sec. V.

II. EXPERIMENT

The $Bi_{4-n}Pb_nSr_3Ca_3Cu_4O_x$ ($n=0.1$, 0.5, 1.0) glasses are prepared by rapid quenching technique discussed earlier[15-17] and the glass samples thus prepared are divided into two batches. The first batch of the samples are annealed at 500 °C for 10 h. These samples are denoted by Pb1*A*, Pb2*A*, and Pb3*A* for $n=0.1$, 0.5, and 1.0, respectively. The second batch of the samples are heated at 840 °C for 24 h and then furnace cooled. These samples are termed as Pb1*S*, Pb2*S*, and Pb3*S* for $n=0.1$, 0.5, and 1.0, respectively. On annealing at these two temperatures in air, these glassy samples become partially (Pb*A*-type) and completely (Pb*S*-type) oxygenated and crystalline (also called glass ceramics). The total copper ion concentrations of the samples were determined from atomic absorption and the values of Cu^{2+} concentration were determined by chemical analysis as discussed earlier [Ref. 1]. The glass transition temperature (T_g) determined by thermal analysis and the results of infrared (IR) spectra showing the presence of BiO_3 and BiO_6 pyramidal and octahedral units have already been reported.[18] Some important parameters of the glasses are shown in Table I for comparison.

Both the as-quenched and the annealed systems are characterized by x-ray powder diffraction (Philips, Model PW 1710) and scanning electron micrographs (Model 425A), Hitachi, Japan). The dc conductivity (σ_{dc}) and thermoelectric power (TEP) measurements were performed on all the samples with different Pb concentrations. The dc conductivity of the glassy samples was measured by two point method, whereas that of the conducting crystallized samples was measured by standard four probe technique using the APD cryocooler (Model: HC-2D) with helium refrigerating system and temperature controller. Conductivity measurements were made in the Ohmic region as tested from the study of the I-V curves. The dc conductivity of the same glass samples in different runs agreed within 2–3 % and samples of the same composition from different batches gave agreement within 5% for room temperature measurements. The temperature was measured with a nanovoltmeter (Keithley 181) with an accuracy of ±0.5 K (or better). The TEP values of the glasses and glass-ceramic samples ($10\times4\times1$ mm^3) were also measured with the use of the APD cryocooler and Keithley nanovoltmeter (Model 181). A temperature difference of 2–4 degrees was maintained between the two parallel surfaces of the samples under investigation.

TABLE I. Value of different parameters of the as-quenched $Bi_{4-n}Pb_nSr_3Ca_3Cu_4O_x$ glasses.

Parameters	Pb1($n=0.1$)	Pb2 ($n=0.5$)	Pb3 ($n=1.0$)
T_g(°C) [a]	400±5	390±5	385±5
$C=\frac{Cu^{1+}}{Cu_{tot}}$	0.78	0.78	0.78
Density (gm/cc)	7.001	6.901	6.760
$N(10^{19}\ cm^{-3})$	2.72	0.63	4.00
R (Å)	4.61	4.69	4.72
r_p (Å)	1.88	1.89	1.90
θ_D (K)	420	412	408
ν_{ph} (10^{12} Hz)	8.75	8.58	8.50
$N(E_F)$ ($10^{21}\ eV^{-1}\ cm^{-3}$)	9.75	9.64	9.47
α ($Å^{-1}$) [b]	0.341	0.384	0.383
α ($Å^{-1}$) [c]	0.407	0.250	0.464
W (eV) (at 300 K)	0.512	0.580	0.443
W_H (eV)	0.295	0.296	0.295
γ	14.261	14.342	14.258

[a]Obtained from the differential thermal analysis (DTA).
[b]Obtained from Eq. (1).
[c]Obtained from Greaves' model [Eq. (4)].

III. RESULTS AND DISCUSSIONS

A. Structural properties of the glasses and glass ceramics

The XRD patterns of the as-quenched glasses shown in Fig. 1 indicate glassy behavior. Figure 2 shows the XRD patterns of the partially annealed (500 °C for 10 h) Pb1*A* Pb2*A*, and Pb3*A* samples and the corresponding XRD patterns of the Pb1*S*, Pb2*S*, and Pb3*S* glass ceramics (annealed at 840 °C for 24 h) are shown in Fig. 3. The appearance of sharp peaks in Fig. 3 is due to the formation of crystalline phases. The identified crystalline peaks in the partially annealed samples (Fig. 2) are found to be of Cu_2O, Ca_2PbO_4, Bi_2O_3, PbO, and Bi-2201, Bi-2212, Bi

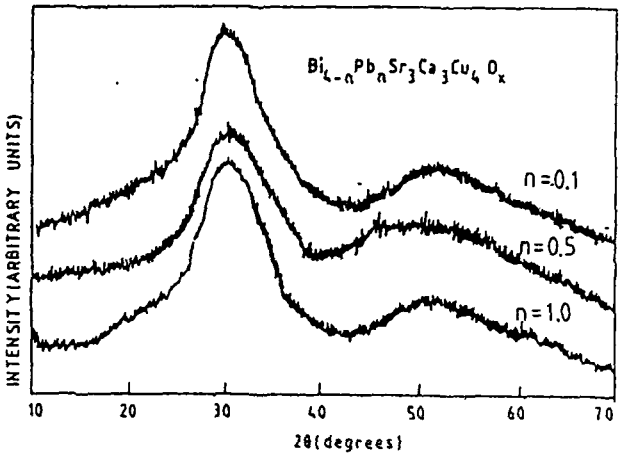

FIG. 1. X-ray-diffraction pattern of $Bi_{4-n}Pb_nSr_3Ca_3Cu_4O_x$ as quenched glasses: (a) $n=0.1$, (b) $n=0.5$, and (c) $n=1.0$

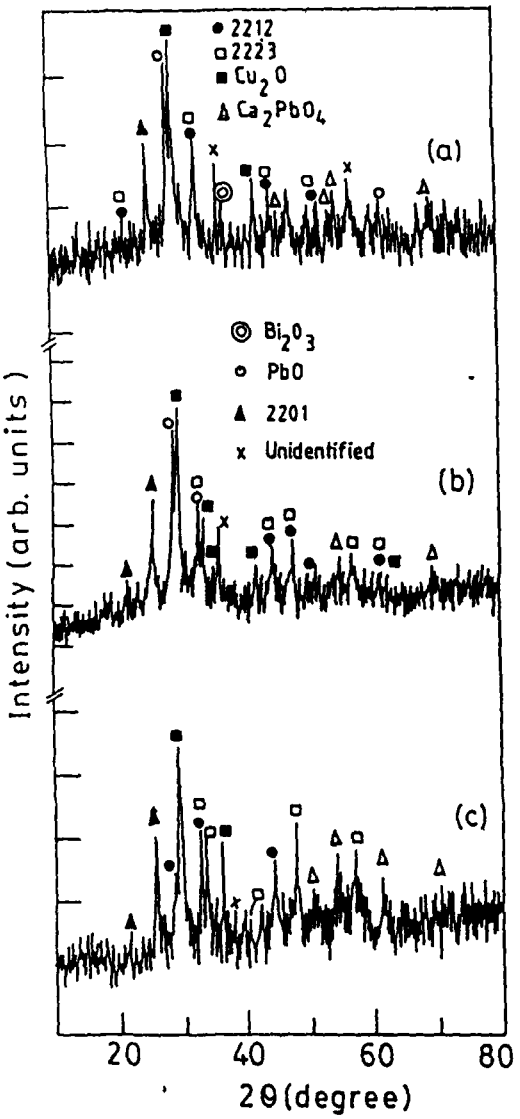

FIG. 2. X-ray-diffraction pattern of $Bi_{4-n}Pb_nSr_3Ca_3Cu_4O_x$ glass ceramics annealed at 500 °C for 10 h: (a) Pb1*A* ($n=0.1$), (b) Pb2*A* ($n=0.2$), and (c) Pb3*A* ($n=1.0$).

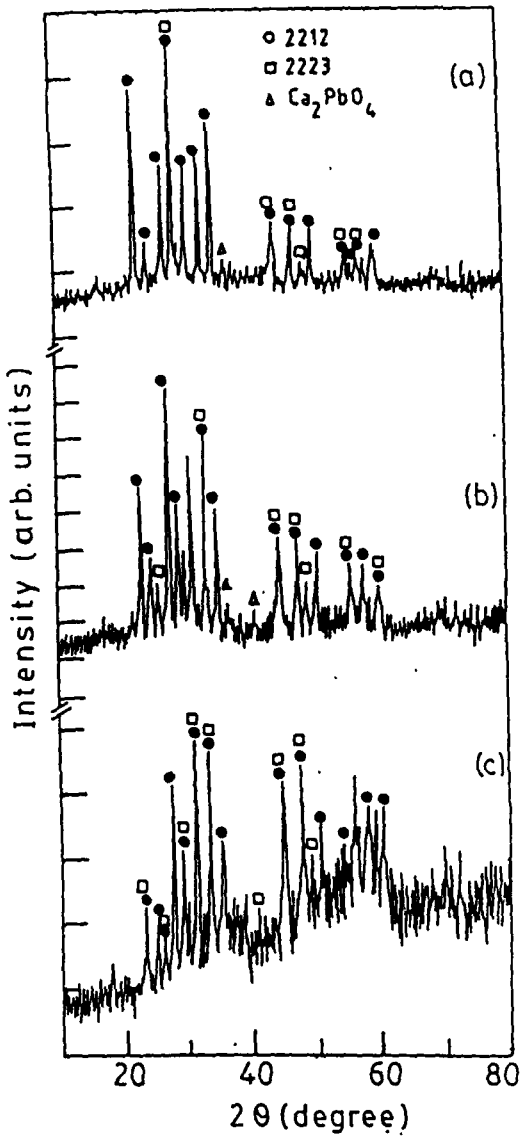

FIG. 3. X-ray-diffraction pattern of $Bi_{4-n}Pb_nSr_3Ca_3Cu_4O_x$ glass-ceramic superconductors (glasses annealed at 840 °C for 24 h): (a) Pb1*S* ($n=0.1$), (b) Pb2*S* ($n=0.5$), and (c) Pb3*S* ($n=1.0$).

2223 phases. There are also some unidentified peaks (indicated by cross marks) in Fig. 2. However, after final heating at 840 °C (for 24 h) the samples become superconductors having mostly superconducting 2212 and 2223 phases along with traces of Ca_2PbO_4 phase. At this annealing temperature the additional phases formed in the samples during the partial heating at 500 °C disappear. Similar crystallization kinetics of this type of glasses was also discussed in a recent review by Bansal.[18] The XRD pattern of the glass-ceramic samples (Fig. 3) annealed at 840 °C for 24 h (which are superconducting as discussed below) can be fitted with the pseudotetragonal structure. The lattice parameters thus obtained for the Pb1*S*, Pb2*S*, and Pb3*S* superconducting samples are given in Table II. These values of the lattice constants agree quite well with the reported values[19] of the corresponding superconducting samples.

The scanning electron micrographs (SEM) of a typical as-quenched glass sample (viz. $Bi_{3.5}Pb_{0.5}Sr_3Ca_3Cu_4O_x$) and the corresponding glass ceramics are shown in Fig. 4.

Other samples also show identical features. The glass samples annealed at 500 °C for 10 h display [Fig. 4(b)] features of 3–10 μm in size. The homogeneously distributed particulate feature of the crystallites seen in the samples annealed at 500 °C is considered to arise from copious nucle-

TABLE II. Values of the lattice constants (fitted with tetragonal structure) and superconducting transition temperatures T_{c0} (zero resistance temperature) of superconducting glass ceramics (the $Bi_{4-n}Pb_nSr_3Ca_3Cu_4O_x$ glasses annealed at 840 °C for 24 h).

	Lattice constants (Å)				
Superconducting	2212 phase		2223 phase		
glass ceramics	*a*	*c*	*a*	*c*	T_{c0} (K)
Pb1*S*	5.4142	30.7460	5.3247	37.7047	72
Pb2*S*	5.4067	30.7333	5.6455	37.0199	73
Pb3*S*	5.3949	30.5793	5.7127	37.5441	78

(a)

(b)

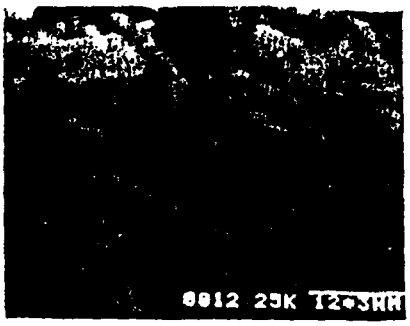

(c)

FIG. 4. Scanning electron micrographs of $Bi_{4-n}Pb_nSr_3Ca_3Cu_4O_x$ (for $n=0.5$) for as-quenched glass (a), the glass-ceramic annealed at 500 °C for 10 h (Pb2A) (b), and the superconducting glass-ceramic annealed at 840 °C for 24 h (Pb2S) (c). [Scale: (a) 23 mm = 120 μm, (b) 20 mm = 20 μm, and (c) 20 mm = 10 μm.]

ation in the phase separated microstructures of the as-quenched glasses. The glass ceramics annealed at 840 °C, however, show pure crystalline structure [Fig. 4(c)].

B. Electrical conductivities of as-quenched glasses

The thermal variation of σ_{dc} of the Pb-doped (4334) glasses are almost similar to those of the Li-doped (4334) glasses discussed earlier [Ref. 1]. Variation of dc conductivity (σ_{dc}) as a function of inverse temperature and $\sigma_{dc}T^{1/2}$ as a function of $T^{-1/4}$ are shown, respectively, in Figs. 5 and 6.

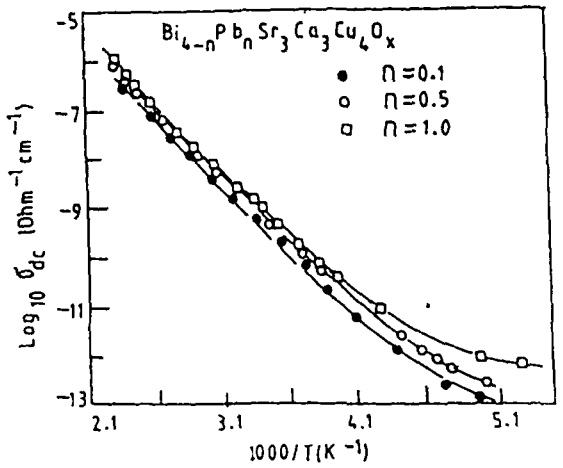

FIG. 5. The logarithm of dc conductivity of the as-quenched $Bi_{4-n}Pb_nSr_3Ca_3Cu_4O_x$ (for $n=0.1$, 0.5, 1.0) glasses as a function of T^{-1}.

These data can be analyzed with nearest-neighbor hopping of small polarons, proposed by Mott[20,21] (for the region of $T > \theta_D/2$, θ_D being the Debye temperature) and Greaves' variable range hopping[22] (for $T < \theta_D/2$) as discussed below. The expression for the dc conductivity (σ_{dc}) as proposed by Mott[20,21] can be written as (for $T > \theta_D/2$)

$$\sigma_{dc}=[\nu_{ph}Ne^2R^2C(1-C)\exp(-2R\alpha)\exp(-W/k_BT)]/k_BT, \quad (1)$$

where N, ν_{ph}, α^{-1}, R, W, and C, are, respectively, the number of transition metal (Cu) ion per unit volume, the optical phonon frequency, localization length of the s-like wave function assumed to describe the localized states at each transition metal (Cu) ion site, average intersite separation, activation energy for the hopping conduction and the ratio of the transition metal (TM) ion concentration in the low valence states to the total TM ion concentrations. In Eq. (1) k_B and T are Boltzmann constant and absolute temperature, respectively. Assuming a strong electron-phonon coupling[23] the activation energy W is given by

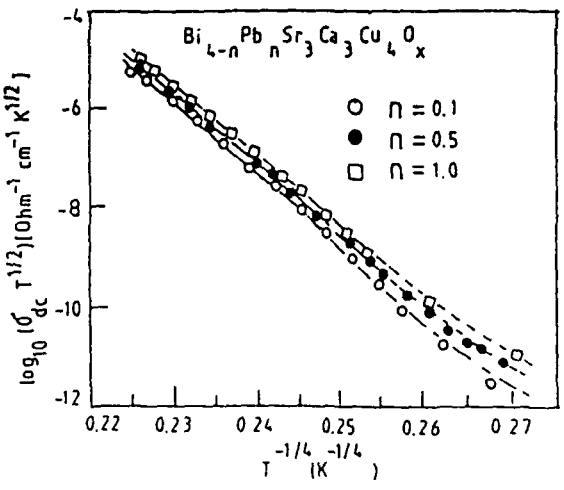

FIG. 6. The variation of $\log_{10}(\sigma_{dc}T^{1/2})$ with $T^{-1/4}$ of the as-quenched $Bi_{4-n}Pb_nSr_3Ca_3Cu_4O_x$ glasses.

$$W = W_H + W_D/2 \quad (\text{for } T > \theta_D/2) = W_D \quad (\text{for } T < \theta_D/4), \tag{2}$$

where W_H and W_D are, respectively, the polaron hopping energy and disorder energy arising from the variation of local arrangements of the ions, and θ_D, defined by $h\nu_{ph} = k_B\theta_D$, is the characteristic Debye temperature. In the adiabatic limit, the overlap integral $I = \exp(-2\alpha R)$ in Eq. (1) reduces to unity.

Schnakenberg[24] also showed theoretically that in amorphous solids, for $T < \theta_D/2$ the contribution to σ_{dc} comes predominantly from acoustic phonon, while for $T > \theta_D/2$, the main contribution to σ_{dc} is the phonon assisted conductivity and hence the temperature dependence of conductivity is different in the temperature ranges on either side of $T_k \sim \theta_D/2$. Schnakenberg model predicts a sharp decrease in activation energy with decrease in temperature at T_k. The temperature dependent conductivity in this model has the form

$$\sigma_{dc} = \sigma_0 T^{-1}[\sinh(h\nu_{ph})]^{1/2}\exp[-(4W_H/h\nu_{ph}) \times \tanh(h\nu_{ph}\beta/4)]\exp(-W_D\beta), \tag{3}$$

where σ_0 is a temperature independent parameter and $\beta = 1/k_BT$.

The experimental conductivity data above a typical characteristic temperature T_k (say) ~250 K (where nonlinearity is observed in Fig. 5) are fitted with Eq. (1). The experimental conductivity data are fitted by least squares method similar to our earlier work [Ref. 1] and the best fit parameters are shown in Table I. The phonon frequency ν_{ph} are obtained from the infrared data.[25] The value of C is estimated from magnetic susceptibility and atomic absorption [Ref. 1]. The values of α shown in Table I are reasonable for localized states and indicate strong localization as in the case of Li-doped (4334) glasses and many other transition metal oxide (TMO) glasses as discussed in Ref. 1. An estimation of polaron radius r_p which is related[26] to W_H ($W_H = 4e^2/\epsilon_p r_p$) has also been made for all the glasses and are shown in Table I. The effective dielectric constant ϵ_p is obtained from dielectric constant data.[15,16] The estimated values of r_p (as shown in Table I) also suggest that the polarons are highly localized in the undoped and Pb-doped $Bi_4Sr_3Ca_3Cu_4O_x$ glasses.

At sufficiently low temperatures where the polaron binding energy is small and static disorder energy of the glass plays a dominant role in the conduction process, Mott's $T^{-1/4}$ analysis for the variable range hopping (VRH) can, in general, be applied for the TMO glasses. But for the Pb-doped glasses, sufficient data at low temperature is not available due to experimental limitations and very high resistivity of the samples which is also found to be true for Li-doped $Bi_4Sr_3Ca_3Cu_4O_x$ glasses [Ref. 1]. An attempt to verify the applicability of this law gives unacceptably large values of α and W_D.

At the intermediate temperature region Greaves[22] suggested a variable range hopping conduction and derived an expression for the conductivity as

$$\sigma_{dc}T^{1/2} = A\exp(-B/T^{1/4}), \tag{4}$$

where A and B are constants and $B = 2.1[\alpha^3/k_BN(E_F)]^{1/4}$, $N(E_F)$ is the density of states at the Fermi level. $N(E_F)$ values (shown in Table I) are obtained from the ac conductivity data of these glasses.[15,25] In Fig. 6 (continuous line), the experimental conductivity data in the low temperature region are fitted with Greaves' VRH model [Eq. (4)]. The values of α estimated from the best fit are also reasonable for localized states[27] and are consistent with the values obtained by the fitting of the conductivity data with Eq. (1) (as shown in Table I). Similar values of α are also obtained for the Li-doped $Bi_4Sr_3Ca_3Cu_4O_x$ glasses and other TMO glasses.[12,15]

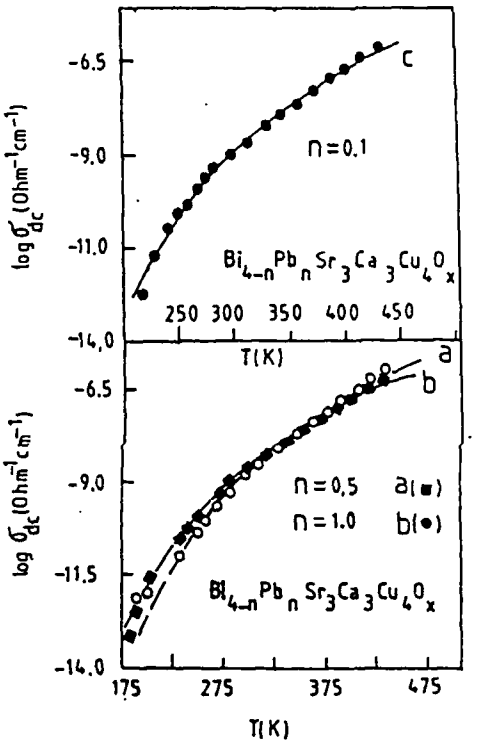

FIG. 7. Theoretical fitting of the dc-conductivity data with Eq. (3) of the as-quenched $Bi_{4-n}Pb_nSr_3Ca_3Cu_4O_x$ glasses: (a) $n = 0.5$, (b) $n = 1.0$, and (c) $n = 0.1$.

The experimental data has also been fitted with Schnakenberg model [Eq. (3)] as shown in Fig. 7. The best fit parameters are shown in Table III. W_H is almost same for all the as-quenched glasses, but it is different from the values obtained by the fitting with Mott's model (Table I). The values of W_D decreases with increase of Pb concentration in the (4334) glasses.

The hopping mechanism (adiabatic or nonadiabatic) of these glasses could be suggested[28] by plotting $\log_{10}(\sigma_{dc})$ vs W at a fixed temperatures. The temperature T_e (say), esti-

TABLE III. Best fit parameters obtained from Schnakenberg's conductivity equation [Eq. (3)] for the as-quenched $Bi_{4-n}Pb_nSr_3Ca_3Cu_4O_x$ glasses with $n = 0.1$ (Pb1), $n = 0.5$ (Pb2), and $n = 1.0$ (Pb3).

Glasses	ν_{ph} (Hz)	W_H (eV)	W_D (eV)
Pb1	2.0×10^{12}	0.468	0.050
Pb2	3.9×10^{12}	0.513	0.012
Pb3	5.2×10^{12}	0.513	0.009

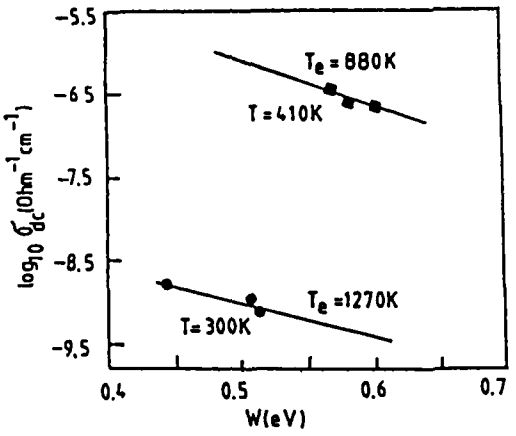

FIG. 8. The logarithm of dc conductivity of the as-quenched glasses as a function of W (activation energy), obtained from Fig. 5, at two fixed temperatures (300 and 410 K). The estimated temperature from slopes of these two curves are 1270 and 880 K, respectively.

mated from the slope of such a plot would be close to the experimental temperature when the hopping is considered to be in adiabatic regime. On the other hand, T_e would be very different from experimental temperature if the hopping is considered to be in the nonadiabatic regime. Such a plot for two fixed temperature (T=300 and 410 K) is shown in Fig. 8 and the corresponding T_e values estimated (1270 and 883 K, respectively) are very much different from experimental temperatures in the Pb-doped (4334) glasses. Thus the hopping mechanism of these as-quenched glasses is in the nonadiabatic regime as in the case of Li-doped $Bi_4Sr_3Ca_3Cu_4O_x$ glasses.[12,15] The nonadiabatic hopping is also supported from the validity of Emil-Holstein relation.[29] According to this relation the polaron bandwidth J satisfies the inequality

$$J \gtrless (2k_BTW_H/\pi)^{1/4}(h\nu_{ph}/\pi)^{1/2}, \quad (5)$$

where the signs > and < are for adiabatic and nonadiabatic hopping, respectively. The values of $(2k_BTW_H/\pi)^{1/4}(h\nu_{ph}/\pi)^{1/2}$ vary from 0.0279 to 0.0284 at 300 K for all the concentrations. The values of J estimated independently from $J \sim \hbar e^3[N(E_F)/\epsilon_p^3]^{1/2}$, are of the order of 0.022 eV. Thus, in Pb-doped glasses $J \lesssim (2k_BTW_H/\pi)^{1/4}(h\nu_{ph}/\pi)^{1/2}$ which suggests that the nearest-neighbor hopping mechanism occurs in the nonadiabatic regime. This behavior is also similar to the Li-doped $Bi_4Sr_3Ca_3Cu_4O_x$ glasses reported earlier [Ref. 1].

C. Electrical conductivity of partially annealed glasses and glass-ceramic superconductors

The dc conductivity data of the corresponding partially annealed (annealed at 500 °C for 10 h) $Bi_{4-n}Pb_nSr_3Ca_3Cu_4O_x$ (n=0.1, 0.5, 1.0) glasses also showing semiconducting behavior (Fig. 9) can also be similarly analyzed by using the polaron hopping conduction mechanism. However, in this case, as discussed below, the nature of the polaron hopping conduction mechanism changes from nonadiabatic regime to adiabatic regime.

The semiconducting character of these samples is clearly observed from the temperature dependence of conductivity

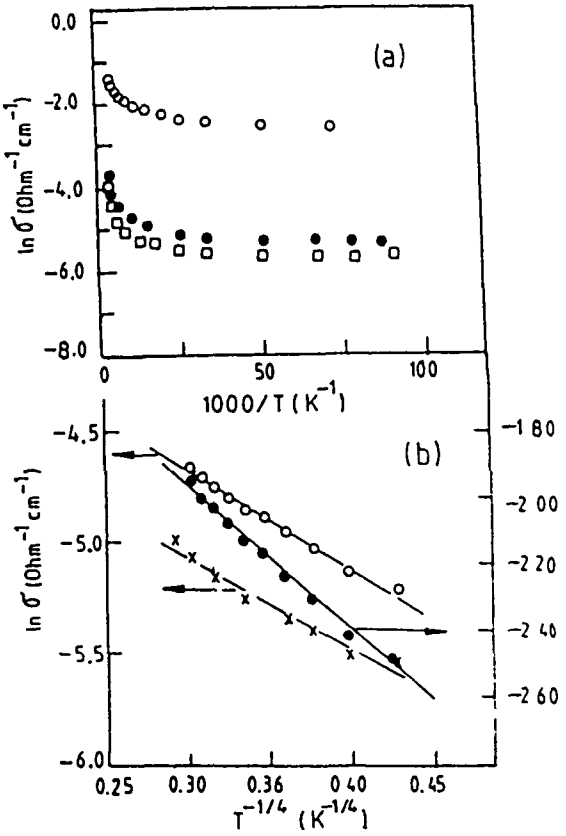

FIG 9. (a) The logarithm of dc conductivity of the partially annealed (at 500 °C for 10 h) $Bi_{4-n}Pb_nSr_3Ca_3Cu_4O_x$ glass ceramics as a function of T^{-1} with n=0.1 (□), 0.5 (●), and 1.0 (○). (b) The logarithm of the low-temperature (T<125 K) conductivity of the partially annealed at 500 °C for 10 h) $Bi_{4-n}Pb_nSr_3Ca_3Cu_4O_x$ [for Pb1A (n=0.1) (×), Pb2A (n=0.5) (○), and Pb3A (n=1.0) (●)] glass ceramics as a function of $T^{-1/4}$.

data plotted in Fig. 9(a). The Debye temperature θ_D, estimated from the temperature where nonlinearity begins, varies from 465 to 488 K with Pb concentration (Table IV) and these θ_D values for these partially annealed glasses are greater than those of the as-quenched glasses (Table I) These values of θ_D (465–488 K) also supports the theoretical value of the superconducting Bi-Pb-Sr-Ca-Cu-O system [30,31] But the Debye temperature shows opposite behaviors with increasing Pb concentration in as-quenched glasses (Table I) and in the partially annealed glass ceramics (Table IV), respectively For the first case θ_D is decreasing with the increase of Pb concentration while for the second case it is increasing with increase of Pb content Actually the procedure used in evaluating θ_D is not usual and quite rough So this strange result might be due to the rough evaluation of θ_D in the partially annealed glass ceramics. Moreover, the multiple phases characterizing the annealed samples (observed from XRD pattern in Fig 2) make the use of the appropriate techniques (ultrasounds and infrared spectroscopy) quite difficult for determining the correct values of θ_D. Therefore the corresponding values of θ_D must be considered only in the light of the order of magnitude The characteristic phonon frequency $\nu_{ph}(=k_B\theta_D/h)$ also changes

TABLE IV. Values of different parameters of the annealed glass ceramics (the $Bi_{4-n}Pb_nSr_3Ca_3Cu_4O_x$ glasses annealed at 500 °C for 10 h.

Parameters	Pb1A ($n=0.1$)	Pb2A ($n=0.5$)	Pb3A ($n=1.0$)
Density (gm/cc)	6.939	6.722	6.776
N (10^{21} cm^{-3})	9.63	9.39	9.49
R (Å)	4.704	4.739	4.723
r_p (Å)	1.88	1.91	1.90
θ_D (K)	465	476	488
ν_{ph} (10^{12} Hz)	9.70	993	10.18
$N(E_F)$ * (10^{21} eV^{-1} cm^{-3})	3.50	4.80	5.10
α (Å^{-1})	0.018	0.019	0.019
W (eV) (at 300 K)	0.11	0.095	0.036
γ	5.49	4.68	1.71

with the increase of Pb as shown in Table IV (corresponding values for the as-quenched glasses as shown in Table I).

The dc conductivity of the partially annealed samples, viz. Pb1A, Pb2A, and Pb3A, in the low temperature region ($T < 125$ K) can be fitted with the equation[23]

$$\sigma_{dc} = A \exp(-B/T^n). \quad (6)$$

The value of the exponent n determines the nature of the conduction mechanism in the semiconducting region of the sample. A and B in Eq. (6) are constants and

$$B = 2.1[\alpha^3/k_B N(E_F)]^{1/4}. \quad (7)$$

Experimental conductivity data are fitted with Eq. (6) using least squares method. The results are presented in Fig. 9(b). Below 125 K ($< \theta_D/2$), the resistivity of the samples may be well described by the relation (6) with $n = 1/4$. This suggests that the conduction in the low temperature region is governed by a three dimensional variable range hopping mechanism.[23]

The $N(E_F)$ values of these partially annealed glass ceramics have been calculated from the corresponding ac conductivity measurement as in the case of as-quenched glasses. Table IV shows that these values of $N(E_F)$ lie between 10^{21}–10^{22} eV^{-1} cm^{-3}. These values of $N(E_F)$ of the partially annealed glass ceramics also agree quite well with those obtained from the superconducting Bi-2212 system.[3]

As mentioned above, the hopping conduction mechanism in all the partially annealed glasses changes to the adiabatic regime. From the plot of $\log_{10}(\sigma_{dc})$ vs W (Fig. 10), the estimated temperatures T_e (as in the case of as-quenched glass samples; Fig. 8) are 304 and 222 K which are very close to the corresponding experimental temperatures, viz. 300 and 220 K, respectively. This suggests[28] that the hopping mechanism is in the adiabatic regime. The Holstein condition[29] for adiabatic hopping [Eq. (5)] is also satisfied for these partially annealed glassy precursors. The values of α estimated from

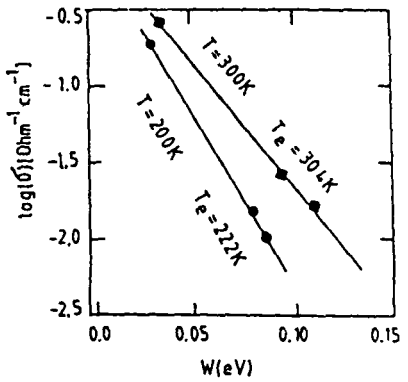

FIG. 10. The logarithm of the dc conductivity of the PbA-type samples as a function of W, at two fixed temperatures (at 220 and 300 K). The estimated temperatures from the slopes of these two curves are 222 and 304 K, respectively.

Eq. (7) using the values of $N(E_F)$ from Table IV are found to be very small and almost constant. These low values of α (Table IV) also support the adiabatic hopping mechanism. Therefore, a change over in hopping mechanism from nonadiabatic to adiabatic regime takes place when the as-quenched glasses are annealed at 500 °C for 10 h (similar behavior is also found for these glasses annealed at 300°C for 24 h or more). Therefore, nonadiabatic hopping mechanism is true for the pure glassy precursors for high-T_c superconductors which is in contrast to the observation of Singh and Zacharias.[14] The adiabatic hopping conduction is observed, due to the presence of more conducting microcrystals in these partially annealed glasses. It is important to mention here that these more conducting microcrystalline clusters might even form in the glass at the time of preparation which changes the conduction mechanism along with other properties.

Assuming the high temperature activation energy W to be close to the hopping energy W_H [Ref. 23], we can roughly estimate the electron-phonon coupling strength $\gamma = W_p/k_B\theta_D$, where W_P is the polaron binding energy and equal to $2W_H$. Activation energy W calculated from Fig. 9(a) (plot of $\ln\sigma$ vs $1000/T$) for a typical Pb1A sample, at room temperature, is about 0.11 eV. The electron-phonon coupling constant γ, calculated with this value of W, is 5.49. The values of γ decrease with increase of annealing time of the samples (Tables I and IV).

To get the idea about the size of polaron we use the formula[26] which has been used in the case of as-quenched glasses. For the Pb2A glass ceramic the radius of the polaron is estimated to be ~2 Å. We have also evaluated all these parameters for the as-quenched unannealed glasses (Table I). The values of r_p for the as-quenched and the partially annealed (at 500 °C for 10 h) glasses remain almost same (Tables I and IV). We have also tried to fit the dc conductivity data of the partially annealed PbA sample with the Schnakenberg model [Eq. (3)], but the fitting parameters obtained are not feasible.

Figure 11 shows the temperature dependences of the resistivity for the $Bi_{4-n}Pb_nSr_3Ca_3Cu_4O_x$ ($n=0.1$, 0.5, 1.0) glass ceramic (heat treated at 840 °C for 24 h). All these samples show metallic behavior above the superconducting transition temperature T_c, varying from 110 to 115 K. The

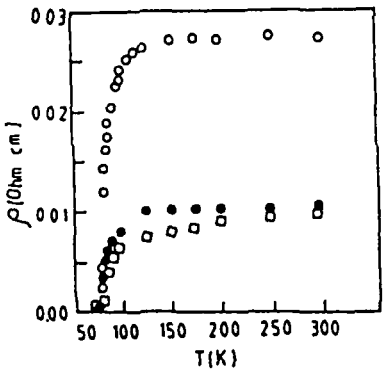

FIG. 11. Thermal variation of the resistivity of the superconducting $Bi_{4-n}Pb_nSr_3Ca_3Cu_4O_x$ glass ceramics [with $n=0.1$ (Pb1S) (□), 0.5 (Pb2S) (●), and 1.0 (Pb3S) (○) annealed at 840 °C for 24 h.

corresponding T_{c0} (zero resistance temperature) values are 72, 73, and 78 K, respectively, for $n=0.1$, 0.5, and 1.0.

D. Thermoelectric power

Thermoelectric power of all the Pb-doped as-quenched glassy semiconductors is found to be positive indicating holes are the carriers, which is due to donation of holes by the Pb ions. However, because of large resistances of the samples reliable TEP data of the glasses cannot be obtained The thermal variation of TEP data of the partially annealed PBA glasses can be measured and are shown in Fig. 12. As observed from this figure, the TEP values increase with increase of temperature unlike many semiconducting oxide glasses where, as suggested by Heikes' model[32] thermoelectric power $S=k/e[\ln(c/(1-c))+a]$, where a is a constant, is almost temperature independent.

It is interesting to note that the temperature dependent TEP is drastically changed for the glass-ceramic superconductors (Fig. 13). Here, for all such samples, the temperature dependent TEP values are negative around 300 K and the sign changes from negative to positive around 290 K. As temperature decreases, the S increases exhibiting a peak around 115 K ($\sim T_c$) and then suddenly drops to zero at 72, 73, and 78 K (the zero resistance temperature, T_{c0}) for the Pb1S, Pb2S, and Pb3S samples, respectively. This behavior is consistent with the fact that in the superconducting state, the S becomes zero. The variation of S above 120 K of these samples is very similar to that obtained[33] for the doped La-Sr-Cu-O.

It has been suggested[34] that the Hubbard model well describes the basic physics of these high-T_c materials For large on-site repulsion, the TEP for a Hubbard model (in the high temperature limit) is given by

$$S=-(k/|e|)\ln 2-(k/|e|)\ln(p/1-p) \qquad (8)$$

Entropy considerations lead to this formula with p equal to the ratio of Cu^{3+} to the Cu_r, if the conduction process involves hopping d electrons and/or holes from one Cu^{2+} to a Cu^{3+} ion. The ln2 term appears from the spin degree of freedom and would be absent if Cu^{2+} ions are magnetically

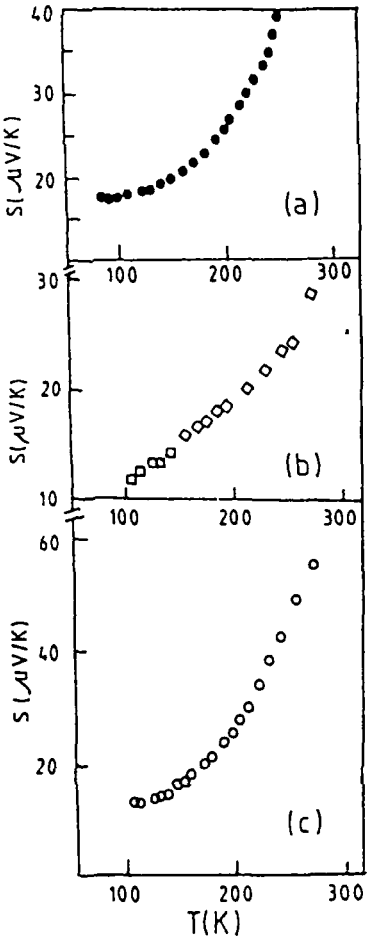

FIG 12 Thermal variation of the thermoelectric power (S) of (a) Pb1A (●), (b) Pb2A (□), and (c) Pb3A (○)

ordered. On the other hand, if Cu^{2+} ions are not ordered and have twofold orbital degeneracy (which occurs for strictly octahedral symmetry) there would be an extra ln2 term from the orbital degrees of freedom. The magnetic ordering is absent in this system[35] and, therefore, the modified expression for TEP is

$$S=-(2k/|e|)\ln 2-(2k/|e|)\ln(p/1-p). \qquad (9)$$

At room temperature for our Pb1S superconducting, sample, the hole concentration is 0 198 per Cu ion For Pb2S and Pb3S the values of hole concentration are almost same ($\sim$0 199 per cu ion) The values are slightly greater than the results obtained by Tarascon *et al*[35] where, for the undoped $Bi_4Sr_3Ca_3Cu_4O_x$ (4334) ceramic superconductor, they found a hole concentration of 0 15 per Cu ion by TGA and titration experiments This increase in hole concentration per Cu ion, in the present system, is simply due to doping of Pb as it acts as a hole donor

We have also fitted the TEP data of our superconducting samples using the expression

$$S=[AT/(B^2+T^2)]+\alpha' T, \qquad (10)$$

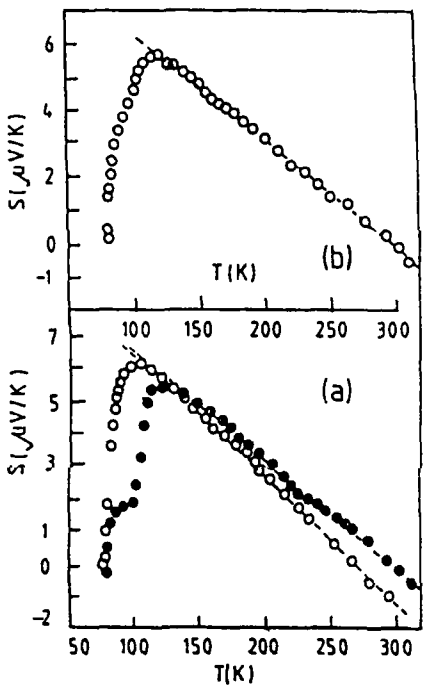

FIG. 13. The thermal variation of the thermoelectric power (S) of the superconducting $Bi_{4-n}Pb_nSr_3Ca_3Cu_4O_x$ glass ceramics annealed at 840 °C for 24 h: (a) $n=0.1$ (Pb1S) (○), $n=0.5$ (Pb2S) (●), and (b) $n=1.0$ (Pb3S) (○). The dotted line represent the best fit curve with Eq. (10). The same best fit curve is obtained with Eq. (12).

which has been used by Forro *et al.*,[36] where the second term is the normal band contribution. The first term, as proposed by Gottwick *et al.*[37] for the analysis of the TEP data of $CeNi_x$ samples, is obtained by assuming superposition of broad band and a localized band with a peak position at ϵ_0 and width Γ. The constants A and B are given by

$$A=2(\epsilon_0-\epsilon_F)/|e| \quad \text{and} \quad B^2=[(\epsilon_0-\epsilon_F)^2+\Gamma^2]/\pi^2k_B^2, \tag{11}$$

where ϵ_F is the Fermi energy. The TEP results of our samples fitted to Eq. (10) in the temperature range of 110–300 K are shown in Fig. 13. The best fit parameters A, B, and α' are given in Table V along with the values of $(\epsilon_0-\epsilon_F)$ and Γ. For all the samples α' is found to be negative and nearly the same. However, with the increase of Pb concentration, $(\epsilon_0-\epsilon_F)$ decreases but Γ increases systematically.

The TEP results of the glass ceramics which become superconductors after annealing at 840 °C for 24 h have also been fitted with the Nagaosa-Lee model[38] which is actually a modification of the model proposed by Ikagawa *et al.*[39] Nagaosa and Lee proposed that for a superconducting cuprate, there are two contributions in the TEP, one coming from bosons (S_B) and another from fermions (S_F): $S=S_B+S_F$ with, $S_B=(k_B/e)[1-\ln(2\pi p/mk_BT)]$ and $S_{qF}=-[k_B/e]k_BT/\epsilon_F$, where p is the concentration of holes per (Cu-O) bond and m is the mass of the bosonic carrier.

TABLE V. Best fit parameters A, B, and α' of Eq. (3) and F, G, and H of Eq. (4) and $(\epsilon_0-\epsilon_F)$, Γ values determined from A and B of the superconducting glass ceramics obtained by annealing the $Bi_{4-n}Pb_nSr_3Ca_3Cu_4O_x$ glasses at 840 °C for 24 h.

Value of	Pb1S ($n=0.1$)	Pb2S ($n=0.5$)	Pb3S ($n=1.0$)
$A(\mu V)$	1880	1840	1800
B (K)	112	124	127
$\alpha'(\mu V/K^2)$	−0.023	−0.018	−0.018
$(\epsilon_0-\epsilon_F)$ (K)	10.9036	10.6716	10.4396
Γ (K)	202.853	224.658	230.116
F	0.0629	0.0637	0.0638
G (K)	5.95×10^7	5.95×10^7	6.00×10^7
H (K)	1.33×10^3	1.48×10^3	1.478×10^3

To fit the TEP results of some superconducting as well as nonsuperconducting compounds, Ikegawa *et al.* modified the above equation in the following form:

$$S=k_B/e[1-F\ \ln(2\pi pG/T)-T/H], \tag{12}$$

where, F, G, and H are the fitting parameters.

The thermoelectric power of the superconducting samples can also be well fitted, like Eq. (10), to Eq. (12). The best fit curves obtained with Eqs. (10) and (12) are almost similar as shown in Fig. 13 [for the best fit with Eq. (10)]. The corresponding fitting parameters, viz. F, G, and H, are also shown in Table V.

IV. SUMMARY AND CONCLUSIONS

The $Bi_{4-n}Pb_nSr_3Ca_3Cu_4O_x$ glass ceramics annealed at 500 °C for 10 h remain semiconductor similar to the corresponding as-quenched glasses. Small polaron hopping conduction mechanism is valid for all these samples. However, a change over from the nonadiabatic small polaron hopping conduction mechanism to the adiabatic hopping conduction mechanism takes place with increase of annealing time and temperature (for instances at 500 °C for 10 h and at 300 °C for 24 h). This is due to the formation of microcrystals in these annealed glasses as observed from XRD patterns and SEM studies. It is important to note that such microcrystals might also form even in the as-quenched glasses (depending on quenching rate, etc.) and as a consequence such glasses would show the adiabatic hopping mechanism instead of the nonadiabatic hopping mechanism as observed by Singh and Zacharias[14] and Som and Chaudhuri.[17] It is further observed that the semiconducting behavior of the as-quenched and the partially annealed glasses, at low temperature, follow the variable range hopping conduction mechanism. The values of the density of states $N(E_F)$ also increase with annealing time. The thermal variation of thermoelectric power indicates that the Pb-doped Bi-Sr-Ca-Cu-O glasses and the corresponding glass ceramics are p-type semiconductors.

All the Pb-doped glasses of our present investigation become superconducting after annealing at 840 °C for 24 h. The positive TEP values of these superconductors again indicate that the Pb-Bi-Sr-Ca-Cu-O type glass ceramics are

hole-type superconductors. It has also been found that the thermoelectric power of the superconducting glass ceramics varies systematically with the carrier concentrations (the carrier concentration is changed by substituting Pb at the Bi site). The zero value of the TEP at temperature T_{c0} is consistent with the corresponding zero resistance temperature of the glass-ceramic superconductor under investigation. The negative value of TEP around 300 K indicates the presence of both electrons and holes in the system. Similar coexistence of holes and electrons has also been very recently reported[40] in the superconducting $BaBi_{0.25}Pb_{0.75}O_{3-\delta}$ and $Ba_{0.74}K_{0.57}Bio_{3-\delta}$ oxides. Again since the Nagaosa-Lee model considers bosonic carriers and also fit the TEP data, the contribution of the bosons in the thermoelectric power appears to be important.

Finally, since the semiconducting behavior of the glassy and partially annealed Pb-doped system can be well explained by the small polaron hopping conduction mechanism, one might argue that the superconductivity in the present glass ceramics (and in other related systems) is bipolaronic in origin.[41,42] These bipolarons (or "spin polarons"[41]), might be created (with lowering of temperature) from the small polarons already existing in the glassy phase. Indeed, experimental evidence of polaron hopping has been reported in a layer structure of superconducting cuprates [43]

ACKNOWLEDGMENTS

The authors are grateful to the University Grants Commission (UGC), and to the Department of Science and Technology (DST) for providing financial assistance. The facilities for the XRD, SEM, EDX, IR, and atomic absorption studies provided by the Departments of Materials Science, Inorganic Chemistry, and Organic Chemistry are also gratefully acknowledged. The authors are also grateful to Professor H Sakata of Tokai University, Japan, for his valuable comments

[1] Y. Abe, H Hosono, M. Hosoe, J. Iwase, and Y. Kubo, Appl. Phys. Lett. 53, 1341 (1988).

[2] S. Mollah, A. K Chakraborty, S. Chakraborty, K. K. Som, and B. K. Chaudhuri, J. Non-Cryst. Solids 165, 192 (1994).

[3] M. Onishi, M. Kyoto, and M. Watanwdabe, Jpn. J. Appl. Phys. 30, L1545 (1991).

[4] E. Takayama-Muromachi, Y. Uchida, A. Ono, F. Izumi, M Onoda, Y. Matsui, K. Kasuda, S. Takekawa, and K. Kato, Jpn. J. Appl. Phys. 27, 1365 (1988).

[5] E. Takayama-Muromachi, Y. Uchida, Y. Matsui, M. Onoda, and K. Kato, Jpn. J. Appl. Phys. 27, L556 (1988).

[6] R. Ramesh, G. Thomas, S. M. Green, C. Jiang, Y. Mei, M. L. Rudee, H. L. Luo, and C. Politis, Phys. Rev. B 38, 7070 (1988).

[7] M. Takano, J. Takada, K. Oda, H. Kitaguchi, Y. Miura, Y. Tomii, and H. Mazaki, Jpn. J. Appl. Phys. 27, L1041 (1988).

[8] U. Endo, S. Koyama, and T. Kawai, Jpn. J. Appl. Phys. 28, L190 (1989).

[9] T. Komatsu, R. Sato, K. Matusita, and T. Yamashita, Appl. Phys. Lett. 54, 1169 (1989).

[10] L. R. Yuan, K. Kurosawa, Y. Takigawa, M. Okuda, H. Naito, K. Nakahigashi, S. Nakanishi, and T. Matsushita, Jpn. J. Appl. Phys. 30, L1545 (1991).

[11] R. C. Baker, W M. Hurng, and H. Stienfink, Appl. Phys. Lett 54, 371 (1989).

[12] S Mollah, K K. Som, K Bose, A. K. Chakraborty, and B K Chaudhuri, Phys Rev B 46, 11 075 (1992).

[13] S Mollah, K K Som, K Bose, and B K Chaudhuri, J Appl Phys 71, 931 (1993)

[14] R Sing and E Zacharias (unpublished).

[15] S Mollah, Ph.D. thesis, Jadavpur University, 1993.

[16] S Mollah, S. Chatterjee, S. Chakraborty, and B K. Chaudhuri, Philos Mag B 71, 151 (1995)

[17] K K Som and B. K. Chaudhuri, Phys Rev. B 41, 1581 (1990)

[18] N P Bansal (unpublished)

[19] A Poddar, P Mandal, A. N Das, B. Ghosh, and P Choudhury, Physica C 161, 567 (1989)

[20] N F. Mott, J Non-Cryst Solids 1, 1 (1968)

[21] E A Davis and N F Mott, Philos Mag. 22, 903 (1970)

[22] G. N. Greaves, J. Non-Cryst Solids 11, 427 (1973)

[23] N F Mott, *Metal Insulator Transitions* (Taylor and Franc, London, 1974)

[24] J. Schnakenberg, Phys. Status Solidi 28, 623 (1968)

[25] S. Mollah, K K. Som, S. Chakraborty, A K. Bera, S Chatterjee, S Banerjee, and B K Chaudhuri, Phys. Rev B 51, 17 512 (1995)

[26] V. N Bogomolov, E K. Kudinov, and Yu A Firsov, Sov Phys Solid State 9, 2502 (1968)

[27] I G. Austin and E. S Garbett, in *Electronic and Structural Properties of Amorphous Semiconductors*, edited by P. G Lecomber and J. Mort (Academic, London, 1973), p. 393.

[28] M. Sayer and A. Mansingh, Phys. Rev. B 6, 4629 (1972)

[29] D. Emin and T. Holstein, Ann. Phys. (N.Y.) 21, 439 (1963)

[30] M. K. Yu, J. P. Frank, and S. Gygax, Physica B 165-166, 1339 (1990).

[31] N. Okazaki, T. Hasegawa, K. Kisluo, K. Kitazawa, A. Kishi, Y Ikeda, M. Takano, K. Oda, H. Kitaguchi, J. Takada, and Y Miura, Phys. Rev. B 41, 4296 (1990).

[32] R. R. Heikes and R. W. Ure, *Thermoelectricity* (Interscience, New York, 1961).

[33] J. R. Cooper, B. Alavi, L. W Zhou, W. P. Beyermann, and G Grüner, Phys Rev B 35, 8794 (1987)

[34] P W Anderson, Science 235, 1196 (1987)

[35] J M Tarascon, Y Le Page, P Barboux, B G Bagley, L H Green, W R Mckinnon, G W Hull, M Giroud, and D M Hwang, Phys Rev B 37, 9382 (1988)

[36] L Forro, J Lukatela, and B Keszei, Solid State Commun 73 501 (1990)

[37] U. Gottwick, K Gloos, S Horn, F Steglich, and N Grewe, J Magn Magn Mater 47&48, 536 (1985)

[38] N Nagaosa and P A Lee, Phys Rev Lett 64, 2450 (1990)

[39] S Ikagawa, T Wada, T Yamashita, A Ichinose, K Matsuura K Kubo, H Ymanchi, and S Tanaka, Phys Rev B 43, 11 508 (1991)

[40] T Hashimoto and R Hirasawa, T Yoshida, Y Yonemura, J Mizusaki, and H Tagawa, Phys Rev B 51, 576 (1995) M Rekala

R. Ratay, A. Pajaezkauska, and B. Gegenheimer, Phys. Status Solidi B 155, K123 (1989).

[41] N. F. Mott, J. Condens. Matter 5, 3487 (1993).

[42] A. S. Alexandrov and N. F. Mott, Rep. Prog. Phys. 57, 1197 (1994); P. Prelovsek, T. M. Rice, and F. C. Zhang, J. Phys. C 20, L229 (1987).

[43] D. Mihailovic, C. M. Foster, K. Voss, and A. J. Heager, Phys. Rev. B 42, 7989 (1990); G. A. Samara, W. F. Hammeter, and E. L. Venturini, Phys. Rev. B 41, 8974 (1990).

ELSEVIER

July 1996

Materials Letters 27 (1996) 187–193

MATERIALS LETTERS

Critical currents of PbBiSCCO Ag/AgCu composites

S. Mollah [1], N. Froumin, M. Polak, J. Baram *

Materials Engineering Department, Ben-Gurion University of the Negev, Beer Sheva, Israel

Received 26 September 1995; revised 13 November 1995; accepted 14 November 1995

Abstract

The superconducting properties of PbBiSCCO containing 10, 20 or 30 wt% of Ag–4 at% Cu additions, as compared to Ag additions, are reported. The highest critical currents have been found for both the 10 wt% Ag–4 at% Cu and Ag composites after 24 h annealing, which are about three times higher than the value measured for pure PbBiSCCO. SEM/EDAX shows that a connectivity effect can account for this finding. The observed superiority of the Ag composites over the Ag–4 at% Cu composites is discussed in terms of the supercurrent transport properties versus interfacial effects.

Keywords: Superconductors; Silver; Silver–copper alloy; Critical temperatures; Critical currents

1. Introduction

Many practical applications of bulk Bi-based high T_c superconductors require high critical current densities. Integration of superconducting devices in electronic circuits, requires maintaining the current carrying ability in ohmic contacts with metals. The volume fraction of the superconducting phases, the relative orientation of the superconducting grains and the connectivity among the grains, all do affect the critical current density, as well as weak links formed at metal-superconductor interfaces [1–3]. High T_c ceramic superconductors are usually brittle and hard to shape. An attractive method for improving their ductility, without impairing the critical current density, is to process it as a composite with a relative high volume fraction of added metal or alloy. In such composite materials, new metal-superconductor interfaces are formed. These composites may be considered as a dispersion of strongly superconductive granular islands embedded in a metallic matrix. In this case, the transport properties are influenced not only by the weak links, but also by the coupling of the superconducting order parameters to Josephson junctions [4]. In the composite material, each Josephson junction is of the SNS, superconductor/normal metal/superconductor, type. The critical current of these SNS junctions is the feature that finally determines the critical current of the whole composite system.

Detrimental chemical reactions may take place at superconductor–metal contacts. Relatively inert metals, such as silver, for example, are therefore prefer-

* Corresponding author.

[1] On leave from the Solid State Physics Department, Indian Association for the Cultivation of Science, Jadavpur, Calcutta-32, India.

SSDI 0167-577X(95)00278-2

able for processing composite superconducting wires and tapes. Apart from improving ductility, silver neither reacts significantly with BiSrCaCuO (BiSCCO), unlike other inert metals belonging to the platinum group, nor does exhibit mutual solubility within the BiSCCO matrix [5].

In Ag/BiSCCO superconductors, the critical current is contradictorily reported to be either improved, or deteriorated, or not affected at all [5–8]. Enhancement in critical current density in Ag/PbBiSCCO is reported to be due to improved connectivity between superconducting grains [7–9]. In Ag/X/PbBiSCCO (X = Cu, In, Pb and Bi) systems, high temperature interdiffusion and segregation phenomena at the interface have been evidenced by wettability measurements combined with Auger electron spectroscopy (AES) [10,11]. X-ray photoelectron spectroscopic (XPS) depth profiling of Ag/PbBiSCCO films annealed up to 700°C has shown Cu enrichment at the interface [11], accompanied by a decrease in contact resistivity [12]. Substituting AgCu for Ag sheeting in powder-in-tube PbBiSCCO caused interfacial Cu segregation [13]. The effect on transport properties has however not been clarified yet. In SNS junctions, the critical current is maximized by high reflection from an SN boundary and by tunneling (in the "clean limit" case [2]), or by the proximity effect [3], which is reduced by high resistivity of the weak link (in the "dirty limit" case) [4].

This paper reports the effects of 10–30% AgCu additions on the electrical properties of the AgCu–PbBiSCCO composite, as compared to those of pure silver. The concentration of copper in the AgCu alloy has been chosen as 4 at%, according to the optimum measured wettability [10], which could be correlated with improvement in transport characteristics. Critical currents values in the composite material are assessed on the basis of possible influence of either interfacial processes or junction transport properties.

[2] "Clean" or "dirty" limits reffer to the amount of impurities which are present in the normal metal [4].

[3] The "proximity" effect is the formation of a superconducting correlation in the normal metal, through the SN interface, and the concommutant suppression of the order parameter in the superconductor, near the SN interface [4,14]

2. Experimental

Commercial PbBiSCCO powders with metal stoichiometry $Pb_{2.82}Bi_{19.26}Sr_{24.94}Ca_{24.24}Cu_{28.23}$, heat treated for superconductivity by the supplier (Hoechst, Germany), were used. The powders were mixed with 10 wt%, 20 wt% and 30 wt% Ag-4 at% Cu chips (in the 30.0 to 50.0 μm size range) or with silver powders (in the 1.7 to 3.3 mm size range), both compacted in 1.5 mm thick pellets, in an hydraulic press (at a pressure of 25 t). The pellets were annealed at 810°C for 24 and 48 h in air, followed by furnace cooling. Table 1 shows the labeling of the samples. Annealing at 840°C, as recommended in the literature [7,9], did invariably result in partial melting of the pellets, enhanced by the presence of the Ag and AgCu additions. The annealed samples were cut into 9.0 × 6.0 mm platelets for critical current and critical temperature measurements. Compositional and microstructural features were analyzed by a Jeol 35C SEM with an EDAX attachment. Elemental mapping has been done in correlation with microstructural features, and is depicted on backscattered electron images. Relative volume fractions of the superconductive (2201, 2212 and 2223) and of the impurity (Ca_2PbO_4) phases have been evaluated by comparing intensities of characteristic X-ray diffraction peaks, obtained by a PW 1050-70 diffractometer with Cu Kα radiation [2]. Electrical resistivity was measured by the four-probe dc method, from room to liquid nitrogen temperatures. The point contacts consisted of copper wires indium-brazed to

Table 1
Sample identification

Sample	Weight fraction of metal in the composite	24 h	48 h
PbBiSCCO	–	AI	AII
	10%	BI(10)	BII(10)
PbBiSCCO/Ag	25%	BI(25)	BII(25)
	30%	BI(30)	BII(30)
PbBiSCCO/Ag–4 at% Cu	10%	CI(10)	CII(10)
	25%	CI(25)	CII(25)
	30%	CI(30)	CII(30)

silver coated PbBiSCCO samples. At room temperature, the contact resistance ranged from 0.1 to 0.3 Ω. When the four-probe dc method is used for critical superconducting currents measurements in bulk material, heat dissipation may cause deleterious heating of the sample. Therefore, for currents in the range of 10 to 100 Å measured in this study, pulsed ac currents have been used [15]. In this method, the critical current I_c is defined, from the dynamic I–V characteristic curve, as the current corresponding to 10 μV cm^{-1}.

3. Results and discussion

3.1. Elemental and phase analyses

No significant compositional changes have been detected in the 48 h annealed, as compared to the 24 h annealed samples, in both the Ag and the AgCu added PbBiSCCO composites. Backscattered electron images of samples BI(10) and BI(30) are shown in Fig. 1a and 1c respectively, and the corresponding elemental mapping is seen in Fig. 1b and 1d. In both samples, clustered silver areas are seen, with sizes ranging from 12.0 to 25.0 μm. Overall area coverage and silver clustering are both more pronounced in the BI(30) samples than in BI(10).

Relative volume fractions of the 2201, 2212, 2223 superconducting and the Ca_2PbO_4 impurity phases are shown on Fig. 2a–2d. No correlation is observed between the evolution of the phases and the amount of metallic addition. Samples with 10% added Ag or Ag–4 at% Cu (series I), contain nearly the same amount of the 2201, 2212 and 2223 phases, though less than the pure PbBiSCCO specimen. Although some of the samples show higher amounts of super-

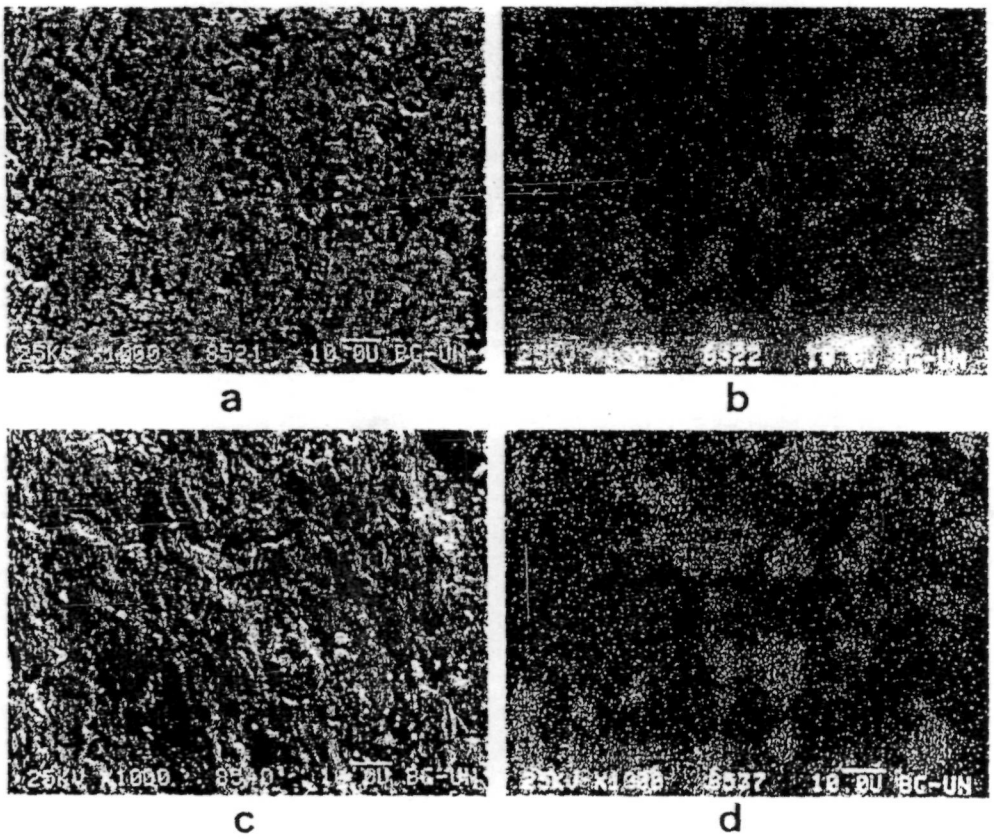

Fig. 1. Scanning electron microscopy of PbBiSCCO/Ag 10 wt% Ag (BI) and 30 wt% Ag (BII) samples: (a) microstructure; (b) Ag elemental mapping of BI(10); (c) microstructure; (d) Ag elemental mapping of BI(30) sample.

conducting phases, no clear correlation with critical currents and critical temperatures can be noted. It therefore appears that there is an additional factor that influences the critical current, probably a morphological one (see below).

3.2. Critical temperatures

Measured critical temperatures are shown in Fig. 3. Among the samples studied, the pure PbBiSCCO sample AI (annealed for 24 h) shows the highest critical temperature T_c, 112.3 K, defined as the temperature where the resistivity is less than 10^{-7} Ω cm. Silver addition causes a slight decrease in T_c, with BI(25) showing the highest critical temperature, 111.3 K. The critical temperatures of all Ag–4 at% Cu added samples are lower than those of the corresponding silver containing samples, and critical temperature values decrease with the increase in Ag–4% Cu volume fraction. The T_c values of series II samples (annealed for 48 h) are lower than the corresponding series I samples (annealed for 24 h) This could be due to the more prolonged exposure of the former samples to atmospheric oxygen, in accordance with similar observations reported in Ref. [8]

Decrease of T_c in Ag-containing BiSCCO samples has been also reported by Chiu et al [16] These authors observed a decrease of 50–70 K in critical temperatures, for samples annealed at 843°C No significant degradation in T_c occurred when the samples were annealed at 827°C [16], in agreement with the observations reported in the present paper

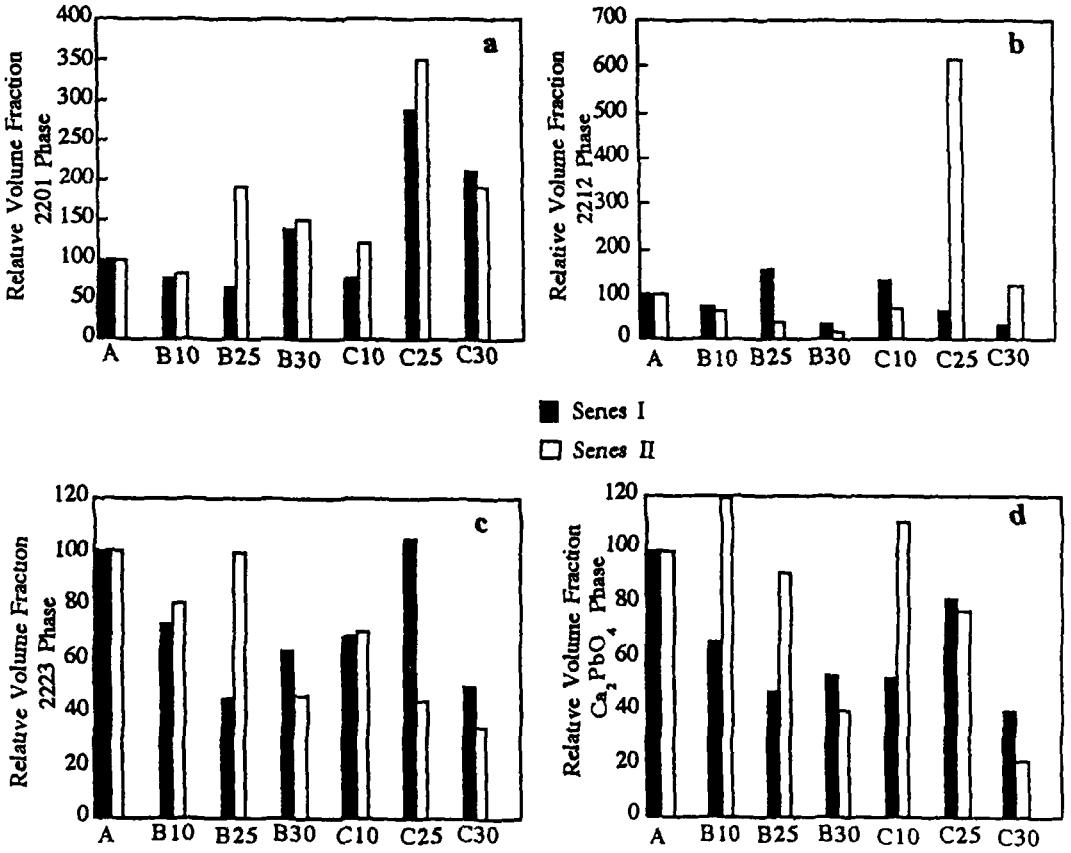

Fig 2 Relative volume fractions from XRD analysis of the PbBiSCCO (A), PbBiSCCO/Ag (B) and PbBiSCCO/Ag–4 at% Cu (C) composites with different metal fractions after air annealing at 810°C for 24 h (series I) and for 48 h (series II) The results are normalized with respect to the fractions observed in the reference, silver free, sample (A)

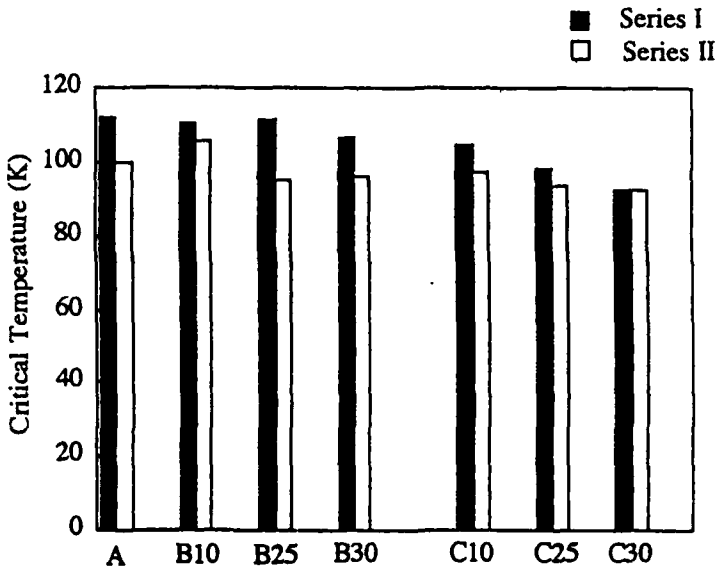

Fig. 3. Critical temperatures of the PbBiSCCO (A), PbBiSCCO/Ag (B) and PbBiSCCO/Ag-4 at% Cu (C) composites with different metal fraction after air annealing at 810°C for 24 h (series I) and for 48 h (series II).

3.3. Critical currents

Critical currents (I_c) measured for the PbBiSCCO, PbBiSCCO/Ag and the PbBiSCCO/Ag–4 at% Cu samples are presented in Fig. 4. The critical current values of all series I samples are substantially higher than the corresponding values for series II. Sample BI(10) shows the highest measured critical current, about 50 Å, more than three times the value observed for the Ag-free sample (AI). Higher

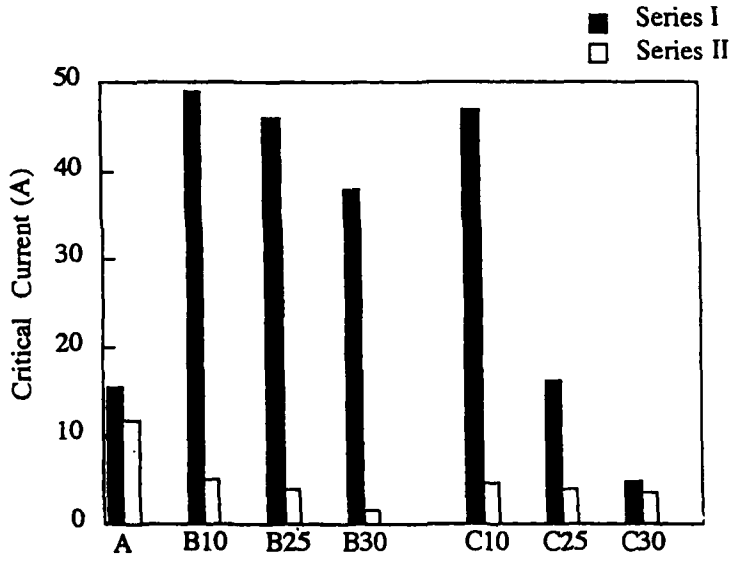

Fig. 4. Critical currents of the PbBiSCCO (A), PbBiSCCO/Ag (B) and PbBiSCCO/Ag-4 at% Cu (C) composites with different metal fraction after air annealing at 810°C for 24 h (Series I) and for 48 h (Series II).

amounts of silver cause I_c to decrease moderately. As for the Ag–4 at% Cu composites, CI(25) and CI(30) exhibit severe deterioration of the critical current, whereas CI(10) is only slightly inferior to BI(10). Degradation of critical currents has been reported for silver addition above 60 wt% [17], while Yufang et al. [9] found that the highest critical current is obtained in samples with a silver optimum concentration of 5.4 wt%, in accordance with the findings of the present study. Apparently, at weight fraction between 5 and 10% silver acts as a good connector between the superconducting grains, resulting in higher critical current values, probably due to a proximity effect. It has indeed been reported that the critical current values depend not only on the amount (volume fraction) of the superconducting phases in the material, but also on the extent of connectivity among bulk superconducting grains, which allows for higher unpinned supercurrent to flow [18,19]. The morphological features seen in Fig. 1 a and b seem indeed to indicate that silver furnishes extended connectivity paths within the PbBiSCCO matrix. When silver or Ag–4 at% Cu contents are increased beyond the 10 wt% limit, the larger clusters of the normal metal (see Fig. 1d) probably act as barriers, causing then reduction of the critical current.

In attempt to account for the observed overall critical currents measured for the Ag–Cu composites as compared to the silver composites, we use an expression given for the critical current density in SNS junctions, at temperatures lower than the critical temperature [4]:

$$j = \frac{A}{(\pi T)^2}\left(\frac{\exp(-\gamma t d/\xi_s)}{\nu^2\gamma^3 d\left[1 + K\sqrt{1 + (\Delta/\pi T)^2}\right]}\right), \quad (1)$$

where $t = T/T_c$, T and T_c are the measuring temperature and critical temperature of the sample, $\nu = m_s/m_n$, with m_s and m_n the critical masses in the superconducting and normal states respectively, $\gamma = \upsilon_s/\upsilon_n$, with υ_s and υ_n the Fermi velocities of the superconducting matrix and normal metal respectively, $K = (1 + \gamma^2)/2\gamma$, d is the thickness of the normal metal, ξ_s is the coherence length in the superconducting state, Δ is an order parameter and A is a constant. Variations in critical current depend mainly on the value of γ, as the other parameters in Eq. (1) are almost constant for the considered material system. Since it is known that $\upsilon_{Cu} < \upsilon_{Ag}$ [20], it can reasonably be assumed that $\upsilon_{AgCu} < \upsilon_{Ag}$. Therefore γ for AgCu is expected to be larger than the one for silver, as the Fermi velocities of the superconducting state are the same in both composites. According to Eq. (1), higher γ results in lower critical current (and density), as observed for the Ag–4 at% Cu versus silver composites.

To conclude, transport and microstructural properties of normal metal inclusions connecting between superconducting grains, seem to play a major role in the composite overall critical current value. This effect appears to be more important than the role of the superconductor–normal metal interface composition. In order to establish this preliminary conclusion, further studies involving PbBiSCCO/AgIn and other silver alloy composites are in progress.

Acknowledgements

The authors are grateful to the Israeli Ministry of Science and Arts for financial support. They like to thank Drs. V. Meerovich and V. Sokolovsky, from the Physics Department, Ben-Gurion University for providing the critical current measurement facility. The assistance of Mr. O. Dor and Eng. M. Luvker, from the Materials Engineering Department, Ben-Gurion University, is highly appreciated.

References

[1] J.M. Tarascon, W.R. McKinnon, P. Barboux, D.M. Hwang, B.G. Bagley, L.H. Greene, G.W. Hull, Y. LePage, N. Stoffel and M. Ground, Phys. Rev. B 38 (1988) 8885.
[2] Y. Massalker, A.N. Sembira and J. Baram, J. Mater. Res. 8 (1993) 2445.
[3] S. Mollah, N. Froumin and J. Baram, in: Studies of high temperature superconductors, Vol. 16, ed. A.V. Narlikar (Nova Sci. Publ., New York, 1995) p.155.
[4] A. Golub and B. Horovitz, Phys. Rev. B 49 (1994) 4222.
[5] S. Jin, R.C. Sherwood, T.H. Tiefel, G.W Kammalott, R.A. Fastnacht, M.E. Davis and S.M. Zahurak, Appl. Phys. Letters 52 (1988) 1628.
[6] C.J. Kim, M.S. Haun, D.S. Suhr, K.B. Kim, H.J. Lee, H.G. Lee, G.W. Hong and D.Y. Won, Mater. Letters 11 (1991) 79.

[7] M.T. Malachevsky, P.L. Villa and L. Gherardi, Appl. Supercond. 2 (1994) 35.
[8] S.X Dou, K.H Song, H.K. Liu and C C. Sorrell, Physica C 160 (1989) 533
[9] R. Yufang, Z. Zuoto, M. Jian and H Ping, Solid State Commun. 75 (1990) 625.
[10] N. Froumin, J Baram and M. Polak, Mater. Letters 18 (1994) 176, Physica C 209 (1993) 315.
[11] M. Polak, J Baram and N. Froumin, Surface Interface Analysis 22 (1994) 387.
[12] E A. Haris, J.L. Bishop, R L. Havill and P.J. Ward, Cryogenics 28 (1990) 685.
[13] K. Nomura, T. Sasaoka, J. Sato, S. Kuma, H Kumakura, K Togano and N Tomita, Appl. Phys Letters 64 (1994) 112
[14] P G De Gennes, Rev Mod Phys 36 (1964) 225
[15] S Goren, G Jung, V Meerovich, V Sokolovsky, I Skoletsky, V V Homjakov, G E Shter and G S Grader Proc of EUCAS '93 Conf, Gottingen, Germany (1993) p 134
[16] Y D Chiu, T S Lei and C H Kao, J Mater Sci 29 (1994) 2678
[17] T Matsushita, A Suzuki, T Kishida, M Okuda and H Naito, Supercond Sci Technol 7 (1994) 222
[18] A K Sarkar, I Maartense and T L Peterson, J Mater Res 7 (1992) 1672
[19] Y Tanaka, T Asano, T Yanagiya, M Fukutomi, K Komori and H Maeda, Jpn J Appl Phys 31 (1992) L235
[20] C Kittel, Introduction to solid state physics (Wiley, New York 1967)

Studies of High Temperature Superconductors
Volume 16

ISBN 1-56072-251-7

PHASES EVOLUTION DURING THE FABRICATION OF BULK Bi-BASED SUPERCONDUCTING GLASS CERAMICS

S. Mollah[#] , N. Froumin and J. Baram[*]
Materials Engineering Department,
Ben-Gurion University of the Negev, BEER-SHEVA, Israel

1. INTRODUCTION

Since the discovery of high temperature superconductivity in the La-Ba-Cu-O system [1], a large number of cuprate superconductors such as Y-Ba-Cu-O (YBCO) [2], Tl-Ba-Ca-Cu-O (TaBCO) [3], Bi-Sr-Ca-Cu-O (BiSCO) [4], Hg-Ba-Ca-Cu-O (HBCCO) [5-7], and A-Cu-O (A = Ca, Sr and/or Ba) [8-11] have been discovered. YBCO was the first system to be superconducting above 77 K, the liquid nitrogen temperature. With this discovery, it was thought that the presence of a rare earth element is essential for superconductors having critical temperature T_c higher than 77 K. However, the later synthesis of the TaBCO and BiSCO systems did contradict this assumption. The TaBCO and BiSCO systems have shown higher critical temperatures, a property believed to be associated with the number of consecutive Cu-O crystallographic planes between Tl-O or Bi-O layers [12-14]. The main disadvantage of the Tl and Bi based systems is the difficulty to synthesize a pure single bulk superconducting phase [15-16]. The Tl based cuprates have slightly higher critical temperatures than the BiSCO family, but are hazardous to synthesize due to the Tl toxicity and volatility. The recently discovered HBCCO system shows the highest T_c (>134 K) so far [7, 17] but the preparation of this superconducting system is also hazardous, due to the volatility of toxic Hg [5-7, 17]. Another newly discovered superconducting system, A-Cu-O, shows high critical temperature (117

[#]. On leave from Solid State Physics Department, Indian Association for the Cultivation of Science, Jadavpur, Calcuuta-32, India.

[*]. To whom correspondance should be addressed.

K) [18] but needs to be synthesized under high pressure [8-11, 18]. All cuprate based ceramic superconductors need oxygenation treatments at elevated temperatures, for prolonged periods of time, in order to become superconducting (at low temperatures). Even so, the various practiced heat treatments, as reported in the literature, are generally not providing a material entirely free from non-superconducting phases in the bulk. Pb doping of BiSCO, resulting in PbBiSCO, has however been shown to increase the volume fraction of the superconducting phases.

BiSCO and PbBiSCO have attracted much attention, compared to other cuprate superconducting systems, due to ease of preparation and low cost of raw materials. They are used in thin film and bulk forms. Critical currents of thin film superconductors are higher than those of bulk materials. However, bulk BiSCO and PbBiSCO are currently used in important technological applications, such as superconducting wires, coils and magnets. Bulk superconducting hollow cylinders serve for magnetic shielding and microwave cavities.

A large number of techniques have used for the preparation of BiSCO and PbBiSCO superconducting bulk materials: the ceramic method [19-22], the sol-gel process [23-24], the coprecipitation and precursor method [25-27], the combustion method [28], the glass to ceramic method [29-37]. In either way, the final product elemental composition and eventual superconducting properties depend on the initial composition used, the temperature and time of the oxygenation heat treatment and the annealing atmosphere. The *ceramic method* is widely used, despite its many limitations: the reaction rates between the constituents are slow, and there is no simple way to monitor the progress of the reaction; compositionally homogeneous product is not always feasible. The *sol-gel and coprecipitation and precursor methods* have the advantage of good mixing of the raw materials, as they are chemical or solution routes. These processes use multivalent organic compounds, like oxalates, for example. Numerous stages of annealing are required to get the final superconductors.

In the past years, the *glass to ceramic route* has attracted much attention [29-37]. This method of preparation requires high temperature for melting. The affinity of the raw materials to the crucible materials generally results in the appearance of impurity phases in the final product. However, this method has the following advantages:

i). melting of the starting materials provides homogeneity;

(ii). the technique provides a convenient means for fabrication of shaped high T_c superconductors; superconducting fibers, wires/tapes may be drown [38-39];

(iii). highly dense superconducting materials are obtained, with nearly zero porosity [31];

(iv). the growth of superconducting crystals can be done in preferential orientation [40].

These last 2 advantages eventually cause significant improvement in the critical current density of the superconductors.

Processing of BiSCO and PbBiSCO superconducting compounds is a major challenge to materials scientists. In these materials, the phase formation depends on numerous parameters. An understanding of the formation of various high T_c phases in BiSCO and PbBiSCO system is critical for materials processing. In this review paper, the preparation of BiSCO and PbBiSCO superconducting materials by the

glass ceramic method, the resulting structures and properties of the different phases and the parameters that lead to the phases evolution are discussed [##].

2. PHASE STRUCTURES AND PROPERTIES

There are three types of Bi-based cuprate oxide superconductors depending on the number of Cu-O planes. Their general formula is: $Bi_2Sr_2Ca_{n-1}Cu_nO_{2n+4+\delta}$ where n = 1, 2, 3, or, in a different notation: 2201, 2212 and 2223 [4, 41-43]. δ stands for small variations in oxygen content from the exact value required for the phase. Another type of classification, not used in the present review, is: $Bi_2(Sr, Ca)_2CuO_x$ [41], $Bi_2(Sr, Ca)_3Cu_2O_x$' [4, 44] and $Bi_2(Sr, Ca)_4Cu_3O_x$'' [4, 44]. The crystallographic structures differ in the number of CuO_2-Ca-CuO_2 planes packed along the c axis [43]. Unit cells of BiSCO and PbBiSCO have lattice constants as follows:

(i). 2201: a = 5.371(2) Å; b = 5.372(2) Å; c = 24.59(1) Å;
(ii). 2212: a = 5.410(2) Å; b = 5.410(2) Å; c = 30.84 Å;
(iii). 2223: a = 5.4101 Å; b = 5.410 Å; c = 37.13 Å.

The three phases have layered structures parallel to the crystallographic a-b plane, consisting of rock-salt-like BiO bilayers that alternate with perovskite-like $Sr_2Ca_{n-1}Cu_n$ units. Figure 1 shows the complex unit cell of the 2223 structure.

The 2212 and 2223 members of the homologous series $Bi_2Sr_2Ca_{n-1}Cu_nO_{2n+4+\delta}$ may be described as double BiO layers alternating with $Sr_2CaCu_2O_6$ and $Sr_2Ca_2Cu_3O_6$ units respectively. Perovskite-like $Sr_2Ca_{n-1}Cu_n$ units contain CuO_2 sheets formed by corner sharing CuO_4 units. The CuO_2 sheets are oriented parallel to the a-b plane. So all the members of this series consist of CuO_2 sheets separated by Ca and "covered" in the c-direction by SrO sheets. These perovskite-like units alternate in the c direction with BiO bilayers [45]. The phases exhibit a modulation in the b axis direction. The spacing of this superstructure is approximately 4.74 times the b axis parameter [46-47] and belongs to the space group *Pcnn* or *Pmnn* [48]. The superstructure is due either to the modulation of BiO bilayers [49-50], or to an alternation of the rock-salt structure and the perovskite-like structure of the BiO bilayer [49], or, alternatively, to an alternation between a quadratic pyramidal coordination of Bi and oxygen and an imperfect rock-salt structure [50].

Tarascon et al. [43] observed that $Bi_2Sr_2Ca_{n-1}Cu_nO_{2n+4+\delta}$ has a pseudo tetragonal structure which can be described as a stacking of a basic $Bi_2Sr_2CuO_6$ unit with either zero, one or two $CaCuO_2$ slabs inserted. The observed increase in c parameter for increasing n value is due to the progressive addition of 2x1 and 2x2 (doubled because of the crystallographic shear) $CaCuO_2$, each about 3 Å thick, to the stacking sequence in the unit cell. The substitution of Bi by Pb promotes a structural change of the superconductors from pseudotetragonal to orthorhombic [51].

[##]. The literature search on which this review is based is updated to September 1994.

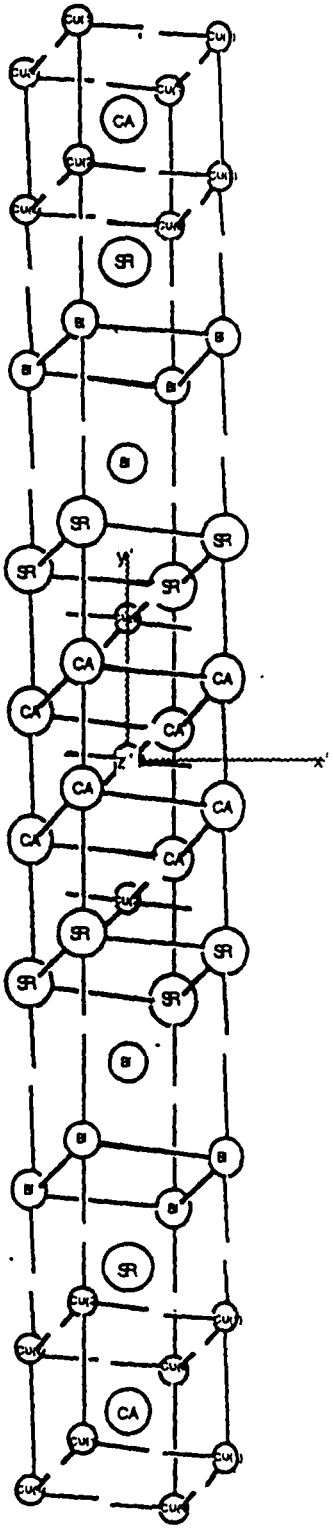

Figure 1. Unit cell of the 2223 structure.

But Kambe et al. [52] found that after annealing the Pb substituted Bi-Sr-Ca-Cu-O samples in N_2, Ar or in very low pressure O_2, a structural change from orthorhombic to monoclinic occurred.

Though most Cu ions in the BiSCO glass exist in the Cu(I) state at elevated temperatures, the CuO dissociates into $Cu_2O(s)$ and $O_2(s)$ [45] with the increase of temperature. The mean copper valances in the $Bi_2Sr_2Ca_{n-1}Cu_nO_{2n+4+\delta}$ superconducting systems for n = 1, 2 and 3 are 1.86, 2.07 and 2.29 respectively [45]. The high T_c phases exhibit a pronounced anisotropy of their properties as expected from their layered structures.

The linear coefficient of thermal expansion, as an example, goes through a transition around 400 C, from $1.15*10^{-5}$ to $1.57*10^{-5}$ C^{-1}, when expansion is checked in a direction parallel to the a-b crystallographic plane, or from $1.79*10^{-5}$ to $3.06*10^{-5}$ C^{-1}, when expansion was checked in a direction parallel to the c crystallographic axis [37]. The anisotropy causes also a 2-dimensional transport superconductivity.

The 2212 and 2223 phases have small coherence length and London penetration depth [45], compared to those of low T_c superconductors like Nb_3Sn and NbTi. The critical temperatures for n = 1, 2, 3 are respectively: 20, 80 and 110 K, but the T_c values strongly depend on the oxygen, calcium and bismuth contents of the phases [45].

3. BULK GLASS AND GLASS CERAMIC PREPARATION TECHNIQUES

Bulk BiSCO and PbBiSCO superconductors can be obtained by the

glass ceramic technique because these systems contain the glass former bismuth oxide. Bismuth and lead oxides form glass if they are mixed with suitable other oxides. The presence of PbO decreases the melting temperature of the Bi-based glasses. The usefulness of the addition of the PbO is also to produce the highest volume fraction of the single high T_c 2223 phase [55]. Bi-based glasses are prepared by twin roller quenching [30, 56-57], splat cooling [31], the metal plate melt-quenching method [22, 37, 58], single roller spinning [32], and quenching of molten material into liquid nitrogen [59-60]. The glasses can be obtained in the form of glassy plates [37, 58, 61-66], glassy rods [67-68], hollow cylinders [69], glass fibers [38, 70], and amorphous films [57]. They are annealed at appropriate temperatures and in appropriate atmospheres to get the desired glass ceramic superconductors.

Carbonates and oxides are generally used as starting materials to prepare the superconducting glass ceramics. Appropriate weights of Bi_2O_3, PbO (or Pb_3O_4), $SrCO_3$, $CaCO_3$ and CuO of high purity are mixed in agate mortars, according to the desired stoichiometric ratio. The powder mixture is calcined at about 800 ^{0}C for 10-24 hours. The calcination procedure is repeated 3 to 4 times, with repeated mixing to improve homogeneity. The calcined powder is then melted in a platinum or alumina crucible at 1100-1250 ^{0}C for 20-90 minutes. The melts are poured on a thoroughly polished copper, steel or iron block and immediately pressed by another highly polished block to get plates a few millimeters in thickness. The as-quenched samples are glossy black in appearance and electrically insulating. The samples are then annealed at various temperatures for 12 - 240 hours in air or in an oxygen atmosphere, and subsequently cooled down to room temperature at different cooling rates. Frequently practiced initial compositions, calcination and annealing durations and temperatures, as well as the resulting critical temperatures and currents of the final superconducting glass ceramics are shown in Table 1. A few typical procedures used to prepare Bi-based glass ceramic superconductors are described in detail below.

The metal plate melt-quenching preparation method uses commercially available Bi_2O_3, $SrCO_3$, $CaCO_3$, CuO and PbO powders as starting materials, in appropriate weight ratios [37]. The amounts of PbO and Bi_2O_3 are according to the Pb:Bi molar ratio of 0.6:1.4. The mixed powders are grounded in a mortar. The decomposition of the carbonates (the calcination step) lasts 12 hours at 800 ^{0}C, in air, in Al_2O_3 crucibles, followed by furnace cooling. The resulting material is then ground again to powders. The powders are given two additional calcination treatments at 820 ^{0}C, and ground again. Melting, in a metallurgical grade Al_2O_3 crucible, is done at 1150 ^{0}C. This melting temperature is maintained for periods varying from 15 to 90 minutes. The melts are then quenched between two highly polished stainless steel (or copper) blocks. The as-quenched amorphous platelets, with smooth surface and glassy appearance, were generally 1 - 2 mm in thickness. The growth of the high T_c superconducting phases in BiSCO ceramics from the amorphous state was then induced by oxygenation in streaming air, at different temperatures and times.

Ibara et al. [63] prepared the PbBiSCO glasses also using carbonates and oxides powders, melted in an alumina crucible at 1150 ^{0}C for 30 - 40 minutes in air. The melts were poured onto a stainless steel plate and pressed quickly by another plate

Table 1. Characteristic processing parameters.

Nominal Composition Bi, Pb, Sr, Ca, Cu	Crucible	Melting Temperature [C]	Melting Time [min]	Annealing Temperature [C]	Annealing Time [h]	Atm.	T_c [K]	Ref
1.6, 0.4, 2.0, 2.0, 3.0	Pt	1100	60	500-820	12-200	air	106	[62]
0.8, 0.2, 1.0, 1.0, x (x=1.5, 1.8, 2.0)	Pt	1250	20	840	100-300	air	106	[65]
0.5, 0.5, 1.0, 1.0, 2.0	Al_2O_3	1150	30-40	820	24	O_2	71	[29]
2.0, 0.4, 2.0, 2.0, 3.0	Al_2O_3	1050	60	850	1-50	O_2-Ar	110	[64]
0.7, 0.3, 1.0, 1.0, 1.8	Pt	1200	2	865	120	-	105	[71]
1.7, 0.3, 2.0, 2.1, 3.1	Al_2O_3	1100	30	700-840	-	-	-	[36]
0.8, (0.1-0.4), 0.8, 1.0, 1.4	Al_2O_3	1150	30-40	840-850	100	O_2-Ar	102	[63]
(0.8, 1.0), 2.0, 1.0, 1.0, 1.5	Al_2O_3	1250	20	830-840	250	air	100	[72]
2.0, 0.0, 2.0, 1.0, 2.0	Pt	1100-1400	5	800-850	5	air	85	[73]
1.5, 0.0, 1.0, (1, 1.5), 2.0	Al_2O_3	1150	30-40	820	24	air	65	[29]

. The glassy samples of 1 mm thickness were then annealed at 840 - 850 ^{0}C for 100 hours in a mixed Ar:O_2 atmosphere, and furnace cooled. Yamanaka et al. [62] used the same type of materials. They mixed the initial powders using ethanol for 1 hour. The melting temperature was 1100 ^{0}C in a Pt crucible. Annealing was done at various temperatures for 12-200 hours. Komatsu et al. [65] calcined the initial powder mixture at 800 ^{0}C for 10 hours in air. The calcinated powders were then melted in an alumina crucible at 1250 ^{0}C for 20 minutes. The glasses were annealed at 840 ^{0}C for 250 hours in air. Egawa et al. [66] prepared BiSCO glassy samples, again using carbonates and oxides as starting materials. Calcination was done at 840 ^{0}C for 30 hours, and grinding performed for several times. The melting temperature was higher than 1000 ^{0}C, the crucible made of Pt. The splat quenched glassy samples were partially melted at 900 ^{0}C for 10 minutes, slowly cooled from 900 to 850 ^{0}C at the rate of 0.5 to 5.0 ^{0}C hour^{-1} in flowing oxygen, and finally cooled to room temperature at the rate of 100 ^{0}C hour^{-1}.

The fabrication of BiSCO glass rods (500 mm long) by melt-casting has been proposed by Abe et al. [67] and Kasuga et al. [68]. In Ref. [67], the low viscosity BiSCO melt is vacuum pumped into a silica glass tube to obtain a rod-shaped glass. In Ref. [68], calcination is performed at 800 ^{0}C for 10 hours in air and melting in an Al_2O_3 crucible at 1150 ^{0}C for 30 minutes. The melt was pumped into a silica glass tube 2 mm in diameter and 40 mm in length. The glassy tubes were oxygenated in air at 850 ^{0}C during 100-500 hours, and then rapidly cooled to room temperature.

PbBiSCO glass fibers were drawn by Mollah et al. [74]. The mixtures stayed at 1150 - 1200 ^{0}C during 1 hour. The melt was drawn to (glassy) fiber. Komatsu et al. [61] prepared BiSCO glassy plates, suspended them inside an electric furnace. The softened plates were then drawn into fibers, that were subsequently annealed to get superconducting fibers.

Abe et al. [69] prepared fully open or half open glass pipes. They casted the melt into a silica glass tube by vacuum pumping. By suction, the inner low viscosity part of the rod is removed while the outer part of the rod like melt is allowed to solidify. The pipes were annealed at 800 ^{0}C for 50 hours in air to obtain glass ceramic pipes.

Seed superconducting crystals have been introduced into amorphous material during the annealing stage [64]. Melting was done in an alumina crucible at 1050 ^{0}C for 1 hour. The melt was quenched to the glassy state between copper blocks. The amorphous plates were ground for 30 minutes, pressed into pellets, and annealed at 850 ^{0}C for 1 to 50 hours in an Ar-7.6% O_2 atmosphere. At this stage, the seed crystals were introduced into the amorphous powders. Additional annealing was performed to obtain the glass ceramics. The seed crystals did enhance the formation of 2223 phase [64].

4. CHARACTERIZATION PROCEDURES

Information on the glass transition and crystallization temperatures, on eventual oxidation/reduction reactions in the glasses and glass ceramics.can be obtained by differential scanning calorimetry (DSC), differential thermal analyses (DTA) or thermogravimetric analyses (TGA). The formation and evolution of the

(superconducting and "impurity") phases can be deduced from X-ray diffractions (XRD) performed at various temperatures or after the practiced heat treatments. Microstructures are investigated on scanning electron micrographs (SEM), reflected light micrographs (RLM) or by transmission electron microscopy (TEM). The chemical composition of the phases analyzed by energy dispersive analysis of X-ray (EDAX) or electron probe microanalysis (EPMA). Atomic vacancy like defects and phase transformations may also be observed by micro-Raman spectroscopy (MRS), electron spin resonance (ESR) or positron annihilation spectroscopy (PAS). Electric and magnetic properties of the superconducting materials are characterized by resistivity and critical current measurements, using either the 4-probe technique or magnetic susceptibility measurements. The following sections provide a review of the use of the above-mentioned techniques for characterizing bulk Bi-based superconducting glass ceramics.

4.1. X-Ray Diffraction

The most efficient way to determine whether the sample is glassy or crystalline is to analyze the XRD pattern. CuK_α, CoK_α, FeK_α radiations are generally used. A glassy sample shows no distinct peaks but a broad hump around the 30^0 2-theta angle. If however some peaks are showing, some unreacted starting material may be still present in the sample. In a glass ceramic XRD, each crystallographic phase, including impurities, is represented by the characteristic peaks. By comparing the peak heights, one can infer about the volume fraction of the different superconducting phases or impurities [36-37]. In BiSCO and PbBiSCO, the phases are the high T_c superconducting 2201, 2212 and 2223 + the (eventually) numerous residual impurities, such as: Ca_2CuO_3, Ca_2PbO_4, CuO, CaO, $(Ca, Sr)_2Cu_5O_8$, $(Ca, Sr)_{14}Cu_{24}O_{41}$, $(Ca, Sr)_2CuO_3$, $(Ca, Sr)_2CuO_3$, $SrBi_2O_4$, $CaPbO_{3-x}$ and $Ca_{1-x}CuO_2$. Massalker et al. [37] analyzed the evolution of the high T_c superconducting phases by adding the intensities of three characteristic and well identified peaks of the 2212 (the 002, 008 and 115 diffractions) [75] and of the 2223 phases (the 002, 113 and 115 diffractions) [76] separately, as a representative value for the volume fraction of each phase. The same procedure has been used to compare the volume fractions of the "impurity" phases, such as the Ca_2PbO_4, Ca_2CuO_3, CuO, CaO, and $(Ca, Sr)_3Cu_5O_8$ compounds. A typical X-ray diffraction of (ground to powder) crystallized PbBiSCO is shown in Figure 2 [37].

Shan et al. [36] estimated the volume fraction V of the high T_c 2223 phase from the peak intensities I reflected by the (115) plane. The corresponding 2θ values for the 2201, 2212 and 2223 phases are 26.2^0, 27.5^0 and 29.8^0 respectively [36]. The volume fraction of the 2223 phase is then given by:

$$V_{2223} = \frac{I_{2223}}{\left(I_{2223} + I_{2212} + I_{2201}\right)}.$$

Zhao and Che [77] have used the peak intensities of (0010) for 2223 and (115) for 2212 phases to estimate the volume fraction of 2223 phase in the same way.

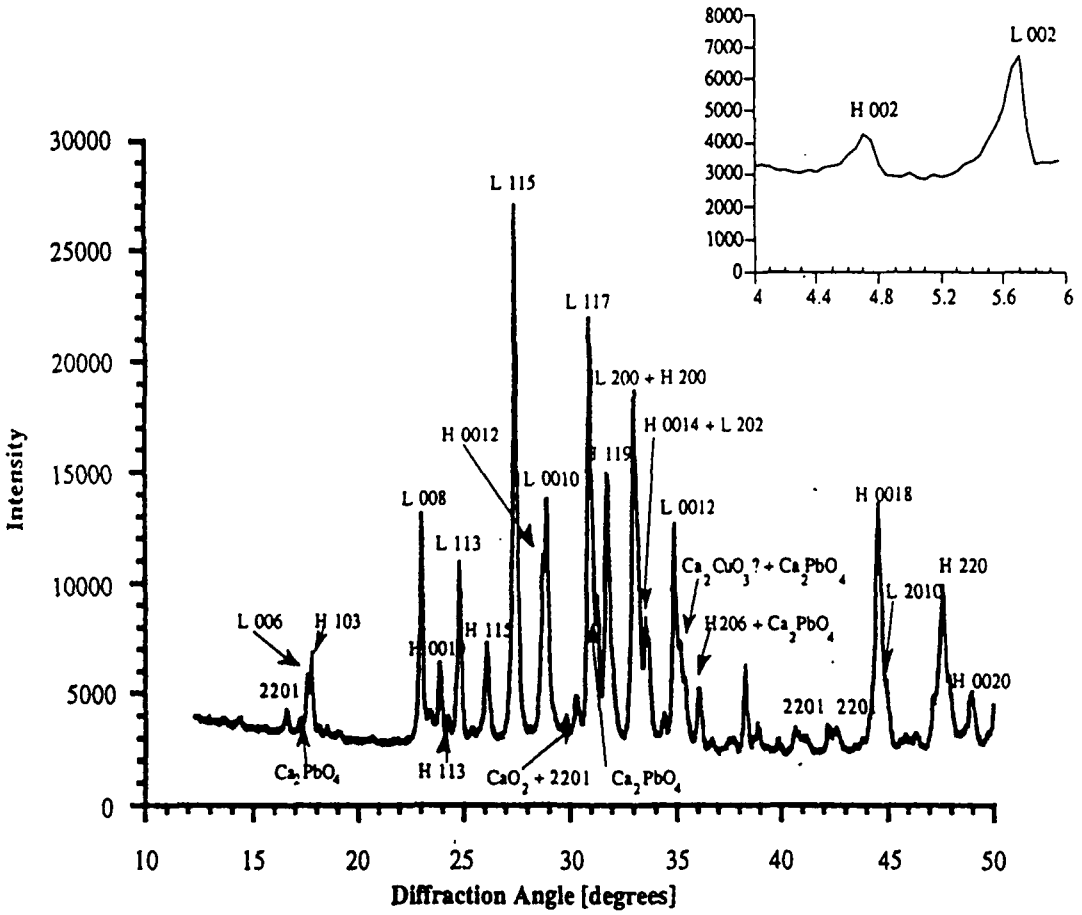

Figure 2. Typical x-ray diffraction of crystallized powder PbBiSCO. The inset represents the diffractogram at small angles, 4-6°. *L hkl* or *H hkl* labels refer to crystallographic planes of the 2212 and 2223 superconducting phases respectively [37].

4.2. Scanning Electron Microscopy and Energy Dispersive Analysis of X-Ray

Grain size and grain size distribution, as well as phase morphologies are visualized by SEM. As observed in electron micrographs [36-37, 62, 65], superconducting phases are plate-like. The lamellar crystals in [37] are characteristic of the 2212 superconducting phase. Komatsu et al. [65] observed plate-like crystals in all superconducting samples. They concluded that the morphology of the superconducting crystals prepared by the melt-quenching method are similar to those prepared by the ceramic method. Kanai et al. [59] observed fine grains with a laminated structure in samples annealed at 754 ^{0}C. The laminated structure developed further, as the annealing temperature increased from 754 ^{0}C to 874 ^{0}C.

Table 2. Changes in 2223 nominal compositions vs heat treatment conditions.

Nominal Composition	Analyzed (by EDAX) Composition (as-quenched or after heat treatment) [at %]						Heat Treatment	
(PbBi)SrCaCu	Pb	Bi	Sr	Ca	Cu	Al	Temp [C]	Time [h]
2223	10.10	16.70	22.20	15.10	35.60	0.30	amorphous	
	9.34±0.61	19.19±0.84	18.84±0.31	16.87±1.00	35.30±0.40	0.46±0.26	850	48
	9.64±0.75	24.68±3.49	21.99±4.97	14.12±2.38	28.45±2.81	1.13±0.91	835	120
	8.66±1.10	15.19±3.26	18.88±3.96	21.85±13.63	31.06±5.10	4.36±1.00	820	216
2223	4.50±0.47	11.59±0.88	21.11±1.83	19.58±2.49	36.64±1.04	6.48±0.99	amorphous	
	4.16±0.21	14.95±0.73	19.96±0.38	16.43±0.61	36.64±1.04	6.48±0.99	850	48
	2.66±0.54	13.22±3.07	20.73±2.58	18.43±2.31	38.03±2.83	7.05±2.18	850	120
	0.65±0.45	11.88±2.28	19.19±3.80	23.87±3.13	39.69±2.49	4.73±2.56	850	240
2223	4.20±0.68	11.49±1.07	25.26±1.44	20.62±5.92	36.22±3.57	2.21±0.94	amorphous	
	1.77±0.29	14.84±1.27	22.79±2.59	23.08±4.02	35.20±3.81	2.32±0.43	840	120
	1.93±1.29	21.87±2.21	24.67±3.81	16.01±2.70	34.34±3.49	1.17±0.63	840	240
	0.00	22.03±0.31	23.52±1.88	12.86±0.33	37.88±1.05	3.71±1.18	840	360

Samples annealed above 803 ^{0}C had a lower density than the samples annealed below 754 ^{0}C. This could be related to the anisotropic growth of phase 2212. If grains grow in random directions, voids tend to be produced among the plate-like grains.

EDAX provides elemental composition analysis, observations on the eventual volatility of constituents [37] and on composition changes with either annealing time, temperature or atmosphere. Microstructure is generally nonuniform in BiSCO and PbBiSCO. EDAX analyses show a great variability, as reflected by standard deviations in elemental analyses. Massalker et al. [37] observed drastic changes in the composition of as-quenched and heat treated specimens, as seen in Table 2.

Generally, the oxides in the BiSCO system are represented by the nominal number of moles of metal elements: 2201, 2212 and 2223. However, elemental analyses do not provide such simple ratios. If during a specific heat treatment, one or more among the constituent elements did evaporate, the reported concentrations of all other elements are affected, as the overall sum of concentrations has to remain 100 %. Lowering the content of one element causes an apparent increase in the amount of others. There is, however, some composition evolution that may be deduced from the values reported in Table 2. [37]. Pb exhibits a very high evaporation rate. The Pb concentrations are invariably lowered as the exposure times are increased, and this effect is enhanced at higher temperatures. The concentration of Cu seems to remain close to nominal composition. Sr decreased in content with time, while Ca evaporated at prolonged exposures [36-37]. The evaporation of Bi started at 860 ^{0}C and a highly significant evaporation was observed at 870 ^{0}C [37]. The presence of Al in the superconducting specimen is almost always reported, as a result of chemical reaction with the alumina crucible. The concentration of Al is higher in samples having been treated at higher temperatures or for a longer time.

4.3. Thermal Analyses

Thermal analysis is widely used to identify crystallization, glass transition and melting temperatures. Glass transition temperatures for Bi-based glass ceramics range from 396 to 408 ^{0}C [37] and crystallization temperatures from 450 to 470 ^{0}C. The coefficient of thermal conductivity can also be extracted from DSC thermograms [37]. The thermal analyses can be performed in air, oxygen, nitrogen or argon.

The formation sequence of the crystalline phases from the amorphous state has been checked by Massalker et al. [37], in flushing argon or air, by DSC. A typical thermogram is shown in Figure 3, for an as-quenched, amorphous sample. An endothermic peak is observed, believed to be due to the glass transition starting at T_g = 401 ^{0}C and two endothermic peaks at T_{x1} = 465 ^{0}C and a stronger one at T_{x2} = 504 ^{0}C, reflecting a 2-stage crystallization process. These two crystallization peaks occurred at higher temperature when heated in argon rather than in air. Some groups [35, 63] observed only one crystallization peak instead of two.

XRD analyses have shown that the broad exothermic peak at 768 ^{0}C is due to the formation of a significant amount of the 2212 superconducting phase, together with the appearance of increased amounts of Ca_2PbO_4 and CuO. The deep endotherm at 856 ^{0}C is attributed to a partial melting reaction of the 2212 phase [78].

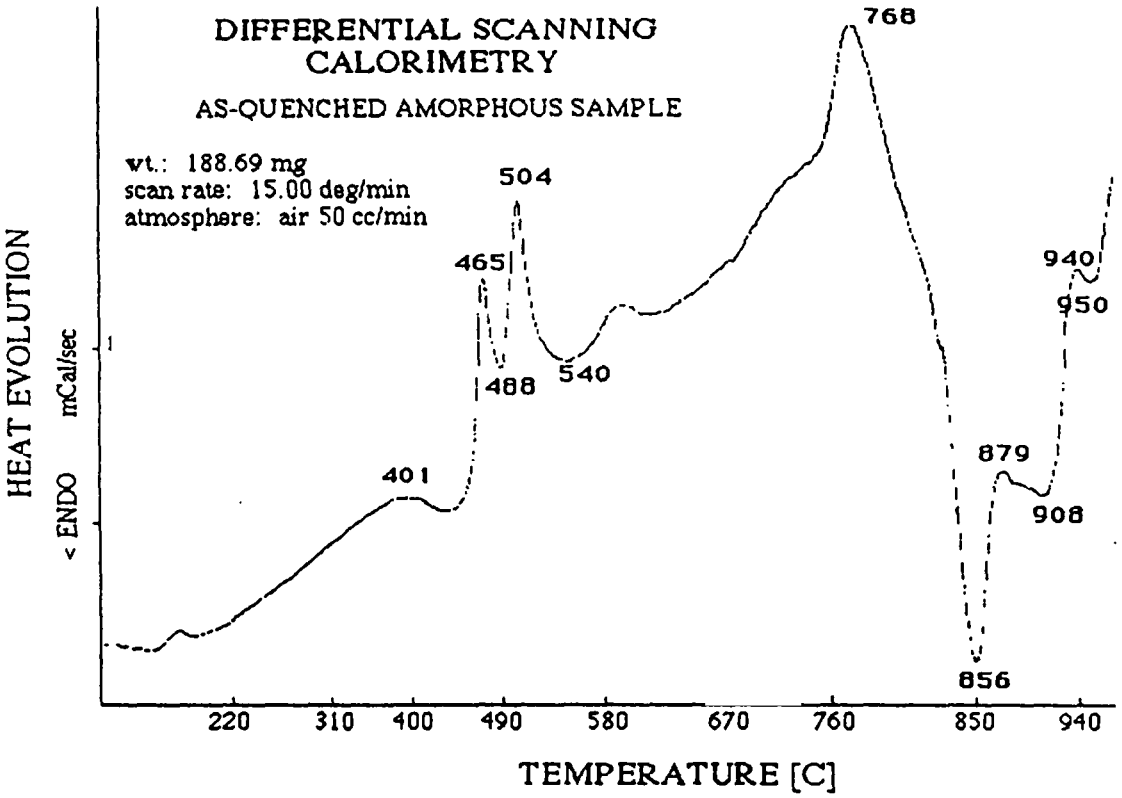

Figure 3. Typical DSC thermogram of an as-quenched, amorphous sample [37].

accompanied by a distinct softening of the specimen in the vicinity of that temperature. However, no reaction has been observed after 800 ^{0}C when the same DSC analysis was performed in argon, instead of air. As the 2223 superconducting phase has higher oxygen content than the 2212 phase, growth of the 2223 phase beyond the initially crystallized amount is connected to a partial melting of the 2212 phase, and addition of oxygen. The authors [37] observed that decomposition of both the 2212 and 2223 phases occurred after 907 ^{0}C, accompanied by some renewed softening of the specimen. Complete melting occurred between 1000 and 1050 ^{0}C.

Hinks et al. [31] observed an endothermic peak around 450 ^{0}C, believed to be due to initial crystallization of the glasses. They also found a second exothermic peak at 570 ^{0}C which they could not identify. An exothermic peak near 800 ^{0}C is due to the formation of superconducting phases. Shan et al. [36] observed the first exothermic peak in PbBiSCO material at 480 ^{0}C which is believed to be due to the crystallization of 2201 phase. They observed a 2212 phase formation at 730 ^{0}C. From DTA and other results, they concluded that the optimum temperature for the 2223 phase formation was ~ 842 ^{0}C. According to Kanai et al. [59], the large endothermic peak around 875 ^{0}C was probably due to the formation of a liquid phase. The peaks at 920 and 970 ^{0}C were attributed to the melting of residual materials.

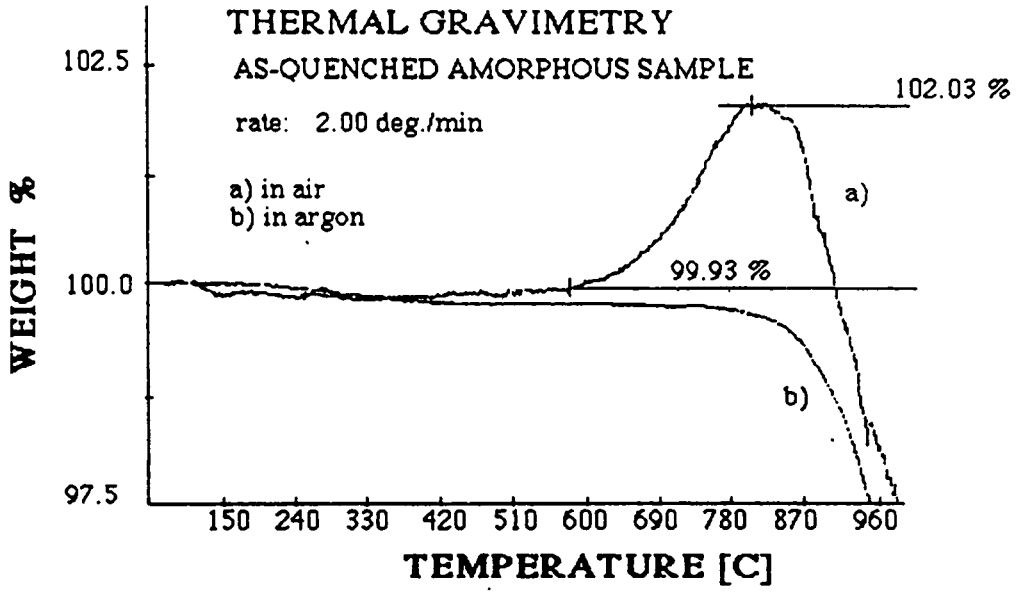

Figure 4. Weight change with temperature of an as-quenched amorphous sample, annealed in air (a) and in argon (b) [37].

Since the quenched glasses are prepared by rapid quenching from a melt well above the melting point, the glassy phase is often strongly oxygen deficient. TGA of the glassy samples in air or in oxygen generally show distinct weight gain, due to absorption of oxygen. According to Kanai et al. [59], the weight of the sample gradually increases from 500 ^{0}C, reaching a maximum between 750 and 850 ^{0}C. The evolution of the oxygen content in as-quenched, amorphous samples, heat treated for oxygenation has been studied by TGA, also used to evaluate the isothermal weight changes at 650 ^{0}C, due to oxygen absorption or desorption.

Figure 4 shows the results of the weight changes with increasing temperature of an amorphous, as-quenched sample $Pb_{0.5}Bi_{0.8}Sr_{1.0}Ca_{0.7}Cu_{1.6}O_y$ in air and argon [37].

In argon, a small weight loss was observed up to about 700 ^{0}C, followed by a drastic and continuous lowering of the weight, up to 960 ^{0}C. Conversely, in air, a small loss was observed up to about 600 ^{0}C, followed by a drastic increase above the nominal weight. The weight was then lowered steadily with increasing temperature. The authors [37] concluded that the gain in weight was due to oxygen

intake solely, as necessary for the formation of the high T_c superconducting phases. It did not occur in argon atmosphere, and may be even higher in air as some amounts of Pb and/or other constituent elements, such as Sr, evaporated after 720 ^{0}C, as suggested by the behavior of the sample in argon, Figure 4b.

Holesinger et al. [35] observed a substantial amount of oxygen intake, when heating BiSCO glass in oxygen. The glass transition was observed at 398 ^{0}C in argon, instead at 415 ^{0}C in oxygen atmosphere. Oxygen intake started near 415 ^{0}C, the maximum amount of oxygen was absorbed by the glass between 600 and 700 ^{0}C. Weight started to decrease above 803 ^{0}C.

The interesting result of the oxygen balance study, obtained by Massalker et al. [37], was the oxygen intake starting as early as at 600 ^{0}C. A comparative study of weight change during annealing of powder- and plate-like sample has shown, see Figure 5, that the platelet shaped sample gains less weight than the powders. During the long time annealing, the powder sample became saturated in oxygen and then a decrease in weight was observed for prolonged annealing. The plate-like sample needed more time to be saturated in oxygen gain. Prolonged annealing did not produce weight loss in this sample. The oxygen intake in solid samples is believed to be due to 3 distinct phenomena: a) absorption of gaseous oxygen onto surfaces and pores; b) surface oxidation, including grain surfaces in polycrystalline material; c) solid state diffusion from grain surface into the bulk. The results presented in that study pointed to the fact that the surface to volume ratio of samples treated for oxygen intake, an unavoidable step for the production of superconducting material, is an essential parameter that controls both the time necessary to achieve optimum intake and the amount of oxygen, and therefore the amount of high T_c phases present after the treatment.

4.4. Critical Temperature Measurement

The critical temperature T_c for the transition from normal to superconducting states is deduced from magnetic susceptibility or electric resistivity changes with temperature. The temperature at which the measured property starts to drop is the critical *onset* temperature $T_{c(onset)}$, while the temperature where zero (less than 10^{-7} ohm cm) resistivity is attained is $T_{c(0)}$. Typical $T_{c(0)}$ temperatures of BiSCO and PbBiSCO glass ceramic superconductors for zero resistivity are shown in Table 1.

4.4.1. Magnetic Susceptibility. The evaluation of the critical temperatures is more accurate by the magnetic susceptibility method. A clear indication that two different superconducting are present in a sample is inferred from two distinct drops in the temperature vs. magnetic susceptibility curve, as shown in Figure 6. 112 K is the $T_{c(onset)}$ temperature for the 2223 phase and 81.5 K the $T_{c(onset)}$ temperature for the 2212 phase.

Two transitions in the real part of the a.c. susceptibility vs. temperature curve, indicating two transitions around 110 K and 75 K are also observed by Komatsu et al. [65]. From the temperature dependence of a.c. susceptibility amplitude, they deduced the existence of weak intergrain coupling between the superconducting crystals in the glass ceramics. The coexistence of non-superconducting phases such as

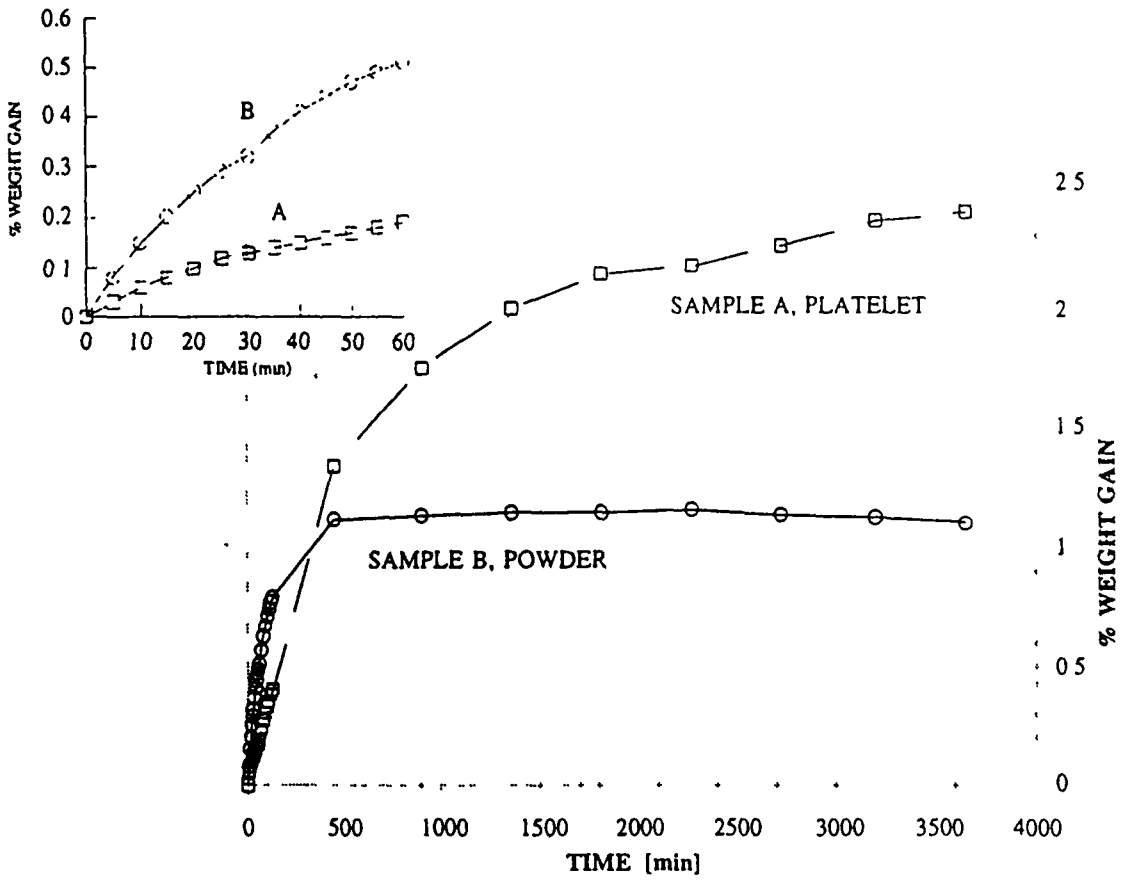

Figure 5. Weight percent oxygen intake at 650 °C, in a powder sample (A) and in a platelet-shaped sample (B) [37].

Ca_2PbO_4 and CuO, and the random orientation of superconducting crystals, are believed to be the cause of the weak coupling at grain boundaries. The coupling could be improved by increasing the annealing time.

Information about mixed volume fraction of superconducting phases can also be obtained from a.c magnetic susceptibility vs. temperature curves [37, 59, 65, 79]. A method has been proposed for the calculation of the actual volume of superconducting phase, using the relation:

$$V(\%) = \frac{V_{sc}}{V_{sample}} = \frac{\frac{E}{c}}{\frac{W}{\sigma}} \times 100$$

where E is an inductance change (dB), c is an equipment constant (in $dBcm^{-3}$), W is the sample weight (gm) and s is the theoretical density of the sample (gm cm^{-3})

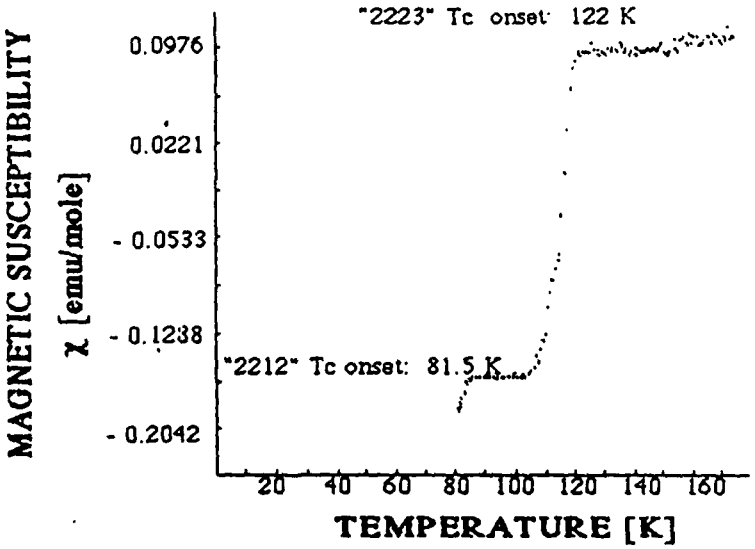

Figure 6. Magnetic susceptibility vs. temperature, 2212 and 2223 phases [37].

4.4.2. Electric Resistivity. The temperature vs. resistivity curves show either a sharp or a broad transition. Massalker et al. [37] studied the critical temperature after successive cooling and heating cycles. They observed close, but different T_c at each cycle. Hysteresis has been evidenced, indicating a dissipation effect during thermal cycling. The resistivity is increased on cooling, as depicted in Figure 7, indicating a semiconducting behavior of the PbBiSCO ceramics studied in Ref. [37].

The semiconducting to normal state transition for the sample having 2223 composition took place between 210 and 220 K. However the series of specimen having Cu in excess, with nominal composition 2234 showed normal, not semiconducting behavior below 300 K. The samples having nominal composition 2224 showed higher $T_c(0)$ and T_c(onset) than the 2223 samples [37].

4.5. Critical Current

Critical current densities (J_c) in superconducting samples are measured in presence or absence of magnetic fields in either liquid helium (4.2 K) or in liquid nitrogen (77 K). That property is highly influenced by the volume percentage of superconducting phases and nonsuperconducting impurities, by the orientation of the superconducting grains and connectivity. The remaining of residual glass causes weak coupling among the superconducting grains, lowering the critical current density.

Komatsu et al. [72] found that J_c of superconducting PbBiSCO glass ceramic was higher for the sample annealed at temperature 400 ^{0}C in oxygen for 24 hours than the same sample annealed at 840 ^{0}C in air for 240 hours. But Yamanaka et al. [62]

observed that the critical current density at 77 K and zero magnetic field increased with the increase of annealing time. Shi et al. [79] were able to increase J_c about 30 times of its initial value by increasing the density of lattice defects in glass ceramic BiSCO superconducting sample. The lattice defects cause increased pinning effects. The critical current decreases with increase of the applied magnetic field. J_c values of BiSCO and PbBiSCO glass ceramic plate superconductors are between 30-250 Acm^{-2} [80-81].

5. PHASE EVOLUTION

In the following subsections the dependence of phase formation on annealing temperature, annealing time, annealing atmosphere and also the role of lead in the formation of 2223 phase are discussed.

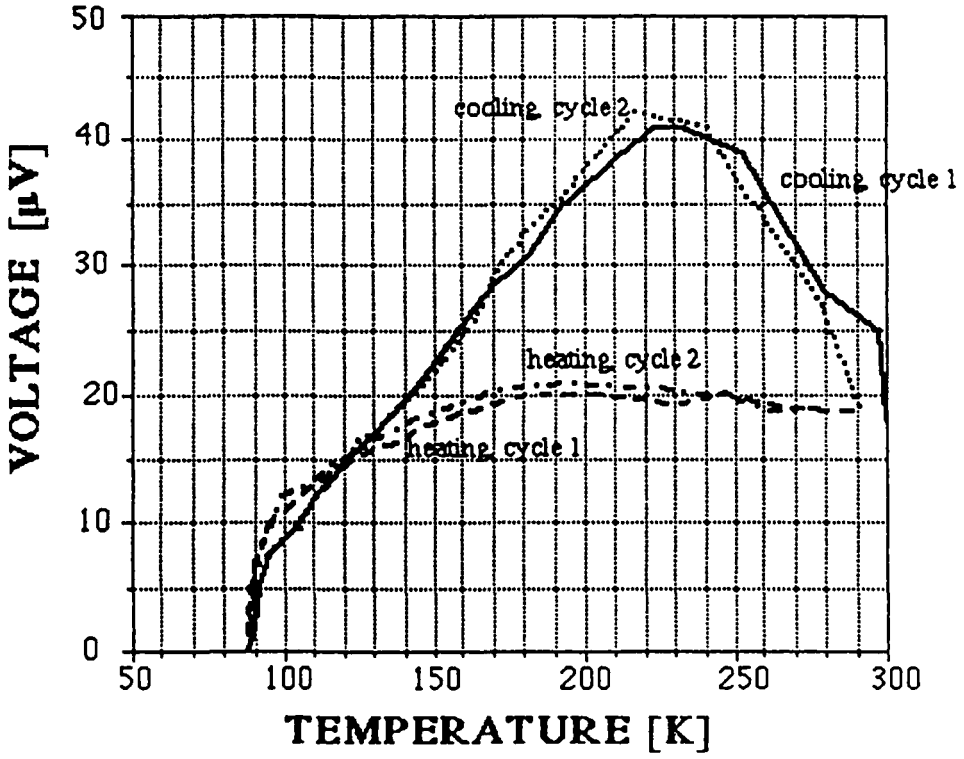

Figure 7. Electric resistivity vs. temperature for 2 cooling-heating cycles [37].

5.1. Annealing Temperature

The formation of the superconducting phases strongly depends on the temperature of annealing [37, 59, 82-87]. Massalker et al. [37] studied the heat treatment of an as-quenched PbBiSCO at different temperatures after flushing air for one hour. The chosen temperatures were 488, 540, 800 and 908 ^{0}C, based on the DSC thermogram shown in Figure 3. The presence, in changing amounts, of the following phases has been deduced from X-ray diffractions analyses: 2201, 2212, 2223, Ca_2PbO_4, Ca_2CuO_3 and the $Bi_2Sr_{3-x}Ca_xO_y$ compound. Small amounts of both the high T_c superconducting phases, 2212 and 2223 were among the first to crystallize. The amount of 2212 increased as the temperature was increased, but that was not the case for 2223. The X-ray diffractions of the samples treated at 488 ^{0}C and at 540 ^{0}C distinctly showed that both samples were not fully crystallized. This was probably due to the short soaking time (one hour) at these temperatures. However, the diffractograms showed that this same short time was enough to produce full devitrifaction at 800 ^{0}C, and of course at 908 ^{0}C also. The amount of CaO decreased steadily with increasing temperature. CaO and Ca_2CuO_3, whose amounts decreased sharply at 800 ^{0}C seemed to be the Ca providing oxides for the formation of 2212. They concluded that the small amount of 2223 that appeared at the lower temperature did not result from "partial melting" of 2212.

A study of the phase formation and crystal growth dependence on annealing temperature has been done by Kanai et al. [59]. With increasing the annealing temperature from 650 ^{0}C to 754 ^{0}C, the peaks from the 2212 phase emerged and increased while the peaks from 2201 phase decreased. At 803 ^{0}C only the peaks from the 2212 phase were observed. Above 865 ^{0}C, the 2201 phase is formed again, together with 2212. The presence of the 2223 phase was observed by resistivity measurement for samples annealed at 840 ^{0}C. The superconducting volume ratio of the sample increased above 705 ^{0}C and showed a maximum value of 70-75 % at 803 - 840 ^{0}C, but decreased by further increase of annealing temperature. The superconducting 2212 and 2223 phases were deduced to decompose into non-superconducting phases above 840 ^{0}C.

Takei et al. [82] claim that crystallization starts at 450 ^{0}C temperature. Rapidly quenched samples were glassy up to 400 ^{0}C. The 500 ^{0}C annealed specimens were in an intermediate state between glassy and crystalline states. SEM observations clarified that no apparent change occurred in the bulk by annealing at 500 ^{0}C. The following changes from amorphous to crystalline were observed:
annealing between 500-800 ^{0}C:
glassy $Bi_2(Sr, Ca)_2CuO_x \Rightarrow$ crystalline $Bi_2(Sr, Ca)_2CuO_x$;
annealing between 600-800 ^{0}C:
glassy $Bi_2(Sr, Ca)_2CuO_x + (Sr, Ca)CuO_2 \Rightarrow$ crystalline $Bi_2(Sr, Ca)_3Cu_2O_x$;
above 600 ^{0}C:
crystalline $Bi_2(Sr, Ca)_2CuO_x + (Sr, Ca)CuO_2 \Rightarrow$ crystalline $Bi_2(Sr, Ca)_3Cu_2O_x$.
The 800 ^{0}C annealed specimens were composed of fine needles of several microns in diameter and 10 μm in length. Small amount of grains and spheres of several millimeters in diameter were also observed. These grains and spheres were analyzed

to be insulative (Sr, Ca)CuO_2 and (Sr, Ca)O respectively. Above 800 ^{0}C, partial melting has bee observed .

A tentative phase diagram of the pseudo-binary system BiSrCaCuO and CaCuO near the melting temperature was presented in Ref. [88], suggesting a solid state disproportionation reaction among 2201, 2212 and 2223 below 800 ^{0}C, in contradiction to the observations by Takei et al. [82]. The results of Takei et al. [82], however, agree to those of Kanai et al. [59] where the formation of 2212 phase was observed by X-ray powder diffraction between 650 and 874 ^{0}C. Massalker et al. [37] also agree with the results of References [59] and [82], but they observed the disproportionation reaction at higher temperature, 908 ^{0}C. Many researchers [82-87] have pointed out that the 2223 phase grows from the 2212 phase, when the latter was in a partially molten condition, between 840 ^{0}C and 900 ^{0}C. Ref. [88] reports that the 2223 phase easily decomposes above 900 ^{0}C. Precipitation of the 2223 phase is not observed between 500 and 600 ^{0}C, though partial melting occurred at 800 ^{0}C. 800 ^{0}C is an eutectic point in that pseudo-binary system [88]. Around 600 ^{0}C, the solid phases 2201 and 2212 are stable. The 2223 phase appeared between 870 and 900 ^{0}C, in air.

5.2. Annealing Time and Annealing Atmosphere

The dependence of annealing time and atmosphere on the high T_c phases evolution has been studied by several groups [35, 37, 62-64, 68, 89]. In Ref. [37], the highest amount (about 95 % in volume) of 2223 detected was after annealing for 120 hours at 850 ^{0}C, in air. The highest amount of the 2212 phase (almost 100 % in volume) was obtained after 240 hours at 840 ^{0}C. The 2212 phase, grown from 2223 initial nominal compositions, appeared in relatively high amounts if treated either at 825, 840 or 850 ^{0}C, for at least 120 hours. However, when the time was increased up to 240 hours, an optimum amount of the phase was attained at 840 ^{0}C. The 2212 phase decomposed either if the temperature exceeded 850 ^{0}C or if the time was increased beyond 240 hours. Conversely, growth of the 2223 phase was enhanced at 840 ^{0}C and prolonged times but was really effective only at 850 ^{0}C after 120 or 240 hours. Exposures at temperatures higher than 850 ^{0}C invariably destroyed almost all of the 2212 and 2223 superconducting phases.

Most of the reviewed studies [35, 37, 59, 82] found the low T_c phase Bi_2(Sr, Ca)$_2CuO_x$, 2201 to crystalline first, though Ibara et al. [63] suggest that the first crystalline product from the glass is (Sr, Ca)$_3Cu_5O_y$. The high T_c phase 2223 does not form in absence of oxygen [37, 90]. For as-quenched material, an uptake of 0.41-0.44 oxygen per copper atoms has been calculated [35, 90].

According to Ref.[35] and [37], crystallization occurs in two steps with the formation of 2201, $Bi_2Sr_{3-x}Ca_xCu_2O_y$ and impurity oxides. $Bi_2Sr_{3-x}Ca_xCu_2O_y$ is converted to other phases upon annealing in oxygen below 700 ^{0}C and melted during heating the glass around 700 ^{0}C. The 2212 phase evolved from the 2201 nuclei formed during the initial crystallization. Its formation from 2201 below 800 ^{0}C was found to be kinetically limited. Holesinger et al. [35] concluded that the majority of the sample could be converted to 2212 after only 1 minute annealing in oxygen at

800 ^{0}C. But extended anneals at these higher temperatures were needed for the system to reach its equilibrium state.

Kanai et al. [64] suggested that the volume fraction of the high T_c phase increased with the decrease of the low T_c phase and the non-superconducting phases, according to the following stoichiometry: 3(2212) + $CaCu_2O_3$ + Ca_2CuO_3 ⇒ 3(2223).

5.3. The Role of Pb

The formation of the 2223 phase is a very slow process, in particular for samples that are not Pb-doped. The doping with lead accelerates the 2223 phase formation kinetics. However, Massalker et al. [37] have shown that the presence of Pb causes also the formation of Ca_2PbO_4 in increasing amounts up to 800 ^{0}C. This oxide provides the Ca necessary for the renewed growth of 2223 at 908 ^{0}C. The 2212 phase could have decomposed somehow, and also contributed to the regeneration of 2223, the amount of which lowers at 800 ^{0}C. The $Bi_2Sr_{3-x}Ca_xO_y$ compound was present at the very first crystallization stage, then decomposed at 800 ^{0}C [37]. Based on all the observed changes in the relative amounts of each phase, the following crystallization and phase evolution sequences, by heating from the amorphous state has been suggested:

at 488 ^{0}C:

$Pb_{0.45}Bi_{1.15}Sr_{2.10}Ca_{2.00}Cu_{3.65}Al_{0.65}$ ⇒ 2201, 2212, 2223, CaO, CuO, Ca_2PbO_4, Ca_2CuO_3 and $Bi_2Sr_{3-x}Ca_xO_y$;

at 540 ^{0}C: increase in Ca_2CuO_3;

at 800 ^{0}C: 2223 + CaO + $Bi_2Sr_{3-x}Ca_xO_y$ + Ca_2CuO_3 ⇒ 2(2212) + 2(Ca_2PbO_4) + CuO;

at 908 ^{0}C, 2 distinct reactions occur simultaneously: 2(2212) ⇒ 2223 + 2201; this is the disproportionation reaction, which is presumed to take place with intake of oxygen in order to comply with the increased oxygen content of the 2223 phase, as compared to the 2212 phase; and: Ca_2PbO_4 + 2201 + 2(CuO) ⇒ 2212 + Ca_2CuO_3 [92]

The mechanism proposed in Ref. [37] suggests that the decomposition of Ca_2PbO_4 causes an increase of 2212, which in turn, favorited the increase of 2223 through the disproportionation reaction. The formation of Ca_2PbO_4 below 850 ^{0}C and its decomposition above this temperature had been reported also by Idemoto et al. [93]. Support for the model reactions as explained above is presented in Figure 8 [37], that shows the evolution of all the phases, superconducting and "impurities", detected by XRD in one specific specimen, heated for 1 hour at the respective temperatures 488, 540, 800 and 908 C.

According to Wong-Ng et al. [94], CaO, CuO and 2201 began to crystallize in the glass at approximately 400 ^{0}C. A small amount of the 2212 phase was also observed, probably already formed during quenching. At 550 ^{0}C, the formation of Ca_2PbO_4 was observed. The 2212 superconducting phase is formed from a 2201 + excess CaO and CuO reaction at 700-730 ^{0}C. At 820 ^{0}C, Ca_2PbO_4 decomposes to form CaO

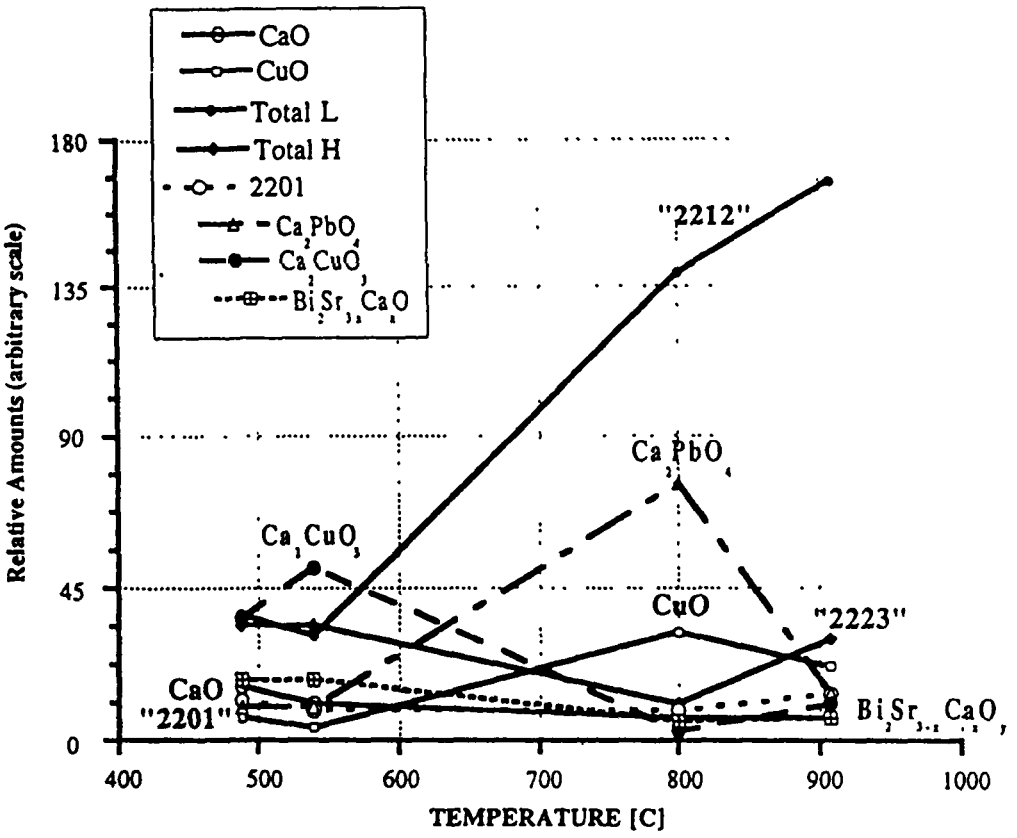

Figure 8. Phases evolution aconsecutive to 1 hour oxygenation treatment of amorphous samples at various temperatures [37].

and PbO [95-97] + a liquid due to an eutectic reaction. That liquid phase accelerates the formation of the 2212 phase, through a process of melt-assisted diffusion of CaO and CuO. CaO reacts with the $(Sr, Ca)_{14}Cu_{24}O_{41}$ phase to form $(Ca, Sr)_2CuO_3$ and 2223. At 860 ^{0}C, the 2223 phase decomposes into Cu_2O, $(Ca, Sr)_2CuO_3$ and a Bi-rich liquid. That Bi-rich liquid subsequently causes the formation of the 2201 phase. The presence of Ca_2PbO_4 seems to help to the formation of 2223 phase [98]. Ca_2PbO_4 melts at 822 ^{0}C and induces a liquid phase below 850 ^{0}C, increasing drastically the diffusion rates of the reactive species Ca^{2+} and Cu^{2+}. The following reaction was consequently proposed: $Ca_2PbO_4 + CuO \Rightarrow Ca_2CuO_3 + PbO_2$ The melted Ca_2PbO_4 contributes to the flux needed for rapid transport of the key elements to the growing 2223 phase. Pb is believed to be the element that acts as a flux. It also substitutes for Bi in the crystal structure of the high T_c phases. Excess CaO and CuO are also needed for the formation of 2223. The temperature for the 2223 phase formation was 840-860 ^{0}C [37, 94]. After the formation of Ca_2CuO_3, the

2223 phase formed in the following manner: 2201 + Ca_2CuO_3 + CuO ⇒ 2212 and 2212 + Ca_2CuO_3 + CuO ⇒ 2223.

Another mechanism has also been proposed [99] to explain the role played by Pb in the development of the 2223 phase. Due to lead substitution of bismuth, the structural properties are modified, and in particular the strength of the bonding between the slabs that constitute the building blocks of the compound. The stacking of these slabs causes intensive intergrowth in the Pb free material. After nucleation, the 2223 phase cannot extend to the adjacent slabs due to very slow kinetics. The intergrowth is absent in the Pb substituted sample. The 2223 nuclei are therefore able to extend up into the entire volume. So the addition of Pb strongly enhances the growth process of the 2223 phase [99]. With the increase of the Pb content, the volume fraction of 2223 phase increased. However, excess Pb lowers the formation temperature of spurious intermediate species, such as strontium-lead oxide [96].

ACKNOWLEDGEMENT

This research is supported by the Israeli Ministry of Sciences and Arts.

REFERENCES

1. J.G. Bendnorz and K.A. Muller, "Possible high T_c superconductivity in the Ba-La-Cu-O system", *Z. Phys. B* , Vol. 64, No. 2, 1986, pp. 189-193.
2. M.K. Wu, J.R. Ashburn, C.J. Torng, P.H. Hor, R.L. Meng, L.Gao, Z.J. Huang, Y.Q. Wang and C.W. Chu, "Superconductivity at 93 K in a new mixed-phase Y-Ba-Cu-O compound system at ambient pressure", *Phys. Rev. Lett.*, Vol. 58, No. 9, 1987, pp. 908-910.
3. Z.Z. Sheng, A.M. Hermann, A. El Ali, C. Almasan, J. Estrada, T. Datta and J. Matson, "Superconductivity at 90 K in the Tl-Ba-Cu-O system", *Phys. Rev. Lett.*, Vol. 60, No. 10, 1988, pp. 937-940.
4. H. Maeda, Y. Tanaka, M. Fukutomi and T. Asano, "A new high T_c oxide superconductor without a rare earth element", *Jpn. J. Appl. Phys.* Vol. 27, No. 2, 1988, pp. L209-L210.
5. S.N. Putilin, E.V. Antipov, O. Chmaissem and M. Marezio, "Superconductivity at 94 K in $HgBa_2CuO_{4+\delta}$", *Nature*, Vol. 362, No. 6417, 1993, pp. 226-228.
6. S.N. Putilin, E.V. Antipov and M. Marezio, "Superconductivity above 120 K in $HgBa_2CaCu_2O_{6+\delta}$", *Physica C*, Vol. 212, No. 3&4, 1993, pp. 266-270.
7. A. Schilling, M. Cantoni, J.D. Guo and H.R. Ott, "Superconductivity above 130 K in Hg-Ba-Ca-Cu-O system", *Nature*, Vol. 363, No. 6424, 1993, pp. 56-58.
8. M. Takano, M. Azuma, Z. Hiroi, Y. Bando and Y. Takeda, "Superconductivity in the Ba-Sr-Cu-O system", *Physica C* , Vol. 176, No. 4-6, 1991, pp. 441-444.

9. M. Azuma, Z. Hiroi, M. Takano, Y. Bando, and Y. Takeda, " Superconductivity at 110 K in infinity-layer compound $(Sr_{1-x}Ca_x)_{1-y}CuO_2$", *Nature* , Vol. 356, No. 6372, 1992, pp. 775-776.
10. S. Adachi, H. Yamauchi, S. Tanaka and N. Mori, "High pressure synthesis of superconducting Sr-Ca-Cu-O samples", *Physica C*, Vol. 208, No. 3&4, 1993, pp. 226-230.
11. S. Adachi, H. Yamauchi, S. Tanaka, and N. Mori, "New superconducting cuprates in the Sr-Ca-Cu-O system", *Physica C*, Vol. 212, No. 1&2, 1993, pp. 164-168.
12. S.S.P. Parkin, V.Y. Lee, A.I. Nazzal, R. Savoy, T.C. Huang, G. Gorman and R. Beyers, "Model family of high temperature superconductors: $Tl_mCa_{n-1}Ba_2Cu_nO_{2(n+1)+m}$ (m = 1, 2; n = 1, 2, 3)", *Phys. Rev. B.*, Vol. 38, No. 10, 1988, pp. 6531-6537.
13. R.M. Hazen, L.W. Finger, R.J. Angel, C.T. Prewitt, N.L. Ross, C.G. Hadidiacos, P.J. Heaney, D.R. Veblen, Z.Z. Sheng, A. El Ali and A.M. Hermann, "100 K superconducting phases in the Tl-Ca-Ba-Cu-O system", *Phys. Rev. Lett.*, Vol. 60, No. 16, 1988, pp. 1657-1660.
14. S.S.P. Parkin, V.Y. Lee, E.M. Engler, A.I. Nazzal, T.C. Huang, G. Gorman, R. Savoy and R. Beyers, "Bulk superconductivity at 125 K in $Tl_2Ca_2Ba_2Cu_3O_x$", *Phys. Rev. Lett.*, Vol. 60, No. 24, 1988, pp. 2539-2542.
15. R.J. Cava, B. Batlogg, C.H. Chen, E.A. Rietman, S.M. Zahurak and D. Werder, "Single phase 60 K bulk superconductor in annealed $Ba_2YCu_3O_{7-\delta}$ ($0.3<\delta<0.4$) with correlated oxygen vacancies in the Cu-O chains", *Phys. Rev. B* , Vol. 36, No. 10, 1987, pp. 5719-5722.
16. Y. Kubo, T. Yoshitake, J. Tabuchi, Y. Nakabayashi, A. Ochi, K. Utsumi, H. Igarashi and M. Yowzawa, "Effect of oxygen on the crystal structure and superconducting properties of the $Ba_2YCu_3O_y$", *Jpn. J. Appl. Phys.*, Vol. 26, No. 5, 1987, pp. L768-L770.
17. L. Gao, Z.J. Haung, R.L. Meng, J.G. Lin, F. Chen, L. Beauvais, Y.Y. Sun, Y.Y. Xue and C.W. Chu, "Study of superconductivity in the Hg-Ba-Ca-Cu-O system", *Physica C*, Vol. 213, No. 3&4, 1993, pp. 261-265.
18. C.Q. Jin, S. Adachi, X.J. Wu, H. Yamauchi and S. Tanaka, "117 K superconductivity in the Ba-Ca-Cu-O system", *Physica C*, Vol. 223, No. 3&4, 1994, pp. 238-242.
19. C.N.R. Rao, L. Ganapathi, R. Vijayaraghavan, G. Ranga Rao, K. Murthy and R.A. Mohan Ram, "Superconductivity in the $Bi_2(Ca, Sr)_{n+1}Cu_nO_{2n+4}$ (n=1, 2, or 3) series: synthesis, characterization and mechanism", *Physica C* , Vol. 156, No. 5, 1988, pp. 827-833.
20. S.S. Sastry, I.K. Gopalakrishnan, A. Sequeira, H. Rajagopal, K. Gangadharan, G.M. Phatak and R.M. Iyer, "On the preparation and structure in the Bi-Sr-Ca-Cu-O system", *Physica C* , Vol. 156, No. 2, 1988, pp. 230-234.
21. B.W. Statt, Z. Wang, M.J.G. Lee, J.V. Yakhmi and P.C. De Camargo, "Stabilizing the high T_c superconductor $Bi_2Sr_2Ca_2Cu_3O_{10+x}$ by Pb substitution", *Physica C* , Vol. 156, No. 2, 1988, pp. 251-255.

22. S.M. Green, C. Jiang, Yu. Mei, H.L. Luo and C. Politis, "Zero resistance at 107 K in the (Bi, Pb)-Sr-Ca-Cu oxide system", *Phys. Rev.* B, Vol. 38, No. 7, 1988, pp. 5016-5018.
23. K. Tanaka, A. Nozue and K. Kaniya, "Preparation of Bi-Pb-Sr-Ca-Cu-O superconductors by the sol-gel method", *J. Mater. Sci.*, Vol. 25, No. 8, 1990, pp. 3551-3556.
24. R.S. Liu, W.N. Wang, C.T. Chang and P.T. Wu, "Synthesis and characterization of high T_c superconducting oxides by the modified citrate gel process", *Jpn. J. Appl. Phys.*, Vol. 28, No. 12, 1989, pp. L2155-L2157.
25. Yu. Zhang, Z. Fang, M. Muhammed, K.V. Rao, V. Skumryev, H. Medelius and J.L. Costa, "The synthesis of superconducting bismuth compounds via oxalate coprecipitation", *Physica C*, Vol. 157, No. 1, 1989, pp. 108-114.
26. G. Marbach, S. Stotz, M. Klee and J.W.C. DeVries, "Superconductivity in Bi-Sr-Ca-Cu-O bulk samples made by thermal decomposition of metal oxalates", *Physica C*, Vol. 161, No. 1, 1989, pp. 111-120.
27. G. Gritzner and K. Bernard, "$Pb_{0.3}Bi_{1.7}Ca_xSr_{4-x}Cu_3O_y$ and $Pb_{0.4}Bi_{1.6}Ca_xSr_{4-x}Cu_3O_y$ superconductors from coprecipitated oxalate precursors", *Physica C*, Vol. 181, No. 1/3, 1991, pp. 201-205.
28. R. Mahesh, V.A. Pavatel, O. Parkash and C.N.R. Rao, "Investigations of the cuprate superconductors prepared by the combustion route", *Supercond. Sci. Technol.*, Vol. 5, No. 3, 1992, pp. 174-179.
29. T. Komatsu, R. Sato, K. Imai, K. Matusita and T. Yamashita, "High T_c superconducting glass ceramics based on Bi-Ca-Sr-Cu-O system", *Jpn. J. Appl. Phys.*, Vol. 27, No. 4, 1988, pp. L550-L552.
30. T. Minami, Y. Akamatsu, M. Tatsumisago, N. Tohge and Y. Kawada, "Glass formation of high T_c compound $BiCaSrCu_2O_x$ by rapid quenching", *Jpn. J. Appl. Phys.*, Vol. 27, No. 5, 1988, pp. L777-L778.
31. D.G. Hinks, L. Soderstrom, D.W. Capone, D. Dabrowski, A.W. Mitchell and D. Shi, "Preparation of Bi-Sr-Ca-Cu-O superconductors from oxide-glass precursors", *Appl. Phys. Lett.*, Vol. 53, No. 5, 1988, pp. 423-425.
32. A. Inoue, H. Kimura, K. Matsuzaki, A. Tsai and T. Masumoto, "Production of Bi-Sr-Ca-Cu-O glasses by liquid quenching and their glass transition and structural relaxation", *Jpn. J. Appl. Phys.*, Vol. 27, No. 6, 1988, pp. L941-L943.
33. F.H. Garzon, J.G. Beery and I.D. Raistrick, "Amorphous-to-crystalline transformations in bismuth-oxide-based high T_c superconductors", *Appl. Phys. Lett.*, Vol. 53, No. 9, 1988, pp. 805-807.
34. H. Sato, W. Zhu and T. Ishiguro, "Preparation of a high-density Bi-Sr-Ca-Cu-O ceramic with a single superconducting phase", *J. Solid State Chem.*, Vol. 75, No. 1, 1988, pp. 207-211.
35. T.G. Holesinger, D.J. Miller and L.S. Chumbley, "Crystallization of Bi-Sr-Ca-Cu-O glasses in oxygen", *J. Mater. Res.*, Vol. 7, No. 7, 1992, pp. 1658-1671.
36. C.H. Shan and S.H. Risbud, "Effect of supercooling on the growth kinetics of the 2223 phase in Bi-Pb-Sr-Ca-Cu-O superconducting glass-ceramics", *Supercond. Sci. Technol.*, Vol. 6, No. 10, 1993, pp. 736-742.

37. Y. Massalker, A.N. Sembira and J. Baram, "Processing characteristics and properties of BiSrCaCuO superconducting glass ceramics prepared by melt-quenching", *J. Mater. Res.*, Vol. 8, No. 10, 1993, pp. 2445-2457.

38. M. Tatsumisago, C.A. Angell, S. Tsuboi, Y. Akamatsu, N. Tohge and T. Minami, "Transition range viscosity of rapidly quenched Bi-Ca-Sr-Cu-O glasses", *Appl. Phys. Lett.*, Vol. 54, No. 22, 1989, pp. 2268-2270.

39. S.E. LeBeau, J. Righi, J.E. Ostenson, S.C. Sanders and D.K. Finnemore, "Preparation of superconducting Bi-Sr-Ca-Cu-O fibers", *Appl. Phys. Lett.*, Vol. 55, No. 3, 1989, pp. 292-294.

40. I. Matsubara, H. Kageyama, H. Tanigawa, T. Ogura, H. Yamashita and T. Kawai, "Preparation of fibrous Bi(Pb)-Sr-Ca-Cu-O crystals and their superconducting properties in a bending state", *Jpn. J. Appl. Phys.*, Vol. 28, No. 7, 1989, pp. L1121-L1124.

41. J. Akimitsu, A. Yamazaki, H. Sawa and H. Fujiki, "Superconductivity in the Bi-Sr-Cu-O system", *Jpn. J. Appl. Phys.*, Vol. 26, No. 12, 1987, pp. L2080-L2081.

42. P. Bordet, J.J. Capponi, C. Chaillout, J. Chenavas, A.W. Hewat, E.A. Hewat, J.L. Hodeau, M. Marezio, J.L. Tholence and D. Tranqui, "Powder X-ray and neutron diffraction study of the superconductor $Bi_2Sr_2CaCu_2O_8$", *Physica C*, Vol. 153-155, No. Part I, 1988, pp. 623-624.

43. J. M. Tarascon, W.R. McKinnon, P. Barboux, D.M. Hwang, B.G. Bagley, L.H. Greene, G.W. Hull, Y. LePage, N. Stoffel and M. Giroud, "Preparation, structure, and properties of superconducting compound series $Bi_2Sr_2Ca_{n-1}Cu_nO_y$ with n = 1, 2, and 3" *Phys. Rev. B*, Vol. 38, No. 13, 1988, pp. 8885-8899.

44. E. Takayama-Muromachi, Y. Uchida, A. Ono, F. Izumi, M. Onoda, Y. Matsui, K. Kosuda, S. Takekawa and K. Kato, "Identification of the superconducting phase in the Bi-Ca-Sr-Cu-O system", *Jpn. J. Appl. Phys.*, Vol. 27, No. 3, 1988, pp. L365-L368.

45. P. Majewski, "BiSrCaCuO high T_c superconductors", *Advanced Materials*, Vol. 6, No. 6, 1994, pp. 460-469.

46. R.M. Hazen, C.W. Prewitt, R.J. Angel, N.L. Ross, L.W. Finger, C.G. Hadidiacos, D.R. Veblen, P.J. Heaney, P.H. Hor, R.L. Meng, Y.Y. Sun, Y.Q. Wang, Y.Y. Xue, Z.J. Huang, L. Gao, J. Bechtold and C.W. Chu, "Superconductivity in the high T_c Bi-Ca-Sr-Cu-O system: phase identification", *Phys. Rev. Lett.*, Vol. 60, No. 12, 1988, pp. 1174-1177.

47. S.A. Sunshine, T. Siegrist, L.F. Schneemeyer, D.W. Murphy, R.J. Cava, B. Batlogg, R.B. van Dover, R.M. Fleming, S.H. Glarum, S. Nakahara, R. Farrow, J.J. Krajewoki, S.M. Zahurk, J.V. Waszczak, J.H. Marshall, P. Marsh, L.W. Rupp, Jr. and W.F. Peck, "Structure and physical properties of single crystals of the 84 K superconductor $Bi_{2.2}Sr_2Ca_{0.8}Cu_2O_{8+\delta}$", *Phys. Rev. B*, Vol. 38, No. 1, 1988, pp. 893-896.

48. E.A. Hewat, P. Bordet, J.J. Capponi, C. Chaillout, J.L. Hodeau and M. Marezio, "Superstructure of the superconductor $Bi_2Sr_2CaCu_2O_8$ by high resolution electron microscopy", *Physica C*, Vol. 153-155, No. Part I, 1988, pp. 619-620.

49. Y. Le Page, W.R. McKinnon, J.M. Tarascon and P.Barboux, "Origin of the incommensurate modulation of the 80 K superconductor $Bi_2Sr_2CaCu_2O_{8.21}$ derived from isostructural commensurate $Bi_{10}Sr_{15}Fe_{10}O_{46}$", *Phys. Rev. B*, Vol. 40, No. 10, 1989, pp. 6810-6816.

50. A. Yamamoto, M. Onada, E. Takayama-Muromachi, F. Izumi, T. Ishigaki and H. Asano, "Rietveld analysis of the modulated structure in the superconducting oxide $Bi_2(Sr, Ca)_3Cu_2O_{8+x}$", *Phys. Rev. B*, Vol. 42, No. 7, 1990, pp. 4228-4239.

51. N. Fukushima, H. Niu, S. Nakamura, S. Takano, M. Hayashi and K. Ando, "Structural modulation and superconducting properties in $Bi_{2-x}Pb_xSr_2CaCu_2O_{8+d}$ and $Bi_{2-y}Pb_ySr_2YCu_2O_{8+\delta}$", *Physica C*, Vol. 159, No. 6, 1989, pp. 777-783.

52. S. Kambe, T. Matsuoka, M. Takahasi, M. Kawai and T. Kawai, "Superconductive transition at 98.5 K in monoclinic $(Bi, Pb)_2Sr_2CaCu_2O_y$", *Phys. Rev. B*, Vol. 42, No. 4, 1990, pp. 2669-2672.

53. T. Kajitami, K. Kusaba, M. Kikuchi, N. Kobayashi, Y. Syono, T. B. Williams and M. Hirabayashi, "Structural study of high T_c superconductor $Bi_{2-x}(Ca, Sr)_3Cu_{2+x}O_{9-y}$", *Jpn. J. Appl. Phys.*, Vol. 27, No. 4, 1988, pp. L587-L590.

54. E. Muromachi, Y. Uchida, Y. Matsui, M. Onoda and K. Kato, "On the 110 K superconductor in the Bi-Ca-Sr-Cu-O system", *Jpn. J. Appl. Phys.*, Vol. 27, No. 4, 1988, pp. L556-L558.

55. M. Takano, J. Takada, K. Oda, H. Kitaguchi, Y. Miura, Y. Akeda, Y. Tomii and H. Mazaki, "High T_c phase promoted and stabilized in the Bi, Pb-Sr-Ca-Cu-O system", *Jpn. J. Appl. Phys.*, Vol. 27, No. 6, 1988, pp. L1041-L1043.

56. S. Shimomura, K. Takahashi, M. Ohta, A. Watanabe, M. Seido and F. Hosono, "Preparation of superconductive Bi-Sr-Ca-Cu-O thick films by rapid quenching", *Jpn. J. Appl. Phys.*, Vol. 27, No. 10, 1988, pp. L1890-L1891.

57. M. Yoshimura, T.H. Sung, Z. Nakagawa, and T. Nakamura, "Preparation of $Bi_2Sr_2CaCu_2O_x$ superconductors from amorphous films by rapid quenching after rapid melting", *Jpn. J. Appl. Phys.*, Vol. 27, No. 10, 1988, pp. L1877-L1879.

58. S. Mollah, K.K. Som, K. Bose, A.K. Chakraborty and B. K. Chaudhuri, "Non-adiabatic small polaron hopping conduction in Li-doped and undoped $Bi_4Sr_3Ca_3Cu_yO_x$ $(0 \leq y \leq 5)$", *Phys. Rev. B*, Vol. 46, No. 17, 1992, pp. 11075-11083.

59. T. Kanai, T. Kumagai, A. Soeta, T. Suzuki, K. Aihara, T. Kamo and S. Matsuda, "Crystalline structures and superconducting properties of rapidly quenched $BiSrCaCu_2O_x$ ceramics", *Jpn. J. Appl. Phys.*, Vol. 27, No. 8, 1988, pp. L1435-L1438.

60. P.J. King, D.S. Misra and W.B. Roys, "The electrical properties of quenched and unquenched superconducting $Bi_2Sr_2CaCu_2O_x$", *Supercond. Sci. Technol.*, Vol. 1, No. 5, 1989, pp. 227-231.

61. T. Komastu, R. Sato, K. Imai, K. Matusita and T. Yamashita, "High T_c superconducting glass ceramics based on the Bi-Ca-Sr-Cu-O system", *Jpn. J. Appl. Phys.*, Vol. 27, No. 4, 1988, pp. L550-L552.

62. H. Yamanaka, M. Matsuda, M. Takata, M. Ishii, T. Yamashita and H. Koinuma, "Preparation of superconducting Bi-Pb-Sr-Ca-Cu-O glass ceramics with $T_{c,zero}$ = 106 K", *Jpn. J. Appl. Phys.*, Vol. 28, No. 12, 1989, pp. L2185-L2187.

63. Y. Ibara, H. Nasu, T. Imura and Y. Osaka, "Preparation and crystallization of the high T_c superconducting phase (T_c (end) > 100 K) in Bi, Pb-Sr-Ca-Cu-O glass ceramics", *Jpn. J. Appl. Phys.*, Vol. 28, No. 1, 1989, pp. L37-L40.

64. T. Kanai, T. Kamo and S.P. Matsuda, "Formation of the high T_c phase in rapidly quenched Bi-Pb-Sr-Ca-Cu-O ceramics", *Jpn. J. Appl. Phys.*, Vol. 28, No. 12, 1989, pp. L2188-L2191.

65. T. Komastu, R. Sato, H. Meguro, K. Matusita and T. Yamashita, "Effect of copper content on glass formation and superconductivity in the Bi-Pb-Sr-Ca-Cu-O system", *J. Mater. Sci.*, Vol. 26, No. 3, 1991, pp. 683-688.

66. K. Egawa, T. Umemura, S. Kinouchi, M. Wakata and S. Utsunomiya, "Microstructures and superconducting properties of Bi-Sr-Ca-Cu-O system prepared by a melt process", *Jpn. J. Appl. Phys.*, Vol. 30, No. 7A, 1991, pp. L1160-L1162.

67. Y. Abe, H. Honsono, M. Hosoe, J. Iwase and Y. Kubo, "Superconducting glass-ceramic rods in $BiCaSrCu_2O_x$ prepared by crystallization under a temperature gradient", *Appl. Phys. Lett.*, Vol. 53, No. 14, 1988, pp. 1341-1342.

68. T. Kasuga, K. Osamura, M. Hirata, W. Lee, and Y. Abe, "Superconducting glass-ceramics in $Bi_{0.7}Pb_{0.3}SrCaCu_{1.8}O_x$: effect of reheating time on T_c", *Supercond. Sci. Technol.*, Vol. 6, No. 1, 1993, pp. 59-62.

69. Y. Abe, H. Honsono, W.H. Lee, M. Hosoe, K. Nakamura and E. Inukai, "New method for fabrication of superconducting pipes in the Bi-Sr-Ca-Cu-O system", *J. Mater. Res.*, Vol. 8, No. 1, 1993, pp. 1-4.

70. T. Komatsu, C. Hirose, T. Okhi, R. Sato, K. Matusita and T. Yamashita, "Preparation of Ag coated superconducting $Bi_2Sr_2CaCu_2O_x$ glass ceramic fibers", *Appl. Phys. Lett.*, Vol. 57, No. 2, 1990, pp. 183-185.

71. B.M. Moon, B. Lalevic, B.H. Kear, L.E. McCandlish, A. Safari and M. Meskoob, "High-density Bi-Pb-Sr-Ca-Cu-O superconductor prepared by rapid thermal melt processing", *Appl. Phys. Lett.*, Vol. 55, No. 14, 1989, pp. 1466-1468.

72. T. Komatsu, R. Sato, K. Matusita and Y. Yamashita, "Superconducting glass ceramics with T_c = 100 K on the Bi-Pb-Sr-Ca-Cu-O system", *Appl. Phys. Lett.*, Vol. 54, No. 12, 1989, pp. 1169-1171.

73. W.H. Lee, H. Kondo, H. Hosono and Y. Abe, "Superconducting $Bi_2Sr_2Ca_1Cu_2O_{8+y}$ glass-ceramics with different melting histories", *Jpn. J. Appl. Phys.*, Vol. 32, No. 3A, 1993, pp. 1082-1090.

74. S. Mollah, S. Chatterjee, S. Chakraborty and B.K. Chaudhuri, "Dielectric properties of semiconducting $Bi_{4-n}Pb_nSr_3Ca_3Cu_4O_x$ ($0 \leq n \leq 1$) glasses: precursors for high T_c superconductors", *Phil. Mag. B*, 1994, in press.

75. P.S. Mukherjee, A. Simon, J. Koshy, P. Guruswamy and A.D. Damodaran, "Superconductivity in Ag added Bi-Pb-Sr-Ca-Cu-O system", *Solid State Commun.*, Vol. 76, No. 5, 1990, pp. 659-661.

76. J.L. Tallon, R.G. Buckley, P.W. Gilberd and M.R. Presland, "Single-phase Pb-substituted $Bi_{2+y}Ca_{n-1}Sr_2Cu_nO_{2n+4+\delta}$ n=2 and 3: structure, T_c, and effects of oxygen stoichiometry", *Physica C* , Vol. 158, No. 1&2, 1989, pp. 247-254.

77. Z.X. Zhao and C.C. Che, "Phase formation and effect of quench treatments on superconductivity of the Bi(Pb)-2223 phase", *Appl. Superconductivity*, Vol. 2, No. 3-4, 1994, pp. 227-235.

78. T. Hatano, K. Aota, S. Akada, K. Nakamura and K. Ogawa, "Growth of the 2223 phase in leaded Bi-Sr-Ca-Cu-O system", *Jpn. J. Appl. Phys.*, Vol. 27, No. 11, 1988, pp. L2055-L2058.

79. D. Shi, J.G. Chen, U. Welp, M.S. Boley, and A. Zangvil, "Lattice defects and flux pinning in crystallized metal-oxide glasses in Bi-Pb-Sr-Ca-Cu-O system", *Appl. Phys. Lett.*, Vol. 55, No. 13, 1989, pp. 1354-1359.

80. R. Sato, T. Komatsu, K. Matushita and T. Yamashita, "Superconducting properties of Bi-Pb-Sr-Ca-Cu-O ceramics prepared by melt-quenching method", *Jpn. J. Appl. Phys.*, Vol. 28, No. 10, 1989, pp. L583-L586.

81. A. Bhargava, R.L. Snyder and A.K. Varshneya, "Prelimenary investigation of superconducting glass-ceramics in Bi-Sr-Ca-Cu-O system", *Mater. Lett.*, Vol. 8, No. 10, 1989, pp. 425-431.

82. H. Takei, M. Koike, H. Takeya, K. Suzuki and M. Ichihara, "Crystallization from a glassy state in the Bi-Sr-Ca-Cu-O system", *Jpn. J. Appl. Phys.*, Vol. 28, No. 7, 1989, pp. L1193-L1196.

83. A. Ono, K. Kosuda, S. Sueno and Y. Ishizawa, "A 105 K superconducting phase in the Bi-Sr-Ca-Cu-O system", *Jpn. J. Appl. Phys.*, Vol. 27, No. 6, 1988, pp. L1007-L1008.

84. T. Wada, N. Suzuki, A. Maeda, S. Uchida, K. Uchinokura and S. Tanaka, "Preparation of high T_c (110 K) superconducting phase by the annealing of low T_c (80 K) superconductor $Bi_2(Sr_{0.5}Ca_{0.5})_{3-x}Cu_2O_y$", *Jpn. J. Appl. Phys.*, Vol. 27, No. 6, 1988, pp. L1031-L1034.

85. A. Ono, "Synthesis of the 107 K superconducting phase in the Bi-Sr-Ca-Cu-O system", *Jpn. J. Appl. Phys.*, Vol. 27, No. 7, 1988, pp. L1213-L1215.

86. Y. Oka, N. Yamamoto, H. Kitaguchi, K. Oda and J. Takada, "Crystallization behavior and partially melted states in Bi-Sr-Ca-Cu-O", *Jpn. J. Appl. Phys.*, Vol. 28, No. 2, 1989, pp. L213-L216.

87. Y. Oka, N. Yamamoto, T. Tomii, H. Kitaguchi, K. Oda, and J. Takada, "Crystalline phase formed in the partially melted states in Bi-Sr-Ca-Cu-O", *Jpn. J. Appl. Phys.*, Vol. 28, No. 5, 1989, pp. L801-L803.

88. K. Kuwahara, S. Yaegashi, K. Kishio, T. Hasegawa and K. Kitazawa, "Microstructural phase analysis of Bi-Sr-Ca-Cu-O system with $T_{c(\rho=0)}$ = 108 K prepared by low temperature treatment", *Proceedings of the 1 LACHTS, First Latin-American Conference on High Temperature Superconduvtivity, Rio de Janeiro, 4-6 May 1988* (Singapore, World Scientific), 1988, pp. 38-48;

89. N. Toghe, S. Tsuboi, M. Tatsumisago and T. Minami, "Crystalline phases precipitated by heat-treatment of rapidly-quenched glasses in the Bi-Ca-Sr-Cu-O system", *Jpn. J. Appl. Phys.*, Vol. 28 , No. 10, 1989, pp. L1742-L1745.

90. K. Nassau, A.E. Miller, E.M. Gryorgy and T. Siegrist, "Rapidly quenched Bi-containing high T_c superconducting oxide composition", *J. Mater. Res.*, Vol. 4, No. 6, 1989, pp. 1330-1338.

91. D. Shi, M. Tang, M. S. Boley, M. Hash, K. Vandervoort, H. Claus and Y. N. Lwin, "Crystallization of metal-oxide glasses in Bi-Sr-Ca-Cu-O systems", *Phys. Rev. B* , Vol. 40, No. 4, 1989, pp. 2247-2253.

92. M. Nagai, T. Nishino, T. Hattori, M. Matsuda, and M. Tanaka, "Effect of annealing on properties of bismuth based high T_c superconductors", *J. Mater. Sci.*, Vol. 26, No. 1-2, 1991, pp. 5681-5684

93. Y. Idemoto, S. Ichikawa and K. Fieki, "Oxygen nonstoichiometry of 2223 phase Bi-Pb-Sr-Ca-Cu-O system superconducting oxides", *Physica C*, Vol. 181, No. 13, 1991, pp. 171-174.

94. W. Wong-Ng, C.K. Chiang, S.W. Feriman, L.P. Cook and M.D. Hill, "Phase formation of high T_c superconducting oxides in the Bi-Pb-Sr-Ca-Cu-O glass", *Amer. Ceram. Soc. Bull.*, Vol. 71, No. 8, 1992, pp. 1261-1267.

95. W. Wong-Ng, C.K. Chiang, S.W. Freiman, L.P. Cook, N.M. Hwang and M.D. Hill, "Phase formation in the Pb-doped Bi-Sr-Pb-Ca-Cu-O Ceramics"; In: *Ceramic Transactions, Vol. 13, Superconductivity and Ceramic superconductors.* (Ed. K.M. Nair and E.A. Giess), Westerville, OH: American Ceramic Society, 1990, pp. 115-128.

96. G. Zorn, B. Seebacher, B. Jobst and H. Gobel, "Investigation of formation reactions in the system Bi-Pb-Sr-Ca-Cu-oxide starting from oxides and carbonates", *Physica C*, Vol. 177, No. 4-6, 1991, pp. 494-508.

97. W. Wong-Ng, C.K. Chiang, S.W. Freiman, L.P. Cook, N.M. Hwang and M.D. Hill, "X-ray characterization of the crystallization process of high T_c superconducting oxides in the Sr-Bi-Pb-Ca-Cu-O system", *Mater. Res. Soc. Symp. Proc.*, Vol. 169, 1990, pp. 123-28.

98. R. Cloots, A. C. Romain, A. Rulmont, P. Diko, P.H. Duvigneaud, C. Hannay, F. Gillet, P.A. Godelaine and M. Ausloos, "Study of the crystallization process in $Bi_{2-x}Pb_xSr_2Ca_2Cu_3O_{10-y}$ glass systems: optical polarized light microscopy, electrical and magnetic properties", *Supercond. Sci. Technol.*, Vol. 6, No. 12, 1993, pp. 850-857.

99. L. Pierre, J. Schneck, D. Morin, J.C. Toledano, J. Primot, C. Daguet and H. Savary, "Role of lead substitution in the production of 110 K superconducting single-phase Bi-Sr-Ca-Cu-O ceramics", *J. Appl. Phys.*, Vol. 68, No. 5, 1990, pp. 2296-2303.

100. N.P. Bansal and D.E. Farrell, "Glass derived superconducting ceramics with zero resistance at 107 K in the $Bi_{1.5}Pb_{0.5}Sr_2Ca_2Cu_3O_x$ system", *Appl. Phys. Lett.*, Vol. 55, No. 15, 1989, pp. 1572-1574.

RAPID COMMUNICATION

Indian J. Phys. **67A** (5), 421 – 424 (1993)

Metallic behaviour of the electrochemically deposited Tl–Bi–Sr–Pb–Ca–Cu–O films down to 10 K

S Chatterjee, S Banerjee, S Mollah, K K Som and B K Chaudhuri
Department of Solid State Physics, Indian Association for the Cultivation of Science, Jadavpur, Calcutta-700 032, India

Received 3 June 1993, accepted 16 July 1993

Abstract : We have deposited, for the first time, $Tl_{1.5}$–$Pb_{0.5}$–$Bi_{0.5}$–Sr_2–Ca_2–Cu_2–O_x films on metal (silver) substrate by electrochemical method. The film is found to be non-superconducting down to 10 K. Electrical resistance of the films measured by four probe method indicates metallic character of the film down to 10 K. The X-ray powder diffraction patterns could be well fitted with tetragonal structure of the unit cell (with lattice constants a = 3.3858 Å and c = 29.8392 Å). The thickness of the films could be varied by changing the time of electrodeposition.

Keywords : Superconducting film, Tl–Bi–Pb–Sr–Ca–Cu–O, electrochemical deposition,

PACS No. : 74.76.Bz.

1. Introduction

Many attempts have so far been made to prepare high T_C superconducting films by various sophisticated techniques like sputtering [1], laser ablation [2], chemical vapour deposition [3] etc. All these techniques are quite sophisticated requiring costly instrumental facilities. It is also found difficult to deposit thin films on large surfaces by using the above mentioned techniques. Superconducting thin films on metal surfaces are suitable for applications in electronic transmission and energy storage using magnetic tapes. However, deposition of thin superconducting films on metal surface is, in general, inconvenient because of thermal expansion or lattice constant mismatch. For all these reasons development of electrochemical or similar other low cost and efficient techniques for the preparation of high T_C superconducting films are important. In our previous report [4,5], we have discussed the development of superconducting Bi–Sr–Ca–Cu–O films on Ag surface by a novel electrodeposition technique. Similar attempt has also been made in the present paper to deposite Tl containing superconducting oxide films. Here, we report on the behaviour of a

typical electrochemically deposited Tl–Bi–Pb–Sr–Ca–Cu–O film (about 200 Å thick) on Ag substrate. Since we find it difficult to deposit Ba on the metal plate, our plan is to replace Ba by Bi and Sr in the Tl–Ba–Ca–Cu–O system and to investigate its superconducting behaviour (if any). The $Tl_{1.5}$ $Bi_{0.5}$ $Pb_{0.5}$ Ca_2 Sr_2 Cu_2O_x films studied are prepared by electrochemical method as discussed below.

2. Experimental

Highly pure (99.99 %) Bi_2O_3, $SrCO_3$, CuO, CaO, Tl_2O_3 and PbO oxides in appropriate proportion are dissolved in 20–25 % HNO_3 solution with pH value between 2 and 3. The solution was taken in a platinum beaker which acts as the anode and pure and highly polished silver plate or wire acts as the cathode on which thin film is deposited. A constant current source (Kiethley 220) is used to supply dc current (80–180 mA) between the electrodes. Uniform black film of Tl–Bi–Pb–Sr–Ca–Cu–O is deposited on the Ag plate which is immediately dried in vacuum and annealed at 780°C for a few minutes in flowing oxygen atmosphere.

3. Results and discussion

The X-ray diffraction patterns of the as grown unannealed and the oxygen annealed (at 780°C for 10 minutes) films are shown in Figure 1 and the scanning electron micrographs of the

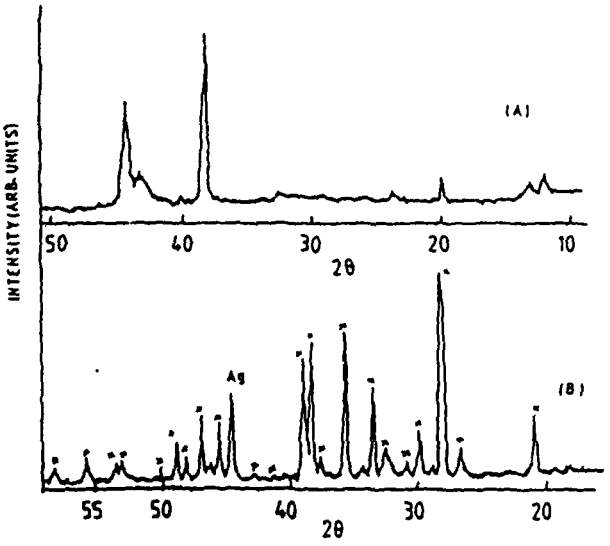

Figure 1. X-ray diffraction pattern of the as grown (unannealed) sample (A) and the final metallic sample after annealing at 780°C (B).

respective films are shown in Figure 2. The infrared spectra of the black unannealed powder collected from the films shown in Figure 3 indicates a band around 1350 cm^{-1} due to the presence of NO_x group in the film. This nitrous group is found to be not present in the final annealed sample. The X-ray patterns (star marked in Figure 1B) could be fitted with a tetragonal structure with lattice constants a = 3.3858 Å and c = 29.8392 Å.

The electrical resistance of the film is measured by four probe technique similar to our earlier works [6] using closed cycle refrigerator unit (APD Cryogenics, USA). Temperature

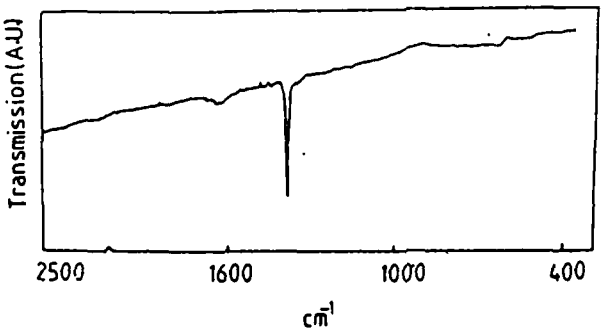

Figure 3. Infra-red spectra of the unannealed powder collected from the film.

down to 10 K was automatically controlled and measured by the unit. Thermal variation of electrical.resistance of the film is shown in Figure 4.

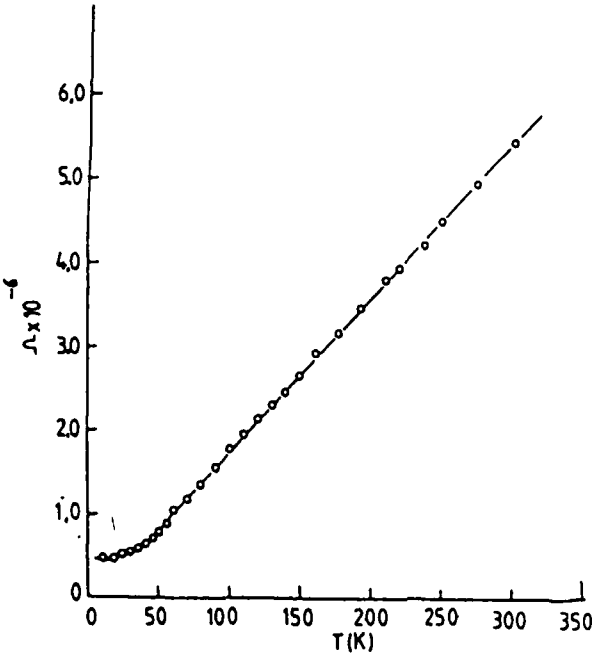

Figure 4. Electrical resistance of the final annealed film showing metallic character.

The metallic character of the film is indicated from the Figure 4. The film is not superconducting down to 10 K. However, improving the annealing technique under controlled oxygen pressure we have observed superconductivity in the Tl–Bi–Pb–Ca–Sr–Cu–O film around 50 K. This work is in progress in our laboratory and would be published elsewhere.

Plate I

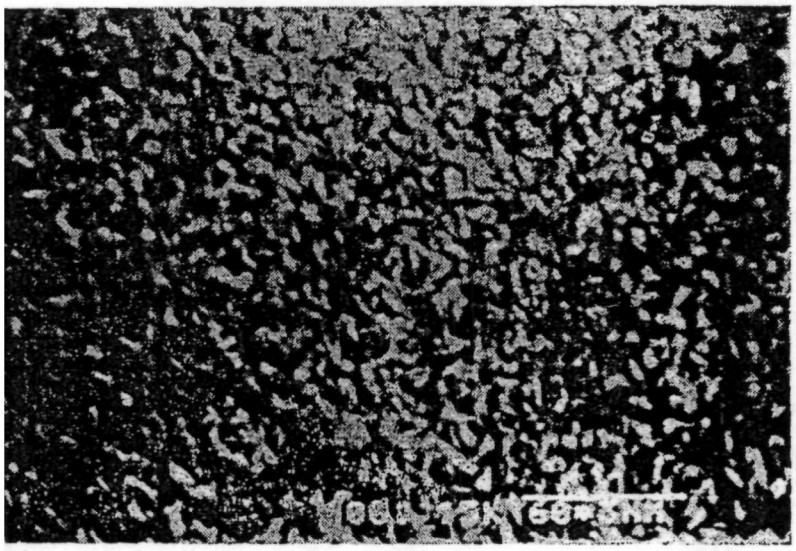

(A)

(b)

Figure 2. Scanning electron micrographs of the unannealed (A) and final annealed (B) films.

Acknowledgment

The authors are grateful to Prof. B G Ghosh (Saha Institute of Nuclear Physics) and Prof. S P Sengupta (Mater. Science, IACS) for providing XRD and EADX (SEM) facilities, respectively, for characterizing the sample.

References

[1] N Savvides and A Katsaros 1993 *Appl. Phys. Lett.* 62 528

[2] C C Chin, H Takahashi and T Morishita 1993 *J. Mater. Res.* 8 951

[3] W Tao, M P Yuan, H T Huang, X Z Liao, X M Xie, H L Zhou and Z L Wu 1993 *Appl. Phys. Lett.* 62 894

[4] S Chatterjee and S Chakravorty 1993 *Proc. Nat. Conf. in Cryogenics (March 28), Calcutta*

[5] S Chatterjee, S Banerjee, S Chakravorty, G De and B K Chaudhuri 1993 *J. Mater. Sci. Electronic Materials* (to be published)

[6] K Bose, P K Dey, P K Pal, K K Som and B K Chaudhuri 1991 *Jpn. J. Appl. Phys. Lett.* 30 L823

JOURNAL OF MATERIALS SCIENCE MATERIALS IN ELECTRONICS 3 (1992) 120–123

Preparation and characterization of superconducting ($YBa_2Cu_3O_x$–Ag) composites obtained by sol-gel method

P. K PAL
Physics Department, Naihati R.B.C. College, West Bengal, India
S. MOLLA, K. BOSE, K. K. SOM, B. K CHAUDHURI
High Temperature Superconductivity Laboratory, Solid State Physics Department, Indian Association for the Cultivation of Science, Calcutta–700032, India

For the first time a simple sol-gel method has been developed for the preparation of [$YBa_2Cu_3O_x$–Ag] composites using nitrates of Y, Ba, Cu, and Ag. For the two composites (with 10 and 20 wt% Ag), the electrical resistivities and magnetic susceptibilities (both alternating and direct current) show critical temperature T_c (zero) around 90–91 K. The X-ray diffraction studies indicate no major change of lattice parameters for the orthorhombic phase The critical current density, J_c, is found to be around 200 A cm^{-2} at zero field and 80 K. The degradation of T_c of the composites in presence of water is also very low, similar to the previous observations. This sol-gel method could be used for the large-scale production of superconducting composite powders necessary for drawing wires/tapes or targets for sputtering.

1. Introduction

The study of high temperature superconducting oxide (HITSO)–Ag composites is of special importance for their technological applications (fabrications of HITSO wires/tapes, etc. [1]) having higher critical current density, J_c, [2] than the corresponding pure $YBa_2Cu_3O_x$ (1 2 3) superconductor. These composites also have very interesting physical properties showing percolative behaviour [3], creep, and pinning effects [4], etc. They are also very stable in moist and other environmental conditions.

The (1 2 3–Ag) composites have mostly been prepared from the mixtures of (1 2 3) superconductor with AgO [5], Ag [6, 7] or Ag_2O [8] powders. In all such cases the problems related to the homogeneity of the material and uniformity of the grain sizes in the final composites might always exist. Therefore, the physical properties of the same composites prepared by different research groups might also vary The sol-gel method of preparation of HITSO materials has the *extra advantage that it gives high yield of HITSO* powders having uniform grain sizes.

Hikichi *et al* [9] developed an interesting nitrate solution method for the preparation of HITSO–Ag composite Using nitrate solutions we also developed [10] a simple sol-gel (SSG) technique for the preparation of $YBa_2Cu_3O_x$ superconductor This (SSG) method has been applied for the preparation of 1 2 3–Ag composites with different wt % of Ag The electrical resistances, magnetic susceptibilities, both a c and d c., and structural properties of two such composites prepared with 10 and 20 wt % of Ag are reported

The method of preparation of 1 2 3–Ag superconducting composites by the SSG method is almost similar to that used for the preparation of (1 2 3) superconductor [10]. Stoichiometric amount of the mixtures of the nitrates of Y, Ba, Cu and Ag (all of 99 99% purity or better purchased from E. Merck, Alfa, and Sigma Chemicals), were separately dissolved in triple distilled water in teflon containers. The metal ionic ratio Y:Ba:Cu = 1:2:3 was maintained for the preparation of the nominal composition of $YBa_2Cu_3O_x$ (1 2 3). The amount of silver nitrate solution was taken in such a way that 10 and 20 wt % of Ag were, introduced in the two composites with (1 2 3) superconductor. The three nitrates of Y, Ba, and Cu were first mixed, stirred, and ice cooled. The calculated amount of silver nitrate was then slowly added to the ice-cooled solution with stirring. For every composite calculated amount [10] of citric acid monohydrate and then ethylene glycol were added to the above nitrate solutions and mixed with constant stirring The *pH value of the mixture was kept between 5 5 and 6* for both the composites by carefully adding ice-cooled ammonia solution diluted with distilled water

The total mixture was then refluxed at about 80 °C for 1 h Any change of pH value was adjusted by adding ammonia, if required The entire solution was then kept below 10 °C overnight The pH value was again adjusted and the solution was heated in an water bath (for gelation) for several hours until blue coloured jelly was obtained. This jelly could be drawn into the form of fibres by pulling the jelly with a glass rod The jelly thus obtained was dried under vacuum and the product was then slowly heated to 300 °C for

0957–4522

TABLE I Sol-gel method for the preparation of (1 2 3)–Ag composites

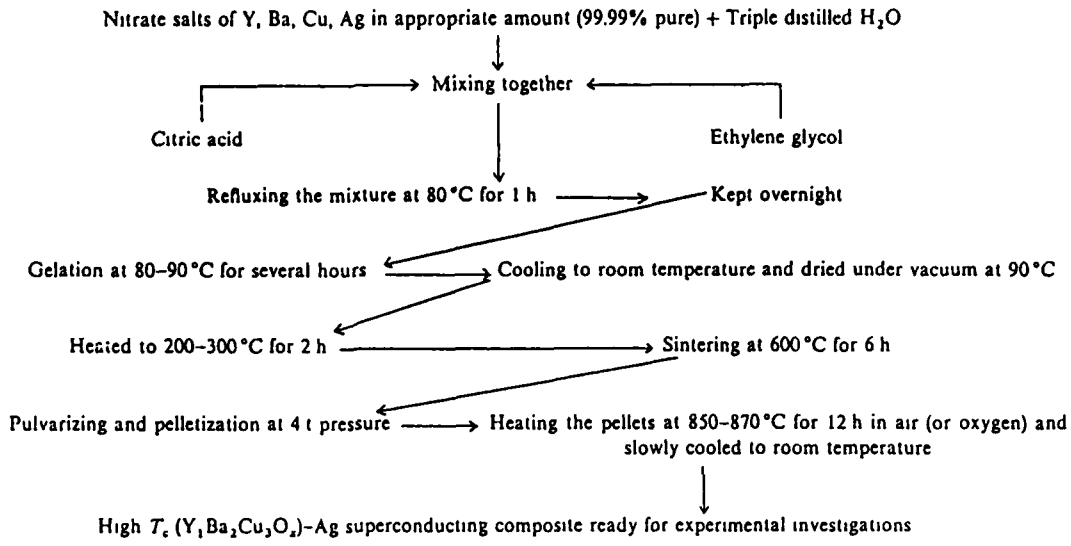

2 h. The loss of water and decomposition of free citric acid, if any, took place around 150 °C.

The black material thus produced was collected, powdered, and sintered at 850 °C (in oxygen) for another 12 h and slowly (~ 5 °C h^{-1}) cooled to 400 °C inside the furnace at which temperature the powdered mass was kept for another 3 h and slowly cooled to 200 °C and quenched to room temperature. The final black powder was the superconducting (1 2 3–Ag) composite powder. The complete SSG process used for the preparation of the composites is shown in Table I. The dried black powder was pressed into pellets or rods which were again sintered at 850 °C for 12 h in air (or in oxygen atmosphere) and slowly cooled to room temperature as before. The room temperature X-ray diffraction patterns (Philips, model 1050/51) are shown in Fig. 1. Comparing the XRD patterns with literature data the materials showed the expected peaks from 1 2 3 superconductor and Ag metal together with a small quantity of $BaCuO_2$. Further improvements of the SSG method of preparation would be necessary for making better superconducting composites. The lattice parameters calculated are $a = 0.3813$ (0.3814) nm, $b = 0.3883$ (0.3873) nm, and $c = 1.1633$ (1.1643) nm for the 10 wt % (20 wt %) Ag–1 2 3 composites. Therefore, no major change in the lattice parameters from those of pure (1 2 3) superconductor was observed in the Ag–(1 2 3) composites which indicates that the silver precipitates in the intergranular spaces as shown in Fig. 2 and it helps retaining the oxygen content fixed in the superconducting lattice as well as increase the electrical connectivity between the grains (Fig. 2). All these might be responsible for the increase of critical current density, J_c, for a low concentration of Ag [2]. For very large concentration of Ag (more than 20 wt %) the silver layers between the grains became thick and the current density reduced. For further increase of Ag (more than 60 wt % of Ag), the resistance did not become zero down to 60 K (in the range of our measurement), but the presence of superconducting grains was observed from the Meissner signal in the oscilloscope. The scanning electron micrographs of the two (1 2 3–Ag) composites (with Hitachi, model S-415A) are shown in Fig. 3, which indicate good connectivity and homogeneity of the materials.

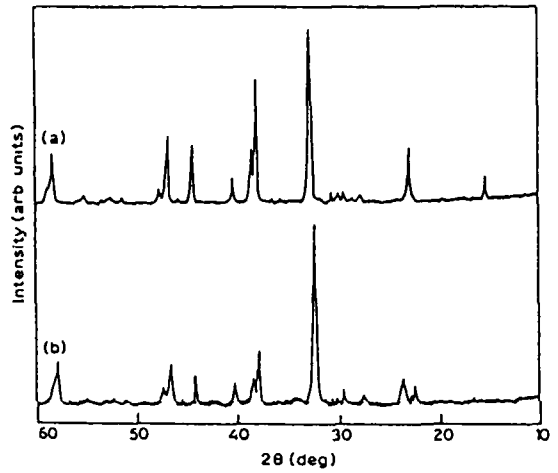

Figure 1 X-ray diffraction patterns of (1 2 3–Ag) composites (a) (1 2 3) 20 wt % Ag, (b) (1 2 3) 10 wt % Ag

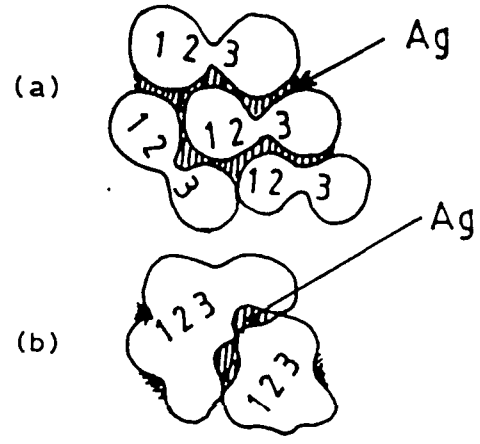

Figure 2 Nature of superconducting and silver grain boundaries (a) Ag trapped in pores between small HITSO grains, (b) Ag precipitation and agglomeration in HITSO grains.

As usual four-probe d.c. resistance measurements were made on a bar-shaped composite sample similar to our earlier work [12–13]. D.c. and a.c magnetic susceptibilities of the composites have also been measured with a Curie type balance and by the mutual inductance method, respectively, similar to our earlier work [12–14]. The thermal variations of d.c. resistance (Fig. 4) and magnetic susceptibilities (Figs 5 and 6) indicate the superconducting behaviour of the composites. The sharp fall of the resistances around T_c (zero) $\approx$ 90–91 K definitely indicates the good quality of the samples. The little kink in the a.c. susceptibility curves might be associated with the percolative behaviour or impure phases of the samples. For detailed information about this behaviour one needs measurements with composites of different Ag concentrations which are in progress.

It appears that the (HITSO–Ag) composite's physical properties (water resistance, J_c, T_c, etc.) are in line with previous results [5–9]. The d.c. magnetic suscep-

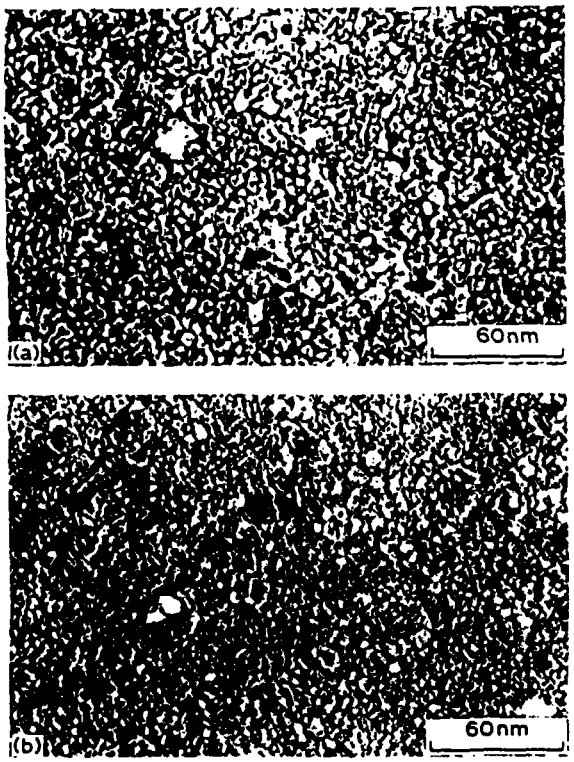

Figure 3 Scanning electron micrographs of (1 2 3–Ag) composites (a) 10 wt % Ag, and (b) 20 wt % Ag.

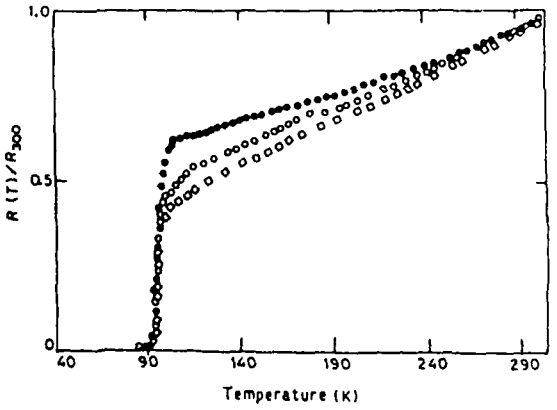

Figure 4 Thermal variation of normalized electrical resistances of the (1 2 3–Ag) composites (R_{300} is the room temperature resistance). (●) $YBa_2Cu_3O_x$, (○) 10 wt % Ag, (□) 20 wt % Ag.

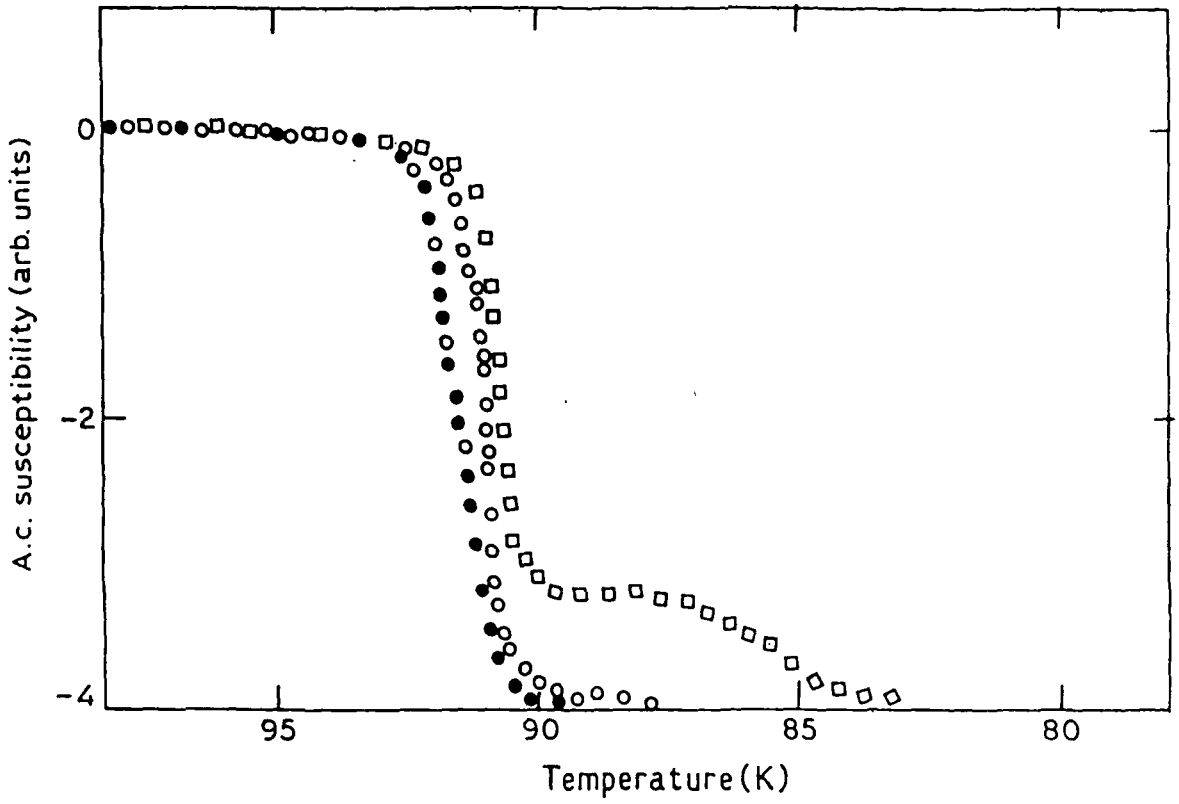

Figure 5 A.c. magnetic susceptibilities of (1 2 3–Ag) composites as a function of temperature. (●) 0 wt % Ag, (○) 10 wt % Ag, (□) 20 wt % Ag

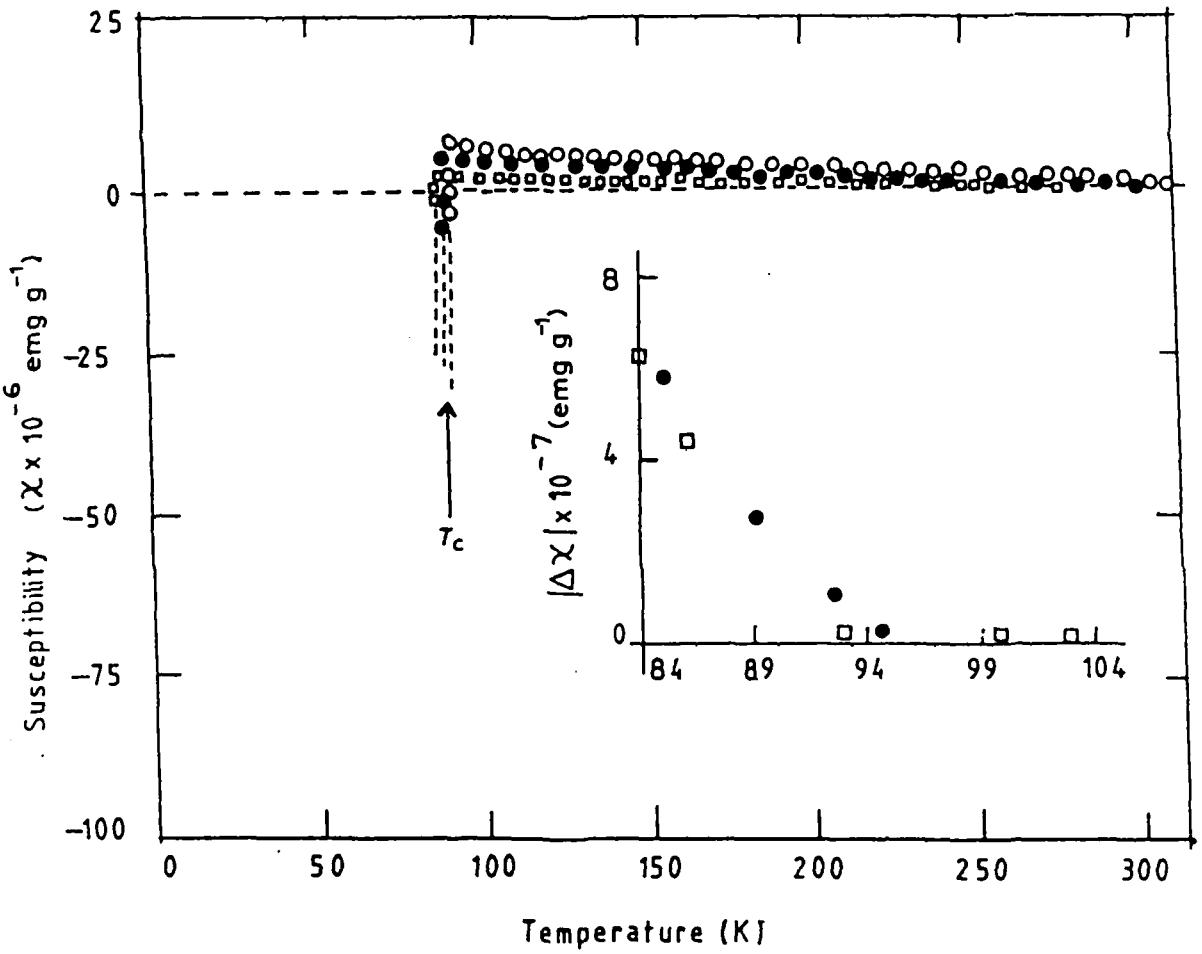

Figure 6 D.c. magnetic susceptibilities of (123–Ag) composites as a function of temperature. (○) (123), (●) (123)–10 wt % Ag, (□) (123)–20 wt % Ag.

tibility, χ, obeys the following Curie–Weiss behaviour:

$$\Delta\chi = (\chi_{300} - \chi_T) + C/(T - \theta)$$

where χ_{300} is the value of d.c. magnetic susceptibility at $T = 300$ K with θ varying from -10 to -15 K for the two composites, respectively. The values of θ and C are found to depend on the samples prepared under different conditions and also on the grain sizes of the samples [11]. This behaviour of χ might be due to the variations of oxygen content in the samples as well as on the incipient AFM character as mentioned above. The process by which antiferromagnetism is suppressed by the appearance of the HITSO phase is yet unexplored.

Finally, we conclude that the simple sol-gel method discussed could be used for the large-scale production of very good quality superconducting composite powders necessary for the fabrications of wires/tapes, films, and targets for sputtering. The SSG method developed might also be extended for the preparation of (Bi–Sr–Ca–Cu–O)–Ag composites and further attempts might also be made to fabricate superconducting thin or thick films or wires directly from this SSG method.

Acknowledgement

The authors thank Professors S. P. Sengupta, R. N. Bhattacharya, B. Bhattacharya, and Mr G. C. Basak for their help in completing the work.

References

1. B. K. CHAUDHURI, in Proceedings 4th Asia Pacific Physics Conference, Seoul, 1990, edited by S. H. Ahy, S. H. Choh, I. C. T. Cheon and C. Lee (World Scientific, Singapore) Vol. I, p. 551.
2. D. LEE and K. SALAMA, *Jpn. J. Appl. Phys.* 29 (1990) L2017.
3. J. J. LIN and T. M. CHEN, *Z. Phys.* 81 (1991) 13.
4. J. JUNG, M. A. K. MOHAMED and J. P. FRANCK, *Physica B* 165, 166 (1990) 1135.
5. H. P. N. PETERS, R. C. SISK, E. W. VRBAN, C. YHVANG and M. K. WU, *Appl. Phys. Lett.* 52 (1988) 2066.
6. N. IMANAKA, F. SAITO, H. IMAI and G. ADACHI, *Jpn. J. Appl. Phys.* 28 (1989) L580.
7. R. PRASAD, N. C. SONI, A. MOHAN, S. K. KHERA, K. U. NAIR, C. K. GUPTA, C. V. TOMY and S. K. MALIK, *Mater. Lett.* 7 (1989) 9.
8. D. PAVUNA, H. BERGER, M. A. AFFRONTE, J. VAN DER MASS, J. J. CAPPONI, M. GUILLOT, P. LEJAY and J. L. THOLENCE, *Solid St. Commun.* 68 (1988) 535.
9. Y. HIKICHI, M. KATO, S. SUZUKI, T. NOMURA and M. MIYAMOTO, *Jpn. J. Appl. Phys. Lett.* 29 (1990) L1615.
10. P. K. PAL, K. BOSE, S. MOLLA and B. K. CHAUDHURI, *Ind. J. Phys.* A65 (1991) 269.
11. B. K. CHAUDHURI and K. BOSE, unpublished.
12. K. BOSE, P. K. DEY, K. K. SOM and B. K. CHAUDHURI, *Jpn. J. Appl. Phys.* 30 (1991) L823.
13. K. K. SOM, A. K. GHOSHAL and B. K. CHAUDHURI, *J. Mater. Sci. Lett.* 8 (1989) 749.
14. B. K. CHAUDHURI, A. K. GHOSHAL and K. K. SOM, *ibid.* 9 (1990) 225.

Received 10 July
and accepted 28 September 1991

Indian J. Phys. 65A (4), 269-275 (1991)

Preparation and characterization of $YBa_2Cu_3O_x$ high temperature superconductor obtained by sol-gel method

P K Pal+, K Bose, S Mollah and B K Chaudhuri

High Temperature Superconductivity Laboratory,
Solid State Physics Department, Indian Association for the
Cultivation of Science, Calcutta-700 032, India

Received 5 April 1991, accepted 18 April 1991

Abstract: Electrical resistivity and magnetic susceptibilities of high temperature superconducting oxide (HITSO) $YBa_2Cu_3O_x$ (123) prepared by a simple sol-gel (SSG) method have been measured down to 80K and results reported in this paper. The (SSG) method developed would be very useful for a large scale production of (HITSO) powders (with T_c=93K and T_{c0}=91K) required for many technological applications (HITSO wires/tapes, thick films etc.).

Keywords: Sol-gel, high T_c superconductor, AC/DC susceptibility.

PACS Nos: 74.70 Mq, 82.70. Gg

1. Introduction

For any R & D programme the development of good quality (large volume fraction of superconductivity, homogeneity, sharp fall of resistance, good connectivity etc.) high temperature superconducting oxide (HITSO) materials is essential. we have developed in our laboratory, like many other researchers in this field, the solid state reaction technique (Som *et al* 1988, 1989, Chaudhuri 1987) and the glass to ceramic technique (Chaudhuri *et al* 1989, 1990 and Som *et al* 1989) for the preparation of (HITSO) materials like $YBa_2Cu_3O_x$, $Bi_4Sr_3Ca_3Cu_4O_x$, $Tl_2Ba_2Ca_2Cu_3O_x$ etc. All these methods have their own advantages and disadvantages as discussed in the above mentioned articles.

However, for the preparation of a large amount of homogeneous (HITSO) powders having uniform grain sizes, the chemical and the sol-gel methods have some special advantages (see for example Brinker *et al* 1984). The sol-gel method for the preparation of (HITSO) materials is, therefore, becoming very popular (Koki 1990, Murakami *et al* 1990). Recently, for the preparation of (HITSO)-Ag and HITSO-polymer precursors for making (HITSO) wires/tapes (Chaudhuri 1990,

+Physics Department, R B C College, Naihati 743 165, West Bengal, India.

Bose *et al* 1991) we have developed a relatively simple sol-gel (SSG) method for the preparation of fine (123) superconducting powders. Since the development of the sol-gel method for the preparation of (HITSO) materials is a bit tricky and the method is also technologically important for the high yield of (HITSO) materials, we described below the detailed method of preparation of (HITSO) with this technique.

Electrical and magnetic properties of the prepared (HITSO) materials have also been studied and compared with those of the (HITSO) prepared earlier by solid state reaction method.

2. Experimental

2.1. *Preparation of materials :*

The method of preparation of (123) superconducting oxide by sol-gel method is almost similar to that discussed in our earlier chemical method (Pal and Chaudhuri 1991). Stoichiometric amount of the nitrates of Y, Ba, and Cu, all of purity 99.99% (Alfa, Germany), were dissolved in triple distilled water. The ratio Y : Ba : Cu = 1 : 2 : 3 was maintained for the preparation of the nominal composition of $YBa_2Cu_3O_x$ (123). Appropriate amount of citric acid monohydrate and ethylene glycol was then mixed with the nitrate solution with stirring. The pH value was maintained between (4.5—5.5) by carefully adding ammonia, if required. We prepared (HITSO) with different pH values of the solution. In this paper, however, we report the properties of only one sample prepared with a fixed pH value ($\sim$5).

The mixture was then refluxed at 80°C for one hour and was then kept overnight. Finally, the solution was heated in an water bath (for gelation) for several hours until bluish coloured jelly like product was obtained. This jelly which could be drawn into the form of fibers was dried under vacuum and then the product was slowly heated to 300°C for two hours. The dry mass is then collected in an alumina crucible and again fired at 600°C for 6 hours and slowly cooled to room temperature. The loss of water and the decomposition of free citric acid occurs around 150°C.

The black material was then powdered, and sintered at 890°C (in oxygen) for another 12 hours and slowly (5°/h) cooled to 400°C inside the furnace and the powder was kept at this temperature for three hours and then slowly cooled to 300°C and quenched to room temperature. The fine black powder thus obtained is superconducting. The complete process for the sol-gel preparation method of (HITSO) is shown in Table 1.

2.2. *Study of physical properties :*

The dried powder thus obtained is pressed into pellets or rods under 4 ton pressure. The pellets are again sintered at 900°C for 12 hours and slowly cooled to room

temperature. No oxygen treatment was made for the pellets but slow cooling rate was always maintained.

Table I. Flow chart of the sol-gel method.

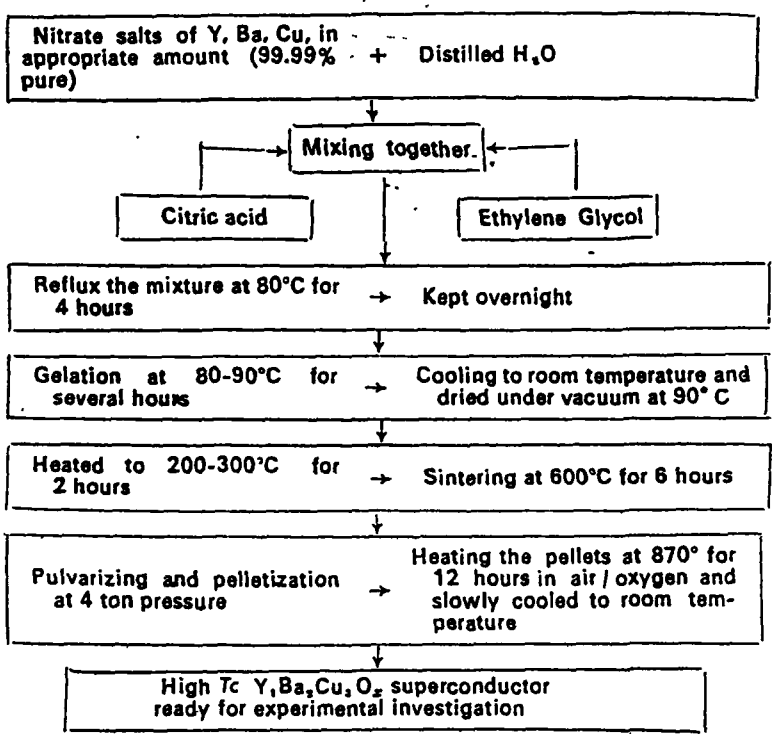

Room temperature X-ray diffraction pattern (Figure 1) shows the superconducting peaks of the (123) sample. The lattice parameters calculated are $a = 3.820$ Å,

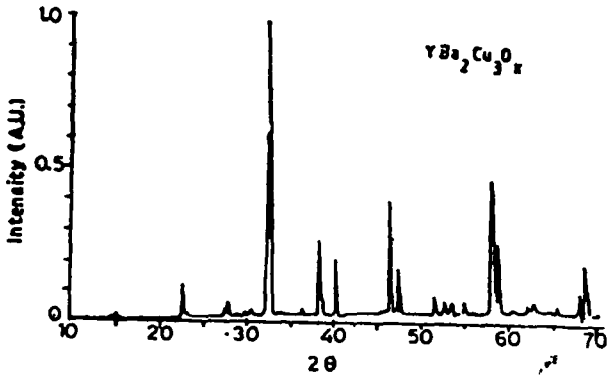

Figure 1. X-ray diffraction pattern of the superconducting (sol-gel) sample.

$b = 3.884$ Å, and $c = 11.682$ Å which agree fairly well with the corresponding values of a, b and c of a typical (123) sample prepared by ceramic route (Som *et al* 1A

1988). The SEM (Hitachi, Japan) picture of the (HITSO) sample is shown in Figure 2 indicating good connectivity between the grains and crystalline nature.

Figure 2. SEM picture of the superconducting (sol-gel) sample.

As usual, four probe dc resistance measurement was made on a bar shaped (123) sample. DC and ac magnetic susceptibilities of the samples were shown in Figures 3 and 4, respectively. The dc and ac magnetic susceptibilities were

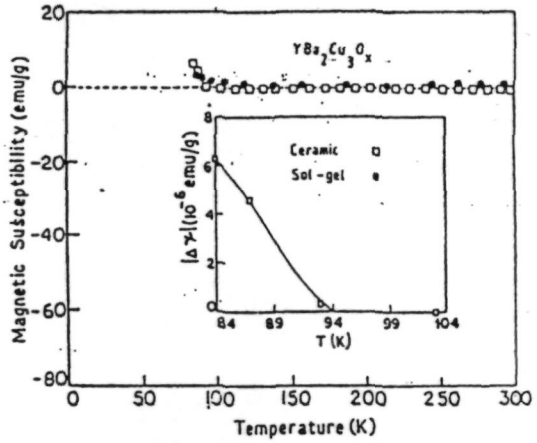

Figure 3. DC magnetic susceptibilities of the superconducting samples prepared by sol-gel and ceramic methods shown as a function of temperature.

measured with similar apparatus used in our earlier work (Chaudhuri *et al* 1989, Bose *et al* 1991).

3. Results and discussion

The thermal variations of dc resistivity (Figure 5) and magnetic susceptibilities as shown in Figures (3-4) indicate the superconducting behaviour of the sample. The

sharp fall of resistance at $T = T_c = 93K$ definitely indicates the good quality of the superconducting sample prepared by sol-gel method. For comparison, the

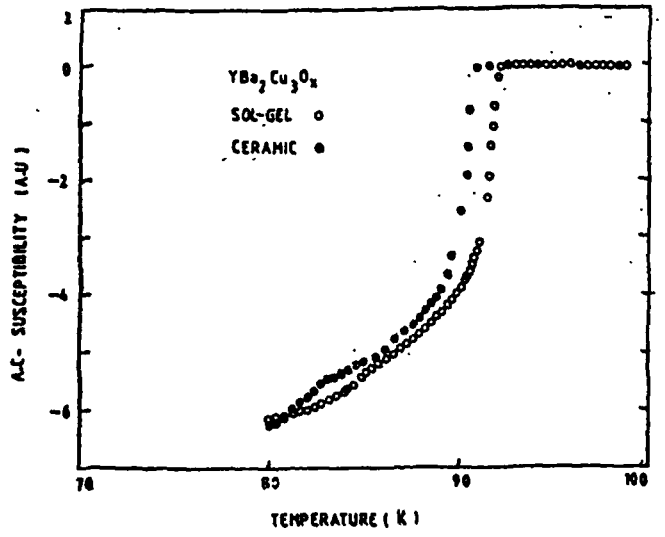

Figure 4. AC magnetic susceptibilities of the superconducting samples prepared by sol-gel and ceramic methods shown as a function of temperature.

resistivity and susceptibility curves for the ceramic sintered samples are also shown in the Figures (3-5). It is interesting to mention that the high field ($\sim$0.3T) dc

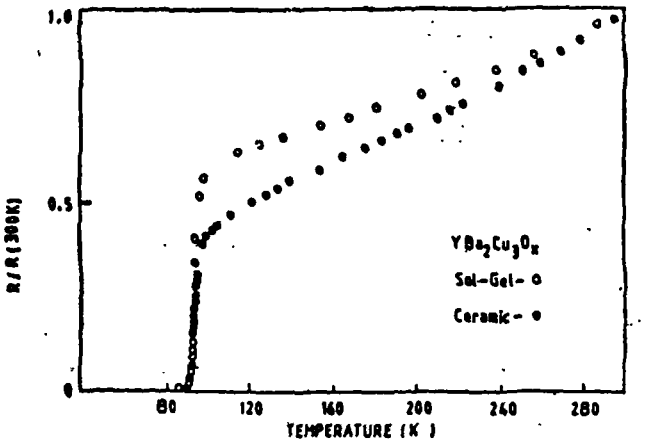

Figure 5. Electrical resistances of the superconducting samples prepared by sol-gel and ceramic methods shown as a function of temperature.

magnetic susceptibility data shows a small rise around the superconducting transition temperature (Figure 3). This type of behaviour has also been observed

by us in our earlier measurements (Chaudhuri *et al* 1989, 1990). It is also observed that $\Delta\chi=(\chi_{300}-\chi_T)$ obey Curie Weirs behaviour of the form,

$$\Delta\chi=(\chi_{300}-\chi_T+C/(T-\theta)$$

χ_{300} is the value of susceptibility χ at $T=300$K with $\theta=\sim(-15\text{K})$. The values of χ and C are found to depend on the samples prepared under different conditions and also on the grain sizes of the samples (Chaudhuri *et al* 1990). This behaviour of magnetic susceptibility might be due to the variation of the oxygen content in the sample as well as on the incipient antiferromagnetic character of the sample. Smaller the values of x (oxygen content in $Y_1Ba_2Cu_3O_x$), larger is the antiferromagnetic character of the sample (showing more prominent rise of χ around T_0 in the $(\chi-T)$ curve as in Figure 3) and lower is the volume fraction of the superconducting grains in the sample. Though it is not yet clear whether antiferromagnetism (AFM) is the origin of pairing mechanism in (HITSO) materials, our present magnetic susceptibility data, however, support the antiferromagnetic origin of superconductivity as was also suggested earlier (Chaudhuri *et al* 1990). The process by which antiferromagnetism is suppressed by superconductivity is yet unexplored (Schriffer 1988). Since we cannot accurately ascertain the oxygen stoichiometry as well as its distribution in the lattice, it is rather difficult to conclude whether the temperature dependent behaviour of χ around T_0 is due solely to oxygen deficiency and/or partly related to antiferromagnetic type ordering.

The problem is actually related to the oxygen ordering in the lattice and hence to the change of ionic state of copper (or other ions). A certain amount of oxygen deficiency causes some kind of disordering in the lattice destroying superconductivity and at the some time stimulating the appearance of antiferromagnetic character and semiconductivity. It appears, as if, there is same competition between superconductivity and antiferromagnetism in such (HITSO) materials. Elaborate investigation in this direction is in progress.

4. Conclusion

We believe that the simple sol-gel method discussed in this paper could be used for the large scale production of very good quality superconducting powders necessary for drawing wires/tapes or films and targets for sputtering. It has also been observed that certain amount of silver could also be added in the superconducting sample while preparing the gel which is of another importance for making (HITSO)-Ag composites suitable for making wires and tapes (Bose *et al* 1991).

If proper care is taken, sol-gel process could provide a sufficient control over the particle sizes of the (HITSO) materials prepared.

We also find that it is better to keep the sintering temperature as low as possible to maintain uniform grain sizes, since the particles are very reactive. Uniform and single sintering cycle would be preferred for the sol-gel (HITSO)

powders. Proper control of pH value is also important. Further attempt are being made to improve the sintering technique at lower temperature.

Acknowledgments

The authors are grateful to K K Som for his various help. The authors are also grateful to Professor S P Sengupta for allowing them to do the X-ray diffraction and SEM studies of the samples in his Department.

References

Bose K, Dey P K, Som K K and Chaudhuri B K 1991 *Jpn. J. Appl. Phys.* **30** No. 3 (In press)

Brinker C J, Clark D E and Ulrich D R 1984 *Better Ceramic through Chemistry* (New York: Elsevier)

Chaudhuri B K 1990 *Proc. 4th Asia Pacific Physics conference, Seoul August 1990* Vol 1 (Singapore: World Scientific) p 551

Chaudhuri B K 1987 *Indian J. Cryogenics* **12** 103

Chaudhuri B K, Ghoshal A K and Som K K 1990 *J. Mater. Sci. Lett.* **9** 225

Chaudhuri B K, Som K K and Sengupta S P 1989 *Mater. Sci. Lett.* **8** 520

Koki A 1990 *Jpn J. Appl. Phys.* **29** L270

Nishino, Shiohara Y and Tanaka S 1990 *Jpn J. Appl. Phys.* **29** 1445

Murakami H, Yabgashi S, Nishino J, Shiohara Y and Taneka S 1990 *Jpn. J. Appl. Phys. Lett.* **29** L445

Pal P K and Chaudhuri B K 1991 *J. Mater. Sc.* (communicated)

Som K K, Sengupta S P and Chaudhuri B K 1988 *Indian J. Phys.* **62A** 106

Som K K, Ghoshal A K and Chaudhuri B K 1989 *J. Mater. Sci. Lett.* **8** 749

Schrieffer J R, Wen X G and Zhang S C 1988 *Phys. Rev. Lett.* **60** 944

——1989 *Advances in Superconductivity* ed Kitazawa K and Ishiguro T (Berlin: Springer-Verlag) p 123

Chapter-III

Chapter-III

The published work on CMR materials is comprised in this chapter. Specific heat (C) of polycrystalline manganites $Pr_{1-x}Ca_xMnO_3$ (113-PCMO) with x = 0.3-0.4, $La_{1-y}Ca_yMnO_3$ (113-LCMO) with y = 0.3 and 0.5, and $La_{2-2z}Sr_{1+2z}Mn_2O_7$ (327-LSMO) are given here. The detailed study of resistivity (ρ), magnetization (M) and specific heat (C) on polycrystalline $Pr_{0.65}Ca_{0.35-x}Sr_xMnO_3$ (x = 0-0.35) perovskite manganites has been included here. This chapter also contains the transport properties of oxygen isotope diffused epitaxial thin films of $La_{0.75}Ca_{0.25}MnO_3$ (LCMO) and $Nd_{0.75}Sr_{0.25}MnO_3$ (NSMO). Temperature dependent magnetization, magnetoresistance and magneto-thermoelectric power of the K doped $La_{1-x}Ca_{x-y}K_yMnO_3$ (x = 0.3 and $0 \leq y \leq 0.15$) has been included in this chapter.

Proc. 49th DAE-Solid State Phys. Symp. 313
(Invited article), 2005

Properties of $Pr_{0.65}Ca_{0.35-x}Sr_xMnO_3$ manganites (x = 0-0.35)

S. Mollah*
Department of Physics, Aligarh Muslim University, Aligarh-202002, India.

We have elaborately investigated the electronic, magnetic and thermal properties of polycrystalline $Pr_{0.65}Ca_{0.35-x}Sr_xMnO_3$ (x = 0-0.35) perovskites. A huge enhancement of magnetoresistance ratio (MRR) [10% at H = 100 Oe and 99% at H = 0.5 T] around metal-insulator (MI) transition temperature (T_{MI}~ 80 K) has been observed in x = 0.1 sample which is induced by the phase separation (PS). Non-adiabatic small polaron hopping conduction mechanism is followed by all the manganites above the respective MI transition temperatures (T_{MI}). The metallic conduction below T_{MI} shows the electron-magnon scattering behaviour similar to other manganites.

I. INTRODUCTION

The complicated phase diagram in colossal magnetoresistive (CMR) materials, $RE_{1-x}A_xMnO_3$ (RE = trivalent rare earths, A = divalent alkaline earth metals), arises due to the interplay between double exchange (DE) interaction and charge/orbital ordering (CO OO). It is well established that the DE interaction prefers the ferromagnetic (FM) metallic state and CO OO results in antiferromagnetic (AFM) insulating state via the super-exchange (SE) interaction. The interplay between DE interaction and CO OO can be tuned by changing the value of x, which in turn alters the ratio of Mn^{3+} and Mn^{4+}, by varying the radius of rare/alkaline earth metals, by applying electric/magnetic fields, by irradiating by x-ray/infrared radiation and by applying external pressure.

However; the DE, CO OO and SE interactions are not sufficient to explain the complicated transport properties of manganites. Recently, it has been suggested that the ground states of manganites tend to be intrinsically inhomogeneous due to the presence of strong tendencies toward phase separation (PS), typically involving FM metallic and AFM/ CO OO insulating domains which can be of several shapes like spherical droplets, curved or stripes.[1-3] Systematic investigations of resistivity, magnetization and specific heat of polycrystalline $Pr_{0.65}Ca_{0.35-x}Sr_xMnO_3$ (x = 0-0.35) manganites are reported here.

II. EXPERIMENTAL TECHNIQUES

Polycrystalline $Pr_{0.65}Ca_{0.35-x}Sr_xMnO_3$ (x = 0-0.35) perovskite manganites are prepared by the standard solid-state-reaction method.[4-6] Electrical resistivity (ρ) is measured by the standard four-probe method. Superconducting quantum interference (SQUID) magnetometer is used to measure the magnetization (M). A high-resolution ac calorimeter is employed to determine the high temperature (80-300 K) relative specific heat (C) using the chopped light as the heat source.[7]

III. RESULTS AND DISCUSSION

Figure 1(a) shows that the $Pr_{0.65}Ca_{0.35-x}Sr_xMnO_3$ manganites respectively

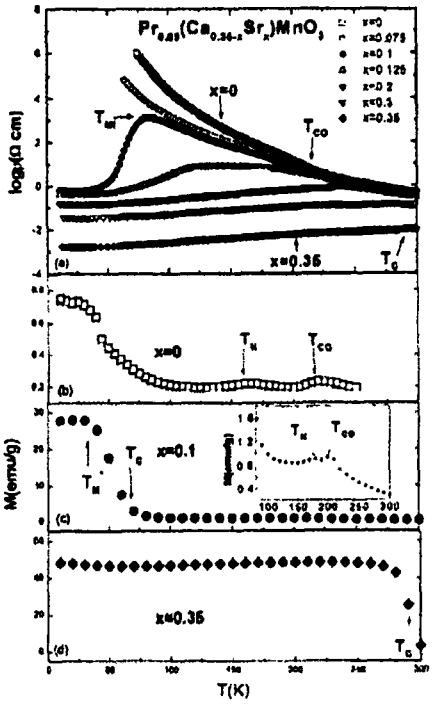

Fig. 1: Temperature variation of (a) logρ of $Pr_{0.65}Ca_{0.35-x}Sr_xMnO_3$ (x = 0-0.35) and M at 1000 Oe of x = 0 (b), 0.1 (c) and 0.35 (d) samples. Inset of c shows the enlarged view.[5]

with x = 0-0.075, 0.1, 0.125-0.3 and 0.35 demonstrate a semiconducting performance, a sharp MI transition at T_{MI} ~ 80 K, a semiconducting followed by a metallic and a metallic behaviour. This also reveals that the charge ordered (CO) transition temperature (T_{CO})

decreases and the T_{MI} increases with the increase of x. The increase of M at 1000 Oe at low temperatures for x = 0 sample with AFM transition temperature, T_N ~ 160 K and T_{CO} ~ 215 K (Fig 1b) may be associated with a small amount of nanosize FM component since the changes of M are insignificant. However, the changes of M for x = 0.1 sample with an unusual magnetic ordering at T_M^* ~ 45 K and FM ordering at T_C ~ 70 K as well as that for x = 0.35 sample with T_C ~ 290 K (Figs. 1c and d) are considerably large presumably due to the occurrence of FM transitions.

Figure 2 shows the temperature (80-300 K) variation of C in absence of magnetic field for

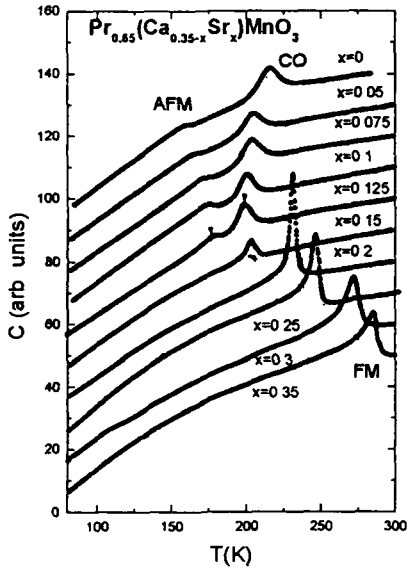

Fig. 2: Temperature dependence of specific heat (C) of $Pr_{0.65}Ca_{0.35-x}Sr_xMnO_3$ (x = 0-0.35).[5]

$Pr_{0.65}Ca_{0.35-x}Sr_xMnO_3$ (x = 0-0.35) perovskites. These specific heat curves can clearly be distinguished into two groups, one for x = 0-0.125 and the other for x = 0.15-0.35. Though the sample with x = 0.1 shows a sharp MI transition at T_{MI} ~ 80 K from temperature dependence of resistivity (Fig. 1), no pronounced anomaly in C around T_{MI} is detected which is because of the unusual magnetic ordering state below T_{MI}.[4-5] On the basis of the temperature variation of ρ, M and C (Figs 1-2), the obtained (T-x) phase diagram for $Pr_{0.65}Ca_{0.35-x}Sr_xMnO_3$ samples is shown in Fig. 3, where paramagnetic insulating (PM-I), charge-ordered insulating (CO-I), antiferromagnetic insulating (AFM-I), ferromagnetic metallic (FM-M) and unusual magnetic metallic (AFM+FM)M regions are clearly indicated. It is evident from

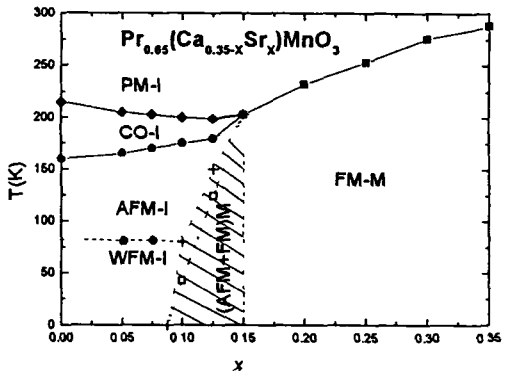

Fig. 3: T-x phase diagram of $Pr_{0.65}Ca_{0.35-x}Sr_xMnO_3$ (x = 0-0.35) samples.[5]

Fig. 3 that the different insulating (PM-I, CO-I and AFM-I) states at various temperatures are observed in samples with x < 0.1 where the nanosize FM phases are embedded in insulating matrix and no percolation is achieved. The

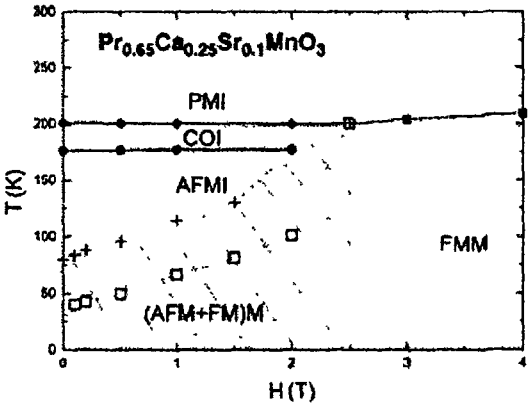

Fig. 4: T-H phase diagram of $Pr_{0.65}Ca_{0.2}Sr_{0.1}MnO_3$.

x = 0.1-0.15 accounts for the (AFM+FM)M region where disorder induced phase separation leads to the unusual magnetic metallic behavior. With x > 0.15, the FM phases start to dominate and finally cover almost the whole matrix leaving nanosize AFM phases for x = 0.35. The T - H phase diagram of x = 0.1 sample is shown in Fig. 4, where PMI, COI, AFMI, FMM and (AFM+FM)M regions are clearly specified. The unusual mixed (AFM+FM)M state may be due to electronic and magnetic instability or the PS of AFM and FM domains in the sample below T_{MI} at low magnetic fields.

To understand the mechanism behind the *maximum MRR* [= $-[\rho(H)-\rho(0)]/\rho(0)$ with $\rho(0)$ and ρ(H) being the resistivities without and with

a magnetic filed H respectively] of each sample, we plot MRR_{max} vs. x in Fig. 5 for $Pr_{0.65}Ca_{0.35-x}Sr_xMnO_3$ series at low magnetic fields of 0.1, 0.2 and 0.5 T. It is fascinating that the MRR_{max} for x = 0.1 sample is as high as 50, 80 and 99% respectively at low magnetic fields of 0.1, 0.2 and 0.5 T. Such a huge MRR at low magnetic fields in polycrystalline samples is rather unusual. Inset of Fig. 5 shows the resistivity ratio vs. low H for the mixed phase (x = 0.1) and FM-M phase (x = 0.35) samples. The resistivity ratio decreases sharply with the increase of magnetic field for x = 0.1 sample whereas that is *almost constant for x = 0.35 sample. Thus, it is*

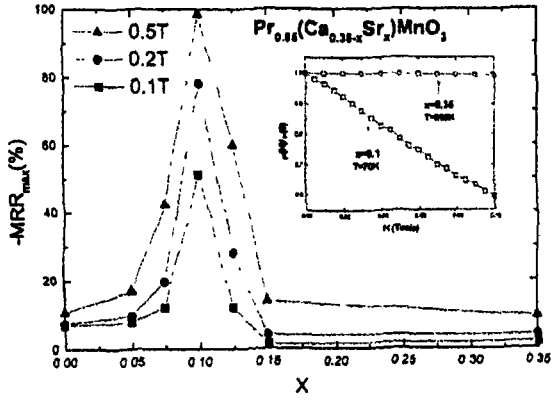

Fig. 5: x vs. MRR_{max} at low magnetic fields. Inset shows the variation of $\rho(H)/\rho(0)$ with H (0-1000 Oe) for x = 0.1 and 0.35 samples near their respective T_{MI}.[5]

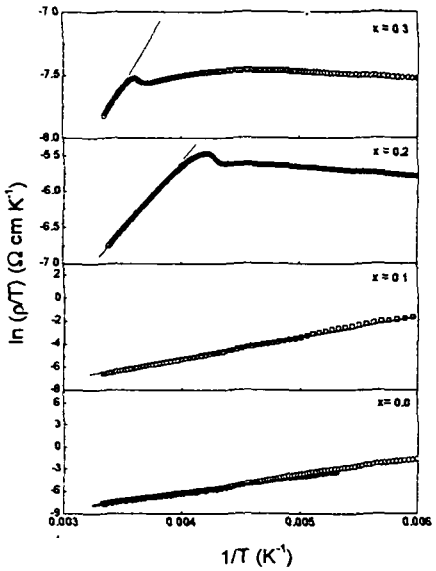

Fig. 6. Inverse temperature variation of ln (ρ/T) of x = 0.0, 0.1, 0.2, and 0.3 samples. Solid lines are the best fit to the SPH model of Mott viz. $\rho/T = \rho_\alpha \exp(E_p/k_BT)$.[6]

evident from Fig. 4 that the mixing phase in any sample plays the dominant role for higher MRR. Our experimental findings may be explained as the following.

The undoped $Pr_{0.65}Ca_{0.35}MnO_3$ exposes an insulating behaviour (with $T_{CO} \sim 215$ K) at all temperatures where as the 100% doped $Pr_{0.65}Sr_{0.35}MnO_3$ reveals a metallic behaviour with MI transition near room temperature, $T_{MI} \sim 290$ K (Fig. 1). Thus a competition between a CO-I phase and a FM-M phase is accomplished in $Pr_{0.65}Ca_{0.35-x}Sr_xMnO_3$. Most probably, the doping of Sr introduces the nanosize FM clusters in CO/AFM matrix of $Pr_{0.65}Ca_{0.35}MnO_3$. At lower concentration of Sr, the number of nanosize FM clusters is very small and the system resembles a regular array of charge short of Wigner crystal and it remains an insulator[8] as no percolation is possible through the AFM matrix. With the increase of Sr concentration, the number as well as volume of FM clusters increase, the percolation among some FM clusters starts and the resistivity decreases (Fig. 1). When x = 0.1, the number and volume of CO/AFM and FM clusters become nearly equal causing to disorder induced phase separation[2] with prominent and intrinsic inhomogeneities in the form of coexisting competing phases and leading to MI transition (Fig. 1). Hence, a particular unstable mixing phase of a weak CO insulating at high temperatures and an (AFM+FM)M phase at low temperatures is obtained for samples with x ~ 0.1. Therefore, the application of a low magnetic field (≤ 0.5 T) on the samples with x ~ 0.1 is enough to partially melt the charge ordering insulating phases and facilitate to percolate the FM phases to enhance the metallicity leading to huge MRR (Fig. 5). The volumes as well as number of FM clusters increase with further increase of x in expense to those of CO/AFM clusters and eventually nearly all the matrix become FM leaving embedded nanosize CO/AFM phases. Subsequently, the x = 0.35 sample is metallic at all temperatures (Fig. 1) as the nanosize AFM phases embedded in FM matrix cannot block the percolation.[8]

Figure 6 shows the inverse temperature variation of ln(ρ/T) of some selective samples. In the high temperature ($T > T_{MI}$) insulating (semiconducting) phase, the conductivity data is dominated by the thermally activated hopping of small polarons[9] and are fitted well with the small polaron hopping (SPH) model (for $T > \theta_D/2$,

where θ_D is the Debye temperature) of Mott[10] viz $\rho/T = \rho_\alpha \exp(E_p/k_BT)$, where $\rho_\alpha = [k_B/\nu_{ph}Ne^2R^2C(1-C)] \exp(2\alpha R)$, k_B is the Boltzmann constant and T is the absolute temperature. N is the number of ion sites per unit volume, $R \sim (1/N)^{1/3}$ is the average inter-site spacing, C is the fraction of sites occupied by a polaron, α is the electron wave function decay constant, ν_{ph} is the optical phonon frequency as estimated from the relation $h\nu_{ph} = k_B\theta_D$, and θ_D is obtained from the temperature where the linearity of ln (ρ/T) vs 1/T curve (Fig 6) disappears in the high temperature region. θ_D as well as ν_{ph} increase with the increase of x. The activation energy (E_p) is determined from the slope of the ln (ρ/T) vs 1/T curve above $\theta_D/2$ (Fig 6) For polaron hopping conduction,[10] $E_p = W_H + W_D/2$ (for $T > \theta_D/2$) and $E_p = W_D$ for $T < \theta_D/4$, where W_H is the polaron hopping energy and W_D is the disorder energy. The difference between E_p and E_s (activation energy estimated from the high temperature thermoelectric power data) gives the polaron hopping energy (W_H) [11] From the values of E_p, E_s and W_H, we notice that with increasing value of strontium concentration (x), the E_p gradually decreases [6] This behaviour can be explained by considering that increasing x causes larger bandwidth and hence charge delocalization occurs due to decrease of electron-phonon (*e-ph*) interaction constant γ_p in the system and thereby the energy required to liberate a free carrier is reduced [6] It is noted that there is a non-linear decrease of E_p and increase in θ_D with the increase of applied magnetic field [6] Similar trend is also observed in other samples of the series Here, it should be mentioned that the activation energy decreases with the increase of magnetic field for any particular x similar to the increase of Sr doping concentration (x) in $Pr_{0.65}Ca_{0.35-x}Sr_xMnO_3$. Thus the role of increasing Sr concentration and magnetic field are the same for delocalization of charge carriers and spin ordering in the CMR system as reported earlier [12]

IV. CONCLUSIONS

The temperature and magnetic field dependence of resistivity, magnetization and specific heat of polycrystalline $Pr_{0.65}Ca_{0.35-x}Sr_xMnO_3$ (x = 0-0.35) perovskite manganites have been systematically studied and explained on the basis of PS scenarios. Unusual magnetic ordering is observed in x = 0.1 sample below MI transition (MIT) temperature. The number of FM clusters become nearly equal to those of AFM clusters for x ~ 0.1 giving rise to disorder induced PS with a huge MRR at low magnetic fields (< 0.5 T) Non-adiabatic small polaron hopping conduction is observed in all the samples above their respective MIT temperature

ACKNOWLEDGEMENTS

The author is grateful to H. D. Yang, H L Huang and B. K Chaudhuri for their active involvement in this work. This is financially supported by the National Science Council, Taiwan

REFERENCES

*Email address: smollah@rediffmail.com

[1] A Moreo, S. Yunoki, and E Dogatto, Science **283**, 2034 (1999).

[2] E Dagotto, T. Hotta, and A. Moreo A, Phys. Rep **344**, 1 (2001).

[3] P Levy, F. Parisi, L. Granja, E. Indelicato, and G Polla, Phys. Rev. Lett. **89**,137001 (2002)

[4] S Mollah, H. L. Huang, P L Ho, W L Huang, C. W. Huang, C P. Sun, J. -Y. Lin, S J Liu, Y. S. Gou, W. -H. Li, and H. D. Yang, J Mag. Mag. Mater. **265**, 215 (2003).

[5] S Mollah, C. P. Sun, H. L. Huang, P. L. Ho, and H. D. Yang, J. Appl. Phys. **95**, 6813 (2004).

[6] S Mollah, H. L. Huang, H. D. Yang, S. Pal, S. Taran, and B. K. Chaudhuri, J. Magn Magn Mater **284**, 383 (2004).

[7] Y -K Kuo, C.S. Lue, F.H. Hsu, H H. Li, and H D Yang, Phys. Rev. B **64**, 125124 (2001)

[8] A L. Malvezzi, S. Yunoki, and E Dagotto, Phys. Rev. B **59**, 7033 (1999).

[9] A. J Millis, P. B. Littlewood, and B I Shraiman, Phys. Rev Lett. **74**, (1995) 5144

[10] N F Mott and E. A. Davis, in *Electronics Process in Non Crystalline Materials* (Clarendon Press, Oxford 1979)

[11] M Jaime, M. B. Salamon, M. Rubenstein, R E Treece, J S. Horwitz, and D B Chrisey, Phys Rev B **54**, (1996) 11914.

[12] Y Tomioka, A Asamitsu, H Kuwahara, and Y Tokura, J Phys Soc Jpn. **66**, (1997) 302

Journal of Magnetism and Magnetic Materials 284 (2004) 383–394
www.elsevier.com/locate/jmmm

Non-adiabatic small-polaron hopping conduction in $Pr_{0.65}Ca_{0.35-x}Sr_xMnO_3$ perovskites above the metal–insulator transition temperature

S. Mollah[a,1], H.L. Huang[a], H.D. Yang[a], Sudipta Pal[b], S. Taran[b], B.K. Chaudhuri[b,*]

[a]*Department of Physics, National Sun Yat Sen University, Kaohsiung 804, Taiwan, ROC*
[b]*Solid State Physics Department, Indian Association for the Cultivation of Science, Jadavpur, Kolkata-700032, India*

Received 18 May 2004; received in revised form 2 July 2004
Available online 28 July 2004

Abstract

We report structural, magnetic and transport properties of $Pr_{0.65}Ca_{0.35-x}Sr_xMnO_3$ ($x = 0 - 0.35$) perovskites. Non-adiabatic small-polaron hopping (SPH) conduction mechanism is followed in all the manganites above the respective metal–insulator transition temperatures (T_{MI}). Variable range hopping has been found less important with the increase of Sr concentration in the low temperature semiconducting region ($T > T_{MI}$). A non-linear change in the activation energy (E_p) and Debye temperature (θ_D) with applied magnetic field has been observed for all the samples. The metallic conduction below T_{MI} shows the electron–magnon scattering behavior similar to other manganites. Activation energy E_s, estimated from the temperature dependent Seebeck coefficient data, was observed to be much smaller than E_p determined from the resistivity data which also supports the SPH conduction.

PACS: 75.47.Jn; 75.47.Gk; 71.30.+h; 72.20.–i

Keywords: CMR manganites; Electrical conductivity; Thermodynamic properties

1. Introduction

Recent explorations on the colossal magnetoresistive (CMR) materials have focused on the role of strong electron–phonon (e–ph) coupling leading to the formation of polarons (i.e. the association of the localized charge carriers with the lattice

*Corresponding author. Tel.: +91-33-247-34971; fax: +91-33-247-32805.
E-mail address: sspbkc@mahendra.iacs.res.in (B.K. Chaudhuri).
[1]Permanent address: Department of Physics, Aligarh Muslim University, Aligarh-202002, India.

0304-8853/$ - see front matter © 2004 Published by Elsevier B.V.
doi:10.1016/j.jmmm.2004.07.004

distortions) in the paramagnetic (PM) insulating phases, supplementing to the double exchange (DE) interactions (for a review, see Ref. [1]) [2,3]. The formation of small polarons is due to the mixed-valance transition metal ions (TMIs) present in the manganites. The lattice distortion arises as a result of the localization of the e_g electrons of Mn^{3+} ions. The different ion sizes $r_{R,A}$ of (R, A)MnO_3 (R = rare earth, A = alkaline earth metals) manganites also lead to disorder owing to size mismatch. It can be qualitatively expressed [4] by the variance factor $\phi^2 = \langle r_{R,A}^2 \rangle - \langle r_{R,A} \rangle^2$. Since there are no 3^+ and 2^+ cations whose ionic radii are identical or close to each other, the (R, A) site disorder will always exist in (R, A)MnO_3 manganites. The polaron formation is believed to be a necessary ingredient for modeling a temperature dependent magnetic and transport behavior of CMR materials [5,6]. The electrical conduction takes place by the hopping/tunneling of the polarons from lower to the higher valance states of TMIs.

Praseodymium (Pr)-based CMR materials have shown numerous remarkable properties like metal–insulator transition (MIT), antiferromagnetic–ferromagnetic (AFM–FM) phase transition, charge ordering (CO), phase separation (PS), etc. [7–10]. The melting of AFM insulating state into FM metallic one has been perceived in $Pr_{0.5}Sr_{0.5}MnO_3$ through the application of magnetic fields [7]. The entropy change associated with the magnetic transitions in $Pr_{0.6}(Ca_{1-x}Sr_x)_{0.4}MnO_3$ ($0 \leqslant x \leqslant 1$) polycrystals is much smaller than the expected value [10] which is attributed to the localization of charge carriers around MIT and the presence of short-range magnetic correlation well above MIT. The occurrence of PS, typically involving FM metallic and AFM/CO insulating (COI) domains of different shapes like spherical droplets, curves or stripes, have been observed [11,12]. Usually, the PS phenomena are pronounced near the MIT temperature of manganites. In this context, the electronic, magnetic and thermal properties of polycrystalline $Pr_{0.65}Ca_{0.35-x}Sr_xMnO_3$ ($x = 0.0 - 0.35$) perovskites have been studied and reported earlier [13,14]. A PS-induced huge enhancement of magnetoresistance (MR) 10% at $H = 100$ Oe and 99% at $H = 0.5$ T around MIT temperature ($T_{MI} \sim 80$ K) has been observed in $x = 0.1$ sample [13,14]. However, the conduction mechanism above and below the T_{MI} of it and other samples of this series has yet not been thoroughly analyzed.

In the present paper, we report in detail the structural, magnetic and magneto-transport properties of polycrystalline $Pr_{0.65}Ca_{0.35-x}Sr_xMnO_3$ ($x = 0-0.35$) manganites. From the temperature dependent resistivity (ρ) and thermoelectric power (TEP) above the respective T_{MI} of the samples, it has been found that the transport property is mainly governed by the non-adiabatic small-polaron hopping (SPH) conduction in high temperature insulating phase.

2. Experimental

Polycrystalline $Pr_{0.65}Ca_{0.35-x}Sr_xMnO_3$ ($x = 0-0.35$) perovskite manganites were prepared by the standard solid-state reaction method [13,14] from the powdered raw materials Pr_6O_{11}, CaO, MnO_2 and $SrCO_3$ (each of purity >99%). Homogeneous stoichiometric mixtures were heat treated at 900 °C for 12 h followed by regrinding and firing at 1200 °C for 12 h. The resultant powder was palletized at a pressure of 2 ton cm^{-2} and sintered in air at 1350 °C for 48 h with in-between grinding, palletizing and annealing for three times. Powder X-ray diffraction (XRD) data of the samples were obtained at room temperature from a SIEMENS D5000 diffractometer using CuKα radiation. Magnetization (M) measurements were performed by the commercial superconducting quantum interface device (SQUID) magnetometer between room temperature (300 K) and 10 K with applied magnetic fields (H) up to 8 T. Magnetic field (0–8 T) dependent electrical resistivity (ρ) of the samples was measured by the standard four-probe method. The TEP (S) of the samples was determined by the standard differential technique in the temperature range of 80–300 K using an APD cryo-cooler unit with a temperature controller in the presence or absence of a magnetic field of 1.5 T.

3. Results and discussion

3.1. Structural study with X-ray diffraction

Powder XRD data of $Pr_{0.65}Ca_{0.35-x}Sr_xMnO_3$ ($x = 0-0.35$) show single-phase character of all the samples without any measurable impurity phases (Fig. 1). Rietveld refinement of the data reveals that the samples crystallize in an orthorhombically distorted perovskite structure with space group Pbmn consistent with the previously reported results [15]. All the structural parameters (a, b and c^*) are listed in Table 1. It clearly shows the increment of the structural parameters with the increase of doping concentration (x) of larger ions Sr in place of Ca. The corresponding increase of a is greater than those of b and c^* indicating a decrease in orthorhombic distortion due to increasing Sr content. This is further supported by the transport data, which clearly indicate a substantial increase in conductivity due to increase of x.

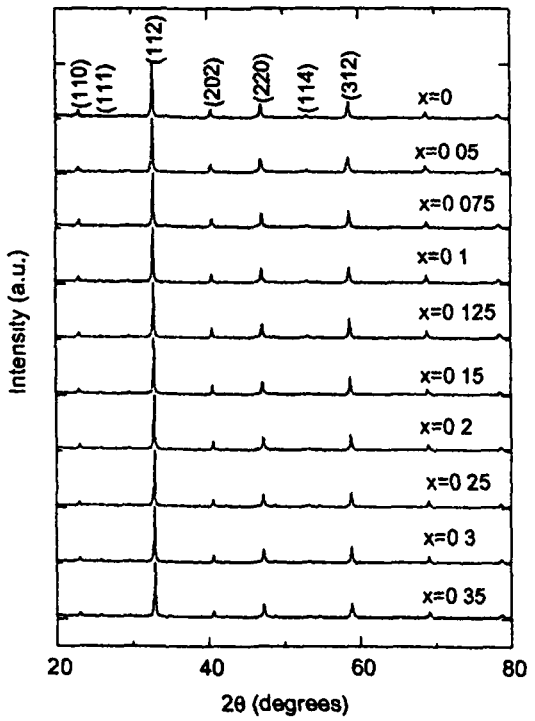

Fig 1 XRD pattern of the samples $Pr_{0.65}Ca_{0.35-x}Sr_xMnO_3$ ($x = 0-0.35$) clearly indicating their single-phase character

Table 1
Structural parameters of $Pr_{0.65}Ca_{0.35-x}Sr_xMnO_3$ perovskites

x	a (Å)	b (Å)	c^* (Å)
0 0	5.447	5 419	5 415
0.05	5 444	5 425	5 421
0 075	5.446	5 429	5 423
0.10	5 444	5 435	5 425
0 125	5 449	5 435	5 437
0 15	5 453	5 438	5 435
0.20	5 446	5 430	5 426
0 25	5 459	5 437	5 435
0 30	5 467	5 437	5 433
0 35	5 481	5 444	5 440

3.2. Magnetic field dependent resistivity and magnetization

The temperature variation of resistivity (ρ) of $Pr_{0.65}Ca_{0.35-x}Sr_xMnO_3$ samples shows a sharp MIT for $x = 0.1$ in the absence of magnetic field (H) [13,14]. Temperature dependent resistivity of two samples (with $x = 0.075$ and 0.125) above and below the Sr concentration ($x = 0.1$) at different H is shown in Fig. 2. The MIT under H of 1 T in $x = 0.075$ sample is quite sharp while that in the sample $x = 0.125$ without H is broad Similarly, the MITs of $x = 0.0$ and 0.05 samples were also observed to be sharp, respectively, at the H of 5 and 3 T. However, the transitions become broader with the increase of x for $x \geq 0.1$ in the absence of H. Magnetization (M) at low H (0.1 T) for three different samples (with different sizes of the A-site cations) is shown in Fig. 3. It is evident that M increases with the increase of A-site cation radius The M–H trace of insulating $Pr_{0.65}Ca_{0.35}MnO_3$ sample at three different temperatures (10, 70 and 300 K) is illustrated in Fig. 4 A large hysteresis effect is seen in the M–H curve at 10 K (Fig. 4) clearly indicating the FM nature of the sample at this temperature. However, the PM ground state of the sample is further verified from the zero hysteresis nature in the M–H curve at 300 K. On the basis of the temperature and magnetic field variation of magnetic as well as transport properties of the $Pr_{0.65}Ca_{0.35-x}Sr_xMnO_3$ samples (Figs. 2–4), three different kinds of

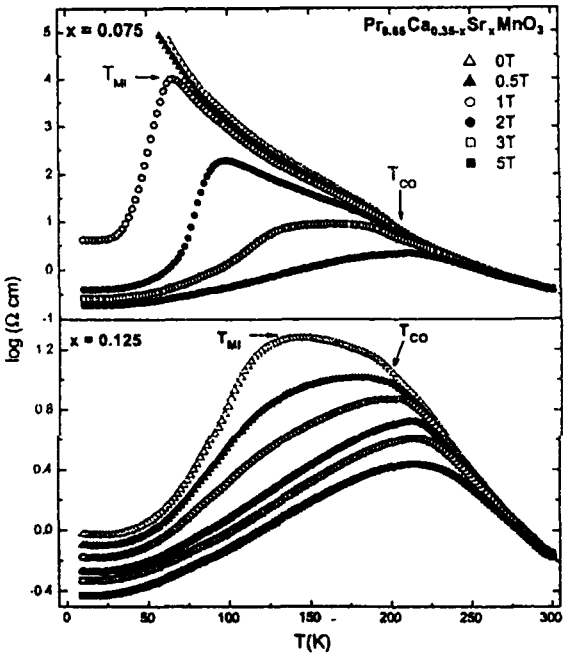

Fig. 2. Temperature variation of resistivity (ρ) of $Pr_{0.65}Ca_{0.35-x}Sr_xMnO_3$ perovskites with $x = 0.075$ and 0.125 at different magnetic fields.

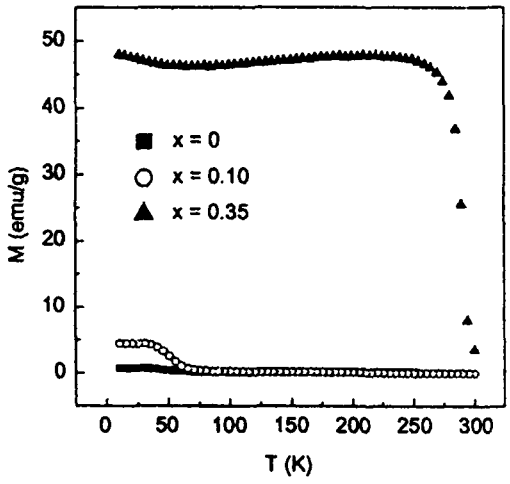

Fig. 3. Magnetization (M) as a function of temperature (T) for three different doping concentrations (x) of $Pr_{0.65}Ca_{0.35-x}Sr_xMnO_3$ at an applied magnetic field of 0.1 T.

magnetic transitions are observed as conversed below.

(i) For smaller values of average ionic radii $\langle r_A \rangle$ corresponding to $0 \leqslant x \leqslant 0.075$, a single magnetic transition from the PM to the AFM/CO states is observed. The T_{MI} increases and the CO transition temperature T_{CO} decreases with the increase of x (Table 2). Actually, at lower concentration of Sr, the number of nanosize FM clusters is very small and the system resembles a regular array of charge short of Wigner crystal and it remains an insulator [16] as no percolation is possible through the AFM matrix and acts as a weak FM insulator (WFMI). With the increase of Sr concentration (x), the number as well as volume of FM clusters increase, the percolation among some FM clusters starts and the M increases.

(ii) For intermediate $\langle r_A \rangle$ corresponding to $x = 0.1$, all the transitions from PM to AFM and AFM to FM phases are observed along with the CO anomaly at lower H. The number and volume of CO/AFM and FM clusters become nearly equal causing to disorder induced PS with prominent and intrinsic

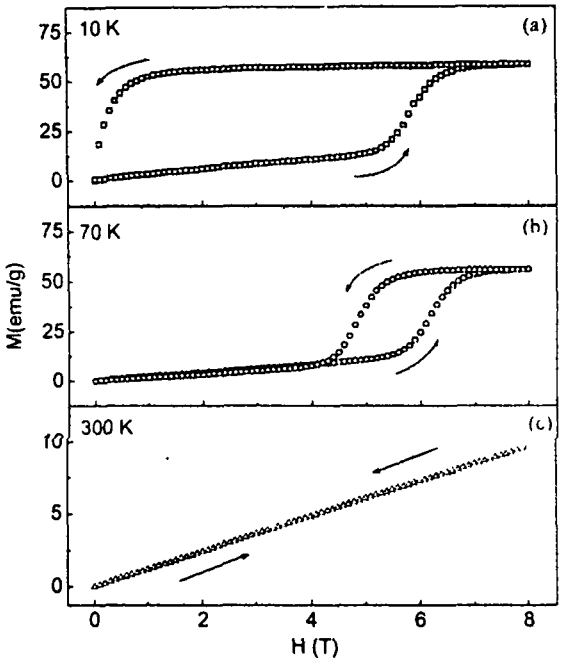

Fig. 4. M–H curve for the $Pr_{0.65}Ca_{0.35}MnO_3$ sample at (a) 10, (b) 70 and (c) 300 K showing the hysteresis nature of the sample at low temperature ferromagnetic phase.

Table 2
Parameters calculated from resistivity and thermoelectric power data of $Pr_{0.65}Ca_{0.35-x}Sr_xMnO_3$ samples

x	T_{MI} (K)	T_{CO} (K)	θ_D (K)	ν_{ph} (Hz)	E_p (meV)	$N(E_F)$ ($eV^{-1}cm^{-3}$)	E_s (meV)	W_H (meV)
0 0	—	214.97	428 27	$8\,91\times10^{12}$	177 45	$1\,43\times10^{17}$	—	—
0 05	—	203 96	434 78	$9\,05\times10^{12}$	170 38	$1\,47\times10^{17}$	—	—
0 075	—	201 97	444 44	$9\,25\times10^{12}$	166 08	$8\,25\times10^{17}$	—	—
0 10	83.9	—	455 69	$9\,49\times10^{12}$	162 10	$1\,43\times10^{18}$	—	—
0 125	143 9	—	465 12	$9\,68\times10^{12}$	156 06	$1\,83\times10^{18}$	—	—
0 15	210 0	—	498 49	$10\,38\times10^{12}$	148 02	$2\,04\times10^{18}$	15 80	132 22
0.20	238 4	—	512 82	$10\,68\times10^{12}$	145 61	$2\,35\times10^{18}$	23 98	121 63
0.25	256 0	—	526 32	$10\,96\times10^{12}$	142 51	$4\,37\times10^{18}$	21 11	121 40
0 30	278.2	—	588 24	$12\,25\times10^{12}$	136 48	$1\,75\times10^{18}$	17 86	118 61
0.35	295.9	—	—		—	—	—	—

inhomogeneities in the form of coexisting competing phases [11,12] and leading to MIT. Therefore, the application of a low H ($\leqslant 0.5$ T) on the samples with $x \sim 0.1$ is enough to partially melt the COI phases and facilitate to percolate the FM phases to enhance the metallicity leading to huge magnetoresistance ratio MRR [13,14].

(iii) For higher $\langle r_A \rangle$ values corresponding to $0.125 \leqslant x \leqslant 0.35$, only a PM to FM phase change is visible. As the temperature is decreased, M starts increasing at T_{MI} and becomes saturated below FM transition temperature T_c. Because of the FM ordering in this doping range, the change in M value is quite high. The T_c increases with the increase of x. The volume as well as the number of FM clusters increase with the increase of x and eventually nearly all the matrix become FM for $x = 0.35$.

3.3. Resistivity above and below T_{MI}

Temperature variation of resistivity (ρ) of manganites can also be explained by the variation of effective one-electron bandwidth (W) or equivalently e_g electron transfer interaction (t) in addition to the PS phenomena discussed earlier. We know that the magnitude of W can be changed [17,18] by varying the ionic averaged radius $r_{R,A}$ or equivalently the tolerance factor $f = (\langle r_{R,A}\rangle + r_O)/[\sqrt{2}(r_{Mn} + r_O)]$. Here r_{Mn} and r_O are the averaged ionic radii for the respective elements. With decrease of f (or $\langle r_{R,A}\rangle$), the average bond angle β of Mn–O–Mn shows a deviation from 180° in the orthorhombic lattice. The W value for the manganite is governed by the degree of the hybridization between the Mn 3d e_g and O 2p σ states which approximately scales with $\cos^2\beta$ due to the d-electron supertransfer process. Therefore, the smaller the average (R, A) site ionic radii or f is, the smaller is the W. Again, W can be increased either by the contraction of Mn–O bond length or straightening of Mn–O–Mn bond angle [19].

The enhanced electron–lattice coupling arises from the charge/orbital correlation and plays an important role in the CMR effect. The DE interaction seems to overcome the AFM fluctuations at lower temperatures, giving rise to the abrupt phase switching to the FM metallic state. According to the DE model [2], the transfer interaction of e_g carriers (t) is governed by the relative angle (θ) of the local t_{2g} spins between neighboring Mn^{3+} and Mn^{4+} ions in a manner that

$$t = t_0 \cos(\theta/2), \tag{1}$$

where t_0 is the normal transfer integral. The t value (or W) can be effectively increased by means of magnetic field induced reduction of θ resulting in the increase of conductivity.

In the present case, the parent compound $Pr_{1-x}Ca_xMnO_3$ is a low bandwidth (W) compound [20] in which a charge ordered ground state is stabilized in the vicinity of $x = 0.5$. It presents a particularly stable CO state [21] in a broad density

region between $x = 0.30$ and 0.75. For $x \geqslant 0.30$, an AFM/CO state is stabilized [21]. Neutron diffraction studies showed that the arrangement of charge/spin/orbital order in samples with $x \geqslant 0.30$ is similar to the charge-exchange (CE)-AFM state [21]. When Ca is successively substituted with Sr, the nominal ratio of Mn^{3+}/Mn^{4+} and hence the hole density in the system remains unchanged due to the same valence of Ca and Sr. The only effect that is prominent is the difference of the atomic size of the Sr and Ca ions which alters the $\langle r_{R,A} \rangle$ value [18]. Due to the larger size of the Sr ions, the electron bandwidth (W) increases and hence the hopping amplitude for the electrons in the e_g band becomes larger causing reduction in resistivity of $Pr_{0.65}Ca_{0.35-x}Sr_xMnO_3$ with the increase of x.

The increase in W stabilizes the FM state by increasing the DE interaction and hence favors the FM metallic state over the COI one. In the minimal W system like $Pr_{1-x}Ca_xMnO_3$, the FM metallic state becomes apparently absent while for the maximal W system, i.e. $Pr_{1-x}Sr_xMnO_3$ the FM metallic state due to DE interaction becomes dominant [1]. Around the middle W region, the subtle balance or competition between the ferromagnetic DE and the antiferromagnetic CO interactions result in versatile phenomena [1] including striction-coupled CMR. It is noted that all the $\rho-T$ curves for $x = 0-0.35$ converge to the constant resistivity around 300 K [14]. This is in contrast to the low temperature region in which only a small variation of W causes a crucial change in transport properties.

Fig. 5 shows the inverse temperature variation of $\ln(\rho/T)$ of some selective samples. In the high temperature ($T > T_{MI}$) insulating (semiconducting) phase, the conductivity data are dominated by the thermally activated hopping of small polarons [22] and are fitted well with the SPH model (for $T > \theta_D/2$) of Mott and Davis [23], viz.

$$\rho/T = \rho_\alpha \exp(E_p/k_B T), \tag{2}$$

where $\rho_\alpha = [k_B/\nu_{ph} N e^2 R^2 C(1-C)] \exp(2\alpha R)$, k_B is the Boltzmann constant and T is the absolute temperature. N is the number of ion sites per unit volume, $R \sim (1/N)^{1/3}$ is the average inter-site spacing, C is the fraction of sites occupied by a polaron, α is the electron wave function decay

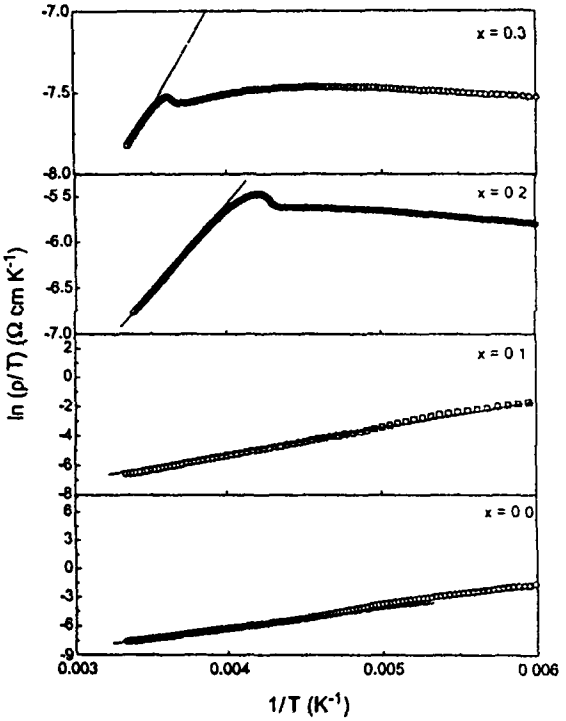

Fig. 5. Variation of $\ln(\rho/T)$ of some of the samples with $x = 0.0$, 0.1, 0.2 and 0.3 as a function of inverse temperature. Solid lines are the best fit to the SPH model of Mott, viz. $\rho/T = \rho_\alpha \exp(E_p/k_B T)$.

constant, ν_{ph} is the optical phonon frequency (Table 2) as estimated from the relation $h\nu_{ph} = k_B\theta_D$, and the Debye temperature θ_D is obtained from the temperature where the linearity of $\ln(\rho/T)$ vs. $1/T$ curve (Fig. 5) disappears in the high temperature region. θ_D as well as ν_{ph} increase with the increase of x (Table 2). The activation energy (E_p) was determined from the slope of the $\ln(\rho/T)$ vs. $1/T$ curve above $\theta_D/2$ (Fig. 5). For polaron hopping conduction [23],

$$E_p = W_H + W_D/2 \quad (\text{for } T > \theta_D/2) \quad \text{and}$$
$$= W_D \quad \text{for } T < \theta_D/4, \tag{3}$$

where W_H is the polaron hopping energy and W_D is the disorder energy. The difference between the E_p and E_s (activation energy estimated from the high temperature TEP data discussed below) is the polaron hopping energy. Therefore, W_H is

estimated from the relation [24]

$$W_H = E_p - E_s \quad (4)$$

From the values of E_p, E_s and W_H, as shown in Table 2, we notice that with increasing value of strontium concentration (x), the E_p gradually decreases. This behavior can be explained by considering that increasing x causes larger bandwidth and hence charge delocalization occurs due to decrease of e–ph interaction constant γ_p (as discussed later) in the system (Table 3) and thereby the energy required to liberate a free carrier is reduced. Using Eq. (2), the magnetic field dependence of E_p and θ_D are calculated for the sample ($x = 0.1$) with electronic and magnetic instability near T_{MI} and is shown in Fig. 6. It is noted that there is a non-linear decrease of E_p and increase in θ_D with the increase of applied magnetic field (Fig. 6). Similar trend is also observed in other samples of the series. Here, it should be mentioned that the activation energy decreases with the increase of magnetic field (Fig. 6) for any particular x similar to the increase of Sr doping concentration (x) in $Pr_{0.65}Ca_{0.35-x}Sr_xMnO_3$ (Table 2). Thus, the role of increasing Sr concentration and magnetic field are the same for delocalization of charge carriers and spin ordering in the CMR system as reported earlier [18]

As mentioned previously in this paper and also reported in our former work [25] that the low temperature ($T_{MI} < T < \theta_D/2$) transport phenomenon in perovskites and in some other semiconducting oxides are described by variable range

Table 3
Parameters of $Pr_{0.65}Ca_{0.35-x}Sr_xMnO_3$ perovskites for non-adiabatic small-polaron hopping conduction

x	J (meV)	H (meV)	$W_H/3$ (meV)	γ_p	exp(γ_p)
0 0	22 3	—	—	—	—
0 05	22 6	—	—	—	—
0 075	23 0	—	—	—	—
0 10	23 4	—	—	—	—
0 125	23 8	—	—	—	—
0 15	25 1	26 9	43 6	6 14	464 05
0 20	25 6	26 7	40 3	5 47	237 46
0 25	26 1	27 1	40 3	5 33	206 43
0 30	28 4	28 5	39 3	4 65	104 58

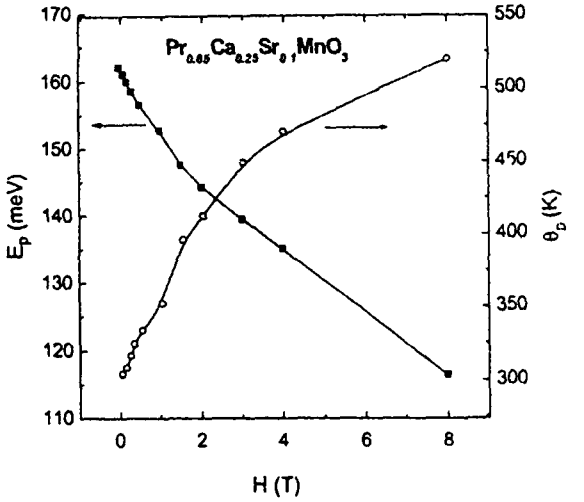

Fig 6 Magnetic field dependence of E_p and θ_D obtained from fitting the resistivity data of $Pr_{0.65}Ca_{0.25}Sr_{0.1}MnO_3$ sample with $\rho/T = \rho_s \exp(E_p/k_BT)$

hopping (VRH) model of charge carriers Recently, Jaime et al. [24] and Viret et al. [26] applied VRH conduction mechanism in La–Ca–Mn–O system for the entire temperature above T_{MI} But as reported earlier [27], the VRH model was applicable for explaining the conductivity data below $\theta_D/2$ For the present samples, the conductivity data are also best fitted with VRH model for $T_{MI} < T < \theta_D/2$ However, for $T > \theta_D/2$, SPH model was applicable as discussed earlier The expression for DC conductivity (σ_{DC}) in the VRH model has the form [23]

$$\sigma_{DC} = \sigma_0 \exp(-T_0/T)^{1/4}, \quad (5)$$

where σ_0 is a pre-exponential factor, T_0 is a constant [$= 18\alpha^3/k_BN(E_F)$] and $N(E_F)$ is the density of states (DOS) at the Fermi level which is calculated from the slope of the log σ_{DC} vs $T^{-1/4}$ curves (Fig 7) For the samples with higher T_{MI} values, the VRH region becomes smaller So it is rather difficult to judge which of the two models (SPH or VRH) is the most appropriate It is, however, noticed that the high temperature ($T > \theta_D/2$) conductivity data are better fitted with the SPH model The calculated values of $N(E_F)$ in the absence of magnetic field ($B = 0$) are shown in Table 2 To estimate the values of $N(E_F)$, we have used $\alpha = 2.22\,nm^{-1}$ (similar to the value used by

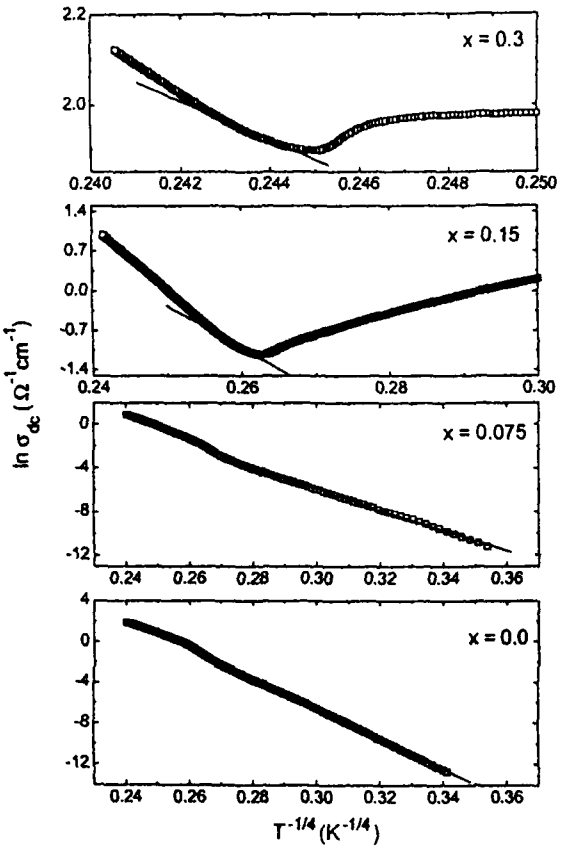

Fig. 7. Plot of $\ln\sigma_{DC}$ as a function of $T^{-1/4}$ for $Pr_{0.65}Ca_{0.35-x}Sr_xMnO_3$ samples with $x = 0$, 0.075, 0.15 and 0.3. Solid lines are the best fit to the VRH model [$\sigma_{DC} = \sigma_0 \exp(-T_0/T)^{1/4}$] between T_{MI} and $\theta_D/2$, where θ_D is the Debye temperature.

Viret et al. [26] for La–Sr–Mn–O samples). T_0 is found to be $\sim 10^6$ for best fit similar to La–Ca–Mn–O and La–Ca–K–Mn–O systems [25]. For any particular composition, T_0 is found to decrease with the increasing magnetic field strength. $N(E_F)$ values are also in good agreement with the previously reported results [27]. The $N(E_F)$ of the present system increases with increasing Sr concentration (Table 2). Application of magnetic field also increases $N(E_F)$ for all Sr concentrations. This increase of $N(E_F)$ with the increase of both by Sr doping and field is also expected, as the increase in conductivity is the obvious effect of the increased number of charges at the Fermi level.

From Holstein's [28] relation, one can confer whether the hopping conduction is in the adiabatic or non-adiabatic region. According to that relation, the polaron bandwidth J should accomplish the following condition:

$J > H$ for adiabatic hopping and

$< H$ for non-adiabatic hopping conduction, (6)

where

$$H = (2k_B T W_H/\pi)^{1/4}(h\nu_{ph}/\pi)^{1/2}. \quad (7)$$

The condition for small-polaron formation is $J < W_H/3$ [28]. An evaluation of J can be made from the approximate relation for high temperature jump site

$$J(T) \approx 0.67 h\nu_{ph}(T/\theta_D)^{1/4} \quad (8)$$

and for ground-state bandwidth $J(0) = 3h\nu_{ph} = 124$ meV with $\nu_{ph} \sim 10^{13}$ Hz. In the present system, from Table 3, we find that H varies from 26.7 to 28.5 meV for a temperature of 290 K (above T_{MI} of all the samples), $J(290\,K) \sim 22.3$–28.4 meV, and $W_H/3 \sim 39.3$–43.6 meV. Since $J(290\,K) < H$ and $J(290\,K) < W_H/3$, we conclude that the DC conduction in the $Pr_{0.65}Ca_{0.35-x}Sr_xMnO_3$ manganites is by reason of SPH in the non-adiabatic regime. The values of small-polaron coupling constant (γ_p), which is a measure of e–ph interaction in these manganites, can be estimated [23,29] from the relation $\gamma_p = 2W_H/h\nu_{ph}$. The accomplished γ_p for the present system alters from 4.65 to 6.14 (Table 3). Austin and Mott [29] suggested that a value of $\gamma_p > 4$ usually indicates strong e–ph interaction. Hence, the e–ph interaction in these manganites is confirmed to be very strong. The polaron mass (m_p) and rigid lattice effective mass (m^*) in the manganites are related by [23]

$$m_p = (h^2/8\pi^2 JR^2)\exp(\gamma_p) = m^* \exp(\gamma_p). \quad (9)$$

The m_P/m^* is found to vary from 104.58 to 464.05 (Table 3) and is very large indicating further strong e–ph interaction in these manganites.

At low temperature ($T < T_{MI}$) the metallic behavior of the samples can be explained in terms of electron–magnon scattering of the carriers (Fig. 8). In this temperature regime, the resistivity

data fit quite well with the following expression:

$$\rho = \rho_0 + \rho_{2.5} T^{2.5}, \quad (10)$$

where the first term ρ_0 corresponds to the resistivity arising due to domain, grain boundary and other temperature independent scattering mechanism [30,31]. The second term $\rho_{2.5}T^{2.5}$ appears as a result of electron–magnon scattering [32]. Thus, the spin scattering cannot be neglected in the low temperature ($T < T_{MI}$) regime as the measured data can be best explained by electron–magnon scattering. The best fitted parameters are given in Table 4. It is noted that the values of both ρ_0 and $\rho_{2.5}$ decrease with the increase of x. However, the decrease of temperature independent

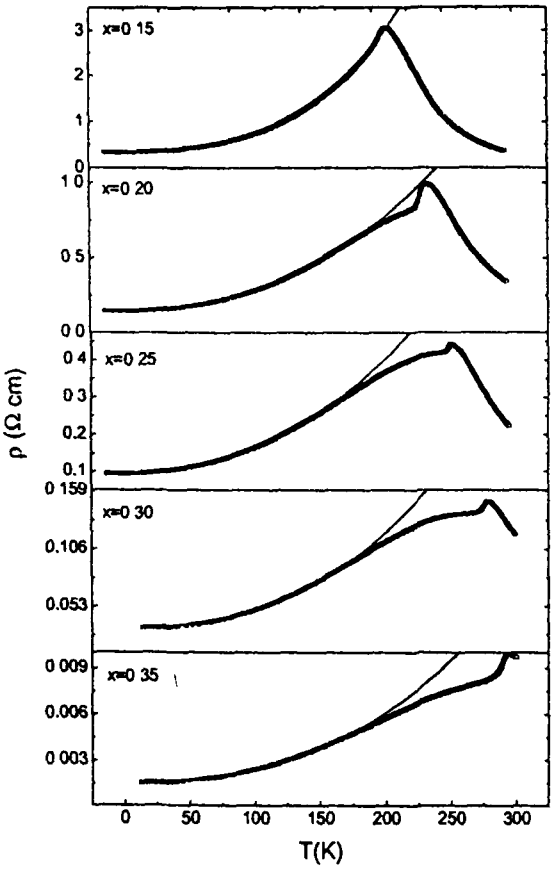

Fig 8 Replotted resistivity data showing $T^{2.5}$ dependence for $Pr_{0.65}Ca_{0.35-x}Sr_xMnO_3$ with $x = 0.15$, 0.20, 0.25, 0.30 and 0.35 below the respective T_{MI} Solid lines are the best fit to the equation $\rho = \rho_0 + \rho_{2.5}T^{2.5}$

Table 4
Best fitted parameters obtained from the fitting of the low temperature resistivity data in the metallic regime of $Pr_{0.65}Ca_{0.35-x}Sr_xMnO_3$ manganites with $\rho = \rho_0 + \rho_{2.5}T^{2.5}$

x	ρ_0 (Ω cm)	$\rho_{2.5}$ (Ω cm K$^{-2.5}$)
0.15	0.33	2.14×10^{-6}
0.20	0.14	1.01×10^{-6}
0.25	0.09	4.94×10^{-7}
0.30	0.03	1.55×10^{-7}
0.35	0.002	8.02×10^{-7}

ρ_0 is more significant with x compared to that of $\rho_{2.5}$ (Table 4). Consequently, the mechanism responsible for huge MRR in this system [13,14] is influenced by the magnetic field for the ordering of magnetic domains. As the magnetic field increases, the size of the domain boundary decreases and ρ_0 becomes smaller (Fig. 2). The decrease of $\rho_{2.5}$ with x is due to the suppression of spin fluctuation due to larger W. The magnitude of $\rho_{2.5}$ is quite similar to that of other CMR compounds [25,33] like La–Pb–Mn–O and La–Ca–Mn–O showing MIT. This indicates a similar low temperature scattering behavior in these CMR compounds.

3.4. Magnetic field dependent thermoelectric power

In order to analyze the TEP data, the crystal structure of the material must be taken into account. Mira et al. [34] have shown that $Pr_{2/3}Sr_{1/3}MnO_3$ clearly shows an anisotropic TEP behavior, which they attributed to the orthorhombic structure of the material. With increasing Sr doping in the present system, the crystal structure becomes less distorted and goes toward an orthorhombic to rhombohedral phase as discussed earlier. The temperature dependence of TEP for the $Pr_{0.65}Ca_{0.35-x}Sr_xMnO_3$ series is illustrated in Fig. 9. Due to their high resistivity, the TEP data for the samples $x < 0.15$ could not be accurately measured. All the measured samples show positive value of Seebeck coefficient (S) in the temperature range 80–300 K unlike La–Ca–K–Mn–O systems [25]. The Seebeck coefficients of the samples with $x \geqslant 0.15$ are found to shift toward more positive

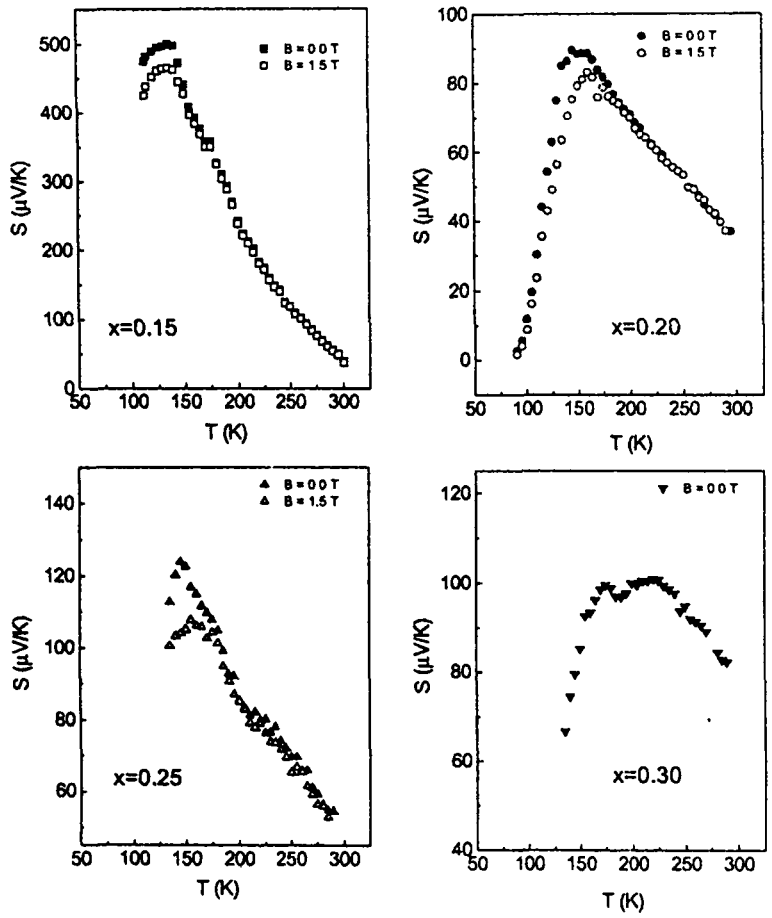

Fig. 9. Temperature dependent Seebeck coefficient (S) for $Pr_{0.65}Ca_{0.35-x}Sr_xMnO_3$ samples with $x = 0.15$, 0.20, 0.25 and 0 30.

with the decrease of x, i.e. with the increase of resistivity. In the $Pr_{0.65}Ca_{0.35-x}Sr_xMnO_3$ series, the decrease of Sr concentration does not affect much on the carrier concentration (Table 2). So the increase in S might attribute to the structural distortion [34] with the decrease of x. A peak is observed near a temperature T_s for all the measured samples. The peak is associated with the AFM–FM ordering below the Neel temperature (T_N). The value of T_s shifts to lower temperature with the decrease of Sr concentration (x). Around the peak temperature T_s, Seebeck coefficient (S) has been found to change with application of magnetic field (1.5 T). The magnetic field (1.5 T) decreases the S value indicating that spin ordering under magnetic fields decreases thermopower of the present manganite samples. It is interesting to observe that the temperature dependence of S data above $\theta_D/2$ follows the Mott's equation [23]:

$$S = \frac{k_B}{e}\left(\frac{E_s}{k_B T} + \alpha'\right), \tag{11}$$

where E_s is the activation energy obtained from the TEP data and α' is a parameter related to the kinetic energy of polarons [35]. The estimated values of E_s (listed in Table 2) have been observed very much lower than E_p. The large difference between E_p and E_s also supports SPH conduction mechanism at the high temperature ($T > T_{MI}$) phase [23]. The change in TEP value with the increase of cationic size for the same Mn valence

state cannot be attributed to a change of carriers from electrons to holes. The high sensitivity of the TEP data to the composition variation of $Pr_{0.65}Ca_{0.35-x}Sr_xMnO_3$ suggests that the strong band structure modifications induced by the size effect are correlated to the overlapping of the atomic Mn–O orbitals. A possibility of interpretation is an evolution of the Jahn–Teller effect, which is larger for the smaller x values (smaller ionic radii of the interpolated cation). On the other hand, it cannot be totally ruled out that the effect of the Coulombian localization, which is often invoked for the CMR properties, also plays a role in the TEP values.

Finally, we would like to mention that in the high temperature semiconducting region (above 220 K), the charge carriers are no more itinerants and the transport properties are governed by the thermally activated carriers (i.e. polarons, which are formed as a result of strong electron–lattice coupling). Above the CO temperature (T_{CO}), the CMR systems are mostly PM and no ferromagnetic cluster exists within the system. So in the high temperature region, possibility of formation of CE bubble does not arise. Above all, the large difference between E_p and E_s signifies that convenient band transport does not occur above Curie temperature (T_c), rather an SPH is dominated by the carrier dependent mobility effects [36]. However, in the high temperature semiconducting phase some kind of clusters or islands might be formed. Such clusters, if formed, are PM. It has also been pointed out that much of the behavior of resistivity above the T_c is indicative of conduction by 'magnetic polarons' [37–39]. In this case, percolation theory could be applied. Considering the correlation of sites in a percolation cluster [40], it can be shown that the expression of conductivity is equivalent to that deduced from the Mott's VRH model [23]. The VRH has also been reported to be applicable in some manganite samples [26,36]. But the VRH model should generally be applicable in low temperature (<100 K) semiconducting phase. Therefore, polaron hopping conduction mechanism used in the present manuscript can, in general, be used to explain the high temperature (above the Curie temperature) semiconducting behavior of the manganite systems even if the conduction process is related to the incipient magnetic polaron or in other complicated mechanism yet to be explored

4. Summary and conclusions

A detailed magnetic field dependent study on the magnetization and transport properties of $Pr_{0.65}Ca_{0.35-x}Sr_xMnO_3$ has been reported. Structural studies show the decrease in orthorhombic distortion with the increase of Sr content. The system gradually transforms to a highly conducting metallic phase from a highly insulating CO/AFM phase with increase of x. MIT appears at higher fields for lower Sr concentration (x) for $x<0.1$ and without field for $x>0.1$. Metallic conduction in these systems follows $T^{2.5}$ dependence indicating the importance of electron–magnon contribution. Non-adiabatic SPH conduction is observed above MIT temperature of all samples The e-ph coupling constant and the ratio of polaron mass to rigid lattice effective mass indicate strong coupling in this system. An appreciable change in the Seebeck coefficient is observed with the application of magnetic field around the peak temperature which is associated with the AFM–FM ordering in these compounds. Formation of ferromagnetic clusters in the high temperature phase is not realized. However, the concept of magnetic polaron may be invoked to analyze the transport behavior of this phase.

Acknowledgements

The author (S. Taran) is grateful to Council for Scientific and Industrial Research (CSIR) for granting research fellowship. This work was supported by National Science Council of Republic of China under contract no. NSC 92-2112-M110-017.

References

[1] Y Tokura (Ed.), Colossal Magnetoresistive Oxides, Gordon and Breach, London, 1999

[2] C. Zener, Phys. Rev. 82 (1951) 403;
P.W. Anderson, H. Hasegawa, Phys. Rev. 100 (1955) 675;
J.B. Goodenough, Phys. Rev. 100 (1955) 564;
E.O. Wollan, W.C. Koehler, Phys. Rev. 100 (1955) 545;
P.G. deGennes, Phys. Rev. 118 (1960) 141.
[3] A. Banerjee, S. Bhattacharya, S. Mollah, H. Sakata, H.D. Yang, B.K. Chaudhuri, Phys. Rev. B 68 (2003) 186401.
[4] L.M. Rodriguez-Martinez, J.P. Attfield, Phys. Rev. B 54 (1996) 15622.
[5] H. Röder, J. Zang, A.R. Bishop, Phys. Rev. Lett. 76 (1996) 1356.
[6] A.J. Millis, B.I. Shraiman, R. Mueller, Phys. Rev. Lett. 77 (1996) 175.
[7] Y. Tomioka, A. Asamitsu, Y. Moritomo, H. Kuwahara, Y. Tokura, Phys. Rev. Lett. 74 (1995) 5108.
[8] C. Martin, A. Maignan, M. Herview, B. Raveau, Phys. Rev. B 60 (1999) 12191.
[9] D. Nicbieskikwiat, R.D. Sanchez, A. Canciro, J. Magn. Magn. Mater. 237 (2001) 241.
[10] M.R. Lees, O.A. Petrenko, G. Balakrishnan, D. McK. Paul, Phys. Rev. B 59 (1999) 1298.
[11] A. Moreo, S. Yunoki, E. Dogatto, Science 283 (1999) 2034.
[12] E. Dagotto, T. Hotta, A. Moreo, Phys. Rep. 344 (2001) 1.
[13] S. Mollah, H.L. Huang, P.L. Ho, W.L. Huang, C.W. Huang, C.P. Sun, J. -Y. Lin, S.J. Liu, Y.S. Gou, W.-H. Li, H.D. Yang, J. Magn. Magn. Mater. 265 (2003) 215.
[14] S. Mollah, C.P. Sun, H.L. Huang, P.L. Ho, H.D. Yang, J. Appl. Phys. 95 (2004) 6813.
[15] M.v. Zimmermann, C.S. Nelson, J.P. Hill, D. Gibbs, M. Blume, D. Casa, B. Keimer, Y. Murakami, C.-C. Kao, C. Venkataraman, T. Gog, Y. Tomioka, Y. Tokura, Phys. Rev. B 64 (2001) 195133.
[16] A.L. Malvezzi, S. Yunoki, E. Dagotto, Phys. Rev. B 59 (1999) 7033.
[17] J.B. Torrance, P. Lacorre, A.I. Nazzal, E.J. Ansaldo, Ch. Nidermayer, Phys. Rev. B 45 (1992) 8209.
[18] Y. Tomioka, A. Asamitsu, H. Kuwahara, Y. Tokura, J. Phys. Soc. Jpn. 66 (1997) 302.
[19] H.Y. Hwang, T.T.M. Palstra, S.-W. Cheong, B. Batlogg, Phys. Rev. B 52 (1995) 15046.
[20] A. Maignan, C. Martin, F. Damay, B. Raveau, Z. Phys. B 104 (1997) 21.
[21] Z. Jirak, S. Krupicka, Z. Simsa, M. Dlouha, Z. Vratislav, J. Magn. Magn. Mater. 53 (1985) 153.
[22] A.J. Millis, P.B. Littlewood, B.I. Shraiman, Phys. Rev. Lett. 74 (1995) 5144.
[23] N.F. Mott, E.A. Davis, in: Electronics Process in Non Crystalline Materials, Clarendon Press, Oxford, 1979.
[24] M. Jaime, M.B. Salamon, M. Rubenstein, R.E. Treece, J.S. Horwitz, D.B. Chrisey, Phys. Rev. B 54 (1996) 11914.
[25] S. Bhattacharya, S. Pal, R.K. Mukherjee, B.K. Chaudhuri, S. Neeleshwar, Y.Y. Chen, S. Mollah, H.D. Yang, J. Magn. Magn. Mater. 269 (2004) 359.
[26] M. Viret, L. Ranno, J.M.D. Coey, Phys. Rev. B 55 (1997) 8067.
[27] S. Pal, A. Banerjee, E. Rozenberg, B.K. Chaudhuri, J. Appl. Phys. 89 (2001) 4955.
[28] T. Holstein, Ann. Phys. (NY) 8 (1959) 343.
[29] I.G. Austin, N.F. Mott, Adv. Phys. 18 (1969) 41.
[30] P. Schiffer, A.P. Ramirez, W. Bao, S.W. Cheong, Phys. Rev. Lett. 75 (1995) 3336.
[31] G.J. Snyder, R. Hiskes, S. Dicarolis, M.R. Beasley, T.H. Geballe, Phys. Rev. B 53 (1996) 14434.
[32] J.M. De Teresa, M.R. Ibarra, J. Blasco, J. Garcia, C. Marquina, P.A. Algarabel, Z. Arnold, K. Kamenev, C. Ritter, R. von Helmolt, Phys. Rev. B 54 (1996) 1187.
[33] A. Banerjee, S. Pal, B.K. Chaudhuri, J. Chem. Phys. 115 (2001) 1550.
[34] J. Mira, A. Fondado, L.E. Hueso, J. Rivas, F. Rivadulla, M.A. López Quintela, Phys. Rev. B 61 (2000) 5857.
[35] K. Sega, Y. Kuroda, H. Sakata, J. Mater. Sci. 33 (1998) 1303.
[36] M. Jaime, M.B. Salamon, K. Pettit, M. Rubinstein, R.E. Treece, J. S Horwitz, D.B. Chrisey, Appl. Phys. Lett. 68 (1996) 1576.
[37] M. Sawicki, T. Dietl, J. Kossut, J. Igalson, T. Wojtowicz, W. Plesiewicz, Phys. Rev. Lett. 56 (1986) 508.
[38] R.M. Kusters, J. Singleton, D.A. Keen, R. McGreevy, W. Hayes, Physica B 155 (1989) 362.
[39] S. Wang, K. Li, Z. Chen, Y. Zhang, Phys. Rev. B 61 (2000) 575.
[40] G.P. Triberis, L.R. Friedman, J. Phys. C:: Solid State Phys. 14 (1981) 4631.

Available online at www.sciencedirect.com
SCIENCE DIRECT®
ELSEVIER
Journal of Magnetism and Magnetic Materials 269 (2004) 359–371
Journal of magnetism and magnetic materials
www.elsevier.com/locate/jmmm

Development of pulsed magnetic field and study of magnetotransport properties of K-doped $La_{1-x}Ca_{x-y}K_yMnO_3$ CMR materials

Sayani Bhattacharya[a], Sudipta Pal[a], R.K. Mukherjee[a], B.K. Chaudhuri[a,*], S. Neeleshwar[b], Y.Y. Chen[b], S. Mollah[c], H.D. Yang[c]

[a] *Department of Solid State Physics, Indian Association for the Cultivation of Science, Kolkata 700032, India*
[b] *Institute of Physics, Academia Sinica, Taipei, Taiwan, ROC*
[c] *Department of Physics, National Sun Yat Sen University, Kaohsiung 804, Taiwan, ROC*

Received 4 March 2003; received in revised form 18 July 2003

Abstract

Temperature-dependent magnetization, magnetoresistance and magneto-thermoelectric power of the K doped $La_{1-x}Ca_{x-y}K_yMnO_3$ type samples with $x = 0.3$ and $0 \leqslant y \leqslant 0.15$ has been studied. All the samples exhibit sharp metal–insulator transition (MIT) around T_p accompanied by a ferromagnetic (metallic) to paramagnetic (semiconducting) phase transition with a well-defined Curie temperature T_C (almost equal to T_p). Doping of monovalent K in the divalent Ca site of $La_{1-x}Ca_{x-y}K_yMnO_3$ drives the system from a high resistivity regime with lower T_p to a lower resistivity regime with higher T_p. Systematic increase of Curie temperature with increase of K doing is observed from the magnetization measurement down to 5 K. Low temperature resistivity (ρ) and thermoelectric power (Seebeck coefficient, S) data well fit the relations $\rho = \rho_0 + \rho_2 T^2$ and $S = S_0 + S_{3/2}T^{3/2} + S_4T^4$, respectively, signifying the importance of electron–magnon scattering process ($\rho_2 T^2$ and $S_{3/2}T^{3/2}$ term). On the other hand, the high temperature ($T > T_p$ upto 320 K) conductivity data satisfy the variable range hopping (VRH) model. For $T > 320$ K small polaron hopping model is more appropriate than the VRH model. High temperature thermoelectric power (TEP) data also indicates the formation of thermally activated small polarons. Even with very small change of y, the density of states at the Fermi level $N(E_F)$ changes considerably. The magnetotransport properties have been measured under pulsed magnetic field of microsecond duration. The decay time of the magnetic pulse within the sample (t) varies with field strength, which indicates that with change of magnetic field, ordering of the spin in the ferromagnetic regime changes.

PACS: 71.38.+i; 71.30.+h; 75.30.Vn

Keywords: Pulse magnetic field; K doping; Electron–magnon

1. Introduction

Colossal magnetoresistivity (CMR) in manganites is an example in which spin, charge and

*Corresponding author. Tel.: +91-33-247-34971; fax: +91-33-247-32805.
E-mail address: sspbkc@mahendra.iacs.res.in (B.K. Chaudhuri).

0304-8853/$ - see front matter © 2003 Elsevier B.V. All rights reserved.
doi:10.1016/S0304-8853(03)00632-2

lattice degrees of freedom conspire to produce a dramatic effect. This system exhibits many significant properties like metal–insulator transition (MIT), ferromagnetic (FM)—paramagnetic (PM) phase change, charge and orbital ordering (CO and OO), etc. depending on the charge density, temperature and atomic structure. Zener proposed that the spin structure and the electronic properties of $R_{1-x}A_xMnO_3$ (R=rare earth metal, A= divalent element) were correlated via the double-exchange (DE) mechanism controlled by the motion of the e_g electrons from Mn^{3+} to Mn^{4+} sites [1]. However, Millis et al. [2] argued that the physics of manganites is dominated by the interplay between a strong electron–phonon coupling and the large Hund coupling effect that optimizes the electronic kinetic energy by the generation of a FM phase. Theoretically, they proved that the effective coupling $\lambda_{eff}(= E_{JT}/t_{eff})$ dominates the physics of the manganites, where E_{JT} is the static trapping energy and t_{eff} is an effective hopping that is temperature-dependent following *DE*. Above the Curie temperature (T_C), λ_{eff} could be greater than the critical value that leads to insulating behavior due to electron localization (caused by the splitting of the degenerate e_g levels at MnO_6 octahedra). Below T_C, λ_{eff} becomes smaller than the critical value and hence metallic behavior is induced. Moreover, other factors viz. average sizes of the R and A site cations, mismatch effect, vacancy in R and Mn sites and the oxygen stoichiometry [3] also play a crucial role. Till now, most of the studies had been concentrated on the divalent ion doped $R_{1-x}A_xMnO_3$ (A = Ca, Sr, Pb, Ba, etc.) compounds and many of these samples crystallize in an orthorhombically distorted perovskite structure (O′-type; $c/2<a<b$; space group Pbmn) with a cooperative ordering of Jahn–Teller distorted $Mn^{3+}O_6$ octahedra [4]. In contrast, there are only few reports of monovalent alkali-metal ion doped compounds [5–8]. Monovalent alkali doping on $LaMnO_3$ can lead to different consequences. Because of the larger valence difference between La^{3+} and alkali-metal ions [7], fewer impurity ions (K ions) are needed to achieve a specific carrier concentration and larger random-potential fluctuations are experienced by the electrons in the σ^*-bond. Consequently, it will cause less inhomogeneity. Since the valence state of the alkali-metal ions is +1, substitution of these ions affect the ratio of $Mn^{3+}(t_{2g}^3e_g^1 \cdot S = 2)$ and $Mn^{4+}(t_{2g}^3e_g^0 \cdot S = 3/2)$ ions which ultimately also affects the DE mechanism

In this paper, we have used pulsed magnetic field of short duration to study the transport properties of the selected samples, which gives identical results with those obtained under DC magnetic field. Earlier Date [9] used a single pulse to study magnetization and resistivity at different magnetic field. Obviously, the advantage of the pulsed field technique is that one can measure transport and magnetic properties low and high magnetic fields, using relatively an easy process without using superconducting magnet Moreover, in the present experimental setup, data can be collected within very short interval of time so that heating effect due to eddy current is not very effective [9]

In this work, we have prepared a novel manganite series $La_{1-x}Ca_xMnO_3$ where Ca^{2+} ions have been partially replaced by K^+ ions. Experimental data both in the high temperature ($T > T_p$) and low temperature ($T < T_p$) phases have been analyzed with theoretical models used in our earlier work [10,11]. Momentary excitation of the magnetic spins with pulsed field and the corresponding time of their return to the normal state (relaxation time) has also been measured indicating spin ordering in the sample.

2. Experimental

2.1 Sample preparation

$La_{1-x}Ca_{x-y}K_yMnO_3$ type samples (with $x = 0.3$ and $y = 0.0$, 0.05, 0.1, 0.15) were prepared by a standard ceramic processing technique [12] Well-mixed stoichiometric mixtures of La_2O_3, CaO, K_2CO_3 and $(CH_3COO)_2Mn$, $4H_2O$ (each of purity >99%) were first heated to 773 K and then to 1073 K for 5 h with intermediate grinding and then again annealing at 1173 K for 48 h. The sintered powder thus obtained was ground, palletized and annealed again at 1073 K for 72 h and then furnace cooled to room temperature. X-ray powder diffraction study has been made with CuK_α

radiation for structural study and the magnetization of the samples are measured by a SQUID magnetometer in the temperature range 4–300 K.

2.2. Arrangement for resistivity measurement under pulsed magnetic field

For the magnetoresistance study under pulsed field, we used a lab-made setup of a pulsed magnetic field produced in an air-core solenoid coil by sudden discharge of a capacitor bank (Fig. 1). The sample was mounted on the tail-end part of the modified closed cycle helium cryostat (Displex, Air Products). For good electrical contacts gold electrodes (films) were first made on the sample surface by vacuum sputtering technique and the electrical contacts of the leads and the sample were made with good-quality quickly drying silver paints. To avoid the induction effect (spurious) that arises due to the introduction of a low resistive sample into the magnetic field, data were taken at the peak of the pulsed field where induction effect is zero. The sample placed nearly at the center of the solenoid coil feels a pulsed magnetic field in a vertical direction whenever a surge of current passes through the coil. The capacitor voltage is changed with the help of a variac to get different magnetic field strengths In the present case, we have measured with a maximum magnetic field of 3.2 T and between 350 and 15 K. The peak value of the magnetic field is measured utilizing the procedure discussed elsewhere [12]. To minimize the heating effect due to eddy current produced by pulse field, the sample was mounted in parallel to the direction of magnetic field so that the effective area of the sample perpendicular to the field is very small [9]

3. Results and discussion

3.1. Structural studies with X-ray diffraction

X-ray powder diffraction (XRD) data of the samples at room temperature were recorded in a Philips PW1710 diffractometer using CuK_α radiation with Ni filter. The XRD pattern of two samples one without K ($y = 0.0$) and the other

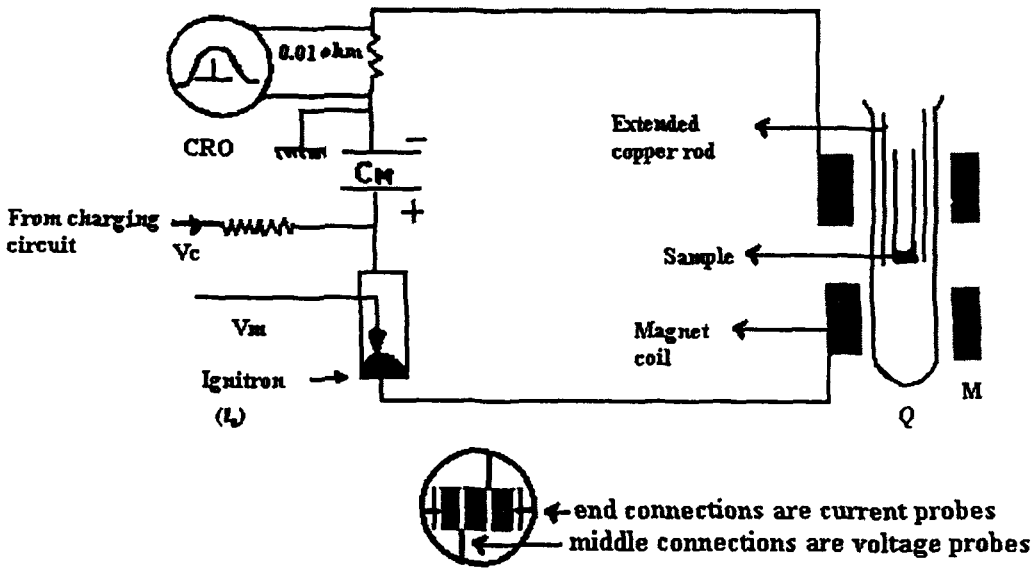

Fig 1 Circuit diagram for pulsed magnetic field generation. *M* Magnet coil, C_M. Main capacitor and *Q* Quartz tube, CRO Digital storage oscilloscope

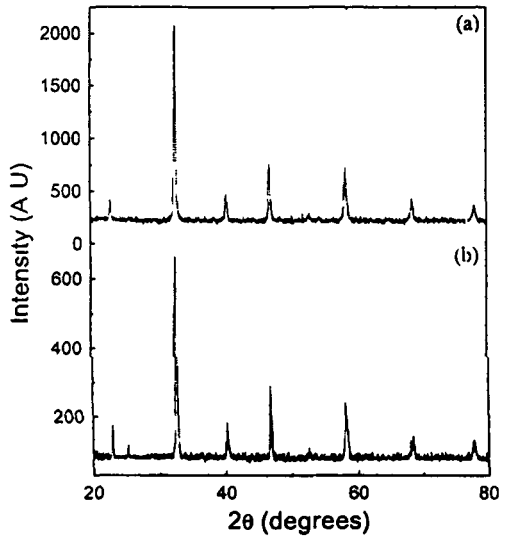

Fig. 2 XRD pattern of the sample $La_{1-x}Ca_{x-y}K_yMnO_3$ taken at room temperature with CuK_α radiation: (a) with $x = 0.3$ and $y = 0.0$ and (b) with $x = 0.3$ and $y = 0.15$.

Table 1
Crystallographic data of $La_{0.7}Ca_{0.3-y}K_yMnO_3$

y	a (Å)	b (Å)	c (Å)	α (deg)	Structure
0.0	5.47	7.736	5.497	—	Orthorhombic (Pbmn)
0.05	5.46	7.728	5.501	—	Orthorhombic (Pnma)
0.10	5.50	—	—	60.32	Rhombohedral (R $\bar{3}$c)
0.15	5.54	—	—	60.27	Rhombohedral (R $\bar{3}$c)

with 15% K substitutions are shown in Fig. 2(a) and (b), respectively. It is clear from the diffraction pattern that the synthesized samples are single phase with no measurable impurity phases. Structural analyses of the samples were performed using the program DBWS. The refined values of the structural parameters are given in Table 1. It was observed that the undoped sample ($y = 0.0$) and the sample with 5% potassium shows an orthorhombic perovskite structure. Space group Pbmn and Pnma were, respectively, used in the refinement whereas, R $\bar{3}$c space group in the hexagonal axes was used for the other two K doped samples. It is clear from the analysis that K doping induces rhombohedral distortion, which is consistent with the previously reported results [5,6]. The transition from the orthorhombic phase to the rhombohedral phase due to K doping indicates that structural disorder decreases and hence Mn–O–Mn bond angle increases. The distortion in the MnO_6 octahedron becomes less with the Mn–O–Mn bond angle moving towards 180°. Less distortion in the crystal structure reduces the possibility of charge localization and hence samples become more conducting, which is further supported by resistivity data. In this regard it should be mentioned that Roy et al. [8] have shown that for the $La_{1-x}Na_xMnO_3$ systems, increased Na doping drives the structure to become more cubic, resulting in an increase of the one-electron bandwidth. Consequently, the possibility of greater overlapping is increased and hence greater conductivity is observed.

3.2. Magnetic properties

Fig. 3(a) shows the temperature-dependent magnetization (M) obtained in the zero-field-cooled (ZFC) and field-cooled (FC) processes with an applied field of 0.01 T for two typical samples ($y = 0.0$ and 0.10). The ZFC curve indicates the samples undergo a paramagnetic (PM) to FM phase transition and like T_p (discussed later), the Curie temperature T_C also increases with increasing K doping. This is explained by considering that with increasing K doping concentration (y), the ratio of Mn^{4+}/Mn^{3+} increases (discussed later) which favors the ferromagnetic DE interaction The number of ferromagnetically aligned domains supercedes the paramagnetically aligned background and hence percolation threshold is attained with increasing K doping. Hence the compound becomes FM throughout the temperature range We also see from the data that magnetization almost saturates for $y \geq 0.1$ and the net magnetic moment decreases with further increase of y (Fig. 3(b)). Almost similar result was explained by Roy et al. [8] as the completion of rhombohedral phase for $y \geq 0.1$ that contributes to the magnetization In the high doping regime the increase in Mn^{4+} ions favors the antiferromagnetic super-exchange interaction (Mn^{4+}–O–Mn^{4+}) over the DE interaction and hence magnetization decreases. The FC and ZFC data do not coincide at low temperatures indicating the presence of some randomly frozen in

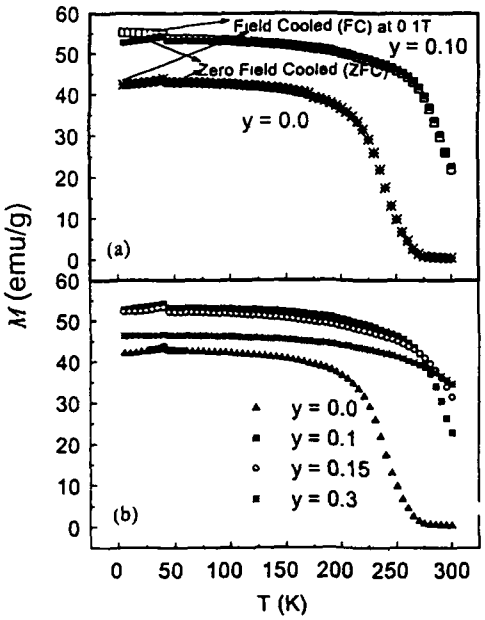

Fig. 3. (a) Zero field cooled (ZFC) and field cooled (FC) magnetization (M) at 0.1 T of $La_{0.7}Ca_{0.3-y}K_yMnO_3$ ($y = 0.0$ and 0.10) as a function of temperature. (b) Field Cooled $La_{0.7}Ca_{0.3-y}K_yMnO_3$ for different K concentrations (y) at 1000 G

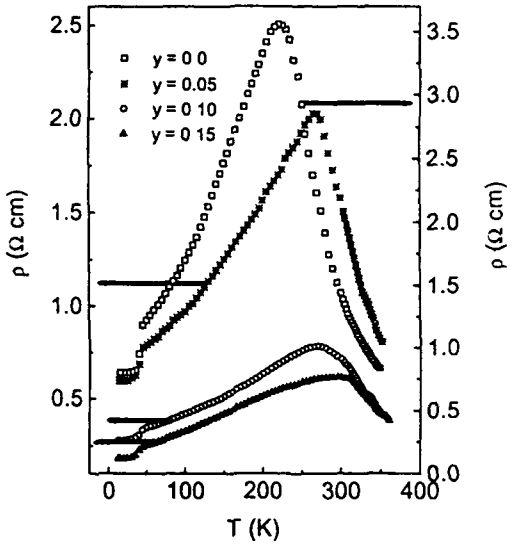

Fig. 4. Resistivity vs. temperature plot at zero magnetic field for different K concentrations.

magnetic clusters. This illustrates that there are possibly large ferromagnetic regions with multi-domain structure and magnetic clusters for $T < T_C$. With increasing magnetic field the magnetic moment value increases rapidly which can be attributed to the FM domain growth under applied field. For a similar kind of sample $La_{0.82}K_{0.08}MnO_{2.89}$ (LKMO), Das et al. [13] have shown that the resultant moment at 14 K is canted at an angle of ~25–27° with respect to [0 0 1] crystallographic axis. The moment values obtained from the magnetization measurements are considerably lower than the values expected for fully aligned Mn spins, which could be due to the disorder induced by the lanthanum and oxygen vacancies. In the low temperature ferromagnetic phase, an anomaly in the magnetic moment is seen around 40 K for all the samples. Such an anomaly has also been reported earlier in composites of La–Ca–Mn–O with $SrTiO_3$ [14] as well as in some substituted La–Ca–Mn–O system. Ju and Shon [15] explained this anomaly on the basis of local microscopic magnetic inhomogeneties arising from the variation in the Mn oxidation state. On the other hand, in Ce doped La–Sr–Mn–O composites, this type of kink has been explained on the basis of the presence of the paramagnetic MnO_2 phase in the compound [16]. In the resistivity vs. temperature plot (Fig. 4 shown later) a corresponding drop in the resistivity is also observed for all the samples which further confirms the existence of this anomaly, which might be due to the same reason as mentioned above. It is also noticed that the strength of this anomaly decreases with increase of K concentration. Room temperature XRD study, however, does not indicate the presence of any paramagnetic MnO_2 phase in the sample. Approximately the same observed values of T_p and T_C (Table 2) indicate good quality of the samples with negligible grain boundary effect.

3.3. Transport properties

3.3.1. Magnetic field-dependent resistivity

All the samples with different K concentrations ($y = 0.0$, 0.05, 0.1, 0.15) show a metallic behavior (i.e. $d\rho/dT > 0$) at low temperatures and with rising temperature, a sharp MIT is seen at T_p, very close to the corresponding Curie temperature T_C

Table 2
Some important data of all the prepared samples from the magnetization and resistivity measurements made in presence and in absence of pulsed magnetic field

y	Mn^{4+}/Mn^{3+}	M (emu/g) ($B = 9.67$ kG) at $T = 300$ K	ρ (Ω-cm)		T_p (K) $B = 0$ T	T_C (K) $B = 0$ T
			$T = 300$ K	$T = T_p$		
0 0	0.428	3 949	1 44	3 24	220 0	220 0
0 05	0.538	15 686	1 58	2 03	280 0	278 5
0 10	0.666	39 903	0 71	0 78	291 5	290 5
0 15	0.818	47.387	0.55	0 61	299.5	295 9

of the sample (Fig. 4). The maximum resistivity ρ_{max} (peak value) decreases and T_p shifts to higher temperature as y increases (Table 2). This increase in conductivity with K doping is considered to be associated with the increase of the ratio of Mn^{4+}/Mn^{3+}, which in turn contribute to the enhancement of holes in the e_g band. This is in accordance with the suggestions made by others [8]. The values of Mn^{4+}/Mn^{3+}, with increasing y, obtained from the valency calculations (Table 2), supports this argument. The cation valency distribution can be represented as $La^{3+}_{1-x}Ca^{2+}_{x-y}K_y(Mn^{3+}_{1-(x+y)}Mn^{4+}_{x+y})O_3$. Hence, y amount increase of K ions will result in a $(x + y)$ amount increase in Mn^{4+} ions and consequently, a small amount of K doping will cause a large number of charge carriers and thus resistivity will be decreased. Rhombohedral distortion introduced by K doping is also an important contributor to the increase of T_C. Similar behavior is also observed with Na doped samples.

Temperature dependence of resistivity measured both in presence and in absence of pulsed magnetic field (maximum 3.2 T) on two typical samples with $y = 0.05$ and 0.15 are shown in Figs. 5a and b. The corresponding changes in %MR as a function of temperature is also shown in the same figure. Similar behavior is also obtained for other samples of this group. Application of pulsed magnetic field causes a significant decrease in the resistivity shifting the resistivity peak to the high temperature region. During the field pulse, the spins favorably orient themselves and consequently the charge carriers suffer less scattering showing a decrease in resistivity. Interestingly, we found that the thermal variation of resistivity measured under constant

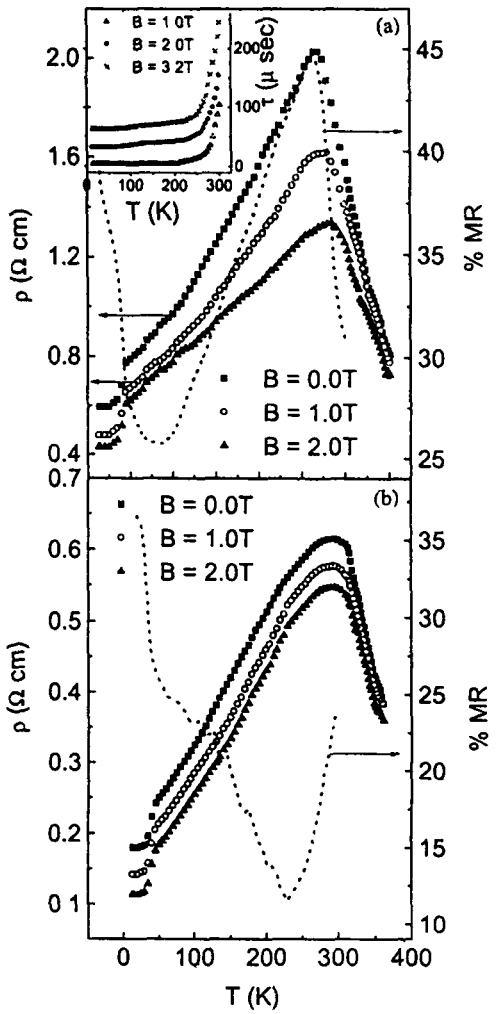

Fig 5 Resistivity and % MR vs temperature plot of (a) $La_{0.7}Ca_{0.25}K_{0.05}MnO_3$ and (b) $La_{0.7}Ca_{0.15}K_{0.15}MnO_3$ with different strengths of the pulsed magnetic fields (a) Inset shows the relaxation time (τ) vs temperature plot for the $y = 0.05$ sample

DC field (1.5 T) is similar to that measured under pulsed field. However, some interesting temperature-dependent relaxation time behavior (time taken by the sample to return to the normal, i.e. zero field state after the pulsed field is switched off) is noticed. The plot of such relaxation time (τ) as a function of temperature for a typical sample (with $y = 0.05$) is shown in the inset of Fig. 5a. It is seen that the relaxation time (τ) depending on magnetic field strength is related to the magnetic spin ordering and falls sharply around T_C and remains almost constant in the low temperature FM phase (Fig. 5a inset). Similar results are also found for the other samples. Nearly constant value of (τ) in the ferromagnetic region indicates most ordered state behavior. In this regard it can be mentioned that, with the application of magnetic field or lowering the temperature below MIT, the FM clusters embedded in the paramagnetic matrix form a connecting path and hence percolation occurs. In the present system, due to momentary excitation (pulsed field), some spins in the paramagnetic matrix become polarized to increase the number of FM clusters, hence enhancing the conductivity. After the withdrawal of the field, these momentarily formed FM clusters will come back to its normal (unpolarized) state with an observed relaxation time (τ). Hence by measuring the relaxation time, the mixed phase tendency of these manganites can be well studied. We believe this is a more important physical issue, for our future investigation, that pulse field measurement could probe.

A plot of T_p vs. alkali metal ion concentration (y) shows almost exponential rise of T_p with increasing potassium content (Fig. 6). With increasing y, ρ_{max} first decreases sharply and then gradually approaches a minimum value (Fig. 6). This observation actually reflects that in the low doping regime ($y \leqslant 0.1$) the Mn^{4+}/Mn^{3+} ratio is favorable to ferromagnetism and hence extension of the FM-metallic phase is obtained. Further increase in the doping level, increases Mn^{4+} concentration and the antiferromagnetic superexchange interaction (Mn^{4+}–O–Mn^{4+}) becomes predominant over the DE interaction and conclusively increase of T_p and decrease of ρ_{max} with increasing y become much smaller. Magnetoresistance $(\Delta\rho/\rho_0) \times 100[= \{\rho(H = 0) - \rho(H)\}/\rho(H = 0) \times 100]$ is found to show a peak around their respective MIT temperature T_p. The dotted lines in Figs. 5(a) and (b) represent % MR of the samples with an applied magnetic field of 3.2 T.

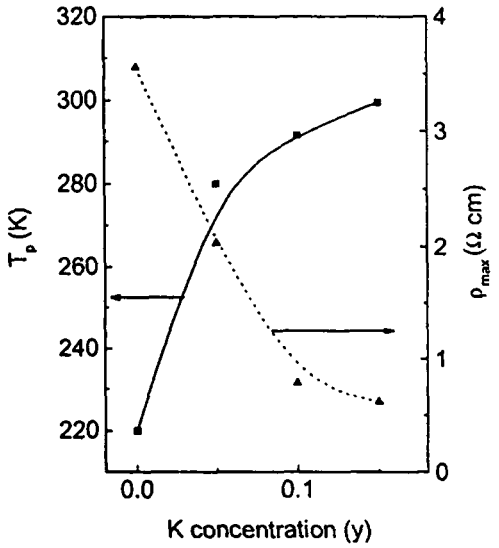

Fig. 6. Transition temperature T_p and maximum resistivity ρ_{max} vs. K concentration y plot for $B = 0$ T.

In the low temperature ferromagnetic metallic phase, the temperature dependence of the resistivity for all the samples both in presence and in absence of the pulsed magnetic field can be well fitted (Fig. 7) by the equation of the form

$$\rho(T) = \rho_0 + \rho_2 T^2, \quad (1)$$

where the temperature independent part ρ_0 is the resistivity due to domain, grain boundary and other temperature independent scattering mechanism [17,18]. Some authors have explained the $\rho_2 T^2$ by the electron–electron scattering process [18] but following Mott [19] $\rho \sim T^2$ behavior in a ferromagnet is due to magnon scattering. We also believe that the spin scattering cannot be neglected in the low T regime as the measured data can be best explained by electron-spin scattering. The best-fit parameters obtained from fitting the low temperature metallic part of the resistivity data with Eq. (1) are shown in Table 3. As expected, the temperature independent term (ρ_0) for all the

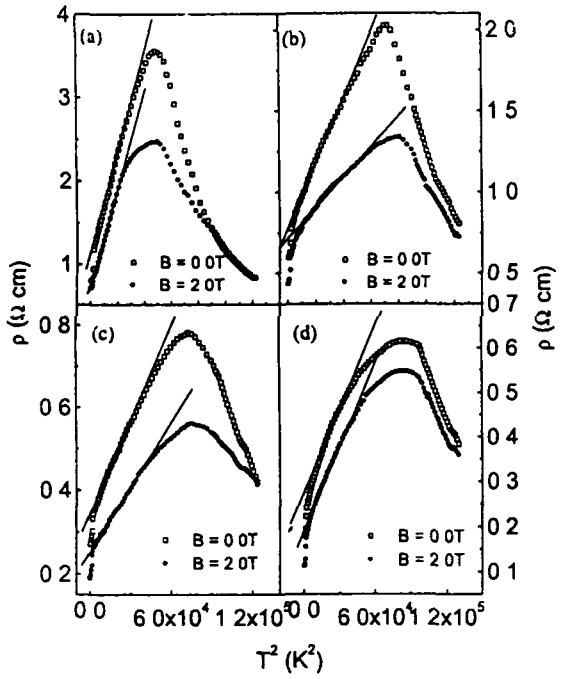

Fig 7 Linear fit of the low temperature (FM region) resistivity data with T^2 term (Eq (1)) for the sample (a) $y = 0\,0$, (b) $y = 0\,05$, (c) $y = 0\,1$ and (d) $y = 0\,15$

Table 3
The values of the parameters ρ_0 and ρ_2 of all the samples obtained from fitting the low temperature ($T < T_p$) resistivity data with Eq (1) in presence and in absence of magnetic field

y	ρ_0 (Ω-cm)		ρ_2 (Ω-cm K^{-2})	
	$B = 0\,0$T	$B = 2\,0$T	$B = 0\,0$T	$B = 2\,0$T
0 0	1 13	0 87	$6\,09 \times 10^{-5}$	$3\,40 \times 10^{-5}$
0 05	0 79	0 70	$1\,86 \times 10^{-5}$	$1\,16 \times 10^{-5}$
0 10	0 35	0 27	$6\,81 \times 10^{-6}$	$5\,92 \times 10^{-6}$
0 15	0 26	0 20	$6\,22 \times 10^{-6}$	$5\,83 \times 10^{-6}$

polycrystalline samples decreases significantly with the magnetic field but the influence of the magnetic field on the ρ_2 term is comparatively small. It is likely that the mechanism responsible for MR in the system, is the influence of the magnetic field on the ordering of magnetic domains As the pulsed magnetic field strength increases, the size of the domain boundary decreases and ρ_0 becomes smaller [20] The decrease of ρ_2 in a magnetic field

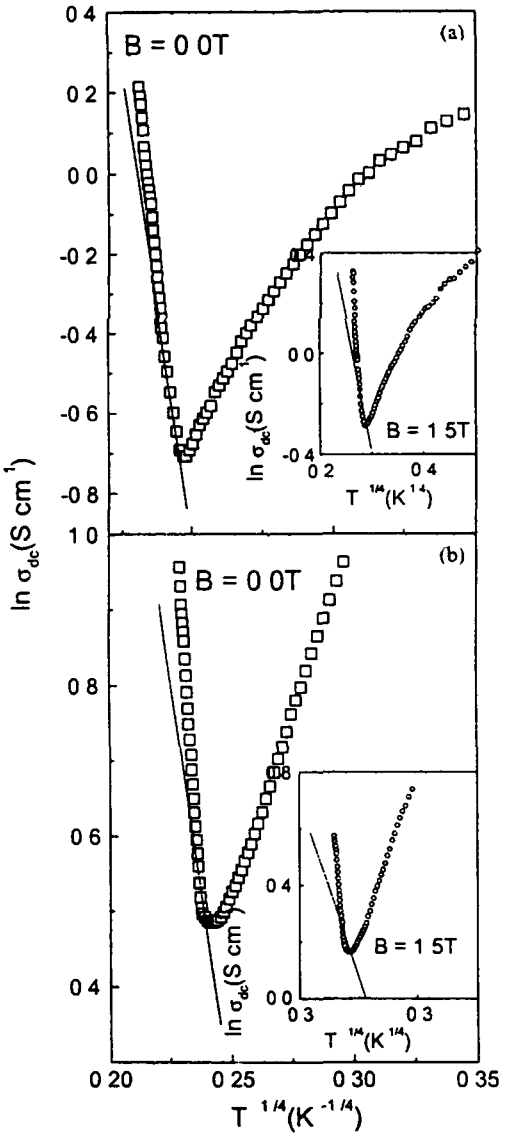

Fig 8 Variation of conductivity log σ_{dc} as a function of $T^{-1/4}$ (Eq (2)) for (a) $y = 0\,05$ with and (b) $y = 0\,15$ with $B = 0$T Insets show the plot with $B = 1\,5$T Solid lines are the best-fit to the VRH model (Eq (2))

is due to the suppression of spin fluctuation in the applied magnetic field (proportional to $B^{-1/3}$) [18]

All the resistivity data, above the transition temperature T_p, have earlier [21] been fitted with variable range hopping (VRH) of charge carriers Recently, Viret et al [22] and Pal et al [10] have applied VRH conduction mechanism in systems

like La–Ca–Mn–O, La–Mn–O, La–Pb–Mn–O, etc. at higher temperatures above T_p. Similarly our data between T_p and 320 K also fit the VRH model quite well. This model in three-dimensional cases, can be written as

$$\sigma_{dc} = \sigma_0 \exp[-(T_0/T)]^{1/4}, \quad (2)$$

where T_0 is a constant [$= 18\alpha^3/k_B N(E_F)$], α is the electron wave function decay constant, k_B is Boltzman's constant and $N(E_F)$ is the density of states at the Fermi level which can be calculated from the slope of the plot of $\log \sigma_{dc}$ vs. $T^{-1/4}$ curves [shown in Figs. 8(a) and (b)]. The best-fit occurs with $T_0 \sim 10^6$ for both La–Ca–Mn–O and La–Ca–K–Mn–O which is in good agreement with the previously reported results [10]. We have also calculated T_0 for different samples in presence of magnetic fields. T_0 is found to decrease with the increasing magnetic field strength. From Eq. (2) we also estimated $N(E_F)$ (Table 4) using $\alpha = 2.22\,nm^{-1}$ as used by Pal et al. [10]. The value of $N(E_F)$ are comparable to those obtained by Coey et al. [21] ($N(E_F) \sim 4 \times 10^{22}/eV\,cm^3$ for La–Ca–Mn–O system) and Pal et al. [10] ($N(E_F) \sim 5.99 \times 10^{22}/eV\,cm^3$ for La–Pb–Mn–O system). The $N(E_F)$ value for the present sample is found to be increasing with the application of magnetic field. It is noticed that for the K doped sample $N(E_F)$ is much higher than that of the undoped sample indicating appreciable increase in the number of charge carriers and consequently showing an increase in the conductivity of the K doped sample. Also the application of magnetic field decreases the localization length which in turn increases the number of delocalized charge carriers causing increased $N(E_F)$.

It should be mentioned here that the VRH model could not be extended to fit well the data above 320 K (between 320 and 350 K). Recently, it has been shown by Banerjee et al. [11] that the conductivity data between T_p and $\theta_D/2$ (θ_D being the Debye temperature) can only be well fitted with VRH model. The high temperature ($T > \theta_D/2$) resistivity data of the Cr doped and undoped La–Pb–Mn–O manganite samples can be well fitted with the thermally activated small polaron hopping (SPH) model. Similar behavior is also exhibited by the present K doped system. For the samples with higher T_p values (like the present samples), the VRH region is small. So it is rather difficult to judge which of the two models is most appropriate. It is, however, noticed that the high temperature ($T > \theta_D/2$) conductivity data between 320 and 350 K for the K doped samples (Figs. 9(a) and (b)) better fit the SPH model of Mott viz. $\rho/T = \rho_\alpha \exp(E_p/k_B T)$, where $\rho_\alpha = [k_B/\nu_{ph} N e^2 R^2 C(1-C)] \exp(2\alpha R)$ where N is the number of ion sites per unit volume (obtained from the density data), R is the average intersite spacing obtained from the relation $R = (1/N)^{1/3}$, E_p is the activation energy for hopping conduction estimated from the conductivity data, C is the fraction of sites occupied by a polaron, α is the electron wave function decay constant obtained from fitting the experimental conductivity data, ν_{ph} is the optical phonon frequency (estimated from the relation $h\nu_{ph} = k_B\theta_D$). We have replotted the resistivity curve as $\ln(\rho/T)$ vs. $1/T$ and from the slope of the curve the activation energy E_p is estimated (Table 4). The activation energies are found to decrease with increasing K doping

Table 4
Values of the density of states (DOS) at the Fermi level ($N(E_F)$), activation energies from resistivity and TEP data (E_p and E_S), polaron hopping energy (W_H) and the constant (α') of Eq (4) both in absence and in presence of a magnetic field (1 5 T)

y	$N(E_F) \times 10^{-21}$ ($eV^{-1}cm^{-3}$)		E_p (meV)		E_S (meV)		W_H (meV)		α'	
	$B = 0$ T	1 5 T	$B = 0$ T	1 5 T	$B = 0$ T	1 5 T	$B = 0$ T	1 5 T	$B = 0$ T	1 5 T
0 0	0 380	1 701	116 3	91 95	13 16	9 38	103 2	82 57	−0 61	−0 45
0)5	0 404	0 636	110 7	91 23	9 89	9 82	100 9	81 40	−0 50	−0 49
0 .0	0 822	2 705	99 07	88 46	8 38	8 32	90 69	80 15	−0 45	−0 43
0 15	1 265	4 609	92 52	82 14	8 01	7 81	84 50	74 33	−0 42	−0 41

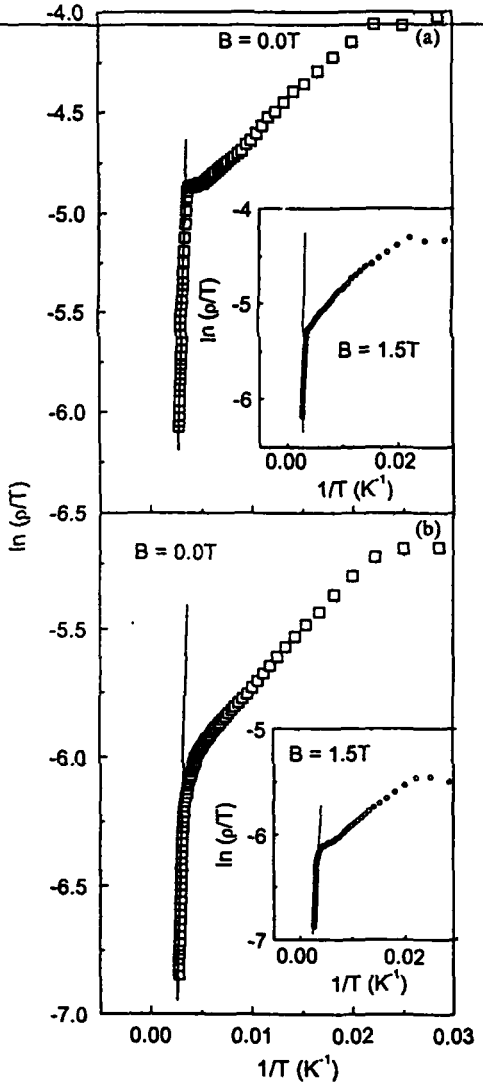

Fig. 9. Variation of $\log(\rho/T)$ as a function of $1/T$ for (a) $y = 0.05$ with and (b) $y = 0.15$ with $B = 0$ T. Insets show the plot with $B = 1.5$ T. Solid lines are the best-fit to the Mott's SPH model (see text).

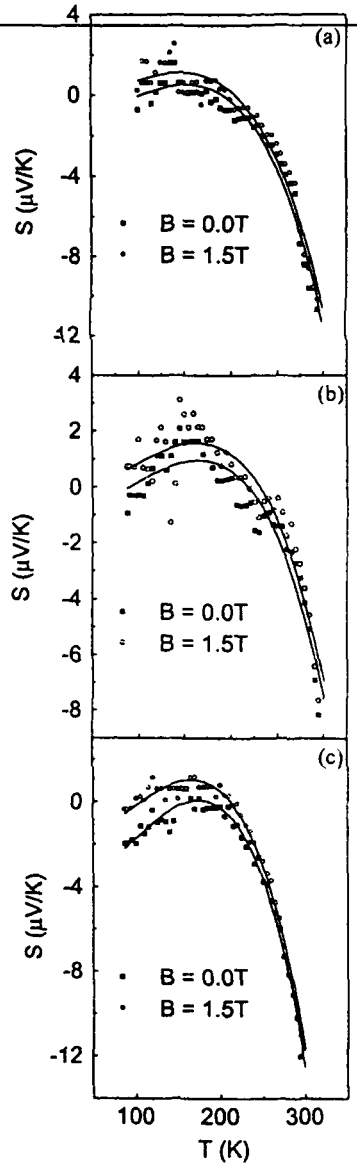

Fig. 10. Temperature and magnetic field ($B = 1.5$ T)-dependent Seebeck coefficient (S) of three different samples $La_{0.7}Ca_{0.3-y}K_yMnO_3$ with (a) $y = 0.05$, (b) 0.1 and (c) 0.15. Solid lines are the best-fit to the Eq. (3).

concentration and with the application of magnetic field. Actually, due to hole doping in the e_g band the delocalization of charge carriers occurs and hence the energy required to liberate a free carrier is reduced. Application of magnetic field enhances this delocalization thereby reducing the activation energy further.

3.3.2. *Magnetic field-dependent thermoelectric power (TEP)*

Magnetic field ($B = 0-1.5$ T)-dependent thermoelectric power (Seebeck coefficient, S) of the K doped $La_{0.7}Ca_{0.3-y}K_yMnO_3$ ($0.0 \leqslant y \leqslant 0.15$) system measured in the temperature range 80–300 K also

supports the conductivity results discussed above. Fig. 10 displays the temperature-dependent thermoelectric power of the samples with different values of $y = 0.05$, 0.1 and 0.15 in presence (1.5 T) and absence of magnetic field. All the K doped samples show a change in the sign of Seebeck coefficient. With the increase of K ions, S tends towards positive value. This increasing trend of S is seen upto $y = 10\%$ which can be attributed to the increase in the number of Mn^{4+} ions due to increasing hole concentration (as discussed above). For $y = 0.15$, the S value is marginally lower but shows the same nature as the other two samples. Addition of K ions causes more hole doping centers, which are localized in character and hence S value increases. This large value of thermopower arising from hole localization may occur due to the narrowing of e_g band and it also indicates distortion of the Fermi surface.

For all the samples, it is observed that with the application of magnetic field ($B = 1.5$ T), S value increases at low temperature and the difference between the two values $\Delta S[= S(0) - S(1.5)]$ decreases near T_p (where $S(0)$ and $S(1.5)$ are the value of S in zero and 1.5 T field). This indicates that spin ordering that occurs under magnetic field, increases thermopower of the present manganite samples. The temperature dependence of S below T_p can be fitted as before [23] with the relation of the form

$$S = S_0 + S_{1.5}T^{1.5} + S_4T^4, \quad (3)$$

where S_0 is a constant term having no physical origin. The low temperature (FM phase below T_p), TEP data of the samples (with $y = 0.0-0.15$) are well fitted with Eq. (3) (some are shown in Figs. 10a–c). From the corresponding fitting parameters shown in Table 5, we find $S_{1.5} \gg S_4$ which suggests that at low temperatures, S is mainly governed by the second term in Eq. (3) arising due to electron–magnon scattering contribution. It is also shown above from the low temperature (FM phase) resistivity data (Eq. (1)) that the electron–magnon scattering process dominates the conduction mechanism in the alkali metal Na-doped manganites. Therefore, from the TEP measurements also, it is reconfirmed that electron–magnon scattering process is predominant in the low temperature FM phase. Decrease of electron–magnon scattering term ($S_{1.5}T^{1.5}$) under magnetic field suggests that spins get favorably oriented under magnetic field and hence electron-spin scattering possibility diminishes and the system behaves like a metal. But in the low temperature metallic phase (below T_p), the exchange coupling strength increases leaving the electrons more delocalized and this makes the system magnetic (ferro- or antiferromagnetic, depending on concentration, strength of exchange interaction). At high temperatures the T^4 term (spin wave fluctuation contribution) cannot be neglected and this term actually fits the data (with Eq. (3)) over the high temperature region. The parameter S_0 (Eq. (3)) is found to increase in presence of magnetic field. However, the interdependency of the parameters S_0, $S_{3/2}$, etc. is not well known and needs further study.

More interesting result is obtained from the high temperature regime ($T > \theta_D/2$) TEP data where there is disorder and localization. In this region

Table 5
The values of the parameters S_0, $S_{1.5}$ and S_4 obtained from fitting the low temperature (ferromagnetic metallic phase) thermoelectric power (TEP) data of $La_{0.7}Ca_{0.3-y}K_yMnO_3$ ($y = 0-0.15$) with Eq. (3) both in presence ($B = 1.5$ T) and in absence ($B = 0$) of magnetic field (B)

y	S_0 (μV/K)		$S_{1.5}$ (μV/K$^{2.5}$)		S_4 (μV/K^5)	
	$B = 0.0$ T	1.5 T	$B = 0.0$ T	1.5 T	$B = 0.0$ T	1.5 T
0.00	−3.84	−3.71	2.34×10^{-3}	2.30×10^{-3}	-4.10×10^{-9}	-5.69×10^{-9}
0.05	−1.66	−0.60	1.85×10^{-3}	1.57×10^{-3}	-2.37×10^{-9}	-2.24×10^{-9}
0.10	−1.38	−0.64	1.76×10^{-3}	1.70×10^{-3}	-1.89×10^{-9}	-1.86×10^{-9}
0.15	−4.72	−2.59	3.34×10^{-3}	2.72×10^{-3}	-3.09×10^{-9}	-2.87×10^{-9}

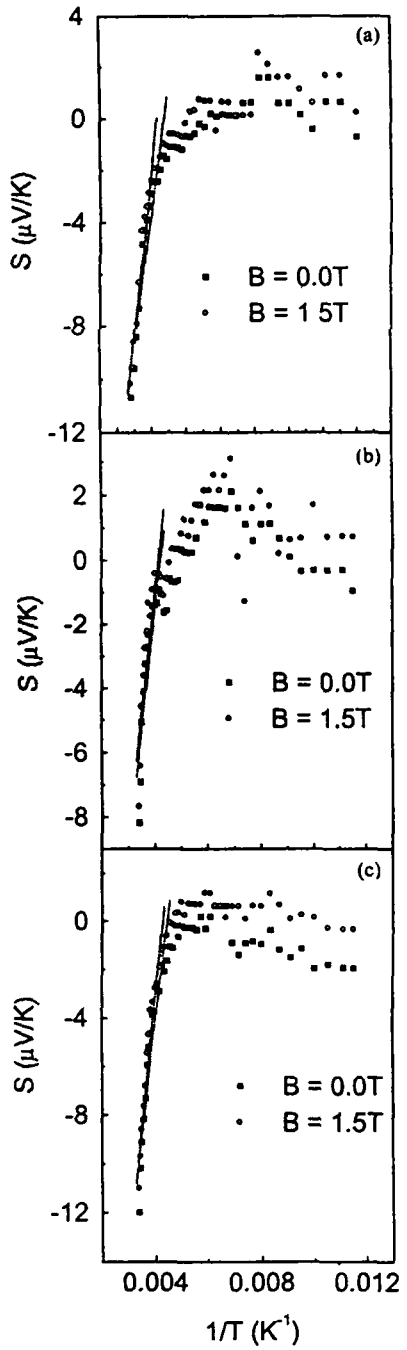

Fig 11 The Seebeck coefficient S vs $1/T$ plot for four different $La_{0.7}Ca_{0.3-y}Na_yMnO_3$ samples with (a) 0 05, (b) 0 1 and (c) 0 15 Solid lines are the best-fit to the Mott's model (Eq (4))

TEP data fits excellently with Mott's well-known equation of Seebeck coefficient based on polaron hopping, viz.

$$S = k_B/e[E_S/k_BT + \alpha'], \quad (4)$$

where E_S is the activation energy obtained from the TEP data and α' is a constant related to the kinetic energy ($\approx k_BT\alpha'$) of the polarons (carriers) For $\alpha' < 1$ small polaron hopping conduction occurs, while for $\alpha' > 2$ the conduction involves large polarons Fig 11 gives the S vs $1/T$ plots for all the samples both in presence and in absence of magnetic field Solid line gives the best-fit of the experimental data with Eq (4) From the slope of S vs $1/T$ curves, we obtain the values of activation energy E_S of the samples shown in Table 4. The constant α' is obtained from the intercept of the plotted curves (Table 4) The estimated values of α' (from Eq (4)), indicated $\alpha' < 1$ for both zero and 1.5T magnetic field Therefore, small polaron hopping conduction mechanism is also supported by the high temperature ($T > T_p$) TEP data

With the application of magnetic field, we noticed (Table 4) that polaron hopping energy ($W_H = E_p - E_S$) and polaron binding energy decreases. This indicates that with increasing K concentration the system becomes more metallic and hence the polaronic conduction regime is gradually converted to electronic conduction regime. This is an interesting observation from the study of K doped manganite system. Similar result is also obtained with Na doped system [24]

4. Conclusion

In conclusion, magnetic and magnetotransport properties of $La_{1-x}Ca_{x-y}K_yMnO_3$ for $x = 0.3$ and $0 \leqslant y \leqslant 0.15$ measured under pulsed magnetic field (0.0–3.2 T) shows monovalent alkali metal K doping in La–Ca–Mn–O system drives the system towards higher conductivity and higher Curie and metal–insulator transition temperature region The low temperature resistivity and TEP data signify the importance of electron–magnon scattering whereas the high temperature transport properties are mainly governed by the small polaron hopping

mechanism. Since both T_C and T_p can be varied around room temperature only by little increase of K at the Ca site, the present K doped system might be a potential candidate for device applications. We also like to state that the pulsed field technique, used in the present measurement, is a convenient technique, which would be very useful for measuring the magnetotransport properties of rare earth manganites, thin films, superconducting and other related materials of current interest. The temperature, magnetic field dependent relaxation time (τ) observed in pulsed field may also be used to determine the field-dependent spin ordering in the low temperature ferromagnetic phase. The relaxation time is also found to be dependent of the grain size of the sample. The pulsed field technique might be an important tool for elaborate investigation of all these features in the future.

Acknowledgements

The authors are grateful to the Department of Science and Technology, Government of India, for financial support. One of the authors (BKC) is also grateful to the NSC, Taiwan for the partial financial support during his stay at the Department of Physics, NSYSU, Taiwan.

References

[1] C. Zener, Phys. Rev. 82 (1951) 403.
[2] A.J. Millis, P.B. Littlewood, B.I. Shraiman, Phys. Rev. Lett. 74 (1995) 5144.
[3] J.M. Gonzalez-Calbet, E. Herrero, N. Rangavittal, J.M. Alonso, J.L. Martinez, M. Vallel-Kegi, J. Solid State Chem. 148 (1999) 158;
N. Abdelmoula, K. Guidara, A. Cheikhrouhou, E. Dhahri, J.C. Joubert, J. Solid State Chem. 151 (2000) 139.
[4] J.A.M. van Roosmalen, P. van Vlaanderen, E.H.P. Cordfunke, J. Solid State Chem. 114 (1995) 516.
[5] C. Boudaya, L. Laroussi, E. Dhahri, J.C Joubert, A Cheikhrouhou, J. Phys.: Condens. Matter 10 (1998) 7485
[6] G.H. Rao, J.R. Sun, K. Bärner, N. Hamad, J Phys Condens. Matter 11 (1999) 1523.
[7] N. Abdelmoula, A. Cheikhrouhou, L. Reversat, J Phys Condens. Matter 13 (2001) 449.
[8] S. Roy, Y.Q. Guo, S. Venkatesh, N. Ali, J Phys Condens. Matter 13 (2001) 9547
[9] M. Date, High Field Magnetism, North-Holland, Amsterdam, 1983.
[10] S. Pal, A. Banerjee, E. Rozenberg, B K Chaudhuri, J Appl. Phys. 89 (2001) 4955.
[11] Anitra Banerjee, S. Pal, B.K. Chaudhuri, J Chem Phys 115 (2001) 1550.
[12] S. Bhattacharya, A. Banerjee, S Pal, R K Mukherjee, B.K. Chaudhuri, J. Appl. Phys. 93 (2003) 356,
S. Bhattacharya, A. Banerjee, S Pal, P Chatterjee, R K Mukherjee, B.K. Chaudhuri, J. Phys Condens Matter 14 (2002) 10221.
[13] A. Das, M. Sahana, S.M. Yusuf, L Madhav Rao, C. Shivkumara, M.S. Hegde, Mater Res Bull 35 (2000) 651.
[14] D. Das, P. Chowdhury, R.N. Das, C M. Srivastava, A K Nigam, D. Bahadur, J. Magn. Magn. Mater. 238 (2002) 178;
D.K. Petrov, L. Krusin-Elbaum, J.Z. Sun, C. Field, P.R Duncombe, Appl. Phys. Lett. 75 (1999) 995.
[15] H.L. Ju, H. Sohn, J. Magn. Magn Mater. 167 (1997) 2041.
[16] J.R. Gebhardt, S. Roy, N. Ali, J. Appl Phys 85 (1999) 5390.
[17] G. Jeffrey Synder, R. Hiskes, S. Dicarolis, M.R Beasley, T.H. Geballe, Phys. Rev. B 54 (1996) R15606
[18] A. Urushibara, Y. Moritomo, T. Amira, A Asamitsu, G Kido, Y. Tokura, Phys. Rev. B 51 (1995) 14103
[19] N.F. Mott, Metal–Insulator Transitions, Taylor & Francis, London, 1974.
[20] P. Schiffer, A.P Ramirez, W Bao, S W Cheong, Phys Rev. Lett. 75 (1995) 3336
[21] J.M.D. Coey, M. Viret, L. Ranno, Phys Rev Lett 75 (1995) 3910.
[22] M. Viret, L. Ranno, J.M D. Coey, Phys. Rev. B 55 (1997) 8067.
[23] S. Anitra Banerjee, S. Pal, H D Bhattacharya, B K Yang, Chaudhuri, Phys. Rev. B 64 (2001) 104428
[24] S. Bhattacharya, S. Pal, A. Banerjee, H D Yang, B K Chaudhuri, J. Chem. Phys. 119 (2003) 3972

JOURNAL OF APPLIED PHYSICS VOLUME 95, NUMBER 11 1 JUNE 2004

Electronic Structure II — Borje Johansson, Chairman

Phase separation and huge enhancement of magnetoresistance in $Pr_{0.65}Ca_{0.35-x}Sr_xMnO_3$

S. Mollah,[a] C. P. Sun, H. L. Huang, P. L. Ho, and H. D. Yang[b]
Department of Physics, National Sun Yat Sen University, Kaohsiung 804, Taiwan

(Presented on 7 January 2004)

The electronic, magnetic, and thermal properties of polycrystalline $Pr_{0.65}Ca_{0.35-x}Sr_xMnO_3$ ($x=0-0.35$) perovskites have been elaborately investigated. A huge enhancement of magnetoresistance (MR) (10% at $H=100$ Oe and 99% at $H=0.5$ T) has been observed in an $x=0.1$ sample around the metal-insulator (MI) transition temperature ($T_{MI}\sim 80$ K) which is induced by the phase separation (PS). This study opens the possibility to search for the polycrystalline colossal magnetoresistive materials with a very high MR at low magnetic fields on the basis of PS phenomena for potential applications. © *2004 American Institute of Physics.*
[DOI: 10.1063/1.1687256]

The mixed-phase ground states of colossal magnetoresistive (CMR) materials containing ferromagnetic (FM) metallic and antiferromagnetic (AFM) insulating domains are found to have two origins.[1,2] (i) An electronic phase separation (PS) between phases with different densities that leads to nanometer scale coexisting clusters, and (ii) a disorder-induced PS with percolative characteristics between equal-density phases, driven by disorder near first-order metal-insulator (MI) transitions. This PS scenario is of particular importance and favorable for the existence of out-of-equilibrium features. A slight change of the fraction or the arrangement of the domains by the application of magnetic field, pressure, or irradiation can induce the percolation.[1-5] The time-dependent relaxation, two-level fluctuations, non-equilibrium fluctuations and relaxor ferroelectric behavior can emerge from the competition of the coexisting phases.[1-5] Here, the systematic investigations of resistivity (ρ), magnetization (M), and specific heat (C) of polycrystalline $Pr_{0.65}Ca_{0.35-x}Sr_xMnO_3$ ($x=0-0.35$) manganites are reported, and the huge enhancement of MR for the $x=0.1$ sample is discussed on the basis of a PS scenario. The details of sample preparation and characterization can be obtained in Refs. 6 and 7.

Figure 1(a) shows that the $Pr_{0.65}Ca_{0.35-x}Sr_xMnO_3$ manganites, respectively with $x=0-0.075$, 0.1, 0.125–0.3, and 0.35, demonstrate a semiconducting performance, a sharp MI transition at $T_{MI}\sim 80$ K, semiconducting followed by a metallic and a metallic behavior. This also reveals that the charge-ordered (CO) transition temperature (T_{CO}) decreases and the T_{MI} increases with the increase of x. Figures 1(b)–1(d) correspondingly illustrate the temperature dependence of M for the $x=0$, 0.1, and 0.35 samples at a fixed magnetic field of 1000 Oe. The increase of M at low temperatures for the $x=0$ sample with an AFM transition temperature of $T_N\sim 160$ K and $T_{CO}\sim 215$ K [Fig. 1(b)] may be associated with a small amount of nanosize FM component, since the changes of M are insignificant. However, the changes of M for the $x=0.1$ sample with an unusual magnetic ordering at $T_M^*\sim 45$ K and FM ordering at $T_C\sim 70$ K, as well as that for the $x=0.35$ sample with $T_C\sim 290$ K [Figs. 1(c) and 1(d)], are considerably large presumably due to the occurrence of FM transitions.

The variation of C with temperature (80–300 K) in the absence of a magnetic field for $Pr_{0.65}Ca_{0.35-x}Sr_xMnO_3$ ($x=0-0.35$) perovskites is demonstrated in Fig. 2. In the $x=0-0.125$ samples, both CO and AFM anomalies are clearly detected and are shifted correspondingly towards lower and higher temperatures with the increase of x. Conversely, only the FM anomalies are detected in the $x=0.15-0.35$ samples and move towards higher temperatures with the increase of x. No pronounced anomaly in C is detected in the $x=0.1$ sample around $T_{MI}\sim 80$ K, although a sharp MI transition is observed from the ρ vs T curve [Fig. 1(a)]. On the basis of the temperature variation of ρ, M, and C (Figs. 1 and 2), the obtained (T-x) phase diagram for $Pr_{0.65}Ca_{0.35-x}Sr_xMnO_3$ samples is shown in Fig. 3, where the paramagnetic insulating (PM-I), CO insulating (CO-I), AFM insulating (AFM-I), weak FM insulating (WFM-I), FM metallic (FM-M), and unusual magnetic metallic [(AFM+FM)M] states are clearly indicated.

To understand the mechanism behind the maximum MRR {$=-[\rho(H)-\rho(0)]/\rho(0)$ with $\rho(0)$ and $\rho(H)$ being the resistivities without and with a magnetic field H, respectively} of each sample, we plot MRR_{max} vs x in Fig. 4 for $Pr_{0.65}Ca_{0.35-x}Sr_xMnO_3$ series at low magnetic fields of 0.1,

[a]Permanent address: Department of Physics, Aligarh Muslim University, Aligarh-202002, India.
[b]Author to whom correspondence should be addressed; electronic mail: yang@mail.phys.nsysu.edu.tw

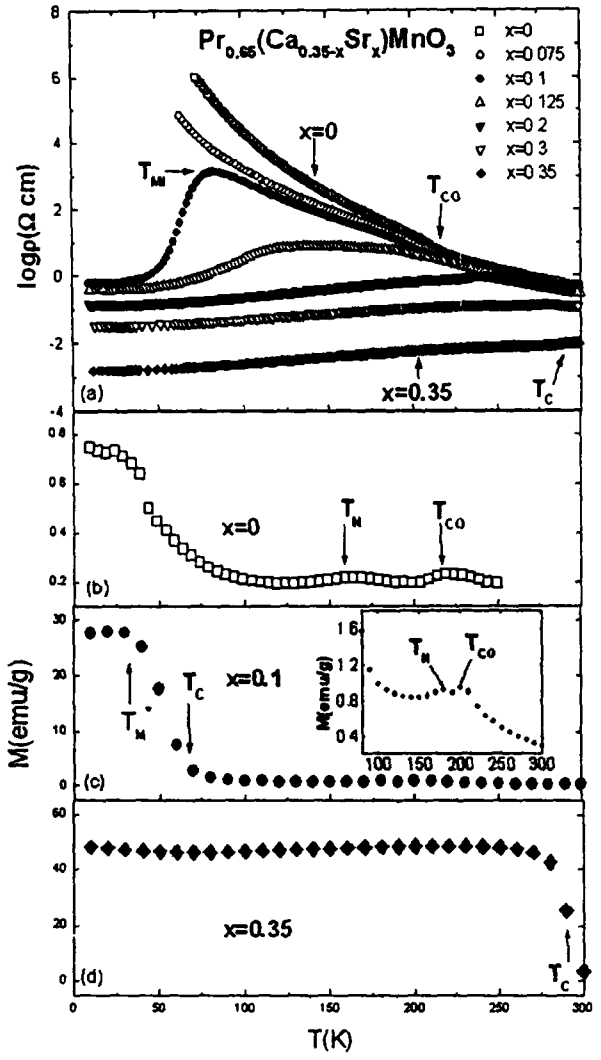

FIG. 1. Temperature variation of (a) $\log \rho$ of $Pr_{0.65}Ca_{0.35-x}Sr_xMnO_3$ ($x=0-0.35$) and M at 1000 Oe of $x=$ (b) 0, (c) 0.1, and (d) 0.35 samples. The inset of (c) shows the enlarged view.

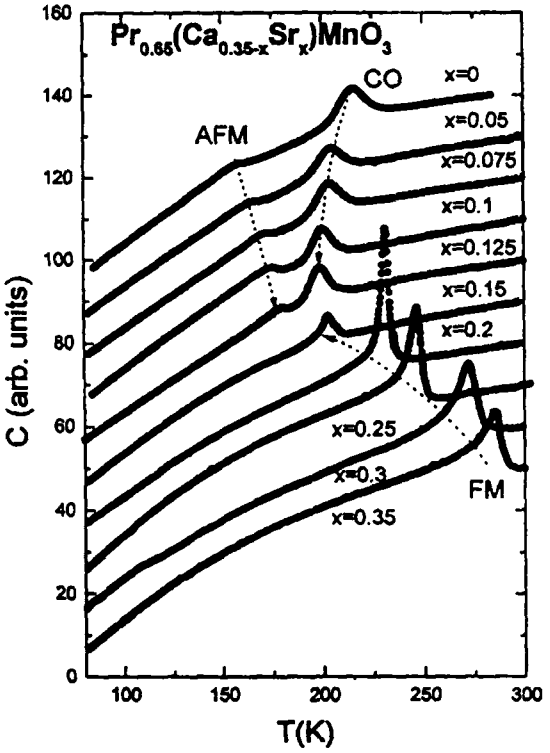

FIG. 2. Temperature dependence of specific heat (C) of $Pr_{0.65}Ca_{0.35-x}Sr_xMnO_3$ ($x=0-0.35$).

0.2, and 0.5 T. It is fascinating that the MRR_{max} for $x=0.1$ sample is as high as 50%, 80% and 99%, respectively, at low magnetic fields of 0.1, 0.2, and 0.5 T. Such a huge MRR at low magnetic fields in polycrystalline samples is rather unusual. For convenient comparison, some of the selective reported[8–10] results are listed in Table I. The inset of Fig. 4 shows the resistivity ratio versus low H for the mixed phase ($x=0.1$) and FM-M phase ($x=0.35$) samples. The resistivity ratio decreases sharply with the increase of the magnetic field for $x=0.1$ sample, whereas that is almost constant for $x=0.35$ sample. Thus, it is evident from Fig. 4 that the mixing phase in any sample plays a dominant role for higher MRR. Our experimental findings may be explained as follows.

Competition between a CO-I and FM-M phase is accomplished in $Pr_{0.65}Ca_{0.35-x}Sr_xMnO_3$ perovskites as the sample for $x=0$ exposes an insulating behavior, and that for $x=0.35$ reveals a metallic behavior [Fig. 1(a)] below room temperature. The doping of Sr introduces the nanosize FM clusters in the CO/AFM matrix of $Pr_{0.65}Ca_{0.35}MnO_3$. At a lower concentration of Sr, the number of nanosize FM clusters is very small, and the system resembles a regular array of charge short of Wigner crystal. It remains an insulator[11] as no percolation is possible through the AFM matrix and acts as a WFM-I (Figs. 1–3). With the increase of Sr concentration (x), the number as well as the volume of FM clusters increase, the percolation among some FM clusters starts, and the ρ decreases [Fig. 1(a)] When $x=0.1$, the number and volume of CO/AFM and FM clusters become nearly equal, causing disorder-induced PS with prominent and intrinsic inhomogeneities in the form of coexisting competing phases[2] and leading to MI transition and unusual magnetic ordering

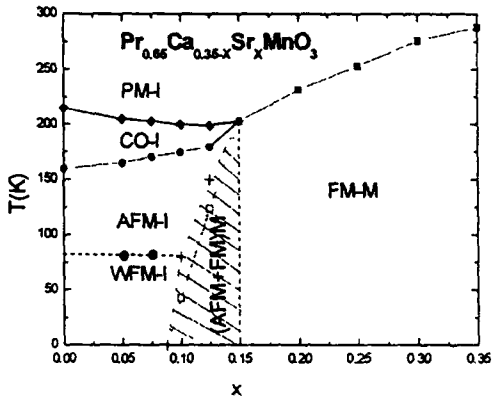

FIG 3 T-x phase diagram of $Pr_{0.65}Ca_{0.35-x}Sr_xMnO_3$ ($x=0-0.35$) samples

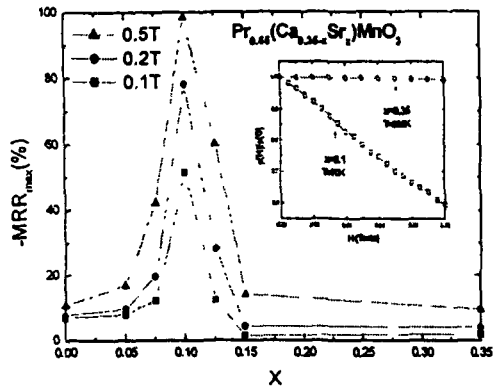

FIG. 4. Dependence of MRR_{max} on x at low magnetic fields. The inset shows the variation of $\rho(H)/\rho(0)$ with H (0–1000 Oe) for $x=0.1$ and 0.35 samples near their respective T_{MI}.

(Figs. 1–3). Therefore, the application of a low magnetic field (≤0.5 T) on the samples with $x\sim0.1$ is sufficient to partially melt the CO-I phases and facilitate to percolate the FM phases to enhance the metallicity leading to huge MRR (Fig. 4). The volumes, as well as the number of FM clusters, increase with further increase of x at the expense of those of CO/AFM clusters. Thus, practically all the matrix become FM, leaving embedded nanosize CO/AFM phases in the $x=0.35$ sample, which is metallic at all temperatures [Figs. 1(a) and 3] as the nanosize CO/AFM phases cannot block the percolation.[11]

In conclusion, the huge enhancement of magnetoresistance in $Pr_{0.65}Ca_{0.35-x}Sr_xMnO_3$ perovskites for $x\sim0.1$ at low magnetic fields (≤0.5 T) near the MI transition temperature is explained on the basis of PS scenarios. This study manifests an important clue that the samples exhibiting phase separation are one of the highly potential candidates for huge MR at low magnetic fields near respective T_{MI}.

TABLE I. MRR_{max}(%) of selective samples at different magnetic fields (≤1 T).

Sample composition	Sample type	T_C (K)	H (T)	MRR_{max} (%)	Reference
$La_{0.72}Ca_{0.25}MnO_3$	Thin film	220	1.0	53	8
$Nd_{0.55}Sr_{0.45}MnO_3$	Single crystal	275	1.0	25	9
$La_{0.7}Ca_{0.3}MnO_3$	Polycrystal	235	0.3	20	10
$Pr_{0.65}Ca_{0.25}Sr_{0.1}MnO_3$	Polycrystal	70	0.1	50	This work
$Pr_{0.65}Ca_{0.25}Sr_{0.1}MnO_3$	Polycrystal	70	0.5	99	This work

This work was supported by National Science Council of the Republic of China under contract No. NSC92-2112-M110-017.

[1] A. Moreo, S. Yunoki, and E. Dogatto, Science **283**, 2034 (1999)
[2] E. Dagotto, T. Hotta, and A. Moreo, Phys. Rep. **344**, 1 (2001).
[3] C. Simon, S. Mercone, N. Guiblin, C. Martin, A. Burlet, and G. Andre, Phys. Rev. Lett. **89**, 207202 (2002).
[4] P. Levy, F. Parisi, L. Granja, E. Indelicato, and G. Polla, Phys. Rev. Lett. **89**, 137001 (2002).
[5] D. Niebieskikwiat, R. D. Sanchez, and A. Caneiro, J. Magn. Magn. Mater. **237**, 241 (2001).
[6] S. Mollah, H. L. Huang, S. J. Liu, P. L. Ho, W. L. Huang, C. W. Huang, C. P. Sun, J.-Y. Lin, Y. S. Gou, W.-H. Li, and H. D. Yang, J. Magn. Magn. Mater. **265**, 215 (2003).
[7] Y.-K. Kuo, C. S. Lue, F. H. Hsu, H. H. Li, and H. D. Yang, Phys. Rev B **64**, 125124 (2001).
[8] K. Chahara, T. Ohno, M. Kasai, and Y. Kozono, Appl. Phys. Lett. 63, 1990 (1993).
[9] Y. Tomioka, T. Okuda, Y. Okimoto, A. Asamitsu, H. Kuwahara, and Y Tokura, J. Alloys Compd. **326**, 27 (2001).
[10] X. L. Wang, S. X. Dou, H. K. Liu, M. Ionescu, and B Zeimetz, Appl Phys. Lett. **73**, 396 (1998).
[11] A. L. Malvezzi, S. Yunoki, and E. Dagotto, Phys. Rev. B **59**, 7033 (1999)

PHYSICAL REVIEW B 68, 186401 (2003)

Comment on "Evidence for the immobile bipolaron formation in the paramagnetic state of the magnetoresistive manganites"

Anitra Banerjee,[1,*] S. Bhattacharya,[1] S Mollah,[2,3] H Sakata,[4] H D Yang,[2] and B K Chaudhuri[1,2,†]
[1]*Department of Solid State Physics, Indian Association for the Cultivation of Science Jadavpur, Kolkata-700 032 India*
[2]*Department of Physics, National Sun Yat-Sen University, Kaohsiung Taiwan 804, Republic of China*
[3]*Department of Physics, Aligarh Muslim University, Aligarh-202 002, India*
[4]*Department of Applied Chemistry, School of Engineering, Tokai University, Hiratsuka, Kanagawa 259-1292 Japan*
(Received 23 September 2002; revised manuscript received 7 March 2003, published 18 November 2003)

Recently, Zhao *et al.* [Phys. Rev. B 62, R11 949 (2000)] reported that bipolarons are formed in the high-temperature paramagnetic phase (above the metal-insulator transition temperature T_p) in oxygen-isotope-diffused epitaxial thin films of $La_{0.75}Ca_{0.25}MnO_3$ and $Nd_{0.75}Sr_{0.25}MnO_3$. But many earlier observations indicated the formation of small polarons in the said temperature range in different manganites. We have confirmed that the transport properties in the high-temperature phase ($T>T_p$) of the above manganites can be well explained by a small-polaron hopping mechanism and the consideration of bipolaron formation is inadequate. We have presented an explanation of the O-isotope effect on the transport properties of the same manganite sample studies by Zhao *et al.*

DOI: 10.1103/PhysRevB.68.186401 PACS number(s): 75.47.Gk, 71.38.−k, 73.43.Qt, 74.20.Mn

The electrical resistivity (ρ) is directly related to the double-exchange (DE) mechanism[1] between the parallel spins of neighboring Mn ions by the arbitration of O ions in $La_{1-x}A_xMnO_3$ manganites. However, the conduction mechanism in these mixed valence materials is a complex interplay between magnetic spin, charge ordering, and structural change.[2] On the other hand, the DE mechanism alone cannot explain the resistivity[3] and small polarons play a major role in the conduction mechanism in the high-temperature ($T>T_P$) regime.[4,5] Hall effect study also indicated small polarons in manganites.[6] But some of the research groups reported in favor of the formation of large polarons or bipolarons to explain the high-temperature ($T>T_P$) conductivity.[7] Zhao *et al.*[8] have studied the oxygen isotope effect on the resistivity of epitaxial thin films of $La_{0.75}Ca_{0.25}MnO_3$ (LCMO) and $Nd_{0.75}Sr_{0.25}MnO_3$ (NSMO) grown on ⟨100⟩ $LaAlO_3$ single-crystal substrates by the laser deposition technique, while the thermoelectric power (TEP) measurements were carried out on isotope-dependent LCMO ceramic pellets. These authors[8] concluded that small polarons formed localized immobile bound pairs (bipolarons) in the high-temperature ($T>T_P$) paramagnetic (PM) phase. The same authors also argued that the coexistence of small polarons and bipolarons in the PM state might lead to a dynamic phase separation into the insulating antiferromagnetically coupled region where the bipolarons resided and the ferromagnetically coupled region where the small polarons sat. But it is to be pointed out that the use of the bipolaron (BP) model is not possible in the present system. Bipolarons are formed in a system when two different defect centers (site) are responsible for the localization of charge carriers.[9–11] In turn, this implies the charge carriers to be two electrons in association and the BP hopping model assumes that carrier motion occurs by means of hopping over the potential barrier separating these two defect sites.[12] The Columbic correlation between these charged defect centers results in a correlation between the barrier height and the intersite separation, and thus the bipolaron hopping model is intimately linked with the correlated barrier-hopping- (CBH) type mechanism.[13] From recent work on the $La_{0.7}Ca_{(0.3-y)}Na_yMnO_3$ ($y=0.0$–0.3) series of samples[4] and similar other works on La-Ca-Mn-O,[5] we find that small-polaron theory can very well explain the conductivity and TEP data in the high-temperature ($T>T_p$) PM phase. Actually the existence of BP's is mainly observed in strongly correlated electron systems of highly disordered materials like semiconducting glasses, chalcogenide glasses, polymers, etc. The CBH mechanism was first used by Pike to explain the frequency-dependent (ac) conduction in scandium oxide.[13] Later application of the BP hopping model was proposed by Elliot to explain the ac conductivity of chalcogenide glasses.[11,12] Pramanik *et al* applied the CBH mechanism in the case of chalcogenide films.[14] Further, recently Brahma *et al* also used the BP hopping mechanism in polycrystalline-antimony-oxide-doped barium hexaferrites.[15] This is quite justified since in the said system two different groups of ions (Sb^{3+}/Sb^{5+} and Fe^{2+}/Fe^{3+}) coexist, which are responsible for the creation of two different types of defect centers.[15] But the colossal magnetoresistive (CMR) manganites of present interest are not so much highly disordered material as indicated by small electron-phonon (el-ph) coupling constant compared to the usual amorphous/disordered oxide semiconductors. Again, in the manganite system, lattice distortion arises due to the localization of the e_g electron of Mn^{3+} ions only.[16] Hence one can say that in rare-earth manganites only one type of defect center exists, which does not support the formation of bipolarons. Thus the transport data, particularly in the high-temperature semiconducting regime of the present system of interest, could only be explained by the small-polaron hopping model[16], on the other hand, the bipolaron hopping mechanism is inadequate to apply for the present system.

This is also confirmed from the analysis of the resistivity (ρ) and TEP (S) data of Zhao *et al*[8] in the PM phase using the small-polaron transport mechanism. In this Comment, we have replotted the resistivity (ρ) and TEP data (of Ref. 8) and found that the small-polaron hopping model[9] well ex-

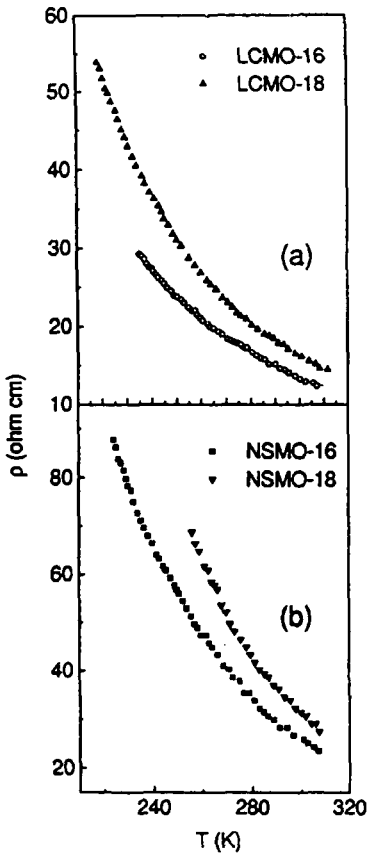

FIG. 1. Temperature-dependent resistivity curves of oxygen isotope exchanged films (Ref. 8) of (a) $La_{0.75}Ca_{0.25}MnO_3$ and (b) $Nd_{0.75}Sr_{0.25}MnO_3$.

plains the transport data of Zhao *et al.* as discussed below. The ^{16}O- and ^{18}O-diffused $La_{0.75}Ca_{0.25}MnO_3$ samples[8] are referred to as LCMO-16 and LCMO-18, respectively. Similarly, the ^{16}O- and ^{18}O-diffused $Nd_{0.75}Sr_{0.25}MnO_3$ samples[8] are referred to as NSMO-16 and NSMO-18, respectively.

Figure 1 represents the temperature-dependent resistivity (ρ) of the LCMO-16, LCMO-18, NSMO-16, and NSMO-18 samples of Ref. 8. The reported Curie temperatures ($T_c \sim T_p$) of the samples[8] are given in Table I. It is noteworthy to mention that the curves reported by Zhao *et al.*[8] showed the thermal variation of resistivity only above the respective Curie temperatures. However, the signature of the small-polaron hopping (SPH) conduction mechanism is observed from the temperature-dependent resistivity data as discussed below. It is perceived that the resistivity data[8] can be well fitted with the thermally activated small-polaron hopping model,[17] similar to many other samples[18,19] of the CMR family. According to this model,[17] the expression for conductivity (σ) is given by

$$\sigma_{sp} = \sigma_{0sp} \exp(-W_M/k_BT), \quad (1)$$

where $\sigma_0 = [\nu_{ph} N e^2 R^2 C(1-C)]/k_BT] \exp(-2R\alpha)$, k_B is the Boltzmann constant, and T is the absolute temperature. N is the number of ion sites per unit volume (calculated from density data), R is the average intersite spacing obtained from the relation $R = (1/N)^{1/3}$, C is the fraction of sites occupied by a polaron, α is the electron wave function decay constant, and ν_{ph} is the optical phonon frequency. W_M is the activation energy given, by the relations[20] $W_M = W_H + W_D/2$ for $T > \theta_D/2$ and $W_M = W_D$ for $T > \theta_D/4$ where W_H is the polaron hopping energy given by $W_H = W_M - E_s$ (discussed later), W_D is the disorder energy, and θ_D is the Debye temperature. Resistivity data are replotted as $\ln\sigma$ vs $1/T$ in Fig. 2. It is customary to determine $\theta_D/2$ from the temperature, where deviation from linearity occurs in the high-temperature region of the $\ln\sigma$ vs $1/T$ curve (Fig. 2). Since the complete range of data is not available from Fig. 1 of Ref. 8, no such deviation is observable from the resistivity data. We have taken $\theta_D = 510.2$ K for the LCMO-16 sample (Table I) from our recent work on $La_{0.7}Ca_{(0.3-y)}Na_yMnO_3$ ($y = 0.0$–0.3) series of samples.[4] Here we should mention that for most of the CMR materials θ_D lies within 400–500 K. This means that the phonon frequency (ν_{ph}) is almost same ($\sim 10^{13}$ Hz) for all CMR materials. The corresponding value of the disorder energy and phonon frequency (ν_{ph}) is also estimated for this sample from the relation $h\nu_{ph} = k_B\theta_D$ and given in Table I. Almost similar values of the phonon frequency are also obtained from the infrared (IR) spectra of the samples.[4] The nature of these curves (Fig. 2) confirms the applicability of Mott's small-polaron hopping mechanism (model) (Ref. 17) in the insulating (semiconducting) region (above T_p), predicting a temperature dependence of the activation energy in this region. The estimated values of the activation energy (W_M) for LCMO and NSMO samples studied by Zhao *et al.*[8] are given in Table I. We also use the same values of the activation energy for fitting the conductivity data.

But in the case of bipolarons, two different defect centers (with energy difference Δ), as mentioned above, are coupled together and the effective potential barrier W over which

TABLE I. Some important physical parameters of the samples (Ref. 8) and the best-fit parameters obtained from fitting with Eqs. (1), (4), and (5). Other relevant parameters are obtained from the conductivity data.

Parameters	LCMO-16	LCMO-18	NSMO-16	NSMO-18
T_p (K)	231.5	216.5	204.0	186.0
θ_D (K)	510.2	–	–	–
ν_{ph} (Hz)	1.06×10^{13}	–	–	–
W_M (meV)	72.8	86.0	78.8	92.9
E_s (meV)	13.2	18.7	–	–
W_H (meV)	59.6	67.4	–	–
W_D (meV)	119.2	134.8	–	–
γ_p	2.71	3.06	–	–
$N(E_F)$ (eV^{-1} cm^{-3})	6.30×10^{18}	3.27×10^{18}	3.06×10^{18}	1.55×10^{18}
α'	−0.47	−0.63	–	–
ϕ (meV)	21.00	–	–	–
J (meV)	2.98	–	–	–
$W_H/3$ (meV)	19.87	–	–	–

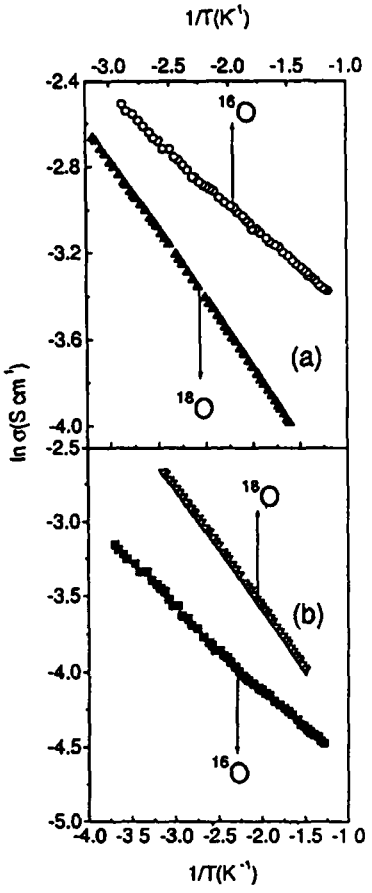

FIG. 2. Variation of $\ln\sigma$ as a function of inverse temperature ($1/T$) of (a) LCMO-16 and LCMO-18 and (b) NSMO-16 and NSMO-18

carriers must hop is the random variable and variations in the W arise from the variations in the distance R separating the two centers.[11,13] W_M is the potential energy associated with a defect site, which actually represents the energy needed for a bipolaron to migrate between centers of infinite separations.[11,13,14] The Coulombic interaction between two neighboring sites lowers the binding energy W_M and the effective barrier height W is then related to the intersite separation R via the equation[11,13,14]

$$W = W_M - 4e^2/\epsilon R_p, \tag{2}$$

where ϵ is the effective dielectric constant and R_p is the critical percolation radius given by $R_p = (2.7\times 3/4\pi N)^{1/3}$ Thus the conductivity equation for the bipolaron is given by[11,13-15]

$$\sigma_{bp} = \sigma_{0bp} \exp[-(W_M - 4e^2/\epsilon R_p)/k_B T], \tag{3}$$

where $\sigma_{obp} = N^2(R_p^5 - R_{min}^5)/15$, and R_{min} is the lower bound for the hopping distance and is given by $R_{min} = 2e^2/\pi\epsilon\epsilon_0 W_M$ (ϵ_0 is the free space permittivity) It is clearly observed that σ_{obp} is largely controlled by the barrier height at the critical percolation radius, i.e, the correlation arising due to Coulombic interactions between two different defect sites plays a major role Further, the preexponential factors in the two processes, σ_{osp} and σ_{obp} [Eqs (1) and (3)] are also quite different So from precisely fitting the experimental resistivity data one can unambiguously indicate the nature of polarons

It is well known[17] that conductivity data of semiconducting oxide systems in the low-temperature regime (below $\theta_D/2$) follow Mott's variable-range hopping (VRH) model of charge carriers Recently, working with similar manganite systems, like La-Sr-Mn-Cu-O and La-Ca-Mn-O, different research groups[21,22] applied the VRH model to fit the conductivity data for the entire high-temperature ($T > T_p$) range Thus, for the present series of samples,[8] we have also tried to fit the conductivity data with the VRH model in the given temperature In the three-dimensional (3D) case, the dc conductivity data according to the VRH model follows the equation[17]

$$\sigma = \sigma_0 \exp(-[T_0/T])^{1/4}, \tag{4}$$

where T_0 is a constant $= 16\alpha^3/k_B N(E_f)$ and $N(E_f)$ the density of states (DOS) at the Fermi level T_0 is obtained from the slope of the $\ln\sigma$ vs $T^{-1/4}$ curve (Fig 3) The straight line of Fig 3 gives the best-fit line obtained from fitting the conductivity data with Eq (4) From the values of T_0, we have also calculated the DOS at the Fermi level, $N(F_f)$ (Table I), using $\alpha = 2.22\ \mathrm{nm}^{-1}$ (Refs 23 and 24), estimated earlier for similar CMR oxide samples

Let us now consider the most important result of temperature-dependent thermoelectric power (S) for two Ca-doped samples, viz, LCMO-16 and LCMO-18, shown in Fig. 4(b) Recently extensive efforts have been made to discuss the polaronic transport in the high-temperature ($T > T_p$) PM phase of the CMR systems [14] We also notice that like resistivity at high temperature, TEP data can also be fitted very well with Mott's equation[17] of the Seebeck coefficient (S) which has the form

$$S = k_B/e[E_S/k_B T + \alpha'] \tag{5}$$

A similar model was also used by Zhao *et al* [8] to fit their TEP data, but they did not estimate α' which gives the condition of small-polaron or bipolaron formation In Eq (5), E_s is the activation energy obtained from the TEP data, which is the same as observed by Zhao *et al* [8] α' is a constant of proportionality between the heat transfer associated with electron and the kinetic energy of the electron It has been shown theoretically by Austin and Mott,[20] Appel,[25] and Mott[26] that $\alpha' > 2$ for large polarons, whereas for small-polaron formation $\alpha' < 1$ Qualitatively, one can argue that for narrow-band semiconductors with small-polaron formation, the polaron bandwidth is very much smaller than $k_B T$ Due to localization of electrons, the heat transfer associated with electrons should be small compared with $k_B T$ and as a consequence the constant α' should be less than 1 (Ref 27)

On the other hand, according to Heikes[28] the term α' is of the form $\alpha' = \Delta S'/k_B$, where $\Delta S'$ is the change in the entropy of the ion (lattice) due to the presence of an electron on the transition-metal site [20,26,28] This must be due to the

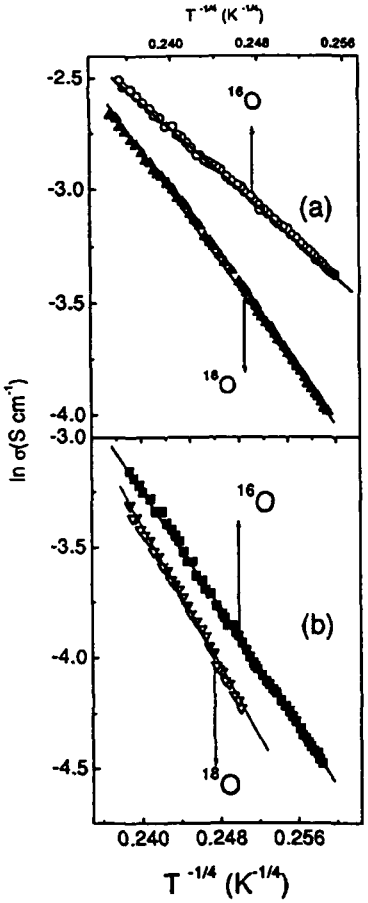

FIG. 3. Plot of $\ln\sigma$ vs $T^{-1/4}$ for the samples of (a) LCMO-16 and LCMO-18 and (b) NSMO-16 and NSMO-18. The solid lines indicate the best fits with Mott's VRH model [Eq. (4)].

change in the vibrational frequency (ω_0) of the surrounding atoms due to the presence of an electron.[26] Detail calculation shows that[20]

$$\Delta S'/k_B = \Delta\omega_0/\omega_0 = 3\lambda W_p/E_a,$$

where $\Delta\omega_0$ is the change in vibrational frequency (w_0), E_a is the energy required to displace an atom, and W_p is polaronic energy ($=2W_H$, where W_H is the polaron hopping energy).[17,20] Now since $E_a \sim eV$ (Refs. 20 and 26) and $W_H \sim 100$ meV (discussed later), α' should be less than unity for small polarons. The solid line in the S vs $1/T$ plot [Fig. 4(a)] gives the best-fit curve to Eq. (5). From the slope of the curve we obtain E_s, the activation energy from the TEP data for two typical samples studied by Zhao *et al.*[8] and are given in Table I. The parameter α', obtained from the fitting of the curves, is shown in Table I. Further, a similar small negative value of α' has also been obtained by other research groups (Ref. 27 and references therein). From the calculated values of α' (Table I), it is seen that $\alpha' < 1$. This again strongly supports the validity of the small-polaron hopping conduction[23] for the system of samples under investigation in contrast to the immobile bipolarons as reported by Zhao

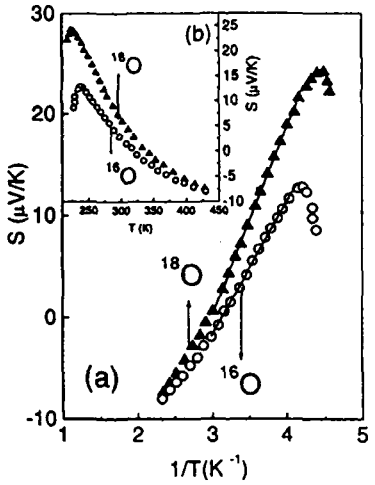

FIG. 4. (a) Variation of thermopower S (Ref. 8) as a function of inverse temperature $1/T$ for LCMO-16 and LCMO-18. The solid lines indicate the best fit with Mott's SPH model of thermoelectric power [Eq. (5)]. (b) Thermal variation of the Seebeck coefficient (S) for the same samples.

et al.[8] The values of E_s obtained from TEP measurements are nearly one order of magnitude smaller than those (W_M, Table I) obtained from the resistivity data. The reason for such a difference, as originally pointed out by Mott and Davis[17] and also recently supported by others,[29] is due to the thermally activated nature of hopping transport at high temperature. This large difference is also an indication of the small-polaron hopping mechanism. The estimated value of the hopping energy W_H ($=W_M - E_s$) is presented in Table I.

We have further attempted to estimate the dimension of the polaron. According to Mott and Davis,[17] small polarons should exist if the condition $J < W_H/3$ is satisfied. The value of the polaron bandwidth J is calculated independently from the model proposed by Mott and Davis,[17] viz.,

$$J \sim e^3[N(E_F)/\epsilon_p^3]^{1/2}. \quad (6)$$

The values of the dielectric constant ϵ_p are calculated from the relation

$$W_H = e^2/4\epsilon_p(1/r_p - 1/R), \quad (7)$$

where the polaronic radius r_p and R, the average intersite spacing, are estimated to have the same value of our recent reported work[4] on the $La_{0.7}Ca_{(0.3-y)}Na_yMnO_3$ ($y = 0.0$–0.3) series of samples and the obtained value of ϵ_p is 12.81. Here we should mention that there is some uncertainty in the estimation of ϵ_p indirectly from Eq. (7). We noticed that for the manganite samples ϵ_p varies from 5 to 15, for which J values vary from 2 to 10 meV (approximately). These values of ϵ_p agree with those obtained from IR reflection spectra. However, all these J values satisfy the condition of small-polaron hopping discussed below. Putting the values of $N(E_F)$ and ϵ_p, the independently calculated value of J is 2.98 meV (Table I). Comparing the values of $W_H/3$ and J given in Table I, we found that $J \ll W_H/3$. Hence the hopping is actually due to small polarons, which is also observed

from the TEP data discussed above. Here also we do not find evidence of large polarons as in the case of thermoelectric power data. This signifies that hopping is actually due to small polarons[30] in the system studied by Zhao *et al.*[8]

An attempt has also been made to confirm the nature of small-polaron hopping conduction for the present samples[8] from Holstein's condition.[31] According to this condition, the polaron bandwidth J should satisfy the inequality[20,31] $J>\phi$ (for adiabatic hopping conduction) and $J<\phi$ (for the nonadiabatic hopping conduction) where

$$\phi=(2k_BTW_H/\pi)^{1/4}(h\nu_{ph}/\pi)^{1/2}. \quad (8)$$

The value of ϕ calculated from Eq. (8) for LCMO-16 is found to be 21.00 meV (Table I). Comparing these values of J and ϕ (Table I), it is observed that for the LCMO-16 sample, $J<\phi$; i.e., the nonadiabatic hopping condition is strictly satisfied. LCMO-18 and other samples also behave similarly.

We have also made an effort to calculate the small-polaron coupling constant γ_p which is a measure of the el-ph interaction strength for these samples, using the relation[20] $\gamma_p=2W_H/h\nu_{ph}$. The estimated values of γ_p are given in Table I. The values of γ_p are less than the strong electron-phonon coupling limit, for which $\gamma_p>4$ (Ref. 20). This indicates the freezing (or melting) of the small polarons and the corresponding increase of electron-electron and spin-spin interactions, leading finally to the metallic state. Dynamic phase separation in the PM state as pointed out by Zhao *et al.*[8] might appear due to the freezing of small polarons and the formation of both ferromagnetic and antiferromagnetic domains depending on the strength of exchange interaction which increases with the freezing of the small polarons. The estimated γ_p values are of the same order of magnitude reported earlier for similar samples,[32] which further supports the theory of lattice distortion and, hence, the formation of small polarons. The γ_p for the ^{16}O diffused system is smaller than the ^{18}O-diffused system. This means that the isotope effect plays a dominant role in the electron-phonon interaction. The isotope effect is related to the electron-phonon interaction constant (γ_p), since the polaron effective mass (m_p) is proportional to $\exp(\gamma_p)$.

Finally, from the above discussion, we may conclude that the hopping mechanism in the LCMO-16, LCMO-18, and other samples is actually due to small polarons; consideration of bipolarons as reported by Zhao *et al.*[8] is inadequate. We further affirm that the isotope effect is actually associated with the polaron effective mass—i.e., the electron-phonon interaction term. The SPH model discussed above is also valid for all other manganites and related materials in the form of both bulk and thin films.

*Present address: Physical Metallurgy Section, Indira Gandhi Center for Atomic Research, Kalpakkam-603 102, India.

†Electronic address: sspbkc@mahendra.iacs.res.in

[1] C. Zener, Phys. Rev. **82**, 403 (1951).

[2] M.B. Salamon and M. Jaime, Rev. Mod. Phys. **73**, 583 (2001).

[3] A.J. Millis, P.B. Littlewood, and B.I. Shraiman, Phys. Rev. Lett. **74**, 5144 (1995).

[4] S. Bhattacharya, Aritra Banerjee, S. Pal, R.K. Mukherjee, and B.K. Chaudhuri, J. Appl. Phys. **93**, 356 (2003).

[5] J.Q. Li, M. Uehara, C. Tsuruta, Y. Matsui, and Z.X. Zhao, Phys. Rev. Lett. **82**, 2386 (1999).

[6] M. Jaime, H.T. Hardner, M.B. Salamon, M. Rubinstein, P. Dorsey, and D. Emin, Phys. Rev. Lett. **78**, 951 (1997).

[7] A.S. Alexandrov and A.M. Bratkovsky, Phys. Rev. Lett. **82**, 141 (1999); L.J. Zou, H.Q. Lin, and Q.-Q. Zheng, J. Appl. Phys. **83**, 7363 (1998).

[8] Guo-meng Zhao, Y.S. Wang, D.J. Kang, W. Prellier, M. Rajeswari, H. Keller, T. Venkatesan, C.W. Chu, and R.L. Greene, Phys. Rev. B **62**, R11 949 (2000).

[9] H. Fritzsche, *Electronic and Structural Properties of Amorphous Semiconductors* (Academic Press, London, 1973).

[10] M. Kastner, D. Adler, and H. Fritzsche, Phys. Rev. Lett. **37**, 1504 (1976).

[11] S.R. Elliot, Philos. Mag. **36**, 1291 (1977).

[12] S.R. Elliot, Philos. Mag. **37**, 553 (1978).

[13] G.E. Pike, Phys. Rev. B **6**, 1572 (1972).

[14] M.H.A. Pramanik, P.N. Butcher, and I.D. Cox, Philos. Mag. B **47**, 437 (1983).

[15] P. Brahma, S. Banerjee, S. Chakraborty, and D. Chakravorty, J. Appl. Phys. **88**, 6526 (2000).

[16] C.N.R. Rao and B. Raveau, *Colossal Magnetoresistance, Charge Ordering, and Related Properties of Manganese Oxides* (World Scientific, Singapore, 1998) and references therein.

[17] N.F. Mott and E.A. Davis, *Electronics Process in Non Crystalline Materials* (Clarendon Press, Oxford, 1971).

[18] R. Mahendiran, R. Mahesh, A.K. RayChaudhuri, and C.N.R. Rao, J. Phys. D **28**, 1743 (1995).

[19] G.J. Snyder, R. Hiskes, S. DiCarolis, M.R. Beasley, and T.H. Geballe, Phys. Rev. B **53**, 14 434 (1996).

[20] G.N. Austin and N.F. Mott, Adv. Phys. **18**, 41 (1969).

[21] L. Pi, L. Zheng, and Y. Zhang, Phys. Rev. B **61**, 8917 (2000).

[22] M. Jaime, M.B. Salamon, M. Rubinstein, R.E. Treece, J.S. Horwitz, and D.B. Chrisey, Phys. Rev. B **54**, 11 914 (1996).

[23] Aritra Banerjee, S. Pal, and B.K. Chaudhuri, J. Chem. Phys. **115**, 1550 (2001).

[24] M. Viret, L. Ranno, and J.M.D. Coey, Phys. Rev. B **55**, 8067 (1997).

[25] J. Appel, Solid State Phys. **21**, 193 (1968).

[26] N.F. Mott, J. Non-Cryst. Solids **1**, 1 (1968).

[27] A. Mansingh and A. Dhawan, J. Phys. C **11**, 3439 (1978).

[28] R.R. Heikes, in *Thermoelectricity*, edited by R.R. Heikes and W. U. Ure (Interscience, New York, 1961).

[29] M. Jaime, M.B. Salamon, K. Pettit, M. Rubinstein, R.E. Treece, J.S. Horwitz, and D.B. Chrisey, Appl. Phys. Lett. **68**, 1576 (1996).

[30] Aritra Banerjee, S. Pal, S. Bhattacharya, B.K. Chaudhuri, and H.D. Yang, Phys. Rev. B **64**, 104428 (2001).

[31] T. Holstein, Ann. Phys. (N.Y.) **8**, 343 (1959).

[32] S. Pal, A. Banerjee, E. Rozenberg, and B.K. Chaudhuri, J. Appl. Phys. **89**, 4955 (2001).

Available online at www.sciencedirect.com
SCIENCE DIRECT®
ELSEVIER
Journal of Magnetism and Magnetic Materials 265 (2003) 215–221
Journal of magnetism and magnetic materials
www.elsevier.com/locate/jmmm

Electronic and magnetic instability in $Pr_{0.65}Ca_{0.25}Sr_{0.1}MnO_3$

S. Mollah[a], H.L. Huang[a,1], S.J. Liu[b], P.L. Ho[a], W.L. Huang[d], C.W. Huang[d], C.P. Sun[a], J.-Y. Lin[c], Y.S. Gou[b], W.-H. Li[d], H.D. Yang[a,*]

[a] *Department of Physics, National Sun Yat Sen University, Kaohsiung 804, Taiwan, ROC*
[b] *Department of Electrophysics, National Chiao Tung University, Hsinchu 300, Taiwan, ROC*
[c] *Institute of Physics, National Chiao Tung University, Hsinchu 300, Taiwan, ROC*
[d] *Department of Physics, National Central University, Chung-Li 320, Taiwan, ROC*

Received 8 March 2003

Abstract

Electronic and magnetic instability in polycrystalline $Pr_{0.65}Ca_{0.25}Sr_{0.1}MnO_3$ manganite has been established from a systematic study of resistivity (ρ), magnetization (M) and specific heat (C). The sample shows a charge ordering transition at $T_{CO} \sim 200$ K, an antiferromagnetic (AFM) ordering transition at $T_N \sim 175$ K, a metal–insulator (MI) transition at $T_{MI} \sim 80$ K and an unusual magnetic ordering transition at $T_M^* \sim 45$ K in the absence of magnetic fields. Though the C data do not show any anomaly at T_{MI} for MI transition, these illustrate a much smaller anomaly than expected one at T_M^* and is suppressed by magnetic fields. This indicates that the unusual magnetic ordering in this sample is of canted, fluctuated or phase separation of AFM and ferromagnetic in nature which is established from the $T-H$ phase diagram, as well as the thermal and magnetic hysteresis in ρ, M and C.

PACS: 75.30.V; 75.30.K; 75.60.E; 75.40.C

Keywords. Manganites; CMR; Phase instability

1. Introduction

The complicated phase diagram in colossal magnetoresistive (CMR) materials [1,2], $RE_{1-x}A_xMnO_3$ (RE = trivalent rare earths, A = divalent alkaline earth metals), arises due to the interplay between double exchange (DE) interaction and charge/orbital ordering (CO–OO). The interplay between DE interaction and CO–OO can be tuned by changing the value of x [1,3], by varying the radius of rare/alkaline earth metals [4], by applying electric/magnetic fields [5–7], by irradiating with X-ray/infrared radiation [8], by applying external pressure [9,10] and by Mn-site substitution [11–14].

Recently, it has been proposed that the ground state of CMR materials have electronic phase separation (PS), which is the simultaneous presence of sub-micrometer FM metallic phase percolated in an insulating charge ordering/

*Corresponding author. Tel.: +886-7-525-3732; fax: +886-7-525-3709.
E-mail address: yang@mail.phys.nsysu.edu.tw (H.D. Yang).
[1] Permanent address: Department of Physics, Aligarh Muslim University, Aligarh-202002, India.

0304-8853/03/$ - see front matter © 2003 Elsevier Science B.V. All rights reserved
doi:10.1016/S0304-8853(03)00268-3

antiferromagnetic (CO/AFM) matrix [15–20]. This PS scenario is of particular importance and favorable for the existence of out-of-equilibrium features. A little change of the fraction or the arrangement of the domains can induce the percolation. There is the possibility of emerging various interesting phenomena like time-dependent relaxation, two level fluctuation, non-equilibrium fluctuation, or relaxor ferroelectric behavior from the competition of the coexisting phases [15–20]. However, those phenomena were observed in different samples at various conditions. Though the Pr-based CMR systems have been widely studied [21–26], there is no report on the detection of instability in phases of these materials from the systematic study of transport, magnetic and thermal properties. Therefore, we chose an interesting system from our studied materials and thoroughly investigated the transport, magnetic and thermal properties to find out the electronic and magnetic instability in it.

In this article, we report the observation of electronic and magnetic instability in polycrystalline $Pr_{0.65}Ca_{0.25}Sr_{0.1}MnO_3$ manganite presumably due to spin fluctuations, canted FM spins or PS of AFM and FM domains. These are concluded to be the possible origins of the occurrence of an unusual magnetic ordering state below T_{MI} in it at low magnetic fields.

2. Experimental details

Polycrystalline $Pr_{0.65}Ca_{0.25}Sr_{0.1}MnO_3$ perovskite manganite was prepared by the standard solid-state reaction method from the powdered raw materials of Pr_6O_{11}, CaO, MnO_2 and $SrCO_3$. Homogenous combination of stoichiometric mixtures were heat treated at 900°C for 12 h, followed by regrinding and firing at 1200°C for 12 h. The resultant powders were palletized at a pressure $\sim 2\,\text{ton cm}^{-2}$ and sintered in air at 1350°C for 48 h with in-between grinding, palletizing and annealing for three times. Powder X-ray diffraction data obtained by SIEMENS D5000 diffractometer using CuKα radiation showed single phase of it. Electrical resistivity (ρ) was measured by the standard four-probe method. Magnetization (M) measurements were performed by the commercial SQUID magnetometer in temperature 10–300 K and magnetic field 0–8 T. A high-resolution AC calorimeter was utilized to measure the relative specific heat, C [27]. Absolute value of C was obtained by using a heat pulse thermal relaxation (HPTR) calorimeter [28] at low temperature (0.6–50 K). The hydrostatic pressure (P) dependent AC magnetic susceptibility (χ_{ac}) data were taken using the piston cylinder self-clamped technique [29]. It is noted that all data on ρ, M, and C were taken on cooling temperature unless when it is particularly specified for warming.

3. Results and discussion

Temperature variation of resistivity (ρ) of $Pr_{0.65}Ca_{0.25}Sr_{0.1}MnO_3$ at various magnetic fields (H) are shown in Fig. 1a. The MI transition becomes broader and the T_{MI} moves to higher temperatures with the increase of H, which is consistent with that observed in other systems [1,2]. The CO state is observed (as indicated by T_{CO} in Fig. 1a) up to a magnetic field of 2.5 T. Dependence of magnetization (M) on temperature at various applied magnetic fields (0.01–8 T) is shown in Fig. 1b. The ferromagnetic transition temperature (T_C), defined as the temperature where magnetization is saturated (indicated by arrow in Fig. 1b), rises with the increase of magnetic fields. Situation at 2 T is very different from others where magnetization starts to increase at $T \sim 200$ K, and exhibits a shoulder at $T \sim 175$ K, then increases and finally becomes saturated at $T \sim 80$ K though these transitions are not so vivid from temperature variation of ρ at 2 T (Fig. 1a).

The temperature dependence of specific heat (C) generally accounts for the anomalies corresponding to different thermodynamic phase transitions [23]. It is a bulk property and shows a rather small (or undetectable) anomaly due to minor impurity, short range or meta-stable ordering phases. Fig. 2 illustrates the temperature distinction of C for this sample at diverse magnetic fields (0–8 T), where anomalies owing to AFM, CO and FM transitions are noticed, respectively, at T_N, T_{CO} and T_C. The AFM and CO anomalies are clearly observed up

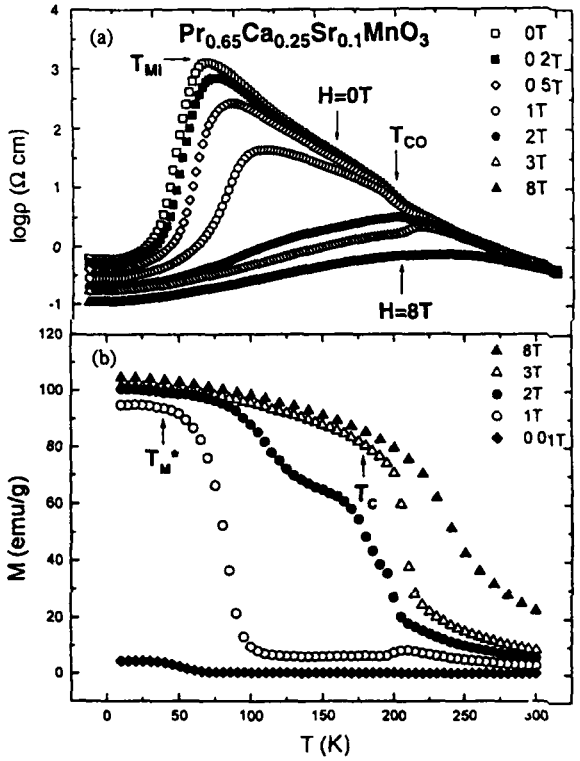

Fig 1 Temperature dependence of (a) resistivity (ρ) in logarithmic scale and (b) magnetization (M) for $Pr_{0.65}Ca_{0.25}Sr_{0.1}MnO_3$ sample at various magnetic fields (0–8 T) The charge ordering (T_{CO}), metal–insulator (T_{MI}), ferromagnetic (T_C) and unusual magnetic ordering (T_M^*) transition temperatures are indicated by arrows For clearness, some data curves are removed

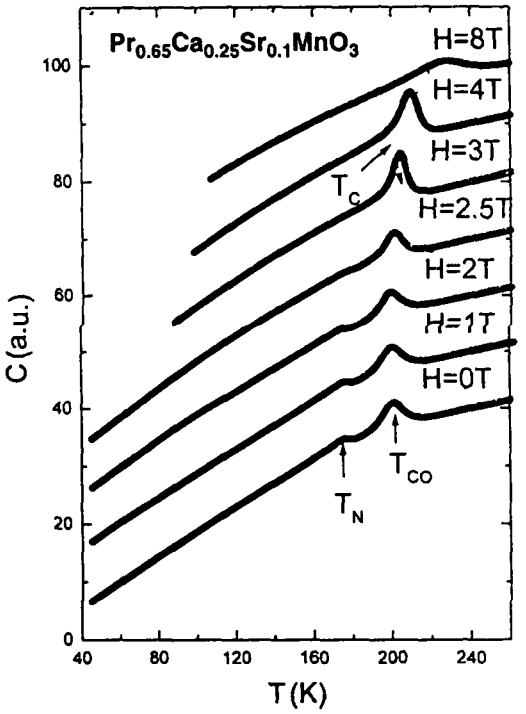

Fig 2 Temperature variation of specific heat (C) for $Pr_{0.65}Ca_{0.25}Sr_{0.1}MnO_3$ sample at various magnetic fields (0–8 T) The anomalies corresponding to charge ordering (T_{CO}), antiferromagnetic (T_N) and ferromagnetic (T_C) transitions are pointed out by arrows

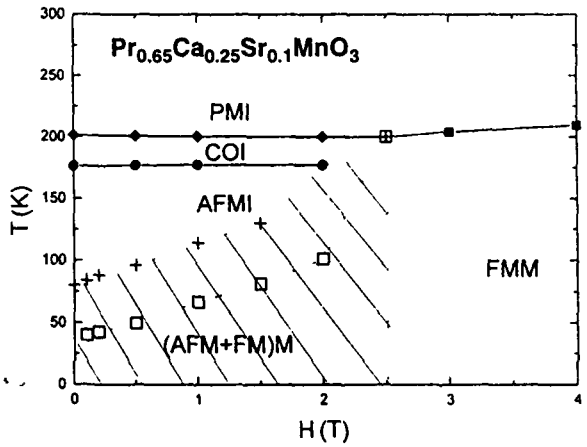

Fig 3 Phase diagram ($T-H$) for $Pr_{0.65}Ca_{0.25}Sr_{0.1}MnO_3$ drawn on the basis of the results of Figs 1 and 2 (AFM + FM)M states are represented by the shaded region

to 2.5 T and the FM anomalies are detected from 3 to 8 T (Fig. 2). These observations are in accordance with the data demonstrated in Figs. 1a and b. However, from Fig. 2 we could not successfully resolve any specific heat anomaly at $T_{MI} \sim 80$ K (for details, see Fig. 6). We thus speculate that the magnetic ordering state at low magnetic fields and low temperatures (below T_{MI}) in this sample is very unusual and denoted as mixing (AFM + FM)M. According to the results of Figs. 1 and 2, the $T-H$ phase diagram of this manganite is shown in Fig. 3, where paramagnetic insulating (PMI), charge-ordered insulating (COI), antiferromagnetic insulating (AFMI), ferromagnetic metallic (FMM) and unusual magnetic metallic (AFM + FM)M regions are clearly indicated The unusual mixed (AFM + FM)M state may be due to electronic and magnetic instability or the PS of AFM and FM domains in the sample below T_{MI}

at low magnetic fields. In the following paragraphs, we present more detailed data and further discuss these phenomena.

3.1. Detection of the unusual magnetic state in $Pr_{0.65}Ca_{0.25}Sr_{0.1}MnO_3$

It is fascinating to note that the maximum magneto-resistance $MR = -[\rho(H) - \rho(0)]/\rho(0)$ at 70 K (near its T_{MI}) obtained from Fig. 1a is as high as 50%, 80% and 99% correspondingly at low magnetic fields of 0.1, 0.2 and 0.5 T. This may be due to a particular unstable mixing phase of a weak CO insulating at high temperatures and a (AFM+FM)M phase at low temperatures in it. Therefore, the application of a low magnetic field ($\leqslant 0.5$ T) is enough to partially melt the CO phase and percolate the FM state to enhance the metallicity. Hence, the large enhancement of MR indicates its electronic and magnetic instability or PS below its T_{MI} at low magnetic fields. This is an indirect evidence that the lattice distortion accompanied with AFM/CO plays an important role to exhibit a huge MR in CMR systems.

Fig. 4 shows the hydrostatic pressure (P) dependent AC magnetic susceptibility (χ_{ac}) measured in warming temperature from 80 to 280 K. At ambient pressure, there is a very small anomaly at 200 K owing to CO transition. With the increase of P, the temperature dependent χ_{ac} profile

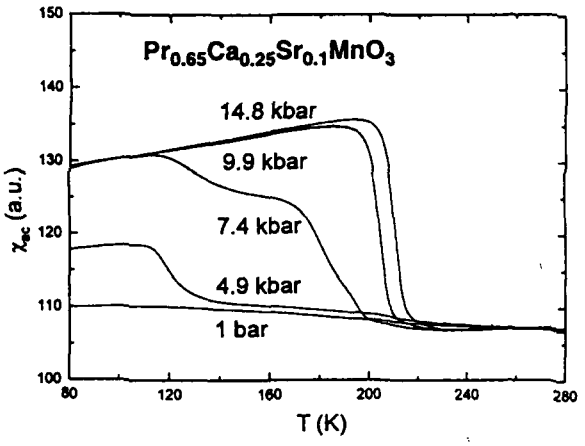

Fig. 4. Hydrostatic pressure (P) dependent AC magnetic susceptibility (χ_{ac}) measured at warming temperature from 80 to 280 K.

becomes very similar to that of temperature dependent magnetization in various magnetic fields (Fig. 1b). The behavior for pressure of 7.4 kbar on AC susceptibility is almost the same as that of magnetic field of 2 T on magnetization shown in Fig. 1b. A sharp transition due to FM ordering is observed at $T_C \sim 200$ K for the pressure of 9.9 kbar. This is similar to that observed in $Pr_{0.7}Ca_{0.3}MnO_3$ [26] and $(Nd_{0.6}La_{0.4})_{0.5}Sr_{0.5}MnO_3$ [30]. However, this is in contrast with that observed in $(Nd_{1-y}Sm_y)_{0.5}Sr_{0.5}MnO_3$ (for $y = 0.875$) where the pressure induces the CO transition and increases T_C [9]. Basically, the external pressure can stabilize the structure (reduce the distortion) and suppress the spin fluctuations in perovskite manganites [31]. It can also melt the CO state and transform the system from PMI to FMM state [26]. Therefore, it is reasonable to see the increase of T_C due to the increased connectivity among the meta-stable FM domains by melting of CO states with the increase of pressure. This also designates the electronic and magnetic instability in this sample due to spin fluctuations or PS below T_{MI}.

The magnetic hysteresis of ρ and M at a fixed temperature of 10 K are shown in Fig. 5. Here, the sample was first cooled down to 10 K at zero magnetic field, then the resistivity and magnetization measurements were taken by sweeping the applied magnetic field up and then down. The resistivity decreases with increasing magnetic fields. It slightly increases from the minimum value in the course of decreasing magnetic fields and the irreversibility occurs at $H \sim 3$ T. Magnetization curves also show similar irreversible performance at a lower magnetic field of ~ 2 T. *In the absence of magnetic field, the FM spins may* be canted, or meta-stable, or fluctuating, or mixed with AFM spins, in this sample. So the magnetization is small as the H is small during increasing and decreasing of magnetic fields. But the FM spins are better aligned, the spin fluctuations are decreased and perhaps the long-range FM order is achieved above 2 T confirming the saturation of magnetization and resistivity. Hence it is once more specified that the canted or fluctuated FM spins are stabilized above 2 T and long range FM ordering is achieved. It is noted that both the ρ

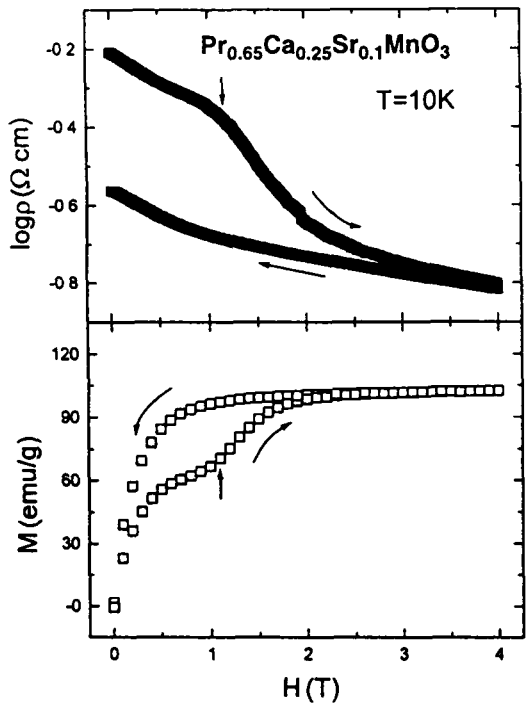

Fig 5 Magnetic hysteresis of resistivity (ρ) in logarithmic scale and magnetization (M) at a fixed temperature (10 K) The curves during sweeping up and down the magnetic fields are indicated by arrows The kinks in ρ and M around 1 T are denoted by arrows

and M curves exhibit a kink at a magnetic field of approximately 1 T (indicated by arrows in Fig. 5) in the sweeping up mode. Similar kink in magnetization at 13 K is also detected by Tomioka et al. [32] at a higher magnetic field (3–4 T) in a $Pr_{0.7}Ca_{0.3}MnO_3$ single crystal, which is insulating at all temperatures\ in the absence of magnetic field. The authors [32] have explained this as the irreversible turn out of canted AFM to FM states and are confirmed from the temperature variation of resistivity curves. The magnetic field dependent resistivity of $Pr_{0.7}Ca_{0.3}MnO_3$ single crystal at 13 K [32] is different from that of our sample at 10 K. In Ref. [32], there is a sharp drop of resistivity (10 orders of magnitude) around 3–4 T (where the kink in magnetization is observed) during the field sweeping up and the resistivity is not increased from the minimum value with the field sweeping down, confirming the irreversible turn out of canted AFM spins to FM ones. However, in our sample the kink of resistivity is observed at 1 T (where the kink in magnetization is also observed) and the ρ slightly increases with the field sweeping down. Therefore, it is likely that the kink in our system is the transformation of canted or fluctuated FM to FM. This implies that the transport mechanism in $Pr_{0.65}Ca_{0.25}Sr_{0.1}MnO_3$ is somewhat different from that in $Pr_{0.7}Ca_{0.3}MnO_3$ single crystal [32] and possibly due to the electronic and magnetic instability or the probable PS of AFM and FM state.

The final verification on the electronic and magnetic instability in $Pr_{0.65}Ca_{0.25}Sr_{0.1}MnO_3$ below T_{MI} at low magnetic fields is attained from the C/T vs. T curves (Fig. 6). It is well established [1,2] that the CO insulating state is unstable under high magnetic fields and a MI transition leading to FMM state can take place due to the melting of CO insulating state. Generally, the FM transition temperature (T_C) and the MI transition temperature (T_{MI}) are close to each other [1,2]. Compre-

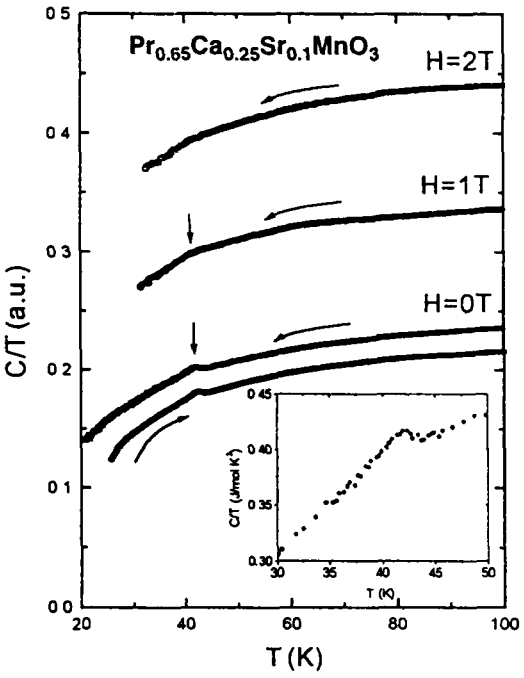

Fig 6 C/T vs T curves at different magnetic fields (0–2 T) The unusual magnetic transition temperature (T_M^*) and the data during cooling and warming are indicated by arrows The inset shows the absolute C/T vs T measured by HPTR calorimeter at zero field

hensible anomalies should be observed in C because of stable FM phase transitions [23]. Within this scenario, the absence of anomaly in C near T_{MI}, the presence of small specific heat anomaly at T_M^* and the substantial difference between T_{MI} and T_M^* would indicate the instability of the (AFM + FM) state below T_{MI}. Here the FM metallic phases may be percolated to the CO/AFM matrix. Fig. 6 shows no anomaly at $T_{MI} \sim 80$ K corresponding to MI transition (observed in Fig. 1), but demonstrates a rather smaller than expected one at $T_M^* \sim 45$ K (shown by arrow in Fig. 6) at low magnetic fields ($\leqslant 1$ T). The zero field C data taken in cooling and warming illustrate that the anomalies occur at same temperature (T_M^*) without resolvable hysteresis. The inset of Fig. 6 shows the absolute values (taken by HPTR calorimeter) of discrete C/T data of the sample at zero magnetic field, in which the anomaly around 45 K is further confirmed. The approximate magnitude of jump seen in the specific heat (ΔC) estimated from the inset of Fig. 6 at $T_M^* \sim 45$ K is only about 0.85 J/mol K, whereas that of CO transition at zero field (Fig. 2) is about 19 J/mol K. The ΔC associated with the magnetic ordering transition at $T_M^* \sim 45$ K (Fig. 6) is also much smaller than that of a typical FM transition (30.4 J/mol K) at $T_C \sim 200$ K and $H = 3$ T (Fig. 2). In addition, this small anomaly (0.85 J/mol K) due to unusual magnetic transition is also smeared at $H = 1-2$ T (Figs. 2 and 6) but resumes at $T_C \sim 200$ K and $H = 3$ T (Fig. 2). Thus we speculate that the unusual magnetic ordering state in $Pr_{0.65}Ca_{0.25}Sr_{0.1}MnO_3$ below $T_{MI} \sim 80$ K at low magnetic fields is different from that of a typical FMM state. Moreover, the existence of unusual magnetic ordering state in this sample below $T_{MI} \sim 80$ K reflects the electronic and magnetic instability in nature due to canted, fluctuated or the PS of AFM and FM.

4. Conclusions

From the systematic studies on the temperature and magnetic field dependence of resistivity, magnetization, pressure effect and specific heat of polycrystalline $Pr_{0.65}Ca_{0.25}Sr_{0.1}MnO_3$ perovskite manganite, it has been confirmed that the sample shows an unusual magnetic metallic state below T_{MI} at low magnetic fields. This unusual state is clearly identified in $T-H$ phase diagram (shaded area in Fig. 3) using various measurements. It has been explained that the unusual magnetic ordering state in this sample is due to the electronic and magnetic instability resulted from the interplay between the CO/AFM insulating state and FM metallic state. Our results have also clearly demonstrated that the spins in this region may be canted, fluctuated or possible PS of AFM and FM in nature and can be stabilized by applying magnetic field or external pressure to achieve the long range FM state.

Acknowledgements

This work was supported by National Science Council of Republic of China under contract Nos. NSC91-2112-M110-005 and NSC90-2112-M009-046.

References

[1] J M D Coey, M Viret, S V Molnar, Adv Phys 48 (1999) 167
[2] D.M Edwards, Adv Phys 51 (2002) 1259
[3] Q Huang, J W. Lynn, R W Erwin, A Santoro, D C Dender, V.N Smolyaninova, K Ghosh, R L Greene, Phys Rev B 61 (2000) 8895
[4] N. Moutis, I. Panagiotopoulos, M Pissas, D Niarchos, Phys. Rev. B 59 (1999) 1129.
[5] A Asamitsu, Y. Tomioka, T. Amira, Y. Tokura, Nature (London) 373 (1995) 407
[6] R. Klingeler, J. Geck, R Gross, L Pinsard-Gaudart, A Revcolevschi, S Uhlenbruck, B Büchner, Phys Rev B 65 (2002) 174404
[7] P Schiffer, A.P Ramirez, W Bao, S -W. Cheong, Phys Rev Lett. 75 (1995) 3336
[8] V Kiryukhin, D Casa, J P Hill, B Keimer, A Vigliante, Y Tomioka, Y Tokura, Nature (London) 386 (1997) 813
[9] Y Tokura, H Kuwahara, Y Moritomo, Y Tomioka, A Asamitsu, Phys Rev Lett 76 (1996) 3184
[10] I Loa, P Adler, A Grzechnik, K Syassen, U Schwarz, M Hanfland, G K Rozenberg, P Gorodetsky, M P Pasternak, Phys. Rev Lett 87 (2001) 125501
[11] K -H Hann, Q Huang, P C Ong, C K Ong, J Phys Condens Matter 14 (2002) 6619

[12] N Kallel, J. Dhahri, S. Zemni, E Dhahri, M. Oumezzine, M. Ghedira, H. Vincent, Phys. Stat Sol. (A) 184 (2001) 319.
[13] A. Barnab, A. Maignan, M. Hervieu, B Raveau, Eur. Phys. J. B 1 (1997) 145.
[14] R.K. Sahu, M.L. Rao, S.S Manoharan, K Dorr, K.-H. Muller, Solid State Commun 123 (2002) 217.
[15] E. Dagotto, T. Hotta, A. Moreo, Phys. Rep. 344 (2001) 1
[16] C. Simon, S. Mercone, N. Guiblin, C. Martin, A. Burlet, G. Andre, Phys. Rev. Lett. 89 (2002) 207202
[17] L.S. Lakshmi, V. Sridharan, D.V. Natarajan, S. Chandra, V S. Sastry, T.S. Radhakrishnan, P Pandian, R J. Joseyphus, A. Narayanasamy, J. Magn Magn. Mater. 257 (2003) 195.
[18] A.S. Lagutin, J. Vanacken, A. Semeno, Y. Bruynseraede, R. Suryanarayanan, Solid State Commun. 125 (2003) 7.
[19] P. Levy, F. Parisi, L. Granja, E. Indelicato, G Polla, Phys. Rev. Lett. 89 (2002) 137001.
[20] N.A. Babushkina, E.A. Chistotina, K I. Kugel, A L. Rakhmanov, O.Y. Gorbenko, A R Kaul, J. Phys. Condens. Matter 15 (2003) 259
[21] C. Martin, A. Maignan, M. Herview, B Raveau, Phys Rev B 60 (1999) 12191.
[22] Y Tomioka, A Asamitsu, Y Moritomo, H Kuwahara, Y Tokura, Phys Rev Lett 74 (1995) 5108
[23] M.R Lees, O.A. Petrenko, G Balakrishnan, D M Paul, Phys. Rev B 59 (1999) 1298
[24] M Ellouze, W Boujelben, A Cheikhrouhou, H Fuess R Madar, J Magn Magn Mater 257 (2003) 319
[25] A Guha, A K Raychaudhuri, A R Raju, C N R Rao, Phys Rev B 62 (2000) 5320
[26] H Yoshizawa, R. Kajimoto, H Kawano, Y Tomioka, Y Tokura, Phys Rev B 55 (1997) 2729
[27] Y-K Kuo, C S Lue, F H Hsu, H H Li, H D Yang, Phys Rev B 64 (2001) 125124
[28] S J Chen, C.F Chang, H L Tsay, H D Yang, J-Y Lin, Phys Rev B 58 (1998) 14753
[29] C.F. Chang, P H. Chou, H L Tsay, S S Weng, S Chatterjee, H D Yang, R S Liu, C H Shen, W-H. Li, Phys Rev B 58 (1998) 12224
[30] Y Moritomo, H Kuwahara, Y Tomioka, Y Tokura, Phys. Rev. B 55 (1997) 7549
[31] K Khazeni, Y.X Jia, L Lu, V H Crespi, M L Cohen, A Zettl, Phys Rev Lett 76 (1996) 295
[32] Y Tomioka, A Asamitsu, Y Moritomo, Y Tokura, J Phys Soc Japan 64 (1995) 3626

Available online at www.sciencedirect.com
SCIENCE DIRECT®
Physica B 329–333 (2003) 801–802
PHYSICA B
www.elsevier.com/locate/physb

Specific heat studies on the charge and magnetic ordering in manganites

H.D. Yang[a,*], H.L. Huang[a], P.L. Ho[a], W.L. Huang[a], C.W. Huang[a], S. Mollah[a], S.J. Liu[b], J.-Y. Lin[c]

[a] *Department of Physics, National Sun Yat-Sen University, Kaohsiung 804, Taiwan, ROC*
[b] *Department of Electrophysics, National Chiao-Tung University, Hsin-Chu 300, Taiwan, ROC*
[c] *Institute of Physics, National Chiao-Tung University, Hsin-Chu 300, Taiwan, ROC*

Abstract

Specific heat (C) studies with a wide range of temperatures ($T = 80$–300 K) on polycrystalline manganites $Pr_{1-x}Ca_xMnO_3$ (113-PCMO) with $x = 0.3$–0.4, $La_{1-y}Ca_yMnO_3$ (113-LCMO) with $y = 0.3$ and 0.5, and $La_{2-2z}Sr_{1+2z}Mn_2O_7$ (327-LSMO) with $z = 0.3$ and 0.5 are reported. Clear anomalies in C are identified which are associated with charge ordering (CO), antiferromagnetic (AFM) and ferromagnetic (FM) transitions. The anomalies in 113-PCMO and 113-LSMO are bigger than those of 327-LSMO. The possible explanations are discussed on the basis of dimensionality effects.

Keywords: Specific Heat; Charge ordering; Magnetic ordering; Manganites

The manganites of the Ruddlesden–Popper series, $R_{n+1}Mn_nO_{3n+1}$ (R = trivalent rare earth metals and n accounts for the dimensionality) illustrate many interesting properties like colossal magnetoresistance (CMR), charge ordering (CO) and magnetic field induced transitions when R is partially substituted by a divalent cation A [1,2]. The temperature dependence of specific heat (C) of these manganites clearly indicates the anomalies corresponding to the various phase transitions [3]. The present paper deals with the comparative specific heat study of 3D infinite layered manganites (113-PSMO and 113-LSMO) and quasi-2D bi-layered 327-LSMO. Polycrystalline $Pr_{1-x}Ca_xMnO_3$ (113-PCMO) with $x = 0.3$–0.4, $La_{1-y}Ca_yMnO_3$ (113-LCMO) with $y = 0.3$ and 0.5, and $La_{2-2z}Sr_{1+2z}Mn_2O_7$ (327-LSMO) with $z = 0.3$ and 0.5 oxides were synthesized by a standard solid-state-reaction method using the powder raw materials Pr_6O_{11}, La_2O_3, CaO, $SrCO_3$ and MnO_2 with purity 99.9 percent or better. For details of preparation, please see Refs. [4,5]. Relative specific heat measurements in high temperature (80–300 K) were performed with a high resolution AC calorimeter using chopped light as the heat source [6].

Fig. 1 shows the temperature variation of specific heat (C) of $Pr_{1-x}Ca_xMnO_3$ (113-PCMO) manganites. Clear anomalies for AFM ($T_N \sim 160$–165 K) and CO ($T_{CO} \sim 215$–227 K) transitions are observed in samples with $x = 0.35$–0.4 and the transition temperatures increase with the increase of x. While $x = 0.3$, the anomaly in C due to AFM or CO transition is smeared out. It is well established that the CO state is most stable with $x = 0.5$ and is destabilized with the decrease of x. As the CO transition vanishes with $x \leqslant 0.3$, the boundary value of x for CO transition in this system is 0.3. Temperature dependence of C for $La_{1-y}Ca_yMnO_3$ (113-LCMO) with $y = 0.3$ and 0.5, and $La_{2-2z}Sr_{1+2z}Mn_2O_7$ (327-LSMO) with $z = 0.3$ and 0.5 samples are displayed in Fig. 2. The anomalies for FM transition ($T_C \sim 100$ K) in $La_{1.4}Sr_{1.6}Mn_2O_7$, CO transition ($T_{CO} \sim 220$ K) in $LaSr_2Mn_2O_7$, FM transition ($T_C \sim 230$ K) in $La_{0.7}Ca_{0.3}MnO_3$ and AFM ($T_N \sim 130$ K) as well as CO

*Corresponding author. Tel.: +886-7-5253700; fax: +886-7-5253709.
E-mail address: hdynag@nsc.gov.tw, yang@mail.phys.nsysu.edu.tw (H.D. Yang).

0921-4526/03/$ - see front matter
doi:10.1016/S0921-4526(02)02562-0

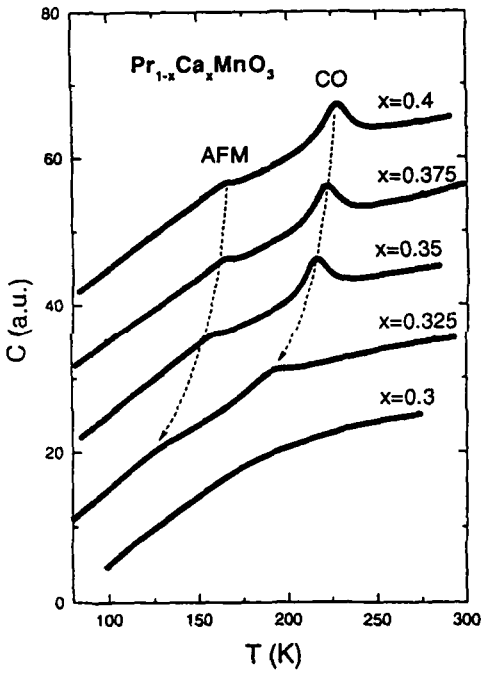

Fig. 1. Temperature variation of specific heat (C) of $Pr_{1-x}Ca_xMnO_3$ (113-PCMO) with $x = 0.3$–0.4 manganites.

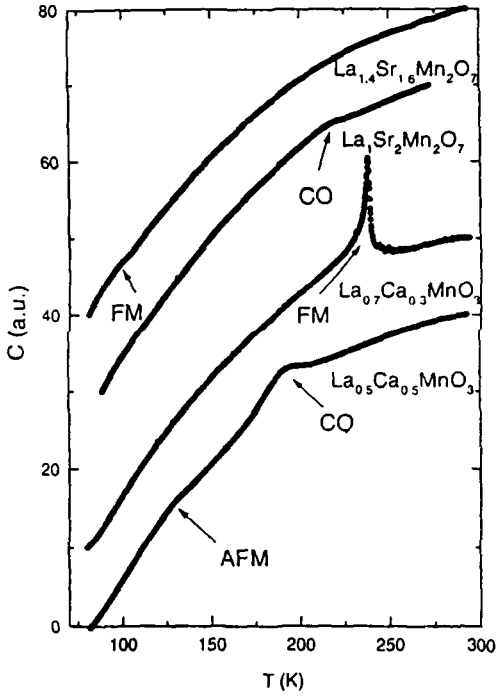

Fig. 2. Temperature dependence of specific heat (C) of $La_{1-y}Ca_yMnO_3$ (113-LCMO) with $y = 0.3$ and 0.5, and $La_{2-2z}Sr_{1+2z}Mn_2O_7$ (327-LSMO) with $z = 0.3$ and 0.5.

($T_{CO} \sim 180$ K) transitions in $La_{0.5}Ca_{0.5}MnO_3$ can be clearly identified. The magnitude and temperature of specific-heat anomalies exhibited in 113-LCMO and 113-PCMO are consistent with those reported [3]. Interestingly the trivalent rare earth plays a dominant role in magnetic transitions as a very large peak is observed in $La_{1-x}Ca_xMnO_3$ for FM transition (Fig. 2) where as no definite peak is detected in $Pr_{1-x}Ca_xMnO_3$ (Fig. 1) for $x = 0.3$ in the temperature range of present investigation. It also deserves noting that the magnitudes of specific heat anomalies observed in quasi-2D manganites (327-LCMO) are much smaller than those in 3D ones (113-PCMO). This may be due to the 40 percent higher density of Mn , atoms (18.23 Mn atom/nm^3) with infinite number of MnO_6 layers along the c direction in 3D systems compared to the quasi-2D one in which the density of Mn atoms is 13.18 Mn atom/nm^3 and has double MnO_6 layers along the same direction. The 2D character of magnetism in bi-layered manganites is also caused by the reduction of exchange coupling along the c direction. Hence the stronger exchange interaction in 3D perovskites compared to 2D bi-layered systems may give rise to bigger specific heat anomaly in the former compared to the latter. This dimensionality effect on the entropy change associated with the thermodynamics of phase transitions in these manganites require further detailed quantitative analysis.

Acknowledgements

This work was supported by the National Science Council of the Republic of China under contract Nos. NSC90-2112-M110-012 and NSC90-2112-M009-025.

References

[1] A. Asamitsu, Y. Tomioka, T. Amira, Y. Tokura, Nature (London) 373 (1995) 407.
[2] M.B. Salamon, M. Jaime, Rev. Mod. Phys. 73 (2001) 583.
[3] M.R. Lees, O.A. Petrenko, G. Balakrishnan, D.McK. Paul, Phys. Rev. B 59 (1999) 1298.
[4] C.F. Chang, P.H. Chou, H.L. Tsay, S.S. Weng, S. Chatterjee, H.D. Yang, R.S. Liu, C.H. Shen, W.-H. Li, Phys. Rev. B 58 (1998) 12224.
[5] S. Chatterjee, P.H. Chou, C.F. Chang, I.P. Hong, H.D. Yang, Phys. Rev. B 61 (2000) 6106.
[6] Y.-K. Kuo C.S. Lue, F.H. Hsu, H.H. Li, H.D. Yang, Phys. Rev. B 64 (2001) 125124.

PERGAMON

Available online at www.sciencedirect.com
SCIENCE DIRECT®

Solid State Communications 27 (2003) 229–232

solid state communications

www.elsevier.com/locate/ssc

Low temperature specific heat of bi-layered manganites $La_{2-2x}Sr_{1+2x}Mn_2O_7$ ($x = 0.3$ and 0.5)

H.D. Yang[a,*], I.P. Hong[a], F.H. Hsu[a], H.H. Li[a], S.Y. Tu[a], H.L. Huang[a], S. Chatterjee[a], S. Mollah[a], Y.-K. Kuo[b], T.I. Hsu[c], H.C. Ku[c], W.-H. Li[d]

[a]*Department of Physics, National Sun Yat-Sen University, Kaohsiung 804 Taiwan, ROC*
[b]*Department of Physics, National Dong-Hwa University, Hualien 974 Taiwan, ROC*
[c]*Department of Physics, National Tsing-Hua University, Hsin-chu 300 Taiwan, ROC*
[d]*Department of Physics, National Central University, Chung-Li 320 Taiwan, ROC*

Accepted 29 April 2003 by G Luke

Abstract

The specific heat (C) of bi-layered manganites $La_{2-2x}Sr_{1+2x}Mn_2O_7$ ($x = 0.3$ and 0.5) is investigated for the ground state of low temperature excitations. A $T^{3/2}$ dependent term in the low temperature specific heat (LTSH) is identified at zero magnetic field and suppressed by magnetic fields for $x = 0.3$ sample, which is consistent with a ferromagnetic metallic-ground state. For $x = 0.5$ sample, a T^2 term is observed and is consistent with a two-dimensional (2D) antiferromagnetic insulator. However, it is almost independent of magnetic field within the range of measured temperature (0.6–10 K) and magnetic field (6 T).

PACS 75.30.Vn, 65.40.−b, 75.40.−s

Keywords A. Magnetically ordered materials, D. Heat capacity; D. Exchange and Superexchange

1. Introduction

Other than a large number of experimental and theoretical studies [1–4] focusing on the extraordinary electronic and magnetic properties of colossal magnetoresistance (CMR) materials $R_{1-x}A_xMnO_3$ (where R is a trivalent rare earth and A is a divalent alkali earth metal), the low temperature specific heat (LTSH) of these materials without [5–13] or with [14–20] magnetic fields has also been extensively studied. However, different results with sample on measurement dependence have been reported. For example, several groups [5–7,11] were unable to resolve a magnetic contribution in their LTSH data on infinite layered ferromagnetic (FM) metallic $R_{1-x}A_xMnO_3$ (R = La, Pr or Nd, A = Ca, Sr or Ba) materials. In contrast, Woodfield et al. [9] and Okuda et al. [15] have included a magnetic $T^{3/2}$ term as fitting their LTSH data of FM metallic $La_{1-x}Sr_xMnO_3$. Moreover, an excess contribution to the LTSH data showing a magnetic field independent non-magnetic origin was observed in charge-ordered (CO) $La_{0.5}Ca_{0.5}MnO_3$ [10] and $Pr_{1-x}Ca_xMnO_3$ [17] systems. However, to our knowledge, there is not many LTSH data on bi-layered manganites $La_{2-2x}Sr_{1+2x}Mn_2O_7$. In analogy with the three-dimensional (3D) manganites, most recently, the bi-layered quasi two-dimensional (2D) $La_{2-2x}Sr_{1+2x}Mn_2O_7$ has also attracted considerable attention due to its reduced dimensionality. Studies have shown that a reduction in the dimensionality of Mn–O–Mn networks in 2D manganites leads to significant changes in the CMR related properties, including enhanced magnetoresistance (MR) effects [21,22] and 2D short range magnetic fluctuation [23–25]. Continuing our previous studies of pressure [22] and ionic-size [26] effects on the transport and magnetic properties, we here report the LTSH of the FM metallic $La_{1.4}Sr_{1.6}Mn_2O_7$ (for $x = 0.3$) and the CO insulating $LaSr_2Mn_2O_7$ (for $x = 0.5$).

* Corresponding author
E-mail address yang@mail.phys.nsysu.edu.tw (H.D. Yang)

0038-1098/03/$ - see front matter
doi:10.1016/S0038-1098(03)00391-0

2. Experimental details

$La_{2-2x}Sr_{1+2x}Mn_2O_7$ ($x = 0.3$ and 0.5) polycrystalline samples were prepared by the standard solid-state reaction method. Detailed preparation and characterization of samples were described elsewhere [22,26]. Electrical resistivity (ρ) of rectangular parallelepiped samples was measured by standard four-probe technique. Magnetization (M) measurement was conducted by the commercial superconducting quantum interference (SQUID) device magnetometer. LTSH was measured from 0.6 to 10 K with a ^{3}He thermal relaxation calorimeter using the heat-pulse technique. Details of the measurement and system calibration can be found in Refs. [27,28].

3. Results and discussion

The temperature dependence of resistivity (ρ) and magnetization (M) of samples $La_{1.4}Sr_{1.6}Mn_2O_7$ and $LaSr_2Mn_2O_7$ are shown in Fig. 1. It is found that the FM transition occurs at 110 K for $La_{1.4}Sr_{1.6}Mn_2O_7$ and the CO transition occurs at 220 K for $LaSr_2Mn_2O_7$. These resistive and magnetic behaviors observed in these polycrystalline samples are fairly consistent with those reported [21–26, 29]. It is noted that an antiferromagnetic transition ($T_N \sim 170$ K) in $LaSr_2Mn_2O_7$ determined by neutron diffraction [30] shows no clear feature in our magnetization data.

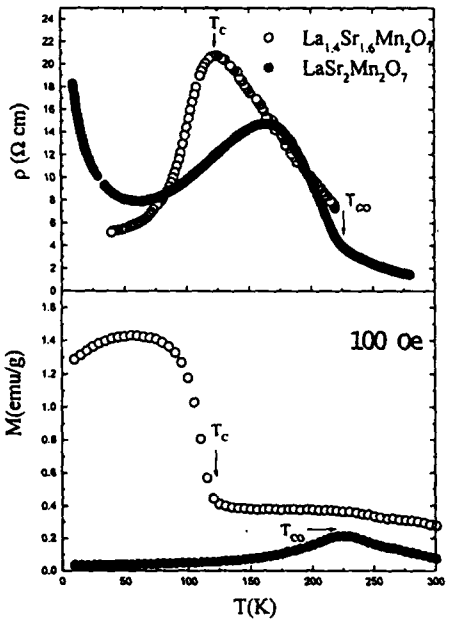

Fig. 1. Temperature dependence of resistivity (ρ) and magnetization (M) of $La_{1.4}Sr_{1.6}Mn_2O_7$ and $LaSr_2Mn_2O_7$ samples. M was measured in a magnetic field of 100 Oe. The ferromagnetic ordering temperature (T_C) and charge ordering temperature (T_{CO}) are marked by arrows.

The low temperature (0.6–10 K) specific heat plotted by C/T vs. T of $La_{2-2x}Sr_{1+2x}Mn_2O_7$ ($x = 0.3$ and 0.5) compounds at zero magnetic field is shown in Fig. 2. We have attempted to model our LTSH data by assuming that the total specific heat is made of four distinct contributions determined by

$$C_{tot} = C_{hyp} + C_{ele} + C_{mag} + C_{lat}, \quad (1)$$

where the $C_{hyp} = A/T^2$ is the hyperfine contribution caused by the local magnetic field at the Mn nucleus due to electrons in unfilled shells, $C_{ele} = \gamma T$ is the electronic term due to free charge carriers, the $C_{lat} = \beta T^3$ is the phonon contribution (T^5 anharmonic term has negligible effect in our fitting range), and the $C_{mag} \sim T^n$ ($T^{3/2}$ for ferromagnetic and T^2 for 2D antiferromagnetic) is the spin wave contribution to the specific heat with the value of the exponent n depending on the nature of magnetic excitations. Thus the data have been fitted using

$$C(T) = A/T^2 + \gamma T + BT^{3/2} + DT^2 + \beta T^3. \quad (2)$$

First, we fit the data using all five terms in Eq. (2) resulting in negative values of parameters. Then we try to fit the data using different assumptions such to set only one or two parameters equal to zero. By varying different combinations in the fitting process, it is found that the best fit (smallest standard deviation, S.D.) occurs as $D = 0$ for $x = 0.3$ and $B = 0$ for $x = 0.5$. The fitting results of zero field data of $La_{2-2x}Sr_{1+2x}Mn_2O_7$ samples are listed in Table 1 where the combinations getting unreasonable S.D. or unphysical fitting parameters are not included. The existence of T and $T^{3/2}$ terms in $x = 0.3$ sample indicates a FM metallic ground state and is consistent with the resistivity and magnetization data (Fig. 1). This result is also similar to that observed in FM metallic $La_{0.7}Sr_{0.3}MnO_3$ [9]. The observation of T^2 term in $x = 0.5$ sample suggests a 2D type-A antiferromagnetic (AFM) order. It is reminded that these $T^{3/2}$ and T^2 magnetic terms were unable to resolve in many reports [5–7,11] on

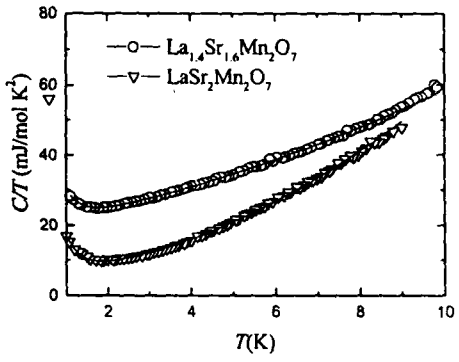

Fig. 2. Low-temperature specific heat C/T vs. T of $La_{1.4}Sr_{1.6}Mn_2O_7$ and $LaSr_2Mn_2O_7$ manganites at zero field. The solid lines are the best fit to Eq. (2). See text for details.

Table 1
Summary of fitting (with Eq. (2)) results to the data in Fig. 2. The units of different quantities are A (mJ K/mol), γ (mJ/mol K^2), B (mJ/mol $K^{5/2}$), D (mJ/mol K^3), and β (mJ/mol K^4). (S.D.) represents the standard deviation of the fitting. The asterisk (*) denotes the best fit (smallest S.D.) parameters. For other combinations getting unreasonable S.D. or unphysical fitting parameters are not included

$La_{2-2x}Sr_{1+2x}Mn_2O_7$	A	γ	B	D	β	$(S.D.)^2$
$x = 0.3$	4.94(0.55)	24.00(0.16)	0	0	0.39(0.005)	0.535
$x = 0.3^*$	10.59(0.28)	13.15(0.24)	6.88(0.28)	0	0.24(0.006)	0.053
$x = 0.3$	9.66 (0.28)	18.47(0.25)	0	2.45(0.11)	0.15(0.01)	0.093
$x = 0.5$	9.68(0.28)	6.83(0.11)	0	0	0.54(0.003)	0.243
$x = 0.5$	11.56(0.34)	2.29(0.64)	2.92 (0.41)	0	0.48(0.01)	0.141
$x = 0.5^*$	11.36(0.29)	4.34(0.32)	0	1.13(0.14)	0.43 (0.014)	0.107
$x = 0.5$	14.49(0.33)	0	0	2.97 (0.7)	0.26(0.01)	0.458

$R_{1-x}A_xMnO_3$ which may be due to the contributions being too small or screened by T^3 lattice term. However, the non-zero value of γ obtained in the insulating $LaSr_2Mn_2O_7$ may be due to disorder effects and similar to that observed in $La_{0.5}Ca_{0.5}MnO_3$ [17]. This probably results from some kind of super-exchange interaction of AFM ordered Mn ions rather than from conduction electrons. The values of Debye temperature $\Theta_D = 459$ and 378 K derived from the lattice term β of $x = 0.3$ and 0.5 samples, respectively, are comparable with those found in $R_{1-x}A_xMnO_3$ [9,11]. It is noted that the non-zero B and D in the fit will obtain the negative γ and a too small β (i.e. very large θ_D) values. Thus it suggests that the mixing of FM and AFM states is unfavorable.

The magnetic field effect on the LTSH of the samples plotted by C/T vs. T^2 is shown in Fig. 3. The LTSH of $x = 0.3$ FM metallic sample is suppressed by a magnetic field of 6 T, particularly more pronounced at lower temperatures. The data in magnetic field (6 T) was fitted to Eq. (2) with the C_{mag} replaced by the spin wave relation

$$C_{spin}(H,T) = \frac{k_B^{5/2}T^{3/2}}{4\pi^2 D^{3/2}} \int_{g\mu_B H/k_B T}^{\infty} \frac{x^2 e^x}{(e^x-1)^2} \times \sqrt{x - \frac{g\mu_B H}{k_B T}}\,dx, \quad (3)$$

where $x = (g\mu_B H + Dk^2)/k_B T$ and $D = 2JSa^2$ is the spin stiffness constant. From the fit, the $\gamma \sim 8.51$ mJ/mol K^2 was obtained. The similar reduction of LTSH by magnetic field has been observed in $La_{1-x}Sr_xMnO_3$ [15] which is consistent with the trend in $La_{1.3}Sr_{1.7}Mn_2O_7$ [30] and is attributed to the suppression of the thermal excitation of spin wave by a magnetic field. It is noted that the thermal excitation of spin wave can be enhanced by the reduction of magnetic dimensionality, while it is also more suppressed by the magnetic field in quasi-2D bi-layered $La_{2-2x}Sr_{1+2x}Mn_2O_7$ compared to 3D cubic $La_{1-x}Sr_xMnO_3$ manganites [30]. The nearly paralleled curves with magnetic fields for each compound suggest the negetive field effect on the lattice contribution. It is striking that the LTSH of $x = 0.5$, CO insulating sample is almost magnetic field independent up to 6 T. This observation is similar to that in $La_{0.5}Ca_{0.5}MnO_3$ reported by Smolyaninova et al. [10,17] and the origin is unclear. Therefore, there is no significant dimensionality effect on the LTSH of quasi-2D and 3D manganites though they have some different CMR related properties.

4. Conclusions

The LTSH of bi-layered $La_{2-2x}Sr_{1+2x}Mn_2O_7$ ($x = 0.3$ and 0.5) has been studied. Several points can be concluded

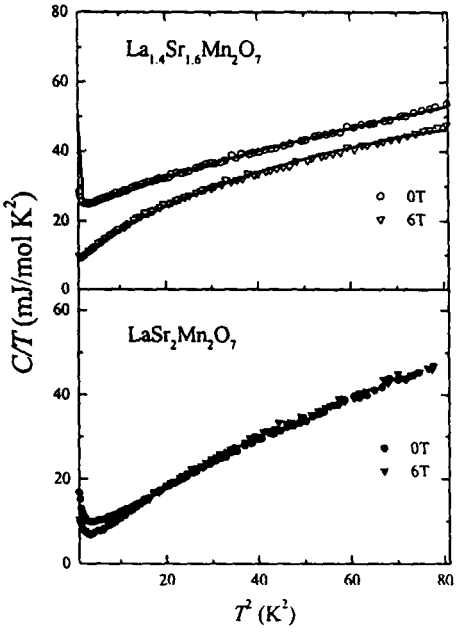

Fig. 3. C/T vs. T^2 of $La_{1.4}Sr_{1.6}Mn_2O_7$ and $LaSr_2Mn_2O_7$ samples with $H = 0$ and 6 T. The solid line in $La_{1.4}Sr_{1.6}Mn_2O_7$ at 6 T is a fit to Eq. (3).

from our data. (1) There exists a $T^{3/2}$ dependent term in LTSH of metallic ferromagnetic $La_{1.4}Sr_{1.6}Mn_2O_7$. (2) The T^2 dependent LTSH was observed in the insulating antiferromagnetic $LaSr_2Mn_2O_7$. (3) The LTSH of metallic FM $La_{1.4}Sr_{1.6}Mn_2O_7$ is reduced by magnetic fields in accordance with the spin wave relation. However, (4) the LTSH of CO $LaSr_2Mn_2O_7$ is magnetic field independent and is similar to that in $La_{0.5}Ca_{0.5}MnO_3$. (5) No significant dimensionality effect is found between quasi-2D and 3D manganites in the feature of LTSH.

Acknowledgment

This work is supported by National Science Council of Republic China under the contract No. NSC91-2112-M110-005.

References

[1] For a review, see, in. C N.R Rao, B Raveau (Eds), Colossal Magnetoresistance, Charge Ordering, and Related Properties of Manganese Oxides, World Scientific, Singapore, 1998
[2] A Asamitsu, Y Tomioka, T. Amira, Y Tokura, Nature (London) 373 (1995) 407
[3] C N R Rao, A.R. Raju, V Ponnambalam, S Parashar, N Kumar, Phys. Rev. B 61 (2000) 594
[4] T. Egami, D. Louca, Phys. Rev B 65 (2002) 094422
[5] J.M.D. Coey, M. Viret, L. Ranno, K. Ounadjela, Phys Rev Lett. 75 (1995) 3910.
[6] S N Bai, Y Y Chen, Y D Yao, L H. Chen, S H Lin, Y Liou, Chin J Phys. 34 (1996) 798.
[7] J.J. Hamilton, E.L. Keatley, H.L. Ju, A.K. Raychaudhuri, V N Smolyaninova, R.L Greene, Phys. Rev B 54 (1996) 14926
[8] S.H. Park, Y.-H. Jeong, K -B. Lee, Phys. Rev. B 56 (1997) 67
[9] B.F. Woodfield, M.L. Wilson, J M Byers, Phys Rev Lett 78 (1997) 3201
[10] V N Smolyaninova, K Ghosh, R L. Greene, Phys Rev B 58 (1998) 14725
[11] M R Lees, O A Petrenko, G Balakrishana, D McK. Paul Phys Rev B 59 (1999) 1298
[12] J Mira, J. Rivas, F Rivadulla, C Vázquez-Vazquez M A López-Quintela, Phys. Rev B 60 (1999) 2998
[13] L. Ghivelder, I.A Gastillo, M A Gusmao, J A Alonso, L F Cohen, Phys. Rev. B 60 (1999) 12184
[14] A K Raychaudhuri, A. Guha, I Das, R Rawat, C N R Rao, Phys. Rev. B 64 (2001) 165111
[15] T. Okuda, A. Asamitsu, Y Tomioka, T Kimura, Y Taguchi, Y Tokura, Phys Rev Lett 81 (1998) 3202
[16] J.E. Gordon, R.A Fisher, Y X Jia, N E Phillips, S F Reklis, D.A Wright, A Zettl, Phys Rev B 59 (1999) 127
[17] V.N. Smolyaninova, A. Biswas, X. Zhang, K H Kim, B -G Kim, S.-W. Cheong, R L Greene, Phys Rev B 62 (2000) 6093.
[18] M. Roy, J.F. Mitchell, S J Potashnik, P Schiffer, J Mag Mag Mater. 219 (2000) 191.
[19] V. Hardy, A. Wahl, C Martin, Ch Simon, Phys Rev B 63 (2001) 224403.
[20] Y. Moritomo, T. Akimoto, H Fujishiro, A Nakamura Phys Rev. B 64 (2001) 64404
[21] Y Moritomo, A. Asamitsu, H Kuwahara, Y Tokura, Nature (London) 380 (1996) 141
[22] C F. Chang, P.H. Chou, H L Tsay, S S Weng, S Chatterjee, H D Yang, R S Liu, C H Shen, W -H Li, Phys Rev B 58 (1998) 12224.
[23] T G Perring, G Apli, Y Moritomo, Y Tokura, Phys Rev Lett 78 (1997) 3197
[24] D N Argyriou, J F Mitchell, J B Goodenough O Chamais sen, S Short, J D Jorgensen, Phys Rev Lett 78 (1997) 1568
[25] R Osborn, S Rosenkrang, D N Argyriou, L Vasiliu-Doloc J W Lynn, S K Sinha, J F Mitchell, K E Gray, S D Bader, Phys. Rev Lett 81 (1998) 3964
[26] S Chatterjee, P H Chou, C F Chang I P Hong H D Yang Phys Rev B 61 (2000) 6106
[27] C F Chang, J -Y Lin, H D Yang, Phys Rev Lett 84 (2000) 14350
[28] H D Yang, J -Y Lin, H H Li, F H Hsu, C J Liu, S -C Li R C. Yu, C -Q Jin, Phys Rev Lett 87 (2001) 167003
[29] J Q Li, Y Matsui, T Kimura, Y Tokura Phys Rev B 57 (1998) 3205
[30] T Okuda, T Kimura, Y Tokura, Phys Rev B 60 (1999) 3370